Friedrich-Schiller-Universität Jena

Chemisch-Geowissenschaftliche Fakultät

Star-shaped drug delivery systems and advanced characterization by mass spectrometry

Dissertation

Zur Erlangung des akademischen Grades

Doctor rerum naturalium (Dr. rer. nat.)

Vorgelegt dem Rat der Chemisch-Geowissenschaftlichen Fakultät der Friedrich-Schiller-Universität Jena

von Diplom-Chemikerin Katrin Knop
geboren am 01.10.1981 in Dresden

Gutachter:

1. Prof. Dr. Ulrich S. Schubert
2. Prof. Dr. Dagmar Fischer

Tag der öffentlichen Verteidigung: 27. 02. 2013

Meinen Eltern

“Non est ad astra mollis e terris via“
Hercules furens, Seneca

#

#

Table of contents

Documentation of authorship

This section contains a list of individual authors' contributions to the publications reprinted in this thesis.

1. K. Knop, R. Hoogenboom, D. Fischer, U. S. Schubert, ″Poly(ethylene glycol) in drug delivery: Pros and cons as well as potential alternatives″ *Angew. Chem. Int. Ed*. **2010**, *49*, 6288–6308. ″Anwendung von Poly(ethylenglycol) beim Wirkstoff-Transport: Vorteile, Nachteile und Alternativen″ *Angew. Chem.* **2010**, *122*, 6430–6452.

   K. Knop: preparation of the manuscript and translation
   R. Hoogenboom: correction of the manuscript
   D. Fischer: conceptual development, correction of the manuscript
   U. S. Schubert: conceptual development, correction of the manuscript, supervision

2. K. Knop, G. M. Pavlov, T. Rudolph, K. Martin, D. Pretzel, B. O. Jahn, D. H. Scharf, V. Makarov, U. Möllmann, A. A. Brakhage, F. H. Schacher, U. S. Schubert, ″Amphiphilic star-shaped block copolymers as unimolecular drug delivery systems: Investigations using a novel fungicide″ *Soft Matter* **2013**, 9, 715–726.

   K. Knop: synthesis and characterization, conceptual contribution, preparation of the manuscript
   G. M. Pavlov: analytical ultracentrifugation experiments and analysis
   T. Rudolph: angle dependent light scattering experiments and analysis
   K. Martin: antifungal tests
   D. Pretzel: *in vitro* biological tests and analysis
   B. O. Jahn: molecular mechanics and dynamics simulations
   D. H. Scharf: isothermal titration calorimetry experiments
   A. A. Brakhage: correction of the manuscript
   V. Makarov: synthesis of fungicide
   U. Möllmann: initial antifungal tests
   F. H. Schacher: correction of the manuscript, supervision
   U. S. Schubert: conceptual contribution, correction of the manuscript, supervision

3. K. Knop, D. Pretzel, A. Urbanek, T. Rudolph, D. H. Scharf, A. Schallon, M. Wagner, S. Schubert, M. Kiehntopf, A. A. Brakhage, F. H. Schacher, U. S. Schubert, ″Star-shaped drug carriers with OEGMA and OEtOxMA brush-like shells: A structural, physical and biological comparison″ *Biomacromolecules* **2013**, submitted.

   K. Knop: synthesis and characterization, conceptual contribution, preparation of the manuscript
   A. Urbanek: doxorubicin encapsulation, *in vitro* doxorubicin cytotoxicity experiments
   D. Pretzel: *in vitro* biological experiments and analysis
   T. Rudolph: angle dependent light scattering experiments and analysis
   D. H. Scharf: isothermal titration calorimetry experiments
   S. Schubert: correction of the manuscript, supervision
   A. A. Brakhage: correction of the manuscript
   M. Kiehntopf: allocation of coagulation assays
   F. H. Schacher: correction of the manuscript, supervision
   U. S. Schubert: conceptual contribution, correction of the manuscript, supervision

4. K. Knop, B. O. Jahn, M. D. Hager, A. C. Crecelius, M. Gottschaldt, U. S. Schubert, ″Systematic MALDI-TOF CID investigation on different substituted mPEG 2000″ *Macromol. Chem. Phys*. **2010**, *211*, 677–684.

   K. Knop: synthesis, MALDI-TOF MS and CID characterization, structure elucidation, conceptual development, preparation of the manuscript
   B. O. Jahn: molecular modeling
   M. D. Hager: supervision, correction of the manuscript
   A. C. Crecelius: correction of the manuscript
   M. Gottschaldt: correction of the manuscript
   U. S. Schubert: correction of the manuscript, supervision

5. A. C. Crecelius, C. R. Becer, K. Knop, U. S. Schubert, ″Block length determination of the block copolymer mPEG-b-PS using MALDI-TOF MS/MS″ *J. Polym. Sci., Part A: Polym. Chem.* **2010**, *48*, 4375–4384.

   A. C. Crecelius: MALDI-TOF MS and CID characterization, structure elucidation, preparation of the manuscript
   C. R. Becer: synthesis
   K. Knop: structure elucidation
   U. S. Schubert: correction of the manuscript, supervision

6. A. Baumgaertel, C. Weber, K. Knop, A. C. Crecelius, U. S. Schubert, ″Characterization of different poly(2-ethyl-2-oxazoline)s via matrix-assisted laser desorption/ionization time-of flight tandem mass spectrometry″, *Rapid Commun. Mass Spectrom*. **2009**, *23*, 756–762.

   A. Baumgaertel: MALDI-TOF MS and CID characterization, structure elucidation, preparation of the manuscript
   C. Weber: synthesis of macromolecules
   K. Knop: synthesis of macromolecules, structure elucidation
   A. C. Crecelius: correction of the manuscript
   U. S. Schubert: correction of the manuscript, supervision

7. L. Tauhardt, K. Kempe, K. Knop, E. Altuntaş, M. Jäger, S. Schubert, D. Fischer, U. S. Schubert, ″Linear polyethyleneimine: Optimized synthesis and characterization – on the way to "pharmagrade" batches″ *Macromol. Chem. Phys*. **2011**, *212*, 1918–1924.

   L. Tauhardt: synthesis, characterization, preparation of the manuscript
   K. Kempe: conceptual contribution, supervision of L. Tauhardt
   K. Knop: MALDI-TOF MS characterization
   E. Altuntaş: ESI-Q-TOF MS characterization
   M. Jäger: supervision of L. Tauhardt, correction of the manuscript
   S. Schubert: correction of the manuscript
   D. Fischer: conceptual contribution, correction of the manuscript
   U. S. Schubert: conceptual contribution, correction of the manuscript

8. E. Altuntaş, K. Knop, L. Tauhardt, Kristian Kempe, A. C. Crecelius, M. Jäger, M. D. Hager, U. S. Schubert, ″Tandem mass spectrometry of poly(ethylene imine)s by electrospray ionization (ESI) and matrix-assisted laser desorption/ionization (MALDI)″ *J. Mass. Spectrom*. **2012**, *47*, 105–114.

   E. Altuntaş: ESI-Q-TOF MS characterization, preparation of the manuscript
   K. Knop: MALDI-TOF MS characterization, preparation of the manuscript
   L. Tauhardt: synthesis of poly(ethylene imine)s
   K. Kempe: supervision of L. Tauhardt
   A. C. Crecelius: correction of the manuscript
   M. Jäger: supervision of L. Tauhardt
   M. D. Hager: correction of the manuscript
   U. S. Schubert: conceptual contribution, correction of the manuscript, supervision

9. K. Knop, S. Stumpf, U. S. Schubert, ″Drugs as matrix to detect their own drug delivery system of PCL-PEG block copolymers in MALDI-TOF MS″ *Rapid Commun. Mass Spectrom.* submitted.

    K. Knop: synthesis and characterization, MALDI experiments conceptual contribution, preparation of the manuscript
    S. Stumpf: AFM measurements
    U. S. Schubert: conceptual development, correction of the manuscript, supervision

10. D. Hölscher, R. Shroff, K. Knop, M. Gottschaldt, A. C. Crecelius, B. Schneider, D. Heckel, U. S. Schubert, A. Svatoš, ″Matrix-free UV-laser desorption/ionization (LDI) mass spectrometric imaging at the single-cell level: Distribution of secondary metabolites of *Arabidopsis thaliana* and *Hypericum* species″ *Plant J.* **2009**, *60*, 907–918.

    D. Hölscher: conceptual development, preparation of the manuscript, phytochemical profiling
    R. Shroff: MALDI experiments, imaging experiments
    K. Knop: LDI imaging measurements and evaluation
    M. Gottschaldt: correction of the manuscript
    A. C. Crecelius: correction of the manuscript
    B. Schneider: progress discussions, correction of the manuscript
    D. Heckel: conceptual development
    U. S. Schubert: correction of the manuscript, supervision of K. Knop
    A. Svatoš: conceptual development, correction of the manuscript, supervision of R. Shroff

11. S. Miosic, K. Knop, D. Hölscher, J. Greiner, C. Gosch, J. Thill, M. Kai, B. Shreshta, B. Schneider, A. C. Crecelius, U. S. Schubert, S. Svatoš, K. Stich, H. Halbwirth, ″4-Deoxyaurone based UV nectar guide formation in *Bidens ferulifolia* (Jacq.) DC.″ *J. Exp. Botany* **2012**, submitted.

    S. Miosic: enzyme characterization
    K. Knop: LDI imaging measurements and evaluation, LDI-TOF CID measurements
    D. Hölscher: identification of pigments and reaction products, sample preparation
    J. Greiner: microscopy
    C. Gosch: UV photography
    J. Thill: enzyme characterization
    M. Kai: LC-MS measurements
    B. Shreshta: enzyme characterization
    B. Schneider: identification of pigments and reaction products
    A. C. Crecelius: correction of the manuscript, supervision of K. Knop
    U. S. Schubert: correction of the manuscript, supervision of K. Knop
    S. Svatoš: correction of the manuscript
    K. Stich: conceptual development and first enzyme demonstration
    H. Halbwirth: conceptual development, data evaluation and manuscript drafting

12. D. Hölscher, K. Knop, M. Kai, R. Maddula, C. Ritter, A. C. Crecelius, D. Heckel, B. Schneider, U. S. Schubert, T. Alexandrov, B. Zimmermann, A. Svatoš, ″Spatially-resolved qualitative and quantitative analysis of *Gossypium hirsutum* L. leaf pigments at single cell level″ *Plant J*. **2012**, submitted.

    D. Hölscher: conceptual development, preparation of the manuscript, phytochemical profiling
    K. Knop: LDI imaging measurements and evaluation, LDI-TOF CID measurements
    M. Kai: UHPLC measurement and evaluation
    R. K. Maddula: LC-MS measurements
    C. Ritter: capillary electrophoresis
    A. C. Crecelius: correction of the manuscript
    D. Heckel: conceptual development
    B. Schneider: progress discussions, correction of the manuscript
    U. S. Schubert: correction of the manuscript, supervision
    T. Alexandrov: statistical analysis of LDI MSI data
    B. Zimmermann: capillary electrophoresis
    A. Svatoš: experimental design, correction of the manuscript, supervision

13. D. Hölscher, S. Dhakshinamoorthy, T. Alexandrov, M. Becker, T. Bretschneider, A. Bürkert, A. C. Crecelius, D. De Waele, A. Elsen, D. G. Heckel, H. Heklau, C. Hertweck, M. Kai, K. Knop, C. Krafft, R. K. Madulla, C. Matthäus, J. Popp, B. Schneider, U. S. Schubert, R. Sikora, A. Svatoš, R. Swennen, ″Phenalenone-type phytoalexins mediate resistance of banana plants (Musa spp.) to the burrowing nematode *Radopholus similis*″ *Nature Chem*. *Biol.* **2013**, in preparation.

    D. Hölscher: conceptual development, preparation of the manuscript, phytochemical profiling
    S. Dhakshinamoorthy: culturing banana plants and nematodes, nematode infection on plants, extraction and identification of phytoalexins, nematode bioassay
    T. Alexandrov: statistical analysis of LDI MSI data
    M. Becker: support of LDI MSI measurements
    T. Bretschneider: LDI imaging measurements and evaluation on nematodes
    A. Bürkert: conceptual development, progress discussions, contribution to the manuscript
    A. C. Crecelius: correction of the manuscript
    D. De Waele: correction of the manuscript, supervision of S. Dhakshinamoorthy
    A. Elsen: supervision of S. Dhakshinamoorthy, correction of the manuscript
    D. G. Heckel: conceptual development
    H. Heklau: leaf and root anatomy of *Musa* spp.
    C. Hertweck: design of research, supervision
    M. Kai: UHPLC measurement and evaluation

K. Knop: LDI imaging measurements and evaluation, LDI-TOF CID measurements and analysis
C. Krafft: correction of the manuscript, supervision of C. Matthäus
R. K. Madulla: LC-MS measurements
C. Matthäus: Raman measurements, data analysis, correction of the manuscript
J. Popp: correction of the manuscript, supervision
B. Schneider: conceptual development, progress discussions, contribution to the manuscript
U. S. Schubert: correction of the manuscript, supervision of K. Knop
R. Sikora: contribution of plant material, correction of the manuscript
A. Svatoš: correction of the manuscript, supervision
R. Swennen: correction of the manuscript, supervision of S. Dhakshinamoorthy

Declaration of the supervisor: _____

(Prof. Dr. U. S. Schubert)

1. Introduction

Drug delivery systems (DDSs) are vehicles to carry drug molecules in a specific way to its site of action in the body. They are for this task designed chemical entities consisting often of polymeric materials. The encapsulation of drugs into a carrier provides beneficial properties as well as alterations of the pharmacokinetic behavior to the guest molecule. Firstly, DDS enable the solubilization of hydrophobic drugs in biological relevant media, *i.e.* water or buffer. Secondly, by using polymeric carrier systems the molar mass of the DDS unity is enhanced leading to a diminished renal clearance.[1–6]

To prevent the fast recognition by the immune system and a subsequent removal from the blood circulation, the carrier systems need to be shielded suchlike that the opsonins are not able to detect it anymore.[7–9] This task is nowadays implemented by *e.g.* poly(ethylene glycol) (PEG), which is frequently used for all kinds of DDSs to hide them from the mononuclear phagocyte system (MPS).[10–14] This shielding effect is not only observed for carriers of hydrophobic drugs but also for transfection agents for gene delivery, *e.g.* poly(ethylene imine)s (PEI). PEG shells reduce the charge density of these systems and, thus, increase their half life in blood.[15–18] Although the exact mode of action is not yet clarified, this polymer has become the gold standard in the so-called “stealth technology”.[19]

However, different disadvantages have arisen from using PEG stimulating the search for alternatives, which have gained increasing interest and importance in literature.[12,20–22] A potential candidate possessing similar properties to PEG are poly(2-oxazoline)s, a polymer class, which provides a multifunctional platform for the synthesis of various architectures with tunable properties. To date, different DDSs containing the hydrophilic poly(2-ethyl-2-oxazoline) (PEtOx) and the poly(2-methyl-2-oxazoline) (PMeOx) have been investigated in view of their ability to act as stealth systems.

Amongst these investigated stealth carrier systems, in particular amphiphilic linear block copolymers play an important role as they assemble in water readily into micellar structures. The hydrophobic cavity formed as core of the DDS is able to take up water insoluble entities. However, the application of block copolymers is limited by their critical micelle concentration (cmc) meaning the disassembling of the aggregate below a certain polymer concentration. This behavior is disadvantageously in medical applications, as the drug would be set free in the body upon administration and sudden dilution of the micelle in the blood. The disassembling of the micellar structure is highly dependent on the chemical nature of the hydrophobic block and the block length.[23,24] By overcoming this drawback other systems have gained significant interest. Dendritic architectures have been proven to act as unimolecular micelles. Nonetheless, this polymer architecture exhibits limitations as well: Their hydrophobic cavity is characterized by a dense architecture leading to poor drug inclusion efficiencies, and their preparation is highly demanding. Unimolecular star-shaped drug delivery systems could offer an approach to combine the advantageous properties of both architectures: The intrinsically linked core should prevent the disassembling of the micelles and the linear arms might offer sufficient space to encapsulate a satisfying number of drug molecules. Both properties require a thorough investigation to prove their physical reality.

However, for biomedical applications a profound analysis is not only necessary for the entire DDS, but also for the synthetic intermediates. There is a high demand for a complete and detailed characterization to understand structure-property relationships. In polymer chemistry, this structural evidence has been proven for a long time by nuclear magnetic resonance (NMR) spectroscopic methods and size exclusion chromatography (SEC). A significant step forward could be made in the 1990s by applying matrix-assisted laser/desorption ionization time of flight mass spectrometry (MALDI-TOF MS) and electrospray ionization (ESI) MS to polymers. By these soft ionization techniques non-fragmented macromolecules and polymer molecules were transferred into the gas phase and ionized allowing the mass spectrometric analysis of the entire macromolecules. These improvements in the volatilization and ionization technique enabled the absolute mass determination of the polymer distribution as well as an end group analysis. However, a deeper insight into polymer architecture by mass spectrometric means was achieved by applying collision induced dissociation (CID). This technique uses the directed fragmentation of selected macromolecules. The obtained fragmentation pattern allows conclusions about the composition and intrinsic structure of the polymer. By elucidating the fragmenting behavior of different polymer classes under CID conditions typical fragments can be assigned leading to more detailed information of the end group, the intrinsic composition of the polymer chain as well as the side group structure.

The choice of matrix plays a crucial role in the success of MALDI-TOF MS measurements.[25] Upon excitation by the laser beam matrix molecules are transferred into the gas phase and co-desorb therewith analyte compounds, *e.g.* polymer molecules, enabling their mass spectrometric analysis.[26] These matrix materials are generally small, organic compounds that are absorbing readily light in the range of, *e.g.*, UV lasers. A basic prerequisite for the absorption of the laser light in the UV range (337 nm for nitrogen lasers and 355 nm for Nd:YAG frequency tripled lasers) represents the existence of a π-system in the matrix molecule.

Many drugs, in particular hydrophobic drug molecules, used up to date exhibit an aromatic entity being thereby principally qualified to act as matrix material. The usage has not yet been investigated for this purpose and would enable the direct analysis of DDSs composed of amphiphilic block copolymers. This approach could further lead to the detection of both, block copolymer as well as drug molecule, in biological media, *i.e.* cell culture or tissue.

If drug molecules are able to volatilize polymeric materials, they can also be detected without application of an established matrix. This comprehension leads to a far more advanced application in mass spectrometry. Mass spectrometry imaging (MSI) is limited to a relatively high spatial resolution (60 to 100 μm) due to the crystallization of the matrix molecules. However, the direct analysis of aromatic analytes without matrix application leads to an improvement of the spatial resolution of the mass image down to the size of the laser diameter (*e.g.* 10 μm for the Smart beam® laser optics of the Ultraflex III instrument, bruker) and even below is possible by using the technique of oversampling.[27]

MSI has been applied to detect and localize substances bearing π-systems in plant materials. Generally, these compounds can be classified as secondary plant metabolites,

which are produced by the plants to defend themselves against herbivores and pathogens. Often these compounds turn out to be of pharmaceutical value, as *e.g.* the hypericin compound family in *Hypericum* species. They are used as antidepressant drug and can be detected on the basis of matrix-free laser desorption/ionization (LDI) MSI in several plant parts.

One aim of this thesis is the localization of different π-system bearing compounds, *e.g.* secondary plant metabolites and drug compounds, in different plant tissues and species by LDI MSI. This approach is further applied to assess drug molecules as matrix material in comparison to established matrices for homopolymers as well as amphiphilic block copolymers. These amphiphilic block copolymers are used to form micelles as carrier systems for drug molecules used as matrix. Secondly, it was aimed to overcome the cmc issues of amphiphilic diblock copolymer micelles. The approach of choice was to construct star-shaped block copolymers, whose hydrophobic ends are linked to each other to prevent a disassembly of the resulting micellar system. This study of star-shaped block copolymers was performed in comparison of PEG polymers and PEtOx polymers as shell forming hydrophilic blocks. Furthermore, the star-shaped block copolymers were investigated regarding the influence of the shell size on the aggregation behavior to ensure a large enough shell to stabilize unimolecular micelles in aqueous systems that would lack a cmc. Their final applicability as DDSs was investigated on the basis of different drug molecules.

2. Drug delivery systems with stealth properties

Parts of this chapter have been published: **P1)** K. Knop, R. Hoogenboom, D. Fischer, U. S. Schubert, *Angew. Chem. Int. Ed*. **2010**, *49*, 6288–6308. *Angew. Chem.* **2010**, *122*, 6430–6452.

One third of the new chemical entities with pharmaceutical background are hydrophobic substances rendering the administration to the body difficult if not impossible.[28,29] Polymeric carriers, which physically entrap hydrophobic molecules of interest, as well as polymer conjugates, play an important role in modern pharmaceutical technology. The shared task of the carriers and conjugates is the targeted delivery of drugs to specific sites of action in the body.[9,30–32]

The entrapment of drug molecules into so-called drug delivery systems (DDSs) leads to several advantageous effects: firstly, the solubility in aqueous media is increased enabling principally the administration of the drug.[29] Secondly, the apparent molar mass of the drug molecule is drastically increased leading to a reduced kidney excretion and resulting in a prolonged blood circulation time.[2] Therewith, the achieved elevated bioavailability allows the optimal use of the enhanced permeability and retention (EPR) effect. Maeda *et al.* discovered that particulate systems are preferentially concentrated in cancer tissues, which are marked by hypervascularization and a leaky vasculature (Figure 2.1).[33] Additionally, an increased production of vascular permeability enhancing factors is observed in tumor tissue, further augmenting the extravasation of macromolecules within the tumor.[34,35] The EPR effect is also known as concept of passive targeting and forms the basic principle that causes the functioning of targeted polymeric drug delivery in different diseases, such as cancer, infection, and inflammation, that show more permeable endothelia.[5,36,37]

To design an efficient DDS, the architecture plays a crucial role as well as the applied material. The polymer used influences the shielding of the drug carrier, which is required to avoid a fast recognition by the immune system followed by rapid clearance from the body. The suppression of non-specific interactions within the body, that is decreased interaction with blood components (opsonization) inducing activation of the complement system and finally leading to a reduced blood clearance of drug carriers, is known as the stealth effect.[7]

Poly(ethylene glycol) (PEG) is the gold standard in stealth technology and a very popular polymer with an overwhelming number of positive properties. These advantageous qualities have led to a very broad usage of PEG in everyday products, industrial applications, as well as in many biomedical DDSs. Its success in the latter field is well reflected by several pharmaceutical products that have reached approval by the Food and Drug Administration (FDA) and European Medicines Agency (EMA) during the last 20 years.[37]

The shielding properties of PEG are not only used to provide particulate or micellar systems with a mononuclear phagocyte system (MPS) evading outer shell, also gene transfection agents, such as poly(ethylene imine) (PEI), take advantage of the reduced renal

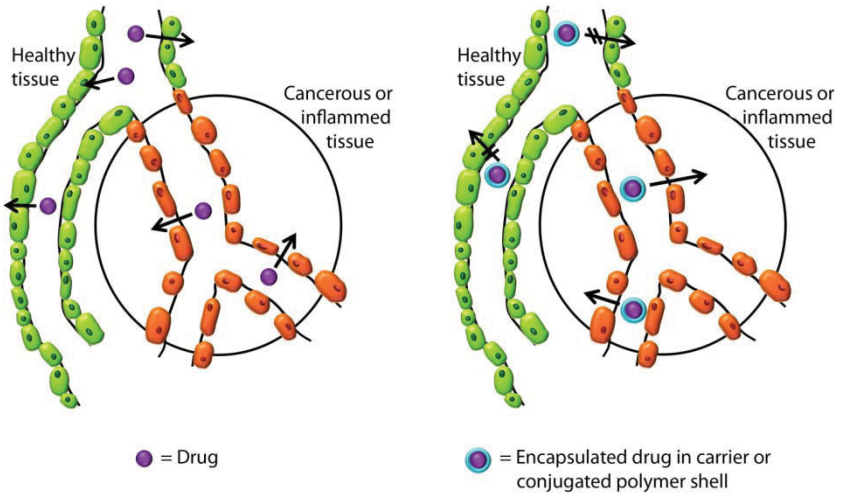

Figure 2.1. Schematic representation of the EPR effect.[38]

filtration and the decreased uptake by the MPS. The cationic charge of the non-viral vectors, which is necessary for electrostatic interaction with the negatively charged DNA, is responsible for toxicity and a low half-life of the carriers in the body. The PEGylation of gene carriers results in a decrease of the disposition in the lung as well as lower initial toxicities compared to unmodified complexes.[15,17,18]

But PEG shows also limitations including the non-biodegradability and the resulting fate of PEG after *in vivo* administration, which is in most studies ignored. Many biological and toxicological data evaluating those points date back to the 1950s and 1970s. They need to be updated and evaluated with contemporary knowledge, especially in terms of the fate at the molecular and cellular level, such as tissue vacuolization and fusion of membranes. At the same time, the polyether structure provides easy targets for peroxide degradation, and although investigations have not been performed under biologically relevant conditions, PEG can be relatively easily degraded compared to polymers with an all-carbon backbone. From a medicinal viewpoint, the unpredictable complement activation, which can lead to hypersensitivity reactions and unclear pharmacokinetics after a second dose (the so called accelerated blood clearance (ABC) phenomenon) complicates the use of PEG therapeutics. Although PEG alone seems to be immunologically harmless, the immunogenicity of PEG is highly dependent on the degree of PEGylation and to which molecule PEG is coupled.

The discussed disadvantages of PEG intensified the search for alternative polymers for use in therapeutics, where a wide range of chemically very different synthetic polymers is available. But not every non-ionic hydrophilic polymer is suitable for biomedical uses and can provide stealth behavior. A number of structural parameters influence the biological and stabilizing effects and have to be carefully taken into consideration.[13] The most promising polymers that do show enhanced circulation time are poly(glycerol)s,[39–41] poly(amino acid)s,[20,42,43] poly (vinylpyrrolidone),[44–46] poly(*N*-(2-hydroxypropyl) methacrylamide),[47–49] and poly(2-oxazoline)s.

Amongst this variety of polymers, poly(2-oxazoline)s have been widely investigated in the last decades. The synthesis of the hydrophilic poly(2-methyl-2-oxazoline) (PMeOx) and

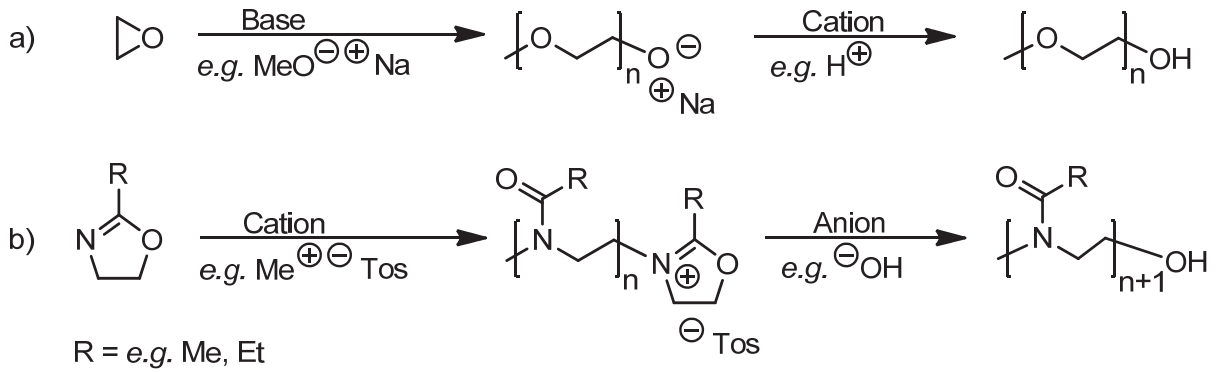

Figure 2.2. Synthesis of poly(ethylene glycol)s and poly(2-oxazoline)s.

poly(2-ethyl-2-oxazoline) (PEtOx) was discovered in the 1960s.[50–53] Since then, a comprehensive chemistry has been built around this class of polymers, which is related to the ease in synthesizing new 2-substituted 2-oxazolines and the post modification of the resulting polymers. Furthermore, the living character of the cationic ring-opening polymerization of 2-oxazolines makes this polymer class attractive to polymer chemists enabling the synthesis of defined polymers with very low polydispersity index (PDI) values and versatile end group chemistry (Figure 2.2).[54,55] Nonetheless, the application of poly(2-oxazoline)s in biomedical fields arose only recently, and the majority of reports dealing with the biological application of these polymers were only published in the last five years.[56,57]

Veronese *et al*. performed one of the first fundamental biological studies. The authors proved the erythrocyte compatibility for PEtOx with molar masses of 5, 10, and 20 kg mol^{-1} at polymer concentrations of 5 mg mL^{-1}.[58] They also showed that 20 kg mol^{-1} PEtOx was safe and non-toxic for intravenous administration in male Sprague Dawley rats every second day at doses of up to 50 mg kg^{-1} over a period of 2 weeks.[58] Bauer *et al*. compared PEtOx polymers with molar masses of 0.4, 2, 4, 10, 20 and 40 kg mol^{-1} to PEG polymers of the same molar mass and commercial PEtOx polymers (5, 50 and 200 kg mol^{-1}) by means of cytotoxicity and hemocompatibility assays. The authors found no cytotoxic effect to L929 mouse fibroblast cells with concentrations up to 80 mg mL^{-1} after 24 h.[59] Only a 0.4 kg mol^{-1} PEtOx showed a cytotoxic effect at concentrations above 1 mg mL^{-1}. No erythrocyte aggregation except for the commercial samples with high molar masses was observed as well as no hemolysis for concentrations up to 80 mg mL^{-1}.[59] In a different study the non-cytotoxicity of PEtOx (4.3, 6.7, 16.2 and 44.7 kg mol^{-1}) was proven by means of a MTT study using RAT-2 fibroblasts and a fluorescein diacetate (FDAc)–propidium iodide (PI) viability assay using P388.D1 macrophages.[60]

For the PEtOx$_{100}$ (10 kg mol^{-1}) and the poly[2-(4-aminophenyl)-2-oxazoline$_{10}$-*co*-2-ethyl-2-oxazoline$_{90}$], the immunomodulatory effects were investigated *via* the induction of TNF-α, IL-1α, and IL-6 cytokines as well as reactive oxygen species (ROS). Both polymers were found to be without strong adverse inflammatory efficacy with respect to their capability to induce proinflammatory cytokines and ROS release at concentrations of 5 mg mL^{-1}.[61] Furthermore, a number of amphiphilic di- and tri block copolymers of poly(2-oxazoline)s (2-butyl-2-oxazoline (BuOx), 2-nonyl-2-oxazoline (NOx), 2-*n*-propyl-2-oxazoline (*n*PrOx), 2-*i*-propyl-2-oxazoline (*i*PrOx) as hydrophobic blocks and PMeOx and PEtOx as hydrophilic

blocks) were shown to posses in general no cytotoxic effect to multi-drug resistant (MCF7-ADR) and non-resistant (MCF7) human adenocarcinoma cells as well as to Madin-Darby canine kidney (MDCK) cells up to 1 mg mL^{-1} after 24 h. Endocytosis studies with MCF7-ADR cells revealed a rather fast uptake of the amphiphilic block copolymers in comparison to the hydrophilic analogs after 60 min, where the uptake rate and efficiency increased with increasing hydrophobicity. The results obtained for the block copolymers were in the range of previously reported uptake rates of other block copolymers.[62]

Drug delivery systems with poly(2-oxazoline)s were developed, for example, based on micelles composed of poly(lactic acid) (PLA) and poly(ε-caprolactone) (PCL), respectively. PLA-*b*-PEtOx-*b*-PLA micelles were applied as carriers for doxorubicin.[63] PEtOx-*b*-PCL micelles loaded with paclitaxel have been shown to possess the same efficiency as Cremophor EL formulated paclitaxel.[64] Amphiphilic ABA di- and triblock copolymers with different compositions ($PMeOx_{27}$-*b*-$PBuOx_{12}$-*b*-$PMeOx_{27}$ (6.2 kg mol^{-1}), $PMeOx_{37}$-*b*-$PBuOx_{23}$-*b*-$PMeOx_{37}$ (9.3 kg mol^{-1}), $PMeOx_{36}$-*b*-$PBuOx_{30}$-*b*-$PMeOx_{36}$ (10 kg mol^{-1}), and $PEtOx_{50}$-*b*-$PBuOx_{19}$ (7.2 kg mol^{-1})) showed no cytotoxic effects to different cell lines up to 1 mg mL^{-1}, and, furthermore, only a small increase of the C3a complement activation was measured in comparison to PBS buffer solution. However, the C3a-desArg concentration was significantly lower than in comparison to Cremophor EL and Taxol. Further investigations revealed that the block copolymers do efficiently encapsulate paclitaxel, which remains fully active as proven in *in vitro* and *in vivo* experiments.[65]

RES evading properties for PEtOx and PMeOx have already been reported in 1994, as liposomes exhibiting hydrophilic shells of both polymers were proven to prolong the blood circulation times in the same range as PEG.[66] In addition, Zalpinsky *et al*. documented similar prolonged blood circulation of PEG-, PMeOx- and PEtOx-modified liposomes with 5 mol% of phospholipid and about 40 repeating units of each polymer.[67] Additionally, the authors found that three different types of liposomes showed a similar tissue distribution profile after 24 h, which means that there is a preferential distribution in the liver, spleen, and kidney.[67] Analogous results have been found for ^{111}In-labeled 4 kg mol^{-1} PMeOx and 4 kg mol^{-1} PEtOx, which showed an augmented blood circulation time but also an increased occurrence of the polymer in the kidney and bladder.[68]

Summarizing the choice of materials for DDSs, PEG as gold standard in stealth technology is currently the most widely used polymer in the biomedical field of drug delivery and the only polymeric therapeutic that has market approval for different drugs. The success of PEG is based on its hydrophilicity, decreased interaction with blood components, and high biocompatibility. However, scientific results obtained in recent years show that PEG has also possible drawbacks, leading to an increased interest in potential substitutes in research. PMeOx and PEtOx are considered as alternatives to PEG, as they reveal a comparable behavior in terms of blood circulation time, opsonization, and organ distribution. Nevertheless, important details of immune activation and mechanical stability require further investigation to evaluate the potential of poly(2-oxazoline)s as alternatives to PEG.

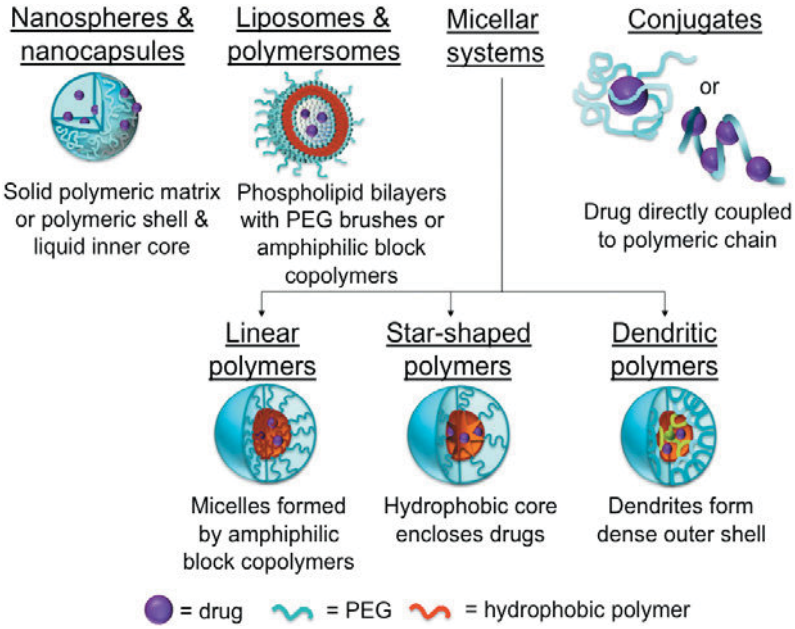

Figure 3.1. Overview of carrier systems for drug delivery.

For a controlled and efficient transport of the drug through the body, not only the material used to construct the DDS plays an important role, also the utilized architecture influences the drug transport. In Figure 3.1, the most prominent carrier systems are depicted. Nanospheres are characterized by a versatile and fast preparation *via* nanoprecipitation or emulsion techniques.[32,69,70] However, the application of these particles is adversely affected by burst release, meaning the uncontrolled liberation of drugs instead of a constant release kinetic.[71]

Liposomes are formed by the assembly of the naturally occurring phospholipids and cholesterols rendering these DDSs non-toxic and highly biocompatible. Furthermore, they can encapsulate a variety of drugs regardless their polarity. This fact is responsible for the wide range of applications of liposomes, *e.g.* as injectable formulations or in clinical medicine.[3,72] Still, some of the commercially available liposomal formulations do not contain PEG or other stealth moieties as outer protecting shell causing their rapid clearance by the mononuclear phagocyte system (MPS). In addition, the recognition is dependent on the size, as larger liposomes are cleared more rapidly than smaller ones, whereas the smaller posses only a small aqueous entrapment volume.[73,74] Their advantageous material design based on naturally occurring lipids causes also a major drawback as the liposomes are destabilized *in vivo* due to a lipid exchange between the liposomes and high-density lipoproteins (HDLs).[75]

Conjugates, where the drug is coupled covalently to the polymer, offer an appealingly simple concept of delivery, as the polymer moiety which increases the molar mass of the system is at the same time the solubility enhancer as well as the protecting shell. The drawback of this approach is system inherent, as the drug needs to be released from the polymer by breaking a covalent bond to regain full activity.[30]

The use of amphiphilic block copolymer micelles as DDSs appears attractive due to several reasons: first, an evidently straightforward structural organization by self-assembly, and, second, the fact that the hydrophilic segments of amphiphilic block copolymers can act

as a protecting shell around the hydrophobic core, which potentially hosts encapsulated cargo.[76] However, such micellar systems can also disassemble into block copolymer unimers, in particular when the concentration within the bloodstream decreases below the critical micelle concentration (cmc) after administration.[77,78] Although this can be influenced to a certain extent by a rational design of the hydrophobic block,[29] dendrimers came into focus as unimolecular micelles at even very dilute concentrations.[79,80] However, the rather dense cores of dendritic structures offer only limited space for the encapsulation of guest molecules and the synthesis is difficult, including up-scaling aspects.[81,82]

This has led to an increased interest in unimolecular star-shaped block copolymers as DDSs as the core in these systems is supposed to provide more space for hydrophobic molecules. In addition, the synthesis of star-shaped polymers and block copolymers is often less tedious if compared to classical approaches used for dendrimer synthesis.[31]

In summary, each of the different architectures used to construct DDSs possesses benefits and drawbacks. Therefore, a potential usage of one of those systems has to be adapted to the specific task that it should fulfill. The combination of the advantages of linear block copolymers and dendrimers encouraged the application of star-shaped DDS. The synthetic easy approach and the circumventing of the cmc should lead to superior polymeric drug carrier systems.

3. Star-shaped drug delivery systems

Parts of this chapter have been published: **P2)** K. Knop, G. M. Pavlov, T. Rudolph, K. Martin, D. Pretzel, B. O. Jahn, D. H. Scharf, V. Makarov, U. Möllmann, A. A. Brakhage, F. H. Schacher, U. S. Schubert, *Soft Matter* **2013***, 9,* 715–726. **P3)** K. Knop, D. Pretzel, A. Urbanek,T. Rudolph, D. H. Scharf, A. Schallon, M. Wagner, S. Schubert, M. Kiehntopf, A. A. Brakhage, F. H. Schacher, U. S. Schubert, *Biomacromolecules,* **2013**, submitted.

3.1. Star-shaped drug delivery systems with a PEG shell

Star-shaped block copolymers comprising an inner hydrophobic and an outer hydrophilic segment represent an attractive approach to construct DDSs. However, a clear distinction between true star-shaped systems and closely related structures (*i.e*. hyperbranched, branched and semi-dendritic frameworks) is not always possible. Dendrimers or hyperbranched polyesters have been applied, *e.g*., as initiators to design star-shaped macromolecules with a dendrimer core, surrounded first by a hydrophobic shell of poly(ε-caprolactone) (PCL) or poly(lactic acid) PLA and an outer hydrophilic shell of PEG.[83–85] Similar systems with brush-like PEG segments have been used to increase the density of the hydrophilic shell.[86,87] Several of these systems have been demonstrated to form unimolecular micelles in aqueous solution and to be suitable for encapsulating guest molecules.[83,86]

Truly star-shaped block copolymers can be engineered using multifunctional initiators. Hydroxy functionalities can be used as initiators for the ring-opening polymerization of ε-caprolactone as hydrophobic segments. PEG has been frequently used as hydrophilic shell, although it has already been shown that linear PEG is not sufficient for the stabilization of unimolecular systems in water as the investigated systems still exhibited a cmc.[88,89]

An alternative design of the hydrophilic shell represents the use of comb-like segments as demonstrated by Schramm *et al*. for a set of four- and six-armed [PCL-*block*-poly(oligo-(ethylene glycol) methacrylate)] ([PCL-*b*-$POEG_9MA$]) block copolymers.[90,91] Nevertheless, for a similar system with four arms and a shell formed by $POEG_5MA$ (M_n = 300 g mol^{-1} for the OEG_5MA monomer) a cmc could be detected, indicating the formation of multimolecular micelles.[92] Consequently, the number and character of arms seem to influence if unimolecular micelles are formed by the star-shaped block copolymers. A unimolecular behavior is favorable for drug delivery applications, because disassembling of the micelles, liberation followed by precipitation of the drug and, therewith, connected negative side effects can be avoided. Therefore, the polymer characteristics and conditions were investigated under which unimolecularity occurs for star-shaped block copolymers with a brush-like hydrophilic shell.

The core-first method was chosen to obtain star-shaped block copolymers with a defined arm number (Scheme 3.1). For the hydrophobic core, pentaerythritol was used as initiator for the ring opening polymerization (ROP) of ε-caprolactone catalyzed by tin(II) ethylhexanoate

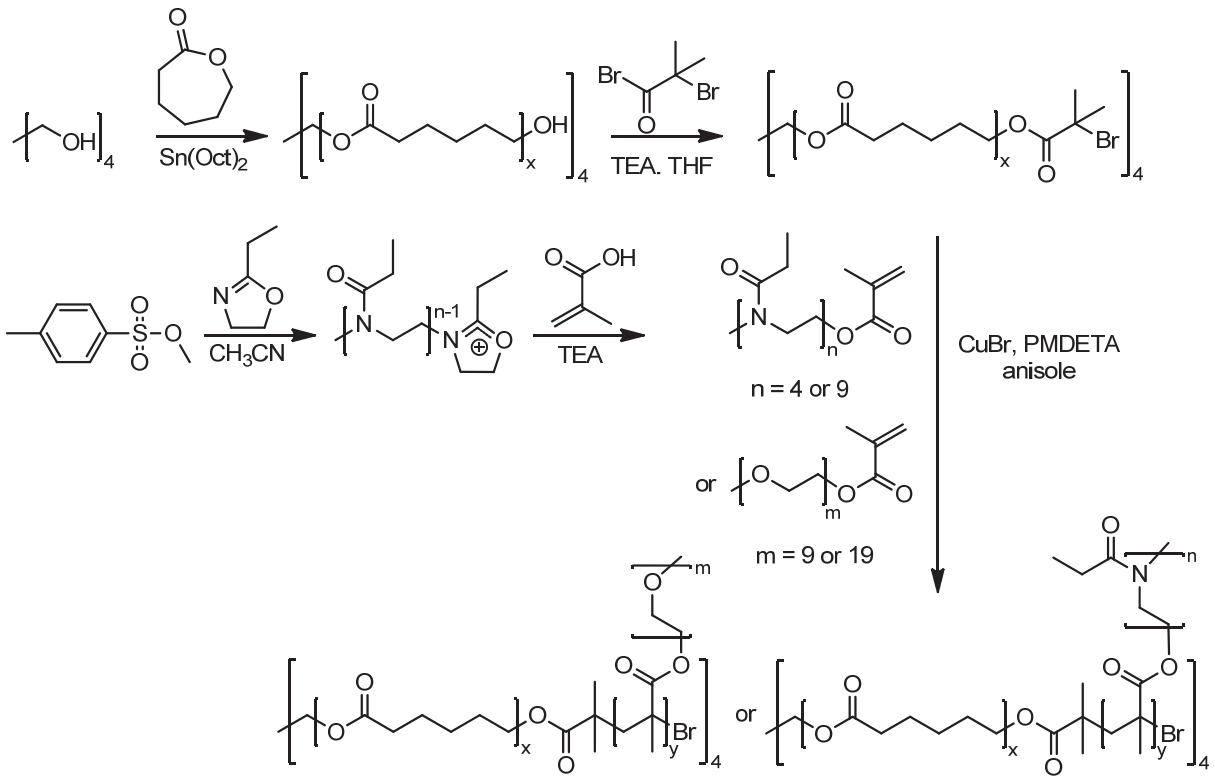

Scheme 3.1. Schematic representation of the synthetic route of the preparation of four-armed star-shaped block copolymers.

($Sn(Oct)_2$) as described in the literature. Different PCL cores were synthesized with varying degrees of polymerization (13 to 23) per arm. For the atom transfer radical polymerization (ATRP) of OEG_9MA, the hydroxy end groups of the prepared star-shaped PCL polymers were esterified with α-bromoisobutyryl bromide. The ATRP of OEG_9MA with the different initiators led to polymers with varying shell size and monomodal molar mass distributions as well as polydispersity index (PDI) values below 1.3 (Table 3.1).

Dynamic light scattering (DLS), light scattering experiments at constant angle and analytical ultracentrifugation (AUC) measurements in the non-selective solvents acetone and THF showed that rather a spheroidal than a spherical geometry is adopted by the unimolecular micelles. These results were confirmed by molecular dynamics calculations.

In water as a selective solvent, both unimolecular micelles as well as loose aggregates of several connected star block copolymer unimers were found. The aggregate formation was confirmed using analytical ultracentrifugation (AUC) measurements, while experiments with nile red as a fluorescence probe led to the conclusion that for all [PCL-*b*-$POEG_9MA]_4$ samples unimolecular hydrophobic cores are present (Figure 3.2). Furthermore, isothermal titration calorimetry (ITC) measurements showed that these amphiphilic systems do not exhibit a cmc. These findings demonstrate that unimolecular micelles can be formed by star-shaped amphiphilic block copolymers also below the typically expected values for the hydrophilic/lipophilic balance.

To elucidate the applicability of these materials as DDS, biological investigations

Table 3.1. Characteristics of the synthesized star-shaped [PCL-*b*-$POEG_9MA$]$_4$ block copolymers.

Polymer	Theoretical DP $POEG_9MA$	Conversion in SEC [%][a]	DP $POEG_9$ MA	Mn [g mol^{-1}] calculated[b]	Mn [g mol^{-1}] measured[c]	PDI
[PCL_{18}-*b*-$POEG_9MA_{12}$]$_4$	12	25	12	31 700	31 000	1.21
[PCL_{18}-*b*-$POEG_9MA_{20}$]$_4$	20	39	20	46 900	36 700	1.19
[PCL_{18}-*b*-$POEG_9MA_{25}$]$_4$	25	51	25	56 400	41 700	1.19
[PCL_{18}-*b*-$POEG_9MA_{51}$]$_4$	50	68	51	100 100	67 800	1.14
[PCL_{23}-*b*-$POEG_9MA_{25}$]$_4$	25	50	25	43 700	43 700	1.23
[PCL_{13}-*b*-$POEG_9MA_{26}$]$_4$	25	53	26	42 300	42 300	1.21

[a] Obtained from SEC ($CHCl_3$:*i*PrOH:NEt_3) using PEG calibration. [b] Calculated from the conversion. [c] Obtained from SEC (DMAc:LiCl) using PMMA calibration.

regarding hemolytic activity, erythrocyte aggregation, and the cytotoxicity were performed. The *in vitro* cytotoxicity experiments were conducted *via* a XTT assay using L929 mouse fibroblasts. After 24 h of incubation with different polymer concentrations (0.1, 1.0 and 10 mg mL^{-1}) of the [$PCL_{13\text{-}23}$-*b*-$POEG_9MA_{25}$]$_4$ and [PCL_{18}-*b*-$POEG_9MA_{12\text{-}25}$]$_4$ star-shaped block copolymers, the metabolic activity of cells treated with test-samples was found to be on the level of untreated controls, which proves the non-toxic effect of the polymers even at the highest concentrations used.

The release of hemoglobin was used to quantify the erythrocyte membrane damaging effect of three different concentrations (5, 25, 50 mg mL^{-1}) of the star-shaped block copolymers. No hemolytic effects up to concentrations of 50 mg mL^{-1} were found, indicating the absence of any membrane destabilizing property of the polymers. Furthermore, the aggregation of erythrocytes, which would indicate a blood incompatibility, was investigated. Visual inspection as well as absorption measurements showed that none of the star-shaped block copolymers led to cluster formation below a concentration of 25 mg mL^{-1}.

Encapsulation studies using fat brown RR as well as nile red revealed that the block copolymers possess a shell large enough to stabilize the micelle and its cargo in water. As a first application, a novel, water insoluble fungicide was encapsulated into the PCL core of [PCL_{18}-*b*-$POEG_9MA_{25}$]$_4$, which was chosen because it exhibited the best inclusion capacity in the model studies with fat brown RR. It is assumed that the drug was not only entrapped in the core but was further taken up by the $POEG_9MA$ shell as well, because within the inclusion study no upper limit of uptake could be determined. However, the antifungal activity of the encapsulated drug increased only up to a ratio of 20 drug molecules per polymer (8 wt%) revealing the true inclusion limit of the star-shaped drug carrier. In fact, the solubility of the drug was drastically enhanced with the star-shaped carrier, and the activity of the fungicide remained in the range of the free drug that was solubilized in a DMSO/methanol/water mixture.

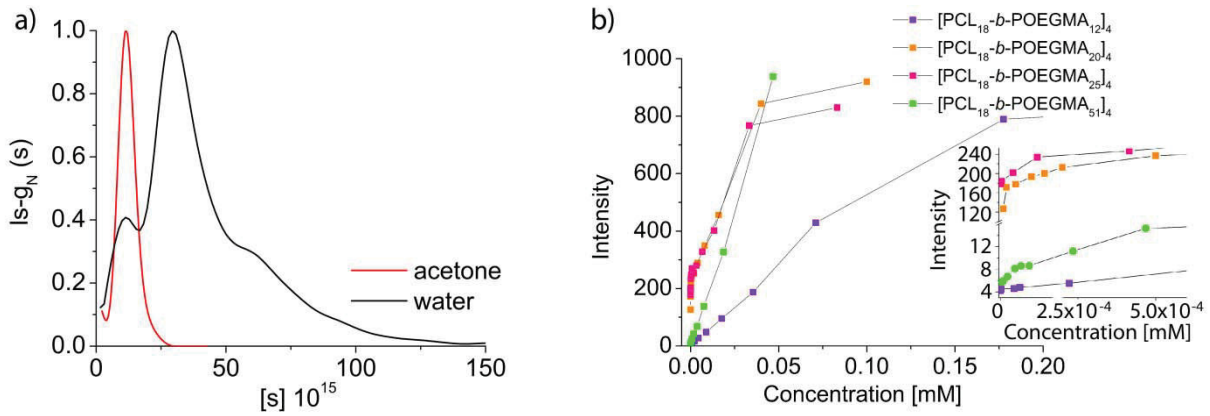

Figure 3.2. a) Normalized distributions of the intrinsic velocity sedimentation coefficients [s] obtained in acetone and in water for $[PCL_{18}$-*b*-$POEG_9MA_{25}]_4$ at a concentration of c = 0.5 mg mL^{-1}. b) Fluorescence emission of nile red at 620 nm with increasing polymer concentration as well as an expanded view of the low concentration regime (inset).

In summary, well-defined star-shaped block copolymers were synthesized, which form unimolecular micelles and aggregates in water. It was shown that the assemblies do not interact by their cores, but only by entangling of their shells. The biocompatibility was proven in terms of cytotoxicity and hemocompatibility. The star-shaped systems were demonstrated to encapsulate hydrophobic model compounds as well as a novel fungicide. In mycobacterial tests the star-shaped block copolymers were proven to transport efficiently drug molecules and to release them, which is the final important issue.

3.2. Star-shaped drug delivery systems with PEtOx shell

To extend the knowledge of the star-shaped poly(*ε*-caprolactone)-*block*-poly(oligo(ethylene glycol)methacrylate) ($[PCL$-*b*-$POEG_9MA]_4$) copolymers, the shielding properties of poly(2-ethyl-2-oxazoline) (PEtOx) accounting as alternative to poly(ethylene glycol) (PEG) (Chapter 2), were investigated in a comparative study of the shell. The shell properties of the star-shaped block copolymers are varied systematically in terms of their shell composition, the brush-length as well as the chemical nature of the shell. Therefore, the hydrophilic shell of the star-shaped block copolymers was constructed using OEGMA (M_n = 950 g mol^{-1}, 19 repeating units, $OEG_{19}MA$) to obtain a brush-like shell with longer brush-arms and oligo(2-ethyl-2-oxazoline) methacrylate (OEtOxMA) macromonomers with similar molar masses ($OEtOx_4MA$, M_n = 500 g mol^{-1}, 4 repeating units) and repeating units ($OEtOx_9MA$, M_n = 1 000 g mol^{-1}, 9 repeating units) in comparison to the OEGMA macromonomers.

Whereas the OEGMA macromonomers were commercially available, the OEtOxMA macromonomers were prepared *via* microwave-assisted cationic ring opening polymerization (CROP) of 2-ethyl-2-oxazolines (EtOx). The reactive chain ends were end-capped with methacrylic acid (MA) according to a reported procedure.[93,94] The following procedure to

Table 3.2. Characteristics of star-shaped $[PCL_{18}$-*b*-POEGMA$]_4$ and $[PCL_{18}$-*b*-POEtOxMA$]_4$ block copolymers.

Polymer	Aimed DP	Conversion in SEC [%][a]	Obtained DP[b]	M_n [g mol^{-1}] calculated[b]	M_n [g mol^{-1}] measured[c]	PDI
$[PCL_{18}$-*b*-$POEG_{19}MA_{14}]_4$	12	28	14	62 200	33 000	1.25
$[PCL_{18}$-*b*-$POEG_{19}MA_{28}]_4$	25	56	28	114 400	55 300	1.28
$[PCL_{18}$-*b*-$POEG_{19}MA_{45}]_4$	50	45	45	180 000	87 700	1.27
$[PCL_{18}$-*b*-$POEtOx_4MA_{15}]_4$	12	29	15	39 000	30 200	1.14
$[PCL_{18}$-*b*-$POEtOx_4MA_{27}]_4$	25	54	27	63 000	29 600	1.24
$[PCL_{18}$-*b*-$POEtOx_4MA_{44}]_4$	50	44	44	97 000	51 600	1.15
$[PCL_{18}$-*b*-$POEtOx_9MA_7]_4$	12	15	7	37 000	76 700	1.21
$[PCL_{18}$-*b*-$POEtOx_9MA_{25}]_4$	25	50	25	109 000	80 000	1.17
$[PCL_{18}$-*b*-$POEtOx_9MA_{51}]_4$	50	51	51	213 000	103 800	1.23

[a] Obtained from SEC ($CHCl_3$:*i*PrOH:NEt_3) using PEG calibration. [b] Calculated from the conversion. [c] Obtained from SEC (DMAc:LiCl) using PMMA calibration.

construct the star-shaped block copolymers was followed as described previously (Scheme 3.1, Table 3.2).

DLS measurements of the star-shaped block copolymers in aqueous solvents revealed larger diameters in comparison to acetone (Figure 3.3). Assuming that in acetone single molecules are observed, only an agglomeration of several unimolecular micelles to larger aggregates can be concluded in water. Spectroscopic investigations by nile red showed that no critical micelle concentration (cmc) can be determined for these block copolymers allowing the conclusion that the hydrophobic cores of the star-shaped block copolymers are not in contact with each other (Figure 3.3). Additionally, isothermal titration calorimetry (ITC) experiments showed no disaggregation behavior upon dilution as no sigmoidal curve can be observed. Therefore, the entanglement of the brush-like shells forming a so-called supermicelle is postulated as reason for the larger diameters observed in water. On the basis of these results, a unimolecular behavior can be assumed for all nine star-shaped block copolymer. This observation leads to the conclusion that rather the molar mass of the hydrophilic shell forming block seems to influence the steric stabilization than the repeating units of the hydrophilic polymer. Since even for the $[PCL_{18}$-*b*-$POEtOx_4MA]_4$ polymers with only 4 repeating units per brush arm, unimers are formed in water.

The evaluation of the biological compatibility is one of the first steps to prove the applicability of the star-shaped POEGMA and POEtOxMA block copolymers for biomedical purpose. The nine polymers were tested in terms of their blood compatibility as this is the first

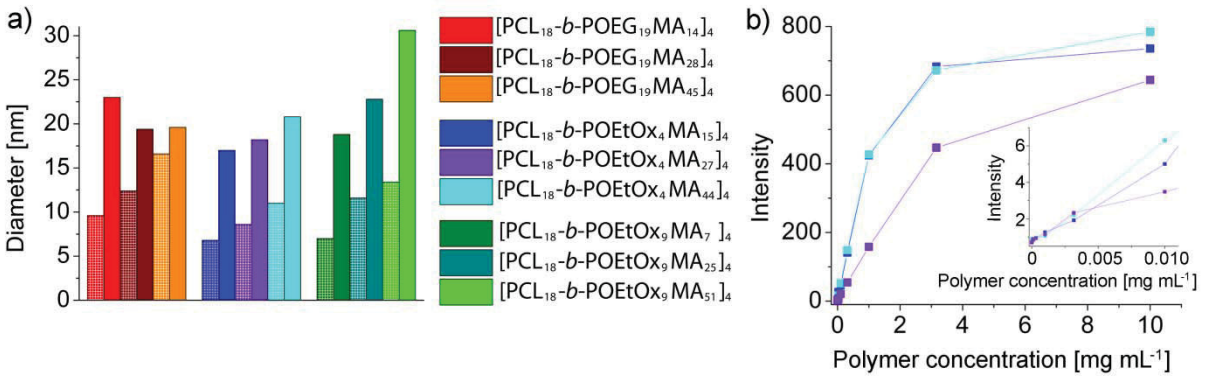

Figure 3.3. a) Diameters obtained in DLS for the $[PCL_{18}$-*b*-$POEG_{19}MA]_4$, $[PCL_{18}$-*b*-$POEtOx_4MA]_4$ and $[PCL_{18}$-*b*-$POEtOx_9MA]_4$ polymers in acetone (checkered columns) and in water (empty columns). b) Fluorescence emission of nile red at 620 nm with increasing polymer concentration representatively shown for the $[PCL_{18}$-*b*-$POEtOx_4MA]_4$ polymers.

part of the body that is exposed to the polymer after intravenous administration. No hemolytic or erythrocyte aggregating activity was observed for the POEGMA and POEtOxMA block copolymers. Furthermore, no effect on the coagulation time of blood plasma could be detected, showing that the star-shaped block copolymers interact neither with the components of the extrinsic nor the intrinsic coagulation pathway. An activation of the complement system of the immune system in the range of the saline control was detected for POEGMA and POEtOxMA containing polymers proving that no unspecific interaction with the alternative pathway can be observed. The *in vitro* cytotoxicity was evaluated on the basis of a XTT assay with a mouse fibroblast L929 cell line. None of the star-shaped block copolymers showed any cytotoxic effect after 24 h incubation at different concentrations of the polymer (0.1, 1 and 10 mg mL^{-1}). Those results confirm the general lack of cytotoxic effects of both PEG as well as PEtOx polymers.

Doxorubicin, an anti-cancer drug frequently used in clinics, was encapsulated to prove the applicability of the star-shaped block copolymer as drug carrier. Cytotoxicity assays revealed that the drug was released from the carrier in a controlled way leading to IC_{50} values above the free drug and the commercial liposomal formulation Doxil/Caelyx proving a retarded release from the carrier.

In summary, the star-shaped block copolymers with a brush-like OEtOxMA shell have been investigated in comparison to the OEGMA shell. Both systems have been proven to form unimers in aqueous solution, even for the very small hydrophilic shell provided by the $[PCL_{18}$-*b*-$POEtOx_4MA]_4$ polymers. Therefore, it can be concluded, that an efficient stabilization of the hydrophobic core in water by the hydrophilic brush-like shell is rather dependent on the molar mass than on the chemical character of the repeating unit of the hydrophilic polymer.

4. Advanced characterization of pharmaceutical relevant polymers by matrix-assisted laser desorption/ionization mass spectrometry and collision induced dissociation

Parts of this chapter have been published: **P4)** A. Baumgaertel, C. Weber, K. Knop, A. C. Crecelius, U. S. Schubert, *Rapid Commun. Mass Spectrom*. **2009**, *23*, 756–762. **P5)** K. Knop, B. O. Jahn, M. D. Hager, A. C. Crecelius, M. Gottschaldt, U. S. Schubert, *Macromol. Chem. Phys*. **2010**, *211*, 677–684. **P6)** A. C. Crecelius, C. R. Becer, K. Knop, U. S. Schubert, *J. Polym. Sci., Part A: Polym. Chem.* **2010**, *48*, 4375–4384. **P7)** L. Tauhardt, K. Kempe, K. Knop, E. Altuntaş, M. Jäger, S. Schubert, D. Fischer, U. S. Schubert, *Macromol. Chem. Phys*. **2011**, *212*, 1918–1924. **P8)** E. Altuntaş, K. Knop, L. Tauhardt, Kristian Kempe, A. C. Crecelius, M. Jäger, M. D. Hager, U. S. Schubert, *J. Mass. Spectrom*. **2012**, *47*, 105–114.

In the emerging field of drug delivery, polymeric materials are widely used for designing drug delivery systems with sufficient *in vivo* stability and delivery efficiency.[29,95] These biological applications of polymers require a very solid and profound characterization of the used materials beyond nuclear magnetic resonance (NMR) spectroscopy and size exclusion chromatography (SEC), as the resulting material properties highly depend on the microstructure of the polymer. For example, the chain architecture, the end group functionality as well as the block length influence the stability of the finally formed drug delivery systems.[96,97]

In the last years, mass spectrometry (MS) arose to a very versatile technique to acquire detailed information of the polymer structure and, in particular, of the end group nature. In former times, MS analysis of polymers has been a difficult task being limited to the analysis of low molar mass compounds. This changed dramatically, when Karas and Hillenkamp developed in the 1980s the matrix-assisted laser desorption ionization (MALDI) process.[98] Tanaka *et al*. improved this technique suchlike that the measurement of molecules with molar masses up to 100 kg mol^{-1} were possible.[99] The therewith achieved advancement in mass spectrometry improved by far the analytical possibilities in polymer chemistry as the implementation of the soft ionization techniques MALDI allowed the analysis of different macromolecules and polymers with little or no fragmentation, leading to an accurate molar mass determination. Since then, a large variety of synthetic polymers has been investigated by MALDI-MS methods, such as polystyrene (PS), poly(methyl methacrylate) (PMMA), poly(ε-caprolactone) (PCL) and many more.

To gain deeper insights into the polymer composition, tandem MS methods, such as collision induced dissociation (CID), have been developed and applied to different synthetic polymers like PMMA, PS or poly(ethylene terephthalate) (PET).[100,101] However, only a few reports exist about the tandem MS analysis of copolymers using MALDI-time-of-flight (TOF) for a detailed analysis of the structure.[102–105]

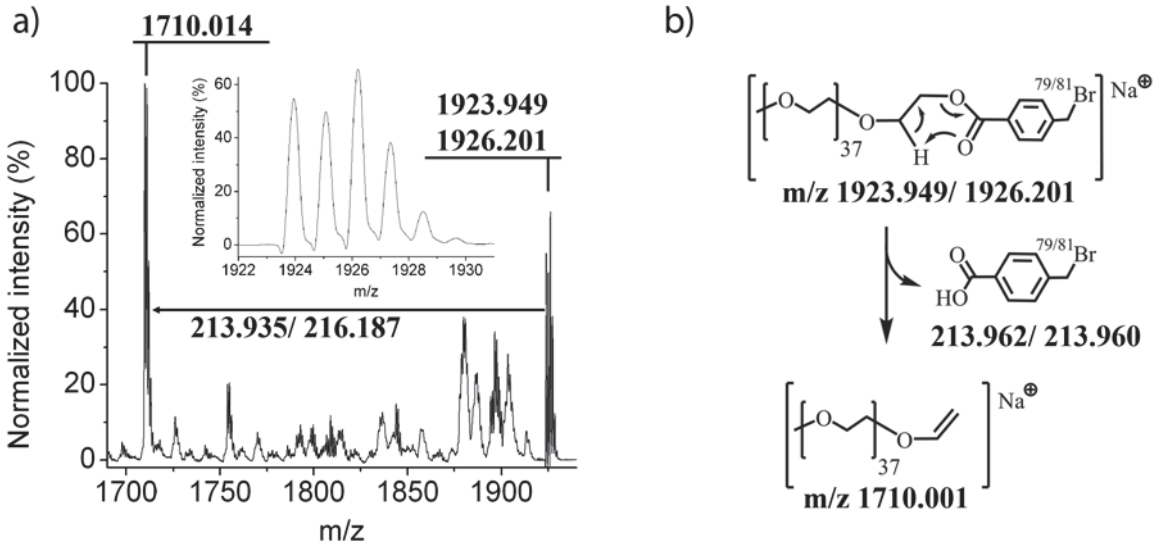

Figure 4.1. a) Zoom into the CID spectrum below the parent peak with 38 repeating units showing the distinct loss of 4-(bromomethyl) benzoic acid (inset: zoom into the parent ion); b) schematic representation of the proposed mechanism for the cleavage of the 4-(bromomethyl) benzoic acid ester bond.

Poly(ethylene glycol) (PEG), of tremendous importance in drug delivery, represents the gold standard in stealth technology as already described in Chapter 2. This broad usage in *in vivo* applications requires a profound structure analysis. PEG is very well investigated by the MALDI-MS techniques as it provides an easily ionizable structure.[106,107] In this study methoxy-poly(ethylene glycol) (mPEG) was substituted with different end groups linked by an ester bond, such as benzyl bromide, benzyl chloride and tosylate. Tandem MS investigations yielded within the CID spectra regions with different analytical information. In the upper region of the mass spectrum the 1,5-hydrogen transfer (McLafferty+1 rearrangement) of the end groups introduced by polymer analogues reactions were cleaved off in a very efficient and characteristic way revealing the exact mass of the end group and providing thereby very direct information on the end group nature (Figure 4.1). Furthermore, in-detail examinations of the spectra of the different end group substituted mPEGs revealed the leaving group qualities of the end groups and a preferentially ionization during the MALDI process by the PEG chain as a crown ether-shaped complex rather than the carbonyl group of the ester end group. These findings were supported by density functional theory (DFT) calculations of the different possible complexation geometries.

The middle part of the CID spectra is marked by a very regular series of fragments of the 1,4-hydrogen elimination process, as proposed by Lattimer *et al*. and Jackson *et al*..[108–110] These fragments confirm the proposed mechanism by their distinguished isotopic pattern revealing the presence or absence, in particular, of the benzyl bromine end group. Multiple fragmentations in combination with the 1,5 hydrogen-transfer were observed additionally, whereas 1,4-ethylene eliminations, in contrast, occured only rarely. In the lower molar mass region, below m/z 500, the appearance of the CID spectrum changes as more fragments appear. They can be attributed to distonic radical cations, which are formed either by single

homolytic bond cleavage or multiple bond cleavages. These fragments are observed additionally to the elimination fragments rendering this region less useful for structure analytical purpose.[108,109]

Furthermore, the block length of the amphiphilic block copolymer mPEG-*b*-PS could be determined in an accurate and reliable manner by performing MALDI-TOF MS/MS analysis. The mPEG macroinitiator of the atom transfer radical polymerization (ATRP) reaction of styrene showed in CID investigations corresponding fragmentation mechanisms to the previously described substituted mPEG samples. However, the 1,5-hydrogen transfer (McLafferty+1 rearrangement) leading to the end group loss, which was predominate in the previous investigations, was surpassed by the loss of bromine. The subsequently performed tandem MS analysis of the block copolymer revealed only fragments of the mPEG block and the PS block, meaning that no signals correlated to fragments bearing the mPEG block as well as the PS block could be detected. From this phenomenon it can be concluded that a scission between both blocks in the tandem MS mode occurs. Interestingly, this separation of the two different blocks does not occur *via* the 1,5-hydrogen transfer but by a 1,4-hydrogen elimination process in the PEG chain. As the PS fragments occur only in the mono-, di- and trimeric region, the block length determination was performed on the basis of the PEG fragments. The ATRP initiating α-bromo isobutyrate could not be verified in the CID fragments.

Poly(2-ethyl-2-oxazoline)s (PEtOx) are regarded as a possible substitute to PEG[12,111] and were also investigated in a detailed tandem MS study. The collision induced dissociation of a PEtOx pentamer, initiated with a methyl group and end functionalized with a methacrylic acid, led to the typical end group loss *via* a charge-remote 1,5-hydrogen transfer (McLafferty+1 rearrangement). Additionally, a charge-induced loss of the methacrylic acid sodium salt induced the formation of an oxazolinium species, leading to the formation of a fragment series of the depolymerizing main chain. For a second PEtOx macromolecule with 19 repeating units, containing a propargyl starting group and a hydroxyl end group, the collision induced dissociation was studied. This macromolecule revealed the formation of twelve different series of fragments, which are mainly formed either by the 1,4-hydrogen- or ethylene elimination from the main chain or a 1,5-hydrogen transfer (McLafferty+1

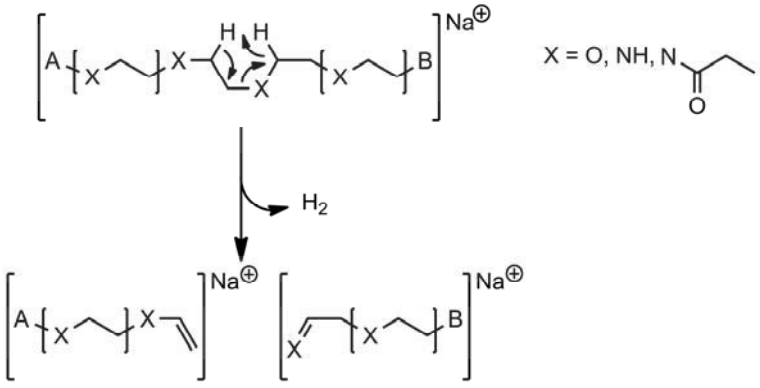

Scheme 4.1. Schematic representation of the proposed charge-remote 1,4-hydrogen elimination mechanisms for the three polymers PEG, PEtOx and PEI.

rearrangement) including the side chain. Further fragment series are formed by ethylene elimination on the side chain and α- and side-group cleavage. This study confirmed the observation of the mPEG analysis that the end group nature plays a key role in the fragment formation in the CID processes.

Poly(ethylene imine)s (PEIs) are established in pharmaceutical science as polymeric vectors for gene delivery.[112–115] Linear PEIs, which are obtained by side-chain cleavage of the above discussed PEtOx, with molar masses similar to branched PEI, show a less efficient electrostatic interaction with nucleic acids, but their *in vivo* application is marked by less cytotoxicity and higher transfection efficiency in comparison to branched PEI.[115–119] Furthermore, the synthesis of linear PEI (*via* hydrolytic cleavage of PEtOx) offers a well-defined architecture, molar mass and purity for reproducible transfection efficiencies and immunological response of the body to the cationic polymer.

PEI with different starting and end groups was analyzed by electrospray ionization-quadrupol time of flight (ESI-Q-TOF) and MALDI-TOF MS to elucidate in detail the macromolecular structures of linear PEIs. It was a challenging task to characterize the resulting PEIs in SEC as well as in MS, due to the multiple charges carried by the polymer. A judicious choice of the matrix for MALDI-TOF MS made the polymers amenable to mass spectrometric measurements, confirming on the one side the molar mass distribution and showing on the other side an incomplete hydrolysis of the PEtOx. Tandem mass spectrometry experiments have been performed to investigate the possible fragmentation mechanisms. In the CID spectra obtained from protonated species, a 1,2-hydride shift *via* a charge-remote rearrangement mechanism through a four membered cyclic transition state provokes the formation of four fragment series and some internal fragments. For PEIs, the type of the cation attached to these polymers was important, because protonated and sodiated species are fragmented through different fragmentation pathways. Thus, the fragmentation of sodiated PEI macromolecules required higher collision energies and occurred *via* the 1,2-hydride shift and the 1,4-hydrogen elimination, as already observed for PEG and PEtOx. Both techniques, MALDI-and ESI-Q-TOF MS and MS/MS, delivered comparable results.

Poly(ε-caprolactone) (PCL) is a biodegradable polymer often used as hydrophobic block in copolymers to form micelles for drug delivery purposes.[96,97,120,121] The wide application is based on its expedient initiation by hydroxyl groups and a convenient synthesis procedure.[120] In particular, the synthesis of star-shaped polymers is enabled by using an initiator with multiple hydroxyl groups. An issue of constant discussion provides the question whether all arms of star-shaped block copolymers feature a similar degree of polymerization. Therefore, the possibility to investigate this open question by mass spectrometric methods was elicited. Two different polymers have been prepared by ring opening polymerization of ε-caprolactone: a linear PCL initiated by 1-bromo-hexanol and a star-shaped PCL initiated by pentaerythritol. The shape of the MALDI-TOF mass spectra of these two polymers showed no apparent difference. The end group analysis by the monoisotopic mass reveals the end group nature but no provides evidence for the different architectures of both polymers (Figure 4.2 a and b). However, the CID spectra revealed a distinct difference in the shape (Figure 4.2 c and d). The CID spectrum of the linear polymer shows the typical pattern of high intensity at

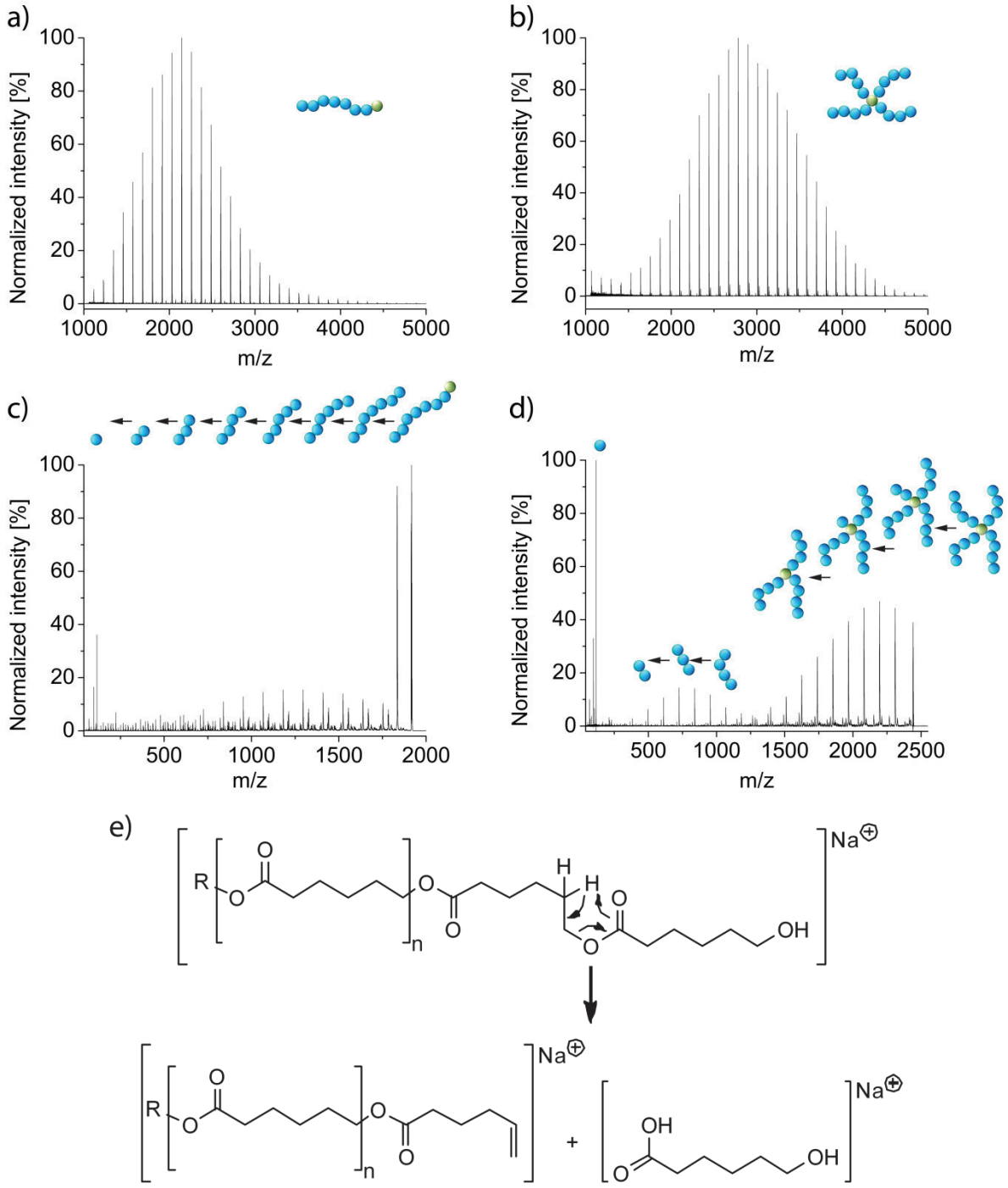

Figure 4.2. a) MALDI-TOF mass spectrum of the linear PCL, b) MALDI-TOF mass spectrum of the four-armed star-shaped PCL, c) CID spectrum of the linear PCL, d) CID spectrum of the four-armed star-shaped PCL and e) schematic representation of the proposed mechanism for cleavage of the PCL ester bond.

high and low molar mass and in between a belt of low intensity peaks formed by regular fragments. These fragments are mainly formed by 1,5-hydrogen transfer (McLafferty+1 rearrangement) typical for ester bonds (Figure 4.2.e). In contrast, the CID spectrum of the star-shaped PCL shows two distributions, one corresponding to the star-shaped polymer with a degrading arm and one formed by the lost arm, both formed by the 1,5-hydrogen transfer

(McLafferty+1 rearrangement). These observations suggest that a determination of the arm length is possible by means of mass spectrometric analysis.

MALDI-TOF MS has been shown to provide more detailed information of macromolecules in addition to SEC and NMR spectroscopy, such as end group analysis, the advantages of an absolute molar mass determination and the possibility to obtain an insight into polymer composition by tandem MS methods. The fragmentation mechanism of different polymer classes was elucidated, showing that macromolecules bearing a heteroatom in the main chain adopt often the 1,4-hydrogen-elimination, whereas polyesters prefer the 1,5-hydrogen transfer (McLafferty+1 rearrangement). The end groups of different polymers could be secured by CID MS.

5. Matrix-free laser desorption/ionization mass spectrometry and imaging

Parts of this chapter have been published: **P9)** K. Knop, S. Stumpf, U. S. Schubert, submitted. **P10)** D. Hölscher, R. Shroff, K. Knop, M. Gottschaldt, A. C. Crecelius, B. Schneider, D. Heckel, U. S. Schubert, A. Svatos, *Plant J.* **2009**, *60*, 907–918. **P11)** S. Miosic, K. Knop, D. Hölscher, J. Greiner, C. Gosch, J. Thill, M. Kai, B. Shreshta, B. Schneider, A. C. Crecelius, U. S. Schubert, S. Svatos, K. Stich, H. Halbwirth, *J. Exp. Botany*, **2012**, submitted. **P12)** D. Hölscher, K. Knop, M. Kai, R. Maddula, C. Ritter, A. C. Crecelius, D. Heckel, B. Schneider, U. S. Schubert, T. Alexandrov, B. Zimmermann, A. Svatos, *Plant J.* **2012**, submitted. **P13)** D. Hölscher, S. Dhakshinamoorthy,T. Alexandrov, M. Becker, T. Bretschneider, A. Bürkert, A. C. Crecelius, D. De Waele, D. G. Heckel, H. Heklau, C. Hertweck, M. Kai, K. Knop, C. Krafft, R. K. Madulla, C. Matthäus, J. Popp, B. Schneider, U. S. Schubert, R. Sikora, A. Svatoš, R. Swennen, *Nature Chem. Biol.* **2013**, in preparation.

5.1. Laser desorption/ionization for drug and drug delivery system mass spectrometry imaging

Matrix-assisted laser desorption/ionization (MALDI) represents an established method to volatilize substances to render them amenable for MS. The choice of matrix plays a crucial role in the success of a MALDI time-of-flight mass spectrometry (TOF MS) measurement.[25] Upon excitation by the laser beam, matrix molecules are transferred into the gas phase and co-desorb therewith analyte compounds, enabling their mass spectrometric analysis.[26] It is generally known that the matrix has to meet several requirements determined by the role the matrix plays in the volatilization process. The matrix has to embed and separate the analytes by co-crystallization as well as absorb the energy from the laser pulse. These materials are generally small, organic compounds that are readily absorbing light in the range of *e.g.* UV lasers.[25]

The hydrophobic character of drug molecules often arises from an extended π-system, either of an aromatic or a conjugated system. These π-systems result in a bathochromic shift of the absorption wavelength into the UV region or even to wavelengths of the visible part of the spectrum. The UV absorption might be used for the volatilization of the drug molecules in the MALDI process.

Hydrophobic drugs are often characterized by a poor distribution in human body and are, therefore, often not suited for pharmaceutical application. In the emerging field of drug delivery, amphiphilic block copolymers are widely used for designing drug delivery systems (DDSs) with sufficient *in vivo* stability and delivery efficiency by solubilization and delivery of hydrophobic drugs.[29,95] The combination of both the approaches, encapsulation into a DDS and evaporation of the drug by the UV laser, leads to the use of the drug molecules as

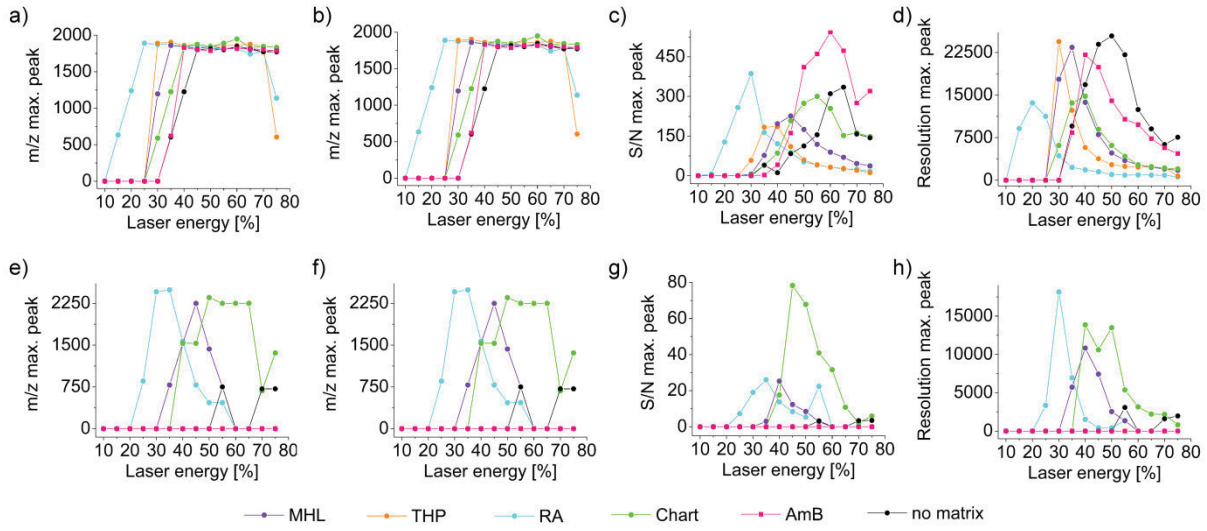

Figure 5.1. Evaluation of the characteristic parameters of the MALDI-TOF MS exemplarily shown for PEG 2 kDa and PS 2 kDa. Spectra have been evaluated on the basis of the maximum peak for PEG 2 kDa as a function of the laser energy against (a) the m/z value, (b) the intensity, (c) the S/N ratio and (d) the resolution. Evaluation of the characteristic parameters of the MALDI-TOF MS spectra on the basis of the maximum peak for PS 2 kDa as a function of the laser energy against (e) the m/z value, (f) the intensity, (g) the S/N ratio and (h) the resolution.

matrix, which might enable the detection of the drug as well as the amphiphilic block copolymer DDS in *ex vivo* and *in vivo* applications.

Five different drug molecules have been chosen for a comparative study as matrix: madurahydroxylactone (MHL),[129] tetrakis(4-hydroxyphenyl)-porphyrine (THP),[125] chartreusin (Chart),[133] amphotericin B (AmB)[135] and retinoic acid (RA).[131] MHL and Chart are natural products with antimicrobial, antimycobacterial and cytotoxic effects. MHL was also found to be useful in HIV therapy[122–124] and Chart was used as antitumor agent.[126,127] THP finds also its application in tumor therapy as a dye for photodynamic therapy.[125] AmB is an established standard drug for the treatment of fungal infections.[128–130] And RA was also tested in cancer therapy for the treatment of acute promyelocytic leukemia.[131]

This choice includes RA as an already established matrix for MALDI measurements of polymers[132–137] and THP that was reported only once to be used as matrix.[138] Firstly, the selected drug molecules were submitted to LDI experiments to study their behavior under laser irradiation, whereas RA has been investigated under LDI conditions previously.[139] For Chart, RA and THP the base peak was provided by the pseudo molecular ion. Both AmB and MHL showed the formation of numerous, intensive fragments, whereas for AmB no molecular ion could be detected. From these LDI investigations, it can be concluded that the investigated drug molecules can be excited and transferred into the gas phase by the laser light, most probably due to their π-system and UV absorption.

Subsequently, the ability to act as matrix was determined for the analysis of a choice of polymers, such as poly(ethylene glycol) (PEG) 2 kDa, poly(methyl methacrylate) (PMMA)

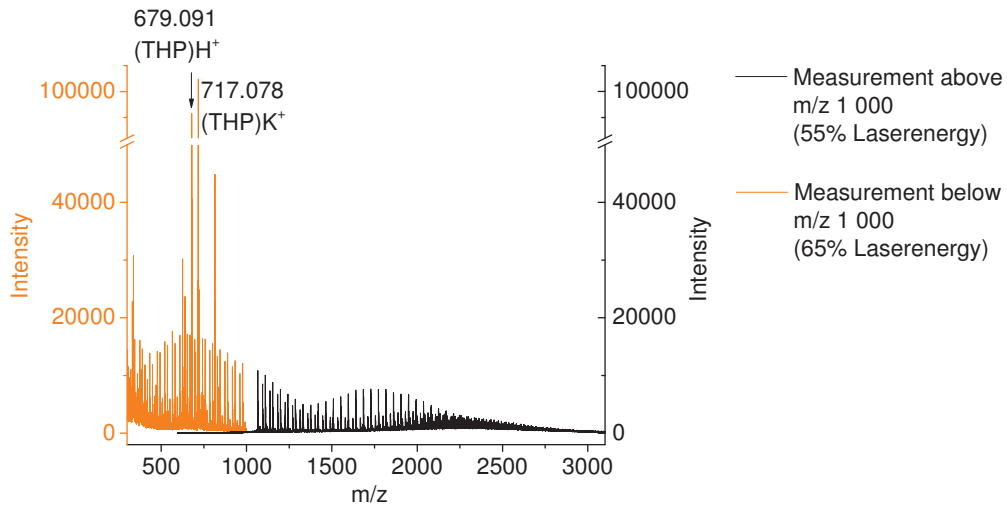

Figure 5.2. Detection of THP and mPEG-*b*-PCL from the micellar solution.

2.5 kDa, poly(styrene) (PS) 2 kDa, poly(2-ethyl-2-oxazoline) (PEtOx) 2 kDa and PEG 2 kDa-*block*- poly(*ε*-caprolactone) 0.9 kDa (PEG-*b*-PCL). The obtained spectra were evaluated according to different quality factors (Figure 5.1). As expected, RA is evaluated as best matrix for all polymers delivering not at all instances the best results but, on the whole, the most steady and robust spectra qualities. For THP, it can be concluded that this matrix is not suited for hydrophobic polymers. Furthermore, Chart and MHL deliver rather good results at relatively high laser energies for all polymers. On the whole, a minor matrix role can be also attributed to AmB by considering the intensity and S/N ratio values obtained for PEG as well as the data obtained for PMMA. The spectra obtained for the block copolymer are not as easily evaluated as the spectra obtained for the homopolymers as the assignment of the peaks is not always performed properly by the software due to their multitude and overlapping character. The visual inspection of the spectra obtained for the block copolymer showed for all matrices a distribution although not with the same resolution of the isotopic pattern.

The block copolymer was subsequently used to encapsulate the five drugs. The micelles were prepared with varying drug molecule to polymer molecule ratios and characterized subsequently in terms of their diameter, zeta potential and inclusion efficiency. It was observed that the drugs Chart and AmB were not hydrophobic enough to be efficiently encapsulated. However, the micellar solutions of RA, MHL and THP with the highest inclusion capacity of the drug were chosen for further MALDI experiments. The solutions were submitted to an analysis whether such a small amount of matrix is sufficient enough to still volatilize the polymer and render it therewith measurable by the MALDI process. As matter of fact, of the three selected samples only the micellar solution containing THP was shown to deliver distinct signals of the matrix and the mPEG-*b*-PCL block copolymer (Figure 5.2). Therefore, the combination of THP and this DDS is suitable for detection of the drug and its carrier.

In summary, it was shown that hydrophobic π-system bearing drug molecules can act as matrix in the MALDI process. Although the spectra qualities of the standard matrix RA were not reached, a matrix effect was shown for the different drug molecules. However, the

analysis of drug and drug carrier was only successful for the THP matrix encapsulated into the mPEG-*b*-PCL copolymer due to the high encapsulation efficiency of THP. These results can serve as basis for *in vitro* and *in vivo* MSI of drug carriers and their cargo.

5.2. Laser desorption/ionization mass spectrometry imaging of secondary plant metabolites

Within this chapter, the spatially resolved detection of aromatic secondary metabolites by laser desorption/ionization mass spectrometry imaging (LDI-MSI) in plant tissues is demonstrated. Metabolites bearing a π-system can be analyzed directly by laser irradiation without application of a matrix that is required for the matrix-assisted LDI (MALDI) process. Therewith, their direct analysis on the untreated plant material without extensive probe preparation and with a spatial resolution in the range of the laser diameter that is not influenced by the matrix crystals is possible.

Many modern drug molecules are of herbal origin or are derivatives of plant metabolites. Pharmacologically interesting compounds are often produced by the plant as secondary metabolites with functions that are not directly related to the immediate survival of the plant. The localization of these compounds within the plant tissue is of basic interest to investigate their biosynthesis and fundamental biological function as well as to analyze seasonal changes

Hypericum perforatum (St. John's wort) is one of the best studied medicinal plants,[140] as their extracts have been shown to possess antidepressant activity.[140–144] Additionally, one of the metabolites, hypericin, revealed multiple pharmacological properties, like anti-bacterial,

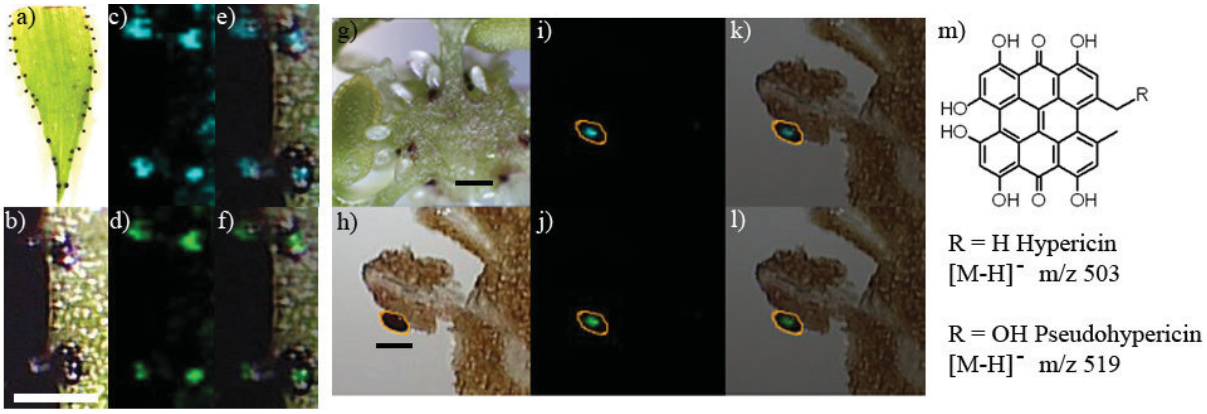

Figure 5.3. a) *H. reflexum* leave, b) zoom into the measured region (bar = 200 µm), c) molecular image of m/z 503, e) overlay of molecular and optical image of m/z 503, d) molecular image of m/z 519 and f) overlay of molecular and optical image of m/z 519. g) Cryosectioned ovary of *H. perforatum* (bar = 500 µm), h) optical image of measured region, orange circle marks expected region of the hypericins (bar = 100 µm), i) molecular image of m/z 503, k) overlay of molecular and optical image of m/z 503, j) molecular image of m/z 519, l) overlay of molecular and optical image of m/z 519 as well as m) chemical structures and ion masses of the detected naphtodianthrones. A measurement raster of 10×10 µm was applied.

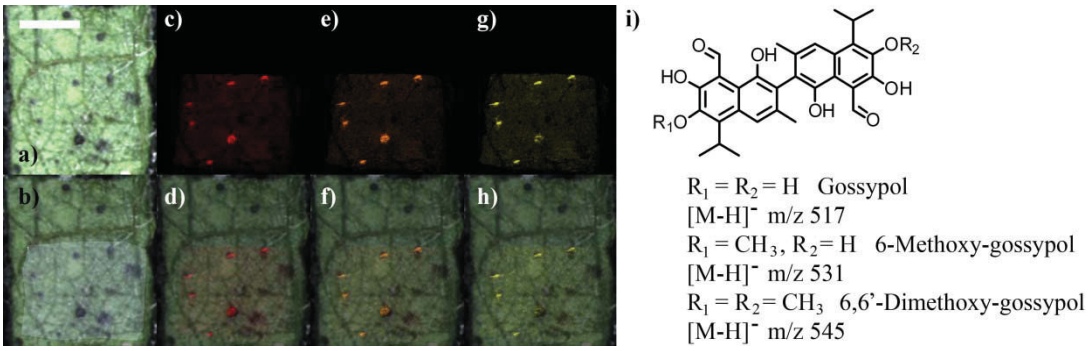

Figure 5.4. a) *Gossypium hirsutum* leaf (bar = 500 µm), b) designation of the measurement region, c) molecular image of m/z 517, d) overlay of molecular and optical image of m/z 517, e) molecular image of m/z 531, f) overlay of molecular and optical image of m/z 531, g) molecular image of m/z 545, h) overlay of molecular and optical image of m/z 545 as well as i) chemical structures and ion masses of gossypol and its derivatives. A measurement raster of 20×20 µm was applied.

of the biosynthesis, which is an important issue for crop plants to determine the most suitable point in time for the harvest.anti-tumor and photodynamic activity.[123,124,129] Although the exact function of the hypericins in the *Hypericum* sp. is only assumed to lay in the field of host defense,[145] the clinical relevance of the mixture of the hypericins in antidepressants has been confirmed.[141] These hypericins have been localized within this study amongst various flavonoids and phloroglucinols in different plant tissues by LDI-MSI. The increased spatial resolution of the LDI-MSI approach in comparison to MALDI-MSI enabled the locally resolved detection of hypericins in the placenta, the stamen und the pollen. On *H. reflexum* leaves, even the spatially resolved detection of hypericins in the glandular trichomes and the secretory cavities has been successfully performed (Figure 5.3).

Similarly, gossypol and its derivatives, compounds of the sesquiterpene family, are produced by *Gossypium* sp. (cotton) as protection against herbivores. Gossypol has been shown to possess anti-cancer activity against breast cancer, prostate cancer as well as melanoma und colon cancer lines.[130-132] In untreated plant materials, gossypol derivatives, hemigossypolone and different heliocides were localized by the LDI-MSI approach in the pigment glands of different plant parts, such as root, stipe, sepal, carpel, seed, cotyledon and leaf (exemplarily shown for gossypol and its derivatives in Figure 5.4). As the compounds are not detectable in the surrounding tissue these pigment glands can be regarded as their centers of biosynthesis

Musa (banana) cultivars with differing susceptibility against the burrowing nematode *Radopholus similis* have been investigated in view of the resistance behavior caused by the biosynthesis of phenylphenalenone compounds.[150,151] In LDI-MSI investigations of the *R. similis* susceptible cultivar Grande Naine (GN) and the resistant cultivar Yangambi Km5 (YKm5), anigorufones and other phenylphenalenone-type compounds have been localized in the region of nematode infection, whereas no distinguishable MS signals were obtained in uninfected tissue. In both *Musa* spp., similar compounds have been detected against the assumption of varying phytochemical profiles causing the different susceptibilities to *R. similis* (Figure 5.5). However, the proton nuclear magnetic resonance (^{1}H NMR) spectroscopy and Ultra High Performance Liquid Chromatography mass spectrometry

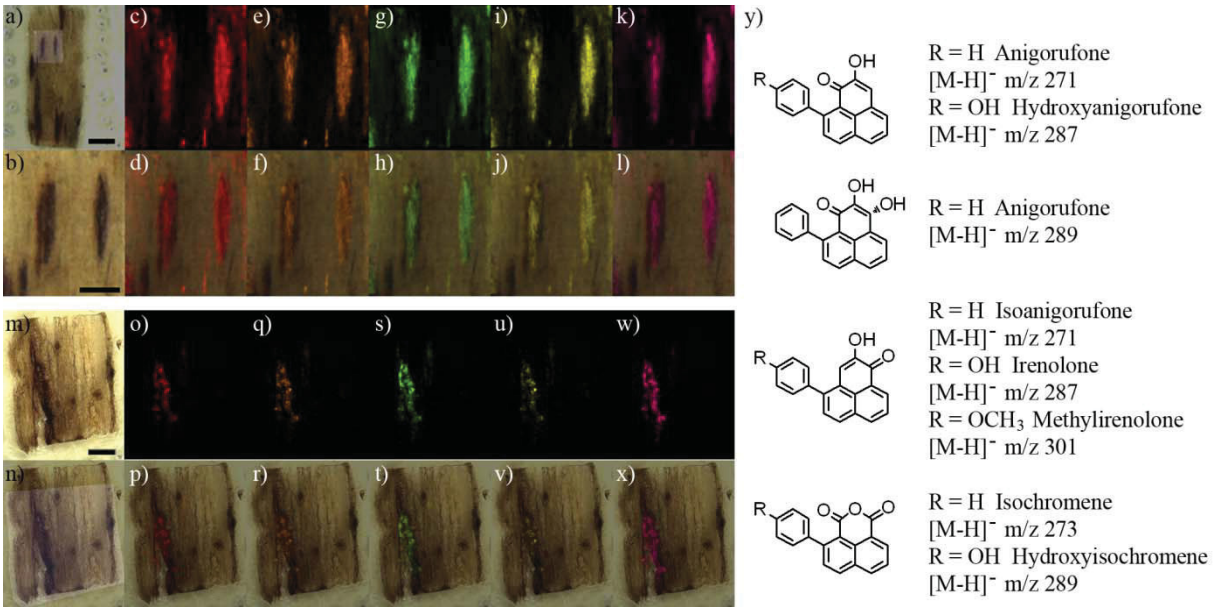

Figure 5.5. a) *Musa* Ykm5 root section (bar = 1 mm), b) zoom into the LDI-MSI measurement region (bar = 500 µm). Molecular images of the *m/z* values c) 271, e) 273, g) 287, i) 289 and k) 301. Overlay of molecular and optical image of the m/z values d) 271, f) 273, h) 287, j) 289 and l) 301. m) *Musa* Grande Naine root section (bar = 1 mm), n) designation of the measurement region. Molecular images for the m/z values o) 271, q) 273, s) 287, u) 289 and w) 301. Overlay of molecular and optical image of the m/z values p) 271, r) 273, t) 287, v) 289 and x) 301. y) Chemical structures and ion masses of anigorufone and related phenylphenalenones. A measurement raster of 10×10 µm was applied.

(UHPLC-MS) based analysis of extracts of both cultivars showed that the resistant cultivar Ykm5 is able to produce the anigorufone and other phytoalexines in higher concentrations. Therewith, a nematode-toxic cellular environment is created leading to the different responses to the nematode. With this investigation the non-quantitative character, which is the main weakness of the LDI-MSI method, is illustrated and demonstrates that complementary methods are necessary to complete the image obtained by this technique.

Secondary metabolites are not only produced by plants to protect against herbivores; they also play a role in the reproduction process. Manifold colored compounds, mainly substances of the flavonoid and carotenoid family, are produced in the petals to attract pollinators. However, hidden from the visible spectrum of human eyes, plants produce guidelines on the petals for UV sensitive insects to lead them to the nectar within the flower.[152,153] The single petals show on the front side a UV active base that forms within the flower a bicolored pattern around the nectar source, the so-called bull's eye. This characteristic can be visualized by staining in ammonia vapor, where the flavonoid compounds undergo a color change most probably due to the change of pH.[154] By LDI-MSI investigations these "honey guidelines" were visualized, and different chalcone and aurone compounds have been localized in the basal part of the petal (representative compounds are depicted in Figure 5.6). The significant different mass spectra obtained for the two regions of the petal are depicted in Figure 5.6. Clearly, the flavonoid attributed signals are only observed in the lower part of the petal. To

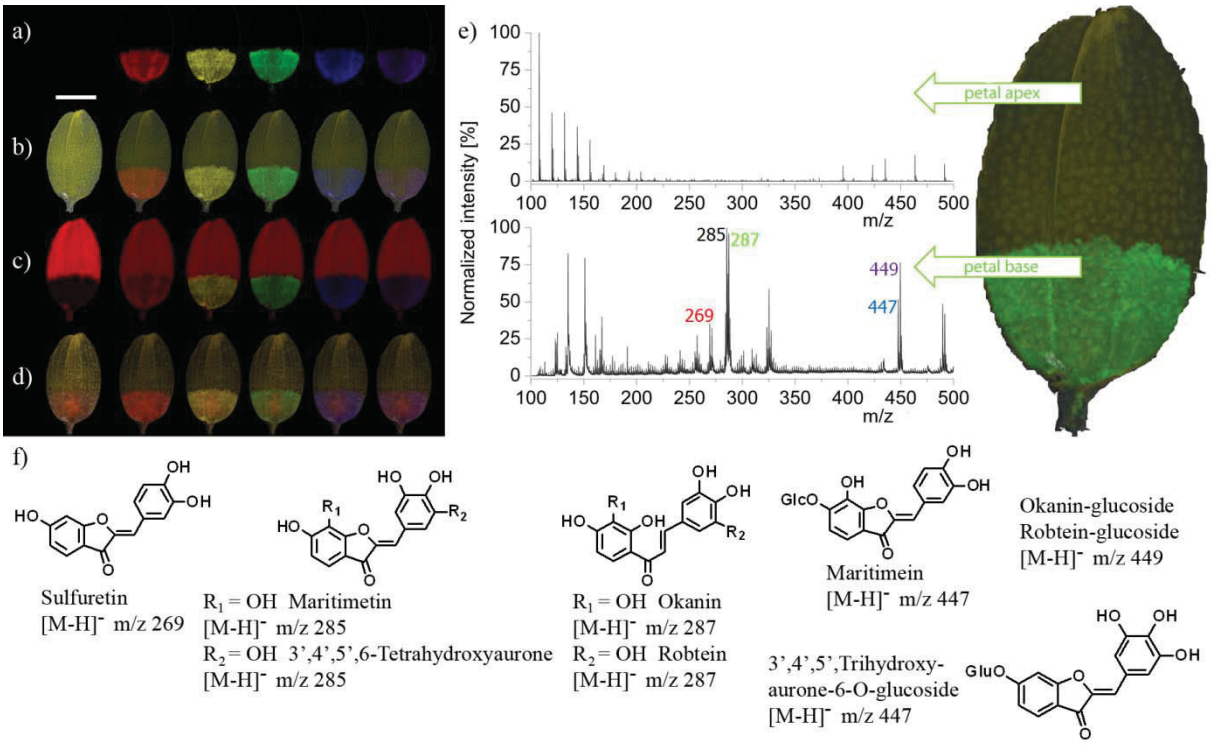

Figure 5.6. a) Molecular images of chalcones and aurones on *Bidens ferulifolia* petals with the color code m/z 269 red, m/z 285 yellow, m/z 287 green, m/z 447 blue, m/z 449 violett, b) overlay of daylight photo and molecular image (bar = 1 mm), c) overlay of UV photo and molecular image, d) overlay of ammonia staining and molecular image, e) representative mass spectra of the petal apex and the petal base as well as f) chemical structures and ion masses of the detected chalcones and aurones. A measurement raster of 75×75 µm was applied.

further confirm the structures of the assigned compounds, collision induced dissociation (CID) investigations have been performed on the petal and with reference compounds.

A directing implication for pollinators is also assumed for the pattern of UV-absorbing flavonoids on *Arabidopsis thaliana* (thale cress). Petals of the model organism in plant biology and genetics were investigated by LDI-MSI and revealed also an apex-basal pattern of analyte distribution (Figure 5.7). Kaempferols and Quercetins of the flavonol family with different degrees of glycosidation have been detected on the petal. Different spatial distributions of the kaempferol compounds in the upper petal and of the quercetin derivatives in the basal petal have been observed as reported earlier in a study using colloidal-graphit assisted LDI (GALDI) MSI to investigate the lipid and flavonoid distribution in the *A. thaliana* petal.[155] The localization of the analytes in different petal parts was attributed to maturation effects allowing the hydroxylation at the 3' position in the B-ring only after the enzyme flavonoid 3'-hydroxylase was biosynthesized.

In conclusion, secondary metabolites of various plant species with different functions and distribution pattern have been localized directly and without pretreatment of the material by the LDI-MSI method. Although no quantitative information can be obtained a good image of the distribution of various analytes was achieved within the biological material. The matrix-

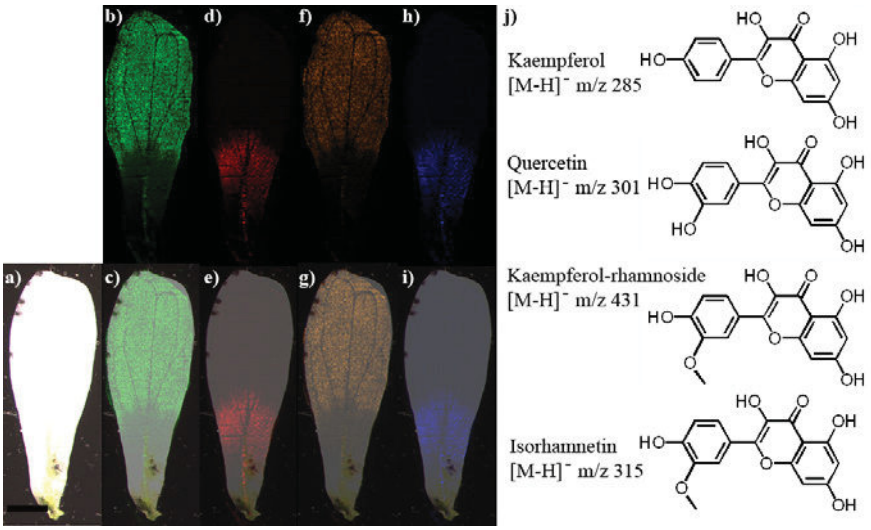

Figure 5.7. a) Petal of *Arabidopsis thaliana* (bar = 200 µm), molecular images of b) m/z 285, d) m/z 301, f) m/z 431 and h) m/z 315. Overlay of the molecular and optical images of c) m/z 285, e) m/z 301, g) m/z 431 and i) m/z 315 as well as j) chemical structures and ion masses of the detected flavonols. A measurement raster of 10×10 µm was applied.

free LDI approach allows the detection of π-system containing compounds on a cellular level, as the measurement raster can be downsized to the diameter of the laser (10 µm). As the probes do not require any pretreatment the direct analysis of fresh plant material is enabled resulting in unbiased images of the biodistribution of the metabolites.

6. Summary

The directed delivery of highly active and toxic drug molecules, to improve their therapeutic index by passive and active targeting, gained enormous attention in the last two decades. Unimolecular micellar systems have been pointed out as superior polymeric drug delivery systems (DDSs) in comparison to conventional micelles as they do not possess a critical micelle concentration. However, the implementation in pharmaceutical applications requires a thorough characterization of the drug and the polymer to enable a reproducible and reliable usage in the human body. Matrix-assisted laser desorption/ionization-time of flight mass spectrometry (MALDI-TOF MS) represents the method of choice to obtain mass related as well as spatially resolved information of relevant molecules. Within this thesis star-shaped amphiphilic polymers have been investigated as unimolecular DDSs. Advanced characterization methods in mass spectrometry have been applied for a detailed characterization such as collision induced dissociation (CID) for the polymer analysis and imaging techniques as localization tool for drug molecules.

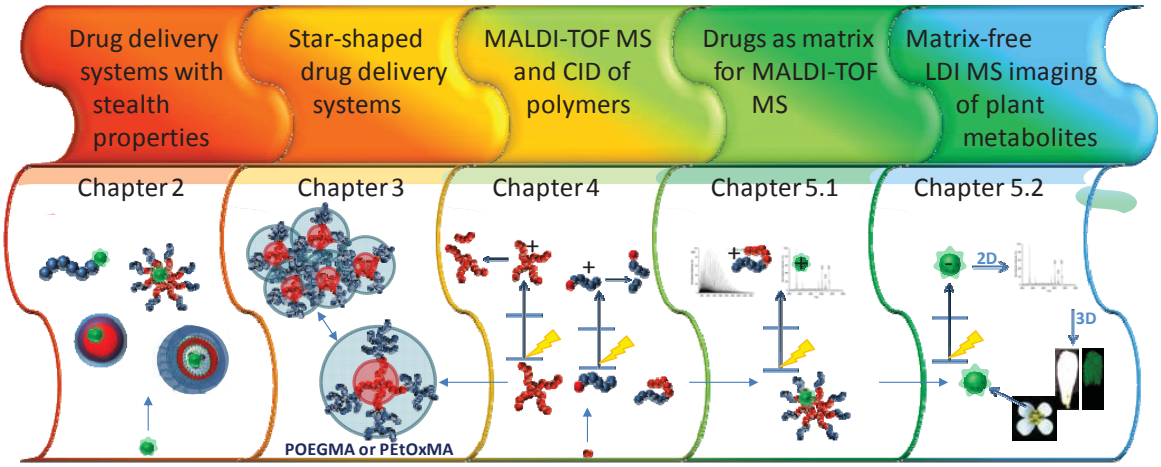

Scheme 6.1. Schematical representation of the summary and the contextual interconnection of the discussed contents within this thesis.

Four-arm star-shaped poly(*ε*-caprolactone) (PCL) macroinitiators have been used for the polymerization of hydrophilic macromonomers (oligo(ethylene glycol)methacrylates (OEGMA) and oligo(2-ethyl-2-oxazoline)methacrylates (OEtOxMA)), which form a comb like outer shell around the hydrophobic PCL core. The resulting amphiphilic block copolymers with different PCL core sizes and various lengths of the hydrophilic backbone as well as of the comb arms of the hydrophilic shell were investigated as DDSs. The unimolecular behavior in aqueous environment of the polymers was proven by spectroscopic investigations with pyrene and nile red as fluorescent probes as well as thermodynamic measurements by means of isothermal titration calorimetry. It was found that even for a hydrophilic/lipophilic balance of as small as 0.8, unimolecular micelles are present in water. These results demonstrate the efficiency of the chosen architecture to stabilize hydrophobic cores in water. The biological compatibility of the polymers has been verified in several *in*

vitro experiments, allowing the conclusion that none of the polymers shows cytotoxic effects or adverse reactions in the blood such as *i.e.* hemolysis, influence on the coagulation or activation of the immune system by the complement cascade. An antifungal drug and the anti-cancer drug doxorubicin have been successfully encapsulated into the star-shaped DDS and its release and efficiency was proven in mycobacterial tests and cytotoxicity experiments, respectively.

For the enhanced characterization in MALDI-TOF MS different pharmaceutically relevant polymers were submitted to CID investigations, such as the afore mentioned poly(ethylene glycol) (PEG), poly(2-ethy-2-oxazoline), PCL and poly(ethylene imine). A successful end group analyses was performed and the fragmentation mechanism for the different polymer classes was elucidated. The 1,4-hydrogen elimination was found as predominating mechanism for all polymers bearing a heteroatom in the main chain. In contrast, esters and polyesters prefer a 1,5-hydrogen transfer (McLafferty+1 rearrangement) as main fragmentation route.

The matrix plays a crucial role in MALDI-TOF MS investigations. As matrix molecules are generally UV-active and π-systems bearing aromatic compounds, drug molecules, such as madurahydroxylactone, tetrakis(4-hydroxyphenyl)-porphyrine, chartreusin, amphotericin B and retinoic acid, have been investigated and proven to act as matrix in the MALDI process for different polymer classes. Furthermore, the drugs have been encapsulated into a classical micellar system assembled by a linear PEG-*b*-PCL block copolymer, to detect in a matrix-free LDI MS set-up the drug as well as the carrier system. However, for the tetrakis(4-hydroxyphenyl)-porphyrine containing micellar system the drug as well as the block copolymer has been detected successfully.

The LDI-MS approach was also used to detect drugs of herbal origin at their point of provenance in the plant tissue. The π-system containing secondary metabolites have been localized by an LDI-MS imaging (LDI-MSI) set-up in different plants and plant parts, revealing, therewith, the multitude of functions of secondary plant metabolites. The characteristic of this newly established method is the high spatial resolution of the measurement down to the laser diameter allowing the detection of the analytes on a cellular level.

To conclude, unimolecular DDSs have been prepared by means of amphiphilic star-shaped block copolymers with a brush-like shell. Investigations on the biological compatibility and drug inclusion efficiencies proved their applicability as drug carrier. The advanced characterization by MALDI-TOF MS and CID was shown for pharmaceutical relevant polymers and drug molecules. The drug molecules were additionally evaluated as matrix for the MALDI process. The approach to use aromatic compounds in a matrix-free set-up enabled the spatially resolved detection of secondary metabolites in plant material.

Future research will focus on the improvement of the star-shaped DDSs by active targeting and increase of the loading capacity. Additionally to the encapsulation of doxorubicin further anti-cancer drugs will be encapsulated. A broad basis for different anti-

cancer drugs should be established to enable also a combined therapy. The up to date performed MALDI-TOF MS investigations will be used to explore this method as elucidation procedure for architectural features of polymers. Basing on the matrix investigations with drug molecules *in vitro* and *in vivo* MSI experiments will be pursued to detect the drug and the drug delivery system in action. The LDI-MSI approach for the detection of secondary plant metabolites will be expanded by a solvent-free matrix application to increase on the on hand the classes of analytes and to maintain, on the other hand, the high spatial resolution of the measurement.

7. Zusammenfassung

In den letzten zwei Jahrzehnten gewann die zielgerichtete Verabreichung von hochaktiven Medikamenten, durch so genanntes aktives und passives *targeting* zur Erhöhung der therapeutischen Breite, enorm an Bedeutung. Unimolekulare Mizellen wurden dabei, im Vergleich zu konventionellen Mizellen, als überlegene Wirkstofftransportsysteme erkannt, da sie keine kritische Mizellbildungskonzentration aufweisen. Nichtsdestotrotz, erfordert die Anwendung in pharmazeutischen Bereichen eine tiefgreifende Charakterisierung von Medikamentmolekülen und Polymeren, um eine reproduzierbare Wirkung im menschlichen Körper zu erreichen. Matrix-unterstützte Laser Desorption/Ionisierung Flugzeit Massenspektrometrie (englisch *matrix-assisted laser desorption/ionization-time of flight mass spectrometry* (MALDI-TOF MS)) ist die Methode der Wahl, um massenbezogene und räumlich aufgelöste Informationen von relevanten Molekülen zu erhalten. In dieser Arbeit wurden sternförmige amphiphile Polymere als unimolekulare Wirkstofftransportsysteme untersucht und hochentwickelte massenspektrometrische Methoden angewandt, wie die Kollisionsinduzierte Dissoziation (englisch *collision-induced dissociation* (CID)) von Polymeren oder bildgebende Verfahren zur räumlich aufgelösten Darstellung von Sekundärmetaboliten und Wirkstoffmolekülen.

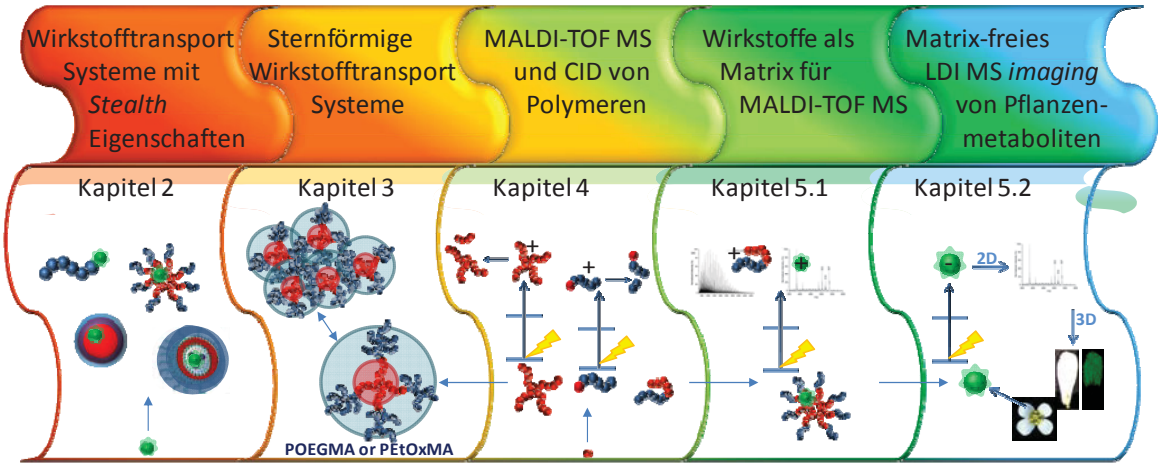

Schema 7.1. Schematischer Überblick der Zusammenfassung sowie der thematische Zusammenhang der einzelnen Themenkomplexe dieser Arbeit.

Vierarmige sternförmige Poly(ε-caprolakton) (PCL) Makroinitiatoren wurden zur Polymerisation von hydrophilen Makromonomeren verwendet (Oligo(ethylenglykol)-methacrylat (OEGMA) und Oligo(2-ethyl-2-oxazolin)methacrylate (OEtOxMA)), welche eine Kamm-förmige Hülle um den hydrophoben PCL Kern bilden. Es wurden amphiphile Kamm-Blockcopolymere mit verschiedenen Kerngrößen und unterschiedlichen Längen des Methacrylatrückkrates und der Seitenkette erhalten. Diese Polymere wurden auf ihre Eignung als Wirkstoff-Transport-Systeme untersucht. Das unimolekulare Verhalten der Polymere in wässriger Lösung konnte durch spektroskopische Untersuchungen mit Pyren und Nilrot als Fluoreszenzsonden und thermodynamische Messungen mittels isothermer

Titrationskalorimetrie bewiesen werden. Es konnte gezeigt werden, dass auch ein HLB Wert (engl. *hydrophilic/lipophilic balance* (HLB)) von 0,8 ausreicht, um die hydrophoben Kerne mit der Kammarchitektur der hydrophilen Hülle als unimolekulare Mizellen in Wasser zu stabilisieren. Die biologische Anwendbarkeit konnte durch zahlreiche *in vitro* Kompatibilitätstests bewiesen werden. So zeigt keines der Polymere zytotoxische Eigenschaften oder Nebenreaktionen mit dem Blut, z.B. Hemolyse, Verzögerung der Blutgerinnung oder Komplementaktivierung. Sowohl ein Fungizidwirkstoff als auch das Krebstherapeutikum Doxorubicin wurden in die Stern-förmigen Transportsysteme eingeschlossen und deren erfolgreiche Freisetzung konnte in Mycobakterientests und Zytotoxizitätsstudien nachgewiesen werden.

Zur Polymercharakterisierung mit Hilfe der MALDI-TOF MS wurden verschiedene pharmazeutisch relevante Polymere herangezogen: Poly(ethylenglykol) (PEG), Poly(2-ethyl-2-oxazolin) (PEtOx), Poly(ethylenimin) (PEI) and PCL. Sowohl die Endgruppenanalyse als auch die Aufklärung des Fragmentierungsmechanismus der verschiedenen Polymerklassen konnte erfolgreich durchgeführt werden. Für Polymere mit einem Heteroatom in der Hauptkette konnte hierbei die 1,4-Wasserstoff-Eliminierung als vorrangiger Mechanismus festgestellt werden. Ester und Polyester fragmentieren hingegen bevorzugt nach einem 1,5-Wasserstoffübertragungsmechanismus (McLafferty+1 Umlagerung).

Die Matrix hat bei MALDI-TOF MS Messungen einen entscheidenden Einfluss auf das Gelingen einer Messung. Da Matrix-Moleküle in der Regel kleine aromatische Verbindungen sind, wurden UV-aktive, π-System tragende Wirkstoffmoleküle, wie Madurahydroxylakton (MHL), Tetrakis(4-hydroxyphenyl)-porphyrin (THP), Chartreusin (Chart), Amphotericin B (AmB) und Retinsäure (RA) auf ihre unterstützende Wirkung im MALDI Prozess hin untersucht. Für alle Moleküle konnte eine Matrix-Wirkung nachgewiesen werden. Zusätzlich wurden diese Wirkstoffmoleküle mittels eines klassischen Mizellsystems eingeschlossen, welches durch ein lineares PEG-*b*-PCL Blockcopolymer gebildet wurde. In einem Matrix-freien LDI Ansatz sollten das Medikamentmolekül und das Wirkstofftransportsystem nachgewiesen werden. Jedoch konnte nur für das THP enthaltende mizellare System sowohl das Medikament als auch das Blockcopolymer nachgewiesen werden.

Der LDI-MS Ansatz konnte nicht nur genutzt werden, um Wirkstoffmoleküle in ihrem Transportsystem nachzuweisen, er wurde auch dazu verwendet, Wirkstoffmoleküle pflanzlichen Ursprungs an seinem Herkunftssort, dem jeweiligen Pflanzengewebe, zu detektieren. π-System enthaltende Moleküle wurden durch LDI-bildgebende Massenspektrometrie (LDI-MS imaging (LDI-MSI)) in verschiedenen Pflanzen und Pflanzenteilen räumlich aufgelöst nachgewiesen und zeigten damit die Bandbreite an Funktionen, die von Sekundärmetaboliten übernommen werden, auf. Der entscheidende Vorteil dieser Methode gegenüber der klassischen MALDI-TOF MSI liegt im Matrix-freien Messen, welches eine hohe räumliche Auflösung, nur beschränkt durch den Durchmesser des Laserstrahls, auf zellulärer Ebene erlaubt.

Zusammenfassend konnten unimolekulare Wirkstofftransportsysteme mittels amphiphiler sternförmiger Blockcopolymere mit einer Kammarchitektur der hydrophilen Hülle hergestellt

werden. Sowohl die biologische Kompatibilität als auch der Einschluss eines Wirkstoffmoleküles beweisen deren Eignung als Wirkstofftransportsystem. MALDI-TOF MS Untersuchungen konnten an pharmazeutisch relevanten Polymeren und Wirkstoffmolekülen durchgeführt werden, welche auch auf ihre Matrixeigenschaften hin untersucht wurden. Der Matrix-freie LDI Ansatz für aromatische Verbindungen konnte auch auf die bildgebende Massenspektrometrie von pflanzlichen Sekundärmetaboliten übertragen werden.

Zukünftige Forschungen werden sich mit der Verbesserung der Wirkstoff-transportsysteme durch aktives *targeting* und die Erhöhung der Beladungseffizienzen beschäftigen. Der Einschluss und Transport weiterer Krebstherapeutika soll etabliert werden, um kombinierte Krebstherapien zu ermöglichen. Die bisher durchgeführten MALDI-TOF MS Experimente sollen dafür genutzt werden, um architektonische Besonderheiten von Polymeren aufzuklären. Ausgehend von den Matrix-Untersuchungen von Wirkstoffmolekülen können *in vitro* und *in vivo* Experimente dazu dienen sowohl den Wirkstoff als auch das Wirkstofftransportsystem in seinem tatsächlichen Wirkungsfeld zu lokalisieren. Der LDI-MSI Ansatz zum Nachweis von Sekundärmetaboliten soll mit einer Lösungsmittelfreien Matrixauftragung erweitert werden, um einerseits die Anzahl möglicher Metabolitklassen zu erhöhen und um andererseits die räumliche Auflösung der Messung nicht einzuschränken.

8. References

[1] T. M. Allen, P. R. Cullis, *Science* **2004**, *303*, 1818–1822.
[2] R. Duncan, *Nat. Rev. Drug Discov.* **2003**, *2*, 347–360.
[3] E. Cukierman, D. R. Khan, *Biochem. Pharmacol.* **2010**, *80*, 762–770.
[4] P. L. Soo, M. Dunne, J. Liu, C. Allen, *Nanotechnology in Drug Delivery*, Springer, **2009**.
[5] R. Haag, F. Kratz, *Angew. Chem. Int. Ed.* **2006**, *45*, 1198–1215.
[6] K. E. Uhrich, S. M. Cannizzaro, R. S. Langer, K. M. Shakesheff, *Chem. Rev.* **1999**, *99*, 3181–3198.
[7] M. Wang, M. Thanou, *Pharm. Res.* **2010**, *62*, 90–99.
[8] D. D. Lasic, D. Needham, *Chem. Rev.* **1995**, *95*, 2601–2628.
[9] U. Kedar, P. Phutane, S. Shidhaye, V. Kadam, *Nanomed. Nanotech. Biol. Med.* **2010**, *6*, 714–729.
[10] D. Bhadra, S. Bahdra, P. Jain, N. K. Jain, *Pharmazie* **2002**, *1*, 5–28.
[11] J. M. Harris, R. B. Chess, *Nat. Rev. Drug Discov.* **2003**, *2*, 214–221.
[12] M. Barz, R. Luxenhofer, R. Zentel, M. J. Vicent, *Polym. Chem.* **2011**, *2*, 1900–1918.
[13] V. P. Torchilin, V. S. Trubetskoy, *Adv. Drug Delivery Rev.* **1995**, *16*, 141–155.
[14] F. M. Veronese, G. Pasut, *Drug Discov. Today* **2005**, *10*, 1451–1458.
[15] H. K. Nguyen, P. Lemieux, S. V Vinogradov, C. L. Gebhart, N. Guérin, G. Paradis, T. K. Bronich, V. Y. Alakhov, A. V Kabanov, *Gene Ther.* **2000**, *7*, 126–138.
[16] M. Nicolaou, P. Chang, M. J. Newman, *Polymeric Gene Delivery*, CRC Press, **2005**.
[17] M. Ogris, S. Brunner, S. Schüller, R. Kircheis, E. Wagner, *Gene Ther.* **1999**, *6*, 595–605.
[18] D. Oupicky, M. Ogris, K. A. Howard, P. R. Dash, K. Ulbrich, L. W. Seymour, *Mol. Ther.* **2002**, *5*, 463–472.
[19] K. Knop, R. Hoogenboom, D. Fischer, U. S. Schubert, *Angew. Chem. Int. Ed.* **2010**, *49*, 6288–6308.
[20] C. Li, S. Wallace, *Adv. Drug Delivery Rev.* **2008**, *60*, 886–898.
[21] B. Romberg, J. M. Metselaar, L. Baranyi, C. J. Snel, R. Bunger, W. E. Hennink, J. Szebeni, G. Storm, *Int. J. Pharm.* **2007**, *331*, 186–189.
[22] O. Hovorka, T. Etrych, V. Subr, J. Strohalm, K. Ulbrich, B. Rihova, *J. Drug Target.* **2006**, *14*, 391–403.
[23] G. S. Kwon, K. Kataoka, *Adv. Drug Delivery Rev.* **1995**, *16*, 295–309.
[24] K. Letchford, H. Burt, *Eur. J. Pharm. Biopharm.* **2007**, *65*, 259–269.
[25] S. M. A. B. Batoy, E. Akhmetova, S. Miladinovic, J. Smeal, C. L. Wilkins, *Appl. Spectrosc. Rev.* **2008**, *43*, 485–550.
[26] K. Dreisewerd, *Chem. Rev.* **2003**, *103*, 395–426.
[27] L. A. McDonnell, R. M. A. Heeren, *Mass Spectrom. Rev.* **2007**, *26*, 606–643.
[28] C. A. Lipinski, *J. Pharmacol. Toxicol.* **2000**, *44*, 235–249.
[29] M. Hamidi, M. A. Shahbazi, K. Rostamizadeh, *Macromol. Biosci.* **2012**, *12*, 144–164.
[30] N. Larson, H. Ghandehari, *Chem. Mater.* **2012**, *24*, 840–853.
[31] J. Khandare, M. Calderón, N. M. Dagia, R. Haag, *Chem. Soc. Rev.* **2012**, *41*, 2824–2848.
[32] S. Schubert, J. Delaney, U. S. Schubert, *Soft Matter* **2011**, *7*, 1581–1588.
[33] Y. Matsumura, H. Maeda, *Cancer Res.* **1986**, *46*, 6387–6392.
[34] H. Maeda, J. Wu, T. Sawa, Y. Matsumura, K. Hori, *J. Controll. Release* **2000**, *65*, 271–284.

[35] J. Fang, H. Nakamura, H. Maeda, *Adv. Drug Delivery Rev.* **2011**, *63*, 136–151.
[36] K. Greish, *J. Drug Target.* **2008**, *15*, 457–644.
[37] Y. Matsumura, K. Kataoka, *Cancer Sci.* **2009**, *100*, 572–579.
[38] Y. Matsumura, H. Maeda, *Cancer Res.* **1986**, *46*, 6387–6392.
[39] S.-E. Stiriba, H. Kautz, H. Frey, *J. Am. Chem. Soc.* **2002**, *124*, 9698–9699.
[40] R. K. Kainthan, D. E. Brooks, *Biomaterials* **2007**, *28*, 4779–4787.
[41] R. K. Kainthan, S. R. Hester, E. Levin, D. V Devine, D. E. Brooks, *Biomaterials* **2007**, *28*, 4581–4590.
[42] J. Pytela, V. Saudek, J. Drobnik, F. Rypacek, *J. Controll. Release* **1989**, *10*, 17–25.
[43] B. Romberg, C. Oussoren, C. J. Snel, M. G. Carstens, W. E. Hennink, G. Storm, *BBA-Biomembranes* **2007**, *1768*, 737–743.
[44] M. Stach, I. Lacik, J. D. Chorvat, M. Buback, P. Hesse, R. A. Hutchinson, L. Tang, *Macromolecules* **2008**, *41*, 5174–5185.
[45] V. P. Torchilin, V. Trubetskoy, K. R. Whiteman, P. Caliceti, P. Ferruti, F. M. Veronese, *J. Pharm. Sci.* **1995**, *84*, 1049–1053.
[46] D. Le Garrec, J. Taillefer, J. E. Van Lier, V. Lenaert, J.-C. Leroux, *J. Drug Target.* **2002**, *10*, 429–437.
[47] R. Duncan, *Nat. Rev. Cancer* **2006**, *6*, 688–701.
[48] Z.-B. Zheng, G. Zhu, H. Tak, E. Joseph, J. L. Eiseman, D. J. Creighton, *Bioconjugate Chem.* **2005**, *16*, 598–607.
[49] Y. Kasuya, Z.-R. Lu, P. Kopeckova, T. Minko, S. E. Tabibi, J. Kopecek, *J. Controll. Release* **2001**, *74*, 203–211.
[50] D. A. Tomalia, D. P. Sheetz, *J. Polym. Sci., Part A: Polym. Chem.* **1966**, *4*, 2253–2265.
[51] W. Seeliger, E. Aufderhaar, W. Diepers, R. Feinauer, R. Nehring, W. Thier, H. Hellmann, *Angew. Chem.* **1966**, *78*, 913–952.
[52] T. Kagiya, S. Narisawa, T. Maeda, K. Fukui, *J. Polym. Sci. Polym. Lett.* **1966**, *4*, 441–445.
[53] T. G. Bassiri, A. Levy, M. Litt, *J. Polym. Sci. Polym. Lett.* **1967**, *5*, 871–879.
[54] S. Kobayashi, *Prog. Polym. Sci.* **1990**, *15*, 751–823.
[55] F. Wiesbrock, R. Hoogenboom, M. A. M. Leenen, M. A. R. Meier, U. S. Schubert, *Macromolecules* **2005**, *38*, 5025–5034.
[56] N. Adams, U. S. Schubert, *Adv. Drug Delivery Rev.* **2007**, *59*, 1504–1520.
[57] R. Hoogenboom, *Angew. Chem. Int. Ed.* **2009**, *48*, 7978–7997.
[58] F. M. Veronese, A. Mero, G. Pasut, Z. Fang, T. X. Viegas, in *36th Ann. Meeting & Exposition CRS*, **2009**.
[59] M. Bauer, C. Lautenschlaeger, K. Kempe, L. Tauhardt, U. S. Schubert, D. Fischer, *Macromol. Biosci.* **2012**, 986–998.
[60] J. Kronek, Z. Kroneková, J. Lustoň, E. Paulovičová, L. Paulovičová, B. Mendrek, *J. Mater. Sci. - Mater. Med.* **2011**, *22*, 1725–1734.
[61] J. Kronek, E. Paulovičová, L. Paulovičová, Z. Kroneková, J. Lustoň, *J. Mater. Sci. - Mater. Med.* **2012**, *23*, 1457–1464.
[62] R. Luxenhofer, G. Sahay, A. Schulz, D. Alakhova, T. K. Bronich, R. Jordan, A. V Kabanov, *J. Controll. Release* **2011**, *153*, 73–82.
[63] C.-H. Wang, C.-H. Wang, G.-H. Hsiue, *J. Controll. Release* **2005**, *108*, 140–149.
[64] S. C. Lee, C. Kim, I. C. Kwon, H. Chung, S. Y. Jeong, *J. Controll. Release* **2003**, *89*, 437–446.
[65] R. Luxenhofer, A. Schulz, C. Roques, S. Li, T. K. Bronich, E. V Batrakova, R. Jordan, A. V Kabanov, *Biomaterials* **2010**, *31*, 4972–4979.
[66] M. C. Woodle, C. M. Engbers, S. Zalipsky, *Bioconjugate Chem.* **1994**, *5*, 493–496.
[67] S. Zalpinsky, C. B. Hansen, J. M. Oaks, T. M. Allen, *J. Pharm. Sci.* **1996**, *85*, 133–137.

[68] F. C. Gaertner, R. Luxenhofer, B. Blechert, R. Jordan, M. Essler, *J. Controll. Release* **2007**, *119*, 291–300.
[69] V. Lassalle, M. L. Ferreira, *Macromol. Biosci.* **2007**, *7*, 767–783.
[70] A. Kumari, S. K. Yadav, S. C. Yadav, *Colloids Surf., B* **2010**, *75*, 1–18.
[71] S. Fredenberg, M. Wahlgren, M. Reslow, A. Axelsson, *Int. J. Pharm.* **2011**, *415*, 34–52.
[72] W. Jiang, B. Y. S. Kim, J. T. Rutka, W. C. W. Chan, *Expert Opin. Drug Deliv.* **2007**, *4*, 621–634.
[73] M. L. Immordino, F. Dosio, L. Cattel, *Int. J. Nanomedicine* **2006**, *1*, 297–315.
[74] D. K. Sarker, *Curr. Drug Discov. Technol.* **2009**, *6*, 52–58.
[75] A. A. Al-Angary, M. A. Bayomi, S. H. Khidr, M. A. Al-Meshal, M. Al-Dardiri, *Int. J. Pharm.* **1995**, *114*, 221–225.
[76] J. F. Gohy, *Adv. Polym. Sci.* **2005**, *190*, 65–136.
[77] S. C. Owen, D. P. Y. Chan, M. S. Shoichet, *Nano Today* **2012**, *7*, 53–65.
[78] R. Savić, T. Azzam, A. Eisenberg, D. Maysinger, *Langmuir* **2006**, *22*, 3570–3578.
[79] G. R. Newkome, C. N. Moorefield, G. R. Baker, A. L. Johnson, R. K. Behera, *Angew. Chem. Int. Ed.* **1991**, *30*, 1176–1178.
[80] S. Kim, Y. Shi, J. Y. Kim, K. Park, J.-X. Cheng, *Expert Opin. Drug Deliv.* **2010**, *7*, 49–62.
[81] H. Liu, Y. Chen, D. Zhu, Z. Shen, S.-E. Stiriba, *React. Funct. Polym.* **2007**, *67*, 383–395.
[82] C. Kojima, K. Kono, K. Maruyama, T. Takagishi, *Bioconjugate Chem.* **2000**, *11*, 910–917.
[83] X. Yang, J. J. Grailer, S. Pilla, D. A. Steeber, S. Gong, *Bioconjugate Chem.* **2010**, *21*, 496–504.
[84] M. Prabaharan, J. J. Grailer, S. Pilla, D. A. Steeber, S. Gong, *Biomaterials* **2009**, *30*, 3009–3019.
[85] F. Wang, T. K. Bronich, A. V Kabanov, R. D. Rauh, J. Roovers, *Bioconjugate Chem.* **2005**, *16*, 397–405.
[86] X. Li, Y. Qian, T. Liu, X. Hu, G. Zhang, Y. You, S. Liu, *Biomaterials* **2011**, *32*, 6595–6605.
[87] W. Yuan, J. Zhang, J. Wei, H. Yuan, J. Ren, *J. Polym. Sci., Part A: Polym. Chem.* **2011**, *49*, 4071–4080.
[88] M. Deng, X. Chen, L. Piao, X. Zhang, Z. Dai, X. Jing, *J. Polym. Sci., Part A: Polym. Chem.* **2004**, *42*, 950–959.
[89] M. R. Nabid, S. J. Tabatabaei Rezaei, R. Sedghi, H. Niknejad, A. A. Entezami, H. A. Oskooie, M. M. Heravi, *Polymer* **2011**, *52*, 2799–2809.
[90] O. G. Schramm, G. M. Pavlov, H. P. van Erp, M. A. R. Meier, R. Hoogenboom, U. S. Schubert, *Macromolecules* **2009**, *42*, 1808–1816.
[91] O. G. Schramm, M. A. R. Meier, R. Hoogenboom, H. P. van Erp, J.-F. Gohy, U. S. Schubert, *Soft Matter* **2009**, *5*, 1662–1667.
[92] T. Ren, A. Wang, W. Yuan, L. Li, Y. Feng, *J. Polym. Sci., Part A: Polym. Chem.* **2011**, *49*, 2303–2313.
[93] C. Weber, C. R. Becer, A. Baumgaertel, R. Hoogenboom, U. S. Schubert, *Des. Monomers Polym.* **2009**, *12*, 149–165.
[94] C. Weber, C. R. Becer, R. Hoogenboom, U. S. Schubert, *Macromolecules* **2009**, *42*, 2965–2971.
[95] G. Gaucher, M. H. Dufresne, V. P. Sant, N. Kang, D. Maysinger, J. C. Leroux, *J. Controll. Release* **2005**, *109*, 169–188.
[96] M. L. Adams, A. Lavasanifar, G. S. Kwon, *J. Pharm. Sci.* **2003**, *92*, 1343–1355.

[97] X. B. Xiong, A. Falamarzian, S. M. Garg, A. Lavasanifar, *J. Controll. Release* **2011**, *155*, 248–261.
[98] M. Karas, F. Hillenkamp, *Anal. Chem.* **1988**, *60*, 2299–2301.
[99] K. Tanaka, H. Waki, Y. Ido, S. Akita, Y. Yoshida, T. Yoshida, *Rapid Commun. Mass Spectrom.* **1988**, *2*, 151–153.
[100] J. H. Scrivens, A. T. Jackson, *Int. J. Mass Spectrom.* **2000**, *200*, 261–276.
[101] A. C. Crecelius, A. Baumgaertel, U. S. Schubert, *Int. J. Mass Spectrom.* **2009**, *2009*, 1277–1286.
[102] C. Wesdemiotis, F. Pingitore, M. J. Polce, V. M. Russell, Y. Kim, C. M. Kausch, T. H. Connors, R. E. Medsker, R. R. Thomas, *Macromolecules* **2006**, *39*, 8369–8378.
[103] S. M. Weidner, J. Falkenhagen, S. Maltsev, V. Sauerland, M. Rinken, *Rapid Commun. Mass Spectrom.* **2007**, *21*, 2750–2758.
[104] S. M. Weidner, J. Falkenhagen, K. Knop, A. Thu, *Rapid Commun. Mass Spectrom.* **2009**, *23*, 2768–2774.
[105] A. Baumgaertel, E. Altuntaş, K. Kempe, A. Crecelius, U. S. Schubert, *J. Polym. Sci., Part A: Polym. Chem.* **2010**, *48*, 5533–5540.
[106] G. Montaudo, M. S. Montaudo, C. Puglisi, F. Samperi, *Macromolecules* **1995**, *28*, 4562–4569.
[107] S. Weidner, G. Kühn, *Rapid Commun. Mass Spectrom.* **1996**, *10*, 942–946.
[108] J. P. Williams, G. R. Hilton, K. Thalassinos, A. T. Jackson, J. H. Scrivens, *Rapid Commun. Mass Spectrom.* **2007**, *21*, 1693–1704.
[109] T. L. Selby, C. Wesdemiotis, R. P. Lattimer, *J. Am. Chem. Soc. Mass Spectrom.* **1994**, *5*, 1081–1092.
[110] A. T. Jackson, H. T. Yates, J. H. Scrivens, G. Critchley, J. Brown, M. R. Green, R. H. Bateman, *Rapid Commun. Mass Spectrom.* **1996**, *10*, 1668–1674.
[111] R. Luxenhofer, G. Sahay, A. Schulz, D. Alakhova, T. K. Bronich, R. Jordan, A. V Kabanov, *J. Controll. Release* **2011**, *153*, 73–82.
[112] W. T. Godbey, M. A. Barry, P. Saggau, K. K. Wu, A. G. Mikos, *J. Biomed. Mater. Res. Part B* **2000**, *51*, 321–328.
[113] B. Brissault, A. Kichler, C. Guis, C. Leborgne, O. Danos, H. Cheradame, *Bioconjugate Chem.* **2003**, *14*, 581–587.
[114] O. Boussif, F. Lezoualch, M. A. Zanta, M. D. Mergny, D. Schermant, B. Demeneixt, J. Behr, *Proc. Nat. Acad. Sci.* **1995**, *92*, 7297–7301.
[115] M. Neu, D. Fischer, T. Kissel, *J. Gene Med.* **2005**, *7*, 992–1009.
[116] J. H. Jeong, S. H. Song, D. W. Lim, H. Lee, T. G. Park, *J. Controll. Release* **2001**, *73*, 391–399.
[117] J. W. Wiseman, C. A. Goddard, D. McLelland, W. H. Colledge, *Gene Ther.* **2003**, *10*, 1654–1662.
[118] U. Lungwitz, M. Breunig, R. Liebl, T. Blunk, A. Goepferich, *Eur. J. Pharm. Biopharm.* **2008**, *69*, 134–148.
[119] Z. Zhong, J. Feijen, M. C. Lok, W. E. Hennink, L. V Christensen, J. W. Yockman, Y.-H. Kim, S. W. Kim, *Biomacromolecules* **2005**, *6*, 3440–3448.
[120] D. J. A. Cameron, M. P. Shaver, *Chem. Soc. Rev.* **2011**, *40*, 1761–1776.
[121] C. Jérôme, P. Lecomte, *Adv. Drug Delivery Rev.* **2008**, *60*, 1056–1076.
[122] C. Marchand, J. A. Beutler, A. Wamiru, S. Budihas, U. Möllmann, L. Heinisch, J. W. Mellors, S. F. Le Grice, Y. Pommier, *Antimicrob. Agents Chemother.* **2008**, *52*, 361–364.
[123] M. Badar, K. Hemmen, M. Nimtz, M. Stieve, M. Stiesch, T. Lenarz, H. Hauser, U. Möllmann, S. Vogt, M. Schnabelrauch, P. P. Mueller, *Open Biomed Eng J.* **2010**, *4*, 263–270.

[124] P. Jütten, W. Schumann, A. Härtl, L. Heinisch, U. Gräfe, W. Werner, H. Ulbricht, *Bioorg. Med. Chem. Lett.* **2002**, *12*, 1339–1342.
[125] W. An, Y. Jiao, C. Dong, C. Yang, Y. Inoue, S. Shuang, *Dyes Pigments* **2009**, *81*, 1–9.
[126] B. E. Leach, K. M. Calhoun, L. E. Johnson, C. M. Teeters, W. G. Jackson, *J. Am. Chem. Soc.* **1953**, *75*, 4011–4012.
[127] Z. Xu, K. Jakobi, K. Welzel, C. Hertweck, *Chem. Biol.* **2005**, *12*, 579–588.
[128] R. B. Greenwald, Y. H. Choe, J. McGuire, C. D. Conover, *Adv. Drug Delivery Rev.* **2003**, *55*, 217–250.
[129] W. Wu, S. Wieckowski, G. Pastorin, M. Benincasa, C. Klumpp, J.-P. Briand, R. Gennaro, M. Prato, A. Bianco, *Angew. Chem. Int. Ed.* **2005**, *44*, 6358–6362.
[130] P. Legrand, M. Chéron, L. Leroy, J. Bolard, *J. Drug Target.* **1997**, *4*, 311–319.
[131] H. Meng-er, Y. Yu-chen, C. Shu-rong, C. Jin-ren, L. Jia-Xiang, Z. Lin, G. Long-jun, W. Zhen-yi, *Blood* **1988**, *72*, 567–572.
[132] S. J. Wetzel, C. M. Guttman, J. E. Girard, *Int. J. Mass Spectrom.* **2004**, *238*, 215–225.
[133] J. W. Leon, J. M. J. Frechet, *Polym. Bull.* **1995**, *35*, 449–455.
[134] D. C. Schriemer, L. Li, *Anal. Chem.* **1996**, *68*, 2721–2725.
[135] D. C. Schriemer, L. Li, *Anal. Chem.* **1997**, *69*, 4169–4175.
[136] L. Przybilla, J.-D. Brand, K. Yoshimura, H. J. Raeder, K. Muellen, *Anal. Chem.* **2000**, *72*, 4591–4597.
[137] M. W. F. Nielen, *Mass Spectrom. Rev.* **1999**, *18*, 309–344.
[138] Y. C. Ling, L. Lin, Y. T. Chen, *Rapid Commun. Mass Spectrom.* **1998**, *12*, 317–327.
[139] T. Wingerath, D. Kirsch, B. Spengler, W. Stahl, *Anal. Biochem.* **1999**, *272*, 232–242.
[140] L. Beerhues, *Phytochemistry* **2006**, *67*, 2201–2207.
[141] F. Gaedcke, *Pharm. Unserer Zeit* **2003**, *2003*, 192–201.
[142] L. Bach-Rojecky, Z. Kalodjera, I. Samarzija, *Acta Pharm.* **2004**, *54*, 157–162.
[143] W. E. Müller, *Pharmacol. Res.* **2003**, *47*, 101–109.
[144] J. Patočka, *J. Appl. Biomed.* **2003**, *1*, 61–70.
[145] P. Agostinis, A. Vantieghem, W. Merlevede, P. A. M. de Witte, *Int. J. Biochem. Cell Biol.* **2002**, *34*, 221–41.
[146] N. Duran, P.-S. Song, *Photochem. Photobiol.* **1986**, *43*, 677–680.
[147] C. van Poznak, A. D. Seidman, M. M. Reidenberg, M. M. Moasser, N. Sklarin, K. Van Zee, P. Borgen, M. Gollub, D. Bacotti, T. J. Yao, R. Bloch, M. Ligueros, M. Sonenberg, L. Norton, C.Hudis, , *Breast Cancer Res. Treat.* **2001**, *66*, 239–248.
[148] F. Shidaifat, H. Canatan, S. K. Kulpa, Y. Sugimotoa, W. Y. Chang, Y. Zhang, R. W. Brueggemeier, W. J. Somersd, Y. C. Lin, *Cancer Lett.* **1996**, *107*, 37–44.
[149] G. P. Tuszynski, G. Cossu, *Cancer Res.* **1984**, *44*, 768–771.
[150] F. Otálvaro, F. Echeverri, W. Quinones, F. Torres, B. Schneider, *Molecules* **2002**, *7*, 331–340.
[151] F. Otálvaro, J. Nanclares, L. E. Vásquez, W. Quiñones, F. Echeverri, R. Arango, B. Schneider, *J. Nat. Prod.* **2007**, *70*, 887–890.
[152] R. Scogin, K. Zakar, *Biochem. Syst. Ecol.* **1976**, *4*, 165–167.
[153] J. B. Harborne, D. M. Smith, *Biochem. Syst. Ecol.* **1978**, *6*, 287–291.
[154] K. Schlangen, S. Miosic, A. Castro, K. Freudmann, M. Luczkiewicz, F. Vitzthum, W. Schwab, S. Gamsjäger, M. Musso, H. Halbwirth, *Phytochemistry* **2009**, *70*, 889–898.
[155] S. Cha, H. Zhang, H. I. Ilarslan, E. S. Wurtele, L. Brachova, B. J. Nikolau, E. S. Yeung, *Plant J.* **2008**, *55*, 348–360.

Supplementary information

Experimental section for Chapter 4

Materials

Tin(II) 2-ethylhexanoate (Aldrich) was used as received. ε-Caprolactone (Aldrich) was dried two days over CaH_2 previous to distillation and stored under argon. Pentaerythritol (Aldrich) and 6-bromo-1-hexanol (Aldrich) were coevaporated with toluene prior to use.

Instrumentation

Proton nuclear magnetic resonance (^{1}H NMR) spectra were recorded in $CDCl_3$ on a Bruker AC 250 MHz spectrometer at 298 K. Chemical shifts are given in parts per million (ppm, δ scale) relative to the residual signal of the deuterated solvent. Size exclusion chromatography (SEC) was performed on a Shimadzu system equipped with a SCL-10A system controller, a LC-10AD pump, and a RID-10A refractive index detector using a solvent mixture containing chloroform, triethylamine, and isopropyl alcohol (94:4:2) at a flow rate of 1 mL min^{-1} on a PSS-SDV-linear M 5 μm column. The system was calibrated with PMMA (410 to 88 000 g mol^{-1}) and PEG (440 to 44 700 g mol^{-1}) standards. MALDI-TOF MS and MS/MS spectra were recorded on an Ultraflex III TOF/TOF of Bruker Daltonics, Bremen, Germany equipped with a Nd:YAG laser and with trans-2-[3-(4-*tert*-butylphenyl)-2-methyl-2-propenylidene] malononitrile (DCTB) as matrix and sodium chlorid as ionizing agent in reflector mode. The instrument was calibrated prior to each measurement with an external PMMA standard from PSS Polymer Standards Services GmbH (Mainz, Germany).

Synthesis of 4-arm poly(ε-caprolactone) and linear poly(ε-caprolactone)

250 mg (1.8 mmol) pentaerythritol or 326 mg (1.8 mmol) of 6-bromo-1-hexanol were weighed into a flame-dried flask and 4.10 g (36 mmol) of ε-caprolactone were added. The quantity of tin(II) 2-ethylhexanoate catalyst, set to 1/20th of the initiating OH-groups. 117 μL (146 mg, 0.36 mmol) of tin(II) 2-ethylhexanoate was added subsequently to the pentaerythritol initiated reaction and 29 μL (37 mg, 0.09 mmol) of tin(II) 2-ethylhexanoate to the reaction initiated by 6-bromo-1-hexanol, respectively. The reaction mixtures were submitted to 3 freeze-pump-thaw-cycles and subsequently set under argon to assure a dry and inert atmosphere during the reaction at 80 °C overnight. The resulting highly viscous polymers were purified by precipitation from concentrated dichloromethane solution into cold methanol and dried in vacuum. The ^{1}H NMR spectra were used to calculate the actual arm length by comparison of the signals at 2.26 ppm with 3.58 ppm for the star-shaped PCL and at 3.64 ppm for the linear PCL, respectively.

4-arm poly(ε-caprolactone): ^{1}H NMR (250 MHz, $CDCl_3$): δ 4.01 (5H, m, CH_2-O), 3.58 (1H, m, CH_2-OH), 2.26 (5H, m, CO-CH_2), 1.60 (10H, m, $COCH_2$-CH_2-$CH_2CH_2CH_2O$ + $COCH_2CH_2CH_2$-CH_2-CH_2O), 1.34 (5H, m, $COCH_2CH_2$-CH_2-CH_2CH_2O).

linear poly(ε-caprolactone): ^{1}H NMR (250 MHz, $CDCl_3$): δ 4.05 (22H, m, CH_2-O), 3.64 (1H, t, CO-O-CH_2-$(CH_2)_5$-Br), 3.41 (1H, t, CO-O-$(CH_2)_5$-CH_2.Br), 2.30 (22H, m, CO-CH_2), 1.86 (1H, quin, CO-O-$(CH_2)_4$-CH_2-CH_2-Br), 1.64 (46H, m, $COCH_2$-CH_2-$CH_2CH_2CH_2O$ + $COCH_2CH_2CH_2$-CH_2-CH_2O + CO-O-CH_2-CH_2-$(CH_2)_4$-Br), 1.39 (24H, m, $COCH_2CH_2$-CH_2-CH_2CH_2O + CO-O-$(CH_2)_2$-CH_2-$(CH_2)_3$-Br + CO-O-$(CH_2)_3$-CH_2-$(CH_2)_2$-Br).

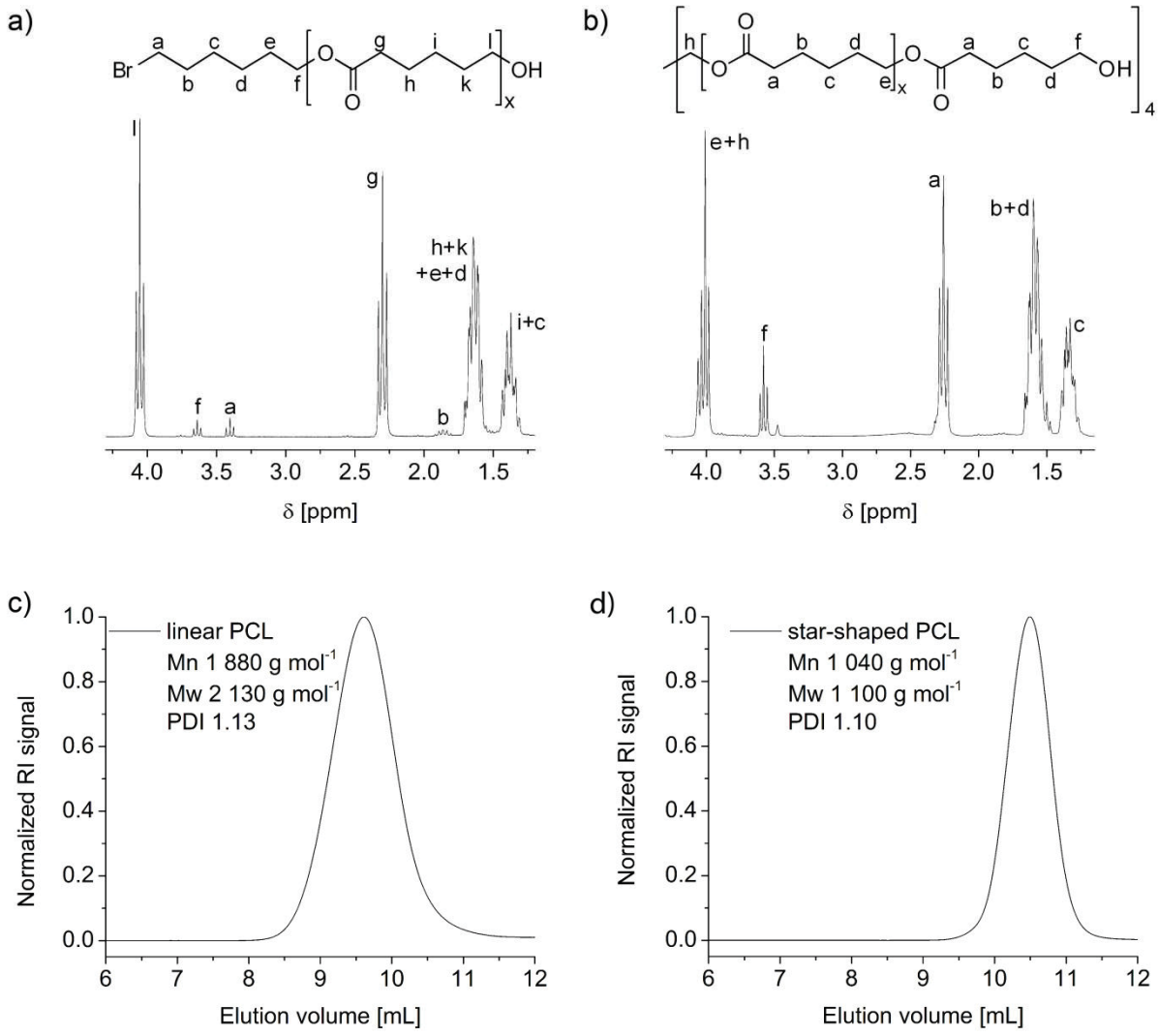

Figure S1. a) ^{1}H NMR spectrum of linear PCL; b) ^{1}H NMR spectrum of star-shaped PCL; c) SEC curves of the linear PCL; d) SEC curves of the star-shaped PCL.

List of abbreviations

^{1}H NMR	proton nuclear magnetic resonance
AAS	atomic absorption spectroscopy
ABC	accelerated blood clearance
AFM	atomic force microscopy
AmB	amphotericin B
ATRP	atom transfer radical polymerization
AUC	analytical ultracentrifugation
BuOx	2-butyl-2-oxazoline
Chart	chartreusin
$CHCl_3$	chloroform
CID	collision induced dissociation
cmc	critical micelle concentration
CROP	cationic ring opening polymerization
DCTB	trans-2-[3-(4-*tert*-butylphenyl)-2-methyl-2- propenylidene] malononitrile
DDS	drug delivery system
DLS	dynamic light scattering
DMAc	*N*,*N*-dimethylacetamide
EMA	European Medicines Agency
EPR	enhanced permeability and retention
ESI	electrospray ionization
EtOx	2-ethyl-2-oxazoline
FDA	Food and Drug Administration
FDAc	fluorescein diacetate
GALDI	colloidal-graphite assisted laser desorption/ionization
GN	Grande Naine
HDLs	high-density lipoproteins
HLB	hydrophilic/lipophilic balance
*i*PrOH	*iso*-propanol
*i*PrOx	2-*iso*-propyl-2-oxazoline
ITC	isothermal titration calorimetry
LDI	laser desorption/ionization
MA	methacrylic acid
MALDI	matrix-assisted laser desorption/ionization
MCF7	non-resistant human adenocarcinoma cells
MCF7-ADR	multi-drug resistant human adenocarcinoma cells
MDCK	Madin-Darby canine kidney
MHL	madurahydroxylactone
mPEG	methoxy-poly(ethylene glycol)
MPS	mononuclear phagocyte system
MS	mass spectrometry

MSI	mass spectrometry imaging
NEt_3	triethylamine
NMR	nuclear magnetic resonance
NOx	2-nonyl-2-oxazoline
*n*PrOx	2-*n*-propyl-2-oxazoline
OEGMA	oligo(ethylene glycol)methacrylates
OEtOxMA	oligo(2-ethyl-2-oxazoline) methacrylate
PCL	poly(ε-caprolactone)
PEG	poly(ethylene glycol)
PEI	poly(ethylene imine)
PET	poly(ethylene terephthalate)
PEtOx	poly(2-ethyl-2-oxazoline)
PI	propidium iodide
PLA	poly(lactic acid)
PMeOx	poly(2-methyl-2-oxazoline)
PMMA	poly(methyl methacrylate)
ppm	parts per million
PS	poly(styrene)
Q	quadrupol
RA	retinoic acid
ROP	ring opening polymerization
ROS	reactive oxygen species
SEC	size exclusion chromatography
Sn(Oct)	tin(II) 2-ethylhexanoate
THP	tetrakis(4-hydroxyphenyl)-porphyrine
TOF	time of flight
UHPLC	ultra high performance liquid chromatography
UV	ultraviolet
YKm5	Yangambi Km5

Curriculum vitae

since 09/2007	PhD student at the Institute of Organic Chemistry and Macromolecular Chemistry (IOMC) of the Friedrich-Schiller-Universität, Jena, in the group of Prof. Dr. U. S. Schubert
04/2007 – 08/2007	Research activities at the Julius-Maximilians-Universität, Würzburg, in the group of Prof. Dr. F. Würthner
09/2006 – 03/2007	Research activities with a Marie Curie EST Fellowship "NANOTOOLS" at the Paul-Sabatier-Université, Toulouse, France, with Dr. J.-P. Souchard and A.-F. Mingotaud
23.03.2006	Academic degree diploma (equivalence to M.Sc.)
09/2005 – 03/2006	Diploma thesis at the Institute of Organic Chemistry and Macromolecular Chemistry (IOMC) of the Friedrich-Schiller-Universität, Jena in the group of Prof. Dr. R. Beckert
09/2004	Vordiplom (equivalence to bachelor)
02/2004 – 06/2004	Study of chemistry at the Paul-Sabatier-Université, Toulouse, France
09/2001 and 03/2006	Internship at Jenapharm GmbH, Jena
10/2000 – 03/2006	Study of chemistry at the Friedrich-Schiller-Universität, Jena
26.06.2000	Graduation: Abitur (University entrance qualification) at Ernst-Haeckel-Gymnasium, Jena
09/1992 – 07/2000	Higher school education in Jena
01.10.1981	Born in Dresden

Jena, den _____

(Katrin Knop)

Publication list

Peer-reviewed publications

[1] K. Knop, G. M. Pavlov, T. Rudolph, K. Martin, D. Pretzel, B. O. Jahn, D. H. Scharf, V. Makarov, U. Möllmann, A. A. Brakhage, F. H. Schacher, U. S. Schubert, *Soft Matter* **2013**, *9*, 715–726.

[2] E. Altuntaş, K. Knop, L. Tauhardt, K. Kempe, A. C. Crecelius, M. Jäger, M. D. Hager, U. S. Schubert, *J. Mass Spectrom*. **2012**, *47*, 105–114.

[3] L. Tauhardt, K. Kempe, K. Knop, E. Altuntas, M. Jäger, S. Schubert, D. Fischer, U. S. Schubert, *Macromol. Chem. Phy.* **2011**, *212*, 1918–1924.

[4] J. Ehrhart, N. El-Akra, K. Knop, A.-F. Mingotaud, F. Violleau, C. Mingotaud, P. Vicendo, J.-P. Souchard, *Bulletin du Cancer* **2010**, *97*, S61–S61.

[5] A. C. Crecelius, C. R. Becer, K. Knop, U. S. Schubert, *J. Polym. Sci., Part A: Polym. Chem.* **2010**, *48*, 4375–4384.

[6] K. Knop, R. Hoogenboom, D. Fischer, U. S. Schubert, *Angew. Chem. Int. Ed.* **2010**, *49*, 6288 – 6308; *Angew. Chem.* **2010**, *122*, 6430–6452.

[7] K. Knop, B. O. Jahn, M. D. Hager, A. C. Crecelius, M. Gottschaldt, U. S. Schubert, *Macromol. Chem. Phys.* **2010**, *211*, 677–684.

[8] D. Hölscher, R. Shroff, K. Knop, M. Gottschaldt, A. C. Crecelius, B. Schneider, D. Heckel, U. S. Schubert, A. Svatos, *Plant J.* **2009**, *60*, 907–918.

[9] S. Weidner, J. Falkenhagen, K. Knop, A. Thünemann, *Rapid Commun. Mass Spectrom.* **2009**, *23*, 2768–2774.

[10] K. Knop, A.-F. Mingotaud, N. El-Akra, F. Violleau, J.-P. Souchard, *Photochem. Photobiol. Sci.* **2009**, *8*, 396–404.

[11] A. Baumgaertel, C. Weber, K. Knop, A. C. Crecelius, U. S. Schubert, *Rapid Commun. Mass Spectrom.* **2009**, *23*, 756–762.

[12] M. Matschke, K. Knop, R. Beckert, *Struct. Chem*. **2008**, *19*, 399–405.

[13] T. Gebauer, R. Beckert, D. Weiß, K. Knop, C. Käpplinger, H. Görls, *Chem. Comm*. **2004**, *16*, 1860–1861.

Submitted manuscripts

[1] D. Hölscher, K. Knop, M. Kai, R. Maddula, C. Ritter, A. C. Crecelius, D. Heckel, B. Schneider, U. S. Schubert, T. Alexandrov, B. Zimmermann, A. Svatos, *Plant J*. **2012**, submitted.

[2] S. Miosic, K. Knop, D. Hölscher, J. Greiner, C. Gosch, J. Thill, M. Kai, B. Shreshta, B. Schneider, A. C. Crecelius, U. S. Schubert, S. Svatos, K. Stich, H. Halbwirth, *J. Exp. Botany* **2012**, submitted.

[3] K. Knop, D. Pretzel, A. Urbanek, T. Rudolph, D. H. Scharf, A. Schallon, M. Wagner, S. Schubert, M. Kiehntopf, A. A. Brakhage, F. H. Schacher, U. S. Schubert, *Biomacromolecules* **2013**, submitted.

[4] G. M. Pavlov, K. Knop, O. V. Okatova, U. S. Schubert, *Macromolecules* **2013**, submitted.

[5] K. Knop, S. Stumpf, U. S. Schubert, *Rapid Commun. Mass Spectrom*. **2013**, submitted.

Manuscripts in preparation

[4] D. Hölscher, S. Dhakshinamoorthy, T. Alexandrov, M. Becker, T. Bretschneider, A. Bürkert, A. C. Crecelius, D. De Waele, D. G. Heckel, H. Heklau, C. Hertweck, M. Kai, K. Knop, C. Krafft, R. K. Madulla, C. Matthäus, J. Popp, B. Schneider, U. S. Schubert, R. Sikora, A. Svatoš, R. Swennen, *Nature Chem. Biol.* **2013**, in preparation.

Poster presentations

[1] K. Knop, K. Martin, V. Schroeckh, U. S. Schubert, A. A. Brakhage, ″A delivery system for a novel rhodane-type antifungal drug″, NanoConSens Meeting, 17.09.2012, Jena.

[2] A. Vollrath, K. Kempe, H. Schäfer, K. Knop, S. Hornig, U. S. Schubert, ″Formation of labeled nanoparticles of polymeric systems for drug delivery applications″, Thüringer Biomaterial-Kolloquium, 17.09.2009, Friedrichroda.

[3] D. Hölscher, R. Shroff, K. Knop, M. Gottschaldt, B. Schneider, D. Heckle, U. S. Schubert A. Svatoš, ″Matrix-free UV-laser desorption/ionization (LDI) mass spectrometric imaging on the single-cell level: distribution of secondary metabolites of Hypericum species″, ICMS, 30.08.–04.09.2009, Bremen.

[4] K. Knop, D. Hölscher, S. Dhakshinamoorthy, A, Elsen, A. C. Crecelius, D. Heckel, B. Schneider, U. S. Schubert, ″LDI imaging of phenylphenalenones in infected banana tissue and pest″, ICMS, 30.08.–04.09.2009, Bremen.

[5] K. Knop, M. Hager, U. S. Schubert, ″Towards star-shaped polymers″, DPI Annual Meeting, 25.–26.11.2008, Antwerpen, Belgien

Oral presentations

[1] K. Knop, U. S. Schubert, ″Star-shaped drug delivery systems″, DPI HTE Cluster meeting, 06.06.2012, Darmstadt, Germany.

[2] K. Knop, D. Hölscher, U. S. Schubert, ″Laser desorption/ionization mass spectrometric imaging on a single cell level of plant tissue″, DPI HTE Cluster meeting, 08.12.2009, Jena, Germany.

[3] K. Knop, U. S. Schubert, ″Matrix-free LDI imaging of secondary plant metabolites″, Bruker Cooperation Meeting, 01.10.2009, Bremen, Germany.

[4] K. Knop, U. S. Schubert, ″Per aspera ad astra – through difficulties to star-shaped polymers″, 29.08.2009, joint seminar at KIT, Karlsruhe, Germany.

[5] K. Knop, U. S. Schubert ″MS-MS on stars: Can MALDI-TOF MS/MS provide valuable information?″, MALDI-Kolloquium of the BAM, 12.05.2009, Berlin, Germany.

[6] K. Knop, U. S. Schubert, ″LDI mass spectrometric imaging on Arabidopsis thaliana″, Bruker Applicators Meeting, 23.–24.04.2009, Bad Soden, Germany.

[7] K. Knop, D. Hölscher, U. S. Schubert, ″Laser desorption/ionization mass spectrometric imaging on a single cell level of plant tissue″, DPI HTE Cluster meeting, 08.12.2009, Jena, Germany.

[8] K. Knop, U. S. Schubert ″MALDI-TOF MS/MS of substituted mPEG″, MALDI-Kolloquium of the BAM, 06.04.2009, Berlin, Germany.

[9] K. Knop, A. Can, U. S. Schubert, ″Star-shaped polymers for drug delivery applications″, DPI Bioinspired Polymer Cluster Meeting, 10.–11.03.2009, Deventer, The Netherlands.

[10] K. Knop, S. Cantekin, U. S. Schubert, ″MALDI-TOF MS/MS of star-shaped PEG″, Bruker Applicators Meeting, 17.–18.02.2008, Bad Schwalbach, Germany.

Acknowledgement/Danksagung

Diese Seiten am Ende beinhalten fast den schwierigsten Teil dieser Arbeit. Es war eine schöne Zeit und ich bin dankbar für die Hilfe und Unterstützung die ich erfahren durfte. Ich möchte gerne an alle diese Worte der Dankbarkeit richten, mit denen ich die letzten Jahre verbracht habe.

Zuerst möchte ich meinem Betreuer Prof. Dr. Ulrich S. Schubert danken, dass ich meine Promotion in seiner Arbeitsgruppe anfertigen durfte. Da dieses Ziel nun kurz davor steht Realität zu werden, möchte ich Dir für die unendlichen Möglichkeiten mich weiter- und fortzubilden, für Deine Energie und Deinen Elan danken. Ich bewundere Deine persönliche Kraft, unsere große Gruppe zu managen und jedem die Möglichkeit zu geben über sich hinaus zu wachsen. Alles begann für mich mit einer Zugfahrt von Würzburg nach Jena und einer Annahme als erster Doktorand in der Arbeitsgruppe in Jena, für diese Chance werde ich Dir immer dankbar sein.

Aus Franken kam auch Jun.-Prof. Dr. Felix Schacher an die Universität in Jena. Ich danke Dir für die ausgiebigen Diskussionen, dass Du die gleichen Probleme mit meinen Ergebnissen hattest wie ich (das beruhigt ungemein) und für die Zeit, die Du für mich hattest, Deine Unterstützung und Deine vielen und schnellen Korrekturen. Ich wünsche Dir alles Gute und viel Glück für die berufliche und private Zukunft. Prof. Dr. Dagmar Fischer möchte ich hiermit besonders danken. Ich habe die Diskussionen mit Ihnen sehr genossen und viele neue Einblicke in die Welt der Pharmazie gewonnen. Ihre systematische, tiefgründige und kritische Analyse meines Reviews hat erst dessen hochrangige Publikation ermöglicht. PD Dr. Dr. Michael Kiehntopf möchte ich danken, dass er die Messung der Gerinnungszeit so schnell und unproblematisch ermöglichte. Einen besonderen Dank möchte ich an dieser Stelle Cora Richert und dem Team der Klinischen Chemie aussprechen, die uns bei den Messungen mit Rat und Tat zur Seite standen und uns so nett unterstützt haben.

Meinen Kooperationspartnern aus sehr verschiedenen Bereichen der Wissenschaft möchte ich auf diesem Wege danken, dass so viele schöne Ergebnisse ermöglicht wurden. Lieber Dr. Dirk Hölscher, nie werde ich die Freitag nachmittage im MALDI Labor vergessen, Ihre Begeisterung für die Wissenschaft im Allgemeinen, für Pflanzenmetabolite im Speziellen und Ihre überschwenglichen Darlegungen von tausenden Details. Es hat Spaß gemacht, dieses Thema so weit ab der synthetischen Arbeiten betreuen zu dürfen. Ich hoffe, Sie werden niemals vergessen, dass (MA)LDI-TOF MS nicht quantitativ ist. Dr. Heidi Halbwirth danke ich für die Überlassung der LDI-TOF MSI Messungen von Zweizahn Blütenblättern (inklusive des tollen Farbspiels der Aurone und Chalcone mit Ammoniak). Dr. Burkhard O. Jahn möchte ich aufs Wärmste für die vielen Rechnungen danken. Diese Zusammenarbeit hat wirklich immer super geklappt, auch wenn (oder vielleicht gerade weil) mein Computerchemiewissen ziemlich begrenzt ist. Karin Martin und Daniel Scharf möchte ich für die Messungen der Fungizid-Aktivitäten sowie der ITC danken. Besonders die Ergebnisse der ITC Messungen konnten viel Verwirrung aufklären und haben mich dementsprechend begeistert. Dear Georgy, thanks for all the wonderful measurements and calculations you did

with your AUC-wonder machine and my stars. Thanks to you I am not regarding physics anymore as avoidable part of the science. Lieber Tobias, vielen Dank für Deine vielen Lichtstreuungen bei konstantem Winkel, für die schnelle Hilfe und Auswertung, dein gutgelauntes Umgehen mit meinem Drängeln besonders als es zeitlich eng wurde. Annett, ich danke Dir von Herzen für Deine viele Zeit und Geduld, die Du für mich hattest, um zum Schluß die vielen MALDI Messungen und besonders die Arbeiten mit Doxorubicin noch durchzuführen. Deine Mitarbeit ist unschätzbar. Ein besonderes Dankeschön geht auch an Alexander, der sich, ohne Groll gegen mich zu hegen, für mehrere Tage in das Fenster- und Lüftungslose UV/Vis Labor hat einschließen lassen, um gefühlte fünf Millionen Proben zu messen.

Un merci unfiniment j'aimerai expresser pour Dr. Anne-Françoise et Dr. Christophe Mingotaud ainsi que Dr. Jean-Pierre Souchard. Merci de m'avoir choisi pour le stage Marie Curie, vous avez donner des ailes à moi. Le temps à Toulouse à l'IMRCP restera à jamais gravé dans mon cœur avec vous, Menana, Valerie, Lacra et les autres.

Ich möchte gerne ein riesiges Dankeschön an alle technischen und mit organisatorischen Angelegenheiten betrauten Angestellten des Institutes aussprechen für die Hilfe die ich in den nicht unerheblich wenigen Jahren an dem Institut erhalten habe. Angefangen ganz unten im Haus im Keller bei Frau Pfeifer (Was wären wir ohne Ihre Organisation und Ordnung?), Dr. Günther und Frau Sentis (Was wären die vielen Publikationen ohne Ihre NMR-Messungen?), die Hausmeister (Was wäre das TO ohne Ihre Fahrleistung?) bis hinauf unters Dach zu Dr. Martin Hager, Dr. Uwe Köhn und PD Dr. Michael Gottschaldt (Was wäre unsere Arbeitsgruppe ohne Euch?). Und in den Etagen dazwischen? Vielen Dank, liebe Grit und Nicole, dass Ihr die SECs in Schuß haltet (Kein Seminar ohne Eure indirekte Arbeit.), liebe (T/H)Anja für ein offenes Ohr, Tanja und Sylvia für all die Arbeit um die Gruppe am Funktionieren zu halten. Liebe Conny ich danke Dir tausendmal für Deine Synthesehilfe während der Schwangerschaft. Und was wären wir ohne Anette's Shop? Tausend Dank für das Besorgen von Spritzen, Kanülen, Vials und unzähligen Kleinigkeiten.

So, liebe Schubert-group, jetzt seid Ihr dran. Was soll ich sagen nach vollen fünf Jahren? Ihr seid mir ans Herz gewachsen und ich weine jetzt schon. (Schreibe ich jetzt zu jedem von Euch etwas und fülle die nächsten drei Seiten? Na klar, Ihr habt es ja auch verdient.)

Ich danke dem kleinen, aber exklusiven Zirkel der Mitstreiter der ersten Stunde: Christine, Andreas, Kristian, Andy, Remzi und Renzo. Es war anstrengend aber auch schön, noch nicht so unübersichtlich viele zu sein. Renzo, thanks a lot for keeping my computer alive throughout the years and for infecting me with Triggerfingers „I follow rivers" (I am just listening to it). Remzi, you put so much effort in building new and old instruments up, to make things run in Jena, thank you for all your energy. Liebe Christine, um nichts möchte ich es missen, Dich kennen gelernt zu haben, Dein kritischer Verstand, Deine Organisation und Klugheit werden mir immer ein Vorbild sein. Und nett bist du auch noch, das ist ja nicht zum aushalten. Auch wenn du es selbst nie glauben willst; du bist toll. Andy, ich wünsche Dir für Deine Familie und deine Zukunft alles erdenklich Gute. Jetzt weine ich gleich (aber ich bin ja nicht blond und ein kleines Mädchen bin ich auch nicht), und eigentlich hat uns der Kristian auch schon verlassen, um einer glorreichen Zukunft entgegen zu streben. Ich glaube fest daran

und weiß es nahezu, dass Du ein Schatz bist, auch wenn du es nicht immer zeigen kannst, Du den Charme offenbar früh mit Löffeln isst und Deine Freundin auf dem Sofa schlafen muss, wenn sie krank ist. Lieber Dauer-Repeat-ABBA-Schnulzen-Mithörer Andreas ich rede gerne mit Dir und im Labor wäre es lange nicht so schön, ohne Dich, Deine Unordnung und das Kopfkino. Ich trauere jetzt schon einer doppeldeutigkeitslosen Zukunft entgegen und der Regeneration meines kompletten Wortschatzes. Was wäre das Leben ohne Hintergrundinformation, einer 34/28 Ritzel Übersetzung, die richtig Ballett macht, halbe Fahrräder an der Wand und ohne den unendlich guten Pietscher? Niemand kümmert sich so wie Du und, ich hoffe, Du bist nicht allzu glücklich, wenn ich Deinen Abzug endlich wieder verlassen habe und praktikumskonformes Arbeiten wieder möglich ist. Meine liebe Antje, einzige Praktikantin, die ich auch behalten wollte, es wäre so schön geworden. Dein Schwung und Deine gute Laune sind ansteckend. Bleib so wie Du bist. Du bist und bleibst in meinem Herzen. Wunderschöne Röcke und T-shirts in beneidenswert bunt mit Blümchen trägt nur Sofia (mit f), ich hoffe, dass sich unsere Wege auch in Zukunft immer wieder finden.

Da bin ich auch schon angelangt im Bio-Büro, welches einen Hühnerstall und David beherbergt. Anja, ich hoffe, Du kannst Deine Energie und Dein Leuchten auch in die Zukunft tragen, das ist so *wusa*. Vielen Dank für das viele Reden und Teilhaben lassen an der Wunderwelt Zellkultur. Stephanie, ich danke Dir für die unglaubliche Hilfe bei der Übersetzung des Reviews im Zeitversatz während Deiner letzten Tage in Kalifornien, den Diskussionen und Deine viele Hilfe am Schluss dieser Arbeit und wünsche Dir für deine Familie alles Gute und viel Kraft. Caro, vielen Dank für die vielen Hemos und Cytotoxis, dass Du so geduldig alle noch so toxischen Sachen heroisch auf Deine liebvoll gezüchteten Zellen geschüttest hast. Alex, toll, dass ich Dich noch kennen lernen durfte, Deine gute Laune und Dein Lachen sind ansteckend. Lieber David, vielen Dank für die in Deinen Augen so langweiligen Bio-Ergebnisse.

Lieber Matthias, Oxazolin-, Methyltosylate- und Triethylamin-Mitbenutzer auf den letzten Metern, vielen Dank für Deine Unterstützung zum Ende hin mit dem nervigen Destillieren. Hoffentlich stirbt die Katze nie. Jürgen, Deine Umsicht ist sprichwörtlich und ich bewundere, wie Du die ganzen alten Instrumente am Laufen hälst. Jetzt sind wir schon am Ende des Ganges im MS-Mädels Büro angelangt. Liebe Banja, schön war es mit Dir und dem MALDI zu starten. Mir fehlt das lange Quatschen im Hotel auf einem der zahlreichen MALDI-Ausflüge. Esra, you are hot-blooded and vivacious, just as it should be for a Turkish girl. We love you, when you are smiling. Thank you for sharing your culture with me. Dear Sarah, thank you for your humor, laughing and for your own theme melody and for being the cat in the Schubert-farm (although it is annoying). I wish you all the best and, ich hoffe, die übergeile Robbe robbt für immer für Dich.

Liebe Anke, vielen Dank für Deine immergewährte, prompte Hilfe bei spontan auftretenden Problemen im Grenzbereich Ink-Jet. Ich hoffe, Du wirst noch oft rot, hinter Deinem Computer und in Deinem Loft, auch wenn der Andreas nicht mehr da ist. Aber vielleicht kann der Sebastian Abhilfe verschaffen. Riesigen Dank geht an Markus, weil ich sein Calciumhydrid aufbrauchen durfte, ohne, dass er mich verhauen hat, obwohl er es dringend brauchte. Schön, dass es noch Gentlemen gibt auf der Welt. Dear Igor, thank you for the viscosity measurements in the last minutes of your and mine thesis. I like meeting you on

the floor, you always smile, keep it for your life. Michael, vielen Dank für Deine unersetzbare Hilfe bei der ITC Auswertung und Dein unerschöpfliches Wissensfundus bei Charakterisierunsfragen. Ohne Dich, hätte ich die ITC sicher doch nicht gemacht.

Der ehemaligen Mensarunde an dieser Stelle meinen Dank für die Freitage und alle Tage davor. Es war eine schöne Zeit und ich denke gerne zurück. Liebe Pia, Stefan, Fenja und Finn schön war es, als Ihr noch oft in Jena zu Besuch wart und traumhaft war es im Heidi-Land, eine tolle Realitätsflucht. Ich hoffe, wir sehen uns noch oft zu Familienurlauben und spätestens auf der Verlobung der beiden Großen (obwohl ich Jonathans letztens versprechen musste, dass er heiraten darf, wen er will). Liebe Anja, lieber Schulzi, ich kann nicht sagen, wie sehr ich das mal-schnell-vorbei-schauen, das James-Bond-schauen und die Spieleabende vermisse auch nach so vielen Jahren. Vielleicht eines Tages, hoffentlich, führen uns unsere Wege wieder zusammen. Liebe Sandra, lieber Uwe, Eure Freundschaft ist Gold wert, Eure Unterstützung hat mich oft gerettet, Ihr verdient nur das Beste im Leben, lasst Euch niemals etwas anderes einreden. Ich hoffe, alle Eure Träume werden war, ein schönes Haus, mit riesigem Garten, nicht so weit weg von Jena und Eure Familie mitten drin.

Schließlich möchte ich meiner gesamten Familie danken; meinen beiden Omas: Inge und Renate, Tanten und Onkeln, Cousinen und Cousins (und ganz besonders allen Sommer-Kind-Betreuern). Ihr seid toll und ich kann mir keine Bessere vorstellen. Meine beiden Schwestern Jana und Karoline möchte ich hier einmal liebevoll explizit erwähnen mit einem dicken Dankeschön für die vielen Zickereien vor vielen Jahren und dass wir uns jetzt so gut vertragen. Meinen Eltern danke ich von tiefstem Herzen. Ich wäre nichts von dem, was ich bin und erreicht habe, ohne Euch.

Lieber Bodo, Deine Liebe ist wie ein warmer Sommerregen und Deine Zuneigung trägt mich über die Schwierigkeiten des Lebens und des Alltags. Unsere Familie macht mich glücklich. Lieber Jonathan, du bist der Sonnenschein in meinem Herzen.

Declaration of authorship/Selbstständigkeitserklärung

Ich erkläre, dass ich die vorliegende Arbeit selbstständig und unter Verwendung der angegebenen Hilfsmittel, persönlichen Mitteilungen und Quellen angefertigt habe.

I certify that the work presented here is, to the best of my knowledge and belief, original and the result of my own investigations, except as acknowledged, and has not been submitted, either in part or whole, for a degree at this or any other university.

Jena, den _____

(Katrin Knop)

Publications P1-P13

Publication P1:

Poly(ethylene glycol) in drug delivery: Pros and cons as well as potential alternatives

---

K. Knop, R. Hoogenboom, D. Fischer, U. S. Schubert

Angew. Chem. Int. Ed. **2010**, *49*, 6288–6308.

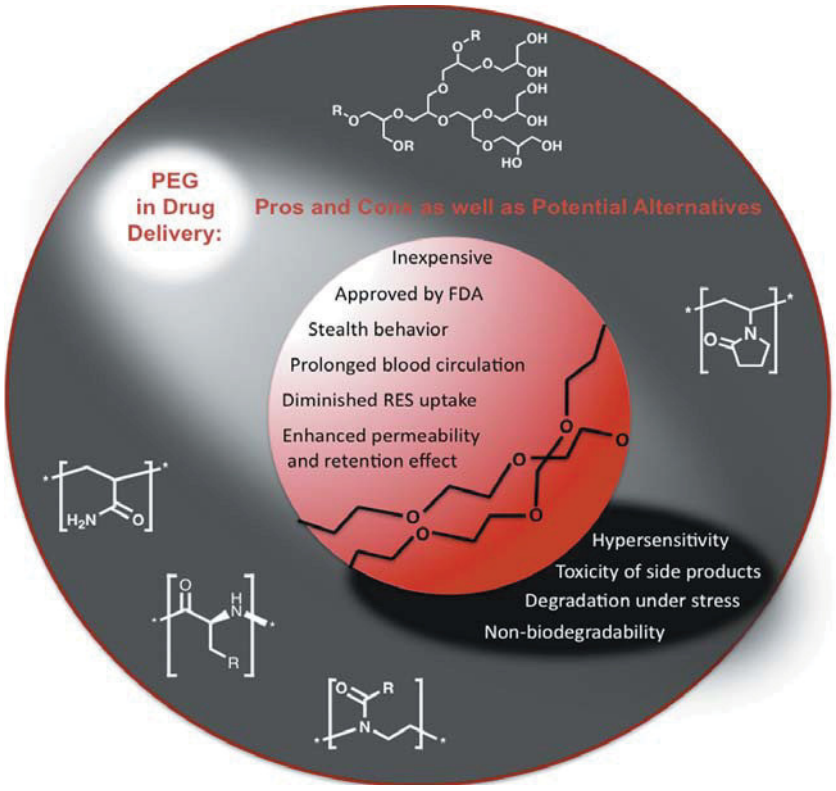

Drug Delivery

DOI: 10.1002/anie.200902672

Poly(ethylene glycol) in Drug Delivery: Pros and Cons as Well as Potential Alternatives

*Katrin Knop, Richard Hoogenboom, Dagmar Fischer, and Ulrich S. Schubert**

Keywords:
drug delivery · nanotechnology · poly(ethylene glycol) · polymers · stealth effect

In memory of Victor A. Kabanov

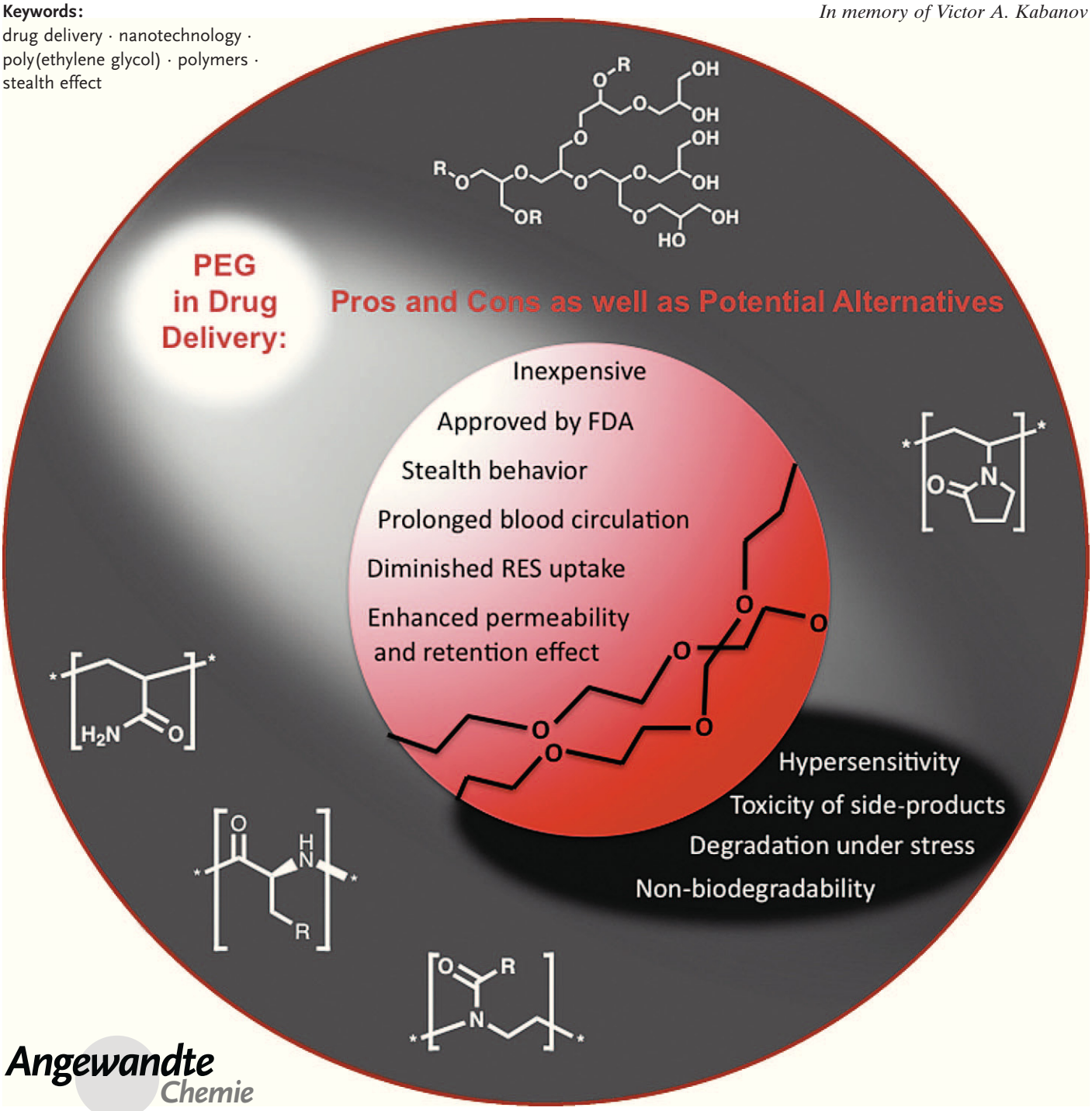

Angewandte International Edition Chemie

Poly(ethylene glycol) (PEG) is the most used polymer and also the gold standard for stealth polymers in the emerging field of polymer-based drug delivery. The properties that account for the overwhelming use of PEG in biomedical applications are outlined in this Review. The first approved PEGylated products have already been on the market for 20 years. A vast amount of clinical experience has since been gained with this polymer—not only benefits, but possible side effects and complications have also been found. The areas that might need consideration and more intensive and careful examination can be divided into the following categories: hypersensitivity, unexpected changes in pharmacokinetic behavior, toxic side products, and an antagonism arising from the easy degradation of the polymer under mechanical stress as a result of its ether structure and its non-biodegradability, as well as the resulting possible accumulation in the body. These possible side effects will be discussed in this Review and alternative polymers will be evaluated.

From the Contents

1. Introduction

Polymeric carriers, which physically entrap molecules of interest, and polymer conjugates, to which such molecules are chemically bound, play an important role in modern pharmaceutical technology. The shared task of carriers and conjugates is the targeted delivery of drugs to specific sites of action in the body. In the case of drug conjugates, in particular, the increase of the molar mass leads to reduced kidney excretion and results in a prolonged blood circulation time of the drug. Shielding of drug carriers and conjugates is required to avoid a fast recognition by the immune system followed by rapid clearance from the body. The suppression of nonspecific interactions with the body, that is, decreased interactions with blood components (opsonization) inducing activation of the complement system, leads to a reduced blood clearance of drug carriers and conjugates, which is known as the stealth effect. Drug-delivery vehicles can be coated with a hydrophilic polymer to allow both inhibition of opsonization and enhancement of water solubility. Poly(ethylene glycol) (PEG) is the most commonly applied non-ionic hydrophilic polymer with stealth behavior. Furthermore, PEG reduces the tendency of particles to aggregate by steric stabilization, thereby producing formulations with increased stability during storage and application.

In the first part of this Review the requirements for hydrophilic polymers in the field of drug delivery will be introduced. In the second part, the overwhelming number of applications of PEG in this field will be briefly discussed, together with the advantages as well as undesired effects observed during the use of this polymer for biomedical purposes. Taking into account these debated deficiencies, potential alternative polymers for forming the hydrophilic shell of carriers for controlled drug release will be introduced and, finally, their actual status will be discussed.

2. Historical Development

The ability of PEG to influence the pharmacokinetic properties of drugs and drug carriers is currently utilized in a wide variety of established and emerging applications in pharmaceutics. The change in the pharmacokinetics of administered drugs by being shielded by or bound to PEG results in prolonged blood circulation times. This consequently increases the probability that the drug reaches its site of action before being recognized as foreign and cleared from the body. Therefore, the majority of conjugated drugs as well as liposomal and micellar formulations on the market or in advanced clinical trials are PEG-containing products.[1] In fact, all polymer-based stealth drug-delivery systems that have been brought to the market up to now contain PEG-functionalized products (PEGylated), and no other synthetic polymer has yet reached this status (Table 1).[1–3]

The concept of PEGylation was first introduced back in the late 1970s; however, it only reached widespread applica-

[*] K. Knop, Prof. U. S. Schubert
Lehrstuhl für Organische und Makromolekulare Chemie (IOMC)
Friedrich-Schiller-University Jena
Humboldtstrasse 10, 07745 Jena (Germany)
Fax: (+49) 3641-948-202
E-mail: ulrich.schubert@uni-jena.de
Homepage: http://www.schubert-group.com
Dr. R. Hoogenboom, Prof. U. S. Schubert
Laboratory of Macromolecular Chemistry and Nanoscience
Eindhoven University of Technology
PO Box 513, 5600 MB Eindhoven (The Netherlands)
K. Knop, Dr. R. Hoogenboom, Prof. U. S. Schubert
Dutch Polymer Institute (DPI)
PO Box 902, 5600 AX Eindhoven (The Netherlands)
Prof. D. Fischer
Department of Pharmaceutical Technology
Friedrich-Schiller-University Jena (Germany)

tion in different carrier systems in the 1990s (for an overview of drug-delivery systems, see Figure 1).[4,5]

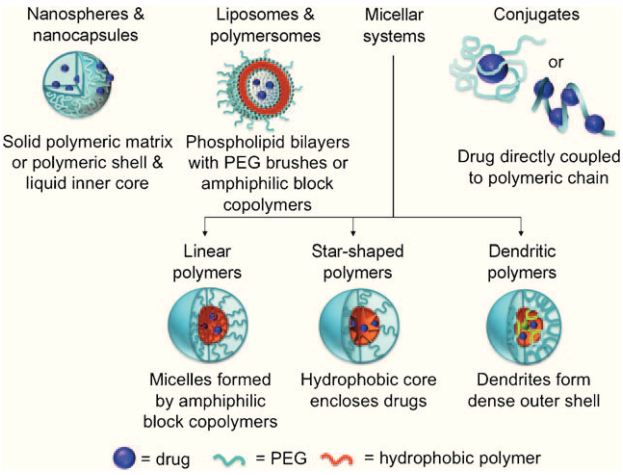

Figure 1. Overview of carrier systems for drug delivery.

The coupling of a protein to PEG was first reported in 1977 by Abuchowski et al. They demonstrated in two studies the non-immunogenicity of PEGylated albumin as well as an extension of the blood circulation time from 12 h to 48 h for PEGylated liver catalase while maintaining the activity of the enzyme.[6,7] A large number of PEG conjugates of proteins, polypeptides, DNA, and RNA as well as of small molecules have since been reported to be more efficient and stable than the native drugs, and several conjugates have reached the market as commercial products. Table 1 shows that PEG conjugates play a very important part in contemporary drug-delivery applications.[1–3] A deeper insight into this topic can be found in two special issues of *Advanced Drug Delivery Reviews*.[8,9]

The effect of PEG surface coverage on the pharmacokinetics of poly(lactic-*co*-glycolic acid) microspheres was reported in 1994 by Gref et al.[10] The authors showed that 66% of the noncoated particles were removed by the liver only 5 minutes after injection, while less than 30% of the 20 kDa PEG-coated nanospheres were captured by the liver 2 h after injection. This study provided the basis for the use of PEG in microsphere technology, whose history already started in the 1950s.[11]

Liposomes have been known since the early 1960s as versatile drug-delivery systems.[12,13] However, a major development was made in 1990 when different research groups reported that the combination of liposome technology and PEGylation by attaching a PEG brush layer to the carriers drastically enhanced blood circulation times of liposomes.[14–16] For example, Klibanov et al. could show that conventional liposomes were completely cleared from blood after 5 h, whereas 49% of the sterically stabilized PEGylated liposomes still circulated in the blood after the same time.[14] This early report provided the basis for the only commercially

Katrin Knop was born in 1981 in Dresden (Germany). She received her MS in Chemistry at the University Jena (Germany) in 2006. She then obtained a Marie Curie Fellowship at the NANOTOOL EST site in Toulouse (France) where she worked on drug-delivery systems for photodynamic therapy. In 2007 she joined the research group of U. S. Schubert as a PhD student at the Friedrich-Schiller-University Jena, where she is working on the synthesis and characterization of drug-transport systems.

Dagmar Fischer was born in Coburg (Germany) in 1967. She studied pharmacy at the University of Würzburg and received her PhD at the University of Marburg in 1997. After research at the Texas Tech University Health Sciences Center in 2002 and 2003, she obtained her Habilitation at the University of Marburg in 2004. From 2004–2008 she was Head of Preclinical Research and Development at Antisense Pharma GmbH. Since 2008 she has been Professor for Pharmaceutical Technology at the University Jena. Her research is focused on the field of nanoparticles as drug-delivery systems, with a focus on polymers.

Richard Hoogenboom was born in 1978 in Rotterdam (The Netherlands) and studied chemical engineering at the TU Eindhoven (The Netherlands). In 2005, he completed his PhD under the supervision of U. S. Schubert and continued working as project leader for the Dutch Polymer Institute. After postdoctoral training with M. Möller at the RWTH Aachen (Humboldt fellowship) and R. J. M. Nolte at the Radboud University Nijmegen (NWO Veni grant), he was appointed as Associate Professor at Ghent University from July 2010.

Ulrich S. Schubert was born in Tübingen in 1969. He studied chemistry in Frankfurt and Bayreuth (both Germany) and the Virginia Commonwealth University, Richmond (USA). His PhD was carried out at the Universities of Bayreuth and South Florida/Tampa. After postdoctoral training with J.-M. Lehn at the Université Strasbourg (France), he moved to the TU München (Germany) and obtained his Habilitation in 1999. 1999–2000 he was professor at the Center for NanoScience, Universität München (Germany), and 2000–2007 Full-Professor at TU Eindhoven. Currently he holds a chair at the Friedrich-Schiller-University Jena.

Table 1: Drug-delivery systems stabilized with PEG that have received regulatory approval in the USA and/or the EU.[a]

PEG drug description	Company	Indication	Year of approval
Adagen (11–17×5 kDa mPEG per adenosine deaminase)	Enzon Inc. (USA & Europe)	severe combined immunodeficiency	1990 (USA)
Oncospar (5 kDa mPEG-L-asparaginase)	Enzon Inc. (USA)/ Rhône–Poulenc Rorer (Europe)	acute lymphoblastic leukemia	1994 (USA)
Doxil/Caelyx (SSL formulation of doxorubicin)	Alza Corp. (USA)/ Schering-Plough Corp. (Europe)	Kaposi's sarcoma, ovarian cancer, breast cancer, multiple myeloma	1995 (USA) 1999 (USA) all 1996 (EU)
PEG-Intron (2×20 kDa mPEG-interferon-α-2a)	Schering- Plough Corp. (USA & EU)	chronic hepatitis C	2000 (EU) 2001 (USA)
Pegasys (12 kDa mPEG-interferon-α-2b)	Hoffmann-La Roche (USA & EU)	chronic hepatitis C	2002 (USA & EU)
Neulasta (20 kDa mPEG-G-CSF)	Amgen Inc. (USA & EU)	febrile neutropenia	2002 (USA & EU)
Somavert (4–6×5 kDa mPEG per structurally modified HG receptor antagonist)	Pfizer (USA & EU)	acromegaly	2002 (EU) 2003 (USA)
Macugen (2×20 kDa mPEG- anti-VEGF- aptamer)	Pfizer (EU)/OSI Pharm. Inc. and Pfizer (USA)	age-related macular degeneration	2004 (USA) 2006 (EU)
Cimzia (2×40 kDa mPEG- anti-TNFα)	UCB S. A. (USA & EU)	Crohn's disease, rheumatoid arthritis	2008 (USA) 2009 (USA) 2009 (EU)

[a] mPEG: methoxypoly(ethylene glycol), SSL: sterically stabilized liposome, G-CSF: granulocyte-colony stimulating factor, HG: human growth, VEGF: vascular endothelial growth factor, TNF: tumor necrosis factor.

available particulate drug-delivery system—Doxil/Caelyx—the stealth liposome encapsulated doxorubicin (Table 1).[17–19]

Even though the use of micelle-forming amphiphilic polymers as drug-delivery vehicles was already proposed by Ringsdorf et al. in the 1970s, Kabanov et al. were the first to propose the use of PEG as a hydrophilic part of linear block copolymers for micellization in 1989.[20] Kwon and Kataoka finally pushed forward the development of PEG-containing block copolymer micelles to drug-delivery carriers.[21] This progress led to the development of dendritic and star-shaped amphiphilic structures, which exhibit enhanced control over the architecture, size, shape, and surface functionality of the micelles at the cost of higher complexity compared to linear block copolymers.[22]

The enormous progress achieved during the last two decades in gene therapy stimulated the development of efficient vectors for gene transfection, but required the polymer to have special properties because of the charged nature of DNA. However, the cationic charge of the nonviral vectors which is necessary for electrostatic interaction with the negatively charged DNA is responsible for toxicity and a low half-life of the carriers in the body. The PEGylation of gene carriers resulted in a decrease in the disposition in the lung as well as lower initial toxicities compared to unmodified complexes.[23–25] This positive influence is most likely related to a decreased interaction with blood constituents, a lower tendency of the complexes to aggregate, and, therefore, a lower rate of filtration by pulmonary capillaries. Furthermore, PEGylated carriers are also characterized by a slower uptake by the organs (liver and spleen) of the reticuloendothelial system (RES).[23,26] A comparison between 25 kDa poly(ethylene imine) (PEI) and a PEGylated derivative grafted with 50 molecules of 550 Da PEG demonstrated that 15 minutes after intravenous (i.v.) injection, the PEGylated copolymer reached only 50% of the values of the unmodified polycation in the liver and spleen. This was correlated with a prolonged circulation of the PEGylated PEI in the blood through an increased (+63%) area under the curve (AUC) and an elevated terminal elimination phase compared to unmodified PEI. This effect of PEGylation could also be proved with other cationic polymers. By using PEGylated poly(L-lysine) (PLL) the amount of polyplex circulating in the blood shifted to 69% from 15% for the non-PEGylated polymer.[23]

PEGylated drugs, liposomes, and nanocarriers are characterized by reduced renal filtration, decreased uptake by the RES, and diminished enzymatic degradation. For this reason, PEGylated drugs show a prolonged half-life in the body and, thus, an enhanced bioavailability. Hence, the frequency of

drug administration and the amount of drug can be diminished, which improves the life quality of the patient and reduces clinical costs.[1,27]

The excretion of PEG conjugates and PEGylated carriers by the kidneys is reduced by using drugs with a higher molar mass, and the enhanced permeability and retention (EPR) effect can be exploited. This EPR effect, discovered by Maeda et al., is mostly observed in cancerous or inflamed tissues.[28] These tissues are marked by hypervascularization and a leaky vasculature. These unorganized and loosely connected endothelial cells allow nanoscopic particles to enter the neoplastic tissue and remain inside as a result of missing or decreased lymphatic drainage (Figure 2). Additionally, an increased

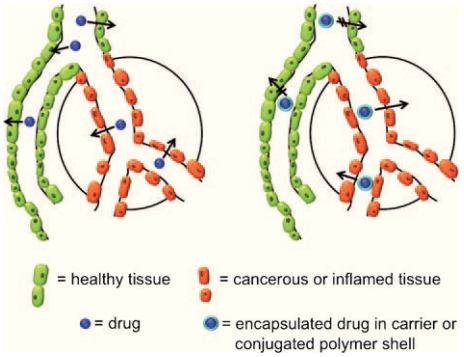

Figure 2. Schematic representation of the EPR effect.

production of vascular permeability enhancing factors is observed in tumor tissue, further augmenting the extravasation of macromolecules within the tumor. The EPR effect is also called passive targeting, and forms the basic principle that causes the functioning of targeted polymeric drug delivery in different diseases, such as cancer, infection, and inflammation, that show more permeable endothelia.[28–30]

Some polymers show a nonlinear behavior in response to an external stimulus, such as a change in temperature or pH value. This response, which could, for example, be a decrease of solubility, can be taken advantage of in drug-delivery applications. The extracellular matrix of cancerous tissue has a decreased pH value of 6.5 to 7.2 compared to blood with a pH value of 7.35 to 7.45. This drop in the pH value can induce precipitation of the polymer and the associated trapping of the polymer and a potentially bound drug or carrier within the cancer tissue. This approach of stimuli-responsive polymers includes manifold stimuli and various responses by the polymers which are ouside the scope of this Review. The interested reader is referred to reviews discussing this topic.[31–34]

These selected examples of applications clearly demonstrate the rising importance of polymers, and in particular of PEG, in biomedical domains such as drug delivery.

3. Advantages of PEG

Not every non-ionic hydrophilic polymer can provide stealth behavior. A number of structural parameters influence the biological and stabilizing effects and have to be carefully taken into consideration.[35]

The molar mass as well as the polydispersity of the polymer has been shown in many applications to be important for biocompatibility and stealth behavior. The molar mass of PEG used in different pharmaceutical and medical applications ranges from 400 Da to about 50 kDa. PEG with a molar mass of 20 kDa to 50 kDa is mostly used for the conjugation of low-molar-mass drugs such as small molecules, oligonucleotides, and siRNA. This results in fast renal clearance being avoided by increasing the size of the conjugates above the renal clearance threshold. PEGs with lower molar masses of 1 kDa to 5 kDa are often used for the conjugation of larger drugs, such as antibodies or nanoparticulate systems. In this way, opsonization and subsequent elimination by the RES is avoided, enzymatic degradation is reduced, and cationic charges are hidden. PEG of about 3 kDa to 4 kDa is given orally as a laxative (as GoLYTELY and MoviPrep).

From a theoretical point of view, a biodegradable polymer would be more beneficial in applications, since difficulties in achieving complete excretion would be avoided, although other issues, such as the toxicity of degradation products and the limited shelf live, would need to be considered. However, it should be kept in mind that the excretion of the polymer is not directly dependent on the molar mass of the polymer, but rather on the hydrodynamic volume, which is affected by the architecture of the polymer. For example, star-shaped polymers and dendrimers show lower hydrodynamic volumes than linear polymers with similar molar masses.[36,37]

In general, a low polydispersity index (PDI) is a basic prerequisite for the polymer to have pharmaceutical applications. A PDI value below 1.1 provides a polymer with an acceptable homogeneity to ensure reproducibility in terms of body-residence time and immunogenicity of the carrier system.[1,38] This demand is readily fulfilled by PEG, since very well defined polymers with PDIs around 1.01 are readily accessible by the anionic polymerization of ethylene oxide.

Furthermore, PEG shows a high solubility in organic solvents and, therefore, end-group modifications are relatively easy. At the same time, PEG is soluble in water and has a low intrinsic toxicity that renders the polymer ideally suited for biological applications. When attached to hydrophobic drugs or carriers, the hydrophilicity of PEG increases their solubility in aqueous media. It provides drugs with a greater physical and thermal stability as well as preventing or reducing aggregation of the drugs in vivo, as well as during storage, as a result of the steric hindrance and/or masking of charges provided through formation of a "conformational cloud".

This "conformational cloud" is generated by the highly flexible polymer chains, which have a large total number of possible conformations. The higher the rate of transition from one conformation to another, the more the polymer exists statistically as a "conformational cloud" which prevents interactions with blood components as well as protein

interactions such as enzymatic degradation or opsonization followed by uptake by the RES.[39] The formation of an efficient sterically hindering cloud on the surface of particles is not only dependent on the polymer, but is also influenced by other factors such as the molar mass of the PEG, the surface density, and the way the PEG is attached to the surface (for example, brush-like or mushroom-like).[40,41]

The diminished interactions with the body result in PEGylated products showing less immunogenicity and antigenicity; hemolysis and aggregation of erythrocytes can also decrease, as can the risk of embolism. The steric hindrance has the additional advantage that the charge in charged carrier systems is shielded and the resulting zeta-potential and charge-induced interactions within the body are decreased. As a consequence, recognition by the immune system through opsonization is suppressed. These favorable properties of PEG in pharmacokinetics are known under the name of the stealth effect, in reference to stealth planes.

Acute and short-term studies as well as pharmacokinetic studies of PEG have been carried out on a wide range of animal species such as rats, mice, guinea pigs, monkeys, and dogs. The gastrointestinal absorption of PEG is decreased as the molar mass increases. Whereas PEGs with a molar mass of 4 kDa to 6 kDa are not absorbed over 5 h in rat intestine, low-molar-mass PEGs of about 1 kDa show a slight absorptive effect of about 2%. The excretion of PEGs is mainly accomplished by the kidneys. In humans, 85% and 96% were excreted in urine in 12 h after intravenous injection of 1 g of 1 kDa and 6 kDa PEG, respectively. LD_{50} values after oral intake were higher than 50 $g\,kg^{-1}$ body weight for 6 kDa PEG (50% solution in water) in mice, rats, rabbits, and guinea pigs. After intraperitoneal (i.p.) administration, the LD_{50} value was 5.9 and 6.8 $g\,kg^{-1}$ in mice and rats, respectively.

In short-term studies in monkeys (*Macaca fascilaris*), daily doses of 2–4 $mL\,kg^{-1}$ of 200 Da PEG were administered over a 13 week period. Intratubular deposition of small numbers of oxalate crystals in the renal cortex were observed, but not related to other clinical or pathological findings. Long-term studies with albino rats with doses of 0.06 $g\,kg^{-1}$ 1 kDa PEG and 0.02 $g\,kg^{-1}$ 4 kDa PEG per day did not cause any significant adverse effects over a two-year period.[42] Toxic effects to the kidney resulting from high PEG doses of 200–600 Da have been observed in laboratory animals and in burn patients whose injured skin was treated topically with PEG.

Evaluating the relative safety of PEG solutions used for bowel cleansing prior to colonoscopy concludes that, in the absence of preexisting renal disease, PEGs are associated with similarly low risks of renal impairment. No significant adverse effects from low-molar-mass PEGs have been observed in inhalation toxicology studies, carcinogen testing, or mutagen assays. Biondi et al. reported that low-molar-mass PEGs of about 200 Da have a genotoxic effect after metabolic activation. However, this was evaluated by induction of chromosome aberrations in CHEL and CHO cells only in the presence of S9 mix. The findings suggested a potential mutagenic risk for PEGs of similar size.[43]

In conclusion, PEGs of different molar masses have essentially similar toxicities, with the toxicity being inverse to the molar mass since the absorption from the gastrointestinal tract decreases with increasing molar mass. The level that caused no toxicological effect in rats was 20000 ppm in a diet equivalent to 1 $g\,kg^{-1}$ body weight. The estimate of the acceptable daily intake for man is 0–10 $mg\,kg^{-1}$ body weight.

The success of PEG in drug-delivery applications also led to its use in other medical fields. Thus, PEG is used in blood and organ storage, where it reduces the aggregation of red blood cells and improves the blood compatibility of poly(vinyl chloride) bags.[44–47] PEG copolymers that are implanted as cardiovascular devices, such as stents, decrease thrombosis.[48]

Furthermore, PEG is not only used in pharmaceutical preparations as an excipient for parenteral, topical, nasal, and ocular applications, it is also used as the active principle in laxatives. The suppression of interactions with biomolecules also led to a variety of antifouling and antiadhesion applications, such as in Merrifield syntheses,[49] ultrafiltration,[50] and the protection of contact lenses from pathogenic bacteria and fungi.[51,52] PEG chains attached to hydrophobic molecules, such as oleic acid, can act as a surfactant, and are found as surface-active, viscosity-increasing, and skin-conditioning agents in all kinds of cosmetics—from toothpaste to cleansing agents, such as shampoos, body and bath soaps, to fragrance, aftershave lotion, face powder, and eye shadow.[53,54] These examples show that PEG, with its special properties, is not only very popular in pharmaceutical applications, it is also a daily consumer product, and is omnipresent in our everyday life.

4. Drawbacks of PEG Polymers

The increasing use of PEG and PEGylated products in pharmaceutical research as well as clinical applications not only provides new insight into the underlying mechanism of the beneficial properties of PEG, it also increases the likelihood of encountering potential side reactions.

The potentially unfavorable effects that might be caused by PEG can be divided into several groups: Adverse side effects in the body can be provoked by the polymer itself or by side products formed during synthesis that lead to hypersensitivity. In addition, unexpected changes in the pharmacokinetic behavior can occur with PEG-based carriers. Furthermore, an antagonism arises from the non-biodegradability of PEG in combination with its relatively easy degradation upon exposure to oxygen. All these potential drawbacks and their importance will be discussed in the following.

4.1. Immunological Response

4.1.1. Intravenous Administration

It was already shown in early studies in 1950 that PEG has the propensity to induce blood clotting and clumping of cells, which leads to embolism. This finding indicates nonspecific interactions of PEG with blood.[42] Since then, it has been shown that PEG, which is not supposed to show any opsonization, can nevertheless induce specific as well as

nonspecific recognition by the immune system, thereby leading to a response of the body to intravenously administered PEG formulations such as liposomal and micellar carrier systems or conjugates.

It was shown that adverse reactions of PEG often occur through complement (C) activation, which leads to hypersensitivity reactions (HSR) that can provoke an anaphylactic shock.[55,56] The complement system, which is part of the immune system, is a biochemical cascade that is started by the hydrolysis of C3, a protein present in blood, whose fragmentation can be triggered by a change in the conformation upon adsorption on a surface. This hydrolysis reaction leads to a biochemical cascade that results in the generation of different C3 and C5 fragments that bind to the surface, thereby labeling the identified foreign body. Leucocytes, mast cells, and macrophages that carry receptors for these complement factors will be activated to remove the foreign body and release inflammatory mediators, such as histamine and proinflammatory cytokines.[57] The release of histamine does not imperatively lead to the hypersensitivity reaction; an additional special susceptibility to one of the other steps is also necessary.[56,58] In earlier studies it was proposed that surface-exposed PEG hydroxy groups provide molecular sites where C3b can covalently bind to the surface and, thus, initiate the pathway of complement activation.[59] However, it should be noted that the vast majority of all currently used PEGylated products are based on methoxy-PEG (mPEG), thereby disproving the validity of this hypothesis.

Although the exact trigger for this phenomenon has not yet been clarified, an immediate HSR in 5–10% of treated patients was shown for different PEG-containing liposomal carriers.[60] Complement activation with subsequent HSR was demonstrated with ^{99m}Tc-labeled 2 kDa mPEG-liposomes for the treatment of Crohn's disease.[61] The Doxil/Caelyx (commercial distearoylphosphatidylethanolamine (DSPE) 2 kDa mPEG) liposome formulation of doxorubicin (Table 1) used in anticancer therapy also causes HSR in up to 25% of the patients, despite pretreatment with corticosteroids and antihistamines and without prior sensitization.[55,58] However, the conclusion that the adverse reaction is only caused by PEG can not be drawn conclusively. In fact, depending on the composition and size of the liposomal formulation, PEG-liposomes cause complement activation even without doxorubicin encapsulation, but Doxil is a more-efficient complement activator than empty PEGylated liposomes (Table 2).[60]

Investigations of the hypersensitivity from side reactions caused by sterically PEG-stabilized liposomes revealed rather opposing results, with complex causal relationships found between PEGylation, size, loading, preparation of the formulation, and different other parameters.[60] For example, small PEGylated liposomes with diameters of less than 70 nm showed no complement activation, in contrast to larger ones.[60] In addition, the beneficial pharmacokinetic effects of covering liposomes with PEG are sometimes absent. Parr et al. found only slight differences in the rates of plasma clearance for PEGylated and non-PEGylated liposome formulations of doxorubicin;[62] Metselaar et al. observed that liposomes without PEG showed the same or even longer circulation half-lives as PEGylated liposomes (36 h and 22 h, respectively).[60]

In summary, these studies indicated complement activation by PEG attached to liposomes, but further investigations are necessary to draw definite conclusions on the mechanism involved and the influence of the various factors that seem to affect the HSR.

The adverse reaction of intravenously administered PEG can also be observed in the application of different contrast agents for echocardiography. Anaphylaxis as a result of hypersensitivity to PEG is observed with SonoVue (commercial contrast agent containing PEG), but not with Optison and Definity (commercial contrast agents without PEG).[63] De Groot et al. reported three cases of anaphylactic shock as a reaction to SonoVue.[64] Dijkmans et al. admit that SonoVue might contain a triggering factor responsible for three fatal cases (0.002% of the treated patients with advanced coronary artery disease as a predisposition) and 18 of 19 adverse anaphylactic or vasovagal reactions (fainting) (0.012%); no such adverse reactions were observed with Optison.[65]

All together, a conclusive statement can not be given as to whether PEG alone or a combination of several factors causes hypersensitivity; further investigations are required. Even though these results argue for a nonspecific recognition of PEG by the body, the binding of antibodies—the specific immune response to PEG—was also observed. In 2005, a case study appeared that showed a severe IgE antibody mediated hypersensitivity reaction to intravenously administered 4 kDa PEG.[66] However, in 1983 Richter et al. already reported the formation of antibodies to PEG conjugates in rabbits. The response to PEG itself was very low, but antibodies were observed for the conjugate of ovalbumin with 6 mPEG chains with a molar mass of 11 kDa anti-PEG as well as anti-ovalbumin. Although the formation of antibodies was highly dependent on the degree of substitution of the protein by PEG and the proportion of animals showing antibody response varied (17% to 50%), this study showed initially that PEG could act as a haptene.[67] Later, the same authors reported that the subcutaneous injection of a mPEG-modified rag-

Table 2: Severity of adverse reactions of different carriers containing PEG and anticancer drugs in a porcine model.[a] Adapted from Ref. [60].

Liposomes	Lipid dose [μmol kg^{-1}]	Frequency of adverse reaction	Severity of adverse reactions		
			mild	severe	lethal
DPPC, PEG-DSPE, Chol	0.17–1.39	4/6	1	1	2
DPPC, PEG-DSPE, Chol	0.16–1.97	2/4	0	1	1
DPPC, Chol (90 nm)	0.16–1.85	5/11	3	2	0
DPPC, Chol (60 nm)	0.16–1.54	0/8	0	0	0
Doxil/Caelyx	0.02–0.27	12/14	3	8	1
DaunoXome	0.18–0.73	7/8	2	1	4

[a] DPPC:dipalmitoyl phosphatidylcholine, PEG-DSPE: 2 kDa mPEG-conjugated distearoyl phosphatidylethanolamine, Chol: cholesterol.

weed allergen in humans triggered the formation of IgM isotype antibodies to PEG, but the only moderate humoral response was classified as not significant for clinics.[68]

However, preexisting IgG and IgM anti-PEG antibodies were identified in over 25% of the healthy donors, and anti-PEG antibodies were induced in 5 of 13 patients in the clinical trial of PEG-asparaginase.[69] The presence of anti-PEG antibodies was strongly related to the rapid blood clearance of PEG conjugates; this effect was also observed for PEG-uricase in 5 of 8 patients.[70]

In summary, PEGylation will continue to be of significant value in medicine to decrease immunogenicity, antigenicity, and toxicity as well as reducing renal clearance. However, it is important to recognize that PEG may possess antigenic and immunogenic properties as haptenes, and the close interaction between complement activation and antibody response should be kept in mind. Further comprehensive studies are required to fully elucidate the effect of anti-PEG antibodies on PEG conjugates.

4.1.2. Oral Administration

Hypersensitivity reactions not only occur when PEG is intravenously injected, but also during the preparation of patients for colonoscopy by oral administration of PEG as a laxative. In general, the gastrointestinal adsorption of PEG decreases as the molar mass increases. Whereas 4 kDa to 6 kDa PEGs are not absorbed over 5 h in rat intestines, low-molar-mass PEGs of about 1 kDa show a slight adsorptive effect of about 2%.[42]

MoviPrep, one of the commercial 3.35 kDa PEG solutions for colonoscopy preparation, is reported to cause hypersensitivity and rash uticaria upon administration. The low absorption rate of 0.2% of high-molar-mass PEG by intestinal mucosa was suggested to be sufficient to cause angioedema as a result of systemic HSR to PEG in susceptible patients.[71] Similarly, GoLYTELY, another 3.35 kDa PEG preparation for colonoscopy, was reported to cause anaphylactic reaction without prior disposition in three separate case studies.[72–74]

4.1.3. Dermal Application

Different examples indicate that cutaneous application of PEG can also cause allergic reactions, such as contact dermatitis. This contact allergy was observed for PEG with molar masses between 4 kDa and 20 kDa used in, for example, dentifrice.[75] Another study found that 8 kDa and 20 kDa PEG present in multivitamin tablets caused hypersensitivity that culminated in unconsciousness in a 36 year old man without predisposition.[76]

Contact dermatitis as a result of hypersensitivity was also reported by Fisher in four patients when drugs containing PEG ranging from 200 to 400 Da were used as an excipient.[77] Quartier et al. reported contact dermatitis to the moisturizing 1 kDa PEG-dodecylglycol block copolymers in 19 of 21 patients.[78] However, both Le Coz et al. and Quartier et al. note a connection between contact dermatitis and 1,4-dioxane, an industrial side product of the PEG synthesis.[54,78]

4.2. Changes in Pharmacokinetic Behavior

Another potential immune reaction to the presence of PEG is the accelerated blood clearance (ABC) phenomenon. Dams et al. first reported that the 2 kDa mPEG liposome concentration in rats was drastically decreased after 4 h compared to a previously injected liposome dose [from $(52.6 \pm 3.7)\%$ to $(0.6 \pm 0.1)\%$ after the second injection].[79] Kiwada and co-workers later observed that the ABC phenomenon also occurred when the second injection was administered within five days. This finding indicated that a preceding injection of PEGylated liposomes can alter the circulation time of repeatedly injected PEG liposomes.[80] In addition, it was also reported that previously administered PEG-containing micelles with a size of at least 30 nm can also induce the ABC reaction,[81] thus indicating that the size of the PEGylated particles is also an important parameter for the reaction. On the other hand, it has been demonstrated that very high doses (5 μmol phospholipid per kg rat) of unprotected liposomes also cause this enhanced blood clearance.[82] This finding shows that the induction and magnitude of the phenomenon is not only determined by PEG, but also by the size and surface of the carrier.[83]

Additionally, the amount of PEGylated lipid can affect the ABC phenomenon. Liposomes containing 0, 5, 10, or 15 mol% PEGylated lipid were tested in rabbits. The ABC phenomenon was found with 5 mol% PEG-covered liposomes to reach a maximum, and with the effect decreasing at higher coverage rates. This observation is in good agreement with the production of anti-PEG as well as anti-ovalbumin antibodies in the presence of an ovalbumin conjugate with 6 molecules of 11 kDa PEG. No antibodies were produced by conjugation with 20 molecules of 11 kDa PEG molecules per ovalbumin molecule.[67]

This ABC phenomenon not only affects the bioavailability of the drug, but passive targeting is also decreased: the second dose was shown to preferentially end up in Kupffer cells of the liver.[79,80,84] This observation proves an involvement of the immune system. This can cause severe liver damage in the case of highly toxic anticancer therapeutics.

The mechanism of ABC is still not fully understood, but it has been suggested that the formation of anti-PEG IgM antibodies by the spleen occurs upon the first injection; the IgM binds to the PEG of the second dose and activates the complement system, thereby leading to opsonization with C3 fragments of PEG and an enhanced uptake by Kupffer cells.[83,85] Since non-PEGylated liposomes can also induce this phenomenon, it seems clear that the mechanism of the occurrence of ABC is much more complex. In any case, these unexpected changes in the pharmacokinetic behavior are undesirable and complicate the therapeutic use of PEGylated liposomes and micelles.

An additional pharmacokinetic irregularity that is shown by PEGylated liposomes is the loss of long-circulating behavior at very low doses (approximately $0.5\ \mathrm{mmol\,kg^{-1}}$).[82] This observation was made with doses much lower than those used during normal therapeutic application (4 to 400 mmol of lipid $\mathrm{kg^{-1}}$); nevertheless, it is important in nuclear medicine, where only trace amounts are

administered.[86] The mechanism accounting for this unexpected behavior is unknown and the question as to whether the loss of long-circulation time is connected to the ABC phenomenon remains unanswered.

4.3. Non-Biodegradability of PEG

A disadvantage of PEG is its non-biodegradability. Therefore, the use of low-molar-mass PEGs would be preferable. However, oligomers with a molar mass below 400 Da were found to be toxic in humans as a result of sequential oxidation into diacid and hydroxy acid metabolites by alcohol and aldehyde dehydrogenase. The oxidative degradation significantly decreases with increasing molar mass and, therefore, a molar mass well above 400 Da should be used.[87,88]

On the other hand, the molar mass should not exceed the renal clearance threshold to allow complete excretion of the polymer. A molar mass limit of 20–60 kDa is reported for nondegradable polymers (corresponding to the albumin excretion limit and a hydrodynamic radius of approximately 3.5 nm).[1,27,38,89–91] Pasut and Veronese assumed that a molar mass below 40–60 kDa is required to prevent accumulation in the liver,[1] but the renal clearance threshold of PEG is not easy to determine.[38] It seems that PEG with a molar mass below 20 kDa is easily secreted into urine, while higher molar mass PEG is eliminated rather slowly, and clearance through the liver becomes predominant.[1] To overcome these uncertainties multiarm and branched biodegradable PEGs were investigated that form low-molar-mass PEGs which can be excreted more easily after cleavage in the body.

Studies concerning toxicity and excretion of PEG mostly date back to the 1950s to 1970s and, therefore, need to be updated with contemporary knowledge and methods.[92–94] In particular, the fate of PEG and PEGylated delivery systems at the cellular level is not known and needs further investigation. It is common practice to assume a fate similar to PEG for PEGylated delivery systems, which are, in general, chemically modified PEGs. Thus, the majority of studies seem to ignore the biological fate of the polymers after disintegration of the liposomes or micelles from which they originate.[91,95]

In fact, there are no systematic long-term studies that show 1) whether PEG is excreted completely or partly remains in the body, 2) where it is accumulated, and 3) its effects at the sites of accumulation.[96]

4.4. Degradation under Stress

The stability of a polymer used for drug delivery is an important factor in achieving and maintaining the stability and therapeutic properties of drugs during storage as well as during treatment.[97] Instabilities observed in polymers can result from chemical changes induced by oxygen, water, and energy such as heat, radiation, or mechanical forces.[97] The effect of these exogenous factors on PEG stability will be discussed in the following.

Mechanical stress on polymers and subsequent degradation can arise during several processes, such as the simple flow of solutions, stirring, or ultrasound treatment. In addition to shear stress during production processes or by injection with a syringe, shear stress can also occur in biological systems. Significant flow of aqueous fluids occurs in the human body, with shear stresses of up to 5 Pa, but the shear behavior of polymers for biomedical applications under these conditions has hardly been considered.[98] Therefore, an examination of the processes that lead to degradation, occurrences that happen during degradation, and the products formed during scission are an important part of the evaluation of polymers for biomedical applications.

Up to now, stress studies have only been carried out on industrial PEG samples with molar masses ranging from 50 kDa to 4000 kDa that are not used in drug-delivery applications. Similarly, shear stresses up to 9 kPa were applied, which significantly exceed the forces occurring in vivo. These forces in vivo are generally around 1 Pa, with maximal shear stresses of around 5 Pa in capillaries and arterioles.[99–104] Even though the investigations on shear stress induced degradation of PEG were not performed with biologically relevant polymers and conditions, the partial degradation of PEG-based therapeutics during prolonged circulation can not be excluded. General findings such as the involvement of oxygen in the rupture of the ether bond and the faster degradation of PEG compared to polymers with a carbon backbone, such as poly(acrylic acid) (PAA) and poly(vinylpyrrolidone) (PVP), should be kept in mind.[103]

PEG is also observed to undergo remarkable degradation under heating in the solid state and solution.[105] Scheirs et al. noted a decrease in the molar mass of solid-state PEG from 100 kDa to 10 kDa after aging for 30 days at 60 °C under air. The authors found by measuring IR spectra that the degradation resulted in the formation of appreciable quantities of aldehyde, carboxylic acid, and alcohol functional groups.[106]

The heating of PEG probes of various molar masses (1–4000 kDa) under a non-oxidative atmosphere at 50 °C also showed slight chain scissions. This finding led the authors to the conclusion that these degradations are induced at so-called weak scissions which have their origin at previously formed peroxides.[107,108] This observation is consistent with others that show that neither the addition of antioxidants nor free radical inhibitors can totally prevent thermal degradation of PEG under inert conditions.[108] Although the discussed conditions might have only limited relevance for biological media, they should be kept in mind during the preparation of the carrier systems.

Even though PEG does not absorb light above 300 nm, it is very sensitive to photooxidation, because of the oxidizability of the α-carbon atom by chromophoric impurities.[107] UV degradation of PEG in the range of 55 to 390 kDa through the formation of ester and formate end groups occurs much faster than in other hydrophilic polymers such as PAA and PVP in the same molar mass range.[103]

Although none of the studies concerning the mechanical stability of PEG involved pharmaceutical grade polymers and the conditions were harsher than those occurring in vivo, it

can be concluded that PEG is more sensitive to degradation than vinylic polymers because of its ether structure and the possible formation of hydroperoxides. These factors have to be taken into consideration, in particular during storage of the polymer as well as the drug formulation.

4.5. Toxicity of Side-Products

The most prominent side product formed during the synthesis of PEG is the cyclic dimer of ethylene oxide, 1,4-dioxane. Currently, 1,4-dioxane is stripped off from the product under reduced pressure. Dioxane is classified by the International Agency for Research on Cancer (IARC) in group 2b (that is, as being possibly carcinogenic in humans with sufficient evidence from animal experiments). Therefore, the European Pharmacopoeia (Ph. Eur.) limits the dioxane content to 10 ppm for pharmaceutical applications. Nonetheless, an evaluation of dioxane by the US Department for Health and Human Services revealed that rats exposed over two years to 111 ppm of 1,4-dioxane in air did not show any evidence of dioxane-caused cancer or any other health effects.

Furthermore, PEG can also contain residual ethylene oxide from polymerization that is classified by the IARC in group 1 (carcinogenic in humans), as well as formaldehyde, which is in the same group. As a consequence, the Ph. Eur. limits the content of ethylene oxide to 1 ppm and the amount of formaldehyde to 30 ppm in PEG for pharmaceutical applications.

The toxicity of these potential side products clearly demonstrates the necessity of using pharmaceutical grade PEG for biomedical applications.

5. Summary of PEG

PEG is a very popular polymer with an overwhelming number of positive properties, as is easily confirmed by searching the literature. These advantageous qualities have led to a very broad usage of PEG in everyday products, industrial applications, as well as in many biomedical drug-delivery systems. Its success in the latter field is well reflected by numerous pharmaceutical products that have reached approval by the Food and Drug Administration (FDA) and European Medicines Agency (EMEA) during the last 20 years (Table 1).

In publications on the use of PEG in drug delivery, an overwhelming enthusiasm is often evident and possible disadvantages are hardly mentioned, with potential difficulties that might be faced with this polymer concealed. Although, the possible disadvantages of PEG are highlighted here, this Review does not wish to create the impression that PEG should be avoided. On the contrary, we believe that PEG is of utmost importance for the development of new drug-release systems that will improve the quality of life. In addition, most of the discussed side effects and instabilities of PEG were only observed in a limited percentage of patients and are not as well investigated and documented as the numerous positive properties. Therefore, we want to increase the awareness that PEG might also exhibit some limitations to complement the multitude of reviews that focus on all the beneficial properties of PEG.

The limitations of PEG include the non-biodegradability and the resulting, and in most studies ignored, fate of PEG after in vivo administration. Many biological and toxicological data evaluating those points date back to the 1950s and 1970s and need to be updated and evaluated with contemporary knowledge, especially in terms of the fate at the molecular and cellular level, such as tissue vacuolization and fusion of membranes. At the same time, the polyether structure provides easy targets for peroxide degradation, and although investigations have not been performed under biologically relevant conditions, PEG can be relatively easy degraded compared to polymers with a carbon backbone.

From a medicinal viewpoint, the unpredictable complement activation, which can lead to hypersensitivity reactions and unclear pharmacokinetics after a second dose (the so called ABC phenomenon) complicate the use of PEG therapeutics. Although PEG alone seems to be immunologically harmless, the immunogenicity of PEG is highly dependent on the degree of PEGylation and to which molecule the PEG is coupled.

Nevertheless, the positive properties of PEG cannot be dismissed and strongly outweigh the sometimes observed negative effects discussed. As a consequence, PEG remains the most used polymer and the gold standard in biomedical applications; potential alternatives with even better properties are difficult to find at the moment. However, the search for alternative polymers is also driven by the strained patent and marketing situation of PEG, since numerous patents protect its applications.

6. Potential Alternatives to PEG

The discussed disadvantages of PEG intensified the search for alternative polymers for use in therapeutics. This section will present the most promising hydrophilic polymers that have been investigated as synthetic alternatives to PEG for different biomedical applications and their properties and potentials are compared to PEG.

A variety of natural polymers such as heparin,[109] dextran,[110,111] and chitosan[112] have also been used in a wide range of drug-delivery systems. However, they fall beyond the scope of this Review, which focuses on synthetic polymers, and will not be discussed here.

6.1. Biodegradable Polymers

6.1.1. Poly(amino acid)s

Different synthetic poly(amino acid)s are currently being investigated as alternatives to PEG and are in different stages of development. Poly(glutamic acid) (PGA), which was first investigated by Li and Wallace, has already entered a phase III clinical trial in the form of a 40 kDa PGA-paclitaxel conjugate (37 wt%; Table 3).[113] Poly(hydroxyethyl-L-aspar-

Table 3: Drug-delivery systems containing alternative polymers to PEG and their current status in clinical trials.[a],[3,196,218,219]

Polymeric drug description	Manufacturer	Indication	Status
36 kDa PG-paclitaxel (21 wt%) (CT 2103, Opaxio)	Cell Therapeutics Inc.	NSCLC, ovarian, colorectal, breast and esophageal cancers	phase III
33 kDa PG-camptothecin (37 wt%) (CT 2106)	Cell Therapeutics Inc.	colorectal, lung and ovarian cancers	phase I/II
28 kDa PHPMA-doxorubicin (8.5 wt%) (PK1, FCE 28068)	Pfizer, Cancer Research Campaign, UK	NSCLC and breast cancers	phase III
25 kDa PHPMA-platinate (8.5 wt%) (AP 5280)	Access Pharmaceuticals	ovarian cancer	phase II
25 kDa PHPMA-doxorubicin (7.5 wt%)-galactosamine (PK2, FCE 28069)	Pfizer, Cancer Research Campaign, UK	hepatocellular carcinoma	phase I/II
25 kDa PHPMA-DACH-platinate (8.5 wt%) (AP 5346)	Access Pharmaceuticals	ovarian, melanoma and colorectal cancers	phase I/II
18 kDa PHPMA-camptothecin (10 wt%) (PNU 166148)	Pfizer, Cancer Research Campaign, UK	refractory solid tumors	phase I, discontinued
17 kDa PHPMA-PGA (37 wt%)-paclitaxel (5 wt%) (PNU 166945)	Pfizer, Cancer Research Campaign, UK	refractory solid tumors	phase I, discontinued

[a] NSCLC: non-small cell lung cancer; DACH: diaminocyclohexyl chelating ligand.

agine) (PHEA) and poly(hydroxyethyl-L-glutamine) (PHEG) were tested for drug delivery in different studies, in particular by Romberg et al. (Scheme 1).[96]

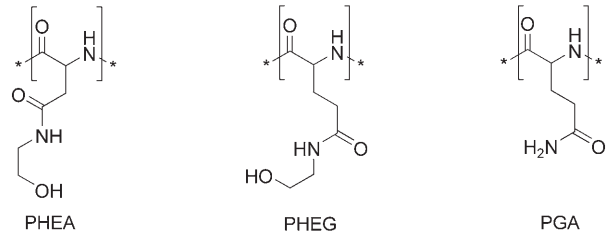

Scheme 1. Structures of poly(hydroxyethyl-L-asparagine) (PHEA), poly-(hydroxyethyl-L-glutamine) (PHEG), and poly(glutamic acid) (PGA).

PGA, PHEA, and PHEG are degraded in vivo to their corresponding amino acids, which can be metabolized by physiological pathways. Their degradation kinetics have been studied in vitro by using different enzymes, which lead either to complete decomposition into single amino acids or degradation to oligomers with 4 to 9 repeating units.[96,114] Biodegradability is the main strength of these polymers together with a prolonged blood circulation time of particles with poly(amino acid)-modified surfaces. This extension was similar to liposomes modified with 5 kDa PEG, 4 kDa PHEG, and 3 kDa PHEA. Similar elimination rates were measured for the poly(amino acid) liposomes as for the PEG liposomes. Additionally, a decrease in the ABC phenomenon has been shown when low doses were injected into rats (Figure 3).[96,115–117]

However, PHEG and PHEA showed increased SC5b-9 (SC5b-9 = complement factor formed by hydrolysis of C3) levels in ELISA tests, thus indicating the explicit activation of the complement system.[96] In addition, the antigenicity of polymers with more than three amino acids in the chain complicates their use in vivo.[118] Nevertheless, both polymers have been used in different drug carriers, such as 100 kDa PHEG-mitomycine conjugate (5.4 wt% mitomycine),[119] histidine-conjugated PHEA as a micelle-forming amphiphilic agent for doxorubicin,[120] or in combination with hyaluronic acid as a hydrogel for the administration of thrombin.[121]

In contrast to PHEA and PHEG, poly(glutamic acid) is already approved by authorities and widely used as a thickener in food and cosmetics, as a wetting agent in cosmetics, and as a fertilizer which slowly releases nitrogen.[122] Despite the known antigenicity of poly(amino acid)s, the paclitaxel-PGA conjugate was the first non-PEG polymer-drug conjugate to reach a phase III clinical trial (under the name Opaxio, formerly Xyotax (CT-2103); Figure 4).[113] It showed less side effects and improved drug efficiency than nonconjugated paclitaxel in some tumors. Although clinical trials have been carried out since 2005, all of them have failed to meet the primary end-point of extended survival compared to gemcitabine or vinorelbine for non-small cell lung cancer (NSCLC in patients with a poor performance status (PS2) is incurable with the therapy available). However, beneficial

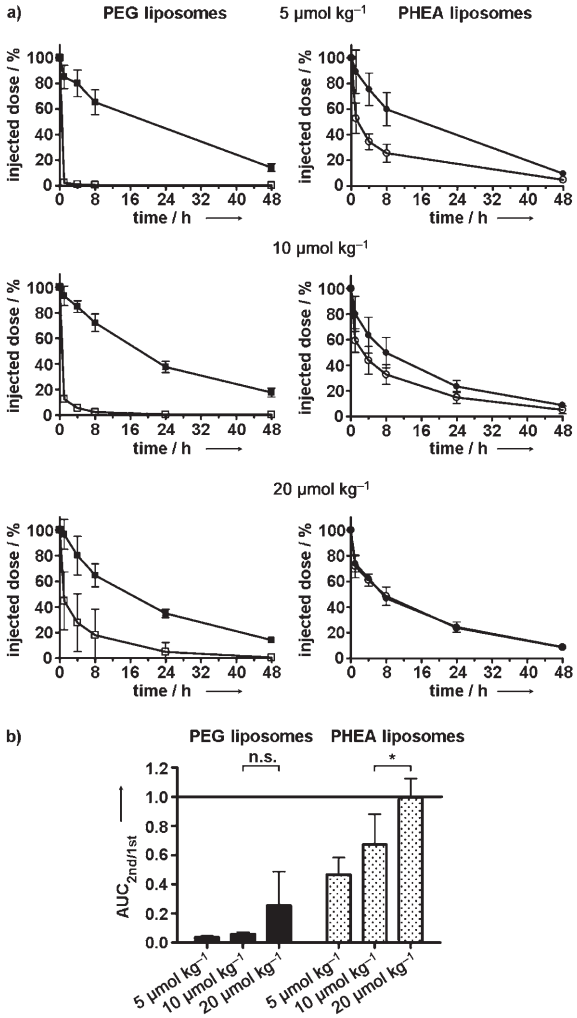

Figure 3. Effect of the polymer-lipid concentration on the pharmacokinetic behavior of PHEA and PEG liposomes after the first and second injection. a) Circulation kinetics of PHEA- (DPPC/cholesterol/PHEA-DODASuc) and PEG liposomes (DPPC/cholesterol/PEG-DSPE) (% of injected dose versus time). The closed symbols represent the results after the first injection; the open symbols those after the second injection of liposomes. b) Ratio of $AUC_{0-48\,h}$ of the second injection to the $AUC_{0-48\,h}$ of the first injection ($AUC_{2nd/1st}$) at the different lipid doses [$AUC_{0-48\,h}$ values were calculated from (a)]. Filled bars represent the $AUC_{2nd/1st}$ of PEG liposomes, dotted bars represent the $AUC_{2nd/1st}$ of PHEA liposomes. All results are expressed as the mean ± standard deviation ($n = 3$–4). $^*p < 0.05$; n.s. = not significant, DODASuc = succinyldioctadecylamine.[115] Reproduced from Ref. [115] with permission from Elsevier B.V.

tolerability, convenience, and safety, such as lower requirement for red blood cell transfusions, fewer hematologic and gastrointestinal adverse events as well as lower incidence of alopecia, fatigue, and weight loss were found.[123] Superior survival was observed among women less than 55 years old, and presumably premenopausal, upon treatment with Opaxio. This effect is attributed to the increased release of paclitaxel.[124,125] Hypersensitivity reactions were only rarely observed, and those that did occur were only mild to moderate.[113] Therefore, Cell Therapeutics, Inc., the pharmaceutical company holding the rights to Xyotax, received fast-

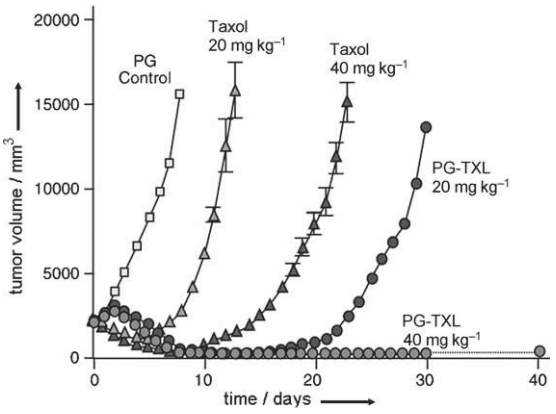

Figure 4. Antitumor activity of PGA-taxol in rats bearing rat breast tumor 13762F (PG = poly(glycerol), TXL = taxol). Each drug was injected intravenously in a single dose at the indicated equivalent paclitaxel concentration. Data are presented as the mean and standard deviations of the tumor volume.[113] Reproduced from Ref. [113] with permission from Elsevier B.V.

track designation from the FDA for paclitaxel-PGA in the indication of advanced non-small cell lung cancer in patients with a poor performance status. Currently, Cell Therapeutics has withdrawn its European marketing application of Opaxio for NSCLC after an EU panel raised concerns over the trial design.[126]

In summary, poly(amino acid)s combine a number of advantageous properties for drug-delivery applications such as prolonged blood circulation, decreased ABC clearance, and—particularly importantly—biodegradability. Their major drawback is complement activation; however, this effect may be tolerable in clinical trials, since it apparently leads to only moderate hypersensitivity reactions.

6.2. Non-Biodegradable Polymers

As the promising biodegradable polymers show an activation of the immune system, non-biodegradable polymers have also been taken into further consideration as alternatives to PEG for drug-delivery applications (Scheme 2).

6.2.1. Polymers with Heteroatoms in the Main Chain

6.2.1.1. Poly(glycerol)

The close structural similarity of poly(glycerol) (PG) to PEG renders the polymer predetermined for biological applications. Indeed, linear as well as hyperbranched PG (HPG) with molar masses ranging from 150 Da to 540 kDa have already been used as hydrophilic shells for conjugates and liposomes, reverse micelles, and hydrogels.[127–131]

The stealth effect and biocompatibility of these polymers have been evaluated in several studies. A prolonged blood circulation time of HPG liposomes compared to unmodified liposomes has been found for poly(glycerol)s with molar masses in the range of 150 Da to 750 Da.[128] Surfaces covered

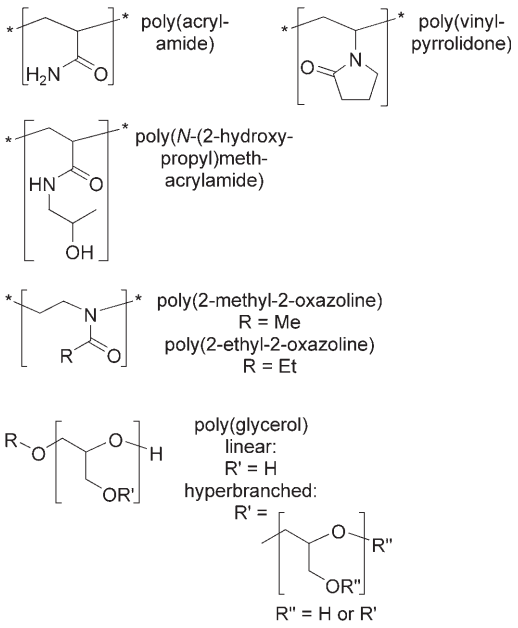

Scheme 2. Structures of the discussed non-biodegradable polymers.

with 1.5–5 kDa HPG showed similar or better protein repulsion than PEG of the same molar mass, probably because of its dense brush-like structure.[132,133]

Only very low in vitro cytotoxicity has been observed at concentrations of 10 mg mL^{-1} after 48 h incubation for HPGs with molar masses between 106 kDa and 870 kDa. In vivo studies on mice did not show any signs of toxicity.[134,135]

The hemocompatibility of HPG has been proven by examination of platelet activation and by coagulation studies.[127,134–136] By examining the generation of C3a, the complement activation of the immune system by poly(glycerol)s has been found to be in the same range as that in saline and PEG (Figure 5). However, since only C3a levels were examined, a direct comparison with the results obtained by Szebeni et al. on PEG is not possible, as their studies were based on SC5b-9 levels. A comparative study between linear PG and HPG of 6.4 kDa showed no significant difference in red blood cell aggregation, complement activation, and cell viability for the two polymer architectures in vitro as well as in vivo. No decrease in the biocompatibility and no increase in complement activation, because of the lower molar mass, was observed relative to the results found with 106 kDa and 870 kDa HPG.[134]

The same non-biodegradability in vivo can be speculated for PG and PEG because of their comparable polyether structures. Michael and Coots found no signs of catabolism of PG, and the predominant excretion in urine after oral administration is similar to PEG.[137] Additionally, accumulation in the liver and spleen (but not in the kidney, lung, or heart) was found for the high-molar-mass HPG, and only very low excretion in urine was reported over 30 days in mice (Figure 5).[131] However, HPGs of lower molar mass were not investigated in terms of their accumulation, thus making an estimation of the excretion limit for HPG impossible. In

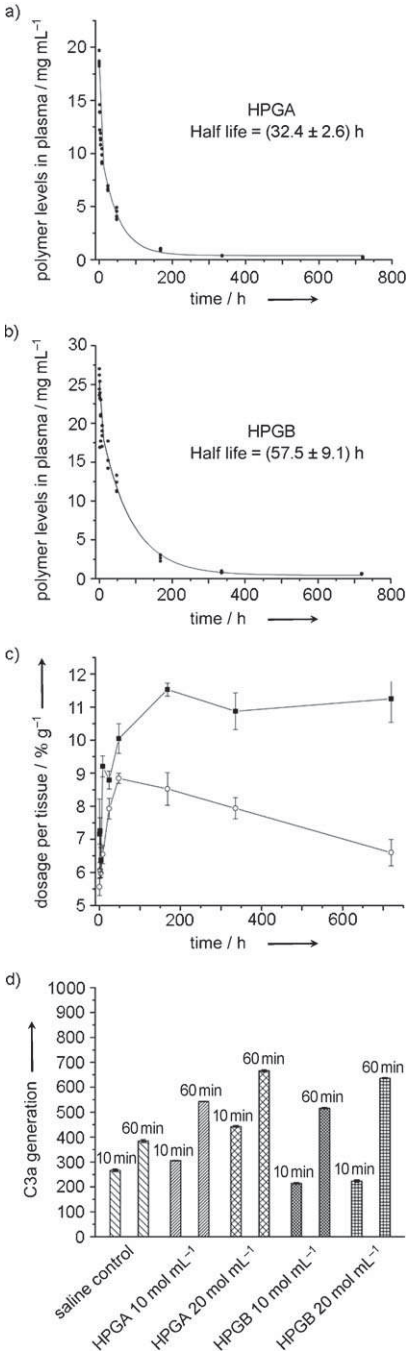

Figure 5. a) b) Plot of the polymer concentration in plasma versus time after intravenous injection into female Balb/C mice. c) Levels of polymer accumulated over time in liver injected intravenously into female Balb/C mice (blank squares: HPGA, filled squares: HPGB).[131] Reproduced from Ref. [131] with permission from Elsevier B.V. d) Generation of the C3a fragment upon incubation of polymers with PPP.[135] Reproduced from Ref. [135] with permission from Elsevier B.V. Abbreviations: HPGA = hyperbranched poly(glycerol) of 106 kDa, HPGB = hyperbranched poly(glycerol) of 540 kDa, PPP = platelet-poor plasma.

contrast to PEG, no degradation studies under mechanical stress have been reported for PG, but as PG possesses a similar ether structure as PEG, an analogous susceptibility to oxygen-induced degradation might be assumed.

The use of glycidol or epichlorhydrine as latent AB_m monomers permits better control over the polymerization to give more defined hyperbranched poly(glycerol)s with the PDI value reduced from 5 to 1.8.[138] While hyperbranched poly(glycerol)s are accessible from glycidol or epichlorhydrine monomers, linear polymers are available by protecting the free hydroxy group of glycidol to prevent branching. The polymerization step is followed by deprotection of the hydroxy groups.[134] The functionalization of PG is feasible via the initiator, and since poly(glycerol)s are hydroxy-rich polymers, all the general substitution reactions of hydroxy groups are possible and result in high degrees of functionalization (Scheme 3).[129,136,139] Diglycerol, PG-3, and PG-4 are commercially available oligomers. Esters of up to PG-10 are approved by the FDA as food and pharma additives.[140]

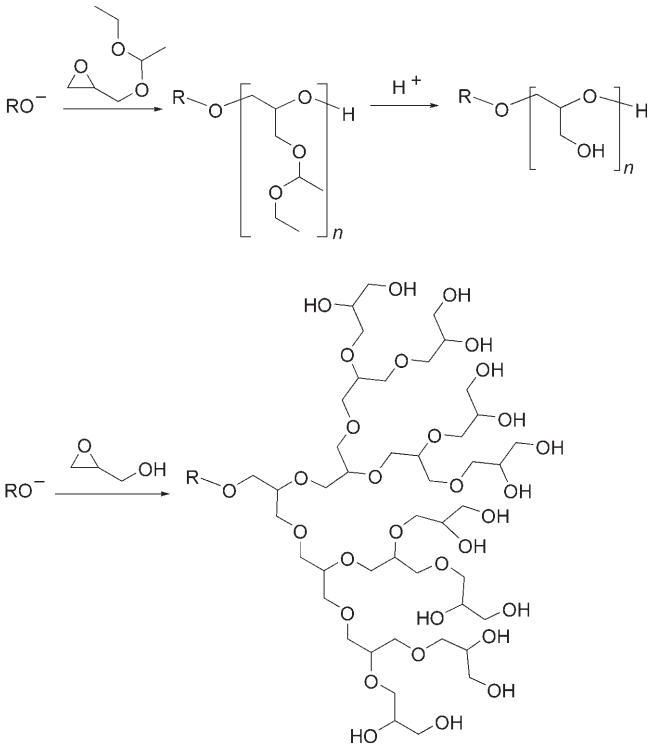

Scheme 3. Synthesis of linear and hyperbranched poly(glycerol).

In conclusion, since PG possesses a similar structure to PEG it shows comparable advantages and disadvantages. An additional interesting possibility is PG branching, since the hyperbranched arrangement allows very high degrees of functionalization, although some end groups will be sterically hidden. The high degree of branching is also advantageous for the circulation time, since branched structures are not as quickly excreted as their linear analogues. Furthermore, highly branched polymers have low intrinsic viscosity and are, therefore, expected to increase the blood viscosity only slightly, which has been shown to cause a variety of complex physiological effects.[141]

6.2.1.2. *Poly(2-oxazoline)s*

The hydrophilic poly(2-methyl-2-oxazoline) (PMeOx) and poly(2-ethyl-2-oxazoline) (PEtOx) were discovered in the 1960s.[142–145] Since then a wide range of chemistry has built up around this class of polymers including the living polymerization method, which yields very low PDI values, and versatile end-group chemistry.[146,147]

Nonetheless, the application of poly(2-oxazoline)s in biomedical fields arose only recently, and although both types of polymers have been quite widely tested for different drug-carrier applications, only a few basic biological and stability studies have been reported.[148,149] Drug-transport systems with poly(2-oxazoline) were developed, for example, based on micelles of PLA-PEtOx-PLA [PLA = poly(lactic acid)] as carriers of doxorubicin.[150] PEtOx-poly(ε-caprolactone) micelles with paclitaxel have been shown to possess the same efficiency as Cremophor EL formulated paclitaxel.[151] A cytosine arabinose conjugate of PEtOx showed IC_{50} values in HeLa cell viability tests in a similar range as the corresponding PEG conjugate.[152] PMeOx-coated surfaces have been shown to possess the same protein repellency as PEG.[153,154]

One of the few fundamental biological studies was performed by Veronese et al. They showed erythrocyte compatibility for PEtOx with molar masses of 5, 10, and 20 kDa at polymer concentrations of 5 mg mL^{-1}. They also showed that 20 kDa PEtOx was safe and nontoxic for intravenous administration every second day at doses of up to 50 mg kg^{-1} over a period of 2 weeks (control: saline).[155] The hydrophilic shells of PMeOx and PEtOx prolonged the blood circulation times of liposomes in the same range as PEG.[156]

In addition, Zalpinsky et al. documented similar prolonged blood circulation of PEG-, PMeOx- and PEtOx-modified liposomes with 5 mol% of phospholipid and about 40 repeating units of each polymer.[157] Additionally, they found that three different types of liposomes showed a similar tissue distribution profile after 24 h, which means there is preferential distribution in the liver, spleen, and kidney (Figure 6).[157] Analogous results have been found for ^{111}In-labeled 4 kDa PMeOx and 4 kDa PEtOx, which showed an augmented blood circulation time but also an increased occurrence of the polymer in the kidney and bladder.[158] Furthermore, PEtOx possesses a lower critical solution temperature (LCST), which can be used for enhanced targeting of specific tissue.[149,159]

The biodegradation of PEtOx was investigated by using proteinase K, a nonhuman enzyme. A partial degradation to PEI was found on incubation, but whether this degradation also takes place in humans was not investigated.[160] Cleavage of this side group generates the cationic derivative PEI, which was shown to be cytotoxic as well as to induce erythrocyte aggregation and hemolysis depending on the molar mass, branching, and number of cationic groups. The lower the molar mass and the degree of branching of the PEI, the higher the bio- and hemocompatibility.[161,162]

In summary, PMeOx and PEtOx show a behavior comparable to PEG in terms of blood circulation time, opsoniza-

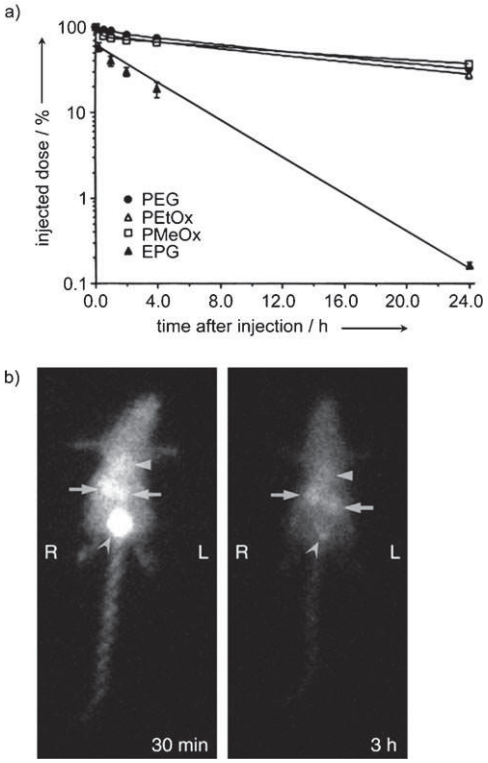

Figure 6. a) Blood lifetimes of ^{67}Ga-labeled liposomes [(90 ± 5) nm] prepared from the EPC, cholesterol, and DSPE conjugate of either PEG, PMeOx, or PEtOx, as well as a control EPG; molar ratio 1.85:1:0.15. Four Sprague–Dawley rats were injected with each liposomal preparation in the tail vein. Samples obtained by retroorbital bleeding at various times were used to determine the radioactivity in the blood (EPC: egg phosphatidylcholine, EPG: egg phosphotidylglycerol).[156] Reproduced from Ref. [156] with permission from the American Chemical Society. b) γ-Camera imaging of the in vivo distribution of $PMeOx_{48}$PipDOTA[^{111}In] in a CD1 mouse 30 min and 3 h after intravenous injection (PipDOTA: piperazine-thiouryl-*p*-benzyl-1,4,7,10-tetraazacyclododecane-*N*′,*N*,*N*,*N*-tetraacetic acid). The highest concentrations were in the bladder (thin arrowhead), the kidneys (arrows), and the blood pool in the heart (thick arrowhead).[158] Reproduced from Ref. [158] with permission from Elsevier B.V.

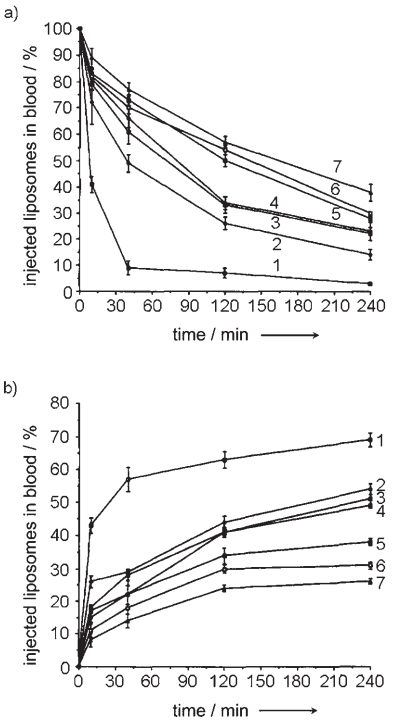

Figure 7. a) Liposome clearance from the blood of mice; b) liposome accumulation in the liver. 1) "plain" liposomes; 2) PVP-L-P-liposomes (2.5 mol% PVP); 3) PAAm-L-P-liposomes (2.5 mol% PAAm); 4) PEG-liposomes (2.5 mol% PEG); 5) PVP-L-P liposomes (6.5 mol% PVP); 6) PAAm-L-P liposomes (6.5 mol% PAAm); 7) PEG liposomes (6.5 mol% PEG) (L: molar mass of polymer 6–8 kDa, P: with terminal palmityl group). Reproduced from Ref. [163] with permission from Elsevier B.V.

tion, and organ distribution. Nevertheless, important details of immune activation and mechanical stability need further investigation to further evaluate the potential of poly(2-oxazoline)s as alternatives to PEG.

6.2.2. *Vinyl Polymers*

6.2.2.1. *Poly(acrylamide)*

Torchilin et al. reported that liposomes covered with 7 kDa poly(acrylamide) (PAAm) showed prolonged blood circulation compared to unmodified liposomes (Figure 7).[163] Microspheres of PAAm containing 5-fluorouracil,[164] hydrogels for ibuprofen release, and ultrafine hydrogel nanoparticles with *meta*-tetra(hydroxyphenyl)chlorin for photodynamic therapy (PDT) have also been tested.[165] Hemoglobin-containing PAAm microspheres have also been investigated as oxygen carriers.[166]

PAAm is often affirmed in such studies to be non-immunogenic, highly protein resistant,[167,168] and not to show cytotoxic effects.[169] However, other reports state an inflammatory response upon implantation of PAAm hydrogels.[170–172]

Other reported drawbacks of PAAm are the following:

1) PAAm can degrade to acrylamide by thermal and photolytic effects;[171]
2) it has a carbon backbone and, as a result, is not biodegradable;[171]
3) a preferential distribution of 7 kDa PAAm liposomes in the liver;[163]
4) PAAm is synthesized by polymerization of acrylamide, a monomer which is known to induce a variety of severe neurotoxic effects[167] so that residual monomer may account for adverse reactions.[171,173]

In view of the controversies and the described disadvantages of PAAm, the wide application of PAAm seems to be surprising. Although PAAm seems to improve blood clearance rates of liposomes, it activates the immune system and even worse, the monomer shows very distinct toxic side effects—it is classified by the International Agency for Research on Cancer in group 2b (meaning the agent is possibly carcinogenic to humans)—and is produced during

thermal and photolytic degradation of the polymer. These drawbacks limit the widespread use of PAAm for biomedical applications.

6.2.2.2. *Poly(vinylpyrrolidone)*

Poly(vinylpyrrolidone) (PVP) is commercially available, for example, under the brand name Kollidon from BASF. In the cosmetic and pharmaceutical industry it is used as, for example, tablet coating and binder as well as an excipient for the formulation of poorly water soluble drugs. PVP is also used in adhesives, coatings and inks, photoresists, paper, photography, textiles, and fiber applications. PVP was used as a plasma expander in the first half of the 20th century, and the iodine complex (Povidone-iodine) possesses disinfectant properties. As a food additive, PVP is used as a stabilizer and has the E number E1201.[40]

This wide range of oral applications indicate that there is already potential compatibility to biomedical fields and, indeed, investigations concerning its suitability for drug-delivery applications look very promising. Its highly hydrated structure makes it suitable to increase the water content of other polymeric materials.[174,175] It is possibly through this high hydration that an interaction with the immune system is suppressed, and distribution studies on poly(hydroxyethyl methacrylate) (PHEMA) and PHEMA-PVP copolymer hydrogels suggest that PVP shows no C3a activation.[176] This leads to the prolonged blood circulation of 6 kDA and 7 kDa PVP liposomes and 6 kDa PVP-superoxiddismutase (SOD) conjugates (Figure 7).[163,177,178]

Nevertheless, contradictory results have also been reported that show an enhanced protein adsorption on 6 kDa PVP-uricase conjugates compared to native uricase as well as the formation of PVP antibodies.[179] Similar observations have been made with PVP-conjugated D-*N*-acetylhexosamidase A, which can interact strongly with antibodies of the native protein.[179] Despite this finding, PVP has been tested in several drug-delivery systems, including a SOD conjugate[178] and liposomes with a stabilizing, hydrophilic PVP shell.[163,177,180] In addition, PLA-PVP micelles[181,182] and microspheres[183] as well as PVP-gelatin hydrogels[184] and PVP have been studied for their formulation assistance.[185,186] PVP has also been used as a gene-delivery system as it can bind presumably through hydrogen bonds with DNA to form a complex. PVP increased the stability and half-life of DNA in vivo by shielding the negative charge and protecting it against enzymatic degradation.[187]

Another promising aspect of PVP is its slower degradation compared to PEG under UV or ultrasound irradiation,[103,188] even though the formation of peroxides during drying can not be prevented.[189] The Ph. Eur. limits the peroxide content of this polymer to 400 ppm. As for PEG, the slow in vitro peroxide-mediated degradation of the polymer is in contrast to its in vivo non-biodegradability. PVP possesses a carbon backbone that is not degraded on exposure to enzymes. This led to the removal of PVP as a plasma expander from the market: patients who received PVP with a molar mass above 25 kDa, which cannot be excreted from the body developed a "PVP storage disease".[190]

PVP can be synthesized by free-radical polymerization of vinylpyrrolidone as well as by controlled radical polymerization methods.[174] The latter method leads to improved PDI values below 1.2,[182,191–193] variable end groups,[182,194] and—most importantly—to the prevention of high-molar-mass PVP. The vinylpyrrolidone monomer is presumed to be a carcinogen and should be removed carefully from the polymer.

In conclusion, the biocompatibility of PVP looks quite promising for polymers with molar masses below the kidney threshold. Nevertheless, PVP has similar problems as PEG: an unclear immunological behavior and non-biodegradability, which leads to accumulation of the polymer above the excretion limit.

6.2.2.3. *Poly(N-(2-hydroxypropyl)methacrylamide)*

The bio-application of poly(*N*-(2-hydroxypropyl)methacrylamide) (PHPMA) was established by Kopecek et al. in the 1970s.[195] The application of PHPMA was further developed by Rihova et al. and Duncan, which led to the use of PHPMA conjugates in clinical trials.[195]

The most successful conjugate, a 28 kDa PHPMA-doxorubicin copolymer (8.5 wt%; doxorubicin PK1; clinical trial FCE 28068 phase III; Scheme 4) was tested against various cancers (Table 3) and showed activity against NSCLC, colorectal cancer, and breast cancer.[196] Additionally, neither cardiotoxicity nor multidrug resistance was observed in these studies, no liver and spleen accumulation was noted, and no immunogenicity or polymer-related toxicity was detected.[195]

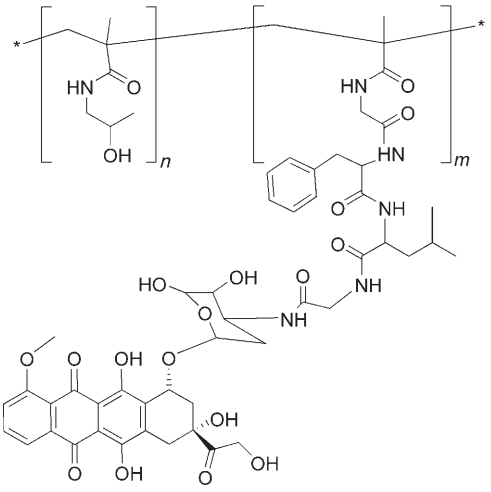

Scheme 4. A doxorubicine-HPMA conjugate.

In addition, 25 kDa PHPMA conjugates with doxorubicin galactosamine (7.5 wt%), carboplatinate (8.5 wt% Pt), and DACH platinate (8.5% w/w) successfully entered phase I/II trials for various cancers.[195] However, the fact that the clinical trials for the PHPMA-paclitaxel and PHPMA-camptothecin conjugates were discontinued because of a lack of antitumor activity shows that biological events that result in efficient drug-delivery systems in vivo are not easily understood and not yet fully explored (Table 3).

Other HPMA-conjugated systems for cancer therapy were also investigated, but have not yet entered clinical trials. These include a glutathione derivative to inhibit human glyoxalase and a cyclohexanone derivative coupled to HPMA with a molar mass of 3–30 kDa and with various drug contents. In vitro studies with murine B16 melanoma cells showed the conjugate was less efficient than the free drug, but this result is not surprising, since the success of conjugates is based on the retarded, slower release of the drug in vivo.[197] A study of 16 to 50 kDa geldanamycin-HPMA conjugates also revealed reduced toxicities in A2780 ovarian cancer cells as well as prostate cancer cell lines (PC-3 and DU145) and endothelial cells (HUVECs). The improved in vivo tolerance of mice against the conjugate was investigated, and showed a tolerance for 80 mg kg^{-1} with no signs of toxicity (compared to 30 mg kg^{-1} for the free drug).[198,199]

Conventional conjugation by PHPMA occurs by binding to the multiple side chains of the polymer. For conjugates with proteins, conjugation of one end of the PHPMA chain (instead of the multiple side groups to yield starlike architectures) turned out to be more advantageous. The PDI value above 3.5 for a conventional protected SOD conjugate was reduced to 2 by conjugation with semitelechelic PHPMA. This probably causes the improved biocompatibility, as significantly larger numbers of antibodies were formed against the classic form of PHPMA-SOD conjugate than the star-shaped PHPMA-SOD conjugate.[200,201]

Drug-delivery systems with different architectures, such as starlike doxorubicin conjugates, conjugation with multiple side groups, or the use of the polymer as an excipient all showed a decreased efficiency in vitro against A2780 ovarian carcinoma cells compared to the free doxorubicin.[202] HPMA conjugates were prepared for active targeting by a Fab antibody, and mesochlorin was introduced as the active principle for photodynamic therapy. This study showed an inhibition of the growth of ovarian carcinoma cells under irradiation.[203] Complexes of poly(L-lysine) and DNA with semitelechelic 5.5 kDa and 8.5 kDa PHPMA were found to display an increased in vitro stability in salt solutions against albumin-induced aggregation, decreased albumin binding, and reduced phagocytic uptake, but have not shown any prolonged circulation times in vivo. The reason for that remains to be elucidated.[204] The blood circulation time for PLL-PEI complexes was found to increase from 5 to 90 minutes by modification with multivalent PHPMA.[23]

Liposomes with PHPMA hydrophilic shells that would transport calcein were prepared.[205] Whiteman et al. showed that liposomes modified with 4.3 kDa PHPMA have longer blood circulation times than unmodified ones (Figure 8).[206] Different types of hydrogels of PHPMA were also tested as drug carriers,[207] for example, for doxorubicin[208] or for PHPMA-adriamycine conjugates to overcome multidrug resistence.[208] PHPMA can be prepared by either free or controlled radical polymerization mechanisms (such as atom-transfer radical polymerization (ATRP) or reversible addition-fragmentation chain transfer (RAFT)),[209–211] and different end groups for chemical modifications were obtained.[212]

The degradation of the polymer under thermal heating was studied.[213] Again, similar to all vinyl polymers, they are degraded under stress, but in general they are not biodegradable under physiological conditions.[214] Nonetheless, it has been shown that a molar mass of 30 kDa ensures elimination of the carrier from the body.[195] The excretion limit is 45 kDa, and long-circulating carriers end up in the liver and spleen.[214–216] However, a DOX-PHPMA conjugate with a molar mass above 30 kDa tested in mice showed a diminished doxorubicin concentration in the heart, but an augmented presence of the conjugate was found in the liver and spleen.[217]

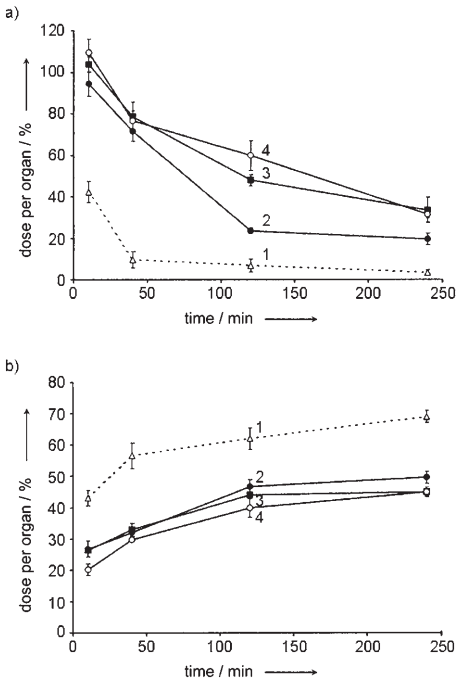

Figure 8. a) Blood clearance and b) liver accumulation for 1) plain liposomes and 2) liposomes with 0.3 mol% PHPMA-oleic acid, M_w 4300 Da; 3) liposomes with 3 mol% PHPMA-oleic acid, M_w 4300 Da; 4) liposomes with 3 mol% PHPMA-oleic acid, M_w 2900 Da.[206] Reproduced from Ref. [206] with permission from Informa Healthcare, Taylor & Francis Group.

In summary, PHPMA conjugates have already entered clinical trials and the results look very promising. However, immunological and stability questions as well as the excretion limit have not yet been investigated and the results of the clinical trials have to be awaited.

7. Conclusions

PEG is currently the most used polymer in the biomedical field of drug delivery and the only polymeric therapeutic that has market approval for different drugs. The success of PEG is based on its hydrophilicity, decreased interaction with blood components, and high biocompatibility. However, scientific results obtained in recent years show that it may also have possible drawbacks, such as interaction with the immune system, possible degradation under stress, and accumulation in the body above an uncertain excretion limit. Furthermore, many of the studies on the biocompatibility of PEG date back to the 1950s to 1970s and, therefore,

additional investigations are required that exploit contemporary techniques and analytical possibilities, in particular at the cellular level.

If an alternative polymer to PEG has to be chosen, a wide range of chemically very different synthetic polymers are available, although only a limited number are water soluble. These water-soluble polymers have to compete with the very high requirements of the gold standard—PEG. It becomes very clear when considering the potential alternatives that, in comparison to PEG, none of the alternative polymers are supported by sufficient studies concerning their biocompatibility, degradation under stress, and excretion limit. Even though the difficult patent situation of PEG pushed the search for alternative polymers, none of them have yet achieved approval for application. Most of the hydrophilic polymers cannot be considered as alternatives because they undergo severe interactions with the immune system and, therefore, are not able to prolong drug-carrier circulation times in the body. The most promising polymers that do show enhanced circulation time are poly(glycerol)s, poly(amino acid)s, poly(vinylpyrrolidone), poly(2-oxazoline)s, and poly(*N*-(2-hydroxypropyl)methacrylamide).

Clearance by the kidneys can be favored by using biodegradable polymers. However, the only polymers that provide both a biodegradable structure and a stealth effect are synthetic poly(amino acid)s. All other considered polymers show the same disadvantage as PEG, namely non-biodegradability and the associated unknown fate after disaggregation of the drug carrier, in particular after frequently repeated administrations. Poly(amino acid)s are the only polymers not to excite the accelerated blood clearance phenomenon, which is an advantage over PEG. An evaluation is not possible for all the other presented polymers, as investigations on this topic have not yet been reported. It should also be considered that the presented polymers, with their rather different chemical structures, might follow different degradation pathways, which may lead to new chemical species of yet unknown biocompatibility.

Degradation under stress has barely been investigated for all of the alternative polymers; thus, conclusions can not be drawn except in the case of PAAm, which degrades to its toxic monomer and is, therefore, unsuitable for biomedical applications. Interestingly, most of the monomers are toxic compounds, whereas the resulting polymers are biocompatible.

Considered as a whole, it appears that when all the polymers are judged with the same severe criteria, PEG remains the gold standard in the field of polymeric drug delivery, as it is the best investigated polymer. However, further studies with more systematic investigations may lead to a different view. In fact, possible substitutes are showing promising results and just need further investigations to allow proper evaluation and comparison with PEG.

The Dutch Polymer Institute (DPI) and the Thüringer Ministerium für Bildung, Wissenschaft und Kultur (TMBWK, ProExzellenz-Programm NanoConSens, B514-09049) are gratefully acknowledged for financial support. We thank Dr. Tobias Pöhlmann, Dr. Stephanie Hornig, and Prof. Dieter Schubert for helpful comments. Additionally, we would like to thank the referees for their kind efforts and helpful remarks.

Received: May 19, 2009
Published online: July 20, 2010

[1] G. Pasut, F. M. Veronese, *Prog. Polym. Sci.* **2007**, *32*, 933 – 961.
[2] T. M. Allen, P. R. Cullis, *Science* **2004**, *303*, 1818 – 1822.
[3] R. Duncan, M. J. Vicent, F. Greco, R. I. Nicholson, *Endocr.-Relat. Cancer* **2005**, *12*, S189 – S199.
[4] D. Bhadra, S. Bahdra, P. Jain, N. K. Jain, *Pharmazie* **2002**, *57*, 5 – 28.
[5] C. Monfardini, F. M. Veronese, *Bioconjugate Chem.* **1998**, *9*, 418 – 450.
[6] A. Abuchowski, T. van Es, N. C. Palczuk, F. F. Davis, *J. Biol. Chem.* **1977**, *252*, 3578 – 3581.
[7] A. Abuchowski, J. R. McCoy, N. C. Palczuk, T. van Es, F. F. Davis, *J. Biol. Chem.* **1977**, *252*, 3582 – 3586.
[8] F. Veronese, J. M. Harris, *Adv. Drug Delivery Rev.* **2002**, *54*, 167 – 252.
[9] F. Veronese, J. M. Harris, *Adv. Drug Delivery Rev.* **2003**, *55*, 1259 – 1350.
[10] R. Gref, Y. Minamitake, M. T. Peracchia, V. Trubetskoy, V. Torchilin, R. Langer, *Science* **1994**, *263*, 1600 – 1603.
[11] J. Kreuter, *Int. J. Pharm.* **2007**, *331*, 1 – 10.
[12] G. Gregoriadis, *N. Engl. J. Med.* **1976**, *295*, 704 – 710.
[13] G. Gregoriadis, *N. Engl. J. Med.* **1976**, *295*, 765 – 770.
[14] A. L. Klibanov, K. Maruyama, V. P. Torchilin, L. Huang, *FEBS Lett.* **1990**, *268*, 235 – 237.
[15] G. Blume, G. Cevc, *Biochim. Biophys. Acta Biomembr.* **1990**, *1029*, 91 – 97.
[16] M. C. Woodle, M. Newman, L. Collins, C. Redemann, F. Martin, *Proc. Int. Symp. Controlled Release Bioact. Mater.* **1990**, *17*, 77 – 78.
[17] M. C. Woodle, *Adv. Drug Delivery Rev.* **1995**, *16*, 249 – 265.
[18] D. D. Lasic, D. Needham, *Chem. Rev.* **1995**, *95*, 2601 – 2628.
[19] V. P. Torchilin, *Nat. Rev. Drug Discovery* **2005**, *4*, 145 – 160.
[20] A. V. Kabanov, V. P. Chekhonin, V. Y. Alakhov, E. V. Batrakova, A. S. Lebedev, N. S. Melik-Nubarov, S. A. Arzhakov, A. V. Levashov, G. V. Morozov, *FEBS Lett.* **1989**, *258*, 343 – 345.
[21] G. S. Kwon, K. Kataoka, *Adv. Drug Delivery Rev.* **1995**, *16*, 295 – 309.
[22] S. Svenson, D. A. Tomalia, *Adv. Drug Delivery Rev.* **2005**, *57*, 2106 – 2129.
[23] D. Oupicky, M. Ogris, K. A. Howard, P. R. Dash, K. Ulbrich, L. W. Seymour, *Mol. Ther.* **2002**, *5*, 463 – 472.
[24] M. Ogris, S. Brunner, S. Schueller, R. Kircheis, E. Wagner, *Gene Ther.* **1999**, *6*, 595 – 605.
[25] H.-K. Nguyen, P. Lemieux, S. V. Vinogradov, C. L. Gebhart, N. Guerin, G. Paradis, T. K. Bronich, V. Y. Alakhov, A. V. Kabanov, *Gene Ther.* **2000**, *7*, 126 – 138.
[26] A. Aigner, D. Fischer, T. Merdan, C. Brus, T. Kissel, F. Czubayko, *Gene Ther.* **2002**, *9*, 1700 – 1707.
[27] S. Parveen, S. K. Sahoo, *Clin. Pharmacokinet.* **2006**, *45*, 965 – 988.
[28] H. Maeda, J. Wua, T. Sawaa, Y. Matsumurab, K. Horic, *J. Controlled Release* **2000**, *65*, 271 – 284.
[29] K. Greish, *J. Drug Targeting* **2007**, *15*, 457 – 464.
[30] R. Haag, F. Kratz, *Angew. Chem.* **2006**, *118*, 1218 – 1237; *Angew. Chem. Int. Ed.* **2006**, *45*, 1198 – 1215.
[31] D. Schmaljohann, *Adv. Drug Delivery Rev.* **2006**, *58*, 1655 – 1670.
[32] J. Kost, R. Langer, *Adv. Drug Delivery Rev.* **2001**, *46*, 125 – 148.
[33] C. de Las Heras Alarcon, S. Pennadem, C. Alexander, *Chem. Soc. Rev.* **2005**, *34*, 276 – 285.

[34] A. W. York, S. E. Kirkland, C. L. McCormick, *Adv. Drug Delivery Rev.* **2008**, *60*, 1018 – 1036.
[35] V. P. Torchilin, V. S. Trubetskoy, *Adv. Drug Delivery Rev.* **1995**, *16*, 141 – 155.
[36] S. M. Grayson, W. T. Godbey, *J. Drug Targeting* **2008**, *16*, 329 – 356.
[37] R. Luxenhofer, M. Bezen, R. Jordan, *Macromol. Rapid Commun.* **2008**, *29*, 1509 – 1513.
[38] F. M. Veronese, G. Pasut, *Drug Discovery Today* **2005**, *10*, 1451 – 1458.
[39] C. Passirani, J.-P. Benoit, *Biomaterials for Delivery and Targeting of Proteins and Nucleic Acids*, CRC, Boca Raton, FL, **2005**.
[40] V. P. Torchilin, *J. Microencapsulation* **1998**, *15*, 1 – 19.
[41] H. Petersen, P. M. Fechner, D. Fischer, T. Kissel, *Macromolecules* **2002**, *35*, 6867 – 6874.
[42] http://www.inchem.org/documents/jecfa/jecmono/v14je19.htm (WHO International Programme on Chemical Safety), last accessed 07.10.2009.
[43] O. Biondi, S. Motta, P. Mosesso, *Mutagenesis* **2002**, *17*, 261 – 264.
[44] I. B. Mosbah, R. Franco-Go, H. B. Abdennebi, R. Hernandez, G. Escolar, D. Saidane, J. Rosello-Catafau, C. Peralta, *Transplant. Proc.* **2006**, *38*, 1229 – 1235.
[45] B. Balakrishnana, D. Kumarb, Y. Yoshidab, A. Jayakrishnan, *Biomaterials* **2005**, *26*, 3495 – 3502.
[46] M. Rahman, C. S. Brazel, *Prog. Polym. Sci.* **2004**, *29*, 1223 – 1248.
[47] S. Lakshmi, A. Jayakrishnan, *Artif. Organs* **1998**, *22*, 222 – 229.
[48] L. J. Suggs, J. L. West, A. G. Mikos, *Biomaterials* **1999**, *20*, 683 – 690.
[49] *Encyclopedia of Polymer Science and Technology* (Ed.: H. F. Mark), Wiley, New York, **2007**.
[50] A. Asatekin, S. Kang, M. Elimelech, A. M. Mayes, *J. Membr. Sci.* **2007**, *298*, 136 – 146.
[51] K. H. Cheng, S. L. Leung, H. W. Hoekman, W. H. Beekhuis, P. G. H. Mulder, A. J. M. Geerards, A. Kijlstra, *Lancet* **1999**, *354*, 179 – 183.
[52] O. H. Kwon, Y. C. Nho, Y. M. Lee, *J. Ind. Eng. Chem.* **2003**, *9*, 138 – 145.
[53] W. Johnson, *Int. J. Toxicol.* **2001**, *20*, 13 – 26.
[54] C.-J. Le Coz, E. Heid, *Contact Dermatitis* **2001**, *44*, 308 – 319.
[55] A. Chanan-Khan, J. Szebeni, S. Savay, L. Liebes, N. M. Rafique, C. R. Alving, F. M. Muggia, *Ann. Oncol.* **2003**, *14*, 1430 – 1437.
[56] J. Szebeni, *Toxicology* **2005**, *216*, 106 – 121.
[57] J. Janatova, *ASAIO J.* **2000**, S53 – S62.
[58] J. Szebeni, L. Baranyi, S. Savay, J. Milosevits, R. Bunger, P. Laverman, J. M. Metselaar, G. Storm, A. Chanan-Khan, L. Liebes, F. M. Muggia, R. Cohen, Y. Barenholz, C. R. Alving, *J. Liposome Res.* **2002**, *12*, 165 – 172.
[59] J. Szebeni, F. M. Muggia, C. R. Alving, *J. Natl. Cancer Inst.* **1998**, *90*, 300 – 306.
[60] J. M. Metselaar, Dissertation, Dept. Pharmaceutics, Utrecht Institute for Pharmaceutical Sciences, Utrecht University, The Netherlands, **2006**.
[61] A. H. Brouwers, D. J. de Jong, E. T. M. Dams, W. J. G. Oyen, O. C. Boerman, P. Laverman, T. H. J. Naber, G. Storm, F. H. M. Corstens, *J. Drug Targeting* **2000**, *8*, 225 – 233.
[62] M. J. Parr, D. Masin, P. R. Cullis, M. B. Bally, *J. Pharmacol. Exp. Ther.* **1997**, *280*, 1319 – 1327.
[63] D. Calvo, J. M. de La Hera, D.-H. Lee, *Rev. Esp. Cardiol.* **2006**, *59*, 399 – 400.
[64] M. C. H. de Groot, B. J. van Zwieten-Boot, A. C. van Grootheest, *Ned. Tijdschr. Geneeskd.* **2004**, *148*, 1887 – 1888.
[65] P. A. Dijkmans, C. A. Visser, O. Kamp, *Eur. J. Echocardiogr.* **2005**, *6*, 363 – 366.
[66] P. Dewachter, C. Mouton-Faivre, *Allergy* **2005**, *60*, 705 – 706.
[67] A. W. Richter, E. Akerblom, *Int. Arch. Allergy Appl. Immunol.* **1983**, *70*, 124 – 131.
[68] A. W. Richter, E. Akerblom, *Int. Arch. Allergy Appl. Immunol.* **1984**, *74*, 36 – 39.
[69] J. K. Armstrong, G. Hempel, S. Koling, L. S. Chan, T. Fisher, H. J. Meiselman, G. Garratty, *Cancer* **2007**, *110*, 103 – 111.
[70] N. J. Ganson, S. J. Kelly, E. Scarlett, J. S. Sundy, M. S. Hershfield, *Arthritis Res. Ther.* **2005**, *8*, R12 – R22.
[71] C. Assal, P. Y. Watson, *Gastrointest. Endocrinol.* **2006**, *64*, 294 – 295.
[72] E. Schuman, P. E. Balsam, *Gastrointest. Endocrinol.* **1991**, *37*, 411.
[73] E. Brullet, A. Moron, X. Calvet, C. Frias, J. Sola, *Gastrointest. Endocrinol.* **1992**, *38*, 400 – 401.
[74] N. Stollman, H. D. Manten, *Gastrointest. Endocrinol.* **1996**, *44*, 209 – 210.
[75] M. Ito, D. Watanabe, M. Kobayashi, Y. Tamada, Y. Matsumoto, *Contact Dermatitis* **2006**, *54*, 225.
[76] Y. N. Kwee, J. Dolovich, *J. Allergy Clin. Immunol.* **1982**, *69*, 138.
[77] A. A. Fisher, *Contact Dermatitis* **1978**, *414*, 135 – 138.
[78] S. Quartier, M. Garmyn, S. Becart, A. Goosens, *Contact Dermatitis* **2006**, *55*, 257 – 267.
[79] E. T. M. Dams, P. Laverman, W. J. G. Oyen, G. Storm, G. L. Scherphof, J. W. M. van der Meer, F. H. M. Corstens, O. C. Boerman, *J. Pharmacol. Exp. Ther.* **2000**, *292*, 1071 – 1079.
[80] T. Ishida, R. Maeda, M. Ichihara, K. Irimura, H. Kiwada, *J. Controlled Release* **2003**, *88*, 35 – 42.
[81] H. Koide, T. Asai, K. Hatanaka, T. Urakami, T. Ishii, E. Kenjo, M. Nishihara, M. Yokoyama, T. Ishida, H. Kiwada, N. Okua, *Int. J. Pharm.* **2008**, *362*, 197 – 200.
[82] T. Ishida, M. Harada, X. Y. Wang, M. Ichihara, K. Irimura, H. Kiwada, *J. Controlled Release* **2005**, *105*, 305 – 317.
[83] T. Ishida, H. Kiwada, *Int. J. Pharm.* **2008**, *354*, 56 – 62.
[84] T. Ishida, K. Masuda, T. Ichikawa, M. Ichihara, K. Irimura, H. Kiwada, *Int. J. Pharm.* **2003**, *255*, 167 – 174.
[85] T. Ishida, S. Kashima, H. Kiwada, *J. Controlled Release* **2008**, *126*, 162 – 165.
[86] P. Laverman, A. H. Brouwers, E. T. M. Dams, W. J. G. Oygen, G. Storm, N. van Rooijen, F. H. M. Corstens, O. C. Berman, *J. Pharmacol. Exp. Ther.* **2000**, *293*, 996 – 1001.
[87] D. A. Herold, K. Keil, D. E. Bruns, *Biochem. Pharmacol.* **1989**, *38*, 73 – 76.
[88] K. D. Hinds, *Biomaterials for Delivery and Targeting of Proteins and Nucleic Acids*, CRC, Boca Raton, FL, **2005**.
[89] V. P. Torchilin, *Adv. Drug Delivery Rev.* **2006**, *58*, 1532 – 1555.
[90] Y. Takakura, A. Takagi, M. Hashida, H. Sezaki, *Pharm. Res.* **1987**, *4*, 293 – 300.
[91] S. M. Moghimi, A. C. Hunter, J. C. Murray, *Pharmacol. Rev.* **2001**, *52*, 283 – 318.
[92] C. B. Schaffer, F. H. Critchfield, J. H. Nair, *J. Am. Pharm. Assoc. Sci. Ed.* **1950**, *39*, 340 – 344.
[93] C. P. Carpenter, M. D. Woddside, E. R. Kinkead, J. M. King, L. J. Sullivan, *Toxicol. Appl. Pharmacol.* **1971**, *18*, 35 – 40.
[94] H. F. Smyth, C. P. Carpenter, C. S. Weil, *J. Am. Pharm. Assoc. Sci. Ed.* **1950**, *39*, 349 – 354.
[95] S. M. Moghimi, J. Szebeni, *Prog. Lipid Res.* **2003**, *42*, 463 – 478.
[96] B. Romberg, J. M. Metselaar, L. Baranyi, C. J. Snel, R. Bunger, W. E. Hennink, J. Szebeni, G. Storm, *Int. J. Pharm.* **2007**, *331*, 186 – 189.
[97] R. S. Porteer, A. Casale, *Polym. Eng. Sci.* **1985**, *25*, 129 – 156.
[98] X. Zhang, S. Granick, *Macromolecules* **2002**, *35*, 4017 – 4022.
[99] T. G. Papaioannou, E. N. Karatzis, M. Vavuranakis, J. P. Lekakis, C. Stefanadis, *Int. J. Cardiol.* **2006**, *113*, 12 – 18.
[100] A. R. D'Almeida, M. L. Dias, *Polym. Degrad. Stab.* **1997**, *56*, 331 – 337.
[101] D. A. White, *Chem. Eng. Sci.* **1970**, *25*, 1255 – 1258.
[102] Y. Minoura, T. Kasuya, S. Kawamura, A. Nakano, *J. Polym. Sci. Part A* **1967**, *5*, 125 – 142.

[103] T. Aarthi, M. S. Shaama, G. Madras, *Ind. Eng. Chem. Res.* **2007**, *46*, 6204 – 6210.
[104] A. Nakano, Y. Minoura, *J. Appl. Polym. Sci.* **1971**, *15*, 927 – 936.
[105] S. Han, C. Kim, D. Kwon, *Polymer* **1997**, *38*, 317 – 323.
[106] J. Scheirs, S. W. Bigger, O. Delatycki, *Polymer* **1991**, *32*, 2014 – 2019.
[107] S. Morlat, J.-L. Gardette, *Polymer* **2001**, *42*, 6071 – 6079.
[108] A. M. Afih-Effat, J. N. Hay, *Eur. Polym. J.* **1972**, *8*, 289 – 297.
[109] J. S. Lee, D. H. Go, J. W. Bae, S. J. Le, K. D. Park, *J. Controlled Release* **2007**, *117*, 204 – 209.
[110] C. Larsen, *Adv. Drug Delivery Rev.* **1989**, *3*, 103 – 154.
[111] S.-I. Sugahara, M. Kajiki, H. Kuriyama, T.-R. Kobayashi, *J. Controlled Release* **2007**, *117*, 40 – 50.
[112] K. A. Janes, P. Calvo, M. J. Alonso, *Adv. Drug Delivery Rev.* **2001**, *47*, 83 – 97.
[113] C. Li, S. Wallace, *Adv. Drug Delivery Rev.* **2008**, *60*, 886 – 898.
[114] J. Pytela, V. Saudek, J. Drobnik, F. Rypacek, *J. Controlled Release* **1989**, *10*, 17 – 25.
[115] B. Romberg, C. Oussoren, C. J. Snel, M. G. Carstens, W. E. Hennink, G. Storm, *Biochim. Biophys. Acta Biomembr.* **2007**, *1768*, 737 – 743.
[116] B. Romberg, F. M. Flesch, W. E. Hennink, G. Storm, *Int. J. Pharm.* **2008**, *355*, 108 – 113.
[117] J. M. Metselaar, P. Bruin, L. W. T. de Boer, T. de Vringer, C. Snel, C. Oussoren, M. H. M. Wauben, D. J. A. Crommelin, G. Storm, W. E. Hennink, *Bioconjugate Chem.* **2003**, *14*, 1156 – 1164.
[118] J. C. Middleton, A. J. Tipton, *Biomaterials* **2000**, *21*, 2335 – 2346.
[119] K. De Winne, E. Roseeuw, J. Pagnaer, E. Schacht, *J. Bioact. Compat. Polym.* **2004**, *19*, 439 – 452.
[120] S. R. Yang, H. J. Lee, J.-D. Kim, *J. Controlled Release* **2006**, *114*, 60 – 68.
[121] G. Pitarresi, P. Pierro, F. S. Palumbo, G. Tripodo, G. Giammona, *Biomacromolecules* **2006**, *7*, 1302 – 1310.
[122] M. Obst, A. Steinbuechel, *Biomacromolecules* **2004**, *5*, 1166 – 1176.
[123] M. E. R. O'Brien, M. A. Socinski, A. Y. Popovich, I. N. Bondarenko, A. Tomova, B. T. Bilynskyi, Y. S. Hotko, V. L. Ganul, I. Y. Kostinsky, A. J. Eisenfeld, L. Sandalic, F. B. Oldham, B. Bandstra, A. B. Sandler, J. W. Singer, *J. Thorac. Oncol.* **2008**, *3*, 728 – 734.
[124] C. Li, J. E. Price, L. Milas, N. R. Hunter, S. Ke, D.-F. Yu, C. Charnsangavej, S. Wallace, *Clin. Cancer Res.* **1999**, *5*, 891 – 897.
[125] C. Li, D.-F. Yu, R. A. Newman, F. Cabrai, L. C. Stephens, N. Hunter, L. Milas, S. Wallace, *Cancer Res.* **1998**, *58*, 2404 – 2409.
[126] http://www.emea.europa.eu/humandocs/PDFs/EPAR/opaxio/601200 09en.pdf (European Medicines Agency), last accessed 07.10.2009.
[127] E. G. R. Fernandes, A. A. A. de Queiroz, G. A. Abraham, J. S. Roman, *J. Mater. Sci. Mater. Med.* **2006**, *17*, 105 – 111.
[128] K. Maruyama, S. Okuizumi, O. Ishida, H. Yamauchi, H. Kikuchi, M. Iwatsuru, *Int. J. Pharm.* **1994**, *111*, 103 – 107.
[129] S.-E. Stiriba, H. Kautz, H. Frey, *J. Am. Chem. Soc.* **2002**, *124*, 9698 – 9699.
[130] M. H. Oudshoorn, R. Rissmann, J. A. Bouwstra, W. E. Hennink, *Biomaterials* **2006**, *27*, 5471 – 5479.
[131] R. K. Kainthan, D. E. Brooks, *Biomaterials* **2007**, *28*, 4779 – 4787.
[132] C. Siegers, M. Biesalski, R. Haag, *Chem. Eur. J.* **2004**, *10*, 2831 – 2838.
[133] P.-Y. J. Yeh, R. K. Kainthan, Y. Zou, M. Chiao, J. N. Kizhakkedathu, *Langmuir* **2008**, *24*, 4907 – 4916.
[134] R. K. Kainthan, J. Janzen, E. Levin, D. V. Devine, D. E. Brooks, *Biomacromolecules* **2006**, *7*, 703 – 709.
[135] R. K. Kainthan, S. R. Hester, E. Levin, D. V. Devine, D. E. Brooks, *Biomaterials* **2007**, *28*, 4581 – 4590.
[136] H. Turk, R. Haag, S. Alban, *Bioconjugate Chem.* **2004**, *15*, 162 – 167.
[137] W. R. Michael, R. H. Coots, *Toxicol. Appl. Pharmacol.* **1971**, *20*, 334 – 345.
[138] H. Frey, R. Haag, *Rev. Mol. Biotechnol.* **2002**, *90*, 257 – 267.
[139] R. Haag, J.-F. Stumbe, A. Sunder, H. Frey, A. Hebel, *Macromolecules* **2000**, *33*, 8158 – 8166.
[140] R. D. O'Brien, *Fats and Oils—Formulating and Processing for Applications*, CRC, Boca Raton, FL, **2004**.
[141] R. K. Kainthan, D. E. Brooks, *Bioconjugate Chem.* **2008**, *19*, 2231 – 2238.
[142] D. A. Tomalia, D. P. Sheetz, *J. Polym. Sci. Part A* **1966**, *4*, 2253 – 2265.
[143] W. Seeliger, E. Aufderhaar, W. Diepers, R. Feinauer, R. Nehring, W. Thier, H. Hellmann, *Angew. Chem.* **1966**, *78*, 913 – 952; *Angew. Chem. Int. Ed. Engl.* **1966**, *5*, 875 – 888.
[144] T. Kagiya, S. Narisawa, T. Maeda, K. Fukui, *J. Polym. Sci. Part B* **1966**, *4*, 441 – 445.
[145] T. G. Bassiri, A. Levy, M. Litt, *J. Polym. Sci. Part B* **1967**, *5*, 871 – 879.
[146] S. Kobayashi, *Prog. Polym. Sci.* **1990**, *15*, 751 – 823.
[147] F. Wiesbrock, R. Hoogenboom, M. A. M. Leenen, M. A. R. Meier, U. S. Schubert, *Macromolecules* **2005**, *38*, 5025 – 5034.
[148] N. Adams, U. S. Schubert, *Adv. Drug Delivery Rev.* **2007**, *59*, 1504 – 1520.
[149] R. Hoogenboom, *Angew. Chem.* **2009**, *121*, 8122 – 8138; *Angew. Chem. Int. Ed.* **2009**, *48*, 7978 – 7997.
[150] C.-H. Wang, C.-H. Wang, G.-H. Hsiue, *J. Controlled Release* **2005**, *108*, 140 – 149.
[151] S. C. Lee, C. Kim, I. C. Kwon, H. Chung, S. Y. Jeong, *J. Controlled Release* **2003**, *89*, 437 – 446.
[152] A. Mero, G. Pasut, L. Dalla Via, M. W. M. Fijten, U. S. Schubert, R. Hoogenboom, F. M. Veronese, *J. Controlled Release* **2008**, *125*, 87 – 95.
[153] R. Konradi, B. Pidhatika, A. Muehlebach, M. Textor, *Langmuir* **2008**, *24*, 613 – 616.
[154] B. Pidhatika, J. Moeller, V. Vogel, R. Konradi, *Chimia* **2008**, *62*, 264 – 269.
[155] F. M. Veronese, A. Mero, G. Pasut, Z. Fang, T. X. Viegas, *36th Ann. Meeting & Exposition CRS* **2009**.
[156] M. C. Woodle, C. M. Engbers, S. Zalipsky, *Bioconjugate Chem.* **1994**, *5*, 493 – 496.
[157] S. Zalpinsky, C. B. Hansen, J. M. Oaks, T. M. Allen, *J. Pharm. Sci.* **1996**, *85*, 133 – 137.
[158] F. C. Gaertner, R. Luxenhofer, B. Blechert, R. Jordan, M. Essler, *J. Controlled Release* **2007**, *119*, 291 – 300.
[159] C. Weber, C. R. Becer, R. Hoogenboom, U. S. Schubert, *Macromolecules* **2009**, *42*, 2965 – 2971.
[160] C. H. Wang, K.-R. Fan, G.-H. Hsiue, *Biomaterials* **2005**, *26*, 2803 – 2811.
[161] J. H. Jeong, S. H. Song, D. W. Lim, H. Lee, T. G. Park, *J. Controlled Release* **2001**, *73*, 391 – 399.
[162] D. Fischer, T. Bieber, Y. Li, H.-P. Elsaesser, T. Kissel, *Pharm. Res.* **1999**, *16*, 1273 – 1279.
[163] V. P. Torchilin, M. I. Shtilman, V. S. Trubetskoy, K. Whiteman, A. M. Milstein, *Biochim. Biophys. Acta Biomembr.* **1994**, *1195*, 181 – 184.
[164] M. Sairam, V. R. Babu, B. V. K. Naidu, T. M. Aminabhavi, *Int. J. Pharm.* **2006**, *320*, 131 – 136.
[165] D. Gao, H. Xu, M. A. Philbert, R. Kopelman, *Angew. Chem.* **2007**, *119*, 2274 – 2277; *Angew. Chem. Int. Ed.* **2007**, *46*, 2224 – 2227.
[166] J. N. Patton, A. F. Palmer, *Langmuir* **2006**, *22*, 2212 – 2221.
[167] M. R. Hynd, J. N. Turner, W. Shain, *J. Biomater. Sci. Polym. Ed.* **2007**, *18*, 1223 – 1244.

[168] D. Saraydin, S. Uenver-Saraydin, E. Karadag, E. Koptagel, O. Gueven, *Nucl. Instrum. Methods Phys. Res. Sect. B* **2004**, *217*, 281 – 292.
[169] E. S. You, H. S. Jang, W. S. Ahn, M. I. Kang, M. G. Jun, Y. C. Kim, H. J. Chun, *J. Ind. Eng. Chem.* **2007**, *13*, 219 – 224.
[170] S. Fernandez-Cossio, M. T. Castano-Oreja, *Plast. Reconstr. Surg.* **2006**, *117*, 1789 – 1796.
[171] L. H. Christensen, V. B. Breiting, A. Aasted, A. Jorgensen, I. Kebuladze, *Plast. Reconstr. Surg.* **2003**, *111*, 1883 – 1890.
[172] H. Gin, B. Dupuyi, D. Bonnemaison-Bourignon, L. Bordenave, R. Bareille, M. J. Latapie, C. Baquey, J. H. Bezian, D. Ducassou, *Biomater. Artif. Cells Artif. Organs* **1990**, *18*, 25 – 42.
[173] T. F. Xi, C. X. Fan, X. M. Feng, Z. Y. Wan, C. R. Wang, L. L. Chou, *J. Biomed. Mater. Res. Part A* **2006**, *78*, 283 – 290.
[174] M. Stach, I. Lacik, J. D. Chorvat, M. Buback, P. Hesse, R. A. Hutchinson, L. Tang, *Macromolecules* **2008**, *41*, 5174 – 5185.
[175] D. Gulsen, A. Chauhan, *J. Membr. Sci.* **2006**, *269*, 35 – 48.
[176] M. S. Payne, T. A. Horbett, *J. Biomed. Mater. Res.* **1987**, *21*, 843 – 859.
[177] V. P. Torchilin, V. S. Trubetskoy, K. R. Whiteman, P. Caliceti, P. Ferruti, F. M. Veronese, *J. Pharm. Sci.* **1995**, *84*, 1049 – 1053.
[178] P. Caliceti, O. Schiavon, M. Morpurgo, F. M. Veronese, L. Sartor, E. Ranucci, P. Ferruti, *J. Bioact. Compat. Polym.* **1995**, *10*, 103 – 120.
[179] P. Caliceti, O. Schiavon, F. M. Veronese, *Bioconjugate Chem.* **2001**, *12*, 515 – 522.
[180] D. Le Garrec, J. Taillefer, J. E. Van Lier, V. Lenaert, J.-C. Leroux, *J. Drug Targeting* **2002**, *10*, 429 – 437.
[181] A. Benahmed, M. Ranger, J.-C. Leroux, *Pharm. Res.* **2001**, *18*, 323 – 328.
[182] L. Luo, M. Ranger, D. G. Lessard, D. Le Garrec, S. Gori, J.-C. Leroux, S. Rimmer, D. Smith, *Macromolecules* **2004**, *37*, 4008 – 4013.
[183] M. Moneghini, D. Voinovich, F. Princivalle, L. Magarotto, *Pharm. Dev. Technol.* **2000**, *5*, 347 – 353.
[184] C. M. A. Lopes, M. I. Felisberti, *Biomaterials* **2003**, *24*, 1279 – 1284.
[185] R. J. Mumper, J. G. Duguid, K. Anwer, M. K. Barron, H. Nitta, A. P. Rolland, *Pharm. Res.* **1996**, *13*, 701 – 709.
[186] W. W. L. Chin, P. W. S. Heng, P. S. P. Thong, R. Bhuvaneswari, W. Hirt, S. Kuenzel, K. C. Soo, M. Olivo, *Eur. J. Pharm. Biopharm.* **2008**, *69*, 1083 – 1093.
[187] M. Nicolaou, P. Chang, M. J. Newman, *Polymeric gene delivery*, CRC, Boca Raton, FL, **2005**.
[188] L. A. Shibaev, E. Y. Melenevskaya, B. M. Ginzburg, A. V. Yakimaskii, O. V. Ratnikova, A. V. Gribanov, *J. Macromol. Sci. Phys.* **2008**, *47*, 276 – 287.
[189] K. J. Hartauer, G. N. Arbuthnot, S. W. Baertschi, R. A. Johnson, W. D. Luke, N. G. Pearson, E. C. Rickard, C. A. Tingle, P. K. S. Tsang, R. E. Wiens, *Pharm. Dev. Technol.* **2000**, *5*, 303 – 310.
[190] P. Dunn, T.-T. Kuo, L.-Y. Shih, P.-N. Wang, C.-F. Sun, M. J. W. Chang, *Am. J. Hematol.* **1998**, *57*, 68 – 71.
[191] S.-I. Yusa, S. Yamago, M. Sugahara, S. Morikawa, T. Yamamoto, Y. Morishima, *Macromolecules* **2007**, *40*, 5907 – 5915.
[192] B. Ray, M. Kotani, S. Yamago, *Macromolecules* **2006**, *39*, 5259 – 5265.
[193] D. Wan, K. Satoh, M. Kamigaito, Y. Okamoto, *Macromolecules* **2005**, *38*, 10397 – 10405.
[194] E. Ranucci, P. Ferruti, R. Annunziata, I. Gerges, G. Spinelli, *Macromol. Biosci.* **2006**, *6*, 216 – 227.
[195] R. Duncan, *Nat. Rev. Cancer* **2006**, *6*, 688 – 701, and references therein.
[196] P. L. Soo, M. Dunne, J. Liu, C. Allen, *Nanotechnology in Drug Delivery*, Springer, Berlin, **2009**.
[197] Z.-B. Zheng, G. Zhu, H. Tak, E. Joseph, J. L. Eiseman, D. J. Creighton, *Bioconjugate Chem.* **2005**, *16*, 598 – 607.
[198] Y. Kasuya, Z.-R. Lu, P. Kopeckova, T. Minko, S. Tabibi, J. Kopecek, *J. Controlled Release* **2001**, *74*, 203 – 211.
[199] M. P. Borgman, A. Ray, R. B. Kolhatkar, E. A. Sausville, A. M. Burger, H. Ghandehari, *Pharm. Res.* **2009**, *26*, 1407 – 1418.
[200] S. Kamei, J. Kopecek, *Pharm. Res.* **1995**, *12*, 663 – 668.
[201] V. Sure, T. Etrych, K. Ulbrich, T. Hirano, T. Kondo, T. Todoroki, M. Jelinkova, B. Rihova, *J. Bioact. Compat. Polym.* **2002**, *17*, 105 – 122.
[202] D. Wang, P. Kopeckova, T. Minko, V. Nanayakkara, J. Kopecek, *Biomacromolecules* **2000**, *1*, 313 – 319.
[203] Z.-R. Lu, J.-G. Shiah, S. Sakuma, P. Kopeckova, J. Kopecek, *J. Controlled Release* **2002**, *78*, 165 – 173.
[204] D. Oupicky, K. A. Howard, C. Konak, P. R. Dash, K. Ulbrich, L. W. Seymour, *Bioconjugate Chem.* **2000**, *11*, 492 – 501.
[205] L. Paasonen, B. Romberg, G. Storm, M. Yliperttula, A. Urtti, W. E. Hennink, *Bioconjugate Chem.* **2007**, *18*, 2131 – 2136.
[206] K. R. Whiteman, V. Subr, K. Ulbrich, V. P. Torchilin, *J. Liposome Res.* **2001**, *11*, 153 – 164.
[207] S. Woerly, S. Fort, I. Pignot-Paintrand, C. Cottet, C. Carcenac, M. Savasta, *Biomacromolecules* **2008**, *9*, 2329 – 2337.
[208] M. Stastny, D. Plocova, T. Etrych, M. Kovara, K. Ulbrich, B. Rihova, *J. Controlled Release* **2002**, *81*, 101 – 111.
[209] M. Save, J. V. M. Weaver, S. P. Armes, P. McKenna, *Macromolecules* **2002**, *35*, 1152 – 1159.
[210] C. W. Scales, Y. A. Vasilieva, A. J. Convertine, A. B. Lowe, C. L. McCormick, *Biomacromolecules* **2005**, *6*, 1846 – 1850.
[211] C.-Y. Hong, C.-Y. Pan, *Macromolecules* **2006**, *39*, 3517 – 3524.
[212] A. W. York, C. W. Scales, F. Huang, C. L. McCormick, *Biomacromolecules* **2007**, *8*, 2337 – 2341.
[213] K. Demirelli, M. F. Coskun, E. Kaya, M. Coskun, *Polym. Degrad. Stab.* **2002**, *78*, 333 – 339.
[214] L. Sprincl, J. Exner, O. Sterba, J. Kopecek, *J. Biomed. Mater. Res.* **1976**, *10*, 953 – 963.
[215] L. W. Seymour, R. Duncan, J. Strohalm, J. Kopecek, *J. Biomed. Mater. Res.* **1987**, *21*, 1341 – 1358.
[216] L. W. Seymour, Y. Miyamoto, H. Maeda, M. Brereton, J. Strohalm, K. Ulbrich, R. Duncan, *Eur. J. Cancer Part A* **1995**, *31*, 766 – 770.
[217] J.-G. Shiah, M. Dvorak, P. Kopeckova, Y. Sun, C. M. Peterson, J. Kopecek, *Eur. J. Cancer* **2001**, *37*, 131 – 139.
[218] R. Duncan, *Adv. Drug Delivery Rev.* **2009**, *61*, 1131 – 1148.
[219] D. P. Nowotnika, E. Cvitkovic, *Adv. Drug Delivery Rev.* **2009**, *61*, 1214 – 1219.

Publication P2:

Amphiphilic star-shaped block copolymers as unimolecular drug delivery systems: Investigations using a novel fungicide

---

K. Knop, G. M. Pavlov, T. Rudolph, K. Martin, D. Pretzel, B. O. Jahn, D. H. Scharf, V. Makarov, U. Möllmann, A. A. Brakhage, F. H. Schacher, U. S. Schubert

Soft Matter **2013**, *9*, 715–726.

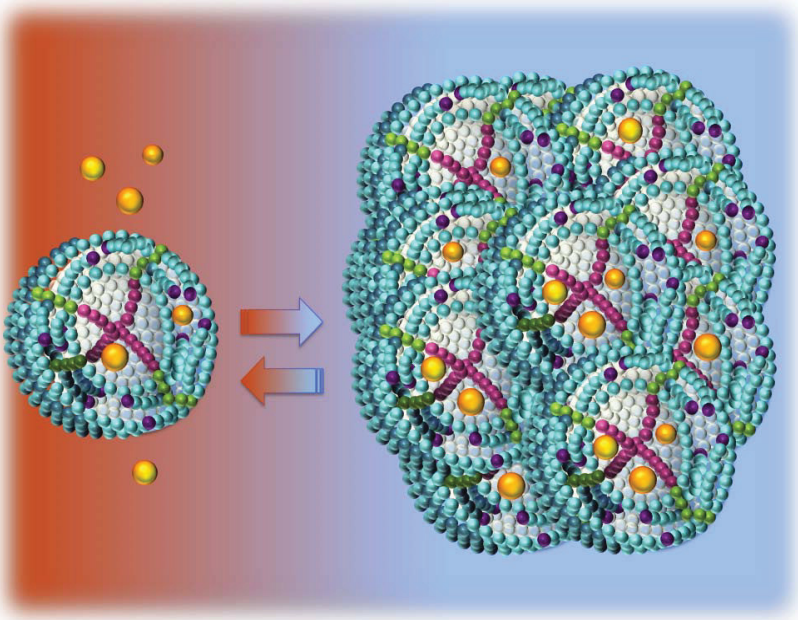

Soft Matter

RSC Publishing

PAPER

View Article Online
View Journal | View Issue

Amphiphilic star-shaped block copolymers as unimolecular drug delivery systems: investigations using a novel fungicide†

Cite this: *Soft Matter*, 2013, **9**, 715

Katrin Knop,[abc] Georges M. Pavlov,[ab] Tobias Rudolph,[ab] Karin Martin,[bd] David Pretzel,[ab] Burkhard O. Jahn,[e] Daniel H. Scharf,[bd] Axel A. Brakhage,[bd] Vadim Makarov,[f] Ute Möllmann,[d] Felix H. Schacher[ab] and Ulrich S. Schubert*[abc]

Amphiphilic star-shaped poly(ε-caprolactone)-*block*-poly(oligo(ethylene glycol)methacrylate) [PCL_a-*b*-$POEGMA_b$]$_4$ block copolymers with four arms and varying degrees of polymerization for the core (PCL) and the shell (POEGMA) were used to investigate the solution behavior in dilute aqueous solution using a variety of techniques, including fluorescence and UV/Vis spectroscopy, dynamic light scattering, analytical ultracentrifugation, and isothermal titration calorimetry. Particular emphasis has been applied to prove that the systems form unimolecular micelles for different hydrophilic/lipophilic balances of the employed materials. *In vitro* cytotoxicity and hemocompatibility have further been investigated to probe the suitability of these structures for *in vivo* applications. A novel fungicide was included into the hydrophobic core in aqueous media to test their potential as drug delivery systems. After loading, the materials have been shown to release the drug and to provoke therewith an inhibition of the growth of different fungal strains.

Received 29th June 2012
Accepted 10th October 2012

DOI: 10.1039/c2sm26509e

www.rsc.org/softmatter

Introduction

Both drug development and modern disease therapies are suffering from the fact that one-third of all newly synthesized and potentially active substances are insoluble in water leading to limited administration if any administration at all is possible.[1] In particular, in the case of cancer therapy, many agents are in general highly hydrophobic and anti-neoplastic, causing very severe side effects during therapy, such as immunosuppression, nausea, and alopecia (hair loss). But also for other cases drugs with a low therapeutic index are used, rendering the specific distribution of the administered substances within the human body desirable. Systemic fungal infections are known as frequent and important complications of modern medicine. Especially for immunocompromised patients with acquired immune deficiency syndrome (AIDS) or cancer, who attended *e.g.* extensive chemotherapy, fungal diseases are known as a major cause of death.[2,3] Until now, the broad band fungicide amphotericin B (AmB) has been the drug of choice for sepsis with fungal strains, but is highly toxic in particular with respect to the kidneys.[4]

Drug delivery systems (DDS) as a kind of packaging for drug molecules were created to overcome the abovementioned adverse issues. They ensure prolonged blood circulation times of drugs, most probably due to an apparently higher molar mass.[5] This leads to a decreased renal filtration of the drugs and to an enhanced uptake in, *e.g.*, the cancer tissue. This can be even further promoted by the enhanced permeability and retention (EPR) effect. As a result of the EPR effect, DDS are preferentially entrapped into the neoplastic tissue and can therefore improve an effective targeting during chemotherapy.[6–8]

To ensure long circulating times, DDS are usually shielded by a suitable shell, preventing recognition by the human immune system and, hence, excretion of the drug carriers. Poly(ethylene glycol) (PEG) is known to prevent unspecific interactions with the human body and is known to act as a so-called "stealth" polymer in DDS.[9] The diversity and versatility of modern polymer synthesis enable the introduction of PEG segments into DDS of different architectures.[10,11]

[a]*Laboratory of Organic and Macromolecular Chemistry (IOMC), Friedrich-Schiller-University Jena, Humboldtstrasse 10, 07743, Jena, Germany. E-mail: ulrich.schubert@uni-jena.de; Web: www.schubert-group.com; Fax: +49 (0) 3641 948202; Tel: +49 (0)3641 948200*

[b]*Jena Center for Soft Matter (JCSM), Friedrich-Schiller-University Jena, Humboldtstrasse 10, 07743, Jena, Germany*

[c]*Dutch Polymer Institute (DPI), John F. Kennedylaan 2, 5612 AB Eindhoven, The Netherlands*

[d]*Leibniz Institute for Natural Product Research and Infection Biology – Hans Knöll Institute, Beutenbergstr. 11a, 07745 Jena, Germany*

[e]*Department of Chemistry, Uppsala University, BMC Box 576, 751 23 Uppsala, Sweden*

[f]*Institute of Biochemistry, Russian Academy of Science, Leninsky pr., 33-2, Moscow 119071, Russia*

† Electronic supplementary information (ESI) available: Synthesis procedures and characterization of the star-shaped block copolymers, experimental details of the biological testing and details of the computational studies. See DOI: 10.1039/c2sm26509e

The use of block copolymer micelles as DDS appears to be attractive due to several reasons: first, an appealingly easy structural build-up using self-assembly and second, the fact that the hydrophilic segments of amphiphilic block copolymers can act as a protecting shell around the hydrophobic core, which potentially hosts encapsulated "cargo".[12] However, such micellar systems can also disassemble into block copolymer unimers, especially if the concentration within the bloodstream falls below the critical micelle concentration (cmc) after administration.[13] Although this can be influenced to a certain extent by a rational design of the hydrophobic block, dendrimers came into focus as unimolecular micelles at even a very dilute concentration.[14,15] One drawback in this particular case is that the rather dense cores of dendritic structures offer only limited space for the encapsulation of guest molecules, besides the difficult synthesis and upscaling.[16,17]

This has led to an increased interest in unimolecular star-shaped block copolymers as DDS as the core in these systems is supposed to provide more space for hydrophobic molecules. In addition, the synthesis of star-shaped polymers and block copolymers is often less tedious when compared to classical approaches used for dendrimer synthesis.[18]

For these reasons, star-shaped block copolymers comprising an inner hydrophobic and an outer hydrophilic segment represent an attractive approach for the macromolecular engineering of DDS. Star-shaped block copolymers can be engineered using multifunctional initiators. Hydroxyl functionalities can be used as initiators for the ring-opening polymerization of ε-caprolactone or lactic acid as hydrophobic segments. PEG has been frequently used as a hydrophilic shell, although it has already been shown that linear PEG is not sufficient for the stabilization of unimolecular systems in water as the investigated systems still exhibited a cmc.[19,20] An exception was reported for amphiphilic starlike macromolecules, which were intensively studied by Uhrich *et al.* Here, no cmc could be determined, although linear PEG served as a hydrophilic shell.[21,22]

Another alternative for a highly hydrophilic shell is the use of comb-like segments as demonstrated by Schramm *et al.* for a set of four- and six-armed [PCL-*block*-poly(oligo(ethylene glycol)methacrylate)] ([PCL-*b*-POEGMA]) block copolymers.[23,24] It is generally acknowledged that a branched or even a brush-like shell lowers the aggregation number and promotes the formation of unimolecular micelles.[25,26] Nevertheless, for a similar system with four arms and a shell formed by POEGMA (M_n = 300 g mol^{-1} for the OEGMA monomer) a cmc could be detected, indicating the formation of multimolecular micelles.[27] Consequently, the number and character of arms seem to influence whether unimolecular micelles are formed by the star-shaped block copolymers. A unimolecular behavior is advantageous for drug delivery applications, because disassembling of the micelles, liberation followed by precipitation of the drug and therewith connected negative side effects can be avoided. Therefore, we were interested in the polymer characteristics and conditions under which unimolecularity occurs for star-shaped block copolymers with a brush-like hydrophilic shell.

Here, we present the synthesis of four-arm PCL-*b*-poly(oligo(ethylene glycol)methacrylate) (POEGMA) star-shaped block copolymers with the general formula $[PCL_a\text{-}b\text{-}POEGMA_b]_x$, where the subscripts a and b represent the degrees of polymerization of the corresponding block, and x refers to the overall number of arms. The aim was to explore under which conditions this system forms unimolecular micelles and how the inclusion capacity for hydrophobic guest substances can be optimized. We therefore synthesized a library with varying degrees of polymerization (DP) for the hydrophobic (PCL) and the hydrophilic block (POEGMA). Our main focus was to elucidate the minimum POEGMA length that is necessary to obtain stable unimolecular micelles in aqueous systems and to define an optimum hydrophilic/hydrophobic balance. Furthermore, we present the first results on the biocompatibility of PCL-*b*-POEGMA and on the encapsulation of a novel fungicide. The inclusion capacity was studied as well as the antifungal activity against the fungal strains *Sporobolomyces salmonicolor* 549, *Candida albicans* BMSY212 and *Penicillium notatum* JP36 in comparison to the free drug.

Experimental part

Materials

Tin(II) 2-ethylhexanoate (Aldrich), α-bromoisobutyryl bromide (Aldrich), anisole (Fluka, 99.0%), copper(I) bromide (Aldrich, 99.999%), trioxane (Aldrich), fat brown RR (Aldrich), nile red (Aldrich), and pyrene (Alfa Aesar) were used as received. ε-Caprolactone (Aldrich) was dried for 2 days over CaH_2 before distillation and stored under argon. Triethylamine was distilled over CaH_2 and stored under argon. Pentaerythritol (Aldrich) was co-evaporated with toluene prior to use. Tetrahydrofuran (THF, Aldrich) was dried in a solvent purification system (Pure Solv EN, Innovative Technology) before use. Oligo(ethylene glycol) methyl ether methacrylate M_n = 475 g mol^{-1} (Aldrich, OEGMA 475) and *N*,*N*,*N*′,*N*″,*N*″-pentamethyldiethylenetriamine (Aldrich, PMDETA) were passed through an aluminum oxide bed containing 5% CaH_2 prior to use. Acetone of spectroscopic purity grade for analytical ultracentrifuge purposes was obtained from Sigma Aldrich showing the following characteristics (at 20 °C): dynamic viscosity $\eta_0 = 0.350 \times 10^{-2}$ mPa s, density $\rho_0 = 0.791$ g cm^{-3}.

Instrumentation

^{1}H and ^{13}C nuclear magnetic resonance (NMR) spectra were recorded in $CDCl_3$ on a Bruker AC 250 or a 300 MHz spectrometer at 298 K. Chemical shifts are given in parts per million (ppm, δ scale) relative to the residual signal of the deuterated solvent.

Size exclusion chromatography (SEC) was performed on a Shimadzu system equipped with a SCL-10A system controller, a LC-10AD pump, a RID-10A refractive index detector, and both a PSS Gram30 and a PSS Gram1000 column in series, whereby *N*,*N*-dimethylacetamide with 5 mmol of LiCl was used as an eluent at a flow rate of 1 mL min^{-1} and the column oven was set to 60 °C. The system was calibrated with PMMA (410 to

88 000 g mol^{-1}) and PEG (440 to 44 700 g mol^{-1}) standards. Furthermore, the kinetics of the polymerization was studied using a Shimadzu system equipped with a SCL-10A system controller, a LC-10AD pump, and a RID-10A refractive index detector using a solvent mixture containing chloroform, triethylamine, and *iso*-propyl alcohol (94 : 4 : 2) at a flow rate of 1 mL min^{-1} on a PSS-SDV-linear M 5 μm column. The system was calibrated with PMMA (410 to 88 000 g mol^{-1}) and PEG (440 to 44 700 g mol^{-1}) standards.

Matrix-assisted laser desorption/ionization time of flight (MALDI-TOF) mass spectra were recorded on an Ultraflex III TOF/TOF (Bruker Daltonics, Bremen, Germany), equipped with a Nd:YAG laser and with *trans*-2-[3-(4-*tert*-butylphenyl)-2-methyl-2-propenylidene] malononitrile (DCTB) as a matrix and lithium chloride as an ionizing agent in reflector and linear modes. The instrument was calibrated prior to each measurement with an external PMMA standard from PSS Polymer Standards Services GmbH (Mainz, Germany).

Dynamic light scattering (DLS) measurements were performed on ALV DLS/SLS equipment consisting of an ALV Laser CGS3 Goniometer with an ALV Avalanche correlator and a He–Ne laser ($\lambda = 632.8$ nm) at 298 K. The aqueous polymer solutions as well as the THF solutions with concentrations of 1 mg mL^{-1} were filtered twice (GF 1–2 μm or PTFE 0.45 μm) and measured at an angle of 150°. The hydrodynamic radius (R_h) was determined using the CONTIN algorithm. Angle-dependent measurements were performed in the same manner in the range of 30 to 150° in 10° steps.

Sedimentation velocity experiments were performed using a Beckman XLI analytical ultracentrifuge (ProteomeLab XLI Protein Characterization System) at a rotor speed of 40 000 rpm and at 20 °C, using interference optics and Al double-sector cells of an optical path of 12 mm. Viscosity measurements were conducted using an AMVn viscometer (Anton Paar, Graz, Austria), with a capillary–ball combination as the measuring system. Density measurements were carried out in a DMA 02 density meter (Anton Paar, Graz, Austria) according to the procedure of Kratky *et al.*[28]

The sedimentation velocity data analysis was performed with the continuous particle size distribution $c(s)$ of Sedfit, where s is the velocity sedimentation coefficient.[29,30] The program Sedfit numerically solves the Lamm equation, the basic differential equation describing the coupled sedimentation and diffusion process.[31] In the $c(s)$ method, this is done for a large number of globular species with different sedimentation and diffusion coefficients. The result is a continuous sedimentation coefficient distribution, which represents the best combination of species for matching the entire collected set of experimental concentration profiles. The numerical analysis is conducted under appropriate statistical criteria of goodness-of-fit. The frictional ratio value (f/f_{sph}), which is the weight-average frictional ratio of all species, was optimized executing a fit command, where f represents the frictional coefficient of the solute macromolecule and f_{sph} the frictional coefficient of a rigid sphere with the same "anhydrous" volume (free of solvent) as the macromolecule. The Tikhonov–Philips 2nd derivative regularization method was used with a confidence level of 0.7 to 0.9 (corresponding F-ratio). The partial specific volume ($\bar{v}$), the solvent density (ρ_0), and the solvent dynamic viscosity (η_0) are additional parameters required to calculate the sedimentation coefficient distributions. Finally, the differential distribution ($dc(s)/ds$) of the sample is obtained and marked as $c(s)$, scaled such that the area under the $c(s)$ curve will give the loading concentration of the macromolecules between the minimum and maximum s-values occurring (expressed, in the case of interference optics, in the number of fringes, J). In addition, the determination of the sedimentation coefficient distribution $g^*(s)$ by least-squares boundary modeling (ls − $g^*(s)$) was used. The values of s obtained by these two software are in good correlation with the accuracy of 0.2–0.3 Svedberg. During the sedimentation experiments, three concentrations of each sample in acetone were studied in the concentration range, which allows a reliable extrapolation to zero concentration in the linear approximation in accordance with the relationship $s^{-1} = {s_0}^{-1}(1 + k_s c + \ldots)$ and an estimation of both values s_0 and the concentration coefficient k_s. The relative viscosities $\eta_r = t/\tau_0$ of the solutions were calculated from the respective time of the fall of the steel ball in a viscous medium of the solvent and polymer solutions, τ_0 and t at 20 °C. The relative viscosities η_r ranged from 2.0 to 1.15. The extrapolation to zero concentration was made by using both the Huggins and the Kraemer equations, and the average values were considered as the value of the intrinsic viscosity.

The ζ potential measurements were performed using a Zetasizer Nano ZS (Malvern instruments, Malvern, UK). The solutions were prepared with 1 mg mL^{-1} polymer in deionized water and passed through 1–2 μm glass frit filters prior to measurement.

Atomic absorption spectroscopy was performed on a nova400 (Analytik Jena, Jena, Germany) instrument. A calibration of five different concentrations of a standard provided by SCP Science (France) was done ($R^2 > 0.999$).

UV-vis absorption measurements were performed on an Analytik Jena SPECORD 250 (Analytik Jena, Jena, Germany) at 298 K. Fluorescence emission as well as excitation spectroscopy were measured on a Jasco FP-6500 spectrometer at 298 K.

For the photometric absorbance measurement, a TECAN Infinite M200 PRO plate reader (TECAN, Crailsheim, Germany) was used to measure the absorption of samples from (a) the XTT cytotoxicity assay (570 nm with a background correction of the optical density (OD) at 690 nm), (b) the hemolysis of erythrocytes (540 nm with a background correction of the OD at 690 nm), and (c) the photometric evaluation of erythrocyte aggregation (645 nm). Each well containing the sample was measured at four different spots each with 10 flashes per scan. To visualize the viability of the L929 cells after incubation with different polymers, the blue/red/green fluorescence signal of cells cultured in a 96 well plate and stained with Hoechst 33342/fluorescein diacetate (FDA)/propidium iodide (PI) was observed on a fluorescence microscope (Cell Observer Z1, Carl Zeiss, Jena, Germany) equipped with a mercury arc UV lamp and the appropriate filter combinations for excitation and detection of emission. Images of a series were captured with a 10× objective using identical instrument settings (*e.g.* UV lamp power,

integration time, and camera gain) and spots of the 96 well plate were addressed using an automated XY table.

The isothermal titration calorimetry (ITC) measurements were performed with a VP-ITC microcalorimeter from MicroCal (Northhampton, MA). Reference cell as well as the sample cell, both filled with a volume of 1.6 mL, were enclosed in an adiabatic jacket. The samples were injected stepwise into the working cell with a syringe of total volume of 288 μL under constant stirring at a stirring rate of 310 rpm. The measurements were performed at a constant temperature of 25 °C. Small aliquots of the sample (6 μL) were successively injected into the water of the working cell. The data treatment was performed as follows: firstly, the baseline was subtracted from the data and secondly each peak was integrated providing the heat per injection.

The energy minimization and the dynamics simulations were performed with the TINKER 6 (J.W. Ponder, freely available at http://dasher.wustl.edu/tinker) molecular-modelling package.[32] All atoms were modelled explicitly by the use of the MM3-2000 force field proposed by Allinger *et al.*[33] Parameterizations as given in the ESI† were used for nonexistent parameters in the original set. Moreover, the MM3-2000 force field was adopted without further modifications. The geometry of the energy minimization calculation was obtained by a quasi-Newton nonlinear optimization routine. The molecular dynamics trajectory was carried out *via* a modified Beeman algorithm in combination with the analytical continuum solvation (ACE) method[34] for water over 100 ps based on a previous run without solvation. For all calculations the default parameters and threshold values of TINKER were used.

Results and discussion

Synthesis

The star-shaped block copolymers were synthesized as described previously.[23] Briefly, the core-first method was applied to build-up different PCL cores (13–23 repeating units of ε-caprolactone per arm), whose hydroxyl end groups were subsequently esterified with α-bromoisobutyryl bromide. The bromine end groups were then used as initiators for the atom transfer radical polymerization (ATRP) of OEGMA to form the hydrophilic outer shell. For the three different cores no influence of the PCL block length on the polymerization rate was observed.

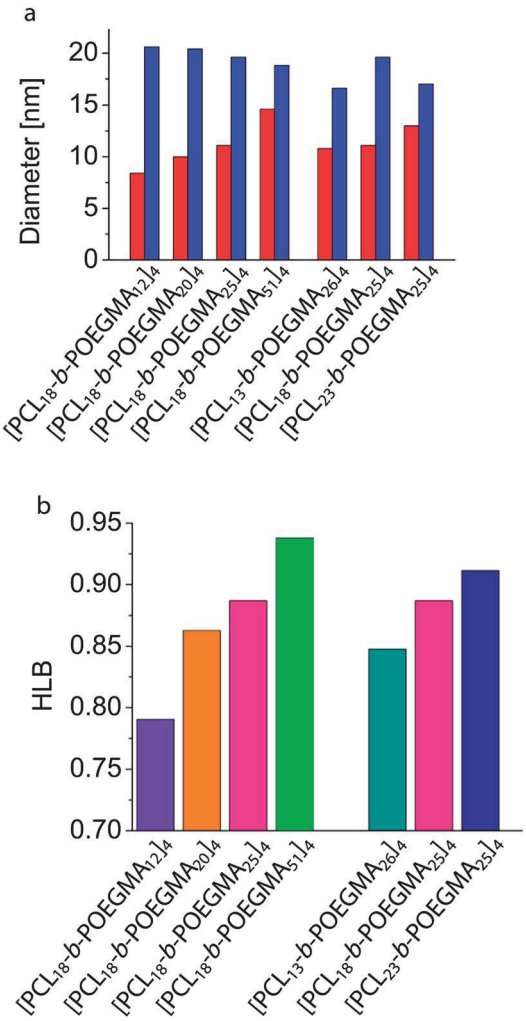

Fig. 1 (a) Hydrodynamic diameters of different [PCL$_a$-*b*-POEGMA$_b$]$_4$ star-shaped block copolymers in THF (red columns) and water (blue columns). (b) Hydrophilic/lipophilic balance values calculated for the star-shaped block copolymers.

The materials were purified by filtration over an aluminum oxide column to remove any copper, which is of importance for the application in the biomedical field. AAS measurements of the final polymers revealed copper concentrations below 40 ppm. The extinction values are even below the lowest standard of 0.1 mg L^{-1} copper of the calibration (Table S4†). Subsequently, the star-shaped block copolymers were

Table 1 Characteristics of star-shaped [PCL$_a$-*b*-POEGMA$_b$]$_4$ block copolymers

Polymer	Theoretical DP POEGMA	Conversion in SEC[a] [%]	DP POEGMA	M_n [g mol^{-1}] calculated[b]	M_n [g mol^{-1}] measured[c]	PDI
[PCL$_{18}$-*b*-POEGMA$_{12}$]$_4$	12	25	12	31 700	31 000	1.21
[PCL$_{18}$-*b*-POEGMA$_{20}$]$_4$	20	39	20	46 900	36 700	1.19
[PCL$_{18}$-*b*-POEGMA$_{25}$]$_4$	25	51	25	56 400	41 700	1.19
[PCL$_{18}$-*b*-POEGMA$_{51}$]$_4$	50	68	51	100 100	67 800	1.14
[PCL$_{23}$-*b*-POEGMA$_{25}$]$_4$	25	50	25	58 700	43 700	1.23
[PCL$_{13}$-*b*-POEGMA$_{26}$]$_4$	25	53	26	56 100	42 300	1.21

[a] Obtained from SEC ($CHCl_3$:*i*PrOH:NEt_3) using PEG calibration. [b] Calculated from the conversion. [c] Obtained from SEC (DMAc:LiCl) using PMMA calibration.

completely separated from the OEGMA macromonomers by a preparative size exclusion column and freeze-dried (Table 1) (synthesis details are given in the ESI†).

Solution behavior

First, the size and the shape of unimolecular [PCL-*b*-POEGMA]$_4$ star-shaped block copolymers were investigated in non-selective solvents, *e.g.* THF and acetone. For this purpose, DLS and analytical ultracentrifugation (AUC) measurements were carried out and compared to molecular calculations.

DLS measurements were performed at the concentration of 1 mg mL^{-1} and provided similar results both in THF and in acetone. The results from THF are depicted in Fig. 1a and show a good correlation between increasing length of the POEGMA block and the diameter of the star-shaped block copolymer unimers. The [PCL$_{18}$–Br]$_4$ macroinitiator shows a diameter of 6.8 nm. The size increases up to 14.6 nm for [PCL$_{18}$-*b*-POEGMA$_{51}$]$_4$ with the longest POEGMA block. In the same way, the diameters of the amphiphilic star-shaped block copolymers increase with higher molar masses of the PCL block while the length of the POEGMA segment was constant.

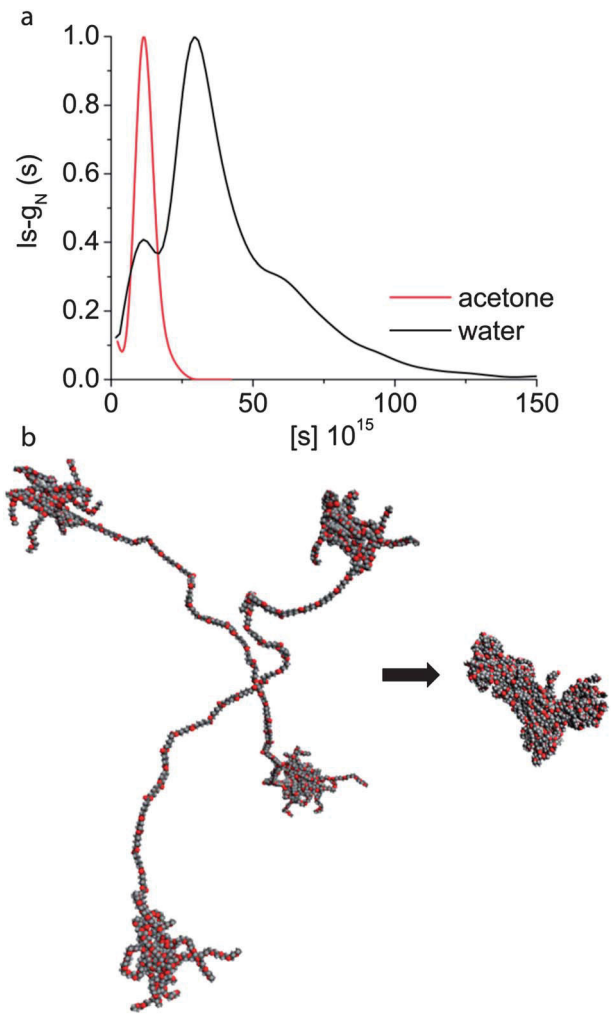

Fig. 2 (a) Normalized distributions of the intrinsic velocity sedimentation coefficients [*s*] obtained in acetone and in water for [PCL$_{18}$-*b*-POEGMA$_{25}$]$_4$ at a concentration of c = 0.5 mg mL^{-1}. (b) Final geometries of the gas phase energy minimization and dynamics calculation of [PCL$_{18}$–POEGMA$_{12}$]$_4$ depicted as a calotte model based on van der Waals radii. Carbon atoms are represented in grey and oxygen atoms in red. Hydrogen atoms are omitted.

Table 2 Hydrodynamic characteristics and molar masses of the initiator [PCL$_{18}$–Br]$_4$ and [PCL$_{18}$–POEGMA$_{12-51}$]$_4$ in acetone

Polymer	$[\eta]$ [cm^3 g^{-1}]	s_0 [10^{13} s]	$(f/f_{sph})_0$	M_{sf} [g mol^{-1}]	M_n [g mol^{-1}]
[PCL$_{18}$–Br]$_4$	10.1	2.99	1.80	9 200	8 900[a]
[PCL$_{18}$-*b*-POEGMA$_{12}$]$_4$	9.6	8.8	1.60	38 000	31 700[b]
[PCL$_{18}$-*b*-POEGMA$_{20}$]$_4$	10.4	9.34	1.62	38 000	46 900[b]
[PCL$_{18}$-*b*-POEGMA$_{25}$]$_4$	9.7	11.2	1.62	59 000	56 400[b]
[PCL$_{18}$-*b*-POEGMA$_{51}$]$_4$	12.7	17.3	1.66	104 000	100 100[b]

[a] Calculated from ^{1}H NMR. [b] Calculated from the conversion.

To obtain further information about the shape of the systems investigated, both [PCL$_{18}$-*b*-POEGMA$_{25}$]$_4$ and [PCL$_{18}$-*b*-POEGMA$_{51}$]$_4$ have been used in angle-dependent light scattering measurements. Due to rather low scattering intensities, the interpretation of the results was not unambiguous (Fig. S4†). Therefore, further experiments were performed using AUC for a series of star-shaped block copolymers with a PCL core of constant DP and an increasing length of the POEGMA segments. This method allowed an estimation of the molar mass of the macromolecules using the hydrodynamic values s_0 (Fig. 2a), the frictional ratio $(f/f_{sph})_0$, and the partial specific volume υ obtained from the modified Svedberg relation:

$$M_{sD} = (RT/(1 - \upsilon\rho_0)\,(s_0/D_0) = M_{sf} = 9\pi 2^{1/2} N_A([s](f/f_{sph})_0)^{3/2}\upsilon^{1/2},$$

where D_0 is the translation diffusion coefficient, $[s] \equiv s_0\eta_0/(1 - \upsilon\rho_0)$ is the intrinsic sedimentation coefficient, υ is the partial specific volume of the solute macromolecules, R is the gas constant, T is the temperature in K, and N_A is Avogadro number. The values of the molar mass calculated on the basis of the AUC measurements (M_{sf}) show a good correlation with the M_n values obtained through ^{1}H-NMR experiments and the conversion (Table 2).

The values for the intrinsic viscosity $[\eta]$ and the frictional ratio $(f/f_{sph})_0$ are in the same region for all investigated [PCL$_{18}$-*b*-POEGMA$_{12-51}$]$_4$ block copolymers. At the same time the velocity sedimentation coefficient s_0 varies by almost 6 times. This behavior of the hydrodynamic values is characteristic of globular species. As the values of both intrinsic viscosity and frictional ratio are superior to those observed for globular proteins ($[\eta]_{protein} \approx 4.5$, $(f/f_{sph})_{protein} \approx 1.25$) the hydrodynamic behavior of the star-shaped block copolymers can be described as a spheroid with constant asymmetry. The degree of asymmetry of the spheroid is estimated from the intrinsic viscosity data calculating the Simha factor $\nu \equiv [\eta]/\upsilon$ and the frictional ratio (Perrin factor),[31] which are determined as $([\eta]/\upsilon)_{av} = 12.3 \pm 0.3$ and $(f/f_{sph})_{av} = 1.62 \pm 0.02$, respectively. Based on these values, an estimation of the asymmetry of the ellipsoids (p) generally is possible. Therefore, for prolate ellipsoids p was determined to be 9.3 (viscosity) and 11.2 (translation friction). For oblate ellipsoids, p was calculated to be

16.2 (viscosity) and 14.0 (translation friction). On this basis, average values for prolate ellipsoids $p_{av} = 10 \pm 1$ and for oblate ellipsoids $p_{av} = 15 \pm 1$ are obtained. However, a final decision whether the investigated star-shaped block copolymers represent prolate or oblate ellipsoids by using only hydrodynamic data is not possible.

These findings are in accordance with the results obtained by molecular mechanics and dynamics simulations performed for $[PCL_{18}$-*b*-$POEGMA_{12}]_4$. Energy minimization of the geometry in the gas phase shows a stretched PCL core carrying dense POEGMA brushes at the end of each arm. By applying a molecular dynamics calculation based on the energetically optimized structure the folding of the PCL arms and, therefore, a strong shrinking of the core is observed. $[PCL_{18}$-*b*-$POEGMA_{12}]_4$ does not adopt a spherical structure, but rather a kidney-shaped morphology as depicted in Fig. 2b. Two arms collapse separately, while the two others merge, leading to an elongated shape of the molecule. This structure shows a length of around 7.6 nm and a width of 2.4 nm to 4.2 nm, which is in good accordance with the values observed in DLS and AUC experiments.

Self-assembly in aqueous media

The solution behavior of the star-shaped block copolymers in water is of crucial importance for their use as DDS. Different samples were dialyzed from a 1 mg mL^{-1} DMF solution against distilled water. In Fig. 1a, the resulting diameters determined by DLS are depicted (striped bars). For the $[PCL_{18}$-*b*-$POEGMA_{12}]_4$, micelles with a hydrodynamic diameter of 20 nm were obtained and similar values were found for samples with a POEGMA shell of up to 51 units. Number-averaged DLS CONTIN plots show diameters of roughly 20 nm.

Investigations in non-selective solvents revealed diameters of 6 to 12 nm, depending on the length of the POEGMA segments. The diameters observed in water with 20 nm are somewhat larger. For this discrepancy, two possible explanations can be given: (1) the inclusion of water into the POEGMA shell increases the observed diameter or (2) multimolecular micelles are formed.

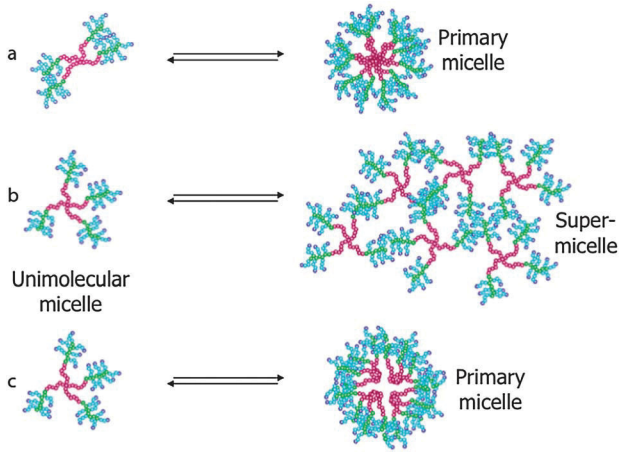

Fig. 3 Schematic representation of possible aggregation models for star-shaped $[PCL_a$-*b*-$POEGMA_b]_4$ block copolymers.

More detailed information on this question can be obtained by the investigation of the $[PCL_a$-*b*-$POEGMA_b]_4$ star-shaped block polymers in water using AUC. The study of the velocity sedimentation of the aqueous solution of $[PCL_{18}$-*b*-$POEGMA_{25}]_4$ shows that predominantly intermolecular clusters of unimolecular micelles are formed. Fig. 2a depicts a comparison of the intrinsic velocity sedimentation coefficient distributions for $[PCL_{18}$-*b*-$POEGMA_{25}]_4$ in acetone and water. The value $[s] \equiv s_0\eta_0/(1 - \upsilon\rho_0) = M/N_A P' \langle R^2\rangle^{1/2}$ is independent of the employed solvent, with P' being the Flory hydrodynamic parameter and $\langle R^2\rangle$ the mean square of the radius of gyration for the moving macromolecule in solution. The distribution of $[s]$ in aqueous solution shows a main central part and two lateral shoulders. The low *s*-shoulder may be attributed to unimolecular micelles (~14%), the main part corresponds to 62%, and the high *s*-shoulder contains ~24% of the material. Therefore, AUC investigations clearly show the presence of larger aggregates.

Although the brush-like shell should prevent aggregation[25,26] and promote the formation of unimolecular micelles, AUC measurements revealed the formation of larger agglomerates of micelles. Further investigations should provide information on the nature of these aggregates. Possible aggregation models are illustrated in Fig. 3: (a) the star-shaped block copolymers behave like a conventional micellar systems (like in the case of linear block copolymers), where multimolecular micelles are formed and the aggregation number is mainly determined by the block length ratio of hydrophilic and hydrophobic segments, (b) the POEGMA shells entangle, forming a kind of supermicelle[35,36] and (c) a system with unimolecular micelles exists at low concentrations, which aggregates at higher values into multimolecular micelles.

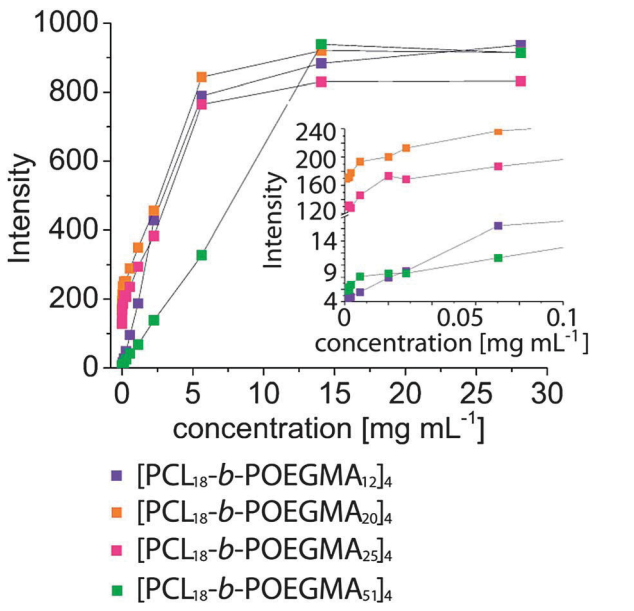

Fig. 4 Intensity of the fluorescence emission of nile red at 620 nm with increasing polymer concentration of $[PCL_{18}$-*b*-$POEGMA_{12}]_4$, $[PCL_{18}$-*b*-$POEGMA_{20}]_4$, $[PCL_{18}$-*b*-$POEGMA_{25}]_4$ and $[PCL_{18}$-*b*-$POEGMA_{51}]_4$ as well as an expanded view of the low concentration regime (inset).

To elucidate the presence of unimolecular micelles, pyrene was used as a fluorescent probe.[37–39] The results obtained for the star-shaped block copolymers $[PCL_{18}$-*b*-$POEGMA_{12-51}]_4$, depicted in Fig. S5,† show changes in the vibrational fine structure (*i.e.* reflected in the change of the ratio of band I to band III) as an indication for a change in the microenvironment of the pyrene,[40] although this must not necessarily correspond to a cmc. The slope can be explained by exceeding the loading capacity of the star-shaped block copolymer (Fig. S8†).

As investigations with pyrene did not allow a final conclusion, additional experiments were performed with nile red as a fluorescent probe: only if hydrophobic cores are present, fluorescence intensity will be detected (Fig. 4). Similar to the preparation of the solutions for the cmc determinations using pyrene, samples were prepared with a constant dye content but varying polymer concentrations. Fig. 4 shows the fluorescence emission of nile red at 620 nm, which is increasing evenly although polymer concentrations down to 3×10^{-8} mM have been used. The inset demonstrates that at very low concentrations no sudden change in the fluorescence intensity can be observed and the intensity is monotonically increasing with increasing polymer concentration. This behavior is an indication of the presence of hydrophobic cores in the whole concentration range, thus confirming the existence of unimolecular micelles even for the smallest hydrophilic shell, $[PCL_{18}$-*b*-$POEGMA_{12}]_4$.

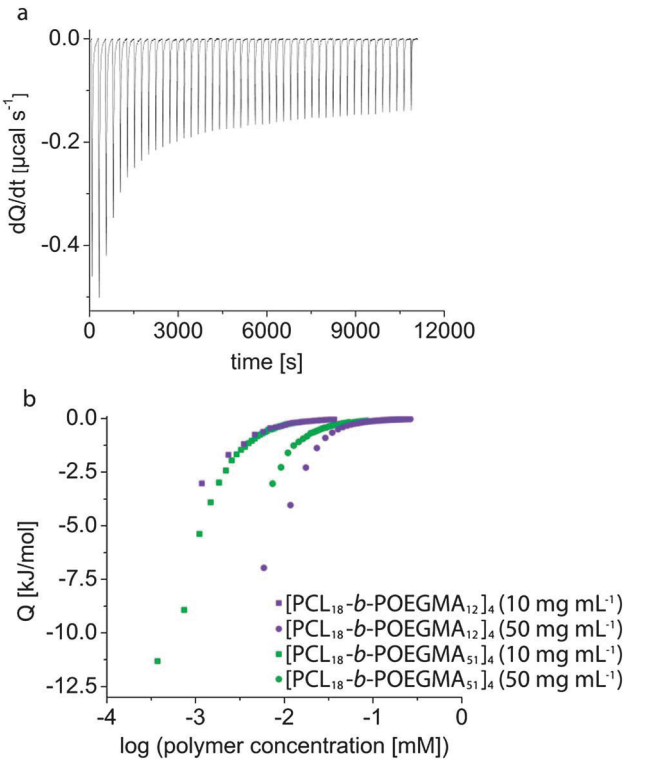

Fig. 5 (a) Experimental titration curve obtained for $[PCL_{18}$-*b*-$POEGMA_{12}]_4$ titrated from a 50 mg mL^{-1} solution into water (baseline corrected). (b) Enthalpograms obtained for the titration of 10 and 50 mg mL^{-1} solutions of $[PCL_{18}$-*b*-$POEGMA_{12}]_4$ and $[PCL_{18}$-*b*-$POEGMA_{51}]_4$.

However, no linear slope is observed as expected for an ideal system. This can be attributed to the entanglement of the POEGMA arms, which is more pronounced at higher concentrations. A penetration of the arms into the core can be conceived by leaving less space for the nile red and prevents the fast and complete inclusion of the appropriate number of molecules as observed earlier by Yang *et al.*[41] Moreover, the authors observed that by further increasing the PEG chain the inclusion capability for pyrene decreases as longer arms hinder molecule diffusion into the core domains. This observation can be confirmed by our findings with nile red, which are particularly visible in the inset of Fig. 4b. $[PCL_{18}$-*b*-$POEGMA_{20}]_4$ and $[PCL_{18}$-*b*-$POEGMA_{25}]_4$ seem to represent an optimum region of the PCL:POEGMA ratio in terms of nile red inclusion efficiency. In contrast, the POEGMA shell of $[PCL_{18}$-*b*-$POEGMA_{51}]_4$ appears to prevent an efficient inclusion of guest molecules.

To confirm the results obtained by spectroscopic methods a complementary approach was used to exclude the presence of multimolecular micelles. Isothermal titration calorimetry (ITC) is an established method to determine the cmc for surfactants and block copolymers.[42] Moreover, the micellization enthalpy together with the free energy of micellization can be calculated.[43,44] For surfactant systems, sigmoidal curves are usually obtained, similar to experiments with pyrene as a fluorescence probe, where the cmc can be deduced from the infliction point of the curve. As initial concentrations, 10 mg mL^{-1} (the maximum concentration used for the cmc determination) and 50 mg mL^{-1} were chosen. In Fig. 5a, the titration curve is illustrated for $[PCL_{18}$-*b*-$POEGMA_{12}]_4$ with an initial concentration of 50 mg mL^{-1}. For $[PCL_{18}$-*b*-$POEGMA_{12}]_4$ and $[PCL_{18}$-*b*-$POEGMA_{51}]_4$ similar results were observed, showing an exothermic incidence for each injection of the sample solution.

Kubowicz *et al.* obtained similar results but used the declining trajectory to determine the cmc as the authors did not observe a sigmoidal shape for the investigated systems.[45] They assumed that the lowest heat value corresponds to the lower linearly extrapolated curve usually used in combination with the upper linearly extrapolated curve to determine the cmc. By measuring two different concentrations for the four different polymers $[PCL_{18}$-*b*-$POEGMA_{12}]_4$, $[PCL_{18}$-*b*-$POEGMA_{20}]_4$, $[PCL_{18}$-*b*-$POEGMA_{25}]_4$ and $[PCL_{18}$-*b*-$POEGMA_{51}]_4$, it was shown that this approach is not appropriate in the case of star-shaped systems. Due to the fact that both curves of the same material show a declining trajectory, hinting towards demicellization enthalpies, these results cannot be attributed to a cmc (Fig. 5b). Rather, the gain of entropy is detected as exothermic amplitude upon dilution of the sample solution. As during the measurement the concentration is increasing, the dilution effect becomes less pronounced. However, it should be noted that the interpretation of these data might be challenging because the dissolution of micelles is probably not a one-step process. Nevertheless the absence of a cmc is assumed, although a stepwise dissolution process should be kept in mind for the system investigated here.[45]

With this background the results obtained by DLS and AUC can be explained in a reasonable manner. In water, the formation of aggregates is observed leading to an increased

hydrodynamic diameter. Although the brush-like POEGMA shells of the star-shaped block copolymers should prevent agglomeration, the formation of a loose network of unimolecular micelles is proposed by entanglement of the POEGMA arms of different molecules. As by spectroscopic methods the absence of multimolecular micelles was confirmed, these star-shaped block copolymers can be employed for drug delivery purpose. Concentration dependent DLS measurements showed an increase of the count rate with increasing concentration. No sudden transition is observed leading to the conclusion that the transition to "supermicelles" is not a spontaneous process at a certain threshold concentration but might rather be connected to an equilibrium between unimolecular micelles and larger aggregates.

These results are somewhat surprising as for drug delivery usually polymers are chosen with large hydrophilic blocks to ensure their solubility in water. To evaluate the proportion of hydrophilic to hydrophobic blocks the concept of the hydrophilic/lipophilic balance (HLB) was introduced. Here, both blocks are compared, the hydrophilic part by its molar mass and the hydrophobic block by its content of methylene groups. The ratio delivers a value, which is recommended to be above 0.9 for conventional micelles. In Fig. 1b, the HLB values calculated according to Uhrich *et al.*,[46] for all star-shaped block copolymers described here are depicted. In our case, only $[PCL_{18}$-*b*-$POEGMA_{51}]_4$ and $[PCL_{13}$-*b*-$POEGMA_{26}]_4$ meet these requirements. $[PCL_{18}$-*b*-$POEGMA_{12}]_4$ even shows a HLB value below 0.8 but still unimolecular micelles seem to be formed. We tentatively assume that this concept might not be applicable for the star-shaped system presented here. In comparison, $[PCL_a$-*b*-$POEGMA_b]_4$ star-shaped block copolymers previously introduced by Schramm *et al.*[23,24] showed HLB values around 0.96. Within this study, it could be clearly demonstrated that even smaller hydrophilic shells of POEGMA are sufficient to stabilize unimolecular micelles.

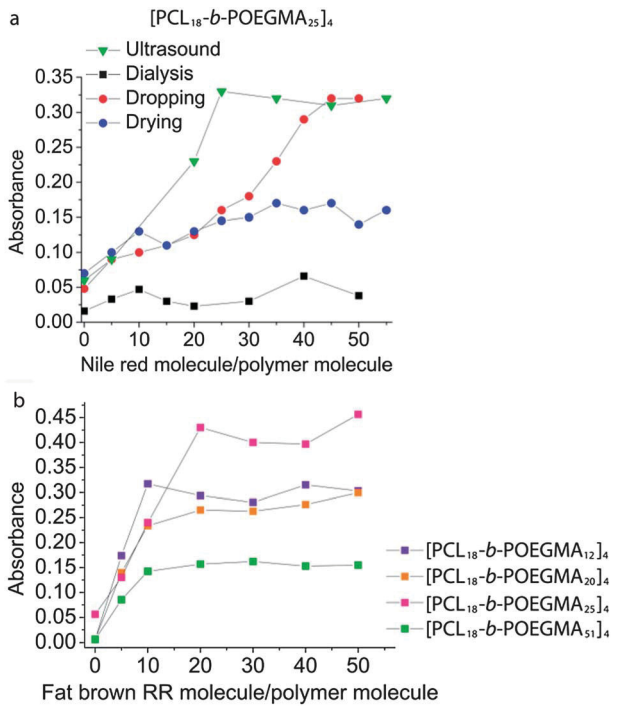

Fig. 6 (a) Absorption intensity of nile red at 525 nm measured for different molar ratios of dye to polymer $[PCL_{18}$-*b*-$POEGMA_{25}]_4$ (1 mg mL^{-1}) in dependence of the preparation method. (b) Absorption intensity of fat brown RR at 460 nm for different molar ratios of dye to polymer for $[PCL_{18}$-*b*-$POEGMA_{12-51}]_4$ polymers.

Encapsulation of guest molecules

To evaluate the uptake and inclusion capacity of the star-shaped block copolymers, fat brown RR and nile red were chosen as model dyes. Different methods for the encapsulation of hydrophobic molecules into amphiphilic polymers have been previously reported; one approach, amongst others, was to apply ultrasound to enhance and to accelerate the uptake of the solid guest molecules by the micellar cores.[23,47] However, ultrasound may damage sensitive drugs; therefore, this method is not useful for DDS. To facilitate the uptake, the use of a co-solvent was found to be beneficial, which is removed either by evaporation or dialysis.[48,49] To identify the best suited preparation conditions for the system, different formulation methods have been tested (Fig. 6a). Therefore, $[PCL_{18}$-*b*-$POEGMA_{25}]_4$ was used and the concentration was adjusted to 1 mg mL^{-1} (corresponding to 0.018 mM) for each method. The concentration of the dye was varied from 0.09 mM to 1.4 mM. Dialysis was found to be very unsuitable as rather low loadings were obtained. For ultrasound-assisted inclusion, a maximum around 25 nile red molecules per polymer was observed, whereas dropping of an acetone solution containing both dye and polymer into water yielded up to 45 nile red molecules per unimolecular micelle. As the best results were obtained with the dropping approach, this method was used for further investigations with different star-shaped block copolymers.

To expand the selection of encapsulated molecules, fat brown RR was utilized, as both dyes are expected to have different hydrophobicity, which will also influence the encapsulation efficiency. Fig. 6b represents the results obtained for $[PCL_{18}$-*b*-$POEGMA_{12-51}]_4$. Surprisingly, no trend with increasing size of the POEGMA shell was observed. The results reflect rather the findings of the cmc determination with nile red. $[PCL_{18}$-*b*-$POEGMA_{25}]_4$ seems to represent an optimum shell to core ratio with an inclusion capacity of around 20 molecules fat brown RR per macromolecule observed from the inclusion saturation ratio. Star-shaped block copolymers with shorter POEGMA shells include less fat brown RR molecules per unimolecular micelle (*ca.* 10). On the other hand, also $[PCL_{18}$-*b*-$POEGMA_{51}]_4$ exhibited the same inclusion capacity, attributed to the shielding effect of the bulky shell. The core size, in contrast, has only a minor influence on the inclusion capacity for this system. For the smallest core $[PCL_{13}$-$Br]_4$, a decreased inclusion maximum of around 10 dye molecules was found when compared to 20 units for a DP of 18 and 23 of PCL (Fig. S6†). To improve the inclusion capacity most probably a more drastic change of the arm length has to be chosen.

Evaluation of *in vitro* biocompatibility

To elucidate the applicability of the star-shaped block copolymers for medical use, an assessment of their biocompatibility

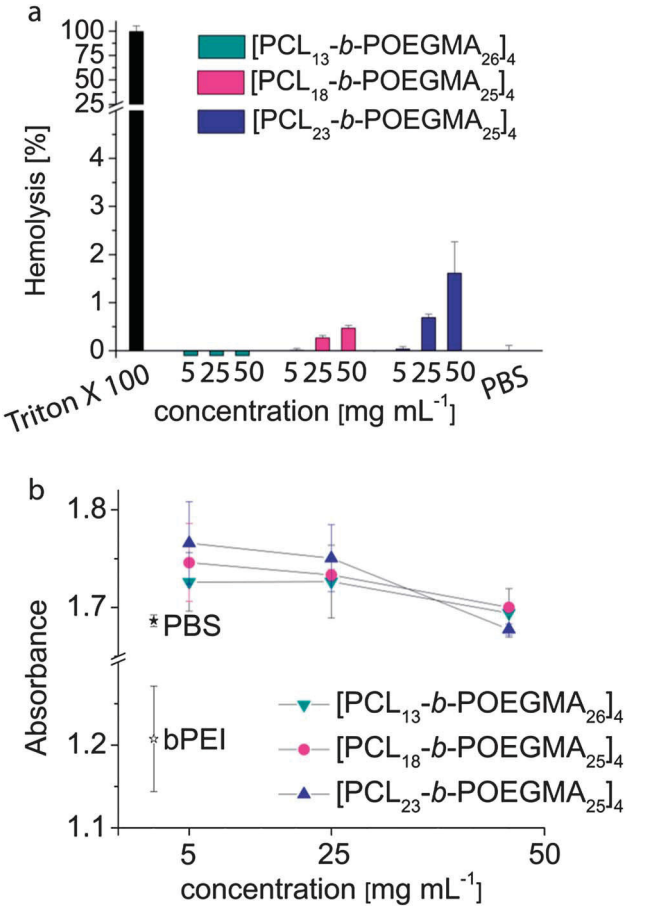

Fig. 7 (a) Photometric determination of the hemolytic activity after incubation with different star-shaped block copolymer concentrations for 1 h at 37 °C. Triton X-100 (1%) served as a positive control and PBS as a negative control. Data are presented as the mean percentage ± SD of hemolytic activity compared to the positive control set as 100%. (b) Photometric determination of the erythrocyte aggregation after 2 h incubation at 37 °C with polymers. 25 kDa bPEI (50 μg mL^{-1}) served as a positive control and PBS as a negative control. Data are presented as the mean measured absorbance ± SD.

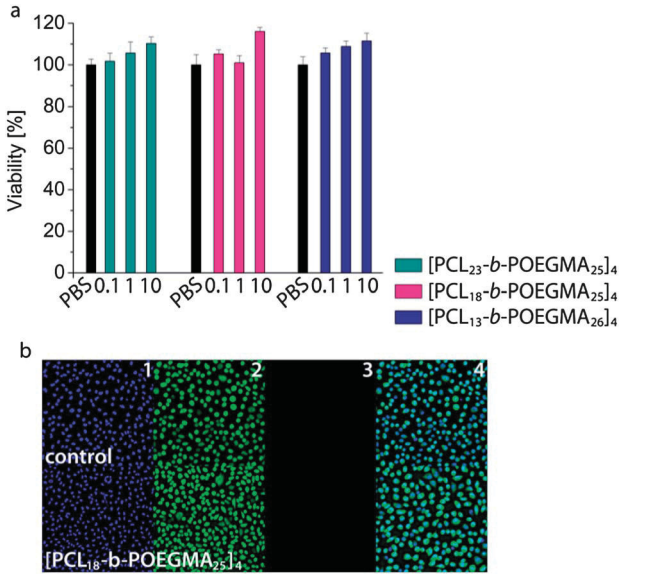

Fig. 8 (a) Cell viability of L929 mouse fibroblasts after incubation with star-shaped block copolymers up to 10 mg mL^{-1} for 24 hours. The cell viability was determined by a XTT assay according to ISO 10993-5. Data are expressed as mean ± SD of six determinations. (b) Representative fluorescence microscopy micrographs of Hoechst 33342/FDA/PI stained L929 mouse fibroblast cells cultured for 24 hours in the presence of 10 mg mL^{-1} of $[PCL_{18}$-*b*-$POEGMA_{25}]_4$ for 24 hours. (1) Blue fluorescent Hoechst 33342 dye labels nuclei of all cells present; (2) green fluorescent FDA dye indicates cytoplasm of vital cells; (3) red fluorescent PI signals tag nuclei of dead cells; (4) overlay of Hoechst 33342 dye fluorescence and green fluorescence of the FDA dye.

in terms of hemocompatibility and possible cytotoxic side effects was performed. Most often, DDS are developed for intravenous administration as they either do not survive in the gastric acid or are not absorbed in the gastrointestinal tract. The interactions of the polymers with erythrocytes as major blood components and one of the first cellular contact partners after systemic administration were investigated regarding red blood cell hemolysis and aggregation. The hemolytic activity of cationic charged polymers, *e.g.* poly(ethylene imine) 600 Da to 1 kDa, poly(L-lysine) 36.6 kDa and also generation dependent poly(amido amine) above G3, is well documented.[50,51] But also uncharged macromolecules of high molar mass, like dextran 60 kDa, poly(vinyl pyrrolidone) 360 kDa and PEG 20 kDa, have been shown to induce red blood cell aggregation.[52] The release of hemoglobin was used to quantify the erythrocyte membrane damaging effect of three different concentrations (5, 25, 50 mg mL^{-1}) of the star-shaped block copolymers (Fig. 7a). The treatment of red blood cells with PBS buffer as a negative control and 1% Triton X-100 solution as a positive control resulted in 0% and 100% hemolysis, respectively. As a hemolysis value of less than 2% of the total release is classified as non-hemolytic, no hemolytic effects up to concentrations of 100 mg mL^{-1} were found, indicating the absence of any membrane destabilizing property of the polymers.

We furthermore investigated whether the $[PCL_a$-*b*-$POEGMA_b]_4$ star-shaped block copolymers would induce the aggregation of erythrocytes, which would represent a sign of blood incompatibility. After incubation with different concentrations (5, 25, 50 mg mL^{-1}) of the materials, the formation of aggregates was studied by both microscopy and photometry. Visual inspection (Fig. S8†) as well as absorption measurements (Fig. 7b) showed that none of the star-shaped block copolymers led to cluster formation below a concentration of 25 mg mL^{-1}. The treatment with 25 kDa branched PEI (bPEI) at 25 μg mL^{-1} served as a positive control causing the clear formation of aggregates, whereas PBS treated samples used as a negative control did not lead to any aggregate formation.

The *in vitro* cytotoxicity experiments were performed *via* a XTT assay using L929 mouse fibroblasts, according to the German standard institution guideline DIN ISO 10993-5 as a reference for biomaterial testing. After 24 h of incubation with different polymer concentrations (0.1, 1.0 and 10 mg mL^{-1}) of the $[PCL_{13-23}$-*b*-$POEGMA_{25}]_4$ and $[PCL_{18}$-*b*-$POEGMA_{12-25}]_4$ star-shaped block copolymers, the metabolic activity of cells treated with test-samples was found to be on the level of untreated controls, which proves the non-toxic effect of the polymers even

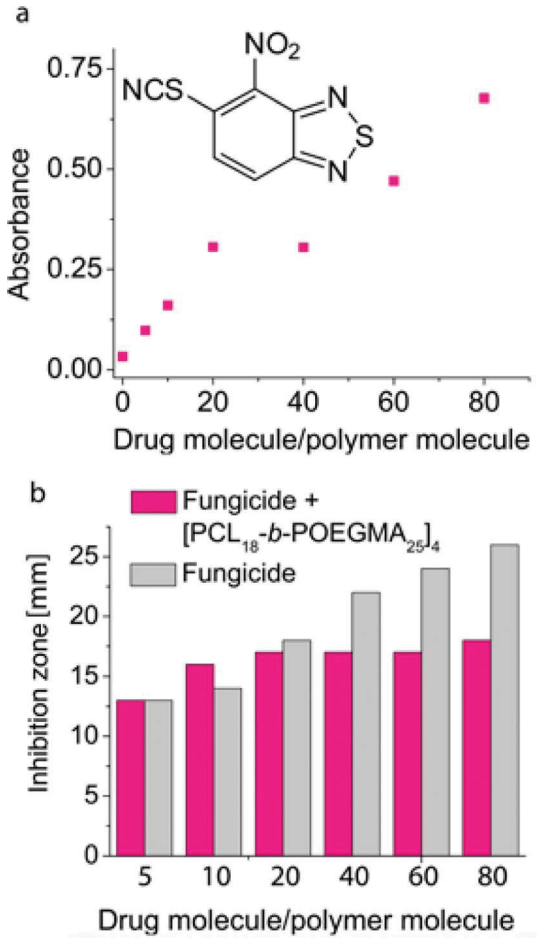

Fig. 9 (a) Absorption intensity of the fungicide (structure given in inset) at 345 nm at constant concentrations of $[PCL_{18}$-*b*-$POEGMA_{25}]_4$ and increasing drug concentration. (b) Inhibition zones of the different fungicide–polymer preparations obtained with *Sporobolomyces salmonicolor* 549.

at the highest concentration used here (Fig. 8a and S9†). A detailed live/dead microscopy study of polymer treated cells confirmed their membrane integrity (exclusion of red fluorescent PI from cell nuclei) and their excellent viability (strong green fluorescence of FDA in cytoplasm) (Fig. 8b).

The zeta potential for the $[PCL_a$-*b*-$POEGMA_b]_4$ star-shaped block copolymers shows values of about −10 mV. The lowest value with −2 mV was obtained in the case of $[PCL_{18}$-*b*-$POEGMA_{51}]_4$. These values are in the typical range for long-circulating PEG protected DDS.[53,54] However, the low values imply also the disadvantage of minor electrostatic repulsion leading to the observed aggregation of the unimolecular micelles.

Heading *e.g.* drug loading and biological activity, those results do confirm that $[PCL_a$-*b*-$POEGMA_b]_4$ star-shaped block copolymers might represent an interesting system for drug delivery issues. In a second step a fungicide was loaded into the star-shaped block copolymers. The development of new fungicides and delivery devices represents a very important step in improving the therapy of systemic fungal infections as frequent and important complications, especially of immunocompromised patients with acquired immune deficiency syndrome (AIDS) or cancer, who attended *e.g.* extensive chemotherapy.[2,3]

The hydrophobic drug with newly discovered promising antifungal activity (structure in Fig. 9a) was encapsulated into the polymer $[PCL_{18}$-*b*-$POEGMA_{25}]_4$ as this polymer has shown the most promising inclusion capacities in previous studies (Fig. 9a).[55] For the dropping method a constant polymer concentration and a growing fungicide concentration were chosen, showing a steady increase of the absorbance with the exception of a step at the drug to polymer ratio of 20, corresponding to the previously determined inclusion limit. A further increase of the absorbance is observed up to a ratio of 80 drug molecules per polymer molecule suggesting that the drug is not only included into the core but also within the hydrophilic shell. Zeta potential measurements are supporting this assumption as the values of the zeta potential are decreasing for the polymer to drug ratios 5, 10 and 20 from −10 mV down to −40 mV. From this ratio the zeta potential remains in the range of −40 mV for the fungicide to polymer ratios 40 to 80.

Similar results were obtained regarding the fungicide activity. Fig. 9b depicts the inhibition zones for the experiments performed with *Sporobolomyces salmonicolor* 549. Further experiments carried out with *Candida albicans* BMSY212 and *Penicillium notatum* JP36 yielded comparable values (results not shown). For fungicide to polymer ratios of 5 to 20, the encapsulated fungicide shows the same antifungal activity as the free drug, which is applied in the same concentration as used for the drug–polymer preparation in a mixture of dimethylsulfoxide, methanol and water to ensure solubility of the hydrophobic drug. The dissolution of the fungicide in pure water, as a comparative experiment, was not successful, no UV signal could be observed and also no inhibition zones in the fungicide test were obtained with the supernatant as well as the suspension of the drug.

For higher ratios of drug to polymer, the free fungicide showed an increased activity, whereas the inhibition zone provoked by the encapsulated drug was observed to lie in the same range as for a ratio of 20. In accordance with the results obtained earlier for the inclusion study and the zeta potential measurements, an inclusion of the fungicide into the POEGMA shell is supposed. This might lead upon administration to the fungal medium to the loss of the shell bound fungicide molecules by precipitation. Only dissolved or in the hydrophobic cavity included fungicide is effective and, hence, the ratio of drug to polymer of 20 resembles the optimum dose for this system. However, the star-shaped polymer is able to solubilize hydrophobic drug molecules in water without the help of a co-solvent and, more importantly, to release them.

Conclusion

4-Arm $[PCL_a$-*b*-$POEGMA_b]_4$ star-shaped block copolymers with varying degrees of polymerization for both PCL and POEGMA have been prepared and exhaustively characterized using mass spectrometry, SEC, DLS, AUC and computational methods. We could show that a spheroidal geometry is adopted in non-selective solvents.

In water as a selective solvent, both unimolecular micelles with a PCL core and a POEGMA shell as well as loose aggregates of several connected star-shaped block copolymer unimers were found. This was confirmed using AUC measurements and, in addition, with nile red as a fluorescence probe, leading to the conclusion that for all [PCL-*b*-POEGMA]$_4$ samples unimolecular hydrophobic cores are present. Furthermore, ITC measurements showed that these amphiphilic systems do not exhibit a cmc. These findings demonstrate that unimolecular micelles can be formed by star-shaped amphiphilic block copolymers also below the typically expected values for the hydrophilic/lipophilic balance.

Inclusion studies using fat brown RR as well as nile red showed an optimum length of 20 to 25 OEGMA units within the hydrophilic shell for a core DP of 18 repeating units.

To elucidate the applicability of these materials as DDS biological investigations regarding hemolytic activity, erythrocyte aggregation, and the cytotoxicity against L929 mouse fibroblast cells were carried out. None of the polymers showed cytotoxic or hemolytic activity.

As a first application, a novel fungicide was encapsulated into the PCL core of [PCL_{18}-*b*-$POEGMA_{25}$]$_4$, which was chosen because it exhibited the best inclusion capacity in our model studies with fat brown RR. It is assumed that the drug was not only entrapped in the core but also further taken up by the POEGMA shell as well. However, the antifungal activity of the encapsulated drug increased only up to a ratio of 20 drug molecules per polymer.

Acknowledgements

We thank Sandra Köhn for the atom absorption measurements and Carolin Fritzsche as well as Christiane Weigel for biological tests. Michael Wagner and Dr Stephanie Schubert are acknowledged for discussions. We thank the Thuringian Ministry for Education, Science and Culture (TMBWK, grant #B514-09051, NanoConSens and TMBWK, grant #B515-10065, ChaPoNano) for financial support.

Notes and references

1 C. A. Lipinski, *J. Pharmacol. Toxicol.*, 2000, **44**, 235–249.
2 G. Medoff, J. Brajtburg, G. S. Kobayashi and J. Bolard, *Annu. Rev. Pharmacol. Toxicol.*, 1983, **23**, 303–330.
3 M. H. Koldin and G. Medoff, *Pediatr. Clin. North Am.*, 1983, **30**, 49–61.
4 B. G. Yu, T. Okano, K. Kataoka and G. Kwon, *J. Controlled Release*, 1998, **53**, 131–136.
5 R. Duncan, *Nat. Rev. Drug Discovery*, 2003, **2**, 347–360.
6 Y. Matsumura and H. Maeda, *Cancer Res.*, 1986, **46**, 6387–6392.
7 H. Maeda, J. Wu, T. Sawa, Y. Matsumura and K. Hori, *J. Controlled Release*, 2000, **65**, 271–284.
8 Y. Matsumura and K. Kataoka, *Cancer Sci.*, 2009, **100**, 572–579.
9 K. Knop, R. Hoogenboom, D. Fischer and U. S. Schubert, *Angew. Chem., Int. Ed.*, 2010, **49**, 6288–6308.
10 N. Hadjichristidis, M. Pitsikalis, S. Pispas and H. Iatrou, *Chem. Rev.*, 2001, **101**, 3747–3792.
11 S. M. Grayson and J. M. J. Frechet, *Chem. Rev.*, 2001, **101**, 3819–3867.
12 J. F. Gohy, *Adv. Polym. Sci.*, 2005, **190**, 65–136.
13 R. Savic, T. Azzam, A. Eisenberg and D. Maysinger, *Langmuir*, 2006, **22**, 3570–3578.
14 G. R. Newkome, C. N. Moorefield, G. R. Baker, A. L. Johnson and R. K. Behera, *Angew. Chem., Int. Ed.*, 1991, **30**, 1176–1178.
15 S. Kim, Y. Shi, J. Y. Kim, K. Park and J.-X. Cheng, *Expert Opin. Drug Delivery*, 2010, **7**, 49–62.
16 H. Liu, Y. Chen, D. Zhu, Z. Shen and S.-E. Stiriba, *React. Funct. Polym.*, 2007, **67**, 383–395.
17 C. Kojima, K. Kono, K. Maruyama and T. Takagishi, *Bioconjugate Chem.*, 2000, **11**, 910–917.
18 J. Khandare, M. Calderón, N. M. Dagia and R. Haag, *Chem. Soc. Rev.*, 2012, **41**, 2824–2848.
19 M. Deng, X. Chen, L. Piao, X. Zhang, Z. Dai and X. Jing, *J. Polym. Sci., Part A: Polym. Chem.*, 2004, **42**, 950–959.
20 M. R. Nabid, S. J. Tabatabaei Rezaei, R. Sedghi, H. Niknejad, A. A. Entezami, H. A. Oskooie and M. M. Heravi, *Polymer*, 2011, **52**, 2799–2809.
21 H. B. Liu, S. Farrell and K. Uhrich, *J. Controlled Release*, 2000, **68**, 167–174.
22 A. M. Harmon and K. E. Uhrich, *J. Bioact. Compat. Polym.*, 2009, **24**, 185–197.
23 O. G. Schramm, G. M. Pavlov, H. P. van Erp, M. A. R. Meier, R. Hoogenboom and U. S. Schubert, *Macromolecules*, 2009, **42**, 1808–1816.
24 O. G. Schramm, M. A. R. Meier, R. Hoogenboom, H. P. van Erp, J. F. Gohy and U. S. Schubert, *Soft Matter*, 2009, **5**, 1662–1667.
25 J. Yun, R. Faust, S. L. Szilagyi, S. Keki and M. Zsuga, *Macromolecules*, 2003, **36**, 1717–1723.
26 M. Zamurovic, S. Christodoulou, A. Vazaios, E. Iatrou, M. Pitsikalis and N. Hadjichristidis, *Macromolecules*, 2007, **40**, 5835–5849.
27 T. Ren, A. Wang, W. Yuan, L. Li and Y. Feng, *J. Polym. Sci., Part A: Polym. Chem.*, 2011, **49**, 2303–2313.
28 O. Kratky, H. Leopold and H. Stabinger, *Methods Enzymol.*, 1973, **27**, 98–110.
29 P. Schuck, *Biophys. J.*, 2000, **78**, 1606–1619.
30 http://www.analyticalultracentrifugation.com/default.htm, last accessed 04 April 2012.
31 C. R. Cantor and P. Schimmel, *Biophysical Chemistry*, Freeman, San Francisco, 1980.
32 J. W. Ponder and F. M. Richards, *J. Comput. Chem.*, 1987, **8**, 1016–1024.
33 N. L. Allinger, Y. H. Yuh and J. H. Lii, *J. Am. Chem. Soc.*, 1989, **111**, 8551–8566.
34 M. Schaefer and M. Karplus, *J. Phys. Chem.*, 1996, **100**, 1578–1599.
35 M. R. Radowski, A. Shukla, H. von Berlepsch, C. Bottcher, G. Pickaert, H. Rehage and R. Haag, *Angew. Chem., Int. Ed.*, 2007, **46**, 1265–1269.
36 H. Y. Hong, Y. Y. Mai, Y. F. Zhou, D. Y. Yan and J. Cui, *Macromol. Rapid Commun.*, 2007, **28**, 591–596.

37 K. Kalyanasundaram and J. K. Thomas, *J. Am. Chem. Soc.*, 1977, **99**, 2039–2044.
38 M. Wilhelm, C. L. Zhao, Y. C. Wang, R. L. Xu, M. A. Winnik, J. L. Mura, G. Riess and M. D. Croucher, *Macromolecules*, 1991, **24**, 1033–1040.
39 G. Kwon, M. Naito, M. Yokoyama, T. Okano, Y. Sakurai and K. Kataoka, *Langmuir*, 1993, **9**, 945–949.
40 A. Hashidzume, M. Mizusaki, K. Yoda and Y. Morishima, *Langmuir*, 1999, **15**, 4276–4282.
41 H. Yang, J. J. Morris and S. T. Lopina, *J. Coll. Int. Sci.*, 2004, **273**, 148–154.
42 Y. Kadam, K. Singh, D. G. Marangoni, J. H. Ma, V. K. Aswal and P. Bahadur, *Colloids Surf., A*, 2010, **369**, 121–127.
43 R. De Lisi, S. Milioto and N. Muratore, *Macromolecules*, 2002, **35**, 7067–7073.
44 P. Taboada, V. Mosquera, D. Attwood, Z. Yang and C. Booth, *Phys. Chem. Chem. Phys.*, 2003, **5**, 2625–2627.
45 S. Kubowicz, A. F. Thunemann, R. Weberskirch and H. Möhwald, *Langmuir*, 2005, **21**, 7214–7219.
46 H. B. Liu, A. Jiang, J. A. Guo and K. E. Uhrich, *J. Polym. Sci., Part A: Polym. Chem.*, 1999, **37**, 703–711.
47 C. J. Hawker, K. L. Wooley and J. M. J. Frechet, *J. Chem. Soc., Perkin Trans. 1*, 1993, 1287–1297.
48 H. M. Aliabadi, S. Elhasi, A. Mahmud, R. Gulamhusein, P. Mahdipoor and A. Lavasanifar, *Int. J. Pharm.*, 2007, **329**, 158–165.
49 H. Cabral, M. Nakanishi, M. Kumagai, W. D. Jang, N. Nishiyama and K. Kataoka, *Pharm. Res.*, 2009, **26**, 82–92.
50 D. Fischer, Y. X. Li, B. Ahlemeyer, J. Krieglstein and T. Kissel, *Biomaterials*, 2003, **24**, 1121–1131.
51 N. Malik, R. Wiwattanapatapee, R. Klopsch, K. Lorenz, H. Frey, J. W. Weener, E. W. Meijer, W. Paulus and R. Duncan, *J. Controlled Release*, 2000, **68**, 299–302.
52 J. K. Armstrong, R. B. Wenby, H. J. Meiselman and T. C. Fisher, *Biophys. J.*, 2004, **87**, 4259–4270.
53 K. Kataoka, A. Harada and Y. Nagasaki, *Adv. Drug Delivery Rev.*, 2001, **47**, 113–131.
54 R. Gref, M. Luck, P. Quellec, M. Marchand, E. Dellacherie, S. Harnisch, T. Blunk and R. H. Müller, *Colloids Surf., B*, 2000, **18**, 301–313.
55 V. G. Pesin and A. M. Chalezkii, *J. Org. Chem.*, 1961, **32**, 3284–3290.

Publication P3:

Star-shaped drug carriers for doxorubicin with POEGMA and POEtOxMA brush-like shells: A structural, physical and biological comparison

---

K. Knop, D. Pretzel, A. Urbanek, T. Rudolph, D. H. Scharf, A. Schallon, M. Wagner, S. Schubert, M. Kiehntopf, A. A. Brakhage, F. H. Schacher, U. S. Schubert

Biomacromolecules, **2013**, submitted.

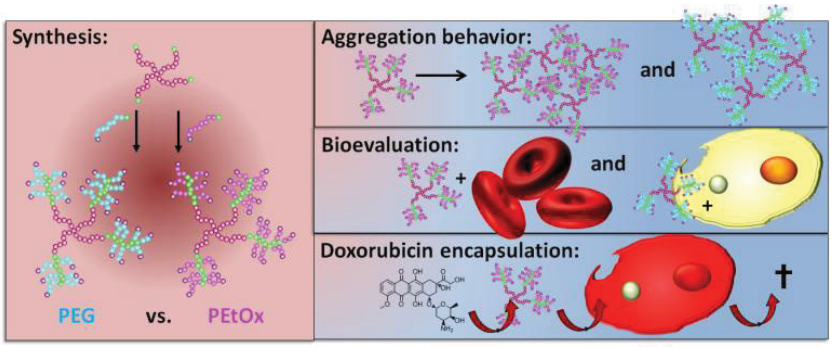

Star-shaped drug carriers for doxorubicin with POEGMA and POEtOxMA brush-like shells: A structural, physical and biological comparison

*Katrin Knop.[1,2] David Pretzel,[1,2] Annett Urbanek,[1,2] Tobias Rudolph,[1,2] Daniel H. Scharf,[3] Anja Schallon,[1,2] Michael Wagner,[1,2] Stephanie Schubert,[2,4] Michael Kiehntopf,[5] Axel A. Brakhage,[3] Felix H. Schacher,[1,2] and Ulrich S. Schubert[1,2]**

[1] Laboratory of Organic and Macromolecular Chemistry (IOMC), Friedrich-Schiller-University Jena, Humboldtstrasse 10, 07743 Germany
[2] Jena Center for Soft Matter (JCSM), Friedrich-Schiller-University Jena, Philosophenweg 8, 07743 Germany
[3] Leibniz Institute for Natural Product Research and Infection Biology – Hans Knöll Institute, Beutenbergstr. 11a, 07745 Jena, Germany
[4] Department of Pharmaceutical Technology, Institute of Pharmacy, Friedrich-Schiller-University Jena, Otto-Schott-Strasse 41, 07745 Jena, Germany
[5] Institute for Clinical Chemistry and Laboratory Diagnostics, Jena University Hospital, Erlanger Allee 101, 07740 Jena, Germany

*Author for correspondence: Prof. Dr. U. S. Schubert. Telephone: +49(0) 3641 948200, Fax: +49(0) 3641 948202, E-mail: ulrich.schubert@uni-jena.de, Internet: www.schubert-group.com

KEYWORDS. Star-shaped block copolymer, unimolecular micelle, drug delivery system, oligo(2-ethyl-2-oxazoline), oligo(ethylene glycol), doxorubicin.

ABSTRACT. The synthesis of amphiphilic star-shaped poly(ε-caprolactone)-*block*-poly(oligo(ethylene glycol)methacrylate)s ([PCL_{18}-*b*-POEGMA]$_4$) and poly(ε-caprolactone)-*block*-poly(oligo(2-ethyl-2-oxazoline)methacrylate)s ([PCL_{18}-*b*-POEtOxMA]$_4$) is presented. Unimolecular behavior in aqueous systems is observed with the tendency to form supermicelles for both hydrophilic shell types. The comparison of OEGMA and OEtOxMA reveals that rather the molar mass of the macromonomer in the hydrophilic shell than the mere length is the crucial factor to form an efficiently stabilizing hydrophilic shell. A hydrophilic/lipophilic balance of 0.8 is shown to stabilize unimolecular micelles in water. An extensive *in vitro* biological evaluation shows neither blood- nor cytotoxicity. The applicability of the polymers as drug delivery systems was proven by the encapsulation of the anti-cancer drug doxorubicin, whose cytotoxic effect was retarded in comparison to the free drug.

Introduction

Amphiphilic star-shaped block copolymers have been shown to have great potential as versatile polymeric drug delivery systems (DDSs) for hydrophobic drugs.[1–4] Their main advantage over micelles based on linear systems is a tailor-made and controlled architecture as no critical micelle concentration (cmc) is observed, which might lead to uncontrolled disassembly and premature drug release directly after administration.[5,6] As an alternative, the concept of unimolecular micelles, which do not disintegrate upon dilution, has been developed by Newkome *et al*..[7] The benefit of star-shaped block copolymers if compared to dendritic DDSs, which also form unimolecular micelles, is that the synthesis is typically more straightforward and an upscaling can be performed more easily.[8,9]

The solution behavior of micelles formed by linear block copolymers depends on several factors, including the architecture. On one side, the architecture of the core-forming block has been shown to have a significant influence on the cmc, which was inversely proportional to the branching parameter of that segment.[10] On the other hand, the design of the hydrophilic shell has a tremendous impact on the micellar properties.[11–13] It was found that sterically demanding hydrophilic shells prevent the formation of larger aggregates.[13] In accordance with these results it was reported for star-shaped block copolymers that a shell composed of linear segments might not be efficient enough to stabilize hydrophobic cores in water.[14] Therefore, the concept of a brush-like shell with improved shielding capabilities was developed.[15,16] In a previous study a poly(ε-caprolactone) (PCL) core was used to attach a hydrophilic shell of poly(oligo(ethylene glycol)methacrylate) (OEGMA, M_n = 475 g mol^{-1}).[17] It was shown that with this concept a lower hydrophilic/lipophilic balance (HLB) is sufficient to stabilize the hydrophobic core. In that particular case, a HLB value of 0.8 was found to stabilize unimers whereas typically a value of 0.9 is expected for linear block copolymers.[18] Moreover, the arm length of the POEGMA brush seemed to play an important role, as for materials with a shorter POEGMA brush-arm length (M_n = 300 g mol^{-1}) multi-molecular micelles were formed.[19]

The influence of the chemical structure of the hydrophilic shell for such systems has been less frequently investigated with respect to chemistry and stability. From a biological point of view the circulation times of different hydrophilic polymers of DDSs in blood have already been studied.[20–22] It was observed that for poly(hydroxyethyl-*L*-asparagine) (PHEA), poly(2-methyl-2-oxazoline) (PMeOx), poly(2-ethyl-2-oxazoline) (PEtOx), and poly(vinyl pyrrolidone) (PVP) the influence of the molar mass of the respective monomer is larger than the influence of the number of repeating units if compared to poly(ethylene glycol) (PEG).[23]

Although different hydrophilic polymers were investigated as substitutes for PEG, it remains the most important material regarding biological applications up to now. However, drawbacks of PEG are a limited biodegradability, prevailing immunological uncertainties, and the often ignored accumulation of PEG after *in vivo* administration.[23] Therefore, amongst a variety of other polymers, poly(2-oxazoline)s have been investigated as potential alternatives to PEG. Several studies on cytotoxicity, blood compatibility and immunomodulatory effects did not reveal any adverse effects at different concentrations and molar masses in case of PEtOx.[24–27]

Additionally, a variety of block copolymers containing poly(2-oxazoline)s segments were shown to be non-cytotoxic.[28] Various formulations containing PEtOx or PMeOx could be assessed as efficient and suitable DDSs, such as liposomes[21,29] and linear amphiphilic poly(lactic acid) (PLA)-*b*-PEtOx-*b*-PLA micelles as carriers for doxorubicin or PEtOx-*b*-PCL micelles loaded with paclitaxel.[30,31] Furthermore, amphiphilic linear ABA di- and triblock copolymers containing different poly(2-oxazoline)s were reported as transport systems for paclitaxel maintaining the drugs activity in *in vitro* and *in vivo* experiments.[32]

The aim of this study was to elucidate the effect of side-chain length and overall molar mass, as well as the chemical structure on the solution properties of the resulting star-shaped DDSs in aqueous media. Therefore, our recent results on star-shaped [PCL-*b*-OEGMA]$_4$ (OEG_9MA, $M_n = 475$ g mol^{-1}, 9 repeating units) block copolymers with four arms were compared to materials with different lengths of POEGMA or poly(oligo(2-ethyl-2-oxazoline)methacrylate) (POEtOxMA) shells. Hence, a library of polymers was synthesized, where both the length of the side-chain as well as the overall length of the corona brushes were varied. In detail, $OEG_{19}MA$ ($M_n = 950$ g mol^{-1}, the subscript denotes the degree of polymerization) and OEG_9MA were compared to $OEtOx_4MA$ ($M_n = 500$ g mol^{-1}) and $OEtOx_9MA$ ($M_n = 1\ 000$ g mol^{-1}) of comparable molar masses. Our aim was to elucidate the effect of side-chain length and overall molar mass, as well as the chemical structure on the solution properties of the resulting star-shaped DDSs in aqueous media. We present a general concept for the use of brush-like amphiphilic star block copolymers as DDS and support this by extensive *in vitro* tests. Furthermore, the potent anti-cancer drug doxorubicin was encapsulated and its activity tested in *in vitro* cytotoxicity assays to investigate the drug delivery potentials of the star-shaped block copolymers.

Experimental Section

Materials

Tin(II) 2-ethylhexanoate ($Sn(oct)_2$, Aldrich), α-bromoisobutyryl bromide (Aldrich), anisole (Fluka, 99.0%), copper(I) bromide (CuBr, Aldrich, 99.999%), poly(ethylene glycol) methyl ether methacrylate (M_n = 950, Aldrich), acetonitrile (ACN, 99.8%, Aldrich) and trioxane (Aldrich) were used as received, if not otherwise stated. ε-Caprolactone (Aldrich) was dried 2 d over CaH_2 before distillation and stored under argon. Triethylamine (TEA) was stored over KOH, distilled over CaH_2 and stored under argon. 2-Ethyl-2-oxazoline (EtOx, Acros Organics) was distilled to dryness over barium oxide (BaO, Sigma Aldrich) and stored under argon. Methyl tosylate (MeTos, Aldrich) was distilled and subsequently stored under argon. Pentaerythritol (Aldrich) was coevaporated with toluene prior to use. Tetrahydrofuran (THF, Aldrich) was dried in a solvent purification system (Pure Solv EN, Innovative Technology) before use. *N*,*N*,*N*′,*N*″,*N*″-Pentamethyldiethylenetriamine (PMDETA, Aldrich) was passed through an aluminum oxide bed

containing 5% CaH_2 prior to use. The dialysis bags with molar mass cut-off of 3 500 g mol^{-1} were supplied by Spectra/Por.

Instrumentation

Proton nuclear magnetic resonance (^{1}H NMR) spectra were recorded in $CDCl_3$ on a Bruker AC 250 or 300 MHz spectrometer at 298 K. Chemical shifts are given in parts per million (ppm, δ scale) relative to the residual signal of the deuterated solvent.

Size exclusion chromatography (SEC) was measured on a Shimadzu system equipped with a SCL-10A system controller, a LC-10AD pump, a RID-10A refractive index detector, and both a PSS Gram30 and a PSS Gram1000 column in series, whereby *N*,*N*-dimethylacetamide with 5 mmol LiCl was used as an eluent at 1 mL min^{-1} flow rate. The column oven was set to 60 °C. The system was calibrated with PMMA (410 to 88 000 g mol^{-1}) and PEG (440 to 44 700 g mol^{-1}) standards. Furthermore, the kinetics of the polymerization was performed on a Shimadzu system equipped with a SCL-10A system controller, a LC-10AD pump, and a RID-10A refractive index detector using a solvent mixture containing chloroform, TEA, and isopropyl alcohol (94:4:2) at a flow rate of 1 mL min^{-1} on a PSS SDV linear M 5 μm column. The system was calibrated with PMMA (410 to 88 000 g mol^{-1}) and PEG (440 to 44 700 g mol^{-1}) standards.

Matrix-assisted laser desorption/ionization time of flight (MALDI-TOF) mass spectra were recorded on an Ultraflex III TOF/TOF (Bruker Daltonics, Bremen, Germany), equipped with a Nd:YAG laser and with *trans*-2-[3-(4-*tert*-butylphenyl)-2-methyl-2-propenylidene] malononitrile (DCTB) as matrix and an appropriate salt as ionizing agent in reflector and linear mode. The instrument was calibrated prior to each measurement with an external PMMA standard from Polymer Standards Services GmbH (Mainz, Germany).

UV/Vis absorption measurements were performed on an Analytik Jena SPECORD 250 (Analytik Jena, Jena, Germany) at 298 K. Fluorescence emission spectroscopy has been measured on a Jasco FP-6500 spectrometer at 298 K.

Dynamic light scattering (DLS) measurements were performed on a ALV DLS/SLS equipment consisting of a ALV Laser CGS3 Goniometer with a ALV Avalanche correlator and a HeNe laser ($\lambda = 632.8$ nm) at 298 K. The aqueous polymer solutions (prepared by dialysis from a dimethylformamide solution at a concentration of 1 mg mL^{-1}) as well as the acetone solutions with concentrations of 5 mg mL^{-1} were filtered twice (GF 1-2 μm or PTFE 0.45 μm) and measured at an angle of 90 °. The hydrodynamic radius (R_h) was determined using the CONTIN algorithm. Angle-dependent measurements were performed in the same manner in the range of 50 to 150 ° in 10 ° steps.

For the photometric absorbance measurement, a TECAN Infinite M200 PRO plate reader (TECAN, Crailsheim, Germany) was used to measure the absorption of samples from a) the XTT cytotoxicity assay (570 nm with a background correction of the optical density (OD) at 690 nm), b) the hemolysis of erythrocytes (540 nm with a background correction of the OD at 690 nm), and c) the photometric evaluation of erythrocyte aggregation (645 nm). Each well containing the sample was measured in four different spots each with 10 flashes per scan.

Isothermal titration calorimetry (ITC) measurements were performed with a VP-ITC microcalorimeter from MicroCal (Northhampton, MA). Reference cell as well as the sample cell, both filled with a volume of 1.6 mL, were enclosed in an adiabatic jacket. The samples were injected stepwise into the working cell with a syringe of a total volume of 288 µL under constant stirring at a stirring rate of 310 rpm. The measurements were performed at a constant temperature of 25 °C. Small aliquots of the sample (6 µL) were successively injected into the water of the working cell. The data treatment was performed as follows: firstly, the baseline was subtracted from the data, secondly each peak was integrated providing the heat per injection.

Experimental details

Determination of the cmc with pyrene. 1 mL of the polymers in acetone solutions were dropped into 5 mL water under stirring to obtain final concentrations between 1.0×10^{-8} µmol mL^{-1} and 1.0×10^{-1} µmol mL^{-1}. 10 µL of a 0.254 mg mL^{-1} concentrated pyrene in acetone solution was added leading to a final pyrene concentration in water of 2.5×10^{-6} M. The acetone was evaporated for two days under constant stirring, the solutions were refilled with water to 5 mL, and the vials were closed to equilibrate for a further week. The emission spectra were recorded between 350 nm and 500 nm with λ_{exc} = 335 nm. Excitation spectra were recorded from 300 nm to 380 nm. The emission wavelength was set to 390 nm.

Determination of the cmc with nile red. The aqueous polymer solutions were prepared in an analogue way as described for the cmc determination with pyrene. To each sample, 10 µL of nile red in acetone (0.4 mg mL^{-1}) were added to result in a final nile red in water concentration of 2.5×10^{-6} M. The acetone was evaporated for two days, refilled to 5 mL and equilibrated for one week. The emission spectra were recorded between 525 nm and 750 nm with $\lambda\lambda_{exc}$ = 520 nm.

Encapsulation. Aqueous solutions of all polymers with a concentration of 1 mg mL^{-1} were prepared by stirring the polymer in the appropriate amount of water. According to a predetermined fat brown RR to polymer molar ratio, aliquots of a fat brown RR acetone solution (4 mg mL^{-1}) were added to a vial and the acetone was allowed to evaporate. 5 mL of the polymer solution were added subsequently, stirred for two days and finally the solutions were refilled to 5 mL. 200 µL of the dye polymer solution were diluted to 1 mL with water, and the UV/Vis absorbance at 460 nm was used to evaluate the inclusion capacity. For doxorubicin encapsulation, doxorubicin hydrochloride was stirred in THF with a 3-fold equivalent of triethylamine overnight in the dark. The appropriate amounts of polymer and subsequently water were added to result a 1 mg mL^{-1} polymer solution. The THF was evaporated and the doxorubicin containing unimolecular micelles were dialyzed against water, freeze dried and weight. The doxorubicin content was determined by dissolving the freeze-fried formulation in DMF and measuring the UV/Vis absorbance at 481 nm (ε = 11 298 cm M^{-1} L^{-1}).

Results and Discussion

Synthesis

The core-first approach has been used for the preparation of star-shaped architectures with a defined number of arms and was, therefore, applied in this study to a four-armed poly(ε-caprolactone) (PCL) star polymer.[16,33,34] The arm length of 18 repeating units ([PCL_{18}-OH]$_4$) was chosen to be comparable to a previous study on star-shaped block copolymers with a $POEG_9MA$ shell.[17] [PCL_{18}-OH]$_4$ was esterified with α-bromoisobutyryl bromide to obtain a [PCL_{18}-Br]$_4$) macroinitiator for the atom transfer radical polymerization (ATRP) of OEGMA or OEtOxMA (synthesis and characterization details for PCL are provided in the SI).

Scheme 1. Schematic representation of the synthetic route to four-arm star block copolymers with different hydrophilic shells.

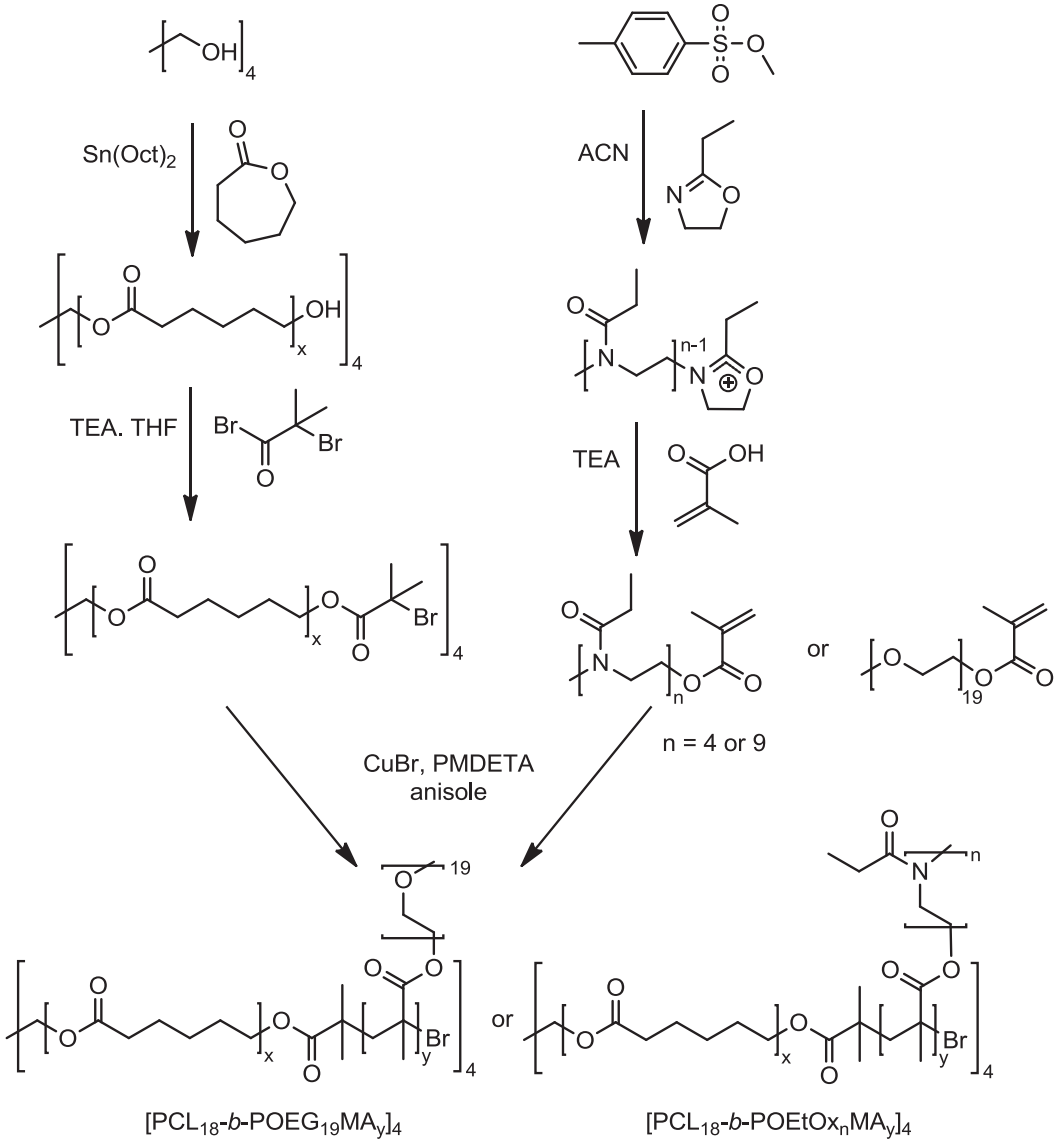

The attachment of a brush-like outer shell by ATRP represents a versatile and straightforward approach (Scheme 1).[15–17] In this study, both length and nature of the outer block have been varied. For this purpose, $OEG_{19}MA$ (M_n = 950 g mol^{-1}) was chosen in comparison to the previous study where OEG_9MA (M_n = 475 g mol^{-1}) has been used.[17] Furthermore, we used oligo(2-ethyl-2-oxazoline)methacrylates (OEtOxMAs) with similar molar masses ((M_n = 500 g mol^{-1}, 4 repeating units, $OEtOx_4MA$) and (M_n = 1 000 g mol^{-1}, 9 repeating units, $OEtOx_9MA$)). The most important aspect here is whether the hydrophilic stabilization of such star-shaped systems in water depends on the backbone length or the length of the side-chain regarding the brush-like shell. Whereas the OEGMA macromonomers were commercially available, the OEtOxMA macromonomers had to be prepared first *via* microwave-assisted cationic ring opening polymerization (CROP) of EtOx, where the reactive chain ends were end-capped with methacrylic acid (MA) according to a reported procedure.[35,36] The resulting macromonomers were characterized by ^{1}H-NMR spectroscopy to ensure a successful end capping. Furthermore, SEC investigations were performed to demonstrate the living cationic polymerization and to exclude autopolymerization reactions of the methacrylic acid (synthetic and characterization details for OEtOxMAs are provided in the SI). The macromonomers were further characterized by matrix-assisted laser desorption/ionization time of flight mass spectrometry (MALDI-TOF MS) and collision induced dissociation (CID) investigations.The detected peaks of the MS analysis were consistent with the presence of a methyl starting group and a methacrylate end group (in-depth characterization is provided in the SI).

The detailed characterization of the macromonomers ensured their suitability as monomer for the shell forming block in well-defined star-shaped drug delivery systems. First, kinetic investigations for the ATRP of the different methacrylate-based monomers were performed to precisely control the backbone length. We used previously determined reaction conditions with a [M]/[I]/[CuBr]/[PMDETA] ratio of 50/1/1.2/3 and a reaction temperature of 60 °C in anisole as solvent.[17] In Figure 2, the corresponding first-order kinetic plots as well as the experimental

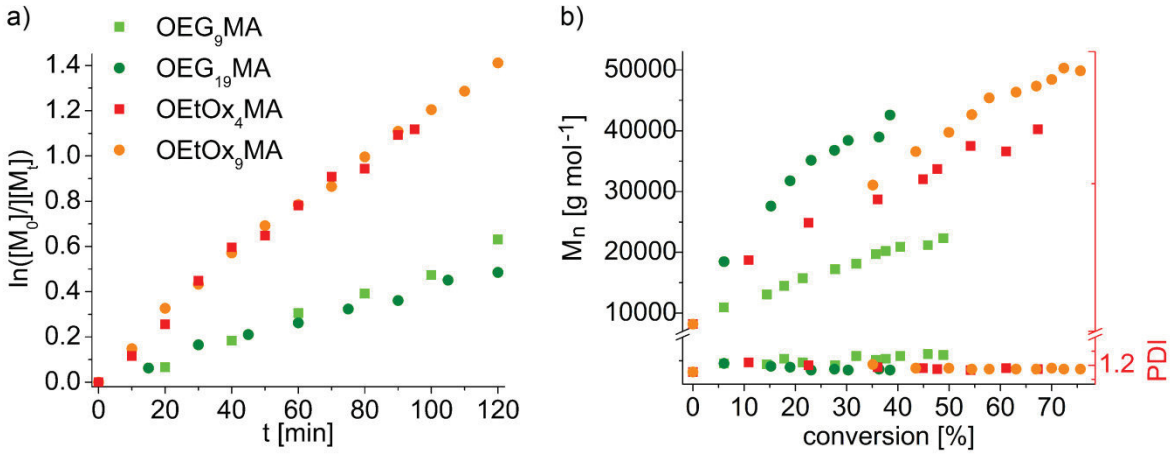

Figure 2. (a) Kinetic plots obtained for the different macromonomers OEG_9MA, $OEG_{19}MA$, $OEtOx_4MA$ and $OEtOx_9MA$ and (b) experimental number-averaged molar mass (M_n). Data for OEG_9MA are taken from a previous investigation.[17]

number average molar masses (M_n) and polydispersity index (PDI) values with increasing conversion are depicted. The kinetic plot shows that the side-chain length of the macromonomers did not influence the reaction rate significantly, whereas the nature of the monomer does. It is assumed that the OEG chains complex copper, thereby decreasing the polymerization rate. As the electron pairs of nitrogen for the OEtOx chains are partially delocalized due to the adjacent carbonyl group, they are less accessible and the reaction proceeds faster. According to the average molar mass values obtained by SEC (Figure 2b), $[PCL_{18}$-*b*-$POEtOx_4MA]_4$ shows an elevated demand of space in dimethylacetamide as solvent in comparison to $[PCL_{18}$-*b*-$POEG_9MA]_4$. The comparison of the star-shaped block copolymers with larger side chains shows a more pronounced effect of the side chain length of the OEGMA containing polymers. In contrast, the polymers with the $OEtOx_4MA$ or $OEtOx_9MA$ shell manifest only a minor difference of the resulting molar mass of the star-shaped block copolymer. This might be attributed to the increased number of repeating units of the OEGMA monomer in comparison to the OEtOxMA monomer.

Based on the kinetic investigations, well-defined star-shaped block copolymers were synthesized. For each of the three hydrophilic macromonomers similar methacrylate backbone lengths were prepared (Table 1). To remove any copper, the reaction solutions were diluted with

Table 1. Characteristics of the star-shaped $[PCL_{18}$-*b*-$POEG_{19}MA]_4$, $[PCL_{18}$-*b*-$POEtOx_4MA]_4$ and $[PCL_{18}$-*b*- $POEtOx_9MA]_4$ block copolymers.

Polymer	aimed DP	Conversion in SEC [%][a]	Obtained DP[b]	M_n [g mol^{-1}] calculated[b]	M_n [g mol^{-1}][c] SEC (DMAc)	PDI[c]
$[PCL_{18}$-*b*-$POEG_{19}MA_{14}]_4$	12	28	14	62 200	33 800	1.25
$[PCL_{18}$-*b*-$POEG_{19}MA_{28}]_4$	25	56	28	115 400	55 300	1.28
$[PCL_{18}$-*b*-$POEG_{19}MA_{45}]_4$	50	45	45	180 000	87 700	1.27
$[PCL_{18}$-*b*-$POEtOx_4MA_{15}]_4$	12	29	15	39 000	30 200	1.14
$[PCL_{18}$-*b*-$POEtOx_4MA_{27}]_4$	25	54	27	63 000	29 600	1.24
$[PCL_{18}$-*b*-$POEtOx_4MA_{44}]_4$	50	44	44	97 000	51 600	1.15
$[PCL_{18}$-*b*-$POEtOx_9MA_7]_4$	12	15	7	37 000	76 700	1.21
$[PCL_{18}$-*b*-$POEtOx_9MA_{25}]_4$	25	50	25	109 000	80 000	1.17
$[PCL_{18}$-*b*-$POEtOx_9MA_{51}]_4$	50	51	51	213 000	103 800	1.23

[a] Obtained from SEC ($CHCl_3$:*i*PrOH:NEt_3) using PEG calibration. [b] Calculated from the conversion. [c] Obtained from SEC (DMAc:LiCl) using PMMA calibration.

chloroform and filtered over aluminum oxide (Brockmann activity II-III) until the bluish color disappeared. The removal of the copper was verified by atomic absorption spectroscopy (AAS), where only two of the samples showed a copper content above the detection limit of 40 ppm (SI, Table S4). Subsequently, the monomer was removed by preparative SEC.

Solution behavior

The solution behavior of the star-shaped block copolymers was investigated in acetone, a non-selective solvent for both blocks (Figure 3a). The $[PCL_{18}\text{-b-}POEG_{19}MA]_4$ polymers showed diameters between 9 and 17 nm, whereas for the $[PCL_{18}\text{-b-}POEtOxMA]_4$ polymers diameters between 6 and 13 nm have been measured. For the three different types of block copolymers an increase in size with increasing shell can be observed. A comparison of the polymers with an $OEtOx_4MA$ shell and an $OEtOx_9MA$ shell, respectively, shows a rather small difference between the polymers with similar methacrylate backbone length and an OEtOx chain of twice the size. This observation reflects the results already obtained during kinetic studies in the DMAc-SEC. The length of the methacrylate backbone has more influence on the micellar size of $[PCL_{18}\text{-b-}POEtOx_4MA]_4$ and $[PCL_{18}\text{-b-}POEtOx_9MA]_4$ than the length of the OEtOx side chain itself. In contrast, the size of the unimers formed by $[PCL_{18}\text{-b-}POEG_{19}MA]_4$ is slightly elevated in comparison to $[PCL_{18}\text{-b-}POEtOx_9MA]_4$ although both systems should have comparable molar masses.

Angle dependent light scattering investigations of different star-shaped block copolymers in acetone showed a slight increase of the diffusion coefficient for $[PCL_{18}\text{-}b\text{-}POEGMA]_4$ at small angles. These observations suggest that rather an ellipsoidal than a spherical shape is adopted as reported previously (Figure S8a).[17] In contrast, for $[PCL_{18}\text{-}b\text{-}POEtOxMA]_4$ this was not the case, hinting towards a truly spherical shape of the unimolecular micelles with a POEtOxMA shell (Figure S8b).

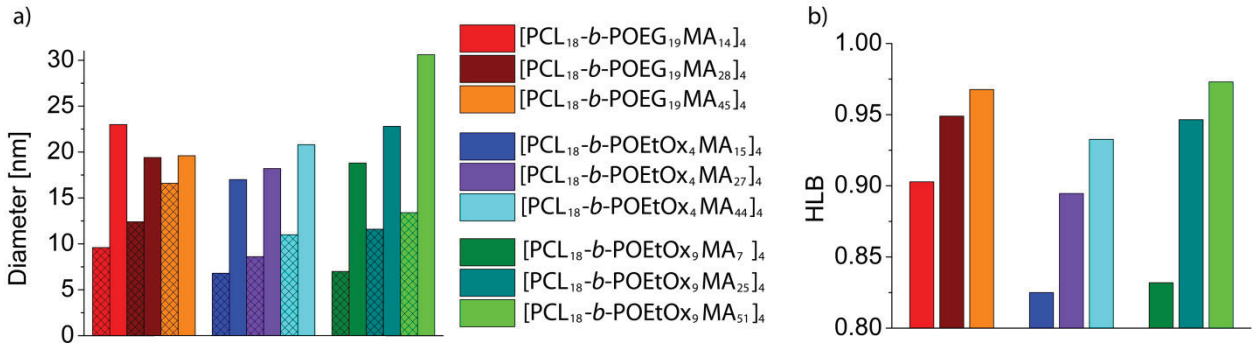

Figure 3. (a) Diameters obtained in DLS for the $[PCL_{18}\text{-}b\text{-}POEG_{19}MA]_4$, $[PCL_{18}\text{-}b\text{-}POEtOx_4MA]_4$ and $[PCL_{18}\text{-}b\text{-}POEtOx_9MA]_4$ polymers in acetone (checkered columns) and in water (empty columns). (b) Hydrophilic/lipophilic balance values calculated for the star-shaped block copolymers.

The hydrodynamic diameters in water were determined to be in the range of 20 nm for the $[PCL_{18}\text{-b-}POEG_{19}MA]_4$ polymers and in the range of 17 to 31 nm for the $[PCL_{18}\text{-b-}POEtOxMA]_4$ based materials, respectively. The diameters in water as a selective solvent for the brush-like shell increase for all investigated samples in comparison to the values obtained in acetone. This observation is hinting towards an agglomeration taking place between the unimers. This effect becomes less pronounced for $[PCL_{18}\text{-b-}POEG_{19}MA]_4$, where the shell occupied the largest volume and causes more steric hindrance. Also here, angle dependent light scattering measurements revealed rather spherical agglomerates (Figure S9).

As unimolecular micelles would be more advantageous for drug delivery purposes, the aggregation behavior was further investigated in detail by the determination of the critical micelle concentration (cmc). Unimolecular micelles would prevent the disassembly after infinite dilution of the system, *e.g.* in the blood stream after administration. We have shown recently that the classical approach for the determination of the cmc using pyrene failed for the system presented here.[17] Also during the course of this study, pyrene was shown to deliver non-interpretable results. As a proof, the inclusion capacity of the star-shaped block copolymers for

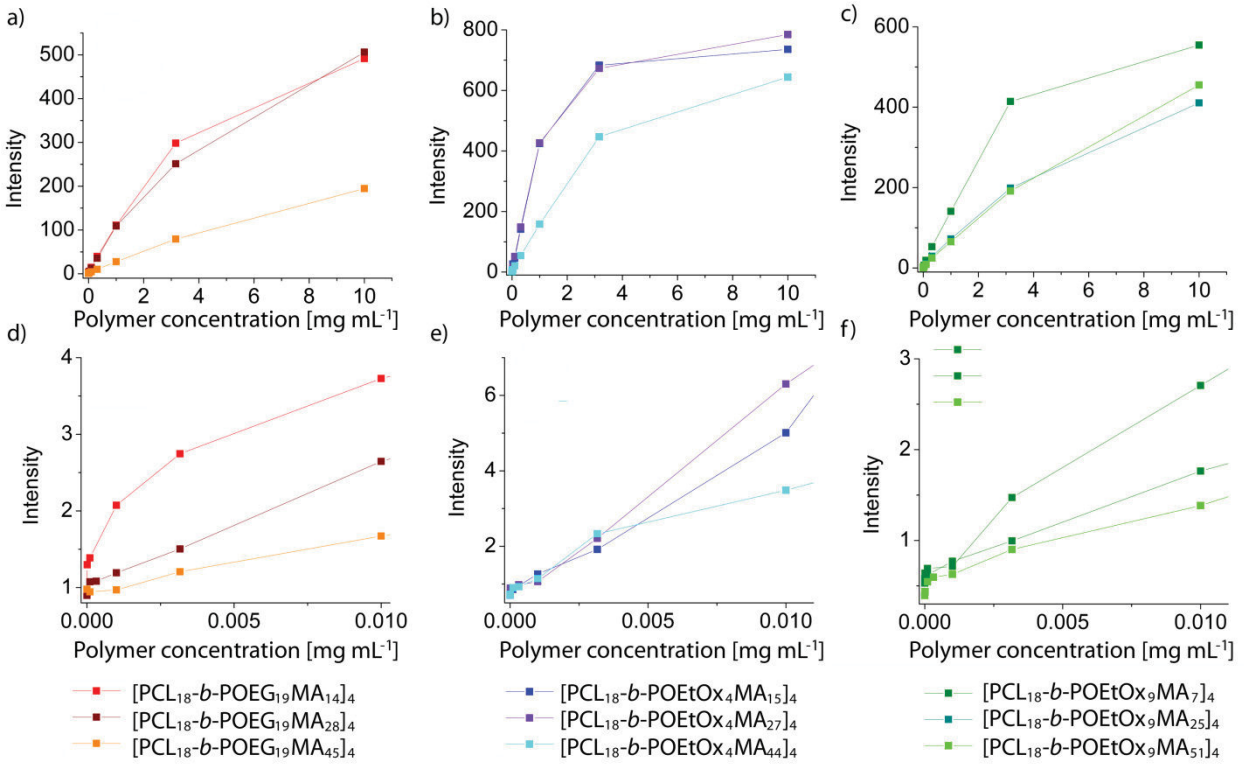

Figure 4. Fluorescence emission of nile red at 620 nm with increasing polymer concentration for (a) the $[PCL_{18}\text{-}b\text{-}POEG_{19}MA]_4$ polymer, (b) the $[PCL_{18}\text{-}b\text{-}POEtOx_4MA]_4$ polymer and (c) the $[PCL_{18}\text{-}b\text{-}POEtOx_9MA]_4$ polymer as well as an expanded view of the low polymer concentration range for (d) the $[PCL_{18}\text{-}b\text{-}POEG_{19}MA]_4$ polymer, (e) the $[PCL_{18}\text{-}b\text{-}POEtOx_4MA]_4$ polymer and (f) the $[PCL_{18}\text{-}b\text{-}POEtOx_9MA]_4$ polymer.

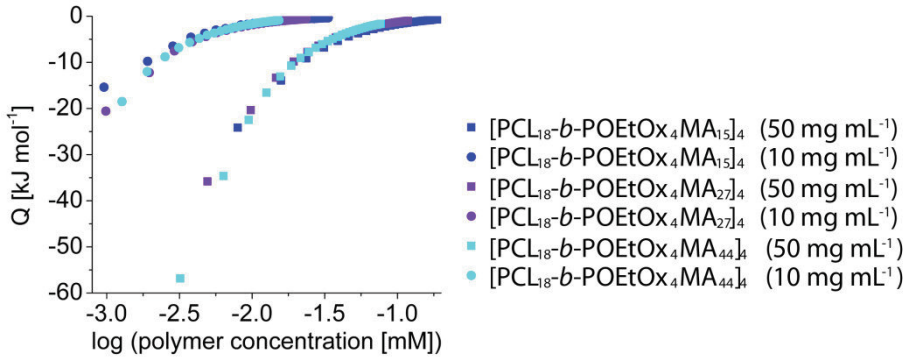

Figure 5. Enthalpograms obtained for the titration of the $[PCL_{18}\text{-b-}POEtOx_4MA]_4$ polymers with a starting concentration of 10 and 50 mg mL^{-1}.

pyrene was measured and was shown to coincide with the change of the vibrational fine structure of the fluorescence emission spectrum of pyrene (Figure S10 and S11). For this reason, nile red was used, which has an extremely low solubility in water and will preferentially be solubilized within the hydrophobic PCL core. Indeed, Figure 4 shows that with increasing block copolymer concentration the nile red fluorescence emission increases as well. This indicates the absence of a cmc in water, even for $[PCL_{18}\text{-b-}POEtOx_4MA_{15}]_4$, the material with the shortest outer block. These conclusions were further confirmed by isothermal titration calorimetry (ITC) and the results obtained for different $[PCL_{18}\text{-b-}POEtOx_4MA]_4$ star block copolymers are shown in Figure 5. In all cases, exothermic reactions after each injection of polymer solutions with concentrations of 50 mg mL^{-1} into water can be observed. No sigmoidal shape of the curve, as expected for surfactants, was found. Comparable results were obtained for lower concentrations (10 mg mL^{-1}) of the materials. For each polymer at two different concentrations, declining trajectories are observed that would result in two different demicellization enthalpies and cmcs. The exothermic effect was, therefore, attributed to a dilution rather than a disaggregation of aggregates. Nevertheless, the interpretation of the thermodynamic data might be hampered by slow demicellization or the occurrence of multi-step processes. However, from the combined results obtained, the absence of a cmc for all nine star block copolymers can be concluded, whereas the DLS results hint towards the formation of aggregates in water, presumably due to entanglement of the hydrophilic shells.

The results obtained within this study confirm the formation of unimers even for $[PCL_{18}\text{-}b\text{-}POEtOx_4MA]_4$ polymers with a rather short shell segment. However, the hydrophilic/lipophilic balance (HLB) for these systems, according to Uhrich *et al.*,[37] corresponds to the value observed previously for $[PCL_{18}\text{-}b\text{-}POEG_9MA]_4$ polymers (Figure 3b).[17] These results confirm the principal applicability of the HLB to different polymer classes on the one hand and support that a HLB value of 0.8 is sufficient to stabilized unimers of star-shaped block copolymers with a brush-like shell in aqueous solution on the other hand.[17] Furthermore, it can be concluded that rather the molar mass of the brush-like shell forming macromonomer plays a key role in the formation of unimolecular micelles than the mere length of the corona-forming block.

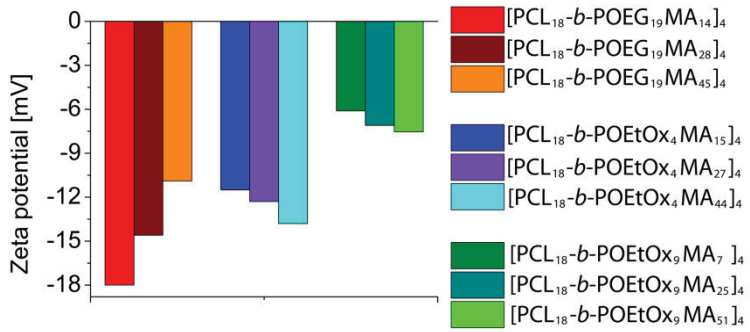

Figure 6. Zeta potentials of the $[PCL_{18}$-b-$POEG_{19}MA]_4$, $[PCL_{18}$-b-$POEtOx_4MA]_4$ and $[PCL_{18}$-b-$POEtOx_9MA]_4$ polymers.

In addition, the zeta potentials were analyzed for all systems presented. For the stars containing $OEG_{19}MA$, negative values between −18 mV and −11mV were detected (Figure 6). For the $[PCL_{18}$-b-$POEtOx_4MA]_4$ polymers zeta potential values around −12 mV and the $[PCL_{18}$-b-$POEtOx_9MA]_4$ polymers values around −7 mV have been measured.

In contrast, for the $OEtOx_4MA$ and the $OEtOx_9MA$ containing block copolymers, respectively, constant zeta potentials were detected. Although the shell size for star-shaped block copolymers with $OEtOx_4MA$ should be smaller if compared to $OEG_{19}MA$, containing polymers, the observed zeta potential is comparable to the $[PCL_{18}$-b-$POEG_{19}MA]_4$ series. For $[PCL_{18}$-b-$POEtOx_9MA]_4$, even lower values were observed. This might be attributed to contributions provided by the nitrogen containing OEtOxMA segments, leading to a shift closer to neutral. For the $OEG_{19}MA$ based polymers the zeta potential is decreasing with increasing shell size and for the $POEtOx_4MA$ and $POEtOx_9MA$ based polymers, respectively, the values are decreasing with increasing arm-length of the brush-like shell. Therefore, the formation of supermicelles, caused by the entanglement of the shells, might be explained by the decreasing zeta potential provoking a diminished electrostatic repulsion.

***In vitro* biocompatibility**

The evaluation of the biocompatibility is one of the first steps to prove the applicability of the herein presented star-shaped systems for biomedical purposes. As blood is the first contact partner with the human body during intravenous administration, all nine materials were tested according to general blood compatibility. Erythrocytes represent the majority of blood cells and are, as carrier of oxygen, the most important blood component. Hence, adverse side reactions with red blood cells were evaluated in terms of erythrocyte aggregation and hemolysis upon polymer incubation.

To assess the influence of the polymeric material on the red blood cells, the hemolytic activity was measured photometrically by means of the hemoglobin release after potential damage of the erythrocytes. The nine polymers were investigated at different concentrations (5, 25 and 50 mg mL^{-1}) showing hemoglobin releases below 2%, proving that in all cases erythrocyte membrane damaging properties are absent (Figure 7b and S12) according to the ASTM F756-00

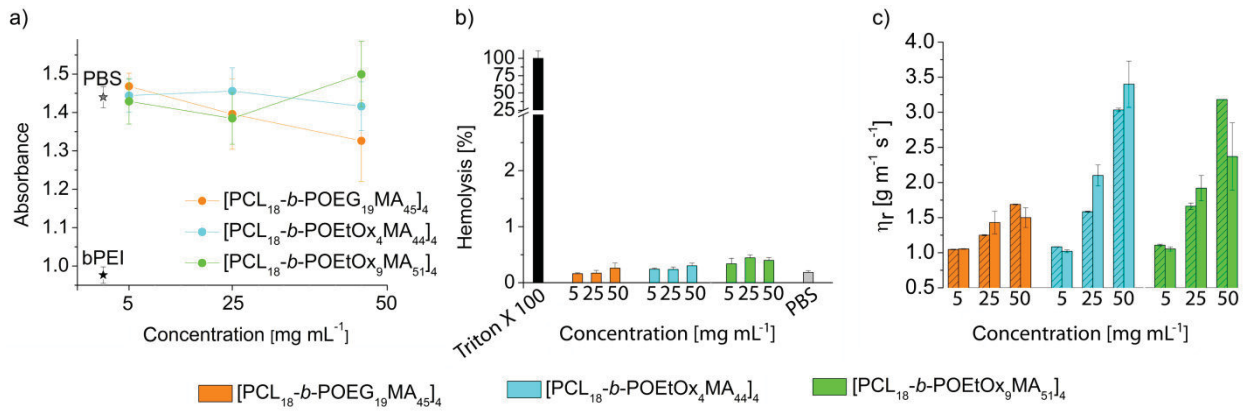

Figure 7. Blood compatibility of $[PCL_{18}$-*b*-$POEG_{19}MA_{45}]_4$, $[PCL_{18}$-*b*-$POEtOx_4MA_{44}]_4$ and $[PCL_{18}$-*b*-$POEtOx_9MA_{51}]_4$. (a) Relative viscosity of the polymer solutions in water (striped bar) and in whole blood (empty bars). Data are presented as the mean percentage ± SD. (b) Photometric determination of hemolytic activity after incubation with different polymer concentrations for 1 h at 37 °C. Triton X-100 (1%) served as positive and PBS as negative control. Data are presented as the mean percentage ± SD of hemolytic activity compared to the positive control set as 100%. (c) Photometric determination of the erythrocyte aggregation after 2 h incubation at 37 °C with polymers. 25 kg mol^{-1} bPEI (50 µg mL^{-1}) served as positive and PBS as negative control. Data are presented as the mean measured absorbance ± SD.

standard. The erythrocyte aggregation represents a further key investigation to prove the blood compatibility as the formation of aggregates could lead to impeded blood flow. This was analyzed by absorption measurements for different concentrations of the block copolymers (5, 25 and 50 mg mL^{-1}) in comparison to phosphate buffered saline (PBS) as negative and branched poly(ethylene imine) (bPEI) as positive controls. The results are depicted in Figure 7c (and Figure S13), where no cluster formation was observed. Within these results no adverse side reactions with red blood cells were observed.

$[PCL_{18}$-b-$POEG_{19}MA_{45}]_4$, $[PCL_{18}$-b-$POEtOx_4MA_{44}]_4$ and $[PCL_{18}$-b-$POEtOx_9MA_{51}]_4$ were submitted to a detailed blood compatibility analysis as these polymers possess the highest ratio of hydrophilic comb polymer and will be later used for encapsulation studies. This included the analysis of possible impacts on platelet activation, complement factor activation and coagulation pathways as well as undesired alterations of the blood viscosity.

The appropriate blood viscosity is essential for the function of blood and alterations will have a severe impact on the cardiovascular system and heart function. The whole blood viscosity is basically influenced by the plasma viscosity, the hematocrit (number of erythrocytes per volume) as well as the geometry/deformability and potential aggregation of erythrocytes induced by interaction with the polymers. Furthermore, a strong mutual reaction with other whole blood components might influence the viscosity. The whole blood viscosity was measured after the addition of $[PCL_{18}$-*b*-$POEG_{19}MA_{45}]_4$, $[PCL_{18}$-*b*-$POEtOx_4MA_{44}]_4$ and $[PCL_{18}$-*b*-$POEtOx_9MA_{51}]_4$ in different concentrations (5, 25 and 50 mg mL^{-1}). To distinguish between a change in viscosity

caused by the intrinsic viscosity of the polymer and a polymer mediated interaction or aggregation of blood components the viscosities of the blood/polymer solutions as well as the corresponding solutions containing only polymer at equivalent concentrations were compared. It turned out, that the increased blood viscosity can be fully attributed to the intrinsic viscosity of the polymer added (Figure 7a). Therefore, no substantial interactions of the polymers with blood components leading to an increase or decrease of the blood viscosity can be observed. The increased values obtained by the addition of highly concentrated polymer solutions are in the physiological tolerable range as a four-fold increase of the whole blood viscosity leads to no adverse effects.[38,39]

Further blood compatibility tests regarding coagulation effects were performed for the [PCL_{18}-*b*-$POEG_{19}MA_{45}$]$_4$, [PCL_{18}-*b*-$POEtOx_4MA_{44}$]$_4$ and [PCL_{18}-*b*-$POEtOx_9MA_{51}$]$_4$ polymers. In general, sulfated naturally occurring polysaccharides and synthetic polymers are known to possess anticoagulant activity.[40,41] However, to exclude an effect of the star-shaped copolymers on the coagulation cascade, the prothrombin time (PT) and the activated partial thromboplastin time (APTT) of polymer exposed citrated plasma were measured in a clinical assay. Both tests are used to indicate an altered coagulation ability of the blood, leading to a risk of uncontrolled bleeding. An elevated APTT is of minor clinical relevance but might indicate an increased risk of thromboembolism.[42] During the secondary hemostasis reaction, so called coagulation factors mediate the strengthening of the platelet plug formed in the primary hemostasis reaction. Coagulation factors are inactive serine proteases or transglutaminases and glycoprotein co-factors which induce a cascade-like cleavage of downstream proteins. In the intrinsic or contact activation pathway this cascade is triggered *in vivo* by the contact of coagulation factors to the collagen exposed in the damaged vessel. The extrinsic or tissue factor pathway is mainly activated by a soluble tissue factor released from damaged tissue. Both pathways end up in the final common pathway characterized by a thrombin based conversion of fibrinogen to the glue like fibrin which supports the formation of a clot.

Since the intrinsic and extrinsic pathway are strongly depending on the presence of calcium ions and in clinical blood samples calcium ions are quenched by complexation with citrate, one can start the coagulation cascade *in vitro* using external calcium ions and for each pathway another specific activator. The APTT indicates the full functioning of the intrinsic coagulation pathway (mediated by the factors V, VIII, IX, X, XI and XIII, respectively) and the performance of the common coagulation pathway. It is specifically activated by the addition of negatively charged silica particles or phospholipids and the value obtained represents the required time (in seconds) to form a fibrin clot in the plasma. For the three polymers APTTs between 23 s and 25 s were measured at different concentrations (5, 25 and 50 mg mL^{-1}) and incubation times (5 min and 30 min) (Figure 8b). Although some of the values show a statistically significant difference to the saline control all observed values are within the clinical normal range of 23 s to 33 s ($p < 0.05$).

On the other hand, the PT assay is specifically activated by the addition with the tissue factor thromboplastin and assesses the activity of the extrinsic coagulation pathway (mediated by the

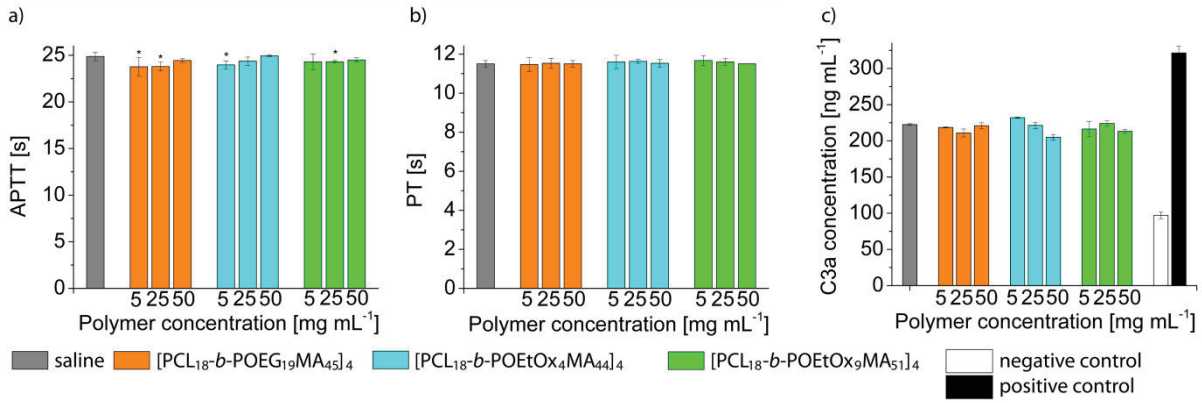

Figure 8. Blood compatibility of $[PCL_{18}$-*b*-$POEG_{19}MA_{45}]_4$, $[PCL_{18}$-*b*-$POEtOx_4MA_{44}]_4$ and $[PCL_{18}$-*b*-$POEtOx_9MA_{51}]_4$. Effects of the polymers on the coagulation detected by (a) the prothrombin time (PT) and (b) the activated partial thromboplastin time (APTT) after 30 min incubation. Data are presented as the mean measured absorbance ± confidence interval. (c) Complement activation by the polymers measured by determination of C3a levels after 60 min incubation. Data are presented as the mean measured absorbance ± SD.

factors VII, X, II and XIII, respectively) and the common coagulation pathway. As the APTT, it measures the time that passes until a fibrin clot is formed in the blood plasma. The three polymers were incubated for two different time periods (5 min and 30 min) with the plasma at three different concentrations (5, 25 and 50 mg mL^{-1}). For both incubation times, PT values in the range of the saline control between 11 s and 12 s were obtained, which are in the clinically normal range of 10 s to 14 s (Figure 8a and S14). From these results an interaction of the star-shaped block copolymers with the components responsible for blood coagulation can be excluded.

Platelet activation represents a very early event in the complex process of blood coagulation in primary hemostasis when damage to the blood vessel occurs. After activation at sites of vessel damage, the platelets aggregate and form a plug by using fibrin. A destabilization of this sensitive system by introduction of a polymeric material can have severe effects leading to a malfunction of platelets provoking excessive bleeding. In the case of a too high platelet activity a spontaneous blood clot formation can be provoked resulting in unwanted pathologies like stroke, myocardial infarcts or pulmonary embolisms.

Besides the platelet specific constitutional expression of CD42 glycoprotein, activated platelets induce the expression of the surface antigen P-Selectin (CD62p), a 140 kDa membrane glycoprotein. This marker was used to identify the status of activation in human platelets upon incubation with the polymers $[PCL_{18}$-*b*-$POEG_{19}MA_{45}]_4$, $[PCL_{18}$-*b*-$POEtOx_4MA_{44}]_4$ and $[PCL_{18}$-*b*-$POEtOx_9MA_{51}]_4$. The measurement of CD42 and CD62p expression in platelet samples treated with the three polymers at different concentrations (5, 25 and 50 mg mL^{-1}) and incubation times (10 and 30 min) revealed, that an effect of the polymers on the CD62p expression was negligible. Since the percentage of the activated platelet phenotype with CD42 and CD62p positive cells remain on the level of the PBS control with less than 1%. Therefore, no platelet activation

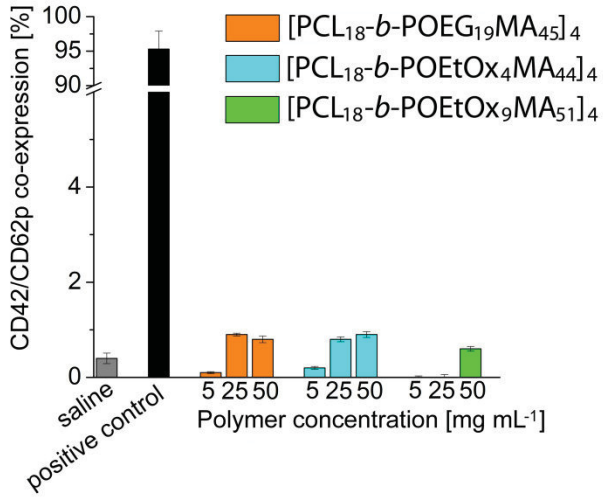

Figure 9. Fluorescence activated cell sorting (FACS) analysis of polymer mediated platelet activation measured by determination of CD62p/CD42 co-expression after 30 min incubation. Data are presented as percentage of platelets positive for both CD62p and CD42 epitopes.

provoked by the tested polymers can be attested. In contrast, platelets exposed to thrombin in the positive control displayed a drastic up-regulation of the CD62 expression already within 10 min up to 95% of all CD42 positive cells. This value was not further increased by a longer incubation time of 30 min (Figure 9 and Figure S15).

A severe issue of polymer interaction with the human body covers the activation of the immunomodulatory complement system upon recognition of the polymer as a foreign body. Whereas the classical pathway of the complement system displays the interaction of complements factors with antibody-antigen-complexes and the lectin pathway is specialized on the recognition of bacterial carbohydrates, the alternative pathway of the complement system is activated by unspecific binding of complements to foreign surfaces and materials. All three pathways share the generation of an enzyme called C3-convertase which cleaves and activates complement component C3 creating C3b and C3a. As a consequence, an inflammatory response in terms of an attraction of macrophages and phagocytosis of opsonized elements is triggered and leads to the recognition and clearance of host components from the body.[43]

The anaphylatoxin C3a is used within a commercial immunoassay kit to detect the activation of the complement system upon interaction with the star-shaped block copolymers. The C3a concentrations were measured in comparison to a saline control and a C3a standard (Figure 8c and S16). For different concentrations of $[PCL_{18}$-*b*-$POEG_{19}MA_{45}]_4$, $[PCL_{18}$-*b*-$POEtOx_4MA_{44}]_4$ and $[PCL_{18}$-*b*-$POEtOx_9MA_{51}]_4$ (5, 25 and 50 mg mL^{-1}) after incubation for 10 min, 30 min and 60 min C3a levels were measured. Since the C3a levels were in the range of the saline control, these results prove that no activation of the complement system is provoked by administration of the star-shaped block copolymers. Similar results were found by Luxenhofer *et al*. whoreported that for PEtOx and poly(2-methyl-2-oxazoline) (PMeOx) containing di- and triblock copolymers

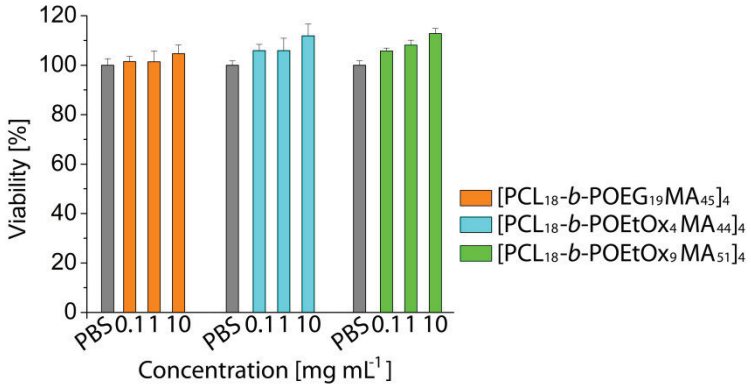

Figure 10. Cell viability of L929 mouse fibroblasts after incubation with star-shaped polymers up to 10 mg mL^{-1} for 24 hours. Cells incubated with polymer free culture medium served as control. The cell viability was determined by XTT assay according to ISO 10993-5. Data are expressed as mean ± SD of six determinations.

only a slight increase of the C3a-desArg concentration occurs in comparison to the PBS control (2-fold).[32]

The *in vitro* cytotoxicity was evaluated on the basis of a XTT assay using mouse fibroblast L929 cells (Figure 10 and S17). None of the star-shaped block copolymers revealed any cytotoxic effect after 24 h incubation at different concentrations (0.1, 1 and 10 mg mL^{-1}). These results confirm the low cytotoxicities generally observed for both PEG as well as PEtOx–based materials. For PEG in general, a very high biocompatibility is attested[44] with exception of oligomers with molar masses below 400 g mol^{-1} that show toxic effects due to oxidation processes.[45,46] PEtOx polymers with different molar masses and PEtOx containing block copolymers were also evaluated in several studies showing no cytotoxic or hemolytic effects.[24,26,27,47,48] An in-detail study with different molar masses of PEtOx revealed that 400 g mol^{-1} PEtOx possesses cytotoxic effects above a concentration of 1 mg mL^{-1}.[25] Such concentrations for OEtOx were also reached by the star-shaped block copolymers at the tested concentration of 10 mg mL^{-1}, because the content of OEtOx within $[PCL_{18}$-*b*-$POEtOx_4MA]_4$ materials ranges from 62 to 73%. The non-cytotoxicity observed in these tests might be attributed to the linkage of the OEtOx to the methacrylate backbone. Due to the fact that the ester bond is slowly cleaved and full degradation can be expected only after 8 days, as shown for the enzymatical degradation of $[PCL$-*b*-$POEGMA]_6$ with a non-human lipase from *Rhizopus arrhizus*,[16] the release of oligomers is retarded. However, for a very safe and reliable non-toxic usage of the star-shaped block copolymers the application of those polymers containing hydrophilic monomers with higher molar masses is recommended. The molar masses of $OEtOx_9$ and $OPEG_{19}$ are well above 400 g mol^{-1} to prevent cytotoxic effects and still small enough to ensure a complete excretion of the polymer after delivery of the drug.

Doxorubicin encapsulation, *in vitro* cytotoxicity assessment and cellular uptake

Doxorubicin is known as a potent anti-cancer drug for a variety of different cancer types. It is regarded to be the drug with the highest single-agent activity and frequently used against breast cancer, amongst other different cancer types.[49,50] The high cardiotoxicity, one of the severe side effects of this drug, accounts together with the red color of the compound for the nickname "red devil".[51] To decrease the toxicity and to improve the patient's overall survival and life quality an increase of the penetration into the neoplastic tissue is regarded as essential. DDS gained importance to implement this task and Caelyx (brand name in the EU, Doxil, respectively, in the US) a liposomal formulation of doxorubicin even reached the commercial market.[52] Different micellar DDS of linear block copolymers have also been investigated to encapsulate this anti-cancer drug.[53–56]

To evaluate the applicability of the star-shaped block copolymers as drug delivery system the specific encapsulation efficiency for doxorubicin was determined for $[PCL_{18}$-*b*-$POEG_{19}MA_{45}]_4$, $[PCL_{18}$-*b*-$POEtOx_4MA_{44}]_4$ and $[PCL_{18}$-*b*-$POEtOx_9MA_{51}]_4$. An uptake of only two molecules doxorubicin per star-shaped block copolymer was found. This low loading capacity might be explained by the size of the doxorubicin molecule and its different hydrophobicity in comparison to a previous study with the orange dye fat brown RR (Figure S18, fat brown RR: $M_n = 262.31$ g mol^{-1}, doxorubicin $M_n = 543{,}52$ g mol^{-1}). The diameters of the obtained loaded micelles are in the range of 10 nm and the zeta potentials between –10 mV and –20 mV as measured before for the unloaded micelles (Figure S19).

The cellular uptake of free doxorubicin as well as of the liposomal and micellar formulation was proven by fluorescence and confocal laser scanning microscopy (Figure 11). An accumulation of the drug within the cytoplasm, independent from the formulation, was observed in L929 mouse fibroblasts as well as in MCF-7 breast cancer cells. However, a nuclear localization of doxorubicin in a less concentrated range might be assumed from the images.

Therefore, the doxorubicin loaded micelles were used in a XTT cytotoxicity assay to evaluate the efficiency of the encapsulated doxorubicin in comparison to free doxorubicin and the commercial liposomal formulation Caelyx. In this study the immortalized mouse fibroblast cell line L929 and the human embryonic kidney (HEK) 293 cell line were used in comparison to the human breast carcinoma cell lines MCF7 and MDA-MB 231.

After 24 h incubation, slight cytotoxic effects of the free doxorubicin and Caelyx were observed in all cell lines except the HEK 293 cells with IC_{50} values in the range 20 000 ng mL^{-1} for Caelyx and 45 000 ng mL^{-1} for free doxorubicin (Table 2). With the micellar formulations, viabilities below 50% were only assessed for the $[PCL_{18}$-*b*-$POEtOx_4MA_{44}]_4$ polymer in the range of 100 000 ng mL^{-1} for the L929 and the MCF-7 cell lines. For the MDA-MB 231 cells an IC_{50} value of 180 000 ng mL^{-1} was determined.

Viabilities below 20% were only assessed after 72 h of incubation. A decrease of the IC_{50} value of free doxorubicin from 45 000 ng mL^{-1} by two to four orders of magnitude after 72 h of incubation was observed for all cell lines. For Caelyx, an IC_{50} value in the range of 600 ng mL^{-1} has been found after 72 h of incubation, whereas the IC_{50} values for the micellar solutions were

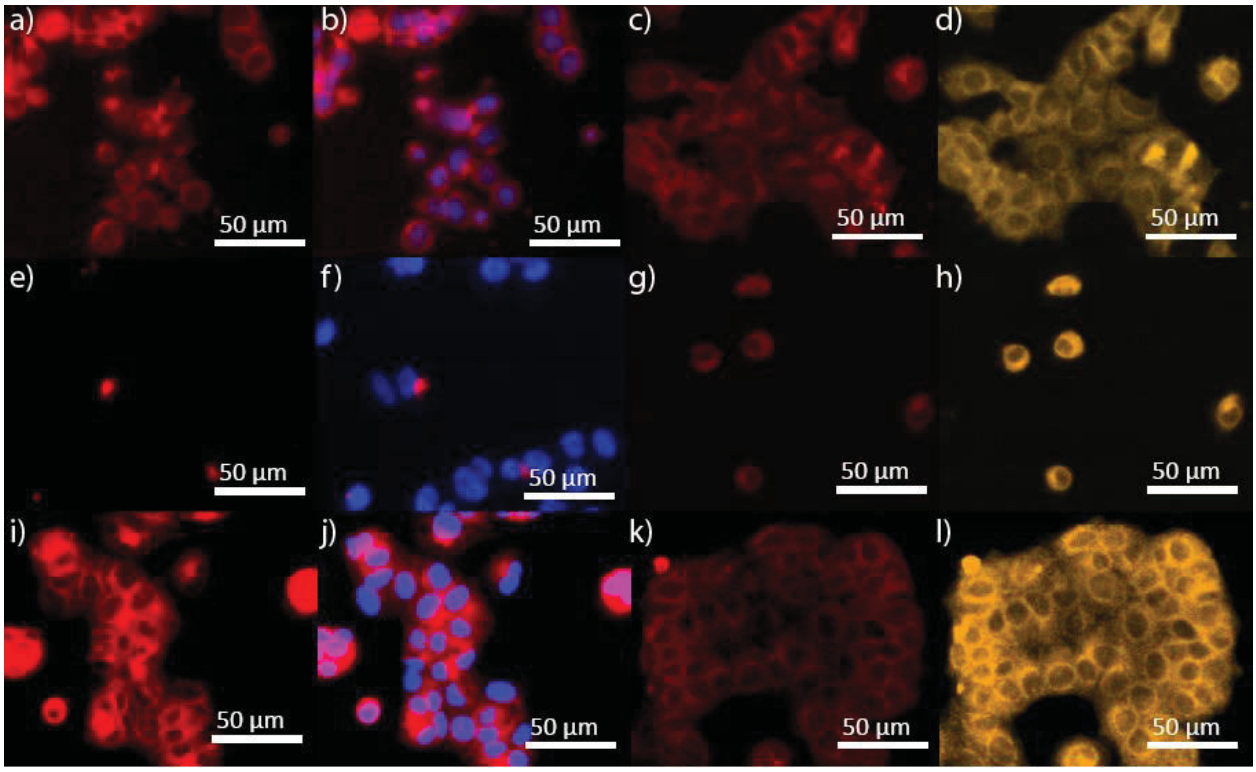

Figure 11. Fluorescence microscopy images (a), b), e), f), i), j)) and confocal laser scanning microscopy images (c), d), g), h), k), l)) of MCF-7 cells treated for 24 h with free doxorubicin (a), b), c), d)), Caelyx (e), f), g), h)) and doxorubicin encapsulated by the [PCL_{18}-*b*-$POEtOx_9MA_{51}]_4$ polymer (i), j), k), l)). a), c), e), g), i, and k) showing the doxorubicin fluorescence emission. b), f) and j) visualizing the cell nuclei stained with Hoechst 33342. d), h) and l) showing the cytoplasm stained with CellTracker Orange CMRA.

determined to be in the range between 30 000 ng mL^{-1} and 100 000 ng mL^{-1}. After further 72 h (in total 6 d) of cell growth without doxorubicin incubation, the viability was again determined. For doxorubicin, the IC_{50} values found after six days were in the range of the values obtained after 72 h. For Caelyx, a significant decrease of the IC_{50} value from 72 h to six day incubation was only detected for the MDA-MB 321 cell line. The L929, HEK 293 and MCF-7 cell lines revealed IC_{50} values in the same order of magnitude as after 72 h. The cancer cell lines MCF-7 and MDA-MB 231 showed after 3 days of incubation and additional 3 days of growth with the micellar solutions an additional decrease of the IC_{50} value from around 100 000 ng mL^{-1} to around 30 000 ng mL^{-1} and the MDA-MB 231 cell line even a decrease down to 7 000 ng mL^{-1} (Figure S20).

The elevated IC_{50} values observed for the formulated doxorubicin, within liposomes or micelles, can be explained either by a delayed doxorubicin release as well as nuclear delivery or an incomplete release from the carrier.[55] The significantly improved IC_{50} values obtained for the three different formulations after a prolonged incubation time might encourage this assumption. Both, the star-shaped block copolymers as well as the commercial liposomal

Table 2. IC_{50} values obtained for doxorubicin, Caelyx and micellar formulated doxorubicin in $[PCL_{18}$-*b*-$POEG_{19}MA_{45}]_4$, $[PCL_{18}$-*b*-$POEtOx_4MA_{44}]_4$ and $[PCL_{18}$-*b*-$POEtOx_9MA_{51}]_4$ star-shaped block copolymers for the L929 mouse fibroblast cell line, the HEK 293 cell line as well as the human breast carcinoma cell lines MCF-7 and MDA-MB 231.

Cell line	24 h				
	Doxorubicin	Caelyx	$[PCL_{18}$-*b*-$POEG_{19}MA_{45}]_4$	$[PCL_{18}$-*b*-$POEtOx_4MA_{44}]_4$	$[PCL_{18}$-*b*-$POEtOx_9MA_{51}]_4$
L929	42 000	20 000	-	80 000	-
HEK 293	-	-	-	-	-
MCF-7	40 000	19 000	-	110 000	-
MDA-MB 231	48 000	20 000	-	180 000	-
	72 h				
L929	100	600	50 000	29 000	29 000
HEK 293	0.1	200	10 800	47 000	47 000
MCF-7	4.2	800	100 000	48 000	-
MDA-MB 231	120	800	100 000	40 000	100 000
	72 h + 72 h				
L929	50	4 000	30 000	30 000	45 000
HEK 293	0.082	38	25 000	21 000	8 900
MCF-7	3	180	39 000	32 000	7 000
MDA-MB 231	3.2	2.8	40 000	32 000	7 000

formulation Caelyx revealed an increased IC_{50} value in comparison to the free drug. Furthermore, the three star-shaped drug delivery systems revealed rather similar cytotoxicity behavior leading to the supposition that they internalize and release the drug according to comparable mechanisms though they possess different shell natures.

The *in vitro* results show a decreased cytotoxicity of the formulated doxorubicin in comparison to the free drug. However, *in vivo* premises differ often drastically from *in vitro* conditions and the obtained results account only as first evidence of the carrier efficacy. As free doxorubicin is characterized by a relatively high hydrophobicity and a low molar mass, a relatively fast

excretion from the body can be assumed. Therefore, the increased cytotoxicity after prolonged incubation might not be exploited by the free drug as it is at this point already excreted from the body, leading to an increased dosage of doxorubicin and more serious side effects for the patient. In contrast, for both the liposomal and the micellar formulation, a prolonged blood circulation time and an increased entrapment in the neoplastic tissue might be assumed. These effects could account for a more cytotoxic environment within the cancer tissue created by the drug formulations, which in turn could decrease the overall drug dosage.

Conclusion

Amphiphilic star-shaped $[PCL_{18}$-*b*-POEGMA$]_4$ and $[PCL_{18}$-*b*-POEtOxMA$]_4$ block copolymers with varying shell size in terms of molar mass of macromonomer and length of methacrylate backbone were prepared. The resulting unimolecular micelles were characterized in a non-selective solvent, showing increasing diameters with increasing shell size in the range of 5 to 15 nm. For the unimers with the OEGMA shell, a spheroidal shape was proposed by angle dependent light scattering experiments, whereas the OEtOxMA containing unimolecular micelles adopt a rather spherical shape. The diameters in water were shown to be in the range of 20 nm, leading to the assumption that aggregates are formed to a certain extent. These aggregates were shown to have a spherical shape for both shell types, OEGMA and OEtOxMA, respectively.

Both spectroscopical investigations using nile red as fluorescent probe and ITC experiments did not reveal any cmc for the systems investigated. Therefore, the steric stabilization was correlated rather to the molar mass of the comb arm forming macromonomer than to its repeating units. As the HLB calculation is based on the molar mass of the hydrophilic and the lipophilic block, it can be supposed that these calculations are true for different polymer classes and not only for PEG. It was confirmed that a HLB value of 0.8 is sufficient to achieve a stabilization of the hydrophobic core in aqueous environment for this star-shaped architecture with a brush-like shell.

In vitro experiments revealed for the POEGMA and the POEtOxMA containing polymers no adverse reaction with human blood in terms of whole blood viscosity, erythrocyte aggregation and hemolysis. No interference with the coagulation pathways or immune activation *via* the complement system was detected. A cytotoxicity assay against L929 mouse fibroblasts showed no short-term cytotoxicity after 24 h incubation with the polymer. These results prove that amphiphilic polymers covered by a POEtOxMA shell can be regarded as alternative shell material in comparison to POEGMA.

The clinically relevant anti-cancer drug doxorubicin was encapsulated into the unimolecular micelles, and their cytostatic effects were evaluated in a comparative study with the L929 and HEK 293 immortalized cell line and the cancer cell lines MCF-7 and MDA-MB 231. For both, the star-shaped block copolymer formulated doxorubicin and Caelyx an enhanced IC_{50} value in comparison to free doxorubicin was determined. As all three micellar formulation showed similar IC_{50} values, corresponding cellular uptake and release mechanisms can be assumed for both the shell types, the POEGMA and the POEtOxMA shell.

Future research will focus on the improvement of the encapsulation efficiency to decrease the dose of polymer given during an administration. Although the star-shaped systems have been shown *in vitro* to possess no adverse side effects and the biodegradation products of the polymer are in a low molar mass range, the polymer dosage should be kept as low as possible. To the best of our knowledge, this study on star-shaped drug delivery systems proves for the first time that a unimolecular drug carrier with an alternative shell chemistry to PEG is possible.

Supporting Information. Includes synthetic details, mass spectrometric in-detail characterization of macromonomers, fluorescence investigations and procedures of the biological experiments. This material is available free of charge *via* the Internet at http://pubs.acs.org.

ACKNOWLEDGMENT

Sandra Köhn and Igor Perevyazko are gratefully acknowledged for AAS and viscosity measurements, respectively. We thank Carolin Fritzsche and Alexander Meier for assistance with the experiments. Cora Richert and the laboratory team of the Institute for Clinical Chemistry and Laboratory Diagnostics are acknowledged for their kind help with the clinical assays. Dr. Ronny Rüger is very gratefully acknowledged for helpful discussions about doxorubicin and kindly providing Caelyx.

REFERENCES

(1) Wang, Y.; Grayson, S. M. *Adv. Drug Deliver. Rev.* **2012**, *64*, 852–865.

(2) Qiu, L. Y.; Bae, Y. H. *Pharm. Res.* **2006**, *23*, 1–30.

(3) Yang, X.; Grailer, J. J.; Pilla, S.; Steeber, D. A.; Gong, S. *Bioconjugate Chem.* **2010**, *21*, 496–504.

(4) Nabid, M. R.; Tabatabaei Rezaei, S. J.; Sedghi, R.; Niknejad, H.; Entezami, A. A.; Oskooie, H. A.; Heravi, M. M. *Polymer* **2011**, *52*, 2799–2809.

(5) Kwon, G. S.; Kataoka, K. *Adv. Drug Delivery Rev.* **1995**, *16*, 295–309.

(6) Letchford, K.; Burt, H. *Eur. J. Pharm. Biopharm.* **2007**, *65*, 259–269.

(7) Newkome, G. R.; Moorefield, C. N.; Baker, G. R.; Johnson, A. L.; Behera, R. K. *Angew. Chem. Int. Ed.* **1991**, *30*, 1176–1178.

(8) Liu, H.; Chen, Y.; Zhu, D.; Shen, Z.; Stiriba, S.-E. *React. Funct. Polym.* **2007**, *67*, 383–395.

(9) Kojima, C.; Kono, K.; Maruyama, K.; Takagishi, T. *Bioconjugate Chem.* **2000**, *11*, 910–917.

(10) Cheng, L.; Cao, D. *Langmuir* **2009**, *25*, 2749–2756.

(11) Yun, J.; Faust, R.; Szilagyi, S. L.; Keki, S.; Zsuga, M. *Macromolecules* **2003**, *36*, 1717–1723.

(12) Pispas, S.; Hadjichristidis, N.; Potemkin, I.; Khokhlov, A. *Macromolecules* **2000**, *33*, 1741–1746.

(13) Zamurovic, M.; Christodoulou, S.; Vazaios, A.; Iatrou, E.; Pitsikalis, M.; Hadjichristidis, N. *Macromolecules* **2007**, *40*, 5835–5849.

(14) Von der Ehe, C.; Kempe, K.; Bauer, Marius Baumgärtel, A.; Hager, M. D.; Fischer, D.; Schubert, U. S. *Macromol. Chem. Phys.* **2012**, *213*, 2146–2156.

(15) Schramm, O. G.; Pavlov, G. M.; Van Erp, H. P.; Meier, M. A. R.; Hoogenboom, R.; Schubert, U. S. *Macromolecules* **2009**, *42*, 1808–1816.

(16) Schramm, O. G.; Meier, M. A. R.; Hoogenboom, R.; Van Erp, H. P.; Gohy, J. F.; Schubert, U. S. *Soft Matter* **2009**, *5*, 1662–1667.

(17) Knop, K.; Pavlov, G. M.; Rudolph, T.; Martin, K.; Pretzel, D.; Jahn, B. O.; Scharf, D. H.; Brakhage, A.; Schacher, F. H.; Schubert, U. S. *Soft Matter* **2013**, *9*, 715–726.

(18) Liu, H.; Farrell, S.; Uhrich, K. *J. Controll. Release* **2000**, *68*, 167–174.

(19) Ren, T.; Wang, A.; Yuan, W.; Li, L.; Feng, Y. *J. Polym. Sci., Part A: Polym. Chem.* **2011**, *49*, 2303–2313.

(20) Romberg, B.; Oussoren, C.; Snel, C. J.; Carstens, M. G.; Hennink, W. E.; Storm, G. *BBA-Biomembranes* **2007**, *1768*, 737–743.

(21) Woodle, M. C.; Engbers, C. M.; Zalipsky, S. *Bioconjugate Chem.* **1994**, *5*, 493–496.

(22) Torchilin, V. P.; Shtilman, M. I.; Trubetskoy, V. S.; Whiteman, K.; Milstein, A. M. *BBA-Biomembranes* **1994**, *1195*, 181–184.

(23) Knop, K.; Hoogenboom, R.; Fischer, D.; Schubert, U. S. *Angew. Chem. Int. Ed.* **2010**, *49*, 6288–6308.

(24) Veronese, F. M.; Mero, A.; Pasut, G.; Fang, Z.; Viegas, T. X. In *36th Ann. Meeting & Exposition CRS*; 2009.

(25) Bauer, M.; Lautenschlaeger, C.; Kempe, K.; Tauhardt, L.; Schubert, U. S.; Fischer, D. *Macromol. Biosci.* **2012**, 986–998.

(26) Kronek, J.; Paulovičová, E.; Paulovičová, L.; Kroneková, Z.; Lustoň, J. *J. Mater. Sci. - Mater. Med.* **2012**, *23*, 1457–1464.

(27) Kronek, J.; Kroneková, Z.; Lustoň, J.; Paulovičová, E.; Paulovičová, L.; Mendrek, B. *J. Mater. Sci. - Mater. Med.* **2011**, *22*, 1725–1734.

(28) Luxenhofer, R.; Sahay, G.; Schulz, A.; Alakhova, D.; Bronich, T. K.; Jordan, R.; Kabanov, A. V *J. Controll. Release* **2011**, *153*, 73–82.

(29) Zalpinsky, S.; Hansen, C. B.; Oaks, J. M.; Allen, T. M. *J. Pharm. Sci.* **1996**, *85*, 133–137.

(30) Wang, C.-H.; Hsiue, G.-H. *J. Controll. Release* **2005**, *108*, 140–149.

(31) Lee, S. C.; Kim, C.; Kwon, I. C.; Chung, H.; Jeong, S. Y. *J. Controll. Release* **2003**, *89*, 437–446.

(32) Luxenhofer, R.; Schulz, A.; Roques, C.; Li, S.; Bronich, T. K.; Batrakova, E. V; Jordan, R.; Kabanov, A. V *Biomaterials* **2010**, *31*, 4972–4979.

(33) Jerome, C.; Lecomte, P. *Adv. Drug Delivery Rev.* **2008**, *60*, 1056–1076.

(34) Cameron, D. J. A.; Shaver, M. P. *Chem. Soc. Rev.* **2011**, *40*, 1761–1776.

(35) Weber, C.; Becer, C. R.; Hoogenboom, R.; Schubert, U. S. *Macromolecules* **2009**, *42*, 2965–2971.

(36) Weber, C.; Becer, C. R.; Baumgaertel, A.; Hoogenboom, R.; Schubert, U. S. *Des. Monomers Polym.* **2009**, *12*, 149–165.

(37) Liu, H. B.; Jiang, A.; Guo, J. A.; Uhrich, K. E. *J. Polym. Sci., Part A: Polym. Chem.* **1999**, *37*, 703–711.

(38) Kainthan, R. K.; Janzen, J.; Levin, E.; Devine, D. V; Brooks, D. E. *Biomacromolecules* **2006**, *7*, 703–709.

(39) Lenz, C.; Rebel, A.; Waschke, K. F.; Koehler, R. C.; Frietsch, T. *Transfus. Altern. Transfus. Med.* **2007**, *9*, 265–272.

(40) Akashi, M.; Sakamoto, N.; Suzuki, K.; Kishida, A. *Bioconj. Chem.* **1996**, *7*, 393–395.

(41) Han, D. K.; Lee, N. Y.; Park, K. D.; Kim, Y. H.; Cho, H. I.; Min, B. G. *Biomaterials* **1995**, *16*, 467–471.

(42) Korte, W.; Clarke, S.; Lefkowitz, J. B. *Am. J. Clin. Pathol.* **2000**, *113*, 123–127.

(43) Gorbet, M. B.; Sefton, M. V *Biomaterials* **2004**, *25*, 5681–5703.

(44) Biondi, O.; Motta, S.; Mosesso, P. *Mutagenesis* **2002**, *17*, 261–264.

(45) Herold, D. A.; Keil, K.; Bruns, D. E. *Biochem. Pharmacol.* **1989**, *38*, 73–76.

(46) Hinds, K. D. *Biomaterials for Delivery and Targeting of Proteins and Nucleic Acids*; Mahato, R. I., Ed.; CRC Press, 2005.

(47) Luxenhofer, R.; Sahay, G.; Schulz, A.; Alakhova, D.; Bronich, T. K.; Jordan, R.; Kabanov, A. V *J. Controll. Release* **2011**, *153*, 73–82.

(48) Gaertner, F. C.; Luxenhofer, R.; Blechert, B.; Jordan, R.; Essler, M. *J. Controll. Release* **2007**, *119*, 291–300.

(49) Sledge, G. W.; Nerberg, D.; Bernardo, P.; Ingle, J. N.; Martino, S.; Rowinsky, E. K.; Wood, W. C. *J. Clin.Oncol.* **2003**, *21*, 588–592.

(50) Steiner, R.; Stewart, J. F.; Cantwell, B. M.; Minton, M. J.; Knight, R. K.; Rubens, R. D. *Eur. J. Cancer Clin. Oncol.* **1983**, *19*, 1553–1557.

(51) Batist, G.; Ramakrishnan, G.; Rao, C. S.; Chandrasekharan, A.; Gutheil, J.; Guthrie, T.; Shah, P.; Khojasteh, A.; Nair, M. K.; Hoelzer, K.; Tkaczuk, K.; Park, Y. C. *J. Clin.Oncol.* **2001**, *19*, 1444–1454.

(52) Mross, K.; Niemann, B.; Massing, U.; Drevs, J.; Unger, C.; Bhamra, R.; Swenson, C. E. *Cancer Chemother. Pharmacol.* **2004**, *54*, 514–524.

(53) Lee, E. S.; Na, K.; Bae, Y. H. *J. Controll. Release* **2005**, *103*, 405–418.

(54) Kwon, G.; Naito, M.; Yokoyama, M.; Okano, T.; Sakurai, Y.; Kataoka, K. *J. Controll. Release* **1997**, *48*, 195–201.

(55) Shuai, X.; Ai, H.; Nasongkla, N.; Kim, S.; Gao, J. *J. Controll. Release* **2004**, *98*, 415–426.

(56) Qiu, L. Y.; Wu, X. L.; Jin, Y. *Pharm. Res.* **2009**, *26*, 946–957.

Supporting information

Star-shaped drug carriers for doxorubicin with POEGMA and POEtOxMA brush-like shells: A structural, physical and biological comparison

*Katrin Knop.[1,2] David Pretzel,[1,2] Annett Urbanek,[1,2] Tobias Rudolph,[1,2] Daniel H. Scharf,[3] Anja Schallon,[1,2] Michael Wagner,[1,2] Stephanie Schubert,[4] Michael Kiehntopf,[5] Axel A. Brakhage,[3] Felix H. Schacher,[1,2] and Ulrich S. Schubert[1,2]**

[1] Laboratory of Organic and Macromolecular Chemistry (IOMC), Friedrich-Schiller-University Jena, Humboldtstrasse 10, 07743 Germany
[2] Jena Center for Soft Matter (JCSM), Friedrich-Schiller-University Jena, Philosophenweg 8, 07743 Germany
[3] Leibniz Institute for Natural Product Research and Infection Biology – Hans Knöll Institute, Beutenbergstr. 11a, 07745 Jena, Germany
[4] Department of Pharmaceutical Technology, Institute of Pharmacy, Friedrich-Schiller-University Jena, Otto-Schott-Strasse 41, 07745 Jena, Germany
[5] Institute for Clinical Chemistry and Laboratory Diagnostics, Jena University Hospital, Erlanger Allee 101, 07740 Jena, Germany

*Author for correspondence: Prof. Dr. U. S. Schubert. Telephone: +49(0) 3641 948200, Fax: +49(0) 3641 948202, E-mail: ulrich.schubert@uni-jena.de, Internet: www.schubert-group.com

General oligo(2-ethyl-2-oxazoline) methacrylate ($OEtOx_4MA$ and $OEtOx_9MA$) synthesis. The oligo(2-ethyl-2-oxazoline) methacrylate monomers were synthesized according to a reported procedure.[11] Briefly, the required amount of initiator (methyl tosylate, for the tetramer: 2.421 g, 13 mmol, for the nonamer: 1.076 g, 5.8 mmol), monomer (2-ethyl-2-oxazoline, 5.155 g, 52 mmol) and solvent (acetonitrile, 7.6 mL) were transferred under argon into a flame-dried microwave vial. The reaction mixtures were heated under heating-while-cooling microwave conditions to 140 °C for 38 s and 86 s, respectively. The end capping was performed by adding methacrylic acid (1.5-fold excess, for the tetramer: 1.65 mL, 19.5 mmol, for the nonamer: 0.74 mL, 8.7 mmol) and triethylamine (2-fold excess, for the tetramer: 3.6 mL, 26 mmol, for the nonamer: 1.6 mL, 11.6 mmol) by syringe to the microwave vials and stirring at room temperature overnight. The reaction solution was diluted with dichloromethane, washed with aqueous sodium hydrogen carbonate solution and brine, dried with sodium sulfate, filtered and dried under vacuum. The repeating units were calculated by comparison of the signals at 6.06 ppm and 3.45 ppm.

Tetramer: ^{1}H NMR (250 MHz, $CDCl_3$): δ 6.06 (1H, m, =CH_2), 5.57 (1H, m, =CH_2), 4.26 (2H, m, CH_2-COO), 3.45 (15H, m, N-CH_2-CH_2), 3.00 (3H, m, N-CH_3), 2.33 (10H, m, C-CH_2-CH_3), 1.91 (3H, m, CH_2=C-CH_3) 1.11 (13H, m, CH_2-CH_3).

Nonamer: ^{1}H NMR (250 MHz, $CDCl_3$): δ 6.06 (1H, m, =CH_2), 5.58 (1H, m, =CH_2), 4.26 (2H, m, CH_2-COO), 3.44 (37H, m, N-CH_2-CH_2), 3.00 (3H, m, N-CH_3), 2.33 (22H, m, C-CH_2-CH_3), 1.91 (3H, m, CH_2=C-CH_3) 1.11 (30H, m, CH_2-CH_3).

Table S1. Overview of analytical data obtained for the $OEtOx_4MA$ and $OEtOx_9MA$ oligomers.

Polymer	M_n [g mol^{-1}]^a ^{1}H NMR	M_n [g mol^{-1}]^b SEC	PDI	M_n [g mol^{-1}]^c MALDI	PDI
$OEtOx_4MA$	500	450	1.27	560	1.10
$OEtOx_9MA$	1000	910	1.23	980	1.05

[a] Calculated from ^{1}H NMR. [b] Obtained from SEC ($CHCl_3$:*i*PrOH:NEt_3) using PMMA calibration. [c] Obtained by MALDI-TOF MS with DCTB, LiCl.

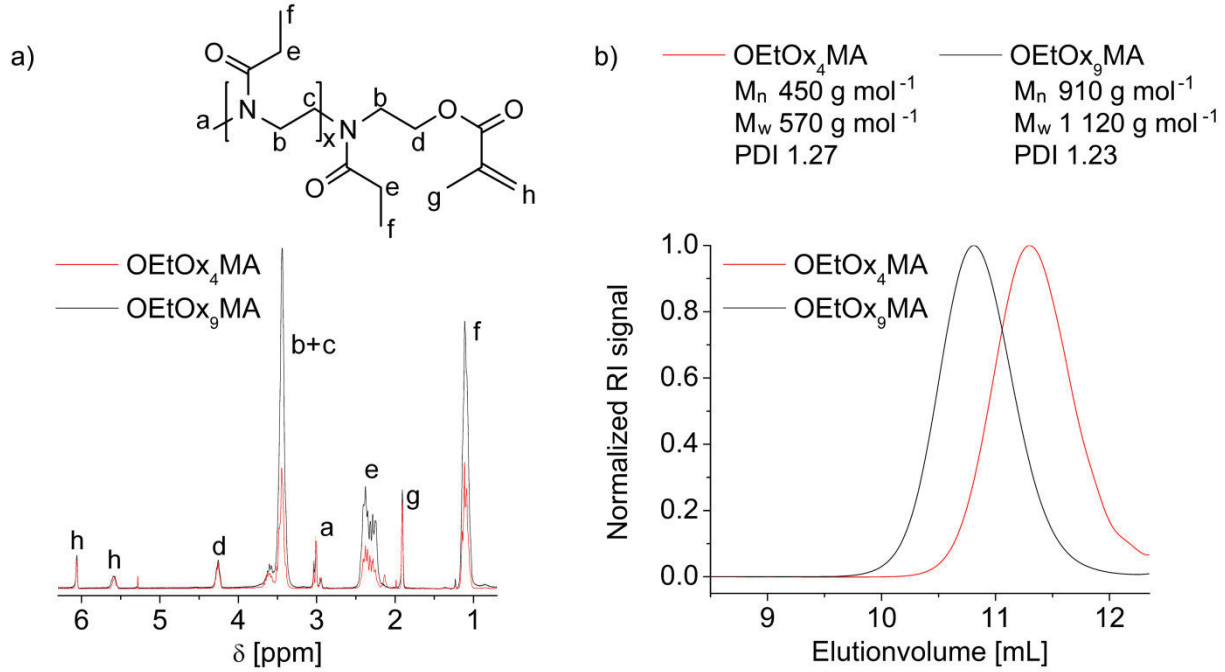

Figure S1. (a) ^{1}H NMR spectra of the $OEtOx_4MA$ and $OEtOx_9MA$ oligomers. (b) SEC curves and molar mass values of the $OEtOx_4MA$ and $OEtOx_9MA$ oligomers.

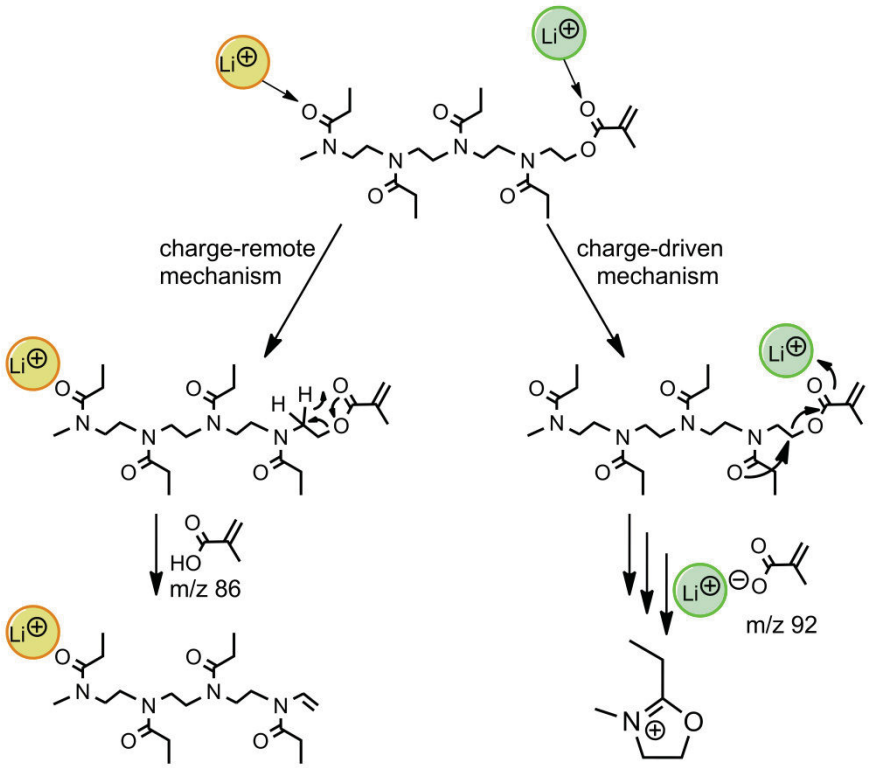

Scheme S1. Schematic representation of the proposed charge-remote and charge-driven fragmentation mechanisms.

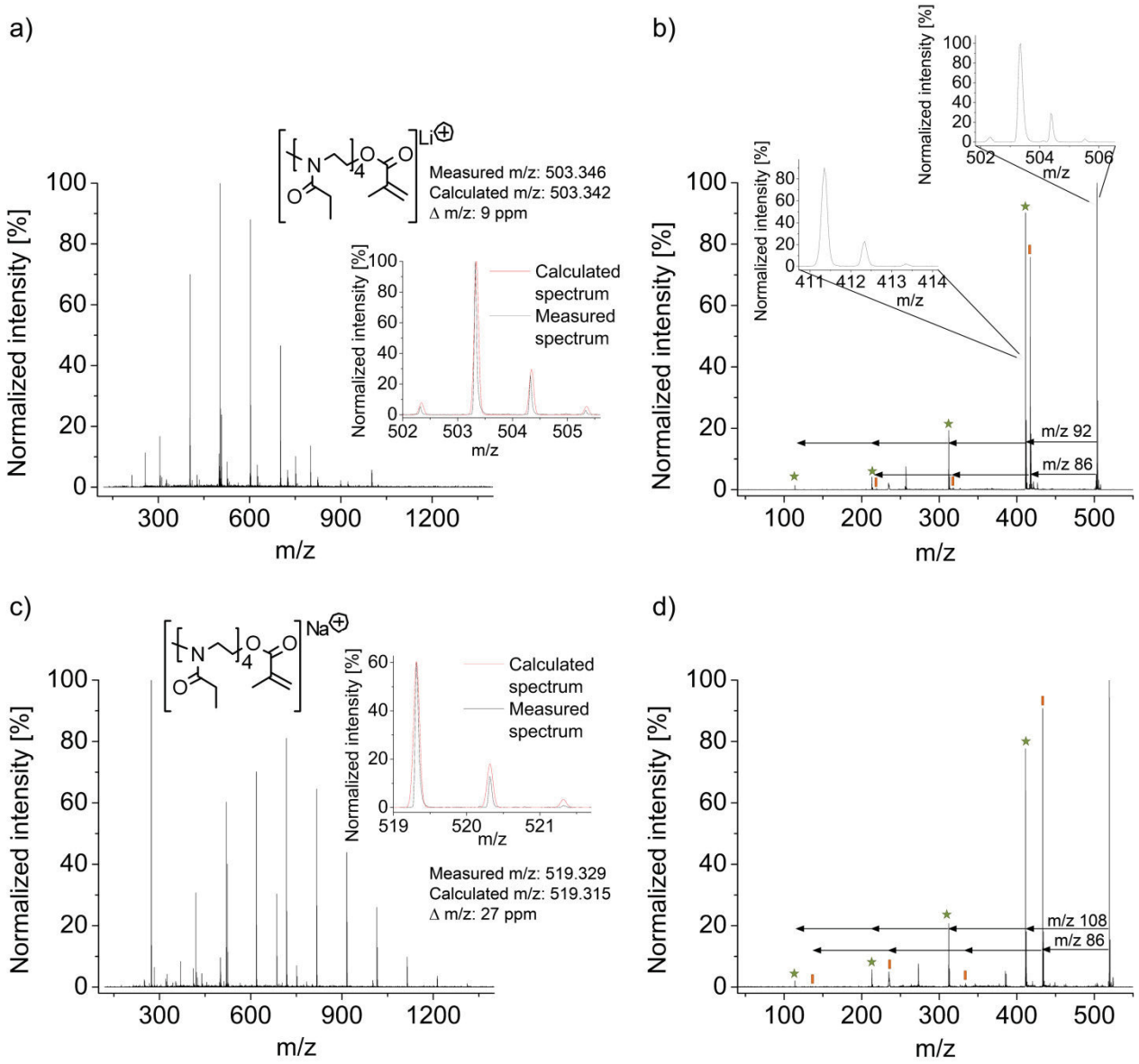

Figure S2. (a) MALDI-TOF MS spectrum of $[OEtOx_4MA]Li^+$; the inset is showing the structure and the calculated and measured isotopic pattern of the tetramer. (b) CID spectrum of $[OEtOx_4MA]Li^+$ with the isotopic pattern of the parent peak and the charge-induced fragmentation peak. (c) MALDI-TOF MS spectrum of $[OEtOx_4MA]Na^+$; the inset is showing the structure and the calculated and measured isotopic pattern of the tetramer. (d) CID spectrum of $[OEtOx_4MA]Na^+$ with the assigned fragmentation pathways. Matrix: *trans*-2-[3-(4-*tert*-Butylphenyl)-2-methyl-2-propenylidene]malononitrile (DCTB).

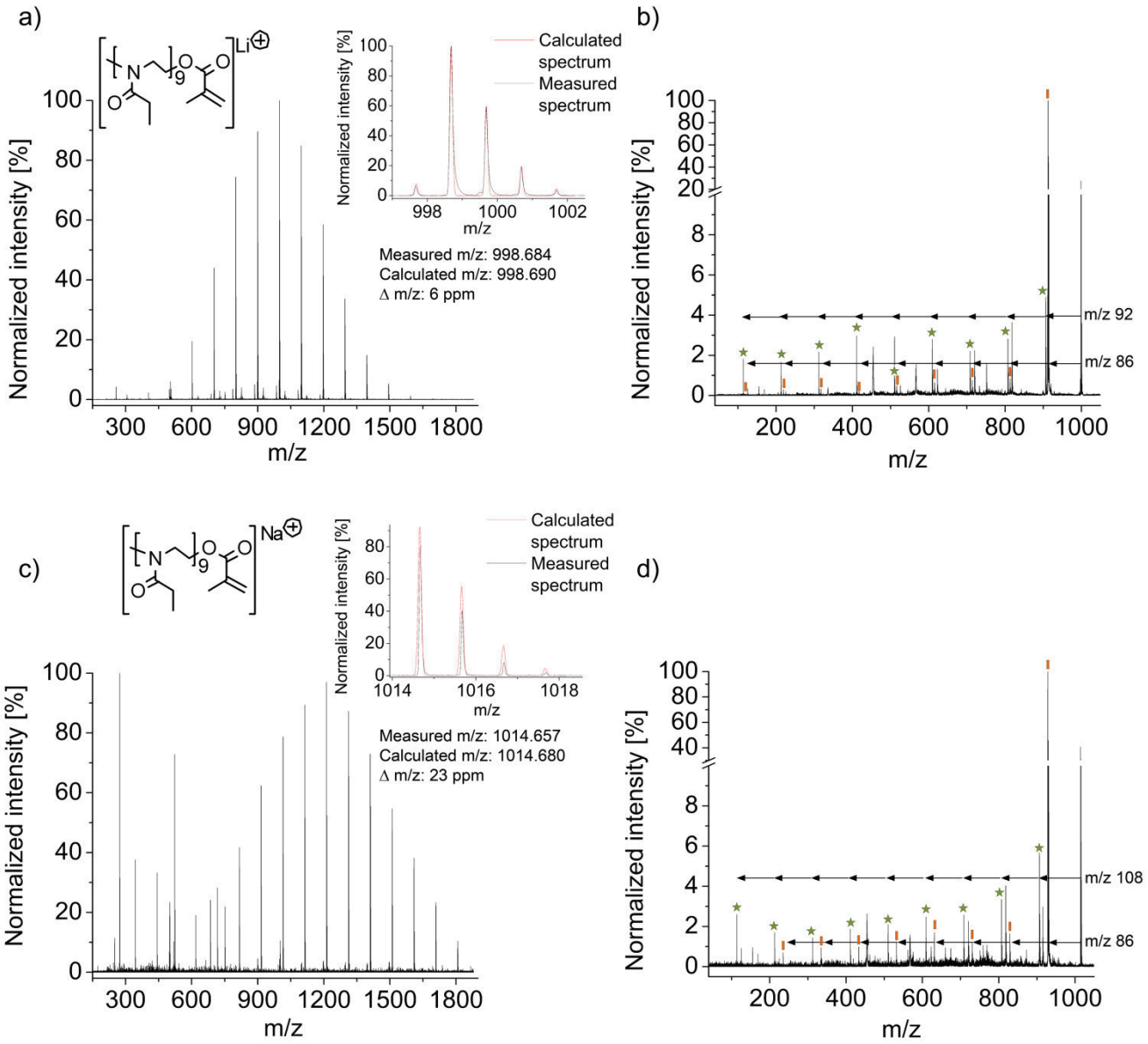

Figure S3. (a) MALDI-TOF MS spectrum of $[OEtOx_9MA]Li^+$; the inset is showing the structure and the calculated and measured isotopic pattern of the tetramer. (b) CID spectrum of $[OEtOx_9MA]Li^+$ with the assigned fragmentation pathways. (c) MALDI-TOF MS spectrum of $[OEtOx_9MA]Na^+$; the inset is showing the structure and the calculated and measured isotopic pattern of the tetramer. (d) CID spectrum with the assigned fragmentation pathways. Not assigned fragments derive from an uncontrolled post-source decay. Matrix: DCTB.

The CID spectra showed the charge-remote 1,5 hydrogen-transfer (McLafferty) loss of m/z 86 from the parent ion, proving that the end group indeed is constituted of a methacrylate (detailed MALDI-TOF MS and CID spectra are given in the SI). The CID investigations of the $OEtOx_4MA$ oligomer with different ionizing agents, namely lithium and sodium ions, showed that in dependence of the ionizing salt two different mechanisms of the end group loss are observed. The 1,5 hydrogen-transfer is leading with both salts to the loss of m/z 86 from the parent ion confirming the charge-remote character of this fragmentation pathway. The associated fragment series with the double bond bearing end group is formed by random main chain fragmentations as reported previously.[2] Additionally, a charge-driven

fragmentation mechanism is observed, induced presumably by the complexation of the carbonyl oxygen of the methacrylic acid. This pathway is leading to the loss of lithium and sodium methacrylate, respectively, and generates in both cases an oxazolinium species at the polymeric chain. This oxazolinium species induces a depolymerization reaction leading to the second fragmentation series. This fragmentation pathway is further confirmed by the characteristic isotopic pattern caused by the ionization with lithium ions. Whereas the parent ion still shows the isotopic pattern of lithium, the fragment formed by loss of lithium methacrylate shows the regular carbon pattern. As the coordination of lithium with the carbonyl oxygen is preferred in comparison to the sodium, the charge-driven mechanism is more pronounced in the CID spectra obtained with lithium ionized $OEtOx_4MA$ chains. For the $OEtOx_9MA$ oligomers, this effect is not anymore observed as the binding sites along the chain increase and the complexation at the carbonyl oxygen of the methacrylate becomes less probable.

4-Arm poly(*ε*-caprolactone) ($[PCL_{18}\text{-}OH]_4$) synthesis. 666 mg (5.2 mmol) of pentaerythritol was weighed into a flame-dried flask, and 35 mL of *ε*-caprolactone (34.4 g, 312 mmol) were added. The quantity of tin(II) 2-ethylhexanoate catalyst was set to $1/20^{th}$ of the initiating OH-groups of the pentaerythritol (corresponding to 336 μL (421 mg, 1.04 mmol) of tin(II) 2-ethylhexanoate) and added. The reaction mixture was submitted to 3 freeze-pump-thaw-cycles and subsequently set under argon to assure a dry and inert atmosphere during the reaction at 80 °C overnight. The resulting highly viscous polymer was purified by precipitation from concentrated dichloromethane solution into cold methanol and dried in vacuum. The ^{1}H NMR spectra were used to calculate the actual arm length by comparison of the signals at 3.63 ppm and 2.80 ppm.

^{1}H NMR (300 MHz, $CDCl_3$): δ 4.05 (18H, m, C*H*$_2$-O), 3.63 (1H, m, C*H*$_2$-OH), 2.30 (18H, m, CO-C*H*$_2$), 1.62 (37H, m, $COCH_2$-C*H*$_2$-$CH_2CH_2CH_2O$ + $COCH_2CH_2CH_2$-C*H*$_2$-CH_2O), 1.37 (18H, m, $COCH_2CH_2$-C*H*$_2$-CH_2CH_2O).

4-Arm poly(ω-(α-bromoisobutyryl)-*ε*-caprolactone) ($[PCL_{18}\text{-}Br]_4$) synthesis. 34 g (4.31 mmol) of the $[PCL_{18}\text{-}OH]_4$ polymer was coevaporated with toluene three times prior to use and dissolved in THF to obtain a 1×10^{-2} M solution. 4.8 mL (24.7 mg, 34.5 mmol) triethylamine and 4.3 mL (8 mg, 34.5 mmol) α-bromoisobutyryl bromide were slowly added under argon in two-fold excess in relation to the hydroxyl end groups of the polymer. After 72 h stirring at room temperature, the solution was passed through an aluminum oxide bed, and, subsequently, the THF was evaporated. The polymer was redissolved in dichloromethane and precipitated in cold methanol to yield a white powder after drying in vacuum. The ^{1}H NMR spectra were used to control the full conversion of the hydroxyl groups.

^{1}H NMR (300 MHz, $CDCl_3$): δ 4.04 (18H, m, C*H*$_2$-O), 2.28 (17H, m, CO-C*H*$_2$), 1.90 (3H, s, C*H*$_3$), 1.62 (34H, m, $COCH_2$-C*H*$_2$-$CH_2CH_2CH_2O$ + $COCH_2CH_2CH_2$-C*H*$_2$-CH_2O), 1.37 (17H, m, $COCH_2CH_2$-C*H*$_2$-CH_2CH_2O).

Table S2. Overview of analytical data obtained for the $[PCL_{18}\text{-}OH]_4$ and $[PCL_{18}\text{-}Br]_4$ polymers.

Polymer	M_n [g mol^{-1}]^a ^{1}H NMR	M_n [g mol^{-1}]^b SEC	PDI	M_n [g mol^{-1}]^c MALDI	PDI
$[PCL_{18}\text{-}OH]_4$	8 400	12 900	1.21	6 900	1.06
$[PCL_{18}\text{-}Br]_4$	9 000	12 800	1.21	7 700	1.04

[a] Calculated from ^{1}H NMR. [b] Obtained from SEC (DMAc:LiCl) using PMMA calibration. [c] Obtained by MALDI-TOF MS with DCTB, LiCl.

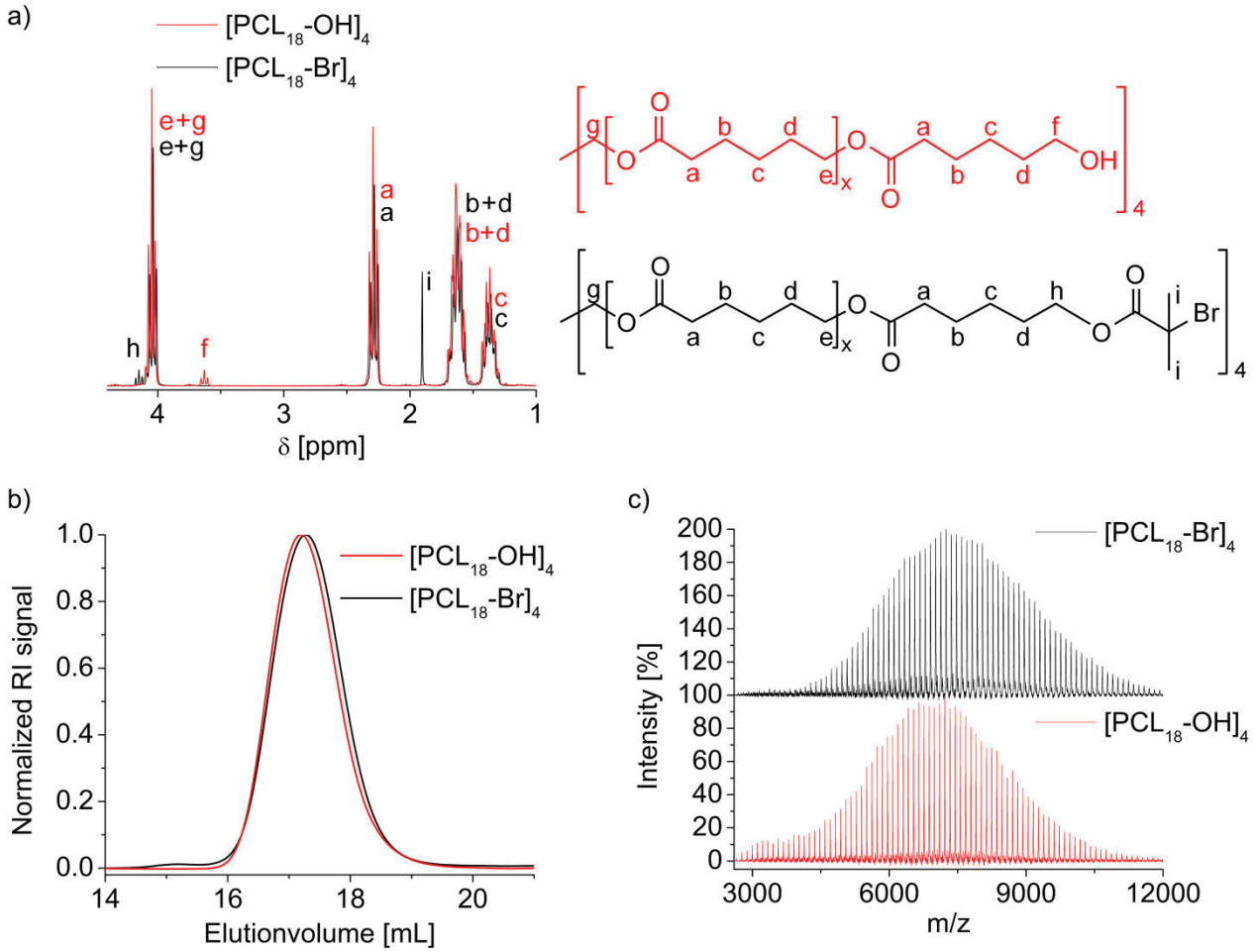

Figure S4. (a) ^{1}H NMR spectra of the $[PCL_{18}\text{-}OH]_4$ and the $[PCL_{18}\text{-}Br]_4$ polymer. (b) SEC curves of the $[PCL_{18}\text{-}OH]_4$ and the $[PCL_{18}\text{-}Br]_4$ polymer obtained with DMAc:LiCl eluent. (c) Full MALDI-TOF MS spectra of the $[PCL_{18}\text{-}OH]_4$ and the $[PCL_{18}\text{-}Br]_4$ polymer. Matrix: DCTB.

General 4-arm poly(ε-caprolactone)-*b*-poly(oligo(ethylene glycol) methacrylate) ([PCL_{18}-*b*-$POEG_{19}MA]_4$) synthesis. 36.5g $OEG_{19}MA$ (37.5 mmol) dissolved in 100 mL anisole were passed through an aluminum oxide/calcium hydride (5%) bed and purged until the resulting solution completes 150 mL. 390 mg *N*,*N*,*N*′,*N*″,*N*″-Pentamethyldiethylenetriamine (PMDETA, 2.25 mmol) were added and purged with argon. While purging the solution, a second flame-dried 2-necked flask equipped with a gas inlet was cooled under argon, and 133 mg CuBr (1.28 mmol) were added. The purged solution was subsequently added and was further purged with argon 10 min. An appropriate amount of initiator according to the [M]/[I]/[CuBr]/[PMDETA] ratio of 50/1/1.2/3 was solved in few milliliters of anisole, purged and added. The reaction flask was immediately closed and heated to 60 °C. For [PCL_{18}-*b*-$POEG_{19}MA_{45}]_4$, a [M]/[I]/[CuBr]/[PMDETA] ratio of 400/1/1.2/3 was used.

For kinetic studies, the flask was closed with a septum, and a sample was taken with an argon flushed syringe very 10 min. The conversions were calculated from the decrease of the integral of the OEGMA signal in the SEC ($CHCl_3$:*i*PrOH:NEt_3).

For the preparation of the different [PCL_{18}-*b*-POEGMA]$_4$ polymers, the flask was closed with a stopper and heated for the calculated amount of time. To terminate the reaction, the solution was aerated and cooled in a freezer to −18 °C. For purification, the reaction mixture was passed twice through an aluminum oxide (Beckmann activity II-III) bed under dilution with chloroform to remove the copper salts. The obtained colorless solution was concentrated and subsequently submitted twice to BioBeads® SX1 (swelled in toluene) separations. After removing the solvent, the polymer was dried in vacuum and finally dispensed in water and freeze-dried.

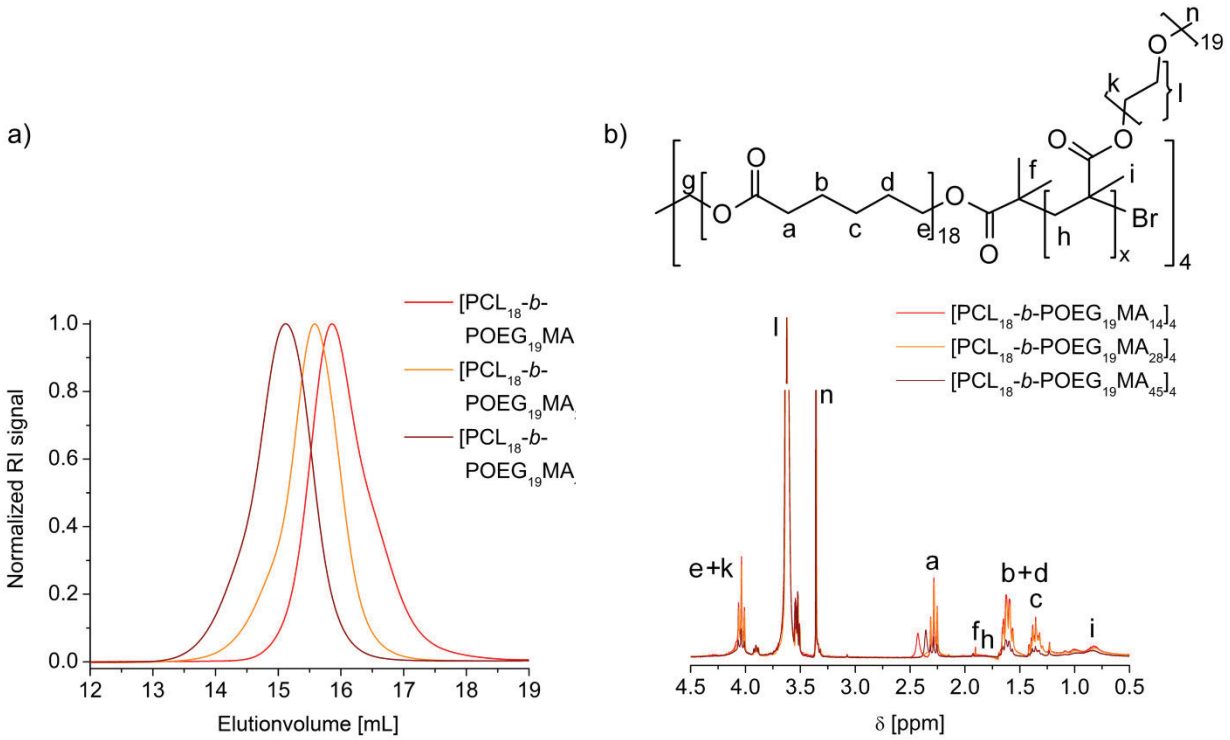

Figure S5. (a) SEC curves of the [PCL_{18}-*b*-$POEG_{19}MA]_4$ polymers obtained with DMAc:LiCl eluent. (b) ^{1}H NMR spectra of the [PCL_{18}-*b*-$POEG_{19}MA]_4$ polymers.

General 4-arm poly(ε-caprolactone)-*block*-poly(oligo(2-ethyl-2-oxazoline) methacrylate) ([PCL$_{18}$-*b*-POEtOx$_4$MA]$_4$ and [PCL$_{18}$-*b*-POEtOx$_9$MA]$_4$) synthesis. 18 g OEtOx$_4$MA (37.5 mmol) or 36.5 g OEtOx$_9$MA (37.5 mmol) dissolved in 100 mL anisole were passed through an aluminum oxide/calcium hydride (5%) bed and purged until the resulting solution completes 150 mL. 390 mg PMDETA (2.25 mmol) were added and purged with argon. While purging the solution, a second flame-dried 2-necked flask equipped with a gas inlet was cooled under argon, and 133 mg CuBr (1.28 mmol) were added. The purged solution was subsequently added and was further purged with argon for 10 min. An appropriate amount of initiator according to the [M]/[I]/[CuBr]/[PMDETA] ratio of 50/1/1.2/3 was dissolved in few milliliters of anisole, purged and added. The reaction flask was immediately closed and heated to 60 °C. For [PCL$_{18}$-*b*-POEtOx$_4$MA$_{44}$]$_4$ and [PCL$_{18}$-*b*-POEtOx$_9$MA$_{51}$]$_4$, a [M]/[I]/[CuBr]/[PMDETA] ratio of 100/1/1.2/3 was used.

For kinetic studies, the flask was closed with a septum and a sample was taken with an argon flushed syringe every 10 min. The conversions were calculated from the decrease of the integral of the OEtOxMA signal in the SEC ($CHCl_3$:*i*PrOH:NEt_3).

For the preparation of the different [PCL$_{18}$-*b*-POEtOxMA]$_4$ polymers, the flask was closed with a stopper and heated for the calculated amount of time. To terminate the reaction, the solution was aerated and cooled in a freezer to −18 °C. For purification, the reaction mixture was passed twice through an aluminum oxide (Beckmann activity II-III) bed under dilution with chloroform to remove the copper salts. The obtained colorless solution was concentrated and subsequently submitted twice to BioBeads® SX1 (swelled in THF) separations. After removing the solvent, the polymer was dried in vacuum and finally dispensed in water and freeze-dried.

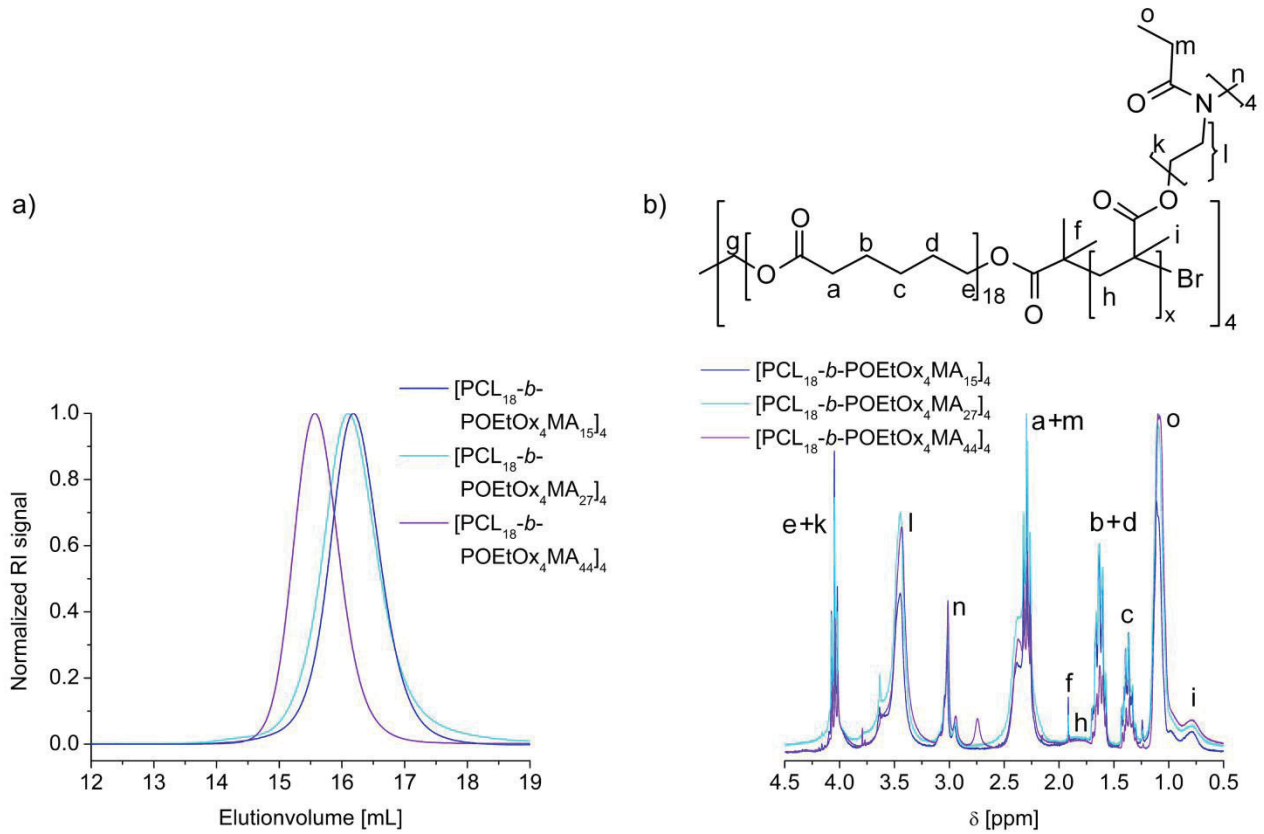

Figure S6. (a) SEC curves of the [PCL$_{18}$-*b*-POEtOx$_4$MA]$_4$ polymers obtained with DMAc:LiCl eluent. (b) ^{1}H NMR spectra of the [PCL$_{18}$-*b*-POEtOx$_4$MA]$_4$ polymers.

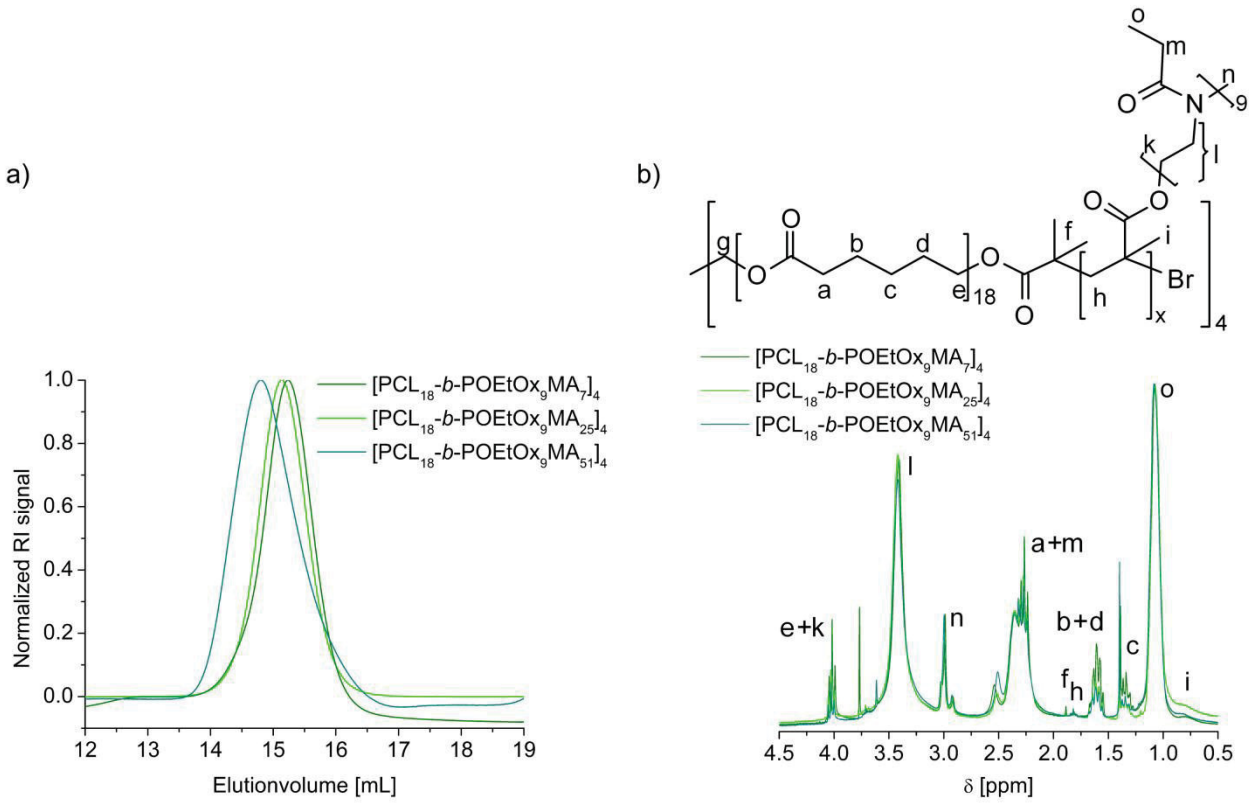

Figure S7. (a) SEC curves of the $[PCL_{18}$-*b*-$POEtOx_9MA]_4$ polymers obtained with DMAc:LiCl eluent. (b) ^{1}H NMR spectra of the $[PCL_{18}$-*b*-$POEtOx_9MA]_4$ polymers.

Table S3. Calibration of copper determination with atom absorption spectroscopy (AAS).

	c_{Cu} M_n [mg L^{-1}]	Extinction [a]
blank	0	0.000386
Standard 1	0.1	0.01749
Standard 2	0.25	0.06625
Standard 3	0.5	0.1055
Standard 4	0.75	0.1581
Standard 5	1	0.2137

[a] Obtained at the wavelength of 324 nm.

Table S4. Copper content determination with atom absorption spectroscopy (AAS) of the $[PCL_{18}$-*b*-POEGMA$]_4$ and $[PCL_{18}$-*b*-POEtOxMA$]_4$ polymers.

Polymer	Extinction [a]	Copper content in polymer [mg g^{-1}]	Copper content in polymer [ppm]
$[PCL_{18}$-*b*-$POEG_{19}MA_{14}]_4$	0.00308	0.02	20
$[PCL_{18}$-*b*-$POEG_{19}MA_{28}]_4$	0.00375	0.02	20
$[PCL_{18}$-*b*-$POEG_{19}MA_{45}]_4$	0.00549	0.01	10
$[PCL_{18}$-*b*-$POEtOx_4MA_{15}]_4$	0.04362	0.04	40
$[PCL_{18}$-*b*-$POEtOx_4MA_{27}]_4$	0.01460	0.02	20
$[PCL_{18}$-*b*-$POEtOx_4MA_{44}]_4$	0.00383	0.02	20
$[PCL_{18}$-*b*-$POEtOx_9MA_7]_4$	0.00458	0.02	20
$[PCL_{18}$-*b*-$POEtOx_9MA_{25}]_4$	0.01909	0.02	20
$[PCL_{18}$-*b*-$POEtOx_9MA_{51}]_4$	0.00661	0.02	20
Tap water	0.1088	(0.52 mg L^{-1})	0.52

[a] Obtained at the wavelength of 324 nm.

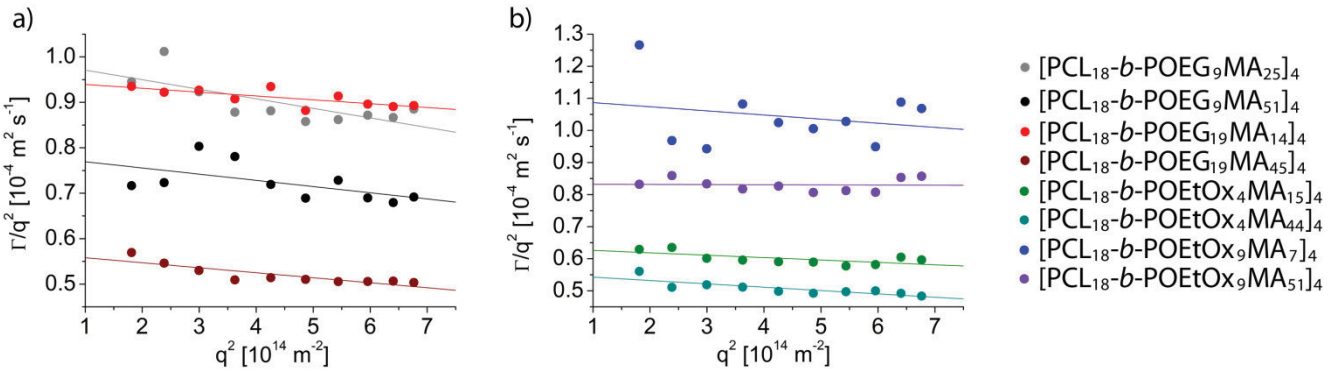

Figure S8. Angle dependent light scattering in acetone of the (a) $[PCL_{18}\text{-b-}POEG_9MA]_4$ and $[PCL_{18}\text{-b-}POEG_{19}MA]_4$ polymers as well as (b) the $[PCL_{18}\text{-b-}POEtOx_4MA]_4$ and $[PCL_{18}\text{-b-}POEtOx_9MA]_4$ polymers. Data of the $[PCL_{18}\text{-b-}POEG_9MA]_4$ polymers taken from a previous publication.[3]

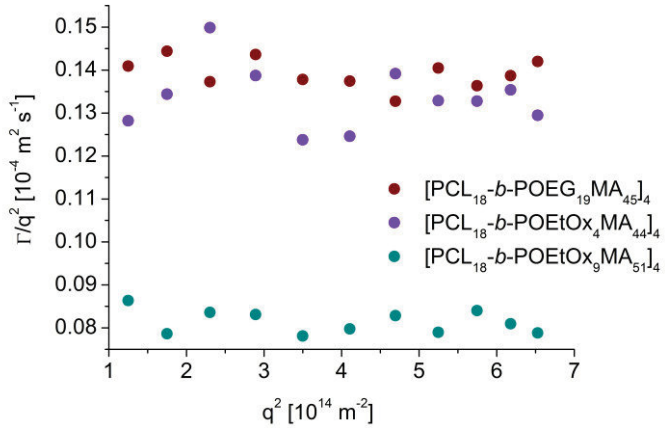

Figure S9. Angle dependent light scattering of the $[PCL_{18}\text{-b-}POEG_{19}MA_{45}]_4$, $[PCL_{18}\text{-b-}POEtOx_4MA_{44}]_4$ and $[PCL_{18}\text{-b-}POEtOx_9MA_{51}]_4$ polymers in water.

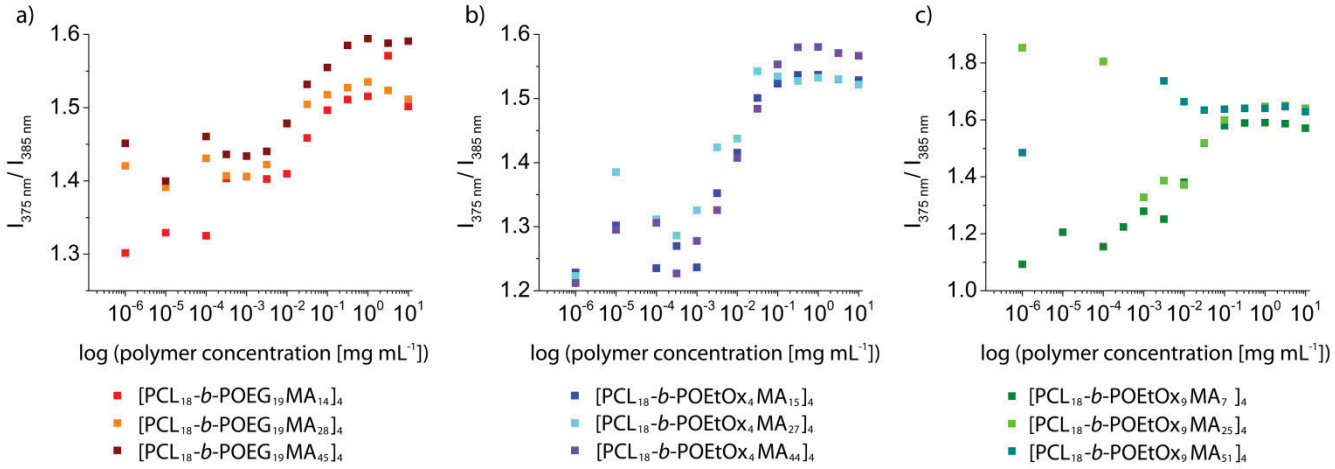

Figure S10. Fluorescence emission of pyrene evaluated according to their intensity ratio of band I to band III for (a) the $[PCL_{18}\text{-b-}POEG_{19}MA]_4$, polymers, (b) the $[PCL_{18}\text{-b-}POEtOx_4MA]_4$ polymers and (c) the $[PCL_{18}\text{-b-}POEtOx_9MA]_4$ polymers.

Similarly to a previous report, the critical micelle concentration (cmc) determined by pyrene does not deliver valuable information on the aggregation behavior.[3] For the three different $[PCL_{18}\text{-b-}POEG_{19}MA]_4$ polymers, an identical cmc in the range of 0.003 mg mL^{-1} was detected with this method. A cmc below 0.001 mg mL^{-1} is determined for the $[PCL_{18}\text{-b-}POEtOx_4MA]_4$ polymers by the band I to band III ratio method. The cmc of the $[PCL_{18}\text{-b-}POEtOx_9MA]_4$ polymers is even more difficult to identify. Apparently, the cmc is only influenced by the chemical characteristics of the hydrophilic shell and not by its length or hydrophilic strength, which is in contradiction to previous reports of classical micelles formed by amphiphilic block copolymers.[4–6]

Therefore, the behavior of the pyrene fluorescence was attributed to the inclusion limit of pyrene in the star-shaped block copolymers, whose hydrophobic core offers only limited space to hydrophobic molecules due to the supposed unimolecular characteristics. The number of maximal encapsulated pyrene was determined and correlated to the cmc curve in comparison to the pyrene molecule to polymer molecule ratio (exemplarily shown for the $[PCL_{18}\text{-}b\text{-}POEtOxMA_{25}]_4$ polymer in Figure S11).

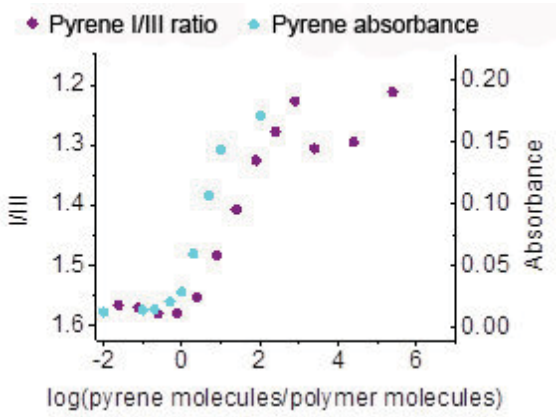

Figure S11. Excimer to monomer ratio of $[PCL_{18}\text{-}b\text{-}POEtOxMA_{28}]_4$ as a function of the pyrene to polymer ratio in comparison to the inclusion limit of the star-shaped block copolymer $[PCL_{18}\text{-}b\text{-}POEtOxMA_{28}]_4$ for pyrene.

HLB value. The hydrophilic/lipophilic balance (HLB) was calculated according to a version reported by Liu et al.:[7]

$$HLB=M_H/(M_L+M_H)$$

M_L represents the molar mass of the hydrophobic moiety, whereas M_H is determined by the molar mass of the hydrophilic moiety. For example, in $[PCL_{18}\text{-}b\text{-}POEtOxMA_{28}]_4$ 18 repeating units of the CL per arm, each containing 5 methylene units (14 amu) give for $M_L=4\times18\times5\times14=5040$. Similarly, 19 ethylene oxide repeating units (44 amu) per comb arm at a total of 28 comb arms per on of the four star arms results in $M_H=19\times44\times28\times4=93\,632$. The resulting HLB value is determined to be 0.95.

Blood-viscosity. The pooled blood of four unmedicated and healthy donors was collected and stabilized by sodium citrate (nine parts blood to one part anticoagulant) (Monovette, Sarstedt, Nümbrecht, Germany). Within 4 hours after collection, 200 µL of PBS or polymer solution (250 mg mL^{-1}, 125 mg mL^{-1} and 25 mg mL^{-1} to obtain final polymer concentrations in the whole blood of 50 mg mL^{-1}, 25 mg mL^{-1} and 5 mg mL^{-1}) were added to 800 µL of whole blood and incubated for 30 min at 37 °C. In a parallel setup, PBS was used instead of the whole blood sample to measure the dynamic viscosity of PBS and the corresponding differently concentrated polymer solutions. Viscosity measurements were conducted at 20 °C using an AMVn (Anton Paar, Graz, Austria) rolling ball viscometer with a manually filled capillary of 0.9 mm internal diameter. The viscosities of the solution, η, were obtained from the rolling times of the steel ball measured at three inclination angles (50°/70°/85°) of the capillary. After x-repetitive measurements, the dynamic viscosity was then calculated by following relationship: $\eta = K \cdot (\rho_b - \rho_s) \cdot t$, where K is a calibration constant, ρ_b and ρ_s are the densities of the ball and the sample respectively, t is the rolling time. The density of the solutions was measured by a densitometer (DMA 4100, Anton Paar, Graz, Austria). For normalization, the dynamic viscosity values of the polymers diluted in whole blood or phosphate buffered saline were divided by the viscosity value of the pure blood or PBS, respectively and results are expressed as relative dynamic viscosity.

Hemolysis of Erythrocytes. For testing the hemolytic activity of the polymer solutions, blood from sheep, collected in heparinized-tubes, was centrifuged at 4.500 × g for 5 min, and the pellet was washed three times with cold 1.5 mM phosphate buffered saline pH 7.4 (PBS). After dilution with PBS in a ratio of 1:7 (number of erythrocytes approx. 2×10^6 mL^{-1}), aliquots of the erythrocyte suspension were mixed 1:1 with the polymer solutions (final polymer concentrations in the erythrocyte suspension of 50 mg mL^{-1}, 25 mg mL^{-1} and 5 mg mL^{-1}) and incubated in a water bath at 37 °C for 60 min. After centrifugation at 2 400 g for 5 min the hemoglobin release into the supernatant was determined spectrophotometrically using a microplate reader at 544 nm wavelength. Complete hemolysis was achieved using 1% Triton X-100 reflecting the 100% value. PBS served as negative control. Less than 5% hemolysis rate were taken as non-hemolytic. Experiments were run in triplicate and were repeated once. The results were analyzed statistically by the Student's *t*-test at a confidence interval of 95%.

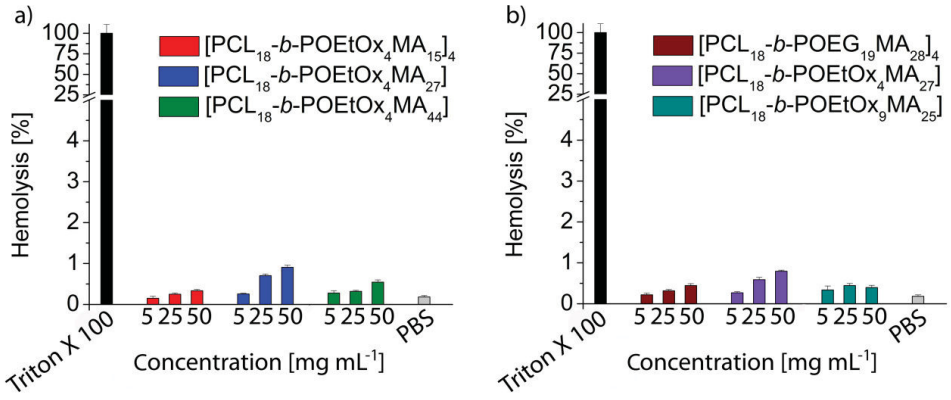

Figure S12. Photometric determination of the hemolytic activity after incubation with different polymer concentrations for 1 h at 37 °C of star-shaped block copolymers with (a) small shell size and (b) medium shell size. Triton X-100 (1%) served as positive and PBS as negative control. Data are presented as the mean percentage ± SD of hemolytic activity compared to the positive control set as 100%.

Erythrocyte Aggregation. Erythrocytes were isolated as described above. Erythrocyte suspensions (100 µL) containing 2 Mio erythrocytes per mL were mixed with the same volume of polymer solutions (100, 50 and 10 mg mL^{-1} PBS buffer) in a clear flat bottomed 96-well plate. The cells were incubated under vigorous shaking at 37 °C for 2 h, and the absorbance was measured at 645 nm in a microplate reader. 25 kDa bPEI (50 µg/mL) was used as positive control. As negative controls, cells were only treated with PBS. Blank values were determined with PBS and subtracted from the sample values. Absorbance values of the test solutions lower than the negative control were regarded as aggregation.

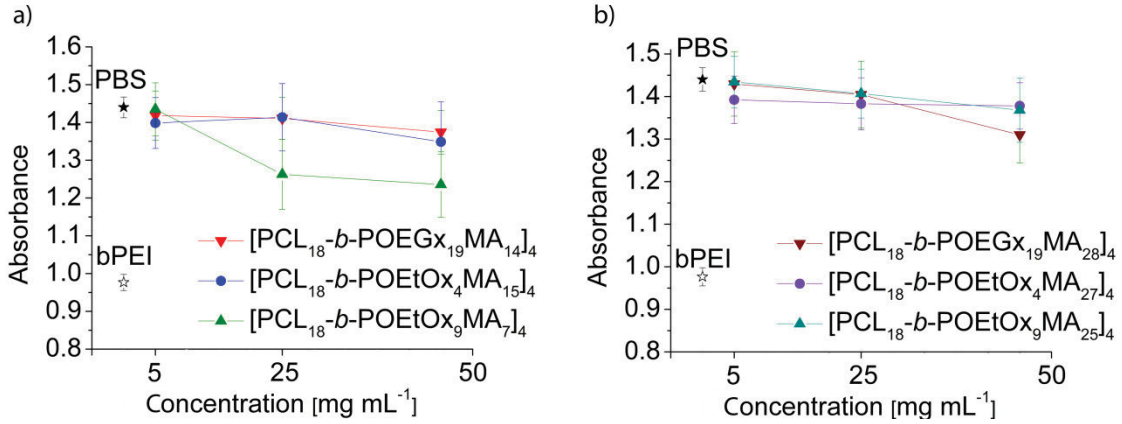

Figure S13. Photometric determination of the erythrocyte aggregation after 2 h incubation at 37 °C with star-shaped block copolymers with (a) small shell size and (b) medium shell size. 25 kDa bPEI (50 µg mL^{-1}) served as positive and PBS as negative control. Data are presented as the mean measured absorbance ± SD.

Blood coagulation. The blood of four unmedicated and healthy donors was collected and stabilized by sodium citrate (nine parts blood to one part anticoagulant) (Monovette, Sarstedt, Nümbrecht, Germany). The plasma was isolated by centrifugation at 3962×g for 4 min at room temperature and used immediately. The prothrombin time (PT) and the activated partial thromboplastin time (APTT) were spectroscopically determined with the clinical coagulation analyzer ACL TOP (Instrumentation Laboratory, Kircheim, Germany). To 240 µL of plasma 60 µL of PBS or polymer solution (250 mg mL^{-1}, 125 mg mL^{-1} and 25 mg mL^{-1} to obtain final polymer concentrations in the plasma of 50 mg mL^{-1}, 25 mg mL^{-1} and 5 mg mL^{-1}) were added and incubated for 5 min or 30 min, respectively. For the APTT determination, 50 µL of the probe were mixed at 37 °C with 50 µL of SyntASiL activator (Instrumentation Laboratory, Milano, Italy) and incubated for 180 to 220 s. Subsequently, the coagulation was triggered by calcium chloride addition (50 µL, 0.02M) and followed spectroscopically at 671 nm for 120 s. The APTT was determined from the maximum of the second derivation of the obtained sigmoidal curve. The PT was determined by addition of 100 µL of RecombiPlasTin activator (Instrumentation Laboratory, Milano, Italy) to 50 µL of the plasma. The coagulation reaction was followed spectroscopically for 120 s at 671 nm. The PT was determined from the maximum of the first derivation of the obtained sigmoidal curve. Each experiment was performed in triplicate and the results were evaluated statistically by the Student's *t*-test at a 95% confidence level.

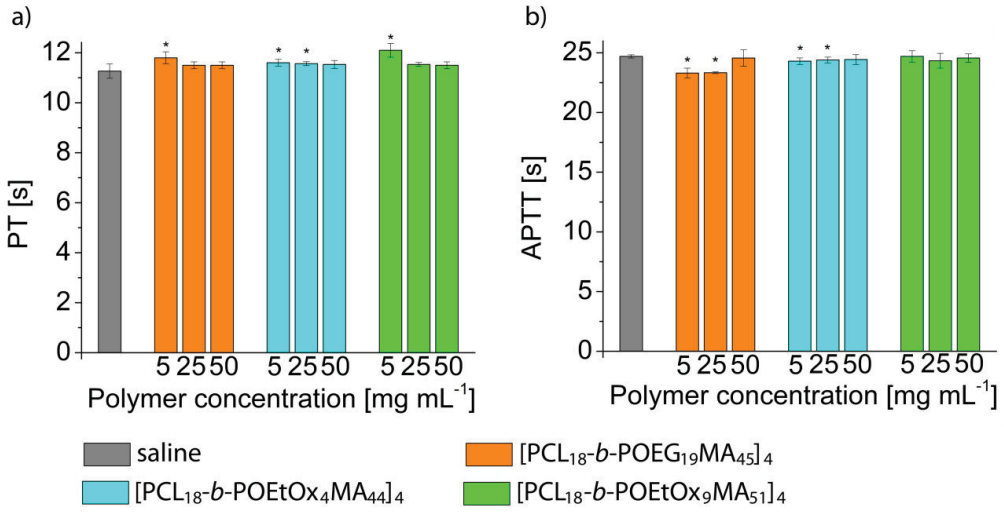

Figure S14. Effects of the polymers on the coagulation detected by (a) the prothrombin time (PT) and (b) the activated partial thromboplastin time (APTT) after 5 min incubation. Data are presented as the mean measured absorbance ± confidence interval.

Platelet activation

The blood of four unmedicated and healthy donors was collected and stabilized by sodium citrate (nine parts blood to one part anticoagulant) (Monovette, Sarstedt, Nümbrecht, Germany). The PRP was isolated by centrifugation and used immediately.

To 240 µL of PRP 60 µL of PBS or polymer solution (250 mg mL^{-1}, 125 mg mL^{-1} and 25 mg mL^{-1} to obtain final polymer concentrations in the PRP of 50 mg mL^{-1}, 25 mg mL^{-1} and 5 mg mL^{-1}) were added and incubated for 10 min or 30 min at 37 °C. To activate platelets 0.5 U mL^{-1} of bovine thrombin (Sigma) were added to the positive control instead of the polymer solution. Aliquots containing 50 µL of the incubated mixture were removed and fixed for 10 min at room temperature using 4% paraformaldehyde in PBS. After washing and centrifugation a double immune-staining was performed using 20 µL of FITC labeled monoclonal antibody directed against CD42 and 20 µL of phycoerythrin (PE) labeled monoclonal antibody directed against CD62P. Isotype controls were incubated with mouse IgG antibodies conjugated with fluorescein isothiocyanate (FITC) or PE dye, respectively (all antibodies were purchased from BD Biosciences, Heidelberg, Germany). After 30 min incubation at room temperature the activation state of the platelets was determined using fluorescence flow cytometry. Expression of the platelet activation marker CD62P and the constitutively present platelet marker CD42 were detected using a Beckmann Coulter Cytomics FC-500 equipped with Uniphase Argon ion laser, 488 nm, 20 mW output. Overall 50 000 platelets were measured per sample and analyzed with the Cytomics CXP software. Results are expressed as percentage of platelets positive for both CD62p and CD42 epitopes.

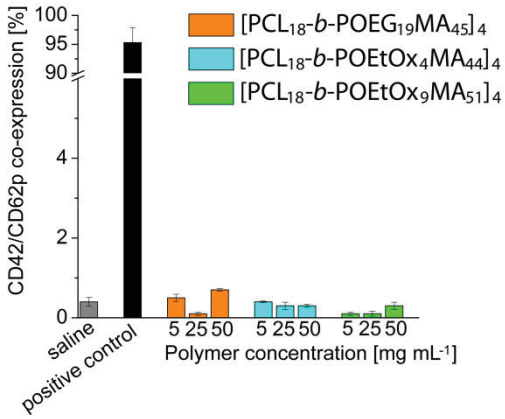

Figure S15. FACS analysis of polymer mediated platelet activation measured by determination of CD62p/CD42 co-expression after 10 min incubation. Data are presented as percentage of platelets positive for both CD62p and CD42 epitopes.

Complement activation

The complement activation was measured on the basis of C3a anaphylatoxins with an ELISA kit (Quidel, San Diego, USA). The blood of four unmedicated and healthy donors was collected and stabilized by sodium citrate (nine parts blood to one part anticoagulant) (Monovette, Sarstedt, Nümbrecht, Germany). The plasma was isolated by centrifugation, pooled and used immediately. 40 µL of plasma were mixed with 10 µL PBS or polymer solution (250 mg mL^{-1}, 125 mg mL^{-1} and 25 mg mL^{-1} to obtain final polymer concentrations in the platelet rich plasma (PRP) of 50 mg mL^{-1}, 25 mg mL^{-1} and 5 mg mL^{-1}) and incubated for 10, 30 or 60 min. Then, samples, standards and controls were diluted in the ratio 1:10 with sample buffer provided by the supplier and applied to a 96 well plate precoated with an antibody directed against C3a epitopes. Further incubation steps were performed according to the instructions of the supplier. The C3a concentrations were measured as absorption (at 450 nm) of the chromogenic substrate added during performance of the assay.

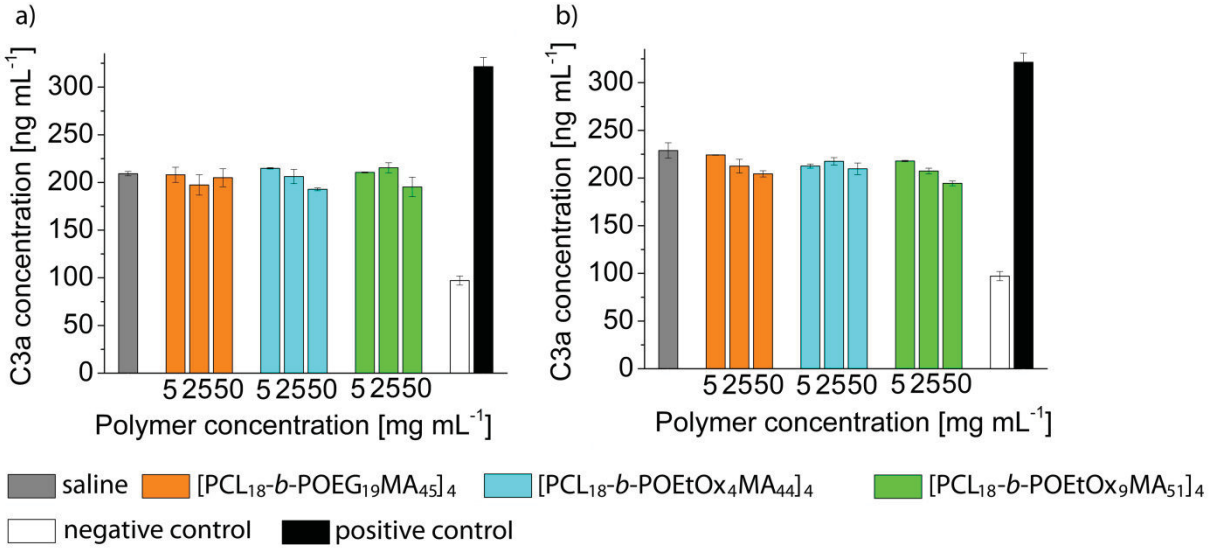

Figure S16. Complement activation by the polymers measured by determination of C3a levels after a) 10 min incubation and b) 30 min incubation. Data are presented as the mean measured absorbance ± SD.

Polymer cytotoxicity. For the cytotoxicity experiments, the mouse fibroblast cell line L929 was purchased from the German Collection of Microorganisms and Cell Cultures (DSMZ, Braunschweig, Germany). The cells were routinely cultured as follows: Dulbecco's modied eagle's medium (DMEM) supplemented with 10% FCS, 100 U mL^{-1} penicillin and 100 µg mL^{-1} streptomycin (all components from Biochrom, Berlin, Germany) at 37 °C in a humidified atmosphere with 5% (v/v) CO_2. The short-term cytotoxicity was determined with a XTT assay following the ISO/EN 10993 part 5 protocol: L929 cells were seeded in 96-well plates at a density of 1×10^4 cells/well and were grown as monolayer cultures for 24 h. The cells were then incubated separately with different polymer concentrations (0.01, 0.1, 1.00 and 10.00 µg mL^{-1} (n = 6)) for 24 h. Control cells were incubated with fresh culture medium. After incubation, 50 µL of a XTT solution prepared according to the manufacturer's instructions were added to each well. After 4 h at 37 °C, 100 µL of each solution were transferred to a new microtiter, plate and the optical density (OD) was measured photometrically. The negative control was standardized as 0% of metabolism inhibition and referred as 100% viability.

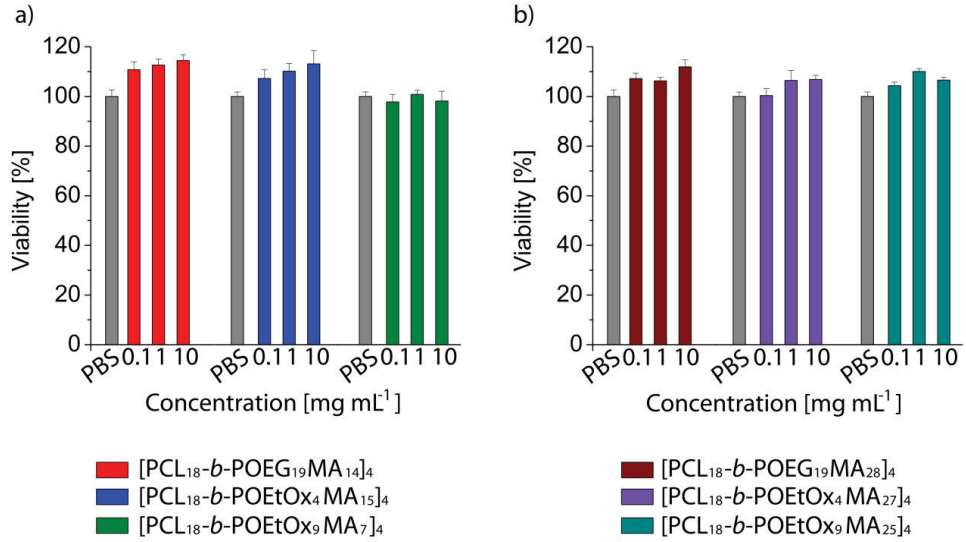

Figure S17: Cell viability of L929 mouse fibroblasts after incubation with star-shaped polymers with (a) small shell size and (b) medium shell size up to 10 mg mL^{-1} for 24 hours. Cells incubated with polymer free culture medium served as control. The cell viability was determined by XTT assay according to ISO 10993-5. Data are expressed as mean ± SD of six determinations.

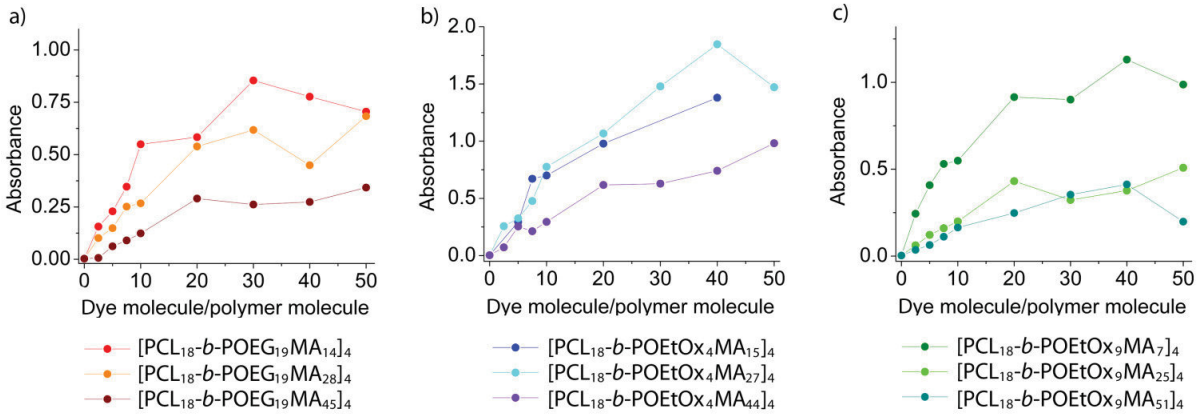

Figure S18: Absorption intensity of fat brown RR at 460 nm for different molar ratios of dye to polymer for (a) the $[PCL_{18}\text{-b-}POEG_{19}MA]_4$, (b) the $[PCL_{18}\text{-b-}POEtOx_4MA]_4$ polymers and (c) the $[PCL_{18}\text{-b-}POEtOx_9MA]_4$ polymers.

Fat brown RR was chosen as model dye to study the encapsulation efficiency of the star-shaped block copolymers (Figure S17). An uptake between 20 and 30 dye molecules per star-shaped block copolymer was determined resulting in loading efficiencies between 4% and 18%. These results show that the encapsulation behavior is rather determined by the core size and characteristics than the shell composition.

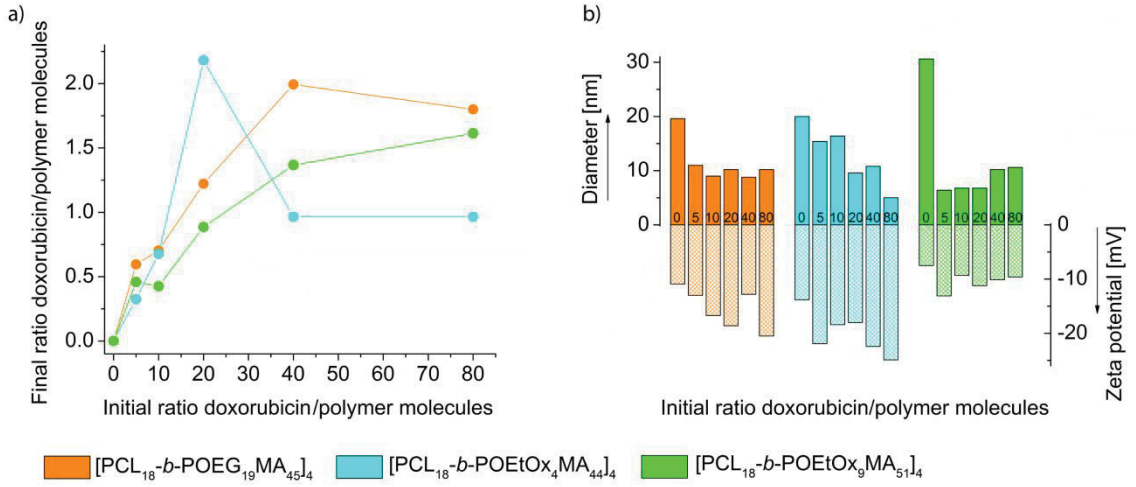

Figure S19: (a) Absorption intensity of doxorubicin at 481 nm for different molar ratios of drug to polymer. (b) Diameters and zeta potentials obtained in DLS for different molar ratios of drug to polymer in water.

Doxorubicin cytotoxicity. For the cytotoxicity experiments, the mouse fibroblast cell line L929, the human breast adenocarcinoma cell lines MCF-7 and MDA-MB 231 as well as the human embryonic kidney (HEK) 293 cell line were purchased from the German Collection of Microorganisms and Cell Cultures (DSMZ, Braunschweig, Germany). The cells were routinely cultured as follows: Dulbecco's modied eagle's medium (DMEM; for L929 cells), DMEM:Ham's F12 (for MDA-MB-231) or Minimum essential medium (MEM; for MCF-7 cells) supplemented with 10% FCS, 100 U mL^{-1} penicillin and 100 µg mL^{-1} streptomycin (all components from Biochrom, Berlin, Germany) at 37 °C in a humidified atmosphere with 5% (v/v) CO_2.

Cells were seeded in 96-well plates (at a density of 1×10^3 cells per well for L929 and MDA-MB-231, and at a density of 3×10^3 cells per well for MCF-7) and were grown as monolayer cultures for 24 h. The cells were then incubated separately with different concentrations of differently formulated doxorubicin (0.01, 0.1, 1.00 and 10.00 µg mL^{-1} (n = 6)) for 24 h, 3 d and 6 d. After 3 d medium was removed and replaced by fresh medium containing doxorubicin. Control cells were incubated with culture medium.

After each incubation time, 50 µL of a XTT solution prepared according to the manufacturer's instructions were added to each well. After 4 h at 37 °C, 100 µL of each solution were transferred to a new microtiter, plate and the optical density (OD) was measured photometrically at 450 nm. The negative control was standardized as 0% of metabolism inhibition and referred to as 100% viability.

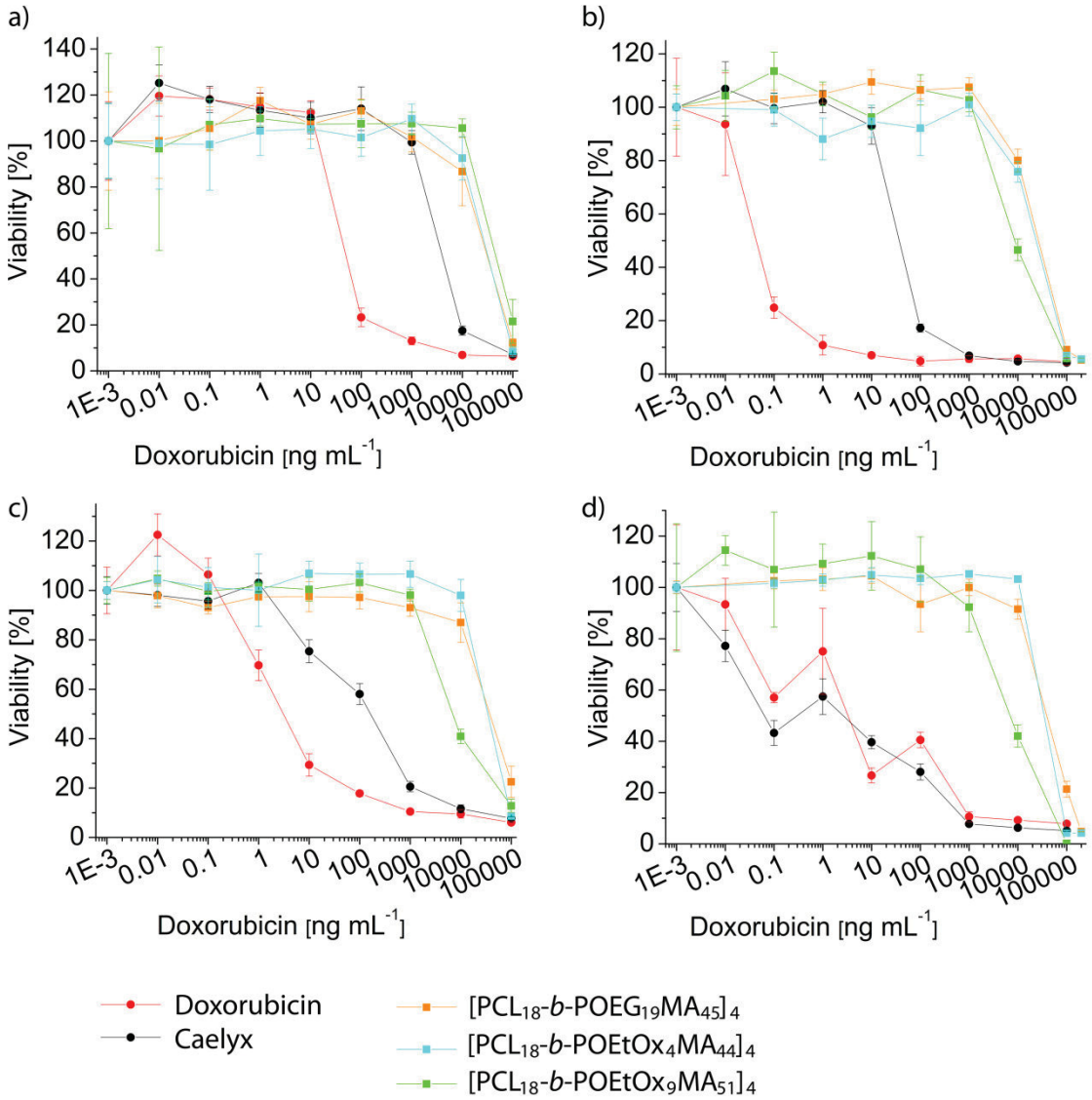

Figure S20. Cell viability of a) L929 mouse fibroblasts, b) HEK 293 cells, c) human breast carcinoma cells MCF7 and d) MDA-MB 231 cells after incubation with doxorubicin differently formulated for six days. Cells incubated with doxorubicin free culture medium served as control. The cell viability was determined by XTT assay. Data are expressed as mean ± SD of six determinations.

Microscopic observation on cellular uptake of doxorubicin and encapsulated doxorubicin. The cellular uptake and distribution of doxorubicin and encapsulated doxorubicin was evaluated using fluorescent microscopy (FM) and confocal laser scanning microscopy (CLSM). For the microscopic imaging, mouse fibroblast cell line L929, human MCF-7 and MDA-MB 231 breast cancer cell line were grown in 8-well Chamber Slide system (Thermo Scientific; Langenselbold, Germany) for 24 h and then incubated with doxorubicin, Caelyx and doxorubicin encapsulated by the $[PCL_{18}$-*b*-$POEtOx_9MA_{51}]_4$ polymer in a concentration of 10.00 µg mL^{-1} (n = 3) for another 24 h. Control cells were incubated with fresh culture medium. For FM, cell nuclei were then stained with Hoechst 33342 (1 µg mL^{-1}) and cells were analysed immediately using a fluorescence microscope (Cell Observer Z1, Carl Zeiss, Jena, Germany) equipped with a mercury arc UV lamp and the appropriate filter combinations for excitation and detection of emission of Hoechst 33342 and doxorubicin. All images were captured with a 10 × objective using identical instrument settings (e.g. UV lamp power, integration time, and camera gain) and spots were addressed using an automated XY table.

For CLSM, cytoplasma of the adherent cells was labeled using 10 µM CellTracker Orange CMRA (Life Technologies, Darmstadt, Germany) according to manufacture instructions and in the next step, cells were fixed for 10 min using PBS with 4% paraformaldehyde. For embedding fixed cells, Moviol 4-88 solution containing 625 µg 1,4-diazabicyclo-(2,2,2)octane (Roth, Karlsruhe, Germany) was used.

Fluorescence images were obtained with confocal laser-scanning microscopes (LSM 510 Meta, Zeiss, Jena, Germany), using a Epiplan Neofluar 20 × objective (NA 0.5 Zeiss). The 488 nm laser line was used for excitation of doxorubicin and emission was collected between 560 and 615 nm. The 543 nm line excited the CellTracker Orange CMRA and the emitted fluorescence was collected with a 560-615 nm bandpass filter. Images were captured in multitrack mode enabling single excitation and emission of fluorescence. To allow a comparison, all images of a series were captured under identical conditions and instrument settings (laser power, pinhole diameter and detector gain).

REFERENZES

(1) Weber, C.; Becer, C. R.; Baumgaertel, A.; Hoogenboom, R.; Schubert, U. S. *Des. Monomers Polym.* **2009**, *12*, 149–165.

(2) Baumgaertel, A.; Weber, C.; Knop, K.; Crecelius, A.; Schubert, U. S. *Rapid Commun. Mass Spectrom.* **2009**, *23*, 756–762.

(3) Knop, K.; Pavlov, G. M.; Rudolph, T.; Martin, K.; Pretzel, D.; Jahn, B. O.; Scharf, D. H.; Brakhage, A.; Schacher, F. H.; Schubert, U. S. *Soft Matter* **2013**, *9*, 715–726.

(4) Kataoka, K.; Kwon, G. S.; Yokoyama, M.; Okano, T.; Sakurai, Y. *J. Controll. Release* **1993**, *24*, 119–132.

(5) Xiong, X. B.; Falamarzian, A.; Garg, S. M.; Lavasanifar, A. *J. Controll. Release* **2011**, *155*, 248–261.

(6) Adams, M. L.; Lavasanifar, A.; Kwon, G. S. *J. Pharm. Sci.* **2003**, *92*, 1343–1355.

(7) Liu, H. B.; Jiang, A.; Guo, J. A.; Uhrich, K. E. *J. Polym. Sci., Part A: Polym. Chem.* **1999**, *37*, 703–711.

Publication P4:

Systematic MALDI-TOF CID investigation on different substituted mPEG 2000

K. Knop, B. O. Jahn, M. D. Hager, A. C. Crecelius, M. Gottschaldt, U. S. Schubert

Macromol. Chem. Phys. **2010**, *211*, 677–684.

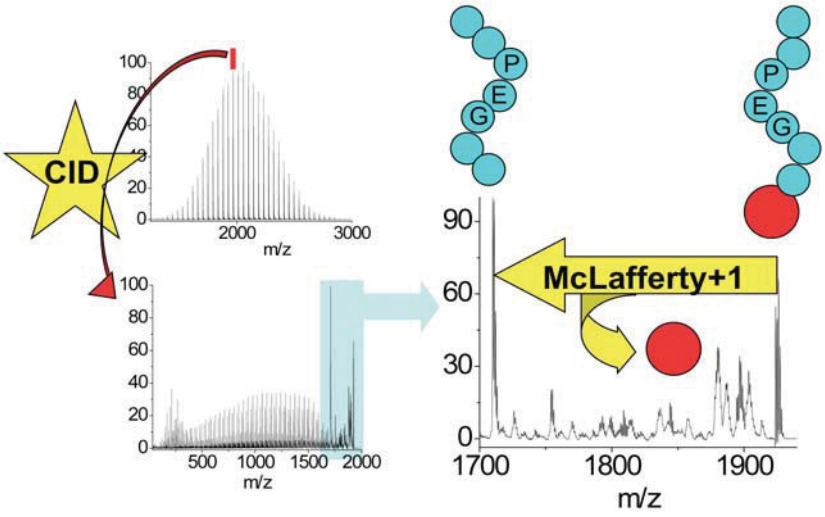

Systematic MALDI-TOF CID Investigation on Different Substituted mPEG 2000[a]

Katrin Knop, Burkhard O. Jahn, Martin D. Hager, Anna Crecelius, Michael Gottschaldt, Ulrich S. Schubert*

Methoxy poly(ethylene glycol) 2000 (mPEG 2000) samples were substituted via esterification reactions to convert the hydroxyl end group of the mPEG into potential initiators for the cationic ring opening polymerization of 2-oxazolines. These substitution products were investigated by matrix-assisted laser desorption/ionization time-of-flight mass spectrometry (MALDI-TOF MS); in addition, detailed MALDI-TOF/TOF-collision induced dissociation (CID) MS studies were performed to introduce this method as complementary structural characterization tool allowing the detailed analysis of the prepared macromolecules. The CID of the macroinitiators revealed 1,4-hydrogen and 1,4-ethylene eliminations forming very regular fragmentation patterns which showed, depending on the end groups, different fragmentation series. Furthermore, very pronounced McLafferty + 1 rearrangements (1,5 hydrogen-transfer) of the introduced ester end groups were observed leaving the mPEG molecule as neutral acid. This incisive loss revealed the exact molar mass for each end group and, therefore, represents an important tool for end group determination of functionalized polymers.

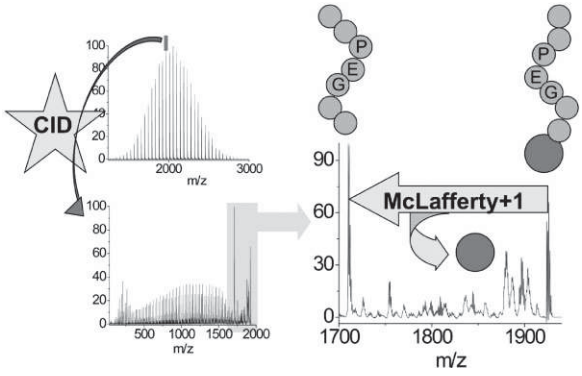

Introduction

In the emerging field of drug delivery, block copolymers are widely used for designing vectors with sufficient in vivo stability and delivery efficiency.[1] These biological applications of polymers require a very solid and profound characterization of the used materials beyond NMR spectroscopic methods and size exclusion chromatography (SEC). In the last few years mass spectrometry (MS) arose to a very versatile technique to acquire detailed information of the polymer structure and, in particular, of the end group nature.

In former times MS analysis of polymers has been a difficult task being limited to the analysis of low molar mass compounds.[2] This changed dramatically when Karas and Hillenkamp developed in the 1980s the matrix-assisted laser desorption ionization (MALDI) process and improved

K. Knop, B. O. Jahn, M. D. Hager, A. Crecelius, M. Gottschaldt, U. S. Schubert
Laboratory of Organic and Macromolecular Chemistry, Friedrich-Schiller-University Jena, Humboldtstr. 10, 07743 Jena, Germany
Fax. +49 3641 948 202; E-mail: ulrich.schubert@uni-jena.de
K. Knop, M. D. Hager, A. Crecelius, M. Gottschaldt, U. S. Schubert
Dutch Polymer Institute (DPI), John F. Kennedylaan 2, 5612 AB Eindhoven, The Netherlands
U. S. Schubert
Laboratory of Macromolecular Chemistry and Nanoscience, Eindhoven University of Technology, Den Dolech 2, 5600 MB Eindhoven, The Netherlands

[a] Supporting information for this article is available at the bottom of the article's abstract page, which can be accessed from the journal's homepage at http://www.mcp-journal.de, or from the author.

DOI: 10.1002/macp.200900309

therewith by far the analytical possibilities in polymer chemistry.[3–5]

Since then, a large variety of synthetic polymers has been investigated by MALDI-MS methods, such as polystyrene (PS) and poly(methyl methacrylate) (PMMA). Also poly(ethylene glycol) (PEG) is very well investigated by MALDI-MS techniques as it provides an easily ionizable structure.[6,7] To gain deeper insight into the polymer composition, tandem MS methods have been developed and applied to different synthetic polymers like PMMA, PS or poly(ethylene terephthalate) (PET).[8,9]

These new techniques have also been used for the fragmentation of different PEG samples. Methoxy poly(ethylene glycol) (mPEG) and dimethoxy poly(ethylene glycol) (2mPEG) of *m/z* 500 ionized with lithium have been fragmented in a fast-atom bombardment (FAB)-collision induced dissociation (CID)-quadrupole instrument. The authors presented the different stability of proton and sodium ion adducts and the following consequences for high and low energy collision processes as well as the fragmentation mechanisms.[10,11]

Equally, PEG 1000 was investigated by sustained-off-resonance-induction (SORI)-CID-Fourier transform (FT)-MS measurements and fragments with very high mass resolution were obtained and could be assigned.[12] Different mono- and disubstituted PEGs in the range of *m/z* 500 were investigated by the group of Williams et al. by using desorption electrospray ionization (DESI).[13]

The MALDI process was also used to obtain ions for post source decay (PSD). Already in 1994 a mechanism for the fragmentation of PEG was proposed by Selby et al. who investigated cyclic polyethers.[14] These 1,4-hydrogen- or 1,4-ethylene elimination mechanisms (Scheme 1) were confirmed by Jackson et al. who observed through fragmentation of PEG additional distonic radical cations, which were formed by homolytic bond cleavage.[15]

Kowalski et al. successfully performed MALDI-PSD analysis of linear and branched PEG 600 and 1500 and established thereby a method to differentiate between various polymer architectures.[4,16] Hoteling et al. fragmented with the aid of a MALDI-CID cell, unsubstituted PEG 1000 confirming therewith the fragmentations of PEG, which were already observed earlier by Lattimer and coworkers.[17]

In order to expand the tool box of block copolymers prepared for biological applications, PEG can be used as macroinitiator for the polymerization of 2-oxazolines. This polymerization can be performed via a microwave assisted cationic ring opening polymerization (CROP) and requires, as the name suggests, a cationic initiator.[18] For this purpose mPEG was converted to a macroinitiator via an esterification reaction of the end groups.[19] These macroinitiators were used for detailed mass spectrometrical and tandem MS investigations to gain insight into the structure

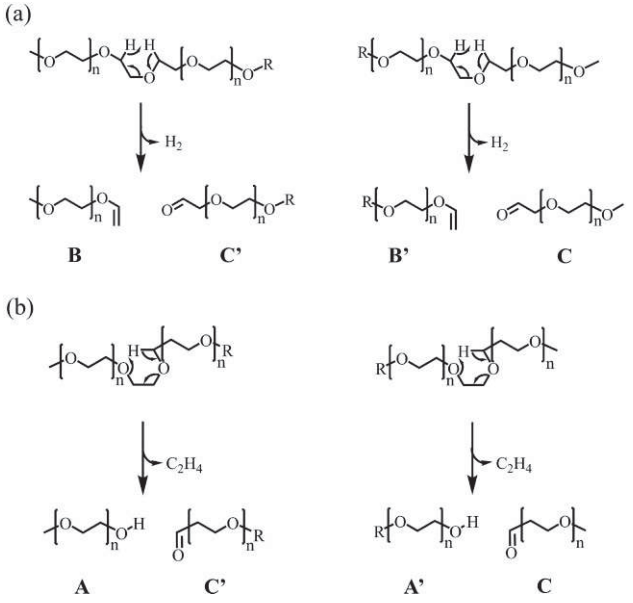

Scheme 1. Schematic representation of the observed fragment series resulting from (a) 1,4-hydrogen elimination mechanism and (b) 1,4 ethylene-elimination mechanism of mPEG.

and to facilitate later the interpretation of the fragmentation behavior of block copolymers, which is still a challenging task.

In this study we performed the synthesis and the fragmentation of substituted mPEG samples (esterified) by MALDI-TOF-MS/MS to obtain detailed information on the molecular structure and the decomposition mechanism of the polymerization precursors. We obtained for the first time a detailed MALDI-TOF CID analysis of the fragmentation of substituted mPEG samples with higher molar masses.

Experimental Part

Materials

mPEG 2000 was purchased from Fluka, triethylamine, 4-(bromomethyl) benzoyl bromide, 4-(chloromethyl) benzoyl chloride and 4-toluenesulfonyl chloride were purchased from Aldrich and used as received unless otherwise stated. Triethylamine was stored over potassium hydroxide and distilled from calcium hydride prior to use. mPEG 2000 was coevaporated with dry toluene (distillation from sodium/benzophenone) before usage and highest available purity grade dichloromethane was purchased from Fluka. The substitution reaction was carried out according to the reported procedure[20] and the products were characterized by ^{1}H NMR spectroscopy, SEC, and MALDI-TOF MS.

α-Methoxy-ω-4-(chloromethyl) benzoic acid ester-poly(ethylene glycol) 2 000: ^{1}H NMR (250 MHz, $CDCl_3$): δ(ppm) = 7.99 (d, 2H), 7.40 (d, 2H), 4.55 (s, 2H), 4.40 (t, 2H), 3.76 (t, 2H), 3.60–3.65 (m, 171H), 3.31 (s, 3H) (Figure S1 of Supporting Information).

Macromol. Chem. Phys. **2010**, *211*, 677–684

Macromolecular Journals

DOI: 10.1002/macp.200900309

SEC: $\overline{M}_n = 1\,760\ g \cdot mol^{-1}$, $\overline{M}_w = 2\,010\ g \cdot mol^{-1}$, PDI = 1.1.

α-Methoxy-ω-4-(bromomethyl) benzoic acid ester-poly(ethylene glycol) 2 000: ^{1}H NMR (250 MHz, $CDCl_3$): δ(ppm) = 8.01 (d, 2H), 7.44 (d, 2H), 4.49–4.44 (m, 4H), 3.81 (t, 2H), 3.62–3.67 (m, 186H), 3.36 (s, 3H) (Figure S2 of Supporting Information).

SEC: $\overline{M}_n = 1\,700\ g \cdot mol^{-1}$, $\overline{M}_w = 1\,870\ g \cdot mol^{-1}$, PDI = 1.1.

α-Methoxy-ω-4-toluenesulfonyl-poly(ethylene glycol) 2 000: ^{1}H NMR (250 MHz, $CDCl_3$): δ(ppm) = 7.77 (d, 2H), 7.32 (d, 2H), 4.13 (t, 2H), 3.61–3.67 (m, 176H), 3.35 (s, 3H) (Figure S3 of Supporting Information).

SEC: $\overline{M}_n = 1\,920\ g \cdot mol^{-1}$, $\overline{M}_w = 2\,070\ g \cdot mol^{-1}$, PDI = 1.1.

For MALDI-TOF MS and MS/MS measurements the matrix material, *trans*-2-[3-(4-*tert*-butylphenyl)-2-methyl-2-propen-ylidene] malononitrile (DCTB) and sodium chloride (NaCl) were obtained from Sigma Aldrich. Lithium chloride (LiCl) and sodium bromide (NaBr) were obtained from Acros Organics. Tetrahydrofuran (THF) of HPLC grade was purchased from Roth and used as received. Bio-beads® S-X3 were obtained from BioRad (Hercules, CA, USA) and prepared in THF according to the supplier's instructions.

Instrumentation

NMR experiments were performed with a Bruker AC 250. Chemical shifts are reported as δ values relative to TMS, defined as $\delta = 0.00$ ppm (^{1}H NMR).

Size exclusion chromatography (SEC) was performed on a Shimadzu system equipped with a SCL-10A system controller, a LC-10AD pump and a RID-10A refractive index detector using a solvent mixture containing chloroform, triethylamine and *iso*-propanol (94:4:2) at a flow rate of $1\ mL \cdot min^{-1}$ on a PSS-SDV-linear M 5 μm column at room temperature. The system was calibrated with PEG standards purchased by PSS Standard.

An Ultraflex III TOF/TOF (Bruker Daltonics, Bremen, Germany) was used for the MALDI-TOF-MS and MS/MS analysis. The instrument was equipped with a Nd:YAG laser and a collision cell. All spectra were measured in the positive reflector mode. For the MS/MS mode, argon was used as the collision gas at a pressure of 2×10^{-6} mbar. The FWHM was calculated to lay in a range between 1 500 for the lower region of the mass spectrum and 3 000 for the higher *m/z* region of the spectra. The instrument was calibrated prior to each measurement with an external standard PMMA from PSS Polymer Standards Services GmbH (Mainz, Germany). MS and MS/MS data were processed using PolyTools 1.0 (Bruker Daltonics) and Data Explorer 4.0 (Applied Biosystems).

Sample Preparation

For the sample preparation, 1 μL of substituted mPEG 2 000 (10 mg mL^{-1}) in THF, 10 μL of DCTB (10 mg mL^{-1}) in THF and 5 μL of lithium chloride, sodium chloride or sodium bromide dissolved in THF at a concentration of $100\ mg \cdot mL^{-1}$ were mixed and the dried-droplet sample preparation method was applied.

Results and Discussion

In order to prepare block copolymers of PEG and poly(2-oxazolines) the hydroxyl end group of mPEG needs to be converted into an initiator for the CROP. Therefore, mPEG 2000 was substituted by esterification reaction with end groups which are suitable as initiators,[19] such as benzyl bromide, benzyl chloride, or tosylate. The reactions with 4-(bromomethyl) benzoyl bromide, 4-(chloromethyl) benzoyl chloride, and toluene sulfonyl chloride yield polymers with the desired end groups; the reactions were performed according to a reported literature procedure.[20] To ensure a full conversion of mPEG the reaction was monitored by MALDI MS, revealing a complete substitution with 4-(bromomethyl) benzoyl bromide after 1 h reaction time and with 4-(chloromethyl) benzoyl chloride as well as toluene sulfonyl chloride after 4 h, respectively.

The reaction products were washed with water and purified by chromatography using a Biobeads column. The converted mPEG samples were characterized by ^{1}H NMR spectroscopy, SEC and MALDI-TOF MS. Whereas the SEC data showed a retention of the molar mass during the reaction, the full conversion of each mPEG sample was confirmed in addition to the MALDI monitoring by ^{1}H NMR spectroscopy within the proton NMR accuracy.

Tosylated mPEG

The MALDI-TOF spectra were measured in reflector mode and contained two distributions for the reaction product of the conversion of mPEG with toluene sulfonyl chloride. Both showed within themselves peak distances of *m/z* 44 corresponding to the PEG repeating unit (Figure 1a). The smaller distribution was shifted by 16 *m/z* units to larger values in comparison to the main distribution. Therefore, both distributions could be assigned to the desired reaction product: the ones ionized with sodium represent the main distribution and the ones ionized with potassium the other, less intense distribution.

For the tandem MS investigations a precursor ion with 38 repeating units was chosen (Figure 1b) and the investigations were performed with lithium chloride and sodium chloride as ionizing agents. The CID spectra showed no differences between sodium and lithium ionized tosylated mPEG except the cation attached, therefore only results obtained with sodiated adducts are presented.

The CID spectrum can be divided into three parts with different emerging fragmentation mechanism respectively as shown in Figure 1c, e and f and presented in the following. In the upper molar mass region of the MS/MS spectrum right after the parent ion a very pronounced loss of small fragments is observed. A zoom into that region revealed the loss of 171.975 (Figure 1c). This neutral loss can be assigned to the corresponding acid of the sulfonic acid ester end group of the substituted mPEG. The very prominent and distinct fragmentation can be explained by a McLafferty + 1 rearrangement (1,5 hydrogen-transfer)[21] that involves the sulfonic acid ester bond leading to the

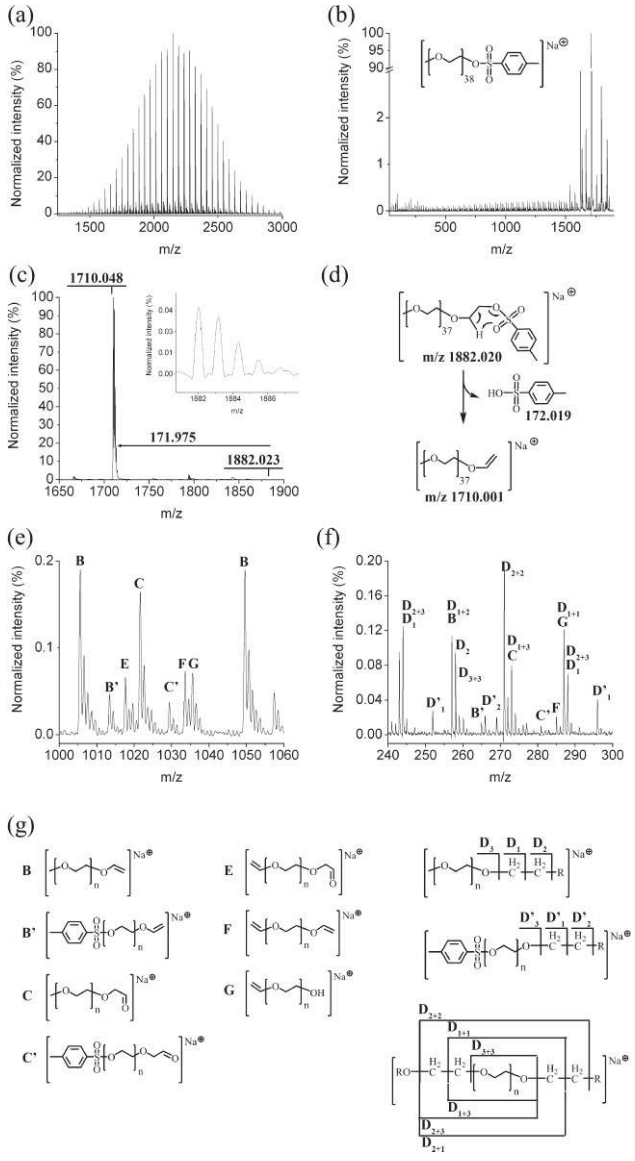

Figure 1. (a) MALDI-TOF spectrum of tosylated mPEG; (b) CID mass spectrum of the parent peak with 38 repeating units (marked with a bar in (a)); (c) zoom into the MS/MS spectrum below the parent peak showing the distinct loss of toluene sulfonic acid (inset: zoom into parent ion); (d) schematic representation of the proposed mechanism for cleavage of the sulfonic acid ester bond; (e) zoom into the MS/MS spectrum at *m/z* values between 1 000 and 1 060 with marked observed fragment series; (f) zoom into the MS/MS spectrum at *m/z* values between 240 and 300 with marked observed fragment series; (g) schematic representation of the observed fragments.

cleavage of the toluene sulfonic acid and the formation of a vinyl ether end group at the PEG chain with a *m/z* value of 1710.048, as observed previously by different groups (Figure 1d).[22–25]

This peak at *m/z* 1710.048 marks the beginning of the fragment series B that can be followed down to *m/z* 125.020. The B series, as well as the C series, are part of different fragment distributions forming eye catching regular structures in the middle molar mass region of the CID spectrum that are certainly much lower in intensity in comparison to the 1,5 hydrogen-transfer (Figure 1e). These series are formed by 1,4-elimination mechanisms, which were already proposed by Lattimer and coworkers and Jackson et al. (Scheme 1).[13–15] Interestingly, the corresponding B′ and C′ fragment series for the 1,4-hydrogen elimination were observed to occur with much lower intensities.

Furthermore, three other fragment series can be observed in the spectrum, which are formed by two subsequently following fragmentations (Figure 1g). Fragment series E and F are formed by 1,4-hydrogen eliminations at both ends of the substituted mPEG molecule or by 1,5 hydrogen-transfer combined with an 1,4-hydrogen elimination. The hydroxyl group of fragment series G is formed by 1,4-ethylene fragmentation. Additionally, to form the series G, 1,4-hydrogen elimination or 1,5 hydrogen-transfer occurs at the other end group of the PEG chain.

In the lower molar mass region, below *m/z* 500, the appearance of the CID spectrum changes as more fragments can be observed (Figure 1f). They can be attributed to distonic radical cations, which are formed either by single homolytic bond cleavage or multiple bond cleavages (Figure 1g).[13,14]

p-(Chloromethyl)-benzoic Acid Ester of mPEG

For the benzyl chloride substituted mPEG the MALDI MS spectra showed only one distribution with the PEG repeating unit of *m/z* 44. The molar masses of the peaks could be assigned to the sodium adducts of the substituted mPEG and, additionally, the isotops of the peaks provided with their distinct chlorine structures a further prove of the substitution reaction (Figure 2a).

The CID experiments were carried out with the parent ion that possessed 38 repeating units and sodium as ionizing agent for better comparability. The benzyl chloride substituted mPEG MALDI MS and tandem MS investigations were carried out in addition with lithium as doping salt. Since the spectra showed – like the tosylated mPEG – no differences compared to the sodium ionized samples, only the prior will be shown and discussed (Figure 2b).

Corresponding to the tosylate substituted sample a division into three parts can be observed. In the upper molar mass region a very distinct neutral loss right after the precursor ion was observed, besides the intense unspecific small fragments of *m/z* 14 and *m/z* 25 (Figure 2c). As this mass loss of *m/z* 170.013 and *m/z* 172.010 corresponds to the *p*-(chloromethyl)-benzoic acid with ^{35}Cl and ^{37}Cl, respectively, a 1,5 hydrogen-transfer is proposed leading, like in the case of tosylated mPEG, to the fragment with *m/z* 1710.102 (Figure 2d).[22–25] Furthermore, the loss of

Macromol. Chem. Phys. **2010**, *211*, 677–684

Macromolecular Journals

DOI: 10.1002/macp.200900309

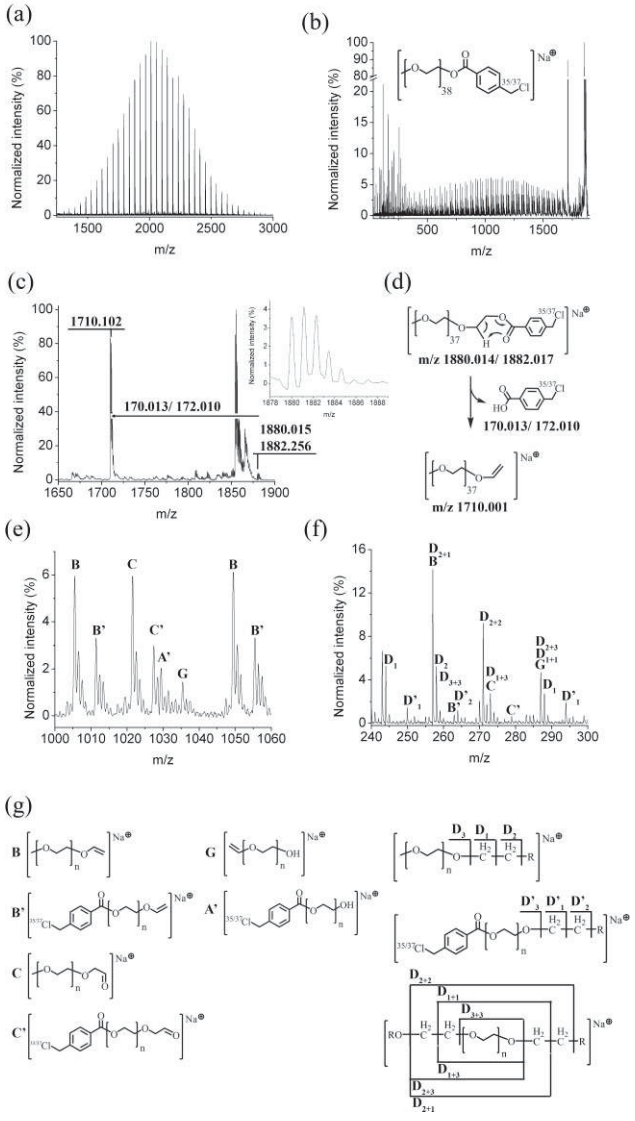

Figure 2. (a) MALDI-TOF spectrum of benzyl chloride substituted mPEG; (b) CID mass spectrum of the parent peak with 38 repeating units (marked with a bar in (a)); (c) zoom into the MS/MS spectrum below the parent peak showing the distinct loss of 4-(chloromethyl) benzoic acid (inset: zoom into parent ion); (d) schematic representation of the proposed mechanism for cleavage of the 4-(chloromethyl) benzoic acid ester bond; (e) zoom into the MS/MS spectrum at *m/z* values between 1 000 and 1 060 with marked observed fragment series; (f) zoom into the MS/MS spectrum at *m/z* values between 240 and 300 with marked observed fragment series; (g) schematic representation of the observed fragments.

the chlorine atom within the acid is underlined by the loss of the chlorine isotopic pattern.

The CID spectrum shows within the middle molar mass region regular series of fragments with intensities below the 1,5 hydrogen-transfer corresponding to fragment series formed by different 1,4-eliminations discussed already by Lattimer coworkers and Jackson et al. (Scheme 1).[14,15]

Again, the dominant fragment series occurring in the middle region of the CID spectrum are formed by 1,4-hydrogen elimination leading to the B and C series that show the methoxy end group of the parent ion and the ethylene ether end group for the B series and the aldehyde end group for the C series (Figure 2e).

Accompanying to the B, B' and C, C' series the A' series is observed with the C series as corresponding opposite fragment (Scheme 1), but no fragments of the A series could be assigned. The series F as product of 1,4-ethylene fragmentation and either 1,4-hydrogen elimination or 1,5 hydrogen-transfer was observed (Figure 2g). In contrast to tosylated mPEG a series A' was observed which still includes the functionalized end group, since the substituted benzoates are less efficient leaving groups.

The region below *m/z* 500 shows multiple fragments, which can be assigned as distonic radical cations, which are formed either by single homolytic bond cleavage or multiple bond cleavages (Figure 1f and g).[13,14]

p-(Bromomethyl)-benzoic Acid Ester of mPEG

The benzyl bromide substitution of mPEG delivers after a very short reaction time a MALDI MS spectrum that contains only one distribution, ionized with sodium. The product peaks showed additionally the very characteristic bromine isotopic patterns (Figure 3a).

Collision induced fragmentation studies were performed on the precursor ion with 38 repeating units and delivered a very prominent loss of *m/z* 213, like already observed for the previous mPEG samples (Figure 3b and c). This mass loss corresponds with the neutral loss of 4-(bromomethyl) benzoic acid caused by a 1,5 hydrogen-transfer (further confirmed by the change of the characteristic bromine isotopic pattern) to a carbon pattern (Figure 3d).[22–25]

In the middle molecular mass region regular series of fragments with lower intensities than the 1,5 hydrogen-transfer were found belonging to fragment series formed by different 1,4-elimination mechanisms discussed already above (Scheme 1).[14,15]

In the case of benzyl bromide substituted mPEG only the B and C series with the corresponding B' and C' series were observed. Whereas the B and C series, not bearing the benzyl bromide group, provide the most intense peaks, the B' and C' series showed the characteristic bromine isotopic pattern in accordance with the fragmentation mechanism. Interestingly, no fragments could be detected that were derived from multiple fragmentations although the applied collision energy was sufficient to induce multiple fragmentations on tosylated and benzyl chloride substituted mPEG (Figure 3e and g).

One new fragment series was detected formed by a backbiting mechanism that substitutes the bromine (Figure 3g). This induced fragmentation, caused by the

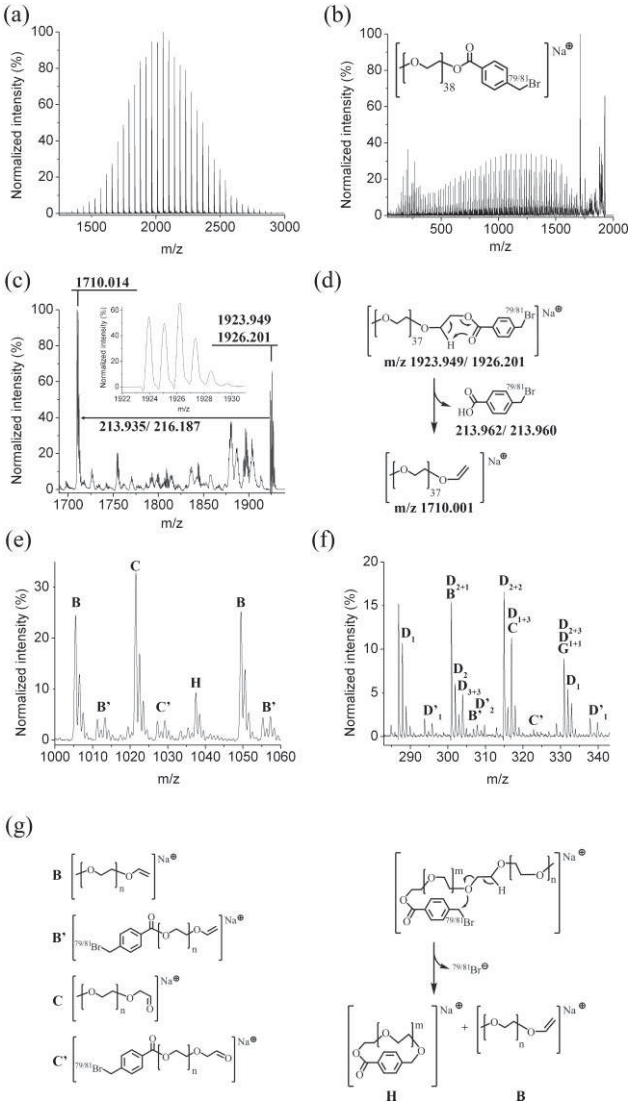

Figure 3. (a) MALDI-TOF spectrum of benzyl bromide substituted mPEG; (b) CID mass spectrum of the parent peak with 38 repeating units (marked with a bar in (a)); (c) zoom into the MS/MS spectrum below the parent peak showing the distinct loss of 4-(bromomethyl) benzoic acid (inset: zoom into parent ion); (d) schematic representation of the proposed mechanism for cleavage of the 4-(bromomethyl) benzoic acid ester bond; (e) zoom into the MS/MS spectrum at *m/z* values between 1000 and 1060 with marked observed fragment series; (f) zoom into the MS/MS spectrum at *m/z* values between 240 and 300 with marked observed fragment series; (g) schematic representation of the observed fragments (D fragments correspond to Fig. 3 substituted with Br, respectively).

very good leaving group quality of bromine, leads to the cyclic structure H and the fragment series B. This additional fragmentation pathway could be observed, in comparison to benzyl chloride substituted mPEG, due to the higher lability of bromine induced by the higher pK_a value of the corresponding acid.

The region of the CID spectrum below *m/z* 500 shows distonic radical cations formed by single homolytic or multiple bond cleavages (Figure 1f).[13,14]

Comparison of the CID Spectra

For the three end group modification reactions a full conversion was achieved proven by ^{1}H NMR spectroscopy as well as MALDI-TOF MS (Figures 1a, 2a and 3a). The MALDI-TOF MS and the MALDI-CID investigations were performed with sodium and lithium as doping salt. Although otherwise reported no difference in signal-to-noise ratio or ion abundance was observed in these cases, possibly caused by the higher *m/z* value of the precursor ions.[22]

For the three different substituted mPEGs the parent peak with 38 repeating units was chosen for the CID experiments. After acid cleavage the same resulting mPEG fragments with the same mass occurred. These very prominent and in the three tandem MS spectra very characteristic acid cleavages are proposed to occur via a 1,5 hydrogen-transfer, as already observed by different groups.[22–25]

For the halogen substituted mPEG precursor ions the loss of the characteristic bromine and respectively chlorine isotopic pattern in the formed 1,5 hydrogen-transfer product at *m/z* 1710 can be observed, which now only show the carbon isotopic pattern.

This mechanism is presented in Figures 1d, 2d, and 3d as concerted reaction although it is not yet clarified whether this mechanism occurs in a concerted or a step-wise electron rearrangement.[26] In MS of small molecules McLafferty + 1 rearrangements are supposed to occur in a charge-induced mechanism. For polymer fragmentation in general and for PEG ionized with sodium in particular, usually a charge-remote mechanism is assumed as ionization of the chains happens in general via the attachment of an ion.[10] Interestingly, the hereby proposed 1,5 hydrogen-transfers occur as charge-remote mechanisms in accordance with the following observation.

For all three substituted mPEG samples regular fragmentation series in the middle molar mass region were observed which are much less intense than the peak obtained by the 1,5 hydrogen-transfer acid cleavage. This difference in intensity between fragments formed during 1,5 hydrogen-transfer and fragments formed during 1,4-elimination can be explained by the energy requirement for these two rearrangements. Although a collision cell is a high energy device and delivers more than enough energy for both mechanisms, apparently, the internal energy conversion leading to a 1,5 hydrogen-transfer associated with the loss of the acid end group occurs more efficient than the energy conversion that is followed by an elimination reaction. Subsequently, it can be deduced that for collision-

Macromol. Chem. Phys. **2010**, *211*, 677–684

Macromolecular Journals

DOI: 10.1002/macp.200900309

induced fragmentation these ester bonds are more easily cleaved than ether bonds corresponding to the general expectation.

A comparison of the CID spectra of polymers with the three end groups (Figures 1b, 2b and 3b) shows also that the intensity of the 1,4-elimination fragments in comparison to the 1,5 hydrogen-transfer peak differs. Whereas tosylate substituted mPEG delivers very low intense 1,4-elimination fragments at only 0.2% normalized intensity, benzyl chloride substituted mPEG shows normalized intensities at 6% and benzyl bromide substituted mPEG delivers values of about 30% normalized intensity. This observation can be explained by the leaving group quality of the end group. Tosylate provides the best leaving group qualities of the three examples leading to a preferred and dominant McLafferty loss. This probably early rearrangement leaves time for further fragmentations explaining the relative high amount of fragments that were derived from multiple dissociations. Ester bonds are not as good leaving groups as tosylate groups; therefore relatively to the 1,5 hydrogen-transfer the 1,4-eliminations occur more often. Apparently, the exchange of the chlorine with the bromine makes a large difference in the fragmentation probability, which can not yet be explained.

In general, the intensity of the two fragments formed during one process should be the same.[21] Nevertheless, it can be clearly observed in the Figures 1e, 2e and 3e that the fragments not bearing the introduced end groups (B and C series) are much more intense, than the ones still holding the introduced end group (series B' and C'). For this observation a possible explanation is connected with the localization of the ionizing sodium on the polymer chain. The ionization of PEG molecules with sodium occurs by coordination of the ion with up to eight oxygen atoms of the polymer chain.[27] As the ester end group might disturb this coordination, the complexation at the methoxy ends of the mPEG molecules might be energetically more favorable and is therefore as ionized fragment more stable during rearrangement and potential following secondary reactions. As the elimination occurs with charge-remote mechanism, the sodium complexed methoxy end remains hence the part of the fragmented molecule, which is detected.

For clarification, density functional theory (DFT) calculations were performed at the B3LYP[28] level of theory in combination with the split valence basis set 6-311 + G(2d,2p) with the aid of the Gaussian03 program package.[29] Energies are given as thermal enthalpies. The *p*-(chloromethyl)-benzoic acid ester and the tosylated mPEG with eight repeating units were used as model systems of the polymer chain. The results show a large difference in energy of over 200 $kJ \cdot mol^{-1}$ between the sodium complex with a crown-shaped mPEG chain and the complexation via the ester end group of a linear polymer chain (Figure 4). In case of the linear mPEG the sodium is situated at the carbonyl oxygen atom of the ester end group. However, the calculations of different geometries of the complex with the crown-shaped PEG chain showed a negligible divergence between the methoxy end group and the ester end group as the top of the crown-shaped complex in comparison to the linear model. In both cases the complex with the ester end group is slightly preferred (p-(chloromethyl)-benzoic acid ester of mPEG $\Delta E = 6$ $kJ \cdot mol^{-1}$; tosylated mPEG $\Delta E = 4$ $kJ \cdot mol^{-1}$). Although the linear model describes only a border case it shows on the one hand, that the MacLafferty + 1 rearrangement might occur more probably via charge-remote mechanism and on the other

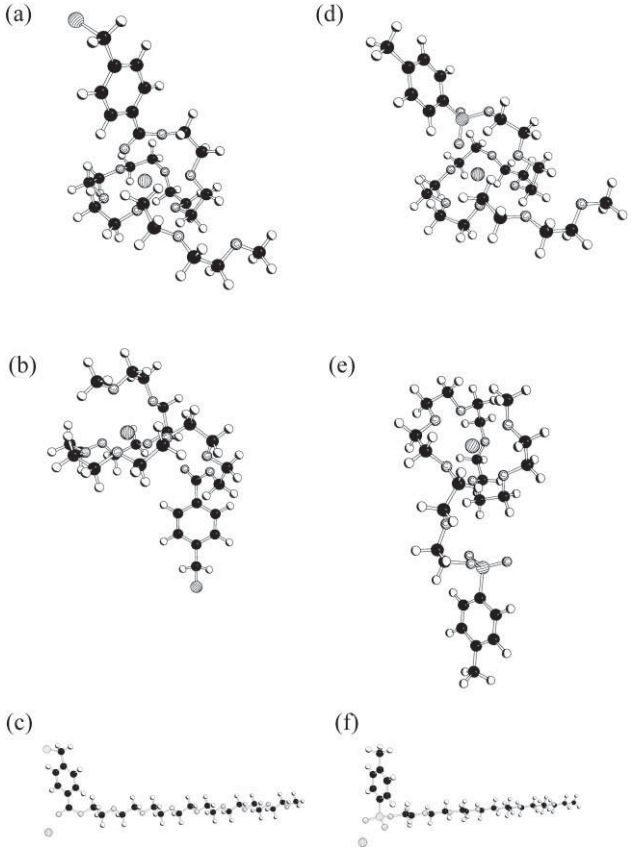

Figure 4. Calculated structures of the ionized sodium adducts with eight repeating units optimized at the B3LYP/6-311 + G(2d,2p) level of theory. Atom descriptions are as follows: coiled: oxygen; black: carbon; white: hydrogen; transverse striped: chlorine resp. sulfur; longitudinal striped: sodium; (a) p-(chlormethyl)-benzoic acid ester, carbonyl group topped crown-shaped sodium complex; (b) p-(chlormethyl)-benzoic acid ester, methoxy topped crown-shaped sodium complex, $\Delta E = 6$ $kJ \cdot mol^{-1}$ in relation to (a); (c) p-(chlormethyl)-benzoic acid ester, linear polymer chain, $\Delta E = 220 \cdot kJ \cdot mol^{-1}$ in relation to (a); (d) tosylated mPEG, carbonyl group topped crown-shaped sodium complex; (e) tosylated mPEG, methoxy topped crown-shaped sodium complex, $\Delta E = 4$ $kJ \cdot mol^{-1}$ in relation to (d); (f) tosylated mPEG, linear polymer chain, $\Delta E = 217$ $kJ \cdot mol^{-1}$ in relation to (d).

hand, that the complexation of the sodium ion by carbonyl group is less favorable.

Distonic radical cations of the fragmented PEG samples were only observed in the lower molar mass region below about *m/z* 500 leading to a rather unspecific overlay of multiple fragments in this range.

Conclusion

mPEG was substituted with different end groups linked by an ester bond. Tandem MS investigations yielded in the middle and the upper molar mass region of the spectra fragments with high analytical value. By 1,5 hydrogen-transfer the end groups introduced by polymer analogs reactions were cleaved off in a very efficient and characteristic way revealing the exact mass of the end group and providing thereby very direct information on the end group nature.

Further, in-detail examinations of the spectra revealed the different leaving group qualities of the end groups and a preferentially ionization during the MALDI process by the PEG chain as a crown ether-shaped complex rather than the carbonyl group of the ester end group. These findings were supported by DFT calculations of the different possible complexation geometries. With these examples of substituted mPEGs MALDI-TOF MS and MS/MS were proven to represent a powerful combination of tools to investigate synthetic polymers and polymer analogs reactions and to elucidate the conversion as well as the exact structure of the reaction products. This study effectively shows that a combination of MALDI-MS and CID fragmentation greatly facilities the determination of end group and architectural modifications to synthetic polymers.

Acknowledgements: The authors wish to acknowledge the *Dutch Polymer Institute* (DPI, technology area high-throughput-experimentation) and the *Thüringer Kultusministerium* (grant no. B515-07008) for the financial support of this study. Many thanks are also expressed to *Bruker Daltonik GmbH* for their cooperation.

Received: June 22, 2009; Revised: October 29, 2009; Published online: January 22, 2010; DOI: 10.1002/macp.200900309

Keywords: block copolymers; CID; collision induced dissociation; mass spectrometry; matrix-assisted laser desorption/ionization mass spectrometry (MALDI MS); poly(ethylene glycol)

[1] G. Gaucher, M.-H. Dufresne, V. P. Sant, Ning Kang D. Maysinger, J.-C. Leroux, *J. Controlled Release* **2005**, *109*, 169.
[2] H.-R. Schulten, R. P. Lattimer, *Mass Spectrom. Rev.* **1984**, *3*, 231.
[3] S. D. Hanton, *Chem. Rev.* **2001**, *101*, 527.
[4] M. W. F. Nielen, *Mass Spectrom. Rev.* **1999**, *18*, 309.
[5] A. C. Crecelius, A. Baumgaertel, U. S. Schubert, *J. Mass Spectrom.* **2009**, *44*, 1277.
[6] G. Montaudo, M. S. Montaudo, C. Puglisi, F. Samperi, *Macromolecules* **1995**, *28*, 4562.
[7] St. Weidner, G. Kuehn, *Rapid Commun. Mass Spectrom.* **1996**, *10*, 942.
[8] J. H. Scrivens, A. T. Jackson, *Int. J. Mass Spectrom.* **2000**, *200*, 261.
[9] P. M. Peacock, C. N. McEwen, *Anal. Chem.* **2004**, *76*, 3417.
[10] R. P. Lattimer, H. Münster, H. Budzikiewicz, *Int. J. Mass Spectrom. Ion Processes* **1989**, *90*, 119.
[11] R. P. Lattimer, *J. Am. Soc. Mass Spectrom.* **1994**, *5*, 1072 and references therein.
[12] S. J. Pastor, C. L. Wilkins, *Int. J. Mass Spectrom.* **1998**, *175*, 81.
[13] J. P. Williams, G. R. Hilton, K. Thalassinos, A. T. Jackson, J. H. Scrivens, *Rapid Commun. Mass Spectrom.* **2007**, *21*, 1693.
[14] T. L. Selby, C. Wesdemiotis, R. P. Lattimer, *J. Am. Soc. Mass Spectrom.* **1994**, *5*, 1081.
[15] A. T. Jackson, H. T. Yates, J. H. Scrivens, G. Critchley, J. Brown, M. R. Green, R. H. Bateman, *Rapid Commun. Mass Spectrom.* **1996**, *10*, 1668.
[16] P. Kowalski, C. Guttman, W. Wallace, *Proc. ASMS Conf. Mass Spectrom. Allied Topics* **1998**, *46*, 1060.
[17] A. J. Hoteling, K. Kawaoka, M. C. Goodberlet, W.-M. Yu, K. G. Owens, *Rapid Commun. Mass Spectrom.* **2003**, *17*, 1671.
[18] R. Hoogenboom, F. Wiesbrock, H. Huang, M. A. M. Leenen, H. M. L. Thijs, S. F. G. M. van Nispen, M. van der Loop, C.-A. Fustin, A. M. Jonas, J.-F. Gohy, U. S. Schubert, *Macromolecules* **2006**, *39*, 4719.
[19] M. W. M. Fijten, R. Hoogenboom, U. S. Schubert, *J. Polym. Sci., Part A: Polym. Chem.* **2008**, *46*, 4804.
[20] K. Jankova, X. Chen, J. Kops, W. Batsberg, *Macromolecules* **1998**, *31*, 538.
[21] F. W. McLafferty, F. Turecek, "*Interpretation of Mass Spectra*", 2nd edition, University Science Books, Mill Valley 1993, p 82.
[22] A. T. Jackson, M. R. Green, R. H. Bateman, *Rapid Commun. Mass Spectrom.* **2006**, *20*, 3542.
[23] A. R. Bottrill, A. E. Giannakopulos, C. Waterson, D. M. Haddelton, K. S. Lee, P. J. Derrick, *Anal. Chem.* **1999**, *71*, 3637.
[24] A. T. Jackson, S. E. Slade, K. Thalassinos, J. H. Scrivens, *Anal. Bioanal. Chem.* **2008**, *392*, 643.
[25] R. Chen, X. Yu, L. Li, *J. Am. Soc. Mass Spectrom.* **2002**, *13*, 888.
[26] D. J. McAdoo, C. E. Hudson, M. Skyiepal, E. Broido, L. L. Griffin, *J. Am. Chem. Soc.* **1987**, *109*, 7648.
[27] J. Gidden, T. Wyttenbach, A. T. Jackson, J. H. Scrivens, M. T. Bowers, *J. Am. Chem. Soc.* **2000**, *122*, 4692.
[28] P. J. Stephens, F. J. Devlin, C. F. Chablowski, M. Frisch, *J. Phys. Chem.* **1994**, *98*, 11623, and references cited therein.
[29] Gaussian 03, Revision C.02, M. J. Frisch, G. W. Trucks, H. B. Schlegel, G. E. Scuseria, M. A. Robb, J. R. Cheeseman, J. A. Montgomery, Jr., T. Vreven, K. N. Kudin, J. C. Burant, J. M. Millam, S. S. Iyengar, J. Tomasi, V. Barone, B. Mennucci, M. Cossi, G. Scalmani, N. Rega, G. A. Petersson, H. Nakatsuji, M. Hada, M. Ehara, K. Toyota, R. Fukuda, J. Hasegawa, M. Ishida, T. Nakajima, Y. Honda, O. Kitao, H. Nakai, M. Klene, X. Li, J. E. Knox, H. P. Hratchian, J. B. Cross, V. Bakken, C. Adamo, J. Jaramillo, R. Gomperts, R. E. Stratmann, O. Yazyev, A. J. Austin, R. Cammi, C. Pomelli, J. W. Ochterski, P. Y. Ayala, K. Morokuma, G. A. Voth, P. Salvador, J. J. Dannenberg, V. G. Zakrzewski, S. Dapprich, A. D. Daniels, M. C. Strain, O. Farkas, D. K. Malick, A. D. Rabuck, K. Raghavachari, J. B. Foresman, J. V. Ortiz, Q. Cui, A. G. Baboul, S. Clifford, J. Cioslowski, B. B. Stefanov, G. Liu, A. Liashenko, P. Piskorz, I. Komaromi, R. L. Martin, D. J. Fox, T. Keith, M. A. Al-Laham, C. Y. Peng, A. Nanayakkara, M. Challacombe, P. M. W. Gill, B. Johnson, W. Chen, M. W. Wong, C. Gonzalez, J. A. Pople, Gaussian, Inc., Wallingford CT, 2004.

DOI: 10.1002/macp.200900309

Publication P5:

Block length determination of the block copolymer mPEG-*b*-PS using MALDI-TOF MS/MS

A. C. Crecelius, C. R. Becer, K. Knop, U. S. Schubert

J. Polym. Sci., Part A: Polym. Chem. **2010**, *48*, 4375–4384.

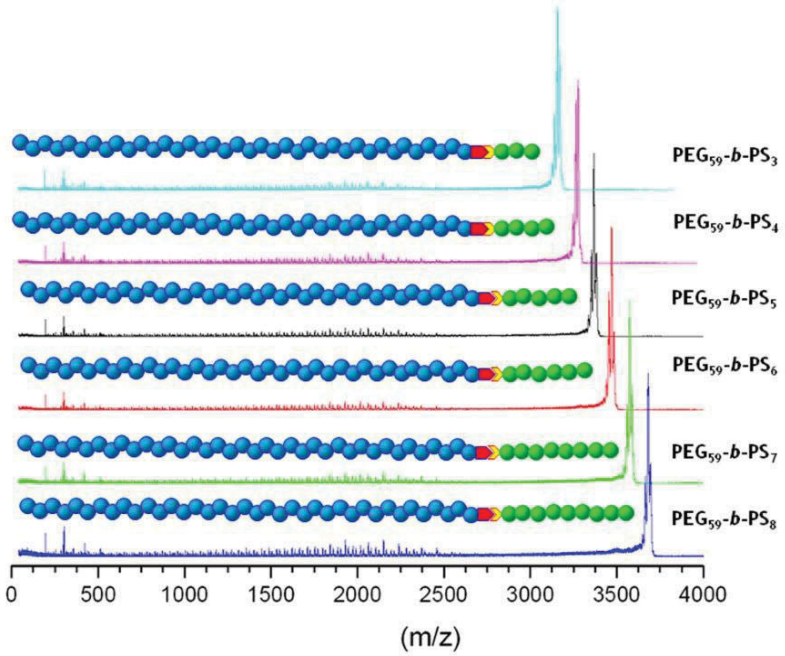

Block Length Determination of the Block Copolymer mPEG-*b*-PS Using MALDI-TOF MS/MS

ANNA C. CRECELIUS,[1,2] C. REMZI BECER,[1,2,3] KATRIN KNOP,[1,2] ULRICH S. SCHUBERT[1,2,3]

[1]Laboratory of Organic and Macromolecular Chemistry, Friedrich-Schiller-University Jena, Humboldtstr. 10, Jena 07743, Germany

[2]Dutch Polymer Institute (DPI), John F. Kennedylaan 2, 5612 AB Eindhoven, The Netherlands

[3]Laboratory of Macromolecular Chemistry and Nanoscience, Eindhoven University of Technology, Den Dolech 2, 5600 MB Eindhoven, The Netherlands

Received 19 May 2010; accepted 1 July 2010
DOI: 10.1002/pola.24223
Published online in Wiley Online Library (wileyonlinelibrary.com).

ABSTRACT: The molar mass determination of block copolymers, in particular amphiphilic block copolymers, has been challenging with chromatographic techniques. Therefore, methoxy poly(ethylene glycol)-*b*-poly(styrene) (mPEG-*b*-PS) was synthesized by atom transfer radical polymerization (ATRP) and characterized in detail not only by conventional chromatographic techniques, such as size exclusion chromatography (SEC), but also by matrix-assisted laser/desorption ionization tandem mass spectrometry (MALDI-TOF MS/MS). As expected, different molar mass values were obtained in the SEC measurements depending on the calibration standards (either PEG or PS). In contrast, MALDI-TOF MS/MS analysis allowed the molar mass determination of each block, by the scission of the weakest point between the PEG and PS block. Thus, fragments of the individual blocks could be obtained. The PEG block showed a depolymerization reaction, while for the PS block fragments were obtained in the monomeric, dimeric, and trimeric regions as a result of multiple chain scissions. The block length of PEG and PS could be calculated from the fragments recorded in the MALDI-TOF MS/MS spectrum. Furthermore, the assignment of the substructures of the individual blocks acquired by MALDI-TOF MS/MS was accomplished with the help of the fragments that were obtained from the corresponding homopolymers. © 2010 Wiley Periodicals, Inc. J Polym Sci Part A: Polym Chem 48: 4375–4384, 2010

KEYWORDS: block copolymer; MALDI-TOF MS/MS; mass spectrometry; poly(ethylene glycol); poly(styrene); structure; tandem MS

INTRODUCTION Amphiphilic block copolymers are of tremendous interest for various applications in which the combination of hydrophilic and hydrophobic properties are utilized, for example, as compatibilizers, dispersion stabilizers, and emulsifiers. Copolymers containing poly(ethylene glycol) (PEG) as hydrophilic and poly(styrene) (PS) as hydrophobic segment are used in many industrial applications, such as stabilizers, surfactants, and templates for the preparation of inorganic nanoparticles.[1,2]

One major breakthrough in block copolymer synthesis in the last two decades was the introduction of controlled radical polymerization techniques (CRP), such as atom transfer radical polymerization (ATRP).[3] ATRP allows the synthesis of well-defined structures of copolymers in industry as well as on the laboratory scale. In ATRP, a transition metal compound acts as a carrier of a halogen atom in a reversible redox process.[4]

The detailed characterization of amphipilic copolymers is crucial, since the properties of such materials depend on the microstructures, such as the ratio of the corresponding block lengths, end group functionality, and the chain architecture.[5] Traditional characterization techniques for this purpose are size exclusion chromatography (SEC) and proton-nuclear magnetic resonance (^{1}H NMR) spectroscopy. However, since the introduction of soft ionization techniques, such as matrix-assisted laser desorption/ionization time-of-flight (MALDI-TOF)[6,7] and electrospray ionization (ESI),[8] mass spectrometry (MS) has been placed in the focus of polymer analysis.[9–12] The addition of tandem MS (MS/MS) analysis in combination with both soft ionization techniques has made the structure analysis of homopolymers, as well as copolymers easier.[13–20] However, only a few reports exist about the MS/MS analysis of copolymers using MALDI-TOF[21–23] and ESI.[24–30] Wesdemiotis et al.[21] performed MALDI-TOF MS/MS measurements on the poly(fluoro oxetane)-*co*-(tetrahydrofuran) copolymer to obtain information regarding its architecture. The block copolymer mono-*n*-butyl ethers of poly(ethylene glycol)-*b*-poly(propylene oxide) (PEG-*b*-PPO) was analyzed by Weidner et al.[22] to determine the correct number of repeating units in the PEG and the PPO block of the

Additional Supporting Information may be found in the online version of this article. Correspondence to: A. C. Crecelius (E-mail: anna.crecelius@uni-jena.de) or U. S. Schubert (E-mail: ulrich.schubert@uni-jena.de)

TABLE 1 Summary of SEC and ^{1}H NMR Spectroscopy Data

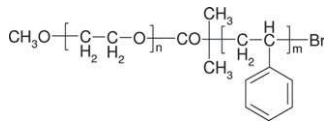

Sample name	Reac time min	$M_{n,SEC}$ g/mol (PEG calibration)	PDI	$M_{n,SEC}$ g/mol (PS calibration)	PDI	NMR (n)	NMR (m)	SEC (m)
Macroinitiator	–	2,050	1.05	4,300	1.04	44	0	0
Sample 1	60	2,500	1.05	5,200	1.05	44	9	8
Sample 2	130	3,250	1.08	6,900	1.09	44	22	25
Sample 3	165	3,600	1.09	7,700	1.10	44	30	33
Sample 4	190	3,850	1.09	8,300	1.11	44	33	38
Sample 5	210	4,100	1.10	8,850	1.12	44	36	44

copolymer. The end-groups and segment information about complex copolyester samples was obtained by Weidner et al.[23] employing MALDI-TOF MS/MS analysis. Adamus[24] investigated two random biodegradable copolyester macromolecules by applying ESI ion trap MS combined with MS^n. Terrier et al.[25] used ESI-MS/MS under low-energy conditions to investigate ammonium adducts of a series of linear triblock and glycerol derivative diblock copolyesters. First the authors performed tandem MS analysis of the homopolymers to identify the structure of the product ions and to propose a possible fragmentation pathway. The authors demonstrated with their work that it is possible to distinguish between copolyesters with the same composition in each repeating unit with inversed block sequences and that information about the block length can be readily obtained. Simonsick and Petkovska[26] performed FT-MS^n for structural characterization and sequencing of a copolymer consisting of poly(glycidyl methacrylate) and methyl methacylate. Girod et al.[27] determined accurately the PS block size in a PEG-*b*-PS block copolymer prepared by a nitroxide-mediated polymerization from the number of styrene losses as observed in the ESI-MS/MS spectrum. In an alternative fragmentation route the junction group between the two blocks could be structurally described. In contrast to the PS block, the PEG block did not show any specific dissociation. The authors expanded their studies by coupling liquid chromatography at critical conditions (LCCC) with on-line ESI tandem MS to characterize a PEG-*b*-PS block copolymer.[28,29] Giordanengo et al.[30] investigated by ESI-MS/MS as well as by NMR spectroscopy the microstructure of a poly(methacrylic acid)-poly(methyl methacrylate) copolymer. The random nature of the copolymer could only be detected by tandem MS analysis.

In this study, we first used the traditional methods, such as SEC, and ^{1}H NMR spectroscopy to characterize the block copolymer mPEG-*b*-PS, which was synthesized by ATRP; afterwards MALDI-TOF MS and MS/MS were applied to determine the size of both blocks. By using MALDI-TOF MS/MS analysis, the hydrolysis of both blocks, as described by Girod et al.[31] was not necessary and therefore the analysis was much faster and easier.

RESULTS AND DISCUSSION

Characterization of the Block Copolymer by SEC and ^{1}H NMR Spectroscopy

The block copolymer mPEG-*b*-PS was synthesized utilizing the ATRP reaction. In total five copolymer samples were obtained besides the macroinitiator and were first characterized by SEC using either a PEG or a PS calibration and, secondly, by ^{1}H NMR spectroscopy. The results obtained from both characterization techniques are summarized in Table 1.

The difference in the calculated number average molar mass values (M_n) by using two different types of calibration standards are arising from the different hydrodynamic volumes of the copolymers obtained. As the calibration standards, either PEG or PS, do not have the same chemical structure to that of the copolymer samples, the relative M_n values should be in between the molar mass values calculated according to PEG or PS calibration. Small polydispersity index (PDI) values as expected from a controlled polymerization were obtained, as presented in Table 1. By integrating the signals of the ^{1}H NMR spectra, the n and m values for the two repeating units of mPEG-*b*-PS were obtained. The integration of the peaks that belong to PEG in the ^{1}H NMR spectrum was taken as 44 repeating units and the corresponding PS content was calculated accordingly. Higher numbers of repeating units were observed at higher monomer conversions, as expected. The SEC graphs were also used to calculate the number of repeating units for PS in the block copolymers. The obtained m values differ slightly from the values obtained by ^{1}H NMR spectroscopy. As depicted in Figure 1, the hydrodynamic volume of the block copolymer is increasing at higher monomer conversions.

There is a shoulder appearing at higher elution time, which corresponds exactly to the PEG macroinitiator. The ratio of this shoulder to the formed polymer peak decreases due to the increased concentration of the polymer. This indicates that the shoulder belongs to unfunctionalized PEG macroinitiator. Nevertheless, the peaks in the SEC curves shift to the lower

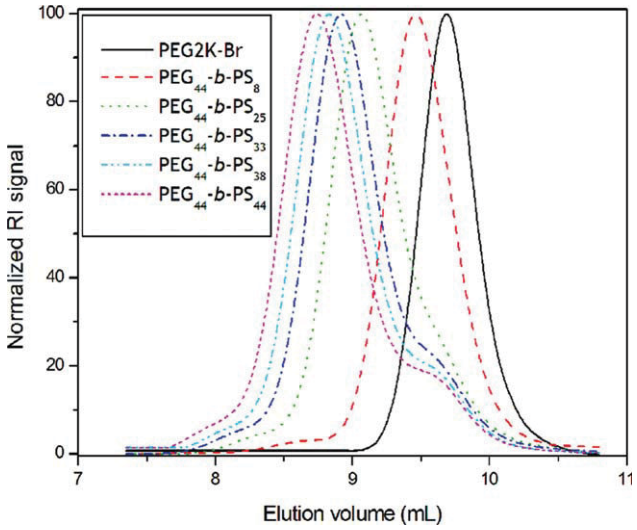

FIGURE 1 SEC curves from PEG-*b*-PS copolymer samples.

elution time proving the growth of the copolymer chain. It should be noted that there is another shoulder appearing at the lower elution time side. This peak corresponds to the chain-chain coupling reaction that is a side reaction during the radical polymerization of styrene. The impurities in the block copolymer, such as unfunctionalized PEG macroinitiator or the coupled block copolymer, have not been removed from the sample using dialysis or any other purification technique. In a follow-up study we are aiming to collect several fractions using 2D-SEC-LC to analyze each adduct, product or side product using MALDI-TOF MS and MS/MS techniques. This will allow us to detect the fingerprints of the polymerization.

MALDI-TOF MS and MS/MS Analysis of Homopolymers

The successful formation of the macroinitiator was investigated by MALDI-TOF MS analysis, as shown in Figure 2. The calculated M_n value for mPEG 2000 was 1907 g/mol and for the macroinitiator 2122 g/mol; the corresponding PDI values

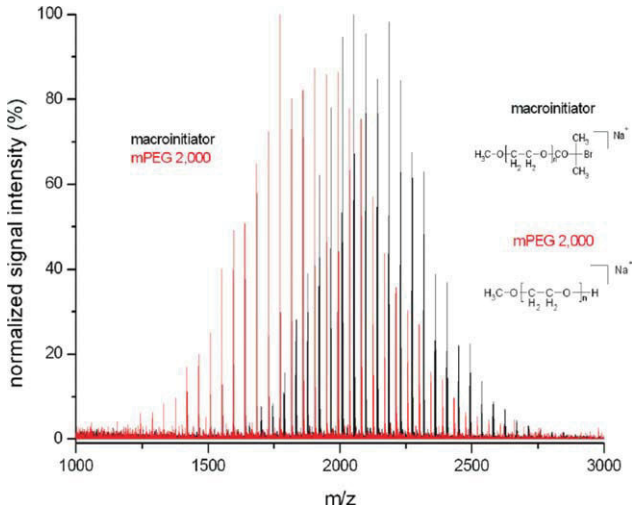

FIGURE 2 MALDI-TOF MS spectrum of mPEG 2000 and macroinitiator (matrix: DCTB, salt: NaI).

using PolyTools for the determination for mPEG 2000 and the macroinitiator were 1.02 and 1.01, respectively.

The experimental mass accuracy assigned for both polymers is around *m/z* 0.1, as presented in Table 2. This is within the mass accuracy achievable with the used instrument.

From the starting material mPEG 2000 and the macroinitiator MALDI-TOF MS/MS analysis was performed to evaluate which fragmentations can occur. The obtained fragments of the homopolymers could be later the basis for the elucidation of the structure of fragment ions in the copolymer analysis. To interpretate the fragment ions obtained for both homopolymers, the structures described by Hoteling et al.[32] were used as possible starting points. Hoteling et al.[32] proposed accordingly to Selby et al.[33] that a 1,4-hydrogen elimination and a 1,2-ethylene elimination are occurring as fragmentation routes. The dissociation of PEG was first described by Lattimer et al. using fast atom bombardment tandem MS.[34] The ions according to these eliminations with the corresponding end groups could be determined in the recorded mass spectra for mPEG 2000 (Supporting Information Fig. 1 and Table 1) and for the macroinitiator (Supporting Information Fig. 2 and Table 2). The product ions arising from the dissociations of mPEG and the macroinitiator were labelled according to the nomenclature established by Lattimer et al.[34] Starting with Supporting Information Figure 1, the MALDI-TOF MS/MS spectrum of mPEG 2000 using AgTFA as salt additives is presented herein. A parent ion with 41 repeating units was selected. The signals of the generated fragment ions in Supporting Information Figure 1(a) reveal a depolymerization reaction. By zooming into the MALDI-TOF MS/MS spectra, as presented in Supporting Information Figure 1(b), it could not be determined accurately if the fragment ions C and A′ are formed or if they can be explained by the silver isotopes of the fragment series B and C′, respectively, since the detected ions are only 2 *m/z* values apart from each other. The MALDI-TOF MS/MS analysis was also performed with NaI, and more or less the same fragments were obtained, except fragment A, as in the AgTFA cationized sample. More detailed information can be found in Supporting Information Figure 1.

mPEG 2000 has a methoxy group on one end and a hydroxyl group on the other end. The hydroxyl group is reacted by α-bromo-iso-butyryl bromide to yield the PEG macroinitiator. As mentioned earlier, the macroinitiator was analyzed as well by MALDI-TOF MS/MS using DCTB as matrix with the addition of NaI. A parent ion with 41 repeating units corresponding to a *m/z* value of 2008 was selected and the

TABLE 2 Measurements of the Mass Accuracy Obtained for the MALDI-TOF MS Analysis of mPEG 2000 and the Macroinitiator (Fig. 2)

Species	m/z^{theo}	m/z^{exp}	Error (*m/z*)
mPEG 2000	1772.04	1771.92	0.12
Macroinitiator	1919.99	1919.86	0.13

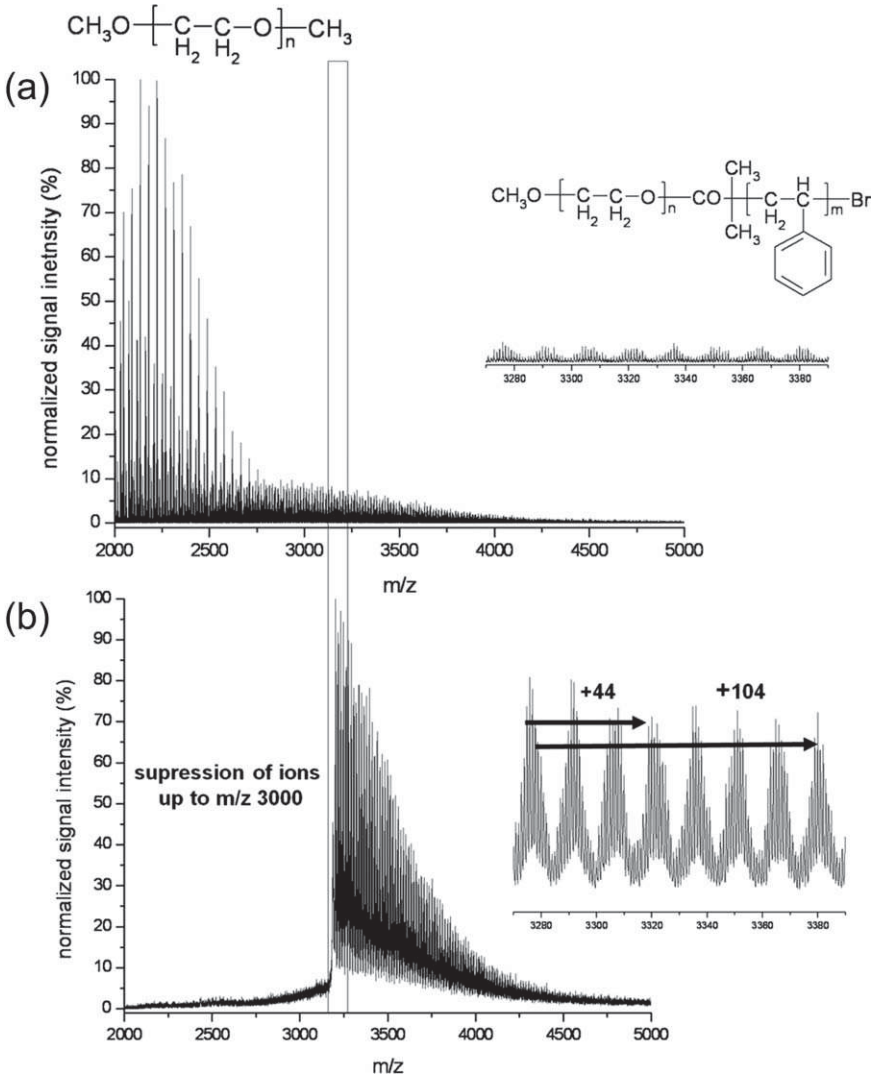

FIGURE 3 MALDI-TOF MS spectra of mPEG-*b*-PS (copolymer 1) in (a) normal mode, and (b) suppressing of ions up to *m/z* 3000. DCTB was used as matrix and AgTFA as salt additive.

resulting MALDI-TOF MS/MS spectrum can be found in Supporting Information Figure 2. The zoom displayed in Supporting Information Figure 2(b) in connection with Supporting Information Table 2 shows the formation of seven fragment series (B, B′, B″, C, C′, C″ and C‴). The fragment series B, B′, C, and C′ are also detected when mPEG 2000 is fragmented, as presented in Supporting Information Figure 1(b), only as sodium adducts instead of silver adducts. Two additional fragment series B″ and C″ could be obtained, showing the characteristic end group of the macroinitiator. At first instance a bromoester moiety was expected as end group, but the distinct isotopic pattern of the bromine atom was not found and cleavage of the bromine atom from the parent ion of the macroinitiator was observed, since a fragment ion with *m/z* 1929 is presented in Supporting Information Figure 2. Fragment series C‴ is as well formed, which contains the unsaturated end group CH_3—C=CH_2. Additionally, a fragment ion, in which the whole bromoester group was cleaved off, was also recorded at the *m/z* value of 1859. Fragment series having a hydrogen atom as end group could be identified. This explains how fragment series B′ and C could be formed bearing a hydrogen atom as end group.

After the MALDI-TOF MS/MS analysis of mPEG 2000 and the macroinitiator was discussed in detail, now the tandem MS analysis of PS will be in the focus of this contribution. PS with a 1,1-dimethylacetic acid ethylester group as initiator moiety and a bromine atom as end group was selected. The matrices DCTB and dithranol and the salt additives NaI and AgTFA were tested for the MALDI-TOF MS analysis of PS. The highest signal-to-noise levels showed the matrix dithranol in combination with AgTFA for the MALDI-TOF MS measurement of PS (spectrum not shown). The corresponding MALDI-TOF MS/MS spectra of PS are presented in Supporting Information Figure 3. As parent ion the silver adduct with 35 repeating units of PS was selected with a *m/z* value of 3864. In the parent ion the bromine as end group was cleaved off and a radical was formed. The instability of the C—Br bond is extensively discussed by Borman et al.[35] on PMMA synthesized by ATRP. The authors showed that methyl bromide gets lost and a ring-closed lactone end group is

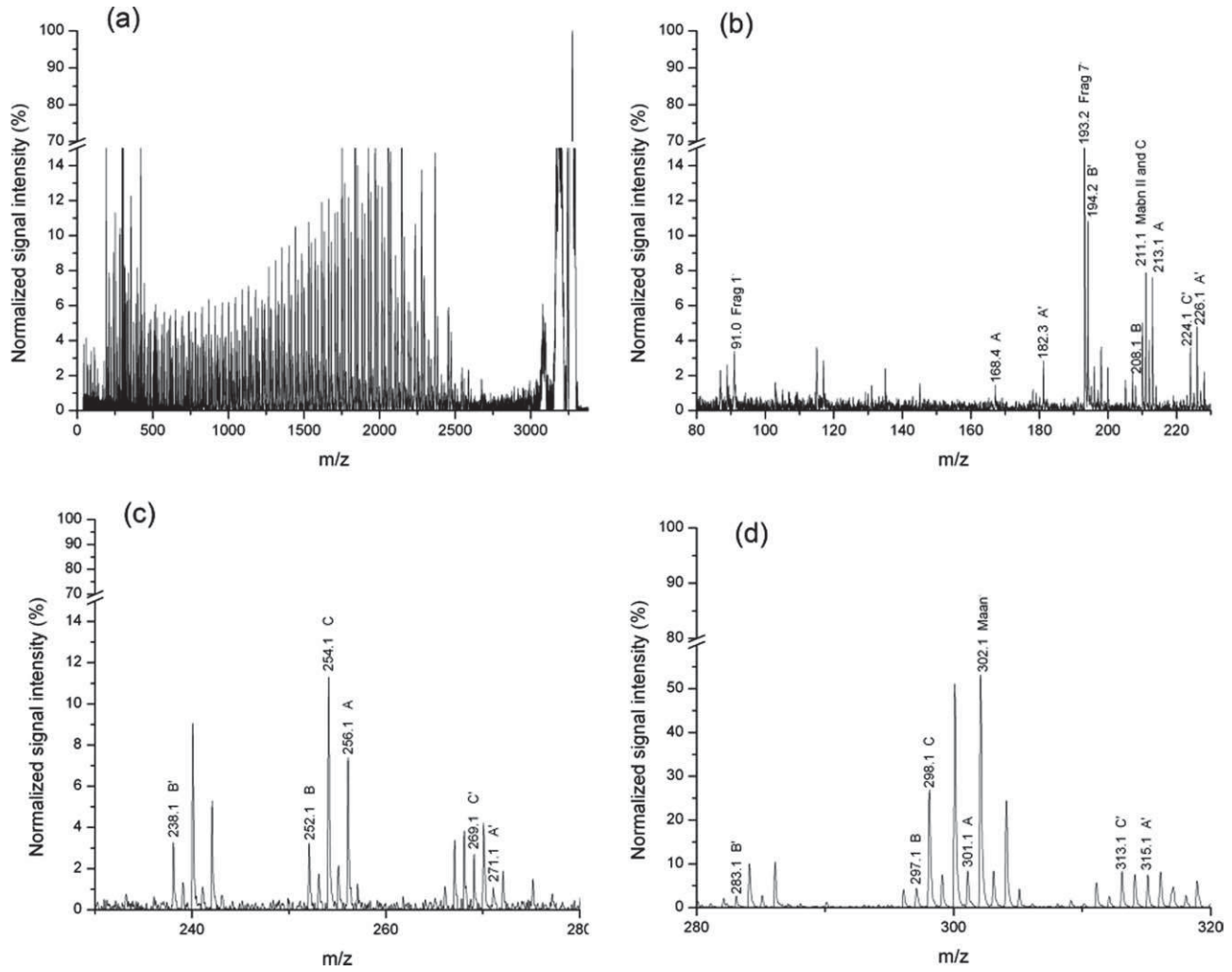

FIGURE 4 MALDI-TOF MS/MS spectra of mPEG-*b*-PS using the highest isotopic peak of $mPEG_{59}$-PS_4 with *m/z* 3305 as precursor ion; (a) complete, (b) monomeric, (c) dimeric, and (d) trimeric region of the mass spectrum.

formed during the MALDI process. The generated fragment ions are annotated in the zoom shown in Supporting Information Figure 3(b) and the structures are summarized in Supporting Information Table 3. The nomenclature, as introduced by Gies et al.,[36] was selected for labeling the fragments produced by the MALDI-TOF MS/MS analysis.

In the elucidation of the structures of the recorded peaks, the reports of Gies et al.[36] as well as Polce et al.[37,38] were used as assistance. All three studies came to the conclusion that free radicals are formed and undergo further fragmentations. In Supporting Information Table 3 only the fragment ions labeled with Ian. and Ibn II show the characteristic 1,1-dimethylacetic acid ethylester group as initiator group, all other fragment ions underwent scission of this initiator moiety and could have also been generated if a butyl group would have been used as initiator instead, corresponding to the measurements by Gies et al.[36] and Polce et al.[37] A detailed mechanism about the formation of these specific product ions has been reported by Gies et al.[36]

The studied block copolymer exhibits the same Br termination, although the cleavage of the C—Br bond does not occur, since the selected precursor ion of the MALDI-TOF MS/MS analysis with a *m/z* value of 3305 corresponds to the intact silver-containing molecule with 59 PEG and 4 PS repeating units, as shown later in this contribution. One possible explanation for this unexpected phenomenon can be that the C—Br bond cleavage is time dependent. PS was synthesized 6 months before the block copolymer was produced and both compounds were analyzed by MALDI-TOF MS and tandem MS at the same date.

Characterization of the Block Copolymer by MALDI-TOF MS and MS/MS Analysis

The MALDI-TOF MS spectrum of the copolymer sample 1 is presented in Figure 3. From Figure 3(a), it is obvious that the unfunctionalized PEG, which is the remaining reagent from the synthesis of the macroinitiator, is masking the signals of the copolymer sample. This effect can be overcome

TABLE 3 Structural Assignments for the Peaks in the MALDI-TOF MS/MS Spectra of Figure 4, Fragments of the PS Block, and mPEG Block

Label	Ions Observed (*m/z*)	Schematic Representation of the Structures
Frag 1	91.0	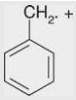
Frag 7	193.2	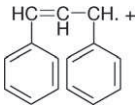
Mabn II	211.1	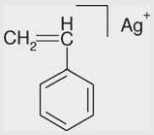
	419.2 ($n = 1$) 523.1 ($n = 2$)	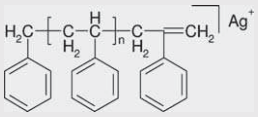
Maan.	302.1($n = 1$) 406.1 ($n = 2$) 510.1 ($n = 3$)	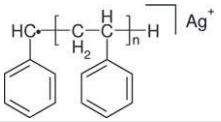
A	168.4 ($n = 1$) 213.1 ($n = 2$) 256.1 ($n = 3$) 301.1 ($n = 4$) 2370.0 ($n = 51$)	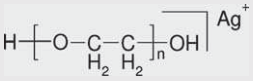
A′	182.3 ($n = 1$) 226.1 ($n = 2$) 271.1 ($n = 3$) 315.1 ($n = 4$) 2516.9 ($n = 53$)	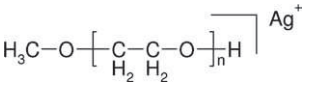
B	208.1 ($n = 1$) 252.1 ($n = 2$) 297.1 ($n = 3$) 2674.9 ($n = 57$)	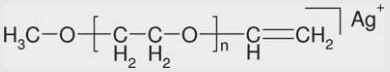
B′	194.2 ($n = 1$) 238.1 ($n = 2$) 283.1 ($n = 3$) 1779.8 ($n = 37$)	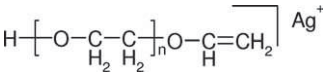
C	211.1 ($n = 1$) 254.1 ($n = 2$) 298.1 ($n = 3$) 2588.2 ($n = 55$)	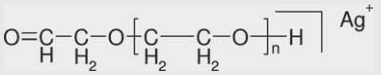
C′	224.1 ($n = 1$) 269.1 ($n = 2$) 313.1 ($n = 3$) 2690.6 ($n = 57$)	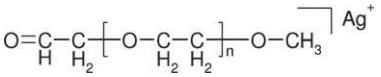

TABLE 4 Measurements of the Mass Accuracy of the Fragment Peaks Presented in the MALDI-TOF MS/MS Spectra Shown in Figure 4

Species	m/z^{theo}	m/z^{exp}	Error (m/z)
Frag 1.	91.0	91.1	0.1
Frag 7.	193.1	193.2	0.1
Mabn II	211.0	211.1	0.1
Maan.	302.0	302.1	0.1
A	301.0	301.1	0.1
A′	315.0	315.1	0.1
B	297.0	297.1	0.1
B′	283.0	283.1	0.1
C	211.0	211.1	0.1
C′	313.0	313.1	0.1

by suppressing the ions up to m/z 3000 reaching the detector.

By using this approach, intense signals of the copolymer sample could be recorded, as shown in Figure 3(b). The zoom of the MALDI-TOF MS spectrum reveals the assignment of the repeating units of both blocks (PEG with m/z 44 and PS with m/z 104). The remaining copolymer samples have been analyzed in the same manner by MALDI-TOF MS. The corresponding MALDI-TOF MS spectra can be found in Supporting Information Figure 4. With rising sample number, the copolymer distribution is shifting to higher m/z values and the MALDI-TOF MS analysis is more and more difficult. Hence, a pre-fractionation, such as two-dimensional liquid chromatography, before the MALDI-TOF MS measurements, would be highly favorable.

The MALDI-TOF MS/MS analysis was performed on the highest isotopic peak (m/z 3305) of mPEG-*b*-PS with 59 repeat units of mPEG and 4 repeat units of PS. Since the window of the precursor ion selector could only be closed up to m/z 4, without losing the precursor ion signal, side products, such as $mPEG_{52}$-*b*-PS_7 with m/z 3309 (highest isotopic peak) and $mPEG_{66}$-*b*-PS_1 with m/z 3301 (highest isotopic peak) could also be fragmented in the analysis. If this would be the case, the fragmentation of $mPEG_{66}$-*b*-PS_1 should reveal a different pattern of fragments due to the short PS block. However, patterns correlated to such a fragmentation could not be found. The only possibility to overcome this phenomenon is the use of an instrument with higher resolution, such as a fourier transform ion cyclotron resonance (FTICR) mass spectrometer or an orbitrap. The resulting mass spectra from the instrument used in this study are presented in Figure 4.

Corresponding structures could be assigned to nearly all peaks in the monomeric, dimeric, and trimeric region of the mass spectrum [see Fig. 4(b–d)]. The structures, which are summarized in Table 3, could be found with the help of the MALDI-TOF MS/MS spectra of the homopolymers. The assignment of the fragment ions was performed over the whole available m/z range, but are not included in Table 3.

To show the validity of our assignments, first the mass accuracy for the identified fragments was calculated. The results are presented in Table 4. The obtained mass accuracy was m/z 0.1, which lies in the specifications of the used mass detector. Additionally, the measured isotopic patterns were compared with the calculated ones for the identified fragments and are shown in Supporting Information Figure 5. In some cases, overlapping m/z value peaks are obtained, making the identification of the fragments demanding. However, in most cases a series of fragments with differing numbers of repeating units was observed and used to judge the assignment.

Obviously only fragments of the mPEG block (Table 3) and the PS block (Table 3) could be detected in the MALDI-TOF MS/MS spectrum of mPEG-*b*-PS, which means that there were no signals detected correlated to fragments bearing the mPEG block as well as the PS block. From this phenomenon it can be concluded that a scission between both blocks in the tandem MS mode occurs.

Three scissions, as shown in Scheme 1, are possible. The first option shown in Scheme 1(a) is that a 1,4-hydrogen elimination starts from the end of the mPEG block, so that the fragment series B and X are formed. The fragment series B, as presented in Table 3, could be identified in the corresponding MALDI-TOF MS/MS spectrum of mPEG-*b*-PS. Fragment series X is only detectable with one repeating unit at the m/z value of 420.1. It might be that it fragments further in the tandem MS mode and is not observed in the corresponding MALDI-TOF MS/MS spectrum, since it possibly does not ionize with Ag^+. A second 1,4-hydrogen-elimination can occur, as presented in Scheme 1(b), so that fragment series X and C′ are formed as a consequence. Fragment series X could only be identified with one repeating unit in the corresponding MALDI-TOF MS/MS spectrum, since it possibly fragments further and does not ionize with Ag^+. Fragment series C′ could be easily detected in the MALDI-TOF MS/MS spectrum (see Fig. 4). The third option, as presented in Scheme 1(c), is the McLafferty rearrangement, where a hydrogen atom is separated from the block copolymer. Here again, as shown in Scheme 1(a), the fragment series B is formed as well as fragment series X, which could not be found in the acquired MALDI-TOF MS/MS spectrum. As in the recorded MALDI-TOF MS/MS spectrum (Fig. 4 and Table 3) fragment series of mPEG with 57 repeating units could be observed, the fragmentation route as presented in Scheme 1(a,b) is possibly favored. If a McLafferty rearrangement would take place one could expect to see 58 repeating units of fragment series B and at least fragment X with one repeating unit.

As mentioned earlier, no fragment series containing both repeating units of mPEG and PS could be observed. This was proven by acquirering MALDI-TOF MS/MS spectra from precursor ions containing the same number of mPEG repeating units and an increasing number of PS repeating units, as

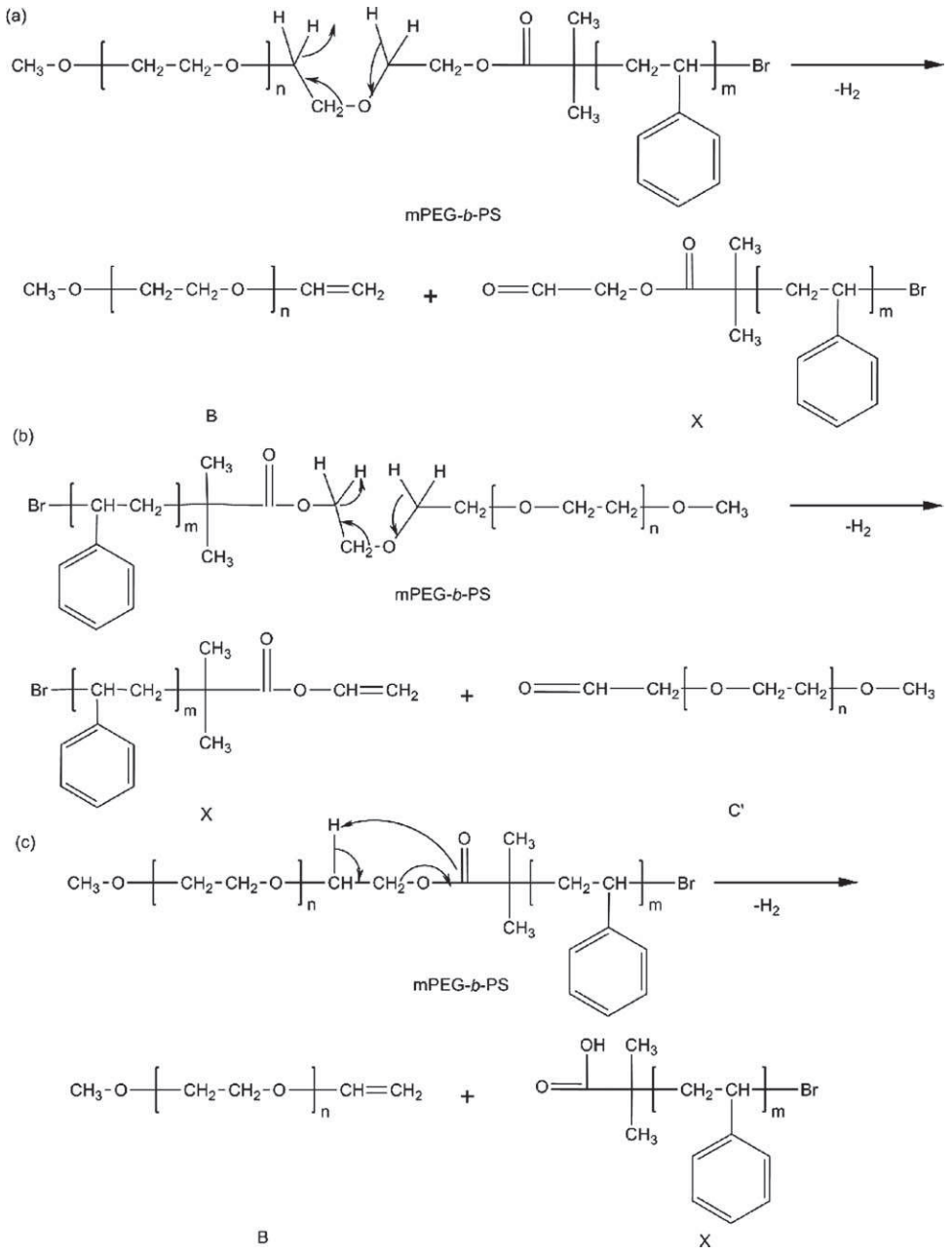

SCHEME 1 Proposed scission of the mPEG block from the PS block. (a), (b) 1,4-Hydrogen-elemination from each side of the copolymer chain, and (c) McLafferty rearrangement.

presented in Figure 5. With increasing the repeating units of PS, the gap in the mass spectrum, where no fragments were obtained at higher molar masses, increased. Therefore a scission between both blocks is proposed as a result for the tandem MS analysis of mPEG-*b*-PS.

EXPERIMENTAL

Materials

Styrene (≥99%, Aldrich) and anisole (Fluka) were passed through neutral alumina oxide column before use. CuBr (99.999%, Aldrich), α–bromo isobutyryl bromine (98%, Aldrich), ethyl-2-bromoisobutyrate (98%, Aldrich), poly(ethylene glycol) methyl ether (M_n = 2000 g/mol, flakes), *N,N,N′,N″,N″*-pentamethyldiethylenetriamine (99%, Aldrich), and triethylamine (≥99%, Aldrich) was used as received.

Instruments

For the determination of the monomer conversions, gas chromatography (GC) measurements were performed on a Shimadzu GC used with a Trace column RTX-5 and an autosampler. ^{1}H NMR spectroscopy was recorded on a Bruker Avance 250 MHz in deuterated methylene chloride. The chemical shifts were calibrated with respect to tetramethylsilane (TMS). SEC was measured on an Agilent system which is equipped with triple detectors that are a diode array detector, a reflactive index detector, and a multiangle light scattering detector. Two PSS SDV (5 μ pore size) columns were placed in series. DMA with 5 mmol LiCl was used as eluent

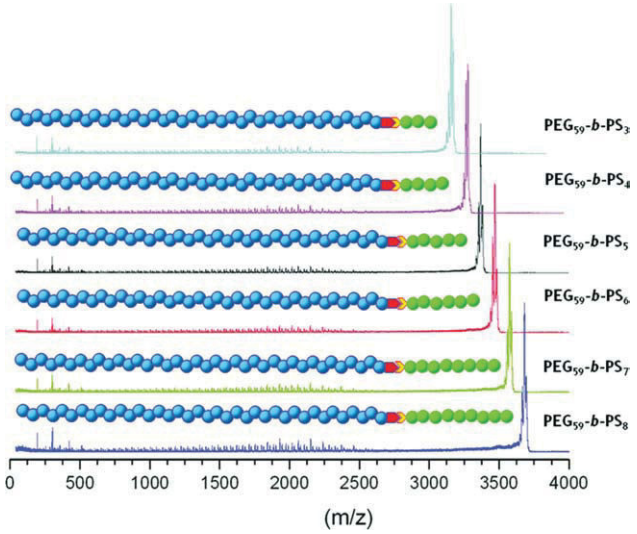

FIGURE 5 MALDI-TOF MS/MS spectra of precursor ions containing 59 repeating units of mPEG and an increasing number of PS repeating units. The selected precursor ions are schematically represented between the spectra. DCTB was used as matrix and AgTFA as salt additive. [Color figure can be viewed in the online issue, which is available at wileyonlinelibrary.com.]

at 1 mL/min flow rate and the column oven was set to 50 °C. An Ultraflex III TOF/TOF (Bruker Daltonics, Bremen, Germany) was used for the MALDI-TOF MS and MS/MS analysis. The instrument is equipped with a Nd:YAG laser and a collision cell. For the MS/MS mode, argon was used as collision gas at a pressure of 2×10^{-6} mbar. The instrument was calibrated before every measurement with an external standard PMMA from PSS Polymer Standards Services GmbH (Mainz, Germany). MS data were processed using PolyTools 1.0 (Bruker Daltonics).

CONCLUSIONS

The block length of the copolymer mPEG-*b*-PS could be determined in an accurate and reliable manner by performing MALDI-TOF MS/MS analysis, since a dissociation of the PEG block was leading to the separation of both blocks. The PEG block showed a depolymerization reaction, while for the PS block fragments in the monomeric, dimeric, and trimeric regions were observed. This fast and easy to perform measurement does not require the hydrolysis of mPEG-*b*-PS followed by the independent MALDI-TOF MS analysis of each individual block to determine the block length of the copolymer. Future experiments will be concentrated on the purification of the block copolymers by performing two-dimensional liquid-chromatography before MALDI-TOF MS and tandem MS analysis.

The authors thank the Dutch Polymer Institute (DPI, technology area high-throughput-experimentation) and the Thüringer Ministerium für Bildung, Wissenschaft und Kultur (grant no. B515-07008) for the financial support of this study. They also thank Bruker Daltonik GmbH for their cooperation.

REFERENCES AND NOTES

1 Dixit, S. G.; Mahadeshwar, A. R.; Haram, S. K. Colloids Surf A 1998, 133, 69–75.

2 Westman, A.; Huthfehre, T.; Demirev, P.; Sundqvist, B. U. R. J Mass Spectrom 1995, 30, 206–211.

3 Kamigatio, M.; Ando, T.; Sawamoto, M. Chem Rev 2001, 101, 3689–3745.

4 Matyjaszewski, K.; Xia, J. H. Chem Rev 2001, 101, 2921–2990.

5 Becer, C. R.; Paulus, R. M.; Hoeppener, S.; Hoogenboom, R.; Fustin, C.-A.; Gohy, J.-F.; Schubert, U. S. Macromolecules 2008, 41, 5210–5215.

6 Karas, M.; Hillenkamp, F. Anal Chem 1988, 60, 2299–2301.

7 Tanaka, K.; Waki, H.; Ido, Y.; Akita, S.; Yoshida, Y.; Yoshida, T. Rapid Commun Mass Spectrom 1988, 2, 151–153.

8 Fenn, J. B.; Mann, M.; Meng, C. K.; Wong, S. F.; Whitehouse, C. M. Science 1989, 246, 64–71.

9 Nielen, M. W. F. Mass Spectrom Rev 1999, 18, 309–344.

10 Hanton, S. D. Chem Rev 2001, 101, 572–569.

11 Montaudo, G.; Samperi, F.; Montaudo, M. S. Prog Polym Sci 2006, 31, 277–357.

12 Grunendling, T.; Weidner, S.; Falkenhagen, J.; Barner-Kowollik, C. Polym Chem 2010, 1, 599–617.

13 McEwen, C. N.; Peacock, P. M. Anal Chem 2002, 74, 2743–2748.

14 Peacock, P. M.; McEwen, C. N. Anal Chem 2004, 76, 3417–3428.

15 Peacock, P. M.; McEwen, C. N. Anal Chem 2006, 78, 3957–3964.

16 Weidner, S. M.; Trimpin, S. Anal Chem 2008, 80, 4349–4361.

17 Crecelius, A. C.; Baumgaertel, A.; Schubert, U. S. J Mass Spectrom 2009, 44, 1277–1286.

18 Baumgaertel, A.; Weber, C.; Knop, K.; Crecelius, A.; Schubert, U. S. Rapid Commun Mass Spectrom 2009, 23, 756–762.

19 Baumgaertel, A.; Becer, C. R.; Gottschaldt, M.; Schubert, U. S. Macromol Rapid Commun 2008, 29, 1309–1315.

20 Knop, K.; Jahn, B. O.; Hager, M. D.; Crecelius, A.; Gottschaldt, M.; Schubert, U. S. Macromol Chem Phys 2010, 6, 677–684.

21 Wesdemiotis, C.; Pingitore, F.; Polce, M. J.; Russell, V. M.; Kim, Y.; Kausch, C. M. T.; Connors, H.; Medsker, R. E.; Thomas, R. R. Macromolecules 2006, 39, 8369–8378.

22 Weidner, S. M.; Falkenhagen, J.; Maltsev, S.; Sauerland, V.; Rinken, M. Rapid Commun Mass Spectrom 2007, 21, 2750–2758.

23 Weidner, S. M.; Falkenhagen, J.; Knop, K.; Thünemann, A. Rapid Commun Mass Spectrom 2009, 23, 2768–2774.

24 Adamus, G. Rapid Commun Mass Spectrom 2007, 21, 2477–2490.

25 Terrier, P.; Buchmann, W.; Desmazieres, B.; Tortajada, J. Anal Chem 2006, 78, 1801–1806.

26 Simonsick, W. J.; Petkovska, V. I. Anal Bioanal Chem 2008, 392, 575–583.

27 Girod, M.; Phan, T. N. T.; Charles, L. J Am Soc Mass Spectrom 2008, 19, 1163–1175.

28 Girod, M.; Phan, T. N. T.; Charles, L. Rapid Commun Mass Spectrom 2008, 22, 3767–3775.

29 Girod, M.; Phan, T. N. T.; Charles, L. Rapid Commun Mass Spectrom 2009, 23, 1476–1482.

30 Giordanengo, R.; Viel, S.; Hidalgo, M; Allard-Breton, B.; Thévand, A.; Charles, L. Anal Chim Acta 2009, 654, 49–58.

31 Girod, M.; Mazarin, M.; Phan, T. N. T.; Gigmes, D.; Charles, L. J Polym Sci Part A: Polym Chem 2009, 47, 3380–3390.

32 Hoteling, A. J.; Kawaoka, K.; Goodberlet, M. C.; Yu, W.-M.; Owens, K. G. Rapid Commun Mass Spectrom 2003, 17, 1671–1676.

33 Selby, T. L.; Wesdemiotis, C.; Lattimer, R. P. J Am Soc Mass Spectrom 1994, 5, 1081–1092.

34 Lattimer, R. P.; Münster, H.; Budzikiewicz, H. Int J Mass Spectrom Ion Processes 1989, 90, 119–129.

35 Borman, C. D.; Jackson, A. T.; Bunn, A.; Cutter, A. L.; Irvine, D. J. Polymer 2000, 41, 6015–6020.

36 Gies, A. P.; Vergne, M. J.; Orndorff, R. L.; Hercules, D. M. Macromolecules 2007, 40, 7493–7504.

37 Polce, M. J.; Ocampo, M.; Quirk, R. P.; Wesdemiotis, C. Anal Chem 2008, 80, 347–354.

38 Polce, M. J.; Ocampo, M.; Quirk, R. P.; Leigh, A. M.; Wesdemiotis, C. Anal Chem 2008, 80, 355–362.

Publication P6:

Characterization of different poly(2-ethyl-2-oxazoline)s *via* matrix-assisted laser desorption/ionization time-of flight tandem mass spectrometry

---

A. Baumgaertel, C. Weber, K. Knop, A. C. Crecelius, U. S. Schubert

Rapid Commun. Mass Spectrom. **2009**, *23*, 756–762.

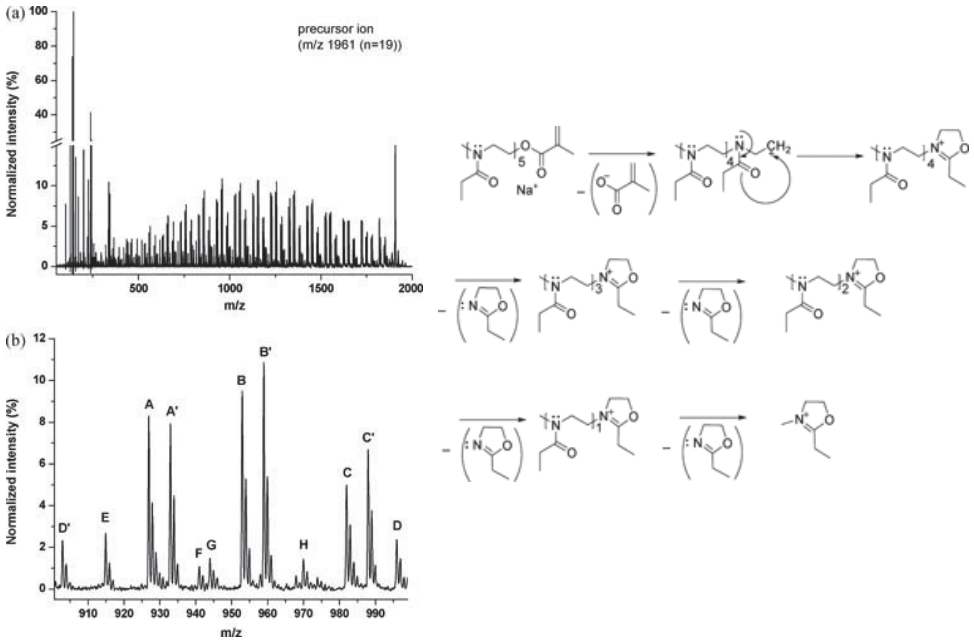

RAPID COMMUNICATIONS IN MASS SPECTROMETRY
Rapid Commun. Mass Spectrom. 2009; **23**: 756–762
Published online in Wiley InterScience (www.interscience.wiley.com) DOI: 10.1002/rcm.3933

RCM

Characterization of different poly(2-ethyl-2-oxazoline)s via matrix-assisted laser desorption/ionization time-of-flight tandem mass spectrometry

Anja Baumgaertel[1], Christine Weber[1,2], Katrin Knop[1,2], Anna Crecelius[1,2] and Ulrich S. Schubert[1,2,3]*

[1]Laboratory of Organic and Macromolecular Chemistry, Friedrich-Schiller-University Jena, Humboldtstr. 10, 07743 Jena, Germany
[2]Dutch Polymer Institute (DPI), John F. Kennedylaan 2, 5612 AB Eindhoven, The Netherlands
[3]Laboratory of Macromolecular Chemistry and Nanoscience, Eindhoven University of Technology, Den Dolech 2, 5600 MB Eindhoven, The Netherlands

Received 28 November 2008; Revised 25 December 2008; Accepted 29 December 2008

Matrix-assisted laser desorption/ionization time-of-flight mass spectrometry (MALDI-TOF MS) coupled with CID (collision-induced dissociation) has been used for the detailed characterization of two poly(2-ethyl-2-oxazoline)s as part of a continuing study of synthetic polymers by MALDI-TOF MS/MS. These experiments provided information about the variety of fragmentation pathways for poly(oxazoline)s. It was possible to show that, in addition to the eliminations of small molecules, like ethene and hydrogen, the McLafferty rearrangement is also a possible fragmentation route. A library of fragmentation pathways for synthetic polymers was also constructed and such a library should enable the fast and automated data analysis of polymers in the future. Copyright © 2009 John Wiley & Sons, Ltd.

Matrix-assisted laser desorption/ionization time-of-flight mass spectrometry (MALDI-TOF MS)[1,2] is an important tool for the characterization of high molar mass substances in biological and chemical fields, such as proteins and peptides, as well as natural and synthetic polymers.[3] The combination of the soft ionization method MALDI-TOF MS[4] with post-source decay (PSD) and collision-induced dissociation (CID) has made it a powerful tool for the structural elucidation of polymers.[5] The arrangement of a collision cell in a TOF analyzer allows the investigation of unimolecular polymer degradation within a single spectrum.[6] The instrument used in this study has a special MS/MS unit, which overcomes the disadvantages of PSD, such as a longer measurement time or less efficient fragmentation.[7]

Poly(2-alkyl-2-oxazoline)s are an important class of polymers with a wide range of potential applications such as in thermosensitive materials, as sensors or as carrier systems for active agents in drug delivery.[8] The cationic ring opening polymerization of 2-oxazolines was first reported in the 1960s by different research groups.[9–12] This method was later modified[13,14] and, more recently, a microwave-assisted process was introduced to achieve better yields.[15,16]

In comparison with conventional heating, microwave irradiation enables the polymerization time to be reduced by up to 400 times, and possible side reactions, like chain transfer or chain coupling, are also reduced. During these investigations a complete library of poly(2-alkyl-2-oxazoline)s was synthesized and the polymerization was investigated by kinetic studies, NMR spectroscopy, size-exclusion chromatography (SEC) and MALDI-TOF MS.[17,18] In addition, to confirm the living polymerization mechanism, all poly(2-oxazoline)s up to a M_n of 7000 Da were analyzed by MALDI-TOF MS to confirm the living polymerization mechanism.[19]

In this study we report for the first time the MALDI-TOF MS and MS/MS analysis of two different poly(2-ethyl-2-oxazoline)s (PEtOx) synthesized under microwave irradiation. The first is a methyl-initiated methacrylate macromonomer and the second is a polymer, initiated with propargyl and terminated with hydroxy.

**Correspondence to*: U. S. Schubert, Laboratory of Organic and Macromolecular Chemistry, Friedrich-Schiller-University Jena, Humboldtstr. 10, 07743 Jena, Germany.
E-mail: ulrich.schubert@uni-jena.de
Contract/grant sponsor: Dutch Polymer Institute.
Contract/grant sponsor: Thüringer Kultusministerium; contract/grant number: B515-07008.

EXPERIMENTAL

Materials

2-Ethyl-2-oxazoline (99%; Acros Organics, Geel, Belgium; EtOx) was dried over barium oxide and distilled under argon prior to use. Methyl tosylate (98%; Sigma Aldrich, Oakville, Canada; MeTos) and propargyl toluene-4-sulfonate (97%; Fluka, Taufkirchen, Germany) were distilled and stored under argon. Acetonitrile (extra dry; Acros Organics) was stored under argon. Methacrylic acid (99%; Sigma Aldrich; MAA) was used as received. Triethylamine was dried over potassium hydroxide and distilled under argon.

The matrix, anthracene-1,8,9-triol (Sigma Aldrich), sodium iodide (Acros Organics) as well as the solvents, chloroform and acetone. (HPLC grade; Roth, Karlsruhe, Germany) were used as purchased.

Synthesis of the oligo(2-ethyl-2-oxazoline) methacrylate macromonomer and the poly(2-ethyl-2-oxazoline)

The oligo(2-ethyl-2-oxazoline) methacrylate macromonomer and the poly (2-ethyl-2-oxazoline) were both synthesized via microwave irradiation.[20] For the reaction, the desired amounts of methyl tosylate (initiator for the macromonomer) (1.485 g, 7.9 mmol) or propargyl tosylate (initiator for the polymer) (0.282 g, 1.3 mmol), 2-ethyl-2-oxazoline (macromonomer: 3.986 g, 40.2 mmol; polymer: 2.573 g, 25.9 mmol) and acetonitrile (macromonomer: 6.1 mL; polymer: 6.7 mL) were transferred to predried microwave vials under inert conditions. These mixtures were first stirred for 10 s, then heated up to 140°C for around 3 min and afterwards cooled down automatically with a nitrogen flow. For end capping of the macromonomer, methacrylic acid (1.02 mL, 12 mmol, 1.5-fold excess) and triethylamine (2.3 mL, 16.6 mmol, 2-fold excess) were added separately by syringe; for the polymer 1 mL of a sodium carbonate water mixture (31.8 mg/mL) was added, and both were heated at 80°C for 15 h. After removing the acetonitrile under reduced pressure the macromonomer and the polymer were dissolved in chloroform, washed with an aqueous sodium hydrogen carbonate solution and saturated brine, dried with sodium sulfate and filtered. The solvent was evaporated under reduced pressure and the resulting white sticky polymer was dried under vacuum.

SEC measurements

Size-exclusion chromatography (SEC) was carried out on a system equipped with a SCL-10A system controller, a LC-10AD pump and a RID-10A refractive index detector (all from Shimadzu, Duisburg, Germany) using a solvent mixture containing chloroform, triethylamine and isopropanol (94:4:2) at a flow rate of 1 mL min^{-1} on a PSS-SDV-linear M 5 μm column (PSS, Mainz, Germany) at room temperature. The system was calibrated with commercial polystyrene (370–67 500 Da) and poly(methyl methacrylate) (2000–88 000 Da) standards from PSS.

MALDI sample preparation

For the sample preparation, oligo(2-ethyl-2-oxazoline) methacrylate macromonomer (10 mg/mL) and poly(2-ethyl-2-oxazoline) (10 mg/mL) in chloroform, dithranol in chloroform (20 mg/mL), and the doping salt (NaI) dissolved in acetone at a concentration of 100 mg/mL were used. The dried-droplet spotting technique[21] (matrix, salt and analyte previously mixed together) was applied. For each sample 1 μL of the mixture was spotted onto a target plate.

MALDI-TOF MS measurements

MALDI-TOF MS measurements were performed with an Ultraflex III TOF/TOF (Bruker Daltonics, Bremen, Germany) mass spectrometer equipped with a Nd:YAG laser and a collision cell. All spectra were measured in the positive ion reflectron mode. For the MS/MS mode, argon was used as collision gas at a pressure of 2×10^{-6} mbar. The instrument was calibrated prior to each measurement with an external PMMA standard $H(CH_2CCH_3COOCH_3)_nH + Na^+$ (*m/z* 425 or 2526, measured with sodium iodide) from PSS in the required measurement range. MS and MS/MS data were processed using the software FlexAnalysis, PolyTools 1.0 and an isotope pattern calculator from Bruker Daltonics.

RESULTS AND DISCUSSION

The polymerization of 2-ethyl-2-oxazoline (EtOx) can be performed in a living manner, as has already been described elsewhere,[22] with the use of microwave irradiation yielding oligomers and polymers with well-defined end groups.[23] In the present study both a methyl-initiated methacrylate macromonomer and a propargyl-initiated and hydroxyl-terminated polymer were synthesized. For the macromonomer the cationic ring-opening polymerization of the 2-ethyl-2-oxazoline monomer was initiated by methyl tosylate and the monomer was end capped by methacrylic acid and triethylamine. The compound was characterized by SEC to obtain values of $M_n = 1170$ Da, $M_w = 1252$ Da and PDI = 1.07 and to confirm the livingness of the polymerization. In addition to the SEC measurements MALDI-TOF MS was used to investigate the possible occurrence of chain-transfer

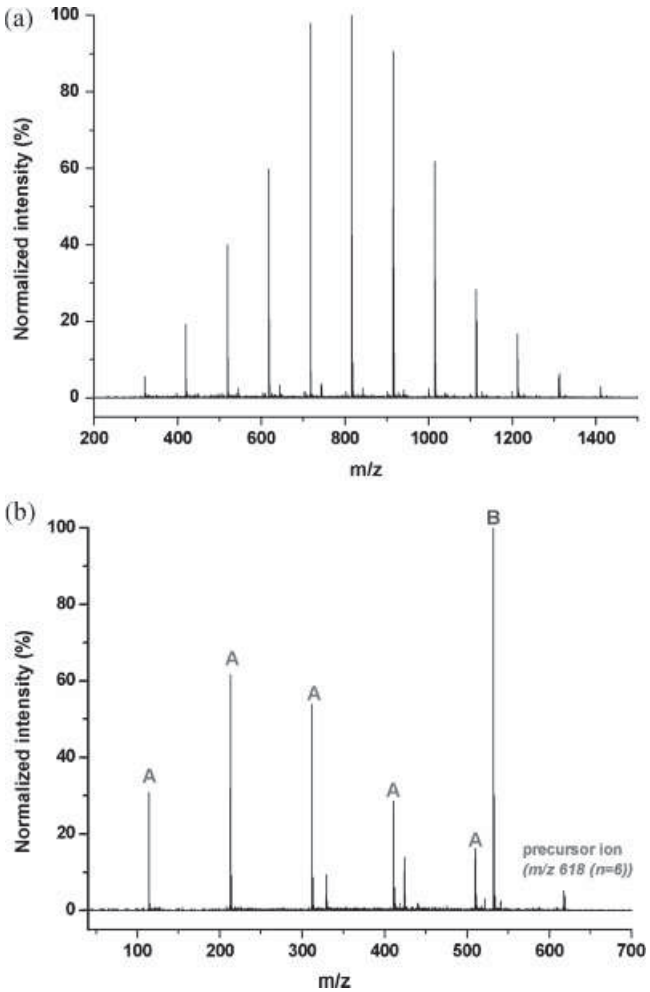

Figure 1. (a) MALDI-TOF MS spectrum of the oligo(2-ethyl-2-oxazoline) methacrylate macromonomer (matrix: dithranol in $CHCl_3$, ionization salt: NaI in acetone, solvent: $CHCl_3$). (b) MALDI-TOF MS/MS spectrum of the selected precursor ion at *m/z* 618. The product ion series (A) is initialized with the loss of the methacrylate end group (B).

DOI: 10.1002/rcm

or chain-coupling reactions as well as to determine the end groups. All spectra were measured in the reflectron mode to verify the polymer structure by comparison of the theoretical calculated and the measured isotopic pattern.[24] The MALDI-TOF MS spectrum, as shown in Fig. 1(a), contains only one distribution from *m/z* 200 to 1500 corresponding to the desired macromonomer structure ionized with a sodium cation ($CH_3[NCOC_2H_5CH_2CH_2]_n\ OCOCH_2CH_3 + Na^+$). All the oligomer ions could be assigned with a mass accuracy of better than 0.2 *m/z* units. The calculation of the number-average and the weight-average molar masses and the polydispersity index using PolyTools 1.0 delivered values that were comparable with those from the SEC measurement ($M_{n,MALDI} = 822$ Da, $M_{w,MALDI} = 873$ Da, $PDI_{MALDI} = 1.06$). For the MALDI-TOF MS/MS measurement the ion with the highest signal intensity within the distribution was chosen as the precursor ion. This ion was selected by the timed ion selector (TIS), which suppress all precursor ions with their product ions except the selected one, which can pass through this deflection gate.[7] As second step the selected precursor ion and its product ions were accelerated into a LIFT™ unit, where an actual potential lift is performed, when the ions are in the unit.[7,25] This unit is followed by a focusing cell to modulate the speed of the ions and a post-acceleration cell. Because metastable fragment ions are suppressed after the LIFT unit only the precursor ion and its associated product ions are detected. Fragmentation of the ion at *m/z* 618 resulted in one product ion series and some lower abundance ions and this spectrum is displayed in Fig. 1(b). After cleavage of the methacrylic end group (B) the more stable cationic oxazolinium species is formed and the depolymerization (A) of the macromonomer can be followed down to one monomer repeating unit with the initiator. This depolymerization probably takes place via a mechanism analogous to the polymerization mechanism of 2-oxazolines and is depicted in Scheme 1.

In comparison with this oligo(2-ethyl-2-oxazoline) macromonomer, a polymer with different end groups was synthesized to determine its MALDI-TOF MS/MS behavior. A propagyl tosylate-initiated polymerization of EtOx followed by a hydroxyl group end capping was chosen for this study. SEC was performed to confirm the molar mass and the PDI value ($M_n = 1{,}955$ Da; $M_w = 2{,}247$ Da; PDI = 1.15). The MALDI-TOF MS spectrum of the PEtOx was measured in the reflectron mode and showed three distributions with distances between the ions of the adjacent oligomers of 99.06 *m/z* units (Figs. 2(a) and 2(b)). The main distribution can be attributed to the desired product with a propargyl starting group and a hydroxyl end group. A second, less abundant distribution with higher molar mass can be assigned to a proton-initiated PEtOx with a hydroxyl end group. For the third distribution there are two possibilities for the starting group and the end group, on the one hand the proton as starting group and the enamine structure of the oxazoline as end group or on the other hand the propargyl group as initiating group and $-NHCH_2CH_2OH$ as end group. These additional ion series are formed via chain transfer and termination during the polymerization reaction. The comparison of these results with those given by NMR demonstrated that the NMR resonances of the -OH or $-NHCH_2CH_2OH$ groups are not observable in the spectrum, because they overlap with the other signals of the polymer or have a too low intensity. The characteristic values of this polymer ($M_n = 1{,}916$ Da; $M_w = 2{,}011$ Da; PDI = 1.05) were similar to those obtained from the SEC results. From the multiplicity of ions, the ion at *m/z* 1961, pertaining to the main distribution, was selected as the precursor ion (marked with a circle in Fig. 2(a)) with no influence from ions belonging to the two other distributions. The corresponding MS/MS spectrum is presented in Fig. 3(a). The product ions in the low mass range, up to *m/z* 250, showed very high signal intensities whereas those

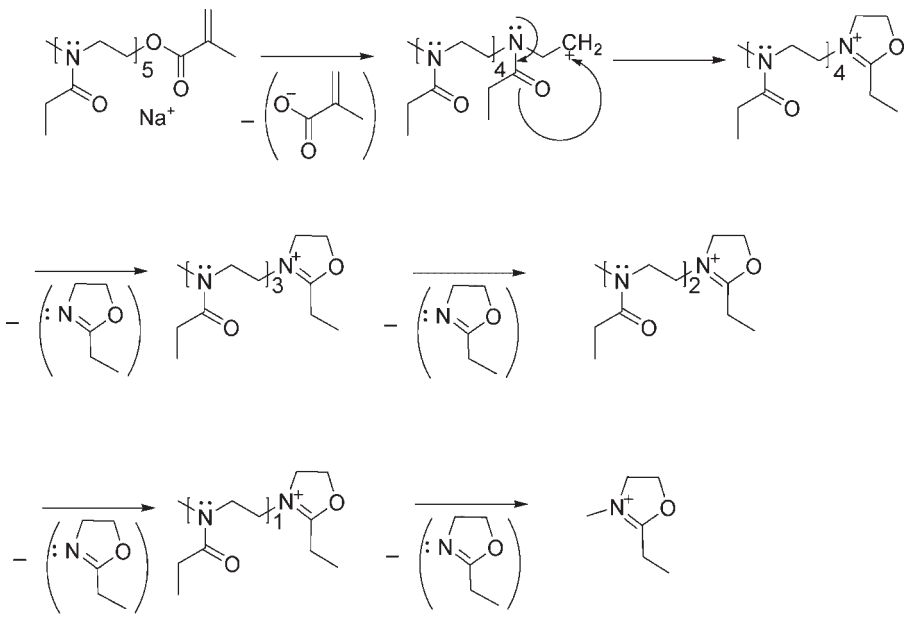

Scheme 1. Schematic representation of the suggested fragmentation pathways for the oligo(2-ethyl-2-oxazoline) methacrylate macromonomer in the MALDI-TOF MS/MS spectrum in Fig. 1(b).

DOI: 10.1002/rcm

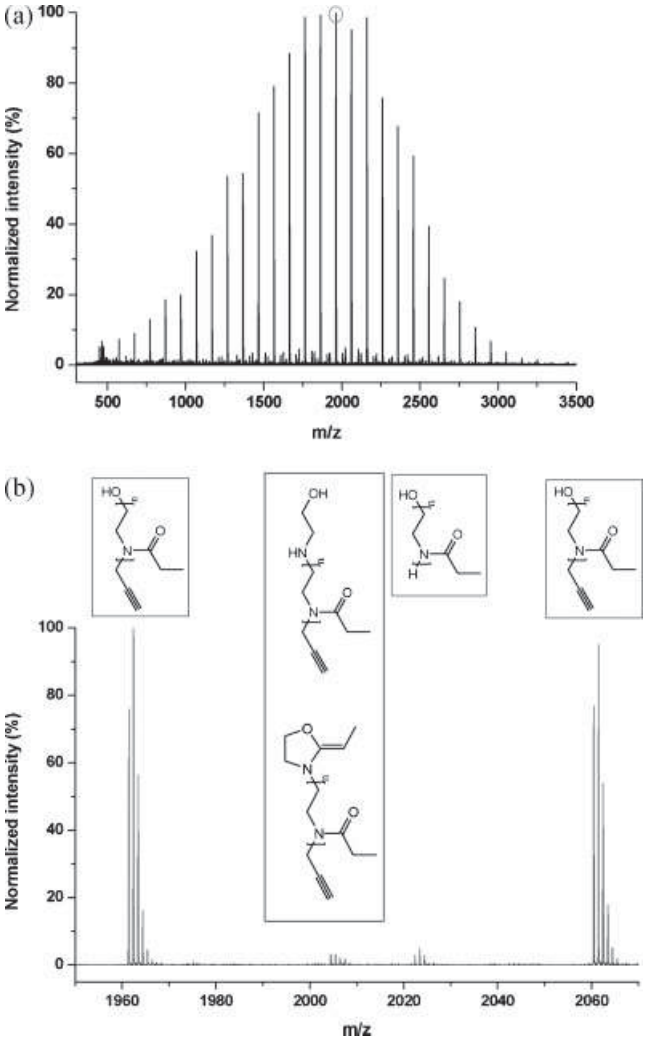

Figure 2. (a) MALDI-TOF MS spectrum of poly(2-ethyl-2-oxazoline) (matrix: dithranol in $CHCl_3$, ionization salt: NaI in acetone, solvent: $CHCl_3$). (b) Zoom of the MALDI-TOF MS spectrum of PEtOx (region from *m/z* 1950 to *m/z* 2070).

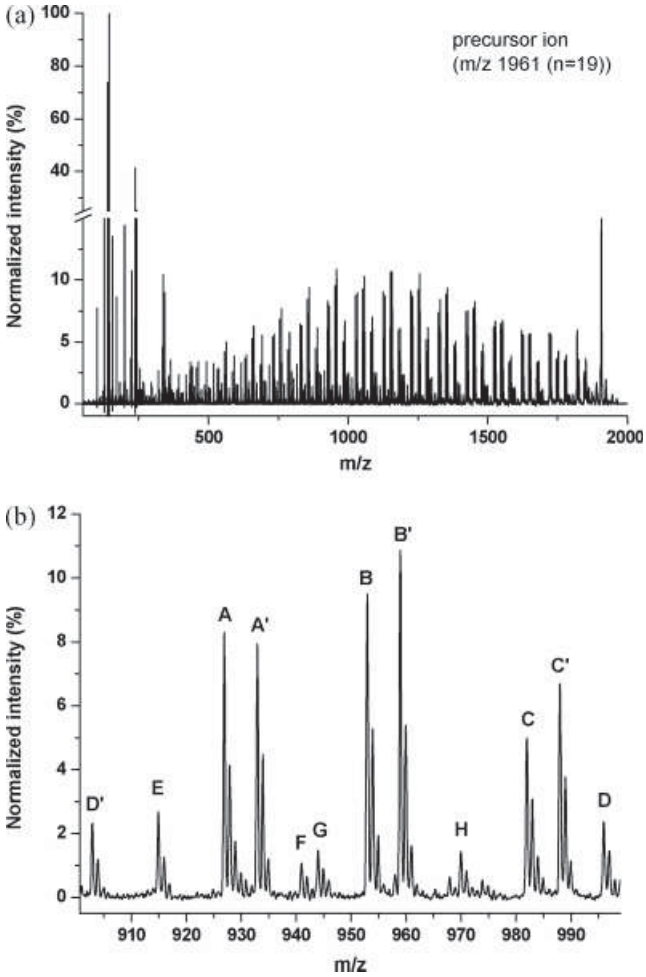

Figure 3. (a) MALDI-TOF MS/MS spectrum of the selected precursor ion at *m/z* 1961. (b) Zoom of the MALDI-TOF MS/MS spectrum of PEtOx (region from *m/z* 900 to *m/z* 1000).

between *m/z* 250 and the precursor ion at *m/z* 1961 had intensities around 10% of those of the low mass ions. In Fig. 3(b) twelve different series can be observed, where eight of them are actually four double series with a distance between the pairs of 6 *m/z* units, a distance which will be explained by the fragmentation mechanisms discussed below. The mass difference between the oligomers in these series was 99.07 *m/z* units, which corresponds to the mass of one repeating unit of EtOx.

Poly(2-ethyl-2-oxazoline)s have the same ethene spacing group between the heteroatom as is found in poly(ethylene glycol)s, which have already been characterized by MALDI-TOF MS/MS by several research groups. Lattimer and co-workers[26] used fast-atom bombardment (FAB) ionization to establish a 1,4-hydrogen or ethene elimination mechanism proceeding via a six-membered transition state. In these mechanisms the ethene spacing groups were only affected by the elimination of H_2 or C_2H_4 from the backbone. Further studies by Owens *et al.* using MALDI-TOF MS/MS confirmed these fragmentation pathways.[27] Transfer of these 1,4-hydrogen and ethene elimination mechanisms to the PEtOx system provided two possible arrangement of the six-membered transition state, starting from each side of the chain. The difference between the two arrangements is always the side group plus the nitrogen atom of the backbone, which causes the double series A, A′, formed by ethene elimination, and B, B′, formed by hydrogen elimination. These mechanisms are shown in Schemes 2(a) and 2(b). However, all the ions labeled with X could not be observed in the MS/MS spectrum. Interestingly, two of these four corresponding ions possess the same structure and, consequently, the same mass. Based on the chemical instability of these X fragments a second elimination of ethene is proposed, leading to the formation of an isocyanate group, providing an explanation for the occurrence of the third double series D, D′ (Scheme 2(c)). An alternative mechanistic possibility is that the double series A, A′ and B, B′ occurs via a McLafferty rearrangement[28] (Scheme 2(d)). The characteristic step in this pathway is the migration of a hydrogen atom in the γ-position to an unsaturated functional group via a six-membered cyclic transition state followed by a β-cleavage to form the double bond. A cleavage could then occur with the aid of the side chain, leading to a double bond end group and a propionic acid amide end group. This kind of rearrangement has already been described in the ESI-MS/MS of carboxylate anions[29] and the esters of *N*-

DOI: 10.1002/rcm

RCM

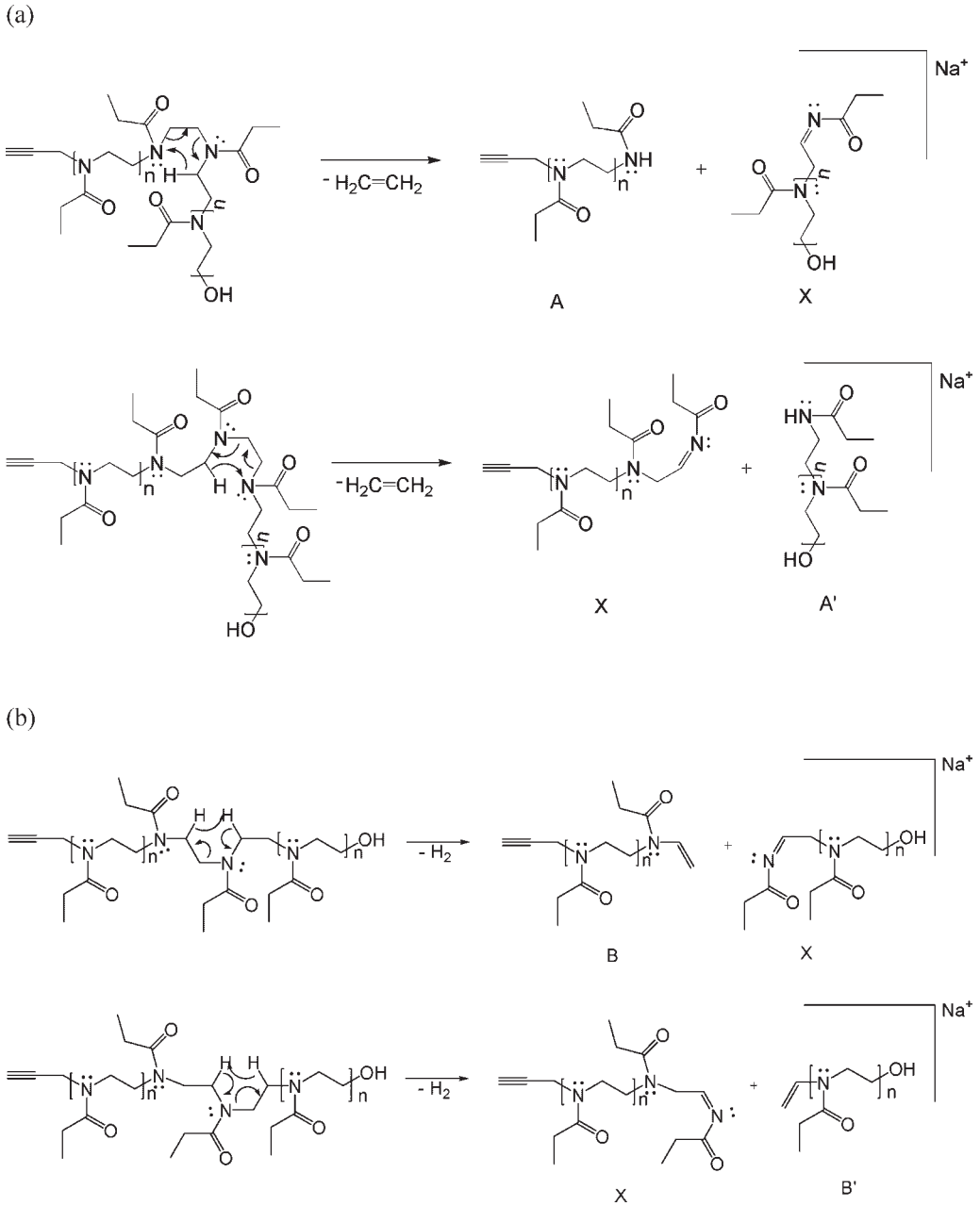

Scheme 2. Schematic representation of: (a) fragmentation pathway for sodiated PEtOx leading to the A and A′ series formed by ethene elimination; (b) fragmentation pathway for sodiated PEtOx leading to the B and B′ series formed by hydrogen elimination; (c) fragmentation pathway for sodiated PEtOx leading to the D and D′ series formed by ethene elimination on the side chain; (d) fragmentation pathway for sodiated PEtOx leading to the series A, A′ and B, B′ formed by McLafferty rearrangement; and (e) fragmentation pathway for sodiated PEtOx leading to the series C and C′ formed by α- and side-group cleavage.

acetylated peptides.[30] In a complementary fashion, the double series C and C′ could be explained by an α-cleavage of the backbone between the CH_2 groups followed by a cleavage of the side group resulting in the formation of a methylene imine end group (Scheme 2(e)). In addition to these related double series there are four additional product ion series, which can be assigned to structures that are formed by combination of the above mechanisms. The series E is explainable by ethene elimination on one side of the chain and hydrogen elimination on the other side of the chain. By performing hydrogen elimination on both sides of the chain the product ion series F can be formed. Finally, the series G and H can be explained by a combination of the α-cleavage and side-group elimination with ethene elimination for G or with hydrogen elimination for H.

In addition, ions belonging to the small distributions in the MALDI-TOF MS spectrum were characterized by tandem mass spectrometry. The side product $H(NCOC_2H_5CH_2CH_2)_nOH + Na^+$, emerging from chain transfer during the reaction, showed nine different product ion series in the MALDI-TOF MS/MS spectrum. These could be explained by the previously described fragmentation mechanisms, although because some of the ions formed by these mechanisms overlapped with each other only these nine series were observable.

DOI: 10.1002/rcm

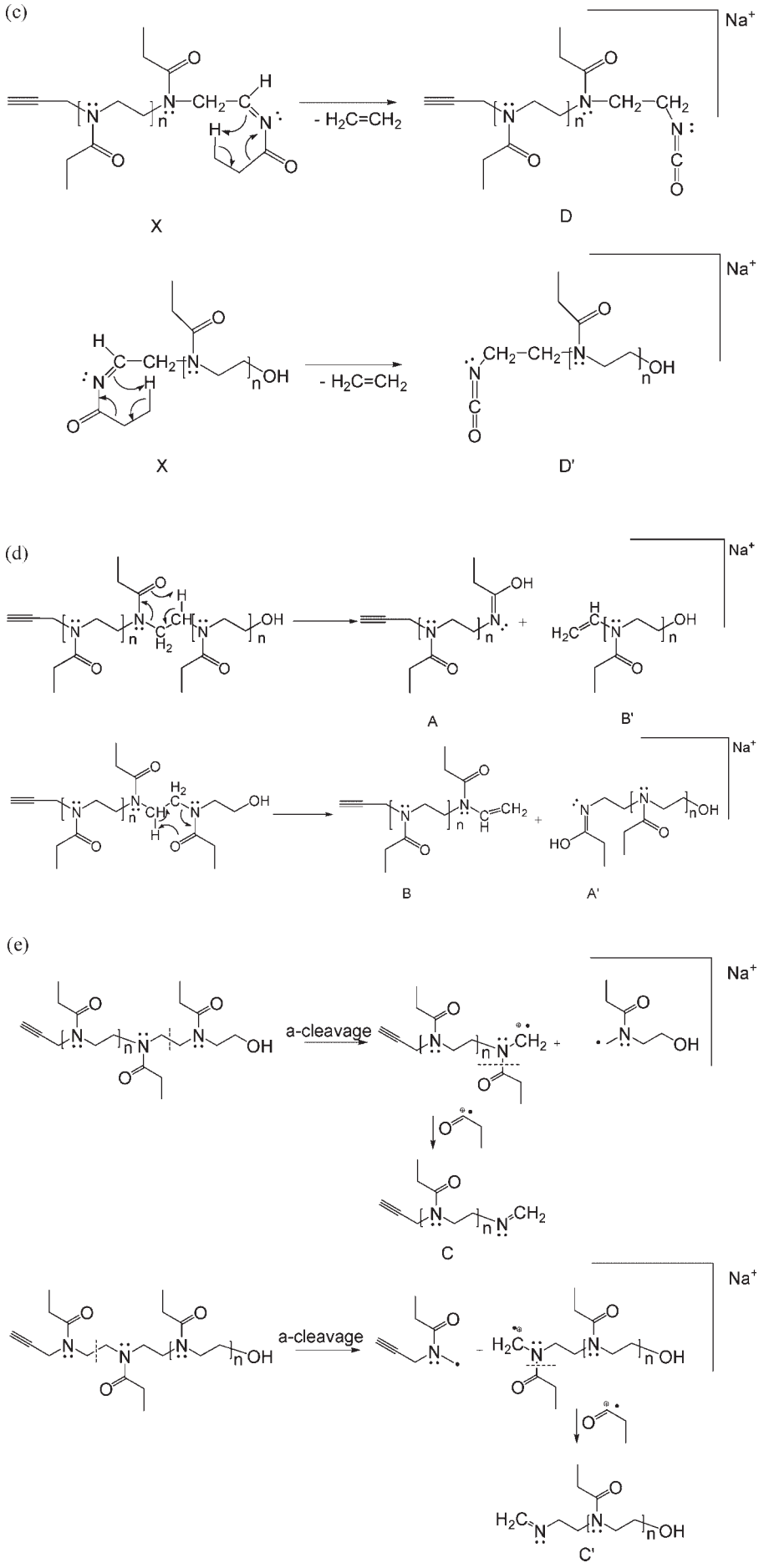

Scheme 2. (Continued).

DOI: 10.1002/rcm

RCM

The third distribution of the MS spectrum was also studied by MS/MS. Because of the two possible structures of the precursor ion, $H(NCOC_2H_5CH_2CH_2)_nNCOC_2H_4CH_2CH_2+Na^+$ or $CHCCH_2(NCOC_2H_5CH_2CH_2)_n\ NHCH_2CH_2OH+Na^+$, fifteen different product ion series were found in the MS/MS spectrum. These series can again be explained by the fragmentation mechanisms mentioned above.

CONCLUSIONS

A detailed characterization of the oligo(2-ethyl-2-oxazoline) methacrylate macromonomer and the 2-ethyl-2-oxazoline polymer was performed by MALDI-TOF MS/MS, which allowed the fragmentation of single ions from the MALDI-TOF MS spectrum. The resulting product ions occurring from fragments of the two poly(2-ethyl-2-oxazoline)s could be explained by the different leaving group qualities of the end groups. Methacrylic acid possessed a high lability leaving a cationic residual poly(oxazoline) chain that depolymerized easily. In contrast, the hydroxyl end group was a poor leaving group and thus it induced a variety of fragmentation mechanisms visible in the more complex MS/MS spectrum of this polymer. For both end groups possible fragmentation pathways like the 1,4 elimination of ethene or hydrogen or the McLafferty rearrangement were proposed and the formed structures were correlated to the obtained masses of the product ions.

The knowledge obtained from this study will be used for a detailed investigation of polyoxazolines synthesized with different end groups, with varying leaving group quality, side groups, i.e. methyl, nonyl or phenyl group, and higher molar masses. These studies will lead to the construction of a MS/MS product ion library of polyoxazolines for a fast and automated analysis of homopolymers and block or random copolymers with different end and side groups of this type of synthetic polymer.

Acknowledgements

The authors wish to acknowledge the Dutch Polymer Institute (DPI, technology area high-throughput-experimentation) and the Thüringer Kultusministerium (Grant No. B515-07008) for the financial support of this study. Many thanks are also expressed to Bruker Daltonics GmbH for their cooperation.

REFERENCES

1. Karas M, Hillenkamp F. *Anal. Chem.* 1988; **60**: 2299.
2. Tanaka K, Waki H, Ido Y, Akita S, Yoshida Y, Yohida T. *Rapid Commun. Mass Spectrom.* 1988; **2**: 151.
3. Hanton SD. *Chem. Rev.* 2001; **101**: 527.
4. Maloney DR, Hunt KH, Lloyd PM, Muir AVG, Richards SN, Derrick PJ, Haddleton DM. *J. Chem. Soc., Chem. Commun.* 1995; **5**: 561.
5. Montaudo G, Samperi F, Montaudo MS. *Prog. Polym. Sci.* 2006; **31**: 277.
6. Gies AP, Vergne MJ, Orndorff RL, Hercules DM. *Macromolecules* 2007; **40**: 7493.
7. Suckau D, Resemann A, Schuerenberg M, Hufnagel P, Franzen J, Holle A. *Anal. Bioanal. Chem.* 2003; **376**: 952.
8. Adams N, Schubert US. *Adv. Drug Deliv. Rev.* 2007; **59**: 1504.
9. Bassiri TG, Levy A, Litt M. *J. Polym. Sci., Part B: Polym. Lett.* 1967; **5**: 871.
10. Tomalia DA, Sheetz DP. *J. Polym. Sci., Part A-1: Polym. Chem.* 1966; **4**: 2253.
11. Seeliger W, Aufderhaar E, Diepers W, Feinauer R, Nehring R, Thier W, Hellman H. *Angew. Chem.* 1966; **78**: 913.
12. Kagiya T, Narisawa S, Maeda T, Fukui K. *J. Polym. Sci., Part B: Polym. Lett.* 1966; **4**: 441.
13. Uyama H, Kobayashi S. *Macromolecules* 1991; **24**: 614.
14. Groß A, Maier G, Nuyken O. *Macromol. Chem. Phys.* 1996; **197**: 2811.
15. Hoogenboom R, Schubert US. *Macromol. Rapid Commun.* 2007; **28**: 368.
16. Wiesbrock F, Hoogenboom R, Schubert US. *Macromol. Rapid. Commun.* 2004; **25**: 1739.
17. Wiesbrock F, Hoogenboom R, Leenen M, Van Nispen SFGM, Van der Loop M, Abeln CH, Van den Berg AMJ, Schubert US. *Macromolecules* 2005; **38**: 7957.
18. Hoogenboom R, Fijten MWM, Meier MAR, Schubert US. *Macromol. Rapid Commun.* 2003; **24**: 92.
19. Meier MAR, Hoogenboom R, Fijten MWM, Schneider M, Schubert US. *J. Comb. Chem.* 2003; **5**: 369.
20. Weber C. *Diploma thesis*, University of Jena, 2008.
21. Raeder HJ, Schrepp W. *Acta Polym.* 1998; **49**: 272.
22. Fijten MWM, Haensch C, Van Lankvelt BM, Hoogenboom R, Schubert US. *Macromol. Chem. Phys.* 2008; **209**: 1887.
23. Weber C, Becer CR, Baumgaertel A, Hoogenboom R, Schubert US. *Des. Monomers Polym.* 2009; in press.
24. Schubert US, Eschbaumer C. *J. Incl. Phenom.* 1999; **35**: 101.
25. Ultraflex III User Manual, version 1.0, September, 2006.
26. Selby TL, Wesdemiotis C, Lattimer RP. *J. Am. Soc. Mass Spectrom.* 1994; **5**: 1081.
27. Hoteling AJ, Kawaoka K, Goodberlet MC, Yu WM, Owens KG. *Rapid Commun. Mass Spectrom.* 2003; **17**: 1671.
28. McLafferty FW, Tureček F. *Interpretation von Massenspektren*. Spektrum Akademischer Verlag: Heidelberg, 1995.
29. Grossert JS, Cook MC, White RL. *Rapid Commun. Mass Spectrom.* 2006; **20**: 1511.
30. Anbalagan V, Patel JN, Niyakorn G, Van Stipdonk MJ. *Rapid Commun. Mass Spectrom.* 2003; **17**: 291.

DOI: 10.1002/rcm

Publication P7:

Linear polyethyleneimine: Optimized synthesis and characterization – on the way to “pharmagrade” batches

---

L. Tauhardt, K. Kempe, K. Knop, E. Altuntaş, M. Jäger, S. Schubert, D. Fischer, U. S. Schubert

Macromol. Chem. Phys. **2011**, *212*, 1918–1924.

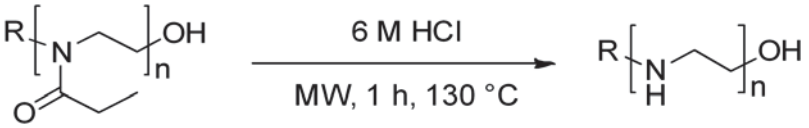

$R = CH_3$, H

Linear Polyethyleneimine: Optimized Synthesis and Characterization – On the Way to "Pharmagrade" Batches

Lutz Tauhardt, Kristian Kempe, Katrin Knop, Esra Altuntaş, Michael Jäger, Stephanie Schubert, Dagmar Fischer, Ulrich S. Schubert*

The synthesis of linear polyethyleneimine (LPEI) by acidic hydrolysis of poly(2-ethyl-2-oxazoline) is studied and optimized to reach the highest degree of hydrolysis within the shortest time range using a microwave synthesizer. In addition, the purification procedure is significantly improved; the fast batch processing combined with an excellent control of the actual heating time represents a well-suited alternative to the conventional synthesis on the way to "pharmagrade" PEI. The developed protocol for the preparation of methyl and proton-initiated LPEIs shows a high reproducibility, and the identity and purity of the LPEIs is proven by means of ^{1}H NMR and IR spectroscopy as well as MALDI-TOF- and ESI-Q-TOF-MS.

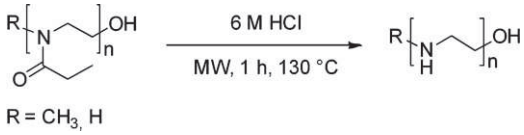

Introduction

Polyethyleneimines (PEIs) are available in two forms – as branched polyethyleneimine (BPEI) and linear polyethyleneimine (LPEI). Both are of highest interest in pharmaceutical research as polymeric vectors for gene delivery as they can electrostatically interact with negatively charged molecules like DNA and RNA.[1] PEIs with a high molar mass and a high degree of branching demonstrated the formation of small and enzymatically stable polyplexes with nucleic acids with a high cell uptake and therapeutic activity. However, their in vivo and clinical administration were limited due to cytotoxic effects and a low hemocompatibility.[1e] Although LPEIs with comparable molar masses were less effective in condensation of nucleic acids, they were found to be more suitable for in vivo applications due to a reduced toxicity and a higher transfection efficiency compared to the branched form.[2] Some of the commercially available LPEIs (e.g., ExGen500, jetPEI) already reached clinical trials, e.g. for the local treatments of bladder carcinoma and HIV disease.[3]

Beside its important role in gene delivery, PEI has some other applications. Based on its ability to form complexes with anionic species, metal complexes, or metal ions, PEI represents an interesting material for technical applications. On account of its chelating properties, PEI is used in waste water treatment for removing heavy metal ions and in hydrometallurgy for the recovery of noble metals.[4] Another field of application of PEI lays in the paper industry, where it is used for the fixation of pigments, as flocculation aid,[5] and as retention agent to improve the wet strength of paper (Epomin, Polymin).

LPEI can be synthesized by the polymerization of *N*-substituted aziridines and their subsequent hydrolysis.[6] The more common method, though, is to obtain LPEI by the

L. Tauhardt, K. Kempe, K. Knop, E. Altuntaş, Dr. M. Jäger, Prof. U. S. Schubert
Laboratory of Organic and Macromolecular Chemistry (IOMC) and Jena Center for Soft Matter (JCSM), Friedrich-Schiller-University Jena, Humboldtstraße 10, 07743 Jena, Germany
E-mail: ulrich.schubert@uni-jena.de
K. Knop, Dr. M. Jäger, Prof. U. S. Schubert
Dutch Polymer Institute (DPI), P.O. Box 902, 5600 AX Eindhoven, The Netherlands
Dr. S. Schubert, Prof. D. Fischer
Department of Pharmaceutical Technology and Jena Center for Soft Matter (JCSM), Institute of Pharmacy, Friedrich-Schiller-University Jena, Otto-Schott-Straße 41, 07745 Jena, Germany

DOI: 10.1002/macp.201100190

acidic[7] or basic[8] hydrolysis of poly(2-oxazoline)s. The living character of the cationic ring-opening polymerization (CROP) of 2-oxazolines allows the preparation of well-defined LPEIs with narrow molar mass distributions. Commercially available LPEIs, e.g. from Polysciences or Polyplus Transfection (jetPEI), are commonly synthesized by acidic hydrolysis of methyl-initiated poly(2-ethyl-2-oxazoline) (PEtOx).[9] However, with reaction times ranging from a few hours up to several days[7c] the acidic hydrolysis of poly(2-oxazoline)s proceeds very slowly. The basic hydrolysis is even slower.[10] More recently, the acceleration of the acidic hydrolysis under microwave irradiation was demonstrated by Schubert et al.[7a] Nevertheless, the reaction conditions were not optimized to reach full hydrolysis to LPEI within the shortest reaction time but rather to prepare partially hydrolyzed poly(2-methyl-2-oxazoline)s and poly(2-ethyl-2-oxazoline)s. Since the degree of hydrolysis significantly influences the transfection efficiency,[1d] a defined and also full degree of hydrolysis is preferred for pharmaceutical and clinical applications. Here, we report the optimization of the hydrolysis conditions of PEtOx using a microwave synthesizer with an autosampler and an improved purification procedure. These techniques were modified on the one hand with regard to reproducibility and controllability. On the other hand, the methods were upscaled to produce PEIs of defined quality in the range of several grams. Moreover, two differently initiated LPEIs, i.e., a methyl- and a proton-initiated, were prepared by acidic hydrolysis of methyl- (**1**) or proton- (**2**) initiated PEtOx. The methyl-initiated LPEI (**3**) contains only secondary amino groups, the proton-initiated LPEI (**4**) exhibits one primary amino group, which allows selective end group functionalization. The differently initiated LPEIs were characterized by proton nuclear magnetic resonance (^{1}H NMR) and infrared (IR) spectroscopy as well as matrix-assisted laser desorption/ionization (MALDI) and electrospray ionization (ESI) time-of-flight (TOF) mass spectrometry (MS). Such an intense structural characterization is essential on the way to "pharmagrade" PEI since up to now only very limited information and protocols, and even less data sheets are available. Consequently, a highly reproducible, time- and yield efficient synthesis protocol allows the preparation of well-defined and in-depth characterized LPEI batches that ensure the absence of impurities and the constancy in structure and, thus, properties.

Experimental Section

Chemicals and Instrumentation

2-Ethyl-2-oxazoline and methyl tosylate were obtained from Acros Organics, distilled to dryness over barium oxide (BaO), and stored under argon. Acetonitrile was purchased from Sigma-Aldrich. An Initiator Sixty single-mode microwave synthesizer from Biotage, equipped with a noninvasive IR sensor (accuracy: ±2%), was used for polymerizations and hydrolyses under microwave irradiation. ^{1}H NMR spectra were recorded on a Bruker AC 300 MHz at 298 K. Chemical shifts are reported in parts per million (ppm, δ scale) relative to the residual signal of the deuterated solvent. ESI-Quadrupole-TOF-MS measurements were performed with a micrOTOF Q-II (Bruker Daltonics) mass spectrometer. The ESI-Q-TOF mass spectrometer was operating at 4.5 kV, at a desolvation temperature of 180 °C, and in the positive ion mode. Methanol or methanol/water mixtures were used as solvents. The ESI-Q-TOF-MS instrument was calibrated in the m/z range 50–3 000 using an internal calibration standard (Tunemix solution), which was supplied from Agilent. The MALDI-TOF-MS spectra were measured on an Ultraflex III TOF/TOF (Bruker Daltonics GmbH, Bremen, Germany). The instrument was equipped with a frequency-tripled Nd:YAG operating at a wavelength of 355 nm. All spectra were measured in the positive reflector mode. For the sample preparation 1 μL of PEI (10 mg · mL^{-1}) and 10 μL of 2,5-dihydroxybenzoic acid (DHB) (10 mg · mL^{-1}), both dissolved in methanol, were mixed. One microliter of this solution was applied to the target using the dried-droplet method. The IR spectra were recorded on a FT-IR spectrometer IRAffinity-1 (Shimadzu). Size-exclusion chromatography (SEC) of the PEtOxs was measured on a Shimadzu system equipped with a SCL-10A system controller, a LC-10AD pump, and a RID-10A refractive index detector using a solvent mixture containing chloroform, triethylamine, and isopropyl alcohol (94:4:2) at a flow rate of 1 mL · min^{-1} on a PSS-SDV-linear M 5 lm column at room temperature. The system was calibrated with polystyrene (370–67 500 g · mol^{-1}) standards.

Synthesis of LPEI

The PEtOxs used in this study as starting materials for the preparation of LPEI were synthesized according to literature.[11] The polymerization of 2-ethyl-2-oxazoline was performed at 140 °C in a microwave synthesizer using methyl tosylate or *p*-toluenesulfonic acid as initiator and acetonitrile as solvent. PEtOxs with molar masses between $\overline{M}_n = 1\ 000$ g · mol^{-1} and $\overline{M}_n = 20\ 000$ g · mol^{-1} and low polydispersity index values (PDI ≤ 1.3) were synthesized. As a general method, methyl- (**1**) or proton-initiated (**2**) PEtOxs were treated with an excess of 6 M aqueous HCl for different periods of time at 100 and 130 °C in a flask and a microwave synthesizer, respectively. The acid was removed under reduced pressure, and the residue was dissolved in water followed by the addition of 3 M NaOH until precipitation occurred. The LPEI was filtered off, recrystallized from water, dissolved in methanol or *N,N*-dimethylformamide (DMF), and precipitated into ice-cold diethyl ether. The white precipitate was filtered off and dried in vacuo at 40 °C (methanol) or 60 °C (DMF) for 5 d. The purity and the degree of hydrolysis of the resulting LPEI **3** (methyl-initiated) and **4** (proton-initiated) were determined by ^{1}H NMR spectroscopy.

Optimized Synthesis Protocol

For the production of "pharmagrade" LPEI, the following optimized synthesis protocol was established: The PEtOx **1** or **2** (5 g) was dissolved in 15 mL of 6 M aqueous HCl and heated in a microwave

synthesizer for 1 h. The acid was removed by vacuum distillation (30 mbar) at 130 °C. The residue was dissolved in water (50 mL), and 3 M aqueous NaOH was added until precipitation occurred. The LPEI was filtered off and recrystallized from water (80 mL). After filtration, the LPEI was dissolved in methanol (40 mL) and precipitated into ice-cold diethyl ether (400 mL). The white precipitate was filtered off and dried in vacuo at 40 °C for 5 d. The purity and the degree of hydrolysis of the resulting LPEI **3** or **4** were determined by ^{1}H NMR spectroscopy.

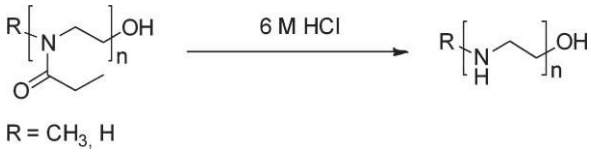

Scheme 1. Schematic representation of the synthesis of the different LPEIs.

Methyl-Initiated LPEI (3)

^{1}H NMR (300 MHz, CD_3OD): $\delta = 3.65$ (t, CH_2-OH), 2.73 (br., $N-CH_2$), 2.39 (s, CH_3-N). IR (FT-IR): $\nu = 3\,217$ (NH), 2 873 (CH_3), 2 804 (CH), 1 446 (CH_2/CH_3), 1 330 (C–N), 1 134 (C–N), 1 103 (C–N) cm^{-1}.

Proton-Initiated LPEI (4)

^{1}H NMR (300 MHz, CD_3OD): $\delta = 3.65$ (t, CH_2-OH), 2.73 (br., $N-CH_2$). IR (FT-IR): $\nu = 3\,271$ (NH_2), 3 217 (NH), 3 116 (NH_2), 2 877 (CH_3), 2 808 (CH), 1 597 (NH), 1 450 (CH_2/CH_3), 1 334 (C–N), 1 103 (C–N) cm^{-1}.

Results and Discussion

Conventional Synthesis of LPEI in a Flask Using Oil-Bath Heating

LPEI can be obtained by acidic[7] or basic[8] hydrolysis of poly(2-oxazoline)s. Since the acidic hydrolysis proceeds much faster than the basic hydrolysis,[10] the acidic treatment was chosen to synthesize LPEI. In a first set of experiments, PEtOx was heated with an excess of 6 M HCl overnight at 100 °C in a flask. LPEIs with two different starting groups, i.e., a methyl group (**3**) and a proton (**4**), and different molar masses were synthesized using this approach (Scheme 1). To the best of our knowledge, it is the first report of a proton-initiated LPEI. The primary amino group renders the possibility for selective end group functionalization. A detailed analysis of the differently initiated LPEIs is feasible by means of ^{1}H NMR spectroscopy (Figure 1). For both types of LPEI, a triplet at $\delta = 1.13$ can be observed. This signal belongs to the methyl group of uncleaved PEtOx side chains. By correlating the integrals of the methyl proton signal of the uncleaved side chain ($\delta = 1.13$) and the protons of the LPEI backbone ($\delta = 2.73$), the degree of hydrolysis can be determined within the limits of the ^{1}H NMR accuracy (98% after 18 h). About 1% of the PEtOx remained uncleaved even by elongation of the reaction time to 26 h. The incomplete hydrolysis is assigned to the precipitation of the LPEI hydrochloride, which is formed during the reaction.

The LPEIs obtained after neutralization with base were soluble in warm water, DMF, and methanol; and insoluble in chloroform, diethyl ether, and dichloromethane. The long reaction times of several hours required an optimization of the reaction conditions in a microwave synthesizer.

Optimized Synthesis of LPEI

The usage of microwave synthesizers is beneficial for the acceleration of the hydrolysis, as already reported.[7a] Based on this previous study, the hydrolysis conditions were further optimized. The usage of a microwave synthesizer enables heating of solvents above their actual boiling points resulting in shorter reaction times. Furthermore, it allows an excellent control of the heating time and rate. Therefore, the synthesis becomes tunable and also highly reproducible, which is important with respect to the pharmaceutical application of LPEI that requires a certified method for the preparation.

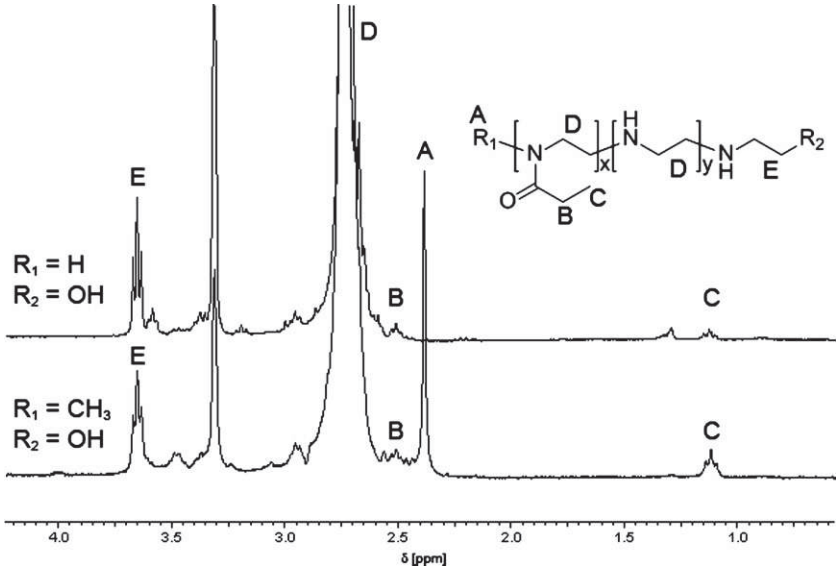

Figure 1. ^{1}H NMR spectra of the different LPEIs (300 MHz, CD_3OD).

Table 1. Degree of hydrolysis of **1** ($n = 20$) under different hydrolysis conditions in a microwave synthesizer.

Entry	Condition [a)]	Time [h]	Temperature [°C]	Degree of hydrolysis[b)] [%]
A	acidic	7	150	99
B	acidic	7	130	99
C	acidic	1	150	99
D	acidic	1	130	99
E	acidic	1/2	130	98
F	basic	1/6	130	12
G	basic	2	130	12

[a)]Acidic: 6 M aqueous HCl, basic: 3 M aqueous NaOH; [b)]Determined by ^{1}H NMR spectroscopy.

For the present study, 100 mg of PEtOx **1** (2 000 g · mol^{-1}, $n = 20$) were dissolved in 4 mL of 6 M HCl and heated in a microwave synthesizer. The degree of hydrolysis of the product was determined by ^{1}H NMR spectroscopy (Table 1). In a first run, compound **1** (2 000 g · mol^{-1}, $n = 20$) was hydrolyzed in a microwave synthesizer for 7 h at 150 and 130 °C (entries A and B), respectively, to yield product **3** (890 g · mol^{-1}, $n = 20$). Both samples showed no difference in their ^{1}H NMR and MALDI-TOF mass spectra, and a degree of hydrolysis above 99% was calculated.

Since the reaction was finished after 7 h, the time dependency of the hydrolysis was investigated in more detail. A test reaction at 150 °C and 1 h reaction time resulted in the same degree of hydrolysis (>99%) as for 7 h (entry C). For the reaction at 130 °C, different hydrolysis times were studied (entries D and E). After 0.5 h 2% of the PEtOx side chains were still uncleaved. Extension to 1 h yielded the maximum degree of hydrolysis (>99%). Longer reaction times did not increase the degree of hydrolysis further. It should be noted that in no event a full PEtOx side chain cleavage could be achieved. Hence, the optimal hydrolysis condition reaching the maximum side chain cleavage within the shortest time is 1 h at 130 °C. Compared to the methods described in literature so far, the reaction time could be significantly reduced.

The optimized microwave-assisted synthesis protocol (130 °C) was used for the synthesis of the LPEIs with molar masses between 430 and 8 600 g · mol^{-1}. The protocol could also be applied for the preparation of proton-initiated LPEI (**4**). In addition, commercially available PEtOx (Aldrich, $\overline{M}_w = 50\,000$ g · mol^{-1}) was hydrolyzed using the microwave-assisted synthesis protocol. 98% of the PEtOx side chains were cleaved within 1 h. Again, prolonged reaction times did not further increase the degree of hydrolysis. However, a subsequent second hydrolysis step increased the degree of hydrolysis slightly from 98 to 99%. Interestingly, commercially available LPEIs exhibit a much lower degree of hydrolysis, e.g. 90% for LPEI 2 500 g · mol^{-1} (Polyscience) and 96% for LPEI 25 000 g · mol^{-1} (Polyscience), according to the ^{1}H NMR measurement protocol described above.

The method established can be applied for a maximum concentration of 0.33 g PEtOx per mL 6 M HCl. At this point, the solubility limit of PEtOx in HCl at room temperature was reached. By using an Initiator Sixty single-mode microwave synthesizer from Biotage, the maximum in reaction volume was limited to 15 mL of stock solution (0.33 g PEtOx per mL 6 M HCl). It is thus possible to hydrolyze 5 g of PEtOx within 1 h, yielding about 2 g of LPEI. The autosampler can handle 24 microwave vials automatically. Due to the limited batch size, the time saving compared to the preparation in the flask is lost in cases of amounts larger than 48 g LPEI to be synthesized. This problem might be overcome by using microwave synthesizers with larger batches or continuous flow microwave reactors. When the concentration was increased to 0.67 g PEtOx per mL of 6 M HCl, the degree of hydrolysis decreased to 87% after 1 h reaction time.

Compared to the fast acidic hydrolysis conditions established above, the basic hydrolysis of PEtOx with 3 M NaOH at 130 °C in a microwave synthesizer proceeded much slower resulting in a degree of cleavage of only 12% after 10 min (entry F). The degree of hydrolysis remained constant even after 2 h reaction time (entry G). This behavior is attributed to the phase separation within the reaction mixture.

Optimized Purification Protocol

For the use of LPEI for polyplex formation in gene delivery, a high purity is essential. In addition, the detailed characterization of the polymer structure, including end group analysis by MALDI-TOF- and ESI-Q-TOF-MS, requires an improved purification procedure. The main impurities are salts. LPEI is known to form complexes with salts (e.g., NaI),[12] which can influence the MS spectra. Thus, the influence of different bases used for the purification of LPEI

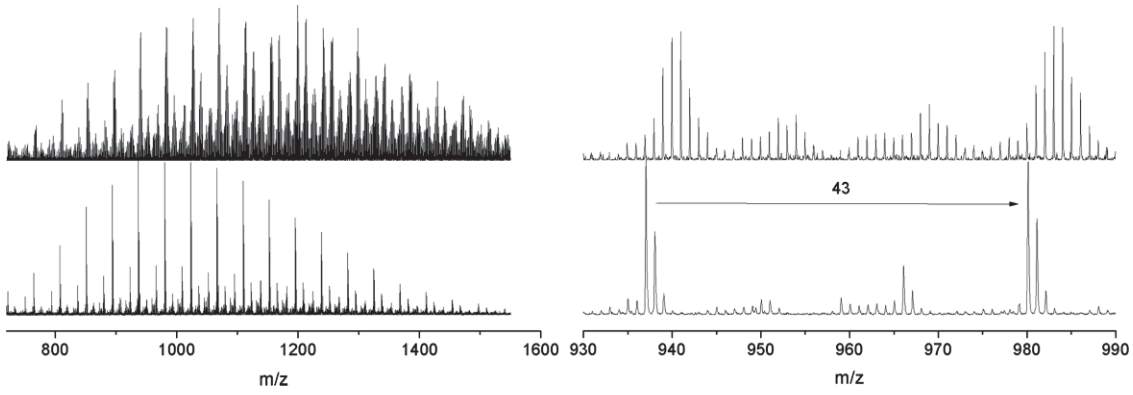

Figure 2. MALDI-TOF-MS spectra of LPEI before (top) and after (bottom) precipitation in diethyl ether (matrix: DHB).

on the resulting MS spectra was investigated, and the purification protocol was optimized.

LPEI was prepared as described above and precipitated using the following bases: NaOH, KOH, LiOH, Cs_2CO_3. Analysis by ^{1}H NMR spectroscopy and MALDI-TOF-MS showed no significant difference between the samples; no influence of the utilized base could be observed. However, the MALDI mass spectra revealed a complex pattern of overlapping peaks preventing a detailed analysis (Figure 2 top). A second recrystallization from water did not improve the quality of the spectra. Nevertheless, for the analysis of differently functionalized LPEIs it is necessary to obtain interpretable MALDI mass spectra for the end group determination. Therefore, the optimization of the purification procedure was investigated.

Since DMF is known to dissolve salts readily, the LPEI was dissolved in DMF and precipitated in a large excess of ice-cold diethyl ether instead of drying directly after the recrystallization from water. The effect of this step on the MALDI-TOF mass spectrum was remarkable (Figure 2 bottom). A disadvantage of this method was the usage of DMF as solvent. High drying temperatures and long drying periods were required to remove DMF completely, even under high vacuum conditions. To overcome this problem, methanol was used to dissolve the LPEI for precipitation in ice-cold diethyl ether. Consequently, the product can be dried in vacuo at 40 °C. ^{1}H NMR spectroscopy as well as ESI-Q-TOF-MS and MALDI-TOF-MS showed no differences to the results of the DMF route. The purity was proven by ^{1}H NMR spectroscopy indicating no solvent signals after drying for 5 d at 40 °C in vacuo.

Characterization of the LPEIs by MALDI-TOF and ESI-Q-TOF-MS

The different LPEIs were characterized by MALDI-TOF as already described for the methyl-initiated LPEI in literature.[7a] In addition, ESI-Q-TOF-MS studies were performed since less fragmentation products, compared to MALDI-TOF-MS measurements, were expected. Caffeic acid (CA) and 2,5-dihydroxybenzoic acid (DHB) without salt addition proved to be the most suitable matrices for LPEIs, as described previously.[13] Although DHB required higher laser intensities, the resolution of the peaks as well as the signal/noise ratio were found to be superior to the results obtained by CA. Hence, all measurements were performed using DHB. For the ESI-Q-TOF-MS measurements, the LPEIs were dissolved in methanol or in a methanol/water mixture.

In both MALDI-TOF and ESI-Q-TOF mass spectra, distributions for the sodium and the proton adduct of LPEI were found. In contrast to the MALDI mass spectra, which showed only singly charged ions, singly (+1) and doubly (+2) charged ionic species appeared in the ESI mass spectra, as depicted in Figure 3. An expanded region of the mass spectra of LPEI **3** ($\overline{M}_n = 860\ g \cdot mol^{-1}$, $n = 20$) is shown in Figure 4. Six of the distributions were assigned to the displayed structures. As expected, proton and sodium adducts of the reaction product could be detected as well as two differently initiated species. The methyl-initiated species derive from the initiation of the polymerization with methyl tosylate. In addition, proton-initiated species, formed by chain transfer reactions occurring during the polymerization of PEtOx, were observed.[14] Moreover, the MALDI-TOF and the ESI-Q-TOF mass spectra showed a species bearing an uncleaved PEtOx side chain. This supports the previous assignment of the triplet at $\delta = 1.13$ in the ^{1}H NMR spectrum. Both MALDI-TOF and ESI-Q-TOF mass spectra showed in principle the same peaks although in the ESI mass spectrum the proton-initiated species in LPEI 3 were hardly visible.

Simple MALDI-TOF and ESI-Q-TOF mass spectra were obtained for the proton-initiated LPEI **4** ($\overline{M}_n = 660\ g \cdot mol^{-1}$, $n = 15$) (Figure 5). Both ESI-Q-TOF and MALDI-TOF mass spectra showed the same peaks. No signals for methyl-initiated LPEI were visible since *p*-toluenesulfonic acid was

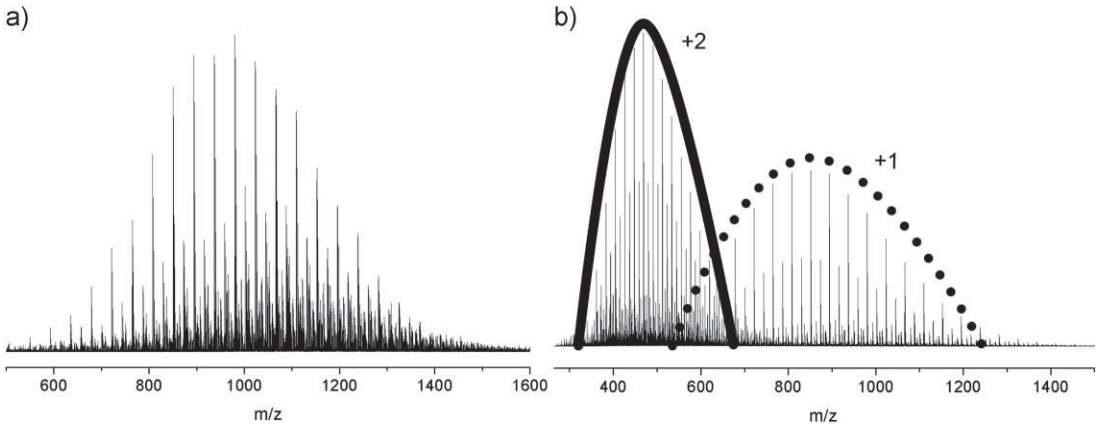

Figure 3. (a) MALDI-TOF-MS and (b) ESI-Q-TOF-MS (straight line: double, dotted line: single charged species) of LPEI **3** (860 g · mol^{-1}, $n = 20$).

used as initiator for the polymerization of the PEtOx. For three of the distributions, corresponding structures could be assigned. In accordance to the spectra of LPEI **3**, a distribution for LPEI with an uncleaved PEtOx side chain was found. The unassigned peaks (mainly in the MALDI-TOF-MS spectrum) belong to fragmentation products. A detailed study on the fragmentation and composition will be published elsewhere.[15] For the hydrolysis performed in both flask and microwave synthesizer, comparable spectra were obtained following the optimized purification protocol.

Since LPEI is a polycation, there is a problem analyzing higher molar masses with ESI-Q-TOF and MALDI-TOF-MS. For high-molar-mass LPEIs, there are numerous multiply charged species, making the ESI-Q-TOF mass spectra very complicated. By means of MALDI-TOF-MS only singly charged species can be detected. Therefore, it is hard to obtain spectra of the multiply charged polycation LPEI, when the degree of polymerization is too large.

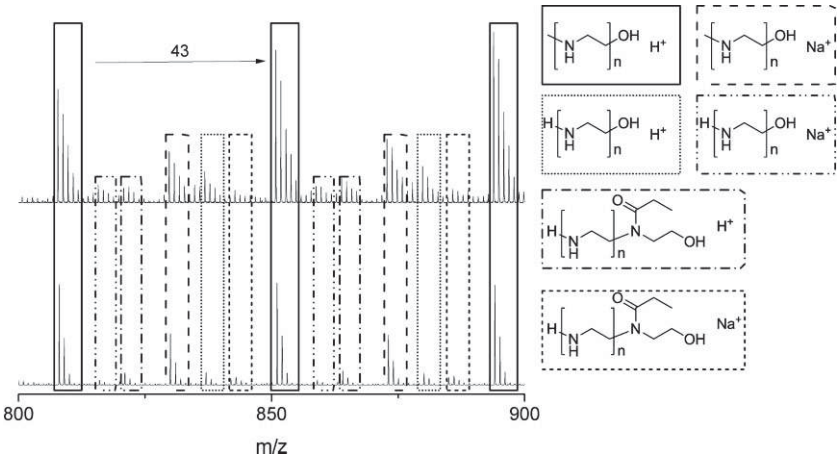

Figure 4. Expanded region of the MALDI- (top) and the ESI-Q-TOF mass spectra (bottom) as well as structural assignments for the different distributions of LPEI **3** (860 g · mol^{-1}, $n = 20$).

Conclusion

In conclusion, both the hydrolysis in a flask and in a microwave synthesizer results in a degree of hydrolysis above 99%. LPEIs with different molar masses (430 g · mol^{-1} to 8 600 g · mol^{-1}) were synthesized using both methods. However, compared to the conventional heating in a flask, the hydrolysis in a microwave synthesizer proceeded much faster. Since the batch processing is automated, it is possible to synthesize larger amounts of LPEI. The fast and efficient hydrolysis and the good heat distribution render the microwave synthesizer to be very energy saving, compared to conventional heating in a flask. Further advantages of a microwave synthesizer are the excellent control of the heating rate and time, making the hydrolysis highly controllable and reproducible. This is important with respect to the development of a certified synthesis method for larger amounts of "pharmagrade" LPEI.

The synthesis conditions were optimized to obtain the maximum of side chain cleavage (99%) within the shortest time range. Although incomplete cleavage (<1%) was obtained even by increasing the reaction time and the temperature, the best and most efficient hydrolysis conditions were found to be 130 °C for 1 h using a microwave synthesizer. The maximum concentration of PEtOx, which can be hydrolyzed, was found to be 0.33 g PEtOx per mL 6 M hydrochloric acid. An increase of the concentration led to a decrease of the degree of hydrolysis.

A methyl and a proton-initiated LPEI were prepared via the improved protocol. Several parameters, which can be used as specification for a "pharmagrade" pro-

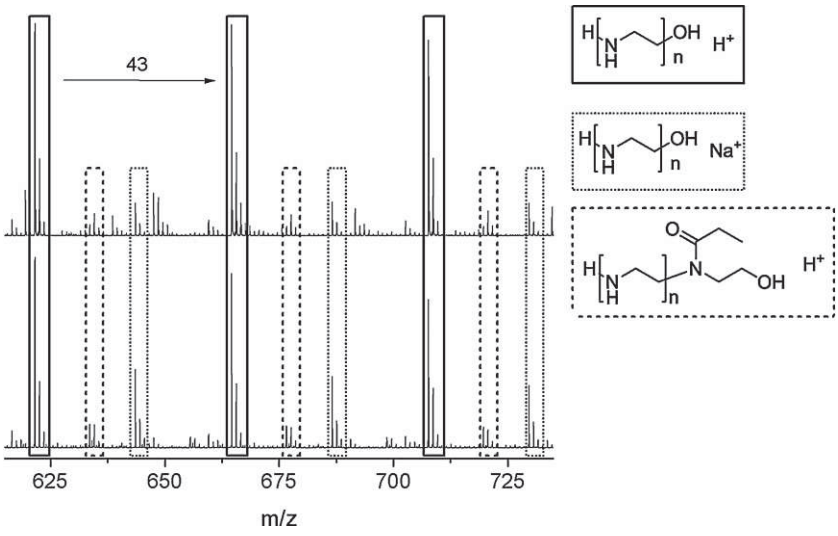

Figure 5. Expanded region of the MALDI- (top) and the ESI-Q-TOF mass spectra (bottom) as well as structural assignments for the different distributions of the proton-initiated LPEI **4** ($\overline{M}_n = 660\ g \cdot mol^{-1}$, $n = 15$).

duction of LPEI, were identified and systematically investigated. The developed protocol showed a high reproducibility, and the identity and purity of the LPEIs was proven by means of ^1H NMR and IR spectroscopy as well as MALDI-TOF- and ESI-Q-TOF-MS. To the best of our knowledge, this contribution contains the first report of a proton-initiated LPEI. The primary amino group of **4** enables the possibility of a selective end group functionalization of the LPEI.

Acknowledgements: The authors thank the Thuringian Ministry for Education, Science and Culture (grant #B514-09051, NanoConSens) and the Dutch Polymer Institute for financial support. K.K. is grateful to the Landesgraduiertenförderung for financial support.

Received: March 29, 2011; Revised: May 9, 2011; Published online: June 30, 2011; DOI: 10.1002/macp.201100190

Keywords: electrospray ionization mass spectrometry; hydrolysis; linear polyethyleneimine; matrix-assisted laser desorption/ionization mass spectrometry (MALDI-TOF MS); poly(2-ethyl-2-oxazoline)s

[1] [1a] O. Boussif, F. Lezoualc'h, M. A. Zanta, M. D. Mergny, D. Scherman, B. Demeneix, J. P. Behr, *Proc. Natl. Acad. Sci. USA* **1995**, *92*, 7297; [1b] B. Brissault, A. Kichler, C. Guis, C. Leborgne, O. Danos, H. Cheradame, *Bioconjugate Chem.* **2003**, *14*, 581; [1c] W. T. Godbey, M. A. Barry, P. Saggau, K. K. Wu, A. G. Mikos, *J. Biomed. Mater. Res.* **2000**, *51*, 321; [1d] J. H. Jeong, S. H. Song, D. W. Lim, H. Lee, T. G. Park, *J. Controlled Release* **2001**, *73*, 391; [1e] M. Neu, D. Fischer, T. Kissel, *J. Gene Med.* **2005**, *7*, 992.

[2] [2a] D. Fischer, A. von Harpe, K. Kunath, H. Petersen, Y. Li, T. Kissel, *Bioconjugate Chem.* **2002**, *13*, 1124; [2b] M. H. Louis, S. Dutoit, Y. Denoux, P. Erbacher, E. Deslandes, J. P. Behr, P. Gauduchon, L. Poulain, *Cancer Gene Ther.* **2005**, *13*, 367; [2c] L. Wightman, R. Kircheis, V. Rössler, S. Carotta, R. Ruzicka, M. Kursa, E. Wagner, *J. Gene Med.* **2001**, *3*, 362; [2d] J. W. Wiseman, C. A. Goddard, D. McLelland, W. H. Colledge, *Gene Ther.* **2003**, *10*, 1654.

[3] [3a] E. R. Toke, O. Lorincz, E. Somogyi, J. Lisziewicz, *Int. J. Pharm.* **2010**, *392*, 261; [3b] M. A. Mintzer, E. E. Simanek, *Chem. Rev.* **2008**, *109*, 259.

[4] [4a] S. Kobayashi, K. Hiroishi, M. Tokunoh, T. Saegusa, *Macromolecules* **1987**, *20*, 1496; [4b] A. von Zelewsky, L. Barbosa, C. W. Schläpfer, *Coord. Chem. Rev.* **1993**, *123*, 229; [4c] E. Bayer, B. Y. Spivakov, K. Geckeler, *Polym. Bull.* **1985**, *13*, 307.

[5] B. A. Bolto, *Prog. Polym. Sci.* **1995**, *20*, 987.

[6] K. F. Weyts, E. J. Goethals, *Polym. Bull.* **1988**, *19*, 13.

[7] [7a] H. M. L. Lambermont-Thijs, F. S. van der Woerdt, A. Baumgaertel, L. Bonami, F. E. Du Prez, U. S. Schubert, R. Hoogenboom, *Macromolecules* **2010**, *43*, 927; [7b] M. H. Litt, C. S. Lin, *J. Polym. Sci., Part A: Polym. Chem.* **1992**, *30*, 779; [7c] R. Tanaka, I. Ueoka, Y. Takaki, K. Kataoka, S. Saito, *Macromolecules* **1983**, *16*, 849.

[8] [8a] J. Bartulín, B. L. Rivas, M. Rodríguez-Baeza, U. Angne, *Makromol. Chem.* **1982**, *183*, 2935; [8b] T. Saegusa, H. Ikeda, H. Fujii, *Polym. J.* **1972**, *3*, 35.

[9] US 20100197888 (2010), Polyplus Transfection (Ilkirch Graffenstaden, FR), invs.: A. Adib, F. Stock, P. Erbacher.

[10] K. M. Kem, *J. Polym. Sci.: Polym. Chem. Ed.* **1979**, *17*, 1977.

[11] R. Hoogenboom, R. M. Paulus, Å. Pilotti, U. S. Schubert, *Macromol. Rapid Commun.* **2006**, *27*, 1556.

[12] C. K. Chiang, G. T. Davis, C. A. Harding, T. Takahashi, *Macromolecules* **1985**, *18*, 825.

[13] J. E. Girard, M. Konaklieva, J. Gu, C. M. Guttman, S. J. Wetzel, *Proceedings of the 51st ASMS Conference on Mass Spectrometry and Allied Products, Montreal (Canada)*, 2003.

[14] [14a] A. Levy, M. Litt, *J. Polym. Sci. [A1]: Polym. Chem.* **1968**, *6*, 1883; [14b] M. Litt, A. Levy, J. Herz, *J. Macromol. Sci. A: Pure Appl. Chem.* **1975**, *9*, 703.

[15] E. Altuntaş, K. Knop, L. Tauhardt, K. Kempe, A. Crecelius, M. Jäger, M. Hager, U. S. Schubert, unpublished.

Publication P8:

Tandem mass spectrometry of poly(ethylene imine)s by electrospray ionization (ESI) and matrix-assisted laser desorption/ionization (MALDI)

E. Altuntaş, K. Knop, L. Tauhardt, Kristian Kempe, A. C. Crecelius, M. Jäger, M. D. Hager, U. S. Schubert

J. Mass Spectrom. **2012**, *47*, 105–114.

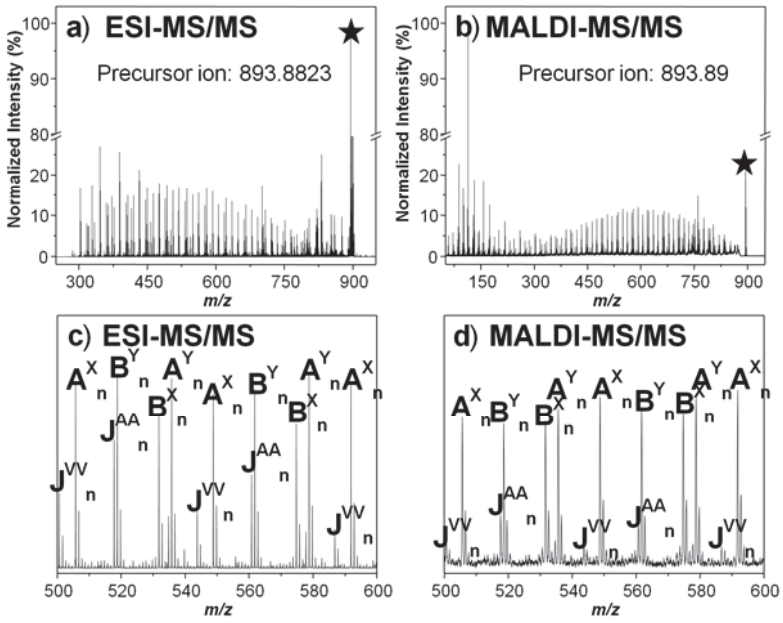

Research Article

Journal of MASS SPECTROMETRY

Received: 16 May 2011 Revised: 13 November 2011 Accepted: 17 January 2011 Published online in Wiley Online Library

(wileyonlinelibrary.com) DOI 10.1002/jms.2032

Tandem mass spectrometry of poly(ethylene imine)s by electrospray ionization (ESI) and matrix-assisted laser desorption/ionization (MALDI)

Esra Altuntaş,[a,b] Katrin Knop,[a,b,c] Lutz Tauhardt,[a,b] Kristian Kempe,[a,b] Anna C. Crecelius,[a,b,c] Michael Jäger,[a,b] Martin D. Hager[a,b] and Ulrich S. Schubert[a,b,c]*

In this contribution, linear poly(ethylene imine) (PEI) polymers, which are of importance in gene delivery, are investigated in detail by using electrospray ionization-quadrupole-time of flight (ESI-Q-TOF) and matrix-assisted laser desorption/ionization-time of flight (MALDI-TOF) mass spectrometry (MS). The analyzed PEIs with different end groups were synthesized using the polymerization of substituted 2-oxazoline via a living cationic ring-opening polymerization (CROP) and a subsequent hydrolysis under acidic conditions. The main goal of this study was to identify linear PEI polymers in a detailed way to gain information about their fragmentation pathways. For this purpose, a detailed characterization of three different linear PEIs was performed by using ESI-Q-TOF and MALDI-TOF MS in combination with collision-induced dissociation (CID) experiments. In ESI-MS as well as MALDI-MS analysis, the obtained spectra of PEIs resulted in fitting mass distributions for the investigated PEIs. In the tandem MS analysis, a 1,2-hydride shift with a charge-remote rearrangement via a four-membered cyclic transition state, as well as charge-induced fragmentation reactions, was proposed as the main fragmentation mechanisms according to the obtained fragmentation products from the protonated parent peaks. In addition, heterolytic and homolytic cleavages were proposed as alternative fragmentation pathways. Moreover, a 1,4-hydrogen elimination was proposed to explain different fragmentation products obtained from the sodiated parent peaks.

Supporting information may be found in the online version of this article.

Keywords: tandem mass spectrometry; poly(ethylene imine)s; collision-induced dissociation; fragmentation mechanism; electrospray ionization

INTRODUCTION

Poly(ethylene imine)s (PEIs) represent an important class of cationic polymers that are widely used in different industrial processes such as paper production, shampoo manufacturing, textile industry, water purification, and in the preparation of electrochemical sensors. However, the most current scientifically interesting topic is related to the usage of PEI as a complexation agent for negatively charged DNA and RNA in gene delivery.[1–8] There are several ways to synthesize PEIs, such as the cationic ring-opening polymerization (CROP) of aziridine by a Lewis acid leading to branched PEIs,[9] the controlled polymerization of *N*-substituted aziridines (which avoids branching reactions),[10] and the polymerization of substituted 2-oxazoline via the living CROP and the subsequent hydrolysis under acidic or basic conditions that yields strictly linear PEIs.[11–16] The living CROP of 2-oxazolines (Ox), and the subsequent hydrolyis of the resulting poly(2-oxazoline)s (POx) enables the possibility to synthesize well-defined linear poly(ethylene imine)s with a narrow molar mass distribution. Saegusa *et al.* published the first detailed synthesis and characterization study of linear PEIs starting from the living CROP of Ox and the subsequent hydrolysis of obtained POx under alkaline conditions. Our group recently published several contributions dealing with the synthesis of PEI homopolymers and copolymers for different possible applications such as temperature and pH responsive micelles.[14,15] A large number of studies have been performed on PEI/DNA complexes to investigate the correlation between the transfection efficiency and different characteristics of the PEI polymer, such as purity, molar mass, and architecture (linear and branched). Molar mass has been found to have a significant impact on the transfection efficiency; an increased transfection efficiency is reached with increased molar mass of PEIs.[17–22] However, the toxicity of PEI increases with a prolonged chain length of PEI; hence, the optimal molar mass that provides

* *Correspondence to: Ulrich S. Schubert, Laboratory of Organic and Macromolecular Chemistry (IOMC), Friedrich-Schiller-Universität Jena, Humboldtstrasse 10, 07743 Jena, Germany. E-mail: ulrich.schubert@uni-jena.de*

a *Laboratory of Organic and Macromolecular Chemistry (IOMC), Friedrich-Schiller-Universität Jena, Humboldtstrasse 10, 07743 Jena, Germany*

b *Jena Center for Soft Matter (JCSM), Friedrich-Schiller-Universität Jena, Humboldtstrasse 10, 07743 Jena, Germany*

c *Dutch Polymer Institute (DPI), P.O. Box 902, 5600 AX Eindhoven, The Netherlands*

low toxicity but high transfection efficiency has to be elucidated. The *in vivo* application of PEI requires a pure and well-defined material to obtain reproducible transfection efficiency results and to minimize the immunological response of the body to the cationic polymer. Therefore, a controlled synthesis and a detailed characterization of these macromolecules have tremendous importance because of its biological usage.

Mass spectrometry, combined with soft ionization techniques such as electrospray ionization mass spectrometry (ESI-MS)[23] and matrix-assisted laser desorption/ionization mass spectrometry (MALDI-MS),[24,25] has been widely utilized for the characterization of different polymer samples. Although each method involve different processes in ion formation, both techniques generally allow the ionization of various macromolecules with little or no fragmentation, enabling an accurate molar mass determination by making the unfragmented structure amenable to mass separation. Both techniques are frequently used for the characterization of different polymers for various purposes, such as to determine the accurate molar mass distributions of polymers, to analyze initiating and terminating end groups of different polymers, to study polymerization mechanisms and kinetics, to determine the initiator efficiency in radical polymerizations, to quantify the efficiency of photoinitiation processes in free radical polymerizations, and to identify the degradation products of different polymers.[26–36] The interfacing of these soft ionization methods with collision-induced dissociation (CID) or post-source decay (PSD) methods presents a modern powerful technique for the detailed structural characterization of polymers including the investigation of the sequence and molecular architecture in copolymers.[37–49] Despite the utmost importance of PEI, for transfection applications, only very few detailed characterizations of this material were reported up-to-date. Furthermore, mass spectrometric analyses of PEI are quite rare. This fact could be caused by the multiple charges of this polymer, which render it very suitable for complexation with negatively charged DNA but also introduces additional challenges in the MS characterization. For this study, PEIs were synthesized with different end groups by using the living CROP of 2-ethyl-2-oxazoline (EtOx) and subsequent hydrolysis under acidic conditions. The main goal was to identify these PEI polymers with different instrumentations to gain information about their fragmentation pathways. For this purpose, a detailed characterization of PEIs was performed by ESI-Q-TOF MS/MS and MALDI-TOF MS/MS. Comprehensive information concerning the fragmentation mechanisms of the PEI polymers and comparison of the tandem mass analysis of these polymers with two different ionization techniques (ESI/MALDI) is reported.

EXPERIMENTAL SECTION

Materials

2-Ethyl-2-oxazoline (99%, Acros, EtOx) was dried over barium oxide and distilled under argon prior to use. Methyl tosylate (98%, Aldrich, MeTos) was distilled and stored under argon. Sodium azide (99%, Sigma Aldrich) and acetonitrile (extra dry, Acros) were stored under argon. The matrix material for the MALDI-TOF MS and MS/MS measurements was 2,5-dihydroxybenzoic acid (DHB), and it was purchased from Sigma Aldrich. All solvents used for the ESI-Q-TOF MS measurements were LC-MS grade solvents; they were purchased from Sigma Aldrich and used as received.

Instrumentation

The polymerizations and hydrolyses were performed in a Biotage Initiator Sixty microwave synthesizer. Proton nuclear magnetic resonance (^{1}H NMR) spectra were recorded on a Bruker AC 300 MHz at 298 K. Chemical shifts are reported in parts per million (ppm, δ scale) relative to the residual signal of the deuterated solvent. The IR spectra were recorded on a FT-IR spectrometer IRAffinity-1 (Shimadzu).

General procedure for the microwave-assisted polymerization of PEtOx

A stock solution containing the initiator, EtOx monomer, and the solvent (acetonitrile) was prepared. The monomer concentration was adjusted to 4 M; and a monomer to initiator ratio of 20 was used, yielding a molar mass at 2000 g/mol. The microwave vials were heated to 140 °C for a predetermined time in the microwave synthesizer. The polymerization was quenched through the addition of trace amount of water or an excess of sodium azide. Subsequently, the solution was filtrated and the solvent was evaporated in vacuum. The polymer was redissolved in chloroform, washed with water, and precipitated in ice-cold diethyl ether. ^{1}H NMR samples were prepared to determine the monomer conversion and the molar masses (M_n) of the polymers.

Acidic hydrolysis of PEtOx to linear PEIs

Linear PEI polymers were synthesized through acidic hydrolysis of the corresponding PEtOx homopolymers. The PEtOx was heated with an excess of 6 M aqueous HCl in a microwave synthesizer at 130 °C for 1 h. After the removal of the acid under reduced pressure at 130 °C, the residue was dissolved in deionized water followed by the addition of 3 M NaOH until precipitation occurred (pH > 9). The PEI was filtered off and precipitated in deionized water for a second and a third time for an improved purification. After the filtration, the PEI was dissolved in methanol or DMF and precipitated into ice-cold diethyl ether. The white precipitate was filtered off and dried at 50 °C in vacuum. The polymers obtained were characterized by ^{1}H NMR and FT-IR spectroscopy. In every case, the degree of hydrolysis was above 99%, as determined by ^{1}H NMR spectroscopy (further information can be found in the supporting information (SI)). A detailed procedure of the synthesis of PEIs can be found elsewhere.[50]

ESI-Q-TOF MS and MS/MS analysis

PEI samples were analyzed by using a micrOTOF Q-II (Bruker Daltonics) mass spectrometer equipped with an automatic syringe pump, from KD Scientific, for sample injection. The ESI-Q-TOF mass spectrometer was running at 4.5 kV, with a desolvation temperature of 180 °C. The mass spectrometer was operating in the positive ion mode. Nitrogen was used as the nebulizer and drying gas. For the CID experiments, a quadrupole was used for the selection of precursor ions, and argon was used as the collision gas. The collision energy was set according to the MS/MS experiments to be carried out by using the tune collision energy function to identify the best collision energy value for these experiments. The standard electrospray ion (ESI) source was used to generate the ions. The concentration of the samples was 10 μg/mL, and all samples were injected with the use of a constant flow rate (180 μL/h) of sample solution. The solvent was methanol or a methanol/water mixture. There was no salt or acid addition prior to analysis, but ionization occured readily from the sodium content that is naturally present in the

glass or in the polymer sample. A total of 60 scans/spectrum were averaged, and the quoted *m/z* values are monoisotopic. The ESI-Q-TOF MS instrument was calibrated in the *m/z* range 50–3000 with the use of an external calibration standard (Tunemix solution), which is supplied from Agilent. All data were processed via Bruker Data Analysis software version 4.0.

MALDI-TOF MS and MS/MS analysis

MALDI-TOF MS experiments were performed with an Ultraflex III TOF/TOF (Bruker Daltonics) equipped with a Nd:YAG laser and a collision cell. All spectra were measured in the positive reflector mode. For the MS/MS measurements (LIFT™ mode), argon was used as the collision gas at a pressure of 2×10^{-6} mbar, and the collision energy amounts to 20 keV. The instrument was calibrated prior to each measurement with an external PMMA standard (molar mass 410 or 2500) from PSS Polymer Standards Services GmbH (Mainz, Germany) in the required measurement range. MS and MS/MS data were processed using Flex Analysis 3.0, PolyTools 1.12 (beta version), Data Explorer 4.0, and an isotope pattern calculator. The ion abundances of several scans were summed up to obtain spectra with good signal/noise ratio for TOF MS and MS/MS experiments. The quoted *m/z* values are monoisotopic.

For the sample preparation, 1 μL of PEI solution in methanol (10 mg/mL) and 10 μL of 2,5-dihydroxybenzoic acid (DHB) solution in methanol (10 mg/mL) were mixed (without salt addition), and the dried-droplet sample preparation method was applied.[51]

RESULTS AND DISCUSSION

Investigated PEIs

The synthesis of linear PEIs can be performed by hydrolyzing linear PEtOxs under alkaline or acidic conditions. The polymerizations of EtOxs were performed using the microwave-assisted living CROP, providing an easy access to well-defined polymers. As useful end groups a hydrogen starting group, as well as a methyl starting group, and a hydroxyl end group were chosen because of their similarity to those used for transfection agent applications. Furthermore, a methyl starting group and an azide end group were chosen to investigate the behavior and to be able to use PEIs in click reactions.[52,53] A schematic representation of the CROP of EtOx and the subsequent hydrolysis under acidic conditions to obtain PEIs is depicted in Scheme 1(a). The studied PEI polymers are displayed in Scheme 1(b).

The subsequent hydrolysis reaction to obtain the corresponding PEIs was executed in a microwave synthesizer. Previously, the hydrolysis reaction was performed overnight (24 h) under conventional heating to reflux; where, at 99% of the PEtOx, side chains were cleaved off. However, using a microwave synthesizer is much faster, and even azide end groups can tolerate the acidic microwave hydrolysis. After purification, a detailed analysis of the PEI polymers was performed with the use of ^{1}H NMR spectroscopy, showing for all macromolecules a 99% conversion of the amide side chains to amine functionalities (SI and [50]). Further characterization was performed with the use of MS techniques, where ESI-MS and MALDI-MS have been utilized. However, it was a challenging task to characterize the resulting PEIs in MS, as the obtained macromolecules contained large salt contaminations. Complicated spectra rendered the MS analysis almost unfeasible. By applying an optimized purification procedure for the PEI polymers and improved measurement conditions (such as the choice of the matrix for MALDI-MS), we found it possible to obtain analyzable MS, as well as MS/MS spectra. Several MALDI matrices have been used to identify the optimum measurement conditions for PEI polymers, such as *t*-2-(3-(4-*t*-butyl-phenyl)-2-methyl-2-propenylidene)malononitrile (DCTB), caffeinic acid (CA), sinnapinic acid (SA), and 2,5-dihydroxybenzoic acid (DHB). DHB was found to be the best suitable matrix for the characterization of PEI samples, as shortly reported previously in a proceeding publication;[54] therefore, all sample preparations were performed using the DHB matrix.

The compositional information on polymers can be obtained by a single-dimensional mass spectrum that can identify the number and types of monomer units, backbone substituents, and end groups incorporated into the studied polymer. In order to obtain the compositional information, the ESI-Q-TOF and MALDI-TOF mass spectra of the studied PEIs were scrupulously examined in terms of chain end group structures and molar mass distributions.

The PEI polymers, PEI-1, PEI-2, and PEI-3, with different initiating and/or terminating end groups were additionally characterized by utilizing ESI-Q-TOF MS/MS and MALDI-TOF MS/MS to identify the fragmentation products. For this purpose, specific oligomers from the distribution of polymer ions formed upon ionization were mass-selected and fragmented using CID. Tandem mass spectra reveal the masses of the fragmentation products, but not directly their structures or their fragmentation pathways. They can only be elucidated with the knowledge of the

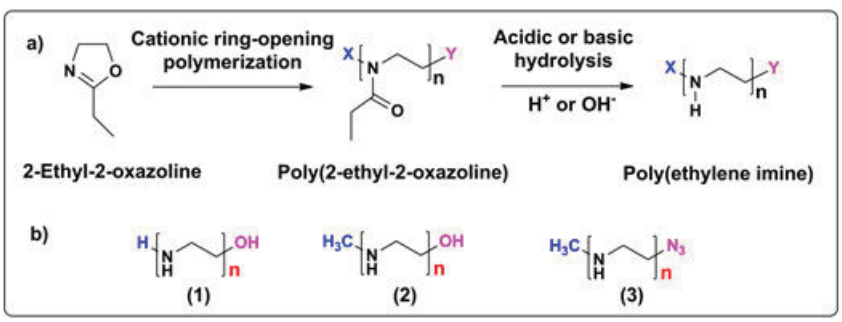

Scheme 1. (a) Schematic representation of the cationic ring-opening polymerization of EtOxs and subsequent hydrolysis into PEIs, (b) schematic representation of the studied PEI polymers 1 to 3.

corresponding fragmentation mechanisms. All three investigated PEI samples will be discussed in detail in the following section.

Mass spectrometry of PEI-1

ESI-Q-TOF and MALDI-TOF mass spectra of PEI-1 with H and OH end groups at the initiating (*X*) and terminating (*Y*) chain end are depicted in Fig. S1(a)–S1(d) (see SI). Both mass spectra reveal the expected signal spacing correlating to the repeating unit of the investigated PEI (43.04 *m/z* for C_2H_5N monomer unit). The expected PEI chains with hydrogen as initiating end group and hydroxyl as terminating end group were observed as the main distribution in the ESI-Q-TOF and MALDI-TOF mass spectra (labeled as **A** and **B** in Figs. S1(c) and S1(d) (SI)). Peak assignments were achieved on the basis of the expected ion *m/z* values and validated by isotopic pattern information. **A** represents the desired protonated distribution $[H(C_2H_5N)_nOH)+H]^+$, and **B** represents the desired sodiated distribution $[H(C_2H_5N)_nOH)+Na]^+$. The minor distribution (***I***) can be explained by the inefficient hydrolysis of PEtOx to PEI, because these oligomer series still have one EtOx monomer unit in their backbone $[H(C_5H_9NO)_1(C_2H_5N)_nOH)+H]^+$ or $[H(C_5H_9NO)_1(C_2H_5N)_nOH)+Na]^+$ (labeled as **I** in Figs. S1(c) and S1(d) (SI)), which are present in the both ESI-Q-TOF and MALDI-TOF mass spectra to a very little extent. This observation is supported by ^{1}H NMR spectroscopy, revealing a degree of hydrolysis around 99%. The only difference between the ESI-Q-TOF and MALDI-TOF mass spectra arises from some fragments (labeled as Fr in Fig. S1(d) (SI)), which are readily observed in the MALDI-TOF mass spectrum. These fragments were not observed in the ESI-Q-TOF mass spectrum, indicating that these fragments were caused by the MALDI-TOF process.

Tandem mass spectrometry of PEI 1

Figures 1 and 2 represent the ESI-Q-TOF and MALDI-TOF tandem mass spectra of PEI-1. The precursor ion at *m/z* 879.8579 (theoretical *m/z* 879.8618) represents the protonated adduct of the hydrogen-initiated and hydroxyl-terminated oligomer with 20 repeating units $[H(C_2H_5N)_{20}OH+H^+]$. There are several series of product ions, which can be distinguished depending on their newly formed end groups. Various kinds of fragmentation mechanisms can be involved in the formation of these ions. The tandem mass spectra contain four major distributions of fragment ion series ($\mathbf{A_n^X}$, $\mathbf{A_n^Y}$, $\mathbf{B_n^X}$, and $\mathbf{B_n^Y}$) and some minor distributions of fragment ion series ($\mathbf{J_n^{VV}}$, $\mathbf{J_n^{VA}}$, and $\mathbf{J_n^{AA}}$). These fragment ion series may be formed via a charge-remote fragmentation pathway, as shown in Scheme 2. This mechanism involves a 1,2-hydride shift via a charge-remote rearrangement mechanism through a four-membered cyclic transition state, resulting in the formation of two different functionalities at the terminal chain ends. The fragment ions were assigned according to the general nomenclature proposed by Wesdemiotis[55] for synthetic polymers to differentiate fragment ions containing different end groups. Superscripts *X* and *Y* are used to represent ions containing initiating (*X*) or termination (*Y*) end groups, respectively ($\mathbf{A_n^X}$, $\mathbf{A_n^Y}$, $\mathbf{B_n^X}$, and $\mathbf{B_n^Y}$). In this proposed mechanism, CID spectra of protonated PEIs occur through a charge-remote process, in which the ionizing proton does not play an active role in the cleavage. The main fragment series ($\mathbf{A_n^X}$, $\mathbf{A_n^Y}$, $\mathbf{B_n^X}$, and $\mathbf{B_n^Y}$) contain one of the original end groups and new end groups ($-NH_2$ or $-CH=CH_2$), which are formed by the proposed charge-remote fragmentation mechanisms. The *m/z* difference between two sequential fragmentation ions within one series corresponds to 43.04 *m/z* units, representing the mass of one repeating unit of PEI. The most abundant fragment ions series ($\mathbf{A_n^X}$, $\mathbf{A_n^Y}$, $\mathbf{B_n^X}$, and $\mathbf{B_n^Y}$) apparently result from this proposed

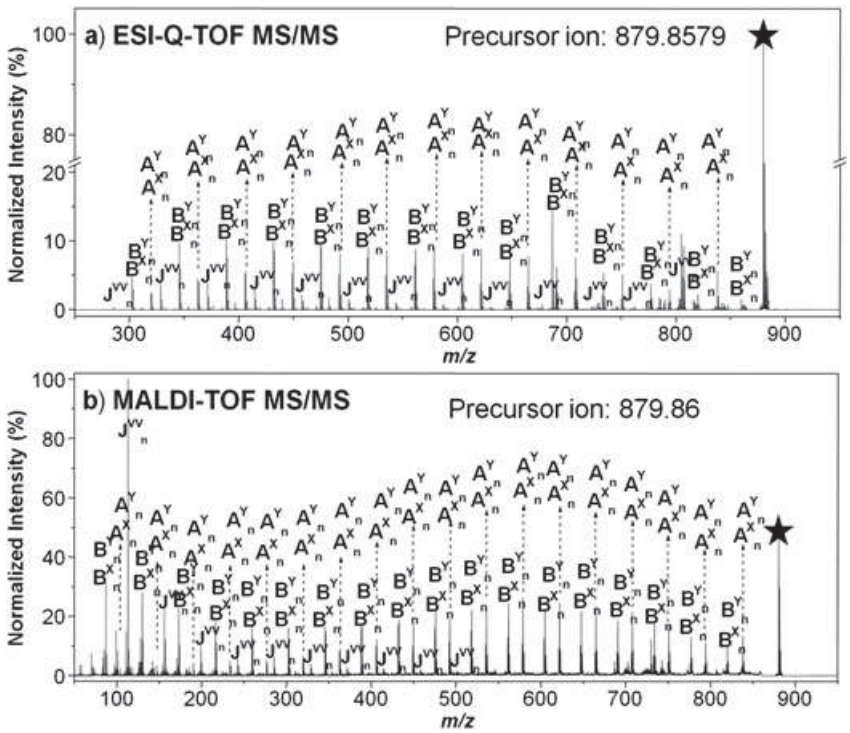

Figure 1. (a, b) ESI-Q-TOF and MALDI-TOF/TOF tandem mass spectra of the protonated PEI-1 parent peak with 20 repeating units marked with a star $[H(C_2H_5N)_{20}OH+H]^+$ (*m/z* 879.8579).

Journal of MASS SPECTROMETRY

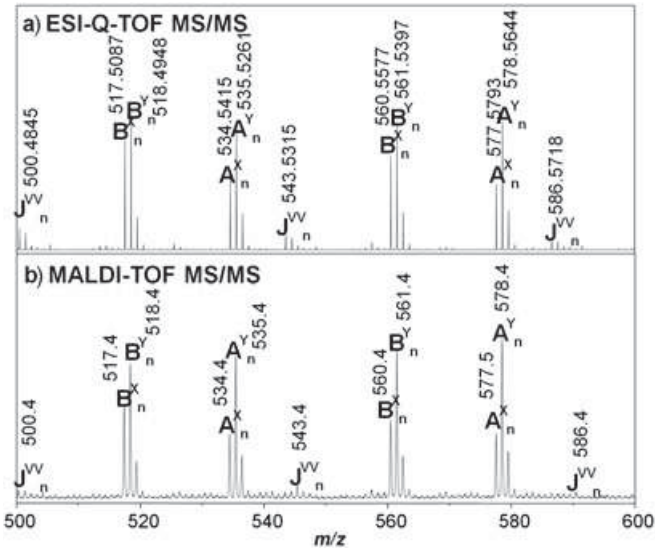

Figure 2. (a, b) ESI-Q-TOF and MALDI-TOF/TOF tandem mass spectra of the protonated PEI-1 and a close up of the range between *m/z* 500 and 600.

mechanism; whereas, the less abundant fragment ion series correspond to internal fragments (J_n^{VV}, J_n^{VA}, and J_n^{AA}) produced by a more complex fragmentation process. This charge-remote fragmentation occurs at both sides of the oligomer chains. Internal fragments with a variety of end groups were named as J_n species with different superscripts that indicate their end groups such as vinyl/amine (J_n^{VA}), vinyl/vinyl (J_n^{VV}), and amine/amine (J_n^{AA}). It must be noted that the ions of the main fragment series can result from both charge-remote and charge-induced dissociation mechanisms, but it is difficult to evaluate the extent of fragment ions from each pathway. Dissociation via competing charge-induced cleavage leads to similar fragments. Charge-induced cleavage of C-N bond followed by an energetically favorable 1,2-hydride shift could be an alternative to the charge-remote fragmentation. Lattimer [56–58] has already described in his earlier studies that a charge-induced dissociation from the protonated PEIs and polyglycols generates some of the fragment ion series via heterolytic or homolytic cleavage (Scheme 3). Polyethylene glycol (PEG) mainly dissociates via a charge-induced fragmentation mechanism and, to a lesser extent, via 1,4-hydrogen eliminations (especially metalated precursor ions). The same situation could be possible for PEI polymers because of the similar backbone. The cationic nature of PEI would imply a charge-induced dissociation at the site where the proton, as charge carrier, is located, as proposed by Lattimer. However, it is noteworthy that the substitution of –O by –NH can significantly change the unimolecular chemistry of the corresponding polymer cation. Because of the larger proton affinity of amines compared to ethers, protonation should take place at the –NH functionality and form an ammonium cation. These ions posses a well-stabilized charge center and might favor the charge-remote fragmentation mechanism upon CID. Moreover, charge-induced fragmentation mechanisms can only explain some of the found fragment ion series. Unfortunately, it is not possible to explain all fragment series with heterolytic or homolytic cleavage mechanisms. The tandem MS analyses of the PEIs were performed under both collision energy conditions (low energy in ESI-CID and high energy in MALDI-CID), yielding fragments, which suggest that the proposed charge-remote fragmentation reactions, as well as the charge-induced fragmentation reactions, are the dissociation mechanisms.

The tandem mass spectra of the protonated and the sodiated PEI precursor ions revealed some differences. A comparison of the ESI-Q-TOF tandem mass spectra of the protonated PEI precursor ions $[M+H]^+$ (observed *m/z* 879.8579, theoretical *m/z* 879.8618) and the sodiated PEI precursor ions $[M+Na]^+$ (observed *m/z* 901.8476, theoretical *m/z* 901.8438) shows that the sodiated precursor ions are more stable than the protonated precursor ions. The protonated species could easily be fragmented at low collision energies (20–60 eV); whereas, the sodiated species could only be fragmented to a small extent even at higher collision energies (60–200 eV). This indicates that sodiated ions are more stable towards collisional dissociation; hence, there is a need to use higher collision energies for obtaining fragments from sodiated species. The fragmentation mechanisms of the collisional dissociation for sodiated and protonated species are also different. The protonated species follow either a 1,2-hydride shift via a charge-remote rearrangement mechanism (Scheme 2) or a charge-induced fragmentation mechanism (heterolytic and homolytic bond cleavage, Scheme 3, similar cleavages were already proposed by Lattimer for PEGs). On the other hand, the sodiated species appear to fragment via a charge-remote 1,4-hydrogen

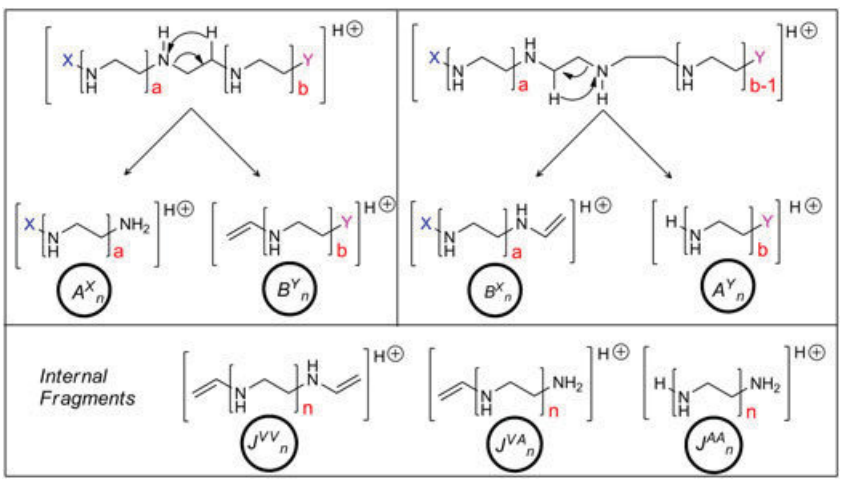

Scheme 2. Schematic representation of the proposed charge-remote rearrangement mechanisms involved in the fragmentation of protonated PEIs and the representation of potential fragmentation products.

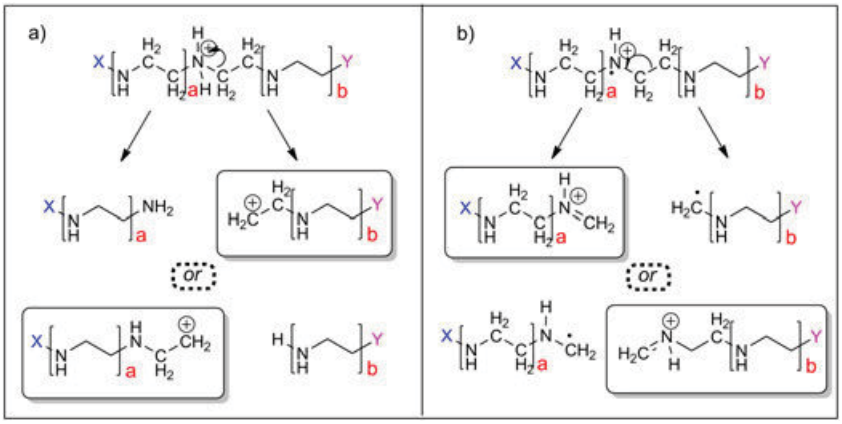

Scheme 3. Schematic representation of (a) heterolytic C-N bond cleavage and (b) homolytic C-C bond cleavage in a PEI chain.

elimination pathway that is analogous to that of PEG (Scheme 4) and a 1,2-hydride shift via charge-remote rearrangement mechanism. For the sodiated parent peaks, possible fragmentation pathways, such as the 1,4-hydrogen elimination, were proposed, and the formed structures ($\mathbf{B}^{X}_{n}$, $\mathbf{B}^{Y}_{n}$, $\mathbf{C}^{X}_{n}$, $\mathbf{C}^{Y}_{n}$, $\mathbf{D}^{X}_{n}$, and $\mathbf{D}^{Y}_{n}$) were correlated to the obtained masses of the fragmentation products. The differences between the sodiated and the protonated species for PEI-1 are depicted in Fig. 3. The schematic representation of the proposed charge-remote 1,4-hydrogen elimination mechanisms involved in the fragmentation of the sodiated PEIs and the resulting fragmentation products are shown in Scheme 4. The fragment product ions from the protonated and sodiated species (Table S1 and Table S2, in SI) are distributed throughout the whole mass range. This observation was valid for both tandem MS measurements (ESI and MALDI MS/MS).

PEI-2 and PEI-3

The ESI-Q-TOF and MALDI-TOF mass spectra of PEI-2, with methyl as initiating end groups and hydroxyl as terminating end groups, and a close up of the ESI-Q-TOF and MALDI-TOF mass spectra of PEI-2 in the range between *m/z* 800 and 900 are depicted in Fig. S2 (SI). **A** represents the protonated distribution of the expected product $[CH_3(C_2H_5N)_nOH)+H]^+$, and **B** represents the sodiated distribution $[CH_3(C_2H_5N)_nOH)+Na]^+$. There are two additional minor distributions obtained in the MS analysis (labeled as **C** and **D** in Figs. S2(c) and S2(d) (SI)). **C** represents the protonated side product distribution $[H(C_2H_5N)_nOH)+H]^+$, and **D** represents the sodiated side product distribution $[H(C_2H_5N)_nOH)+Na]^+$. These side products are formed during the living CROP of EtOx, and they can be explained by known chain transfer reactions during

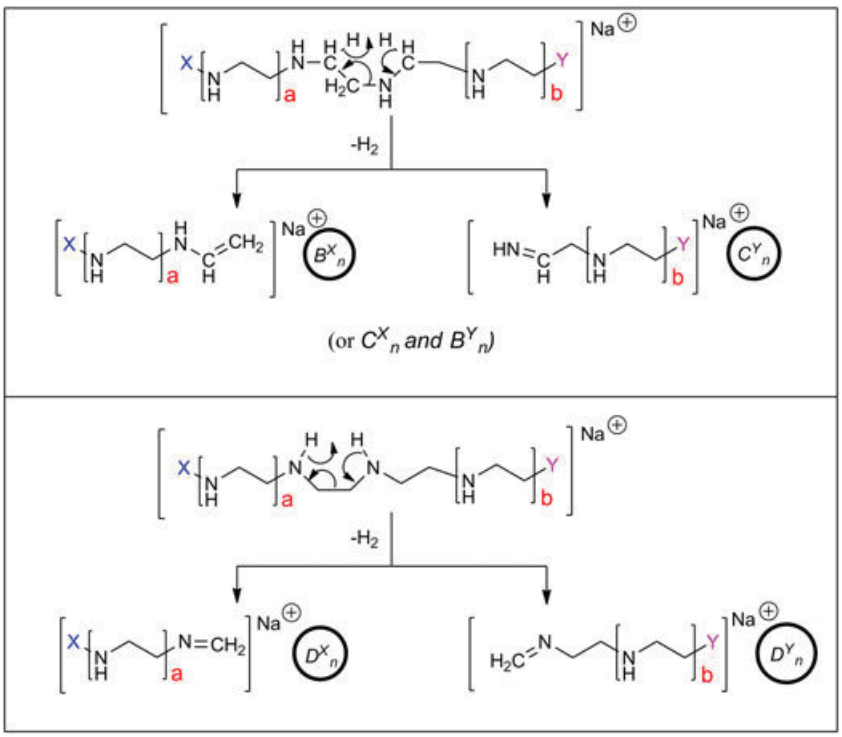

Scheme 4. Schematic representation of the proposed charge-remote 1,4-hydrogen elimination mechanisms involved in the fragmentation of the sodiated PEIs and the representation of the potential fragmentation products.

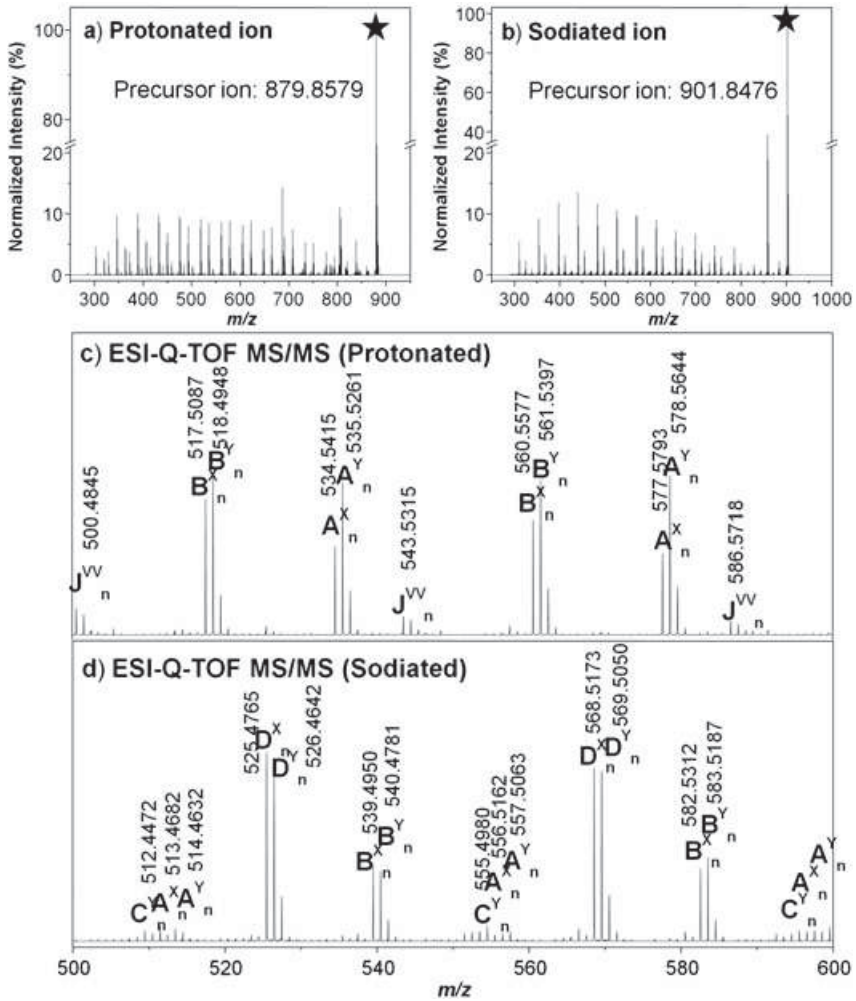

Figure 3. (a, b) ESI-Q-TOF tandem mass spectra of the protonated $[H(C_2H_5N)_{20}OH + H]^+$ (*m/z* 879.8579) and sodiated $[H(C_2H_5N)_{20}OH + Na]^+$ PEI-1 parent peak with 20 repeating units (*m/z* 901.8476) and (c, d) a close up of the ESI-Q-TOF tandem mass spectra of the protonated and sodiated PEI-1 in the range between *m/z* 500 and 600.

the CROP, which lead to proton-initiated PEtOx instead of methyl-initiated PEtOx. These proton-initiated PEtOx polymers are later turned into PEIs side products by acidic hydrolysis. The minor distribution (**I**) can be explained by the inefficient hydrolysis of PEtOx to PEI, as mentioned before. These oligomer series still bear one EtOx monomer unit in their backbone $[CH_3(C_5H_9NO)_1(C_2H_5N)nOH) + H]^+$ or $[CH_3(C_5H_9NO)_1(C_2H_5N)nOH) + Na]^+$ (labeled as I in Figs. S2(c) and S2(d) (SI)). They are present in both ESI-Q-TOF and MALDI-TOF mass spectra to a minor extent. Figure , 4(a)–4(d) represent the ESI-Q-TOF and MALDI-TOF/TOF tandem mass spectra of PEI-2. For the tandem mass analysis, the precursor ion (*m/z* 893.8823), which is the protonated adduct of the methyl-initiated and hydroxyl-terminated oligomer with 20 repeating units $[CH_3(C_2H_5N)_{20}OH + H]^+$, was selected. The fragment ion series can be explained by the previously mentioned charge-remote fragmentation pathway (Scheme 2), which involves a 1,2-hydride shift via a charge-remote rearrangement mechanism through a four-membered cyclic transition state resulting in the formation of two different functionalities ($-NH_2$ or $-CH=CH_2$) at the terminal chain ends.

Figure S3(a)–S3(d) displays the ESI-Q-TOF and MALDI-TOF mass spectra of PEI-3 with methyl as initiating end groups and azide as terminating end groups and a close up of the ESI-Q-TOF and MALDI-TOF mass spectra of PEI-3 in the range between *m/z* 800 and 900 (SI). **A** represents the protonated distribution of the desired product $[CH_3(C_2H_5N)_nN_3) + H]^+$, and **B** represents the sodiated distribution $[CH_3(C_2H_5N)_nN_3) + Na]^+$. Again, there are two minor distributions obtained in the MS analysis, which are formed by chain transfer reaction in the CROP that led to the proton-initiated PEtOx and were later turned into the proton-initiated PEIs during subsequent hydrolysis (labeled as **C** and **D** in Figs. S3(c) and S3(d) (SI)). The comparison of the ESI-Q-TOF and MALDI-TOF mass spectra of PEI-3 shows some differences between these two techniques. In the ESI-Q-TOF mass spectrum, there is one extra distribution (**N**) obtained for this polymer, which is formed because of the decomposition of the azide end group into nitrene through losing nitrogen (shown in Fig. S3(f)).[59] In a number of cases, loss of nitrogen from azides results in uncharged monovalent nitrogen intermediates called nitrenes. Nitrenes have triplet ground states and a short lifetime.[60] There were several additional distributions (**E, F, G**, and **H**) in the MALDI-TOF mass spectrum. A possible explanation for this situation is that the nitrene intermediate is very unstable, and different reactions might occur to stabilize it. The matrix material (2,5-dihydroxybenzoic acid (DHB)) used for this study is acidic. Therefore, it acts as a proton source to promote the

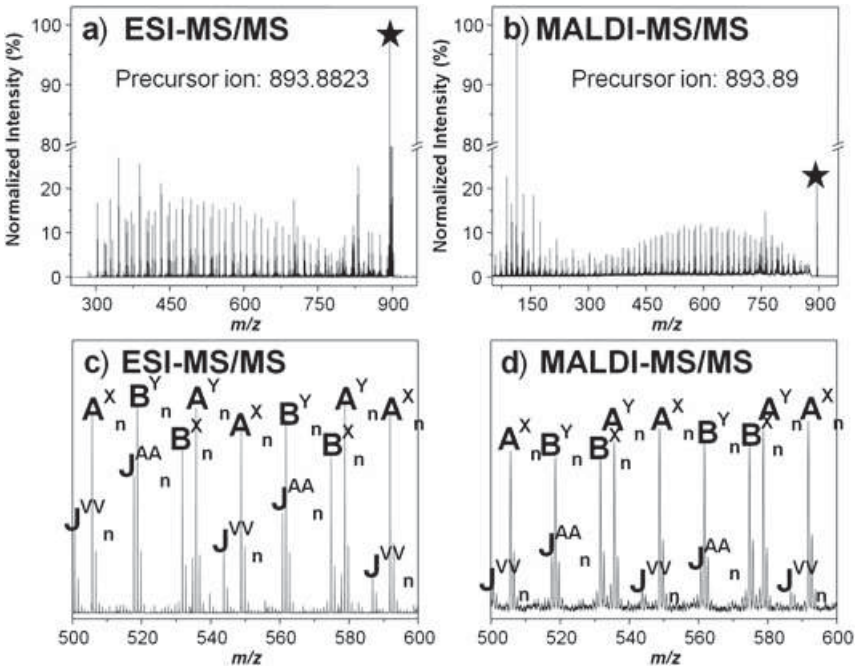

Figure 4. (a, b) ESI-Q-TOF and MALDI-TOF/TOF tandem mass spectra of the protonated PEI parent peak with 20 repeating units marked with a star $[CH_3(C_2H_5N)_{20}OH + H]^+$ (*m/z* 893.8823) and (c, d) a close up of the ESI-Q-TOF and MALDI-TOF/TOF tandem mass spectra of PEI-2 in the range between *m/z* 500 and 600.

formation of amine end groups from these nitrene intermediates. As a consequence, the main distribution in the MALDI-TOF mass spectrum was the PEI with methyl as the initiating end group and amine as the terminating end group. In contrast, the main distribution in the ESI-Q-TOF mass spectrum was the desired PEI structure with methyl and azide end groups, proving that the ESI technique is the softer ionization method, compared to MALDI, for the analysis of fragile azide end groups. The structural explanation of all distributions (**E, F, G**, and **H**) for PEI-3 polymer is depicted in Fig. S3(e) (SI).

The tandem mass experiment was carried out with the precursor ion (observed *m/z* 1069.9859, theoretical *m/z* 1069.9924) that possessed 23 repeating units and with sodium as the ionizing agent $[CH_3(C_2H_5N)_{23}N_3) + Na]^+$. Figure 5(a) and 5(b) represent the ESI-Q-TOF tandem mass spectrum of PEI-3 which showed some differences compared to PEI-1 and PEI-2. In the upper molar mass region of the tandem mass spectrum right after the precursor ion, a pronounced loss of nitrogen was observed. This neutral loss can be assigned to the decomposition of the azide end group into nitrene, which was also observed in the single-dimensional MS analysis.[59] The tandem mass spectrum shows the fragment ion series corresponding to the fragment series formed by a 1,2-hydride shift via charge-remote rearrangement mechanism (Scheme 2) and a charge-remote 1,4-hydrogen elimination pathway (Scheme 4), which are already discussed for the previous PEI polymers, within the medium and low molar mass region. A proper selection of a precursor ion for the fragmentation experiments was not possible because of the multiple overlapping fragments observed in the MALDI-MS; therefore, no tandem MS data were obtained for PEI-3 polymer.

A comparison of the tandem mass spectra of PEIs with different end groups reveals that only the azide end group has a tendency to cleave easily through the loss of nitrogen in the formation of an unstable nitrene end group which can also be turned into an amine end group in the MALDI-MS analysis. On the other hand, hydrogen, hydroxyl, and methyl end groups do not show any direct fragmentation. This behavior can be explained by the leaving group ability of these end groups; they have no tendency to fragment. Therefore, different charge-remote fragmentation mechanisms may occur along the whole

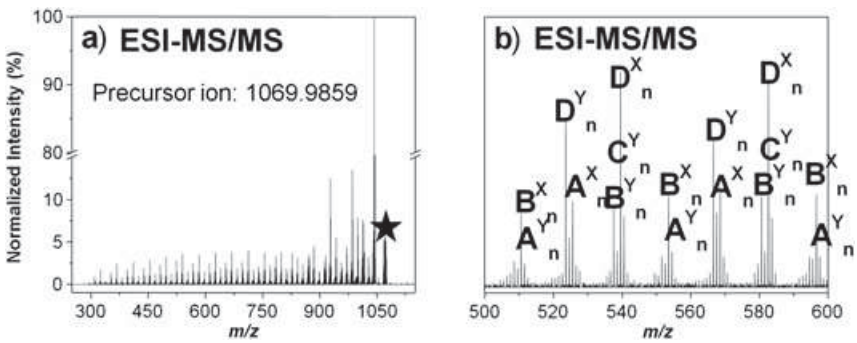

Figure 5. (a) ESI-Q-TOF tandem mass spectrum of the sodiated PEI parent peak with 23 repeating units marked with a star $[CH_3(C_2H_5N)_{23}N_3 + Na]^+$ (*m/z* 1069.9859) and (b) a close up of the ESI-Q-TOF tandem mass spectrum of PEI in the range between *m/z* 500 and 600.

backbone of the PEIs and form various main fragment series that contain one of the original initiating or terminating end groups (A_n^X, A_n^Y, B_n^X, B_n^Y, C_n^X, C_n^Y, D_n^X, and D_n^Y). Meanwhile, the less abundant fragment ion series can correspond to internal fragments (J_n^{VV}, J_n^{VA}, and J_n^{AA}) produced by a more complex fragmentation process where this charge-remote fragmentation occurs in both sides of the oligomer chains. Overall, it is possible to explain all fragmentation products within the whole molar mass region in the tandem mass spectra of PEIs with these proposed mechanisms and the combination of these mechanisms.

CONCLUSIONS

In this contribution, ESI-Q-TOF and MALDI-TOF mass spectrometers were utilized to elucidate in detail the macromolecular structures of linear PEIs. Tandem mass spectrometry experiments have been performed to investigate the possible fragmentation mechanisms with different initiating and terminating end groups. For PEIs, the type of the cation attached to these polymers was important, because protonated and sodiated species are fragmented via different fragmentation pathways. The presented study provides important information on the fragmentation mechanisms of PEI polymers and the comparison of the tandem mass analysis of these polymers with two different ionization techniques (ESI/MALDI). The information gained from this study will also help to build up a tandem MS product ion library for PEIs with different end groups including fragmentation pathways. This will provide necessary knowledge for the future to make the fast and automated identification of these polymers possible. This kind of studies will form a new research field that can be named as 'Polymeromics', and the obtained information will facilitate the structural elucidation of polymers (i.e. analysis of the initiating/end groups, the accurate molar mass distributions).

Acknowledgements

The authors thank the Dutch Polymer Institute (DPI, Technology area HTE, #667) and the Thüringer Ministerium für Bildung, Wissenschaft und Kultur (grant no. B715-07011 and B515-07008) for the financial support of this study. Kristian Kempe is grateful to the Landesgraduiertenförderung Thüringen for financial support.

Supporting Information

Supporting information may be found in the online version of this article.

REFERENCES

[1] O. Boussif, F. Lezoualc'h, M. A. Zanta, M. D. Mergny, D. Scherman, B. Demeneix, J. P. Behr. A versatile vector for gene and oligonucleotide transfer into cells in culture and *in vivo*: polyethylenimine. *Proc. Natl. Acad. Sci. U. S. A.* **1995**, *92*, 7297.
[2] W. T. Godbey, M. A. Barry, P. Saggau, K. K. Wu, A. G. Mikos. Poly(ethylenimine)-mediated transfection: a new paradigm for gene delivery. *J. Biomed. Mater. Res.* **2000**, *51*, 321.
[3] B. Brissault, A. Kichler, C. Guis, C. Leborgne, O. Danos, H. Cheradame. Synthesis of linear polyethylenimine derivatives for DNA transfection. *Bioconjugate Chem.* **2003**, *14*, 581.
[4] M. M. Ramos-Tejada, A. Ontiveros-Ortega, E. Gimenez-Martin, M. Espinosa-Jimenez, A. Molina Diaz. Effect of polyethyleneimine ion on the sorption of a reactive dye onto Leacril fabric: electrokinetic properties and surface free energy of the system. *J. Colloid Interface Sci.* **2006**, *297*, 317.
[5] A. von Zelewsky, L. Barbosa, C. W. Schläpfer. Poly(ethylenimines) as Broensted bases and as ligands for metal ions. *Coord. Chem. Rev.* **1993**, *123*, 229.
[6] S. Kobayashi, K. Hiroishi, M. Tokunoh, T. Saegusa. Chelating properties of linear and branched poly(ethylenimines). *Macromolecules* **1987**, *20*, 1496.
[7] B. A. Bolto. Soluble polymers in water purification. *Prog. Polym. Sci.* **1995**, *20*, 987.
[8] G. Jones, H. Roth, Substituted acylated polyimine resins. US Patent 3,40909, **1972**.
[9] G. D. Jones, A. Langsjoen, M. M. C. Neumann, J. Zomlefer. The polymerization of ethyleneimine. *J. Org. Chem.* **1944**, *9*, 125.
[10] K. F. Weyts, E. J. Goethals. New synthesis of linear polyethyleneimine. *Polym. Bull.* **1988**, *19*, 13.
[11] T. Saegusa, H. Ikeda, H. Fujii. Crystalline polyethylenimine. *Macromolecules* **1972**, *5*, 108.
[12] T. Saegusa, S. Kobayashi, A. Yamada. Graft copolymerization of 2-methyl-2-oxazoline onto chloromethylated polystyrene and hydrolysis of graft copolymer to a chelating resin of poly(styrene-g-ethylenimine). *Macromolecules* **1975**, *8*, 390.
[13] S. Kobayashi, M. Kaku, T. Saegusa. Grafting of 2-oxazolines onto cellulose and cellulose diacetate. *Macromolecules* **1988**, *10*, 1921.
[14] H. M. L. Lambermont-Thijs, F. S. van der Woerdt, A. Baumgaertel, L. Bonami, F. E. Du Prez, U. S. Schubert, R. Hoogenboom. Linear poly (ethylene imine)s by acidic hydrolysis of poly(2-oxazoline)s: kinetic screening, thermal properties, and temperature-induced solubility transitions. *Macromolecules* **2010**, *43*, 927.
[15] H. M. L. Lambermont-Thijs, J. P. A. Heuts, S. Hoeppener, R. Hoogenboom, U. S. Schubert. Selective partial hydrolysis of amphilic copoly (2-oxazoline)s and responsive micellization of the resulting poly (ethylene imine) copolymers. *Polym. Chem.* **2011**, *2*, 313.
[16] S. Navarro, A. Shkilnyy, B. Tiersch, A. Taubert, H. Menzel. Preparation, characterization, and thermal gelation of amphiphilic alkyl-poly (ethyleneimine). *Langmuir* **2009**, *25*, 10558.
[17] J. H. Jeong, S. H. Song, D. W. Lim, H. Lee, T. G. Park. DNA transfection using linear poly(ethylenimine) prepared by controlled acid hydrolysis of poly(2-ethyl-2-oxazoline). *J. Controlled Release* **2001**, *73*, 391.
[18] L. Wightman, R. Kircheis, V. Rössler, S. Carotta, R. Ruzicka, M. Kursa, E. Wagner. Different behavior of branched and linear polyethylenimine for gene delivery in vitro and *in vivo*. *J. Gene Med.* **2001**, *3*, 362.
[19] U. Lungwitz, M. Breunig, R. Liebl, T. Blunk, A. Goepferich. Methoxy poly(ethylene glycol) – low molecular weight linear polyethylenimine-derived copolymers enable polyplex shielding. *Eur. J. Pharm. Biopharm.* **2008**, *69*, 134.
[20] J. W. Wiseman, C. A. Goddard, D. McLelland, W. H. Colledge. A comparison of linear and branched polyethylenimine (PEI) with DCChol/DOPE liposomes for gene delivery to epithelial cells in vitro and in vivo. *Gene Ther.* **2003**, *10*, 1654.
[21] M. Neu, D. Fischer, T. Kissel. Recent advances in rational gene transfer vector design based on poly(ethylene imine) and its derivatives. *J. Gene Med.* **2005**, *7*, 992.
[22] Z. Zhong, J. Feijen. Low molecular weight linear polyethylenimine-*b*-poly(ethylene glycol)-*b*-polyethylenimine triblock copolymers: synthesis, characterization, and *in vitro* gene transfer properties. *Biomacromolecules* **2005**, *6*, 3440.
[23] J. B. Fenn. Electrospray wings for molecular elephants (Nobel lecture). *Angew. Chem. Int. Ed.* **2003**, *42*, 3871.
[24] K. Tanaka, H. Waki, Y. Ido, S. Akita, Y. Yoshida, T. Yohida. Protein and polymer analyses up to m/z 100 000 by laser ionization time-of-flight mass spectrometry. *Rapid Commun. Mass Spectrom.* **1988**, *2*, 151.
[25] M. Karas, F. Hillenkamp. Laser desorption ionization of proteins with molecular mass exceeding 10 000 Daltons. *Anal. Chem.* **1988**, *60*, 2299.
[26] C. Barner-Kowollik, T. P. Davis, M. H. Stenzel. Probing mechanistic features of conventional, catalytic and living free radical polymerizations using soft ionization mass spectrometric techniques. *Polymer* **2004**, *45*, 7791.
[27] M. Buback, H. Frauendorf, F. Günzler, P. Vana. Electrospray ionization mass spectrometric end-group analysis of PMMA produced by radical polymerization using diacyl peroxide initiators. *Polymer* **2007**, *48*, 5590.
[28] F. Bennet, T. M. Lovestead, P. J. Barker, T. P. Davis, M. H. Stenzel, C. Barner-Kowollik. Degradation of poly(methyl methacrylate) model compounds in the solid state studied via high resolution electrospray ionization mass spectrometry (ESI-MS). *Macromol. Rapid Commun.* **2007**, *28*, 1593.

[29] T. Gruendling, M. Guilhaus, C. Barner-Kowollik. Quantitative LC-MS of polymers: determining accurate molecular weight distributions by combined size exclusion chromatography and electrospray mass spectrometry with maximum entropy data processing. *Anal. Chem.* **2008**, *80*, 6915.
[30] T. Gruendling, M. Guilhaus, C. Barner-Kowollik. Design of experiment (DoE) as a tool for the consistent optimization of source conditions in SEC-ESI-MS of functional synthetic polymers synthesized via ATRP. *Macrom. Rapid Commun.* **2009**, *30*, 589.
[31] F. Günzler, E. H. H. Wong, S. P. S. Koo, T. Junkers, C. Barner-Kowollik. Quantifying the efficiency of photo-initiation processes in methyl methacrylate free radical polymerization via electrospray ionization mass spectrometry. *Macromolecules* **2009**, *42*, 1488.
[32] F. Günzler, T. Junkers, C. Barner-Kowollik. Studying the mechanism of thioketone mediated polymerization (TKMP) via electrospray ionization mass spectrometry. *J. Polym. Sci., Part A: Polym. Chem.* **2009**, *47*, 1864.
[33] M. Buback, H. Frauendorf, F. Günzler, F. Huff, P. Vana. Determining initiator efficiency in radical polymerization by electrospray ionization mass spectrometry. *Macromol. Chem. Phys.* **2009**, *210*, 1591.
[34] T. L. Selby, C. Wesdemiotis, R. P. Lattimer. Dissociation characteristics of $[M + X]^+$ ions (X = H, Li, Na, K) from linear and cyclic polyglycols. *J. Am. Soc. Mass Spectrom.* **1994**, *5*, 1081.
[35] T. Gruendling, S. Weidner, J. Falkenhagen, C. Barner-Kowollik, Mass spectrometry in polymer chemistry: a state-of-the-art up-date. *Polym. Chem.* **2010**, *1*, 599.
[36] S. M. Weidner, S. Trimpin. Mass spectrometry of synthetic polymers. *Anal. Chem.* **2010**, *82*, 4811.
[37] A. T. Jackson, H. T. Yates, J. H. Scrivens, G. Critchley, J. Brown, M. R. Green, R. H. Bateman. The application of matrix-assisted laser desorption/ionization combined with collision-induced dissociation to the analysis of synthetic polymers. *Rapid Commun. Mass Spectrom.* **1996**, *10*, 1668.
[38] A. T. Jackson, H. T. Yates, W. A. MacDonald, J. H. Scrivens, G. Critchley, J. Brown, M. J. Deery, K. R. Jennings, C. Brookes. Time-lag focusing and cation attachment in the analysis of synthetic polymers by matrix-assisted laser desorption-ionization time-of-flight mass spectrometry. *J. Am. Soc. Mass Spectrom.* **1997**, *8*, 132.
[39] J. H. Scrivens, A. T. Jackson, H. T. Yates, M. R. Green, G. Critchley, J. Brown, R. H. Bateman, M. T. Bowers, J. Gidden. The effect of the variation of cation in the matrix-assisted laser desorption/ionisation-collision induced dissociation (MALDI-CID) spectra of oligomeric systems. *Int. J. Mass Spectrom. Ion Processes* **1997**, *165/166*, 363.
[40] A. R. Bottrill, A. E. Giannakopulos, C. Waterson, D. M. Haddleton, K. S. Lee, P. J. Derrick. Determination of end groups of synthetic polymers by matrix-assisted laser desorption/ionization: high-energy collision-induced dissociation. *Anal. Chem.* **1999**, *71*, 3637.
[41] T. Yalcin, W. Gabryelski, L. Li. Structural analysis of polymer end groups by electrospray ionization high-energy collision-induced dissociation tandem mass spectrometry. *Anal. Chem.* **2000**, *72*, 3847.
[42] A. T. Jackson, S. E. Slade, J. H. Scrivens. Characterisation of poly(alkyl methacrylate)s by means of electrospray ionisation–tandem mass spectrometry (ESI–MS/MS). *Int. J. Mass Spectrom.* **2004**, *238*, 265.
[43] M. Girod, Y. Carissan, S. Humbel, L. Charles. Tandem mass spectrometry of doubly charged poly(ethylene oxide) oligomers produced by electrospray ionization. *Int. J. Mass Spectrom.* **2008**, *272*, 1.
[44] K. Chaicharoen, M. J. Polce, A. Singh, C. Pugh, C. Wesdemiotis. Characterization of linear and branched polyacrylates by tandem mass spectrometry. *Anal. Bioanal. Chem.* **2008**, *392*, 595–607.
[45] A. C. Crecelius, A. Baumgaertel, U. S. Schubert. Tandem mass spectrometry of synthetic polymers. *J. Mass Spectrom.* **2009**, *44*, 1277.
[46] K. Knop, B. O. Jahn, M. D. Hager, A. C. Crecelius, M. Gottschaldt, U. S. Schubert. Systematic MALDI-TOF CID investigation on different substituted mPEG 2000. *Macromol. Chem. Phys.* **2010**, *211*, 677.
[47] A. Baumgaertel, C. Weber, K. Knop, A. C. Crecelius, U. S. Schubert. *Rapid Commun. Mass Spectrom.* **2009**, *23*, 756.
[48] E. Altuntaş, K. Kempe, A. C. Crecelius, R. Hoogenboom, U. S. Schubert. Electrospray ionization–mass spectrometric (ESI-MS and MS/MS) analysis of poly(2-oxazoline)s with different side groups. *Macromol. Chem. Phys.* **2010**, *211*, 2312.
[49] A. Baumgaertel, E. Altuntaş, K. Kempe, A. C. Crecelius, U. S. Schubert. Characterization of different poly(2-oxazoline) block copolymers by MALDI-TOF MS/MS and ESI-Q-TOF MS/MS. *J. Polym. Sci., Part A: Polym. Chem.* **2010**, *48*, 5533.
[50] L. Tauhardt, K. Kempe, K. Knop, E. Altuntaş, M. Jäger, S. Schubert, D. Fischer, U. S. Schubert. Linear Poly(ethylene imine) – Optimized Synthesis and Characterization, On the Way to 'Pharmagrade' Batches. *Macromol. Chem. Phys.* **2011**, *212*, 1918.
[51] H. J. Raeder, W. Schrepp. MALDI-TOF mass spectrometry in the analysis of synthetic polymers. *Acta Polym.* **1998**, *49*, 272.
[52] C. R. Becer, R. Hoogenboom, U. S. Schubert. Click chemistry beyond metal-catalyzed cycloaddition. *Angew. Chem. Int. Ed.* **2009**, *48*, 2.
[53] D. Fournier, R. Hoogenboom, U. S. Schubert. Clicking polymers: a straightforward approach to novel macromolecular architectures. *Chem. Soc. Rev.* **2007**, *36*, 1369.
[54] J. E. Girard, M. Konaklieva, J. Gu, C. M. Guttman, S. J. Wetzel. Proc. 51st ASMS Conf. Mass Spectrometry and Allied Products, Montreal, Canada, June 8–12, **2003**.
[55] C. Wesdemiotis, N. Solak, M. J. Polce, D. E. Dabney, K. Chaicharoen, B. C. Katzenmeyer. Fragmentation pathways of polymer ions. *Mass Spectrom. Rev.* **2011**, *30*, 523.
[56] R. P. Lattimer, H. R. Schulten. Field desorption and fast atom bombardment mass spectrometry of poly(ethylene imine). *Int. J. Mass Spectrom. Ion Proc.* **1985**, *67*, 277.
[57] R. P. Lattimer. Tandem mass spectrometry of lithium-attachment ions from polyglycols. *J. Am. Soc. Mass Spectrom.* **1992**, *3*, 225.
[58] R. P. Lattimer. Tandem mass spectrometry of poly(ethylene glycol) lithium-attachment ions. *J. Am. Soc. Mass Spectrom.* **1994**, *5*, 1072.
[59] Y. Li, J. N. Hoskins, S. G. Sreerama, S. M. Grayson. MALDI – TOF mass spectral characterization of polymers containing an azide group: evidence of metastable ions. *Macromolecules* **2010**, *43*, 6225.
[60] G. L'abbe. Decomposition and addition reactions of organic azides. *Chem. Rev.* **1969**, *69*, 345.

Publication P9:

Drugs as matrix to detect their own drug delivery system of PCL-PEG block copolymers in MALDI-TOF MS

K. Knop, S. Stumpf, U. S. Schubert

Rapid Commun. Mass Spectrom. **2013**, submitted.

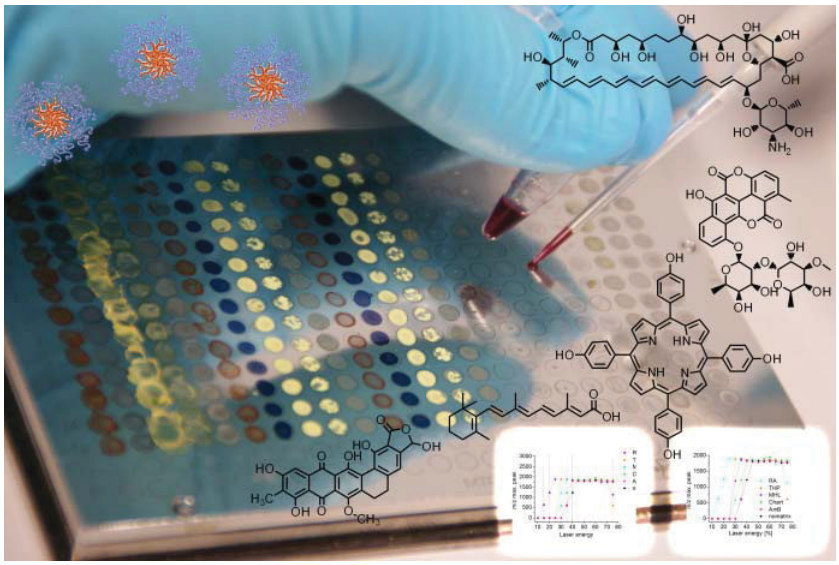

Drugs as matrix to detect their own drug delivery system of PEG-*b*-PCL block copolymers in MALDI-TOF MS

*Katrin Knop,[1,2] Steffi Stumpf,[1,2] and Ulrich S. Schubert[1,2]**

[1] Laboratory of Organic and Macromolecular Chemistry (IOMC), Friedrich-Schiller-University Jena, Humboldtstrasse 10, 07743 Germany

[2] Jena Center for Soft Matter (JCSM), Friedrich-Schiller-University Jena, Philosophenweg 7, 07743 Germany

*Author for correspondence: Prof. Dr. U. S. Schubert. Telephone: +49(0) 3641 948200, Fax: +49(0) 3641 948202, E-mail: ulrich.schubert@uni-jena.de, Internet: www.schubert-group.com

Abstract. Five drug molecules, *i.e.* madurahydroxylactone (MHL), tetrakis(4-hydroxyphenyl)-porphyrine (THP), chartreusin (Chart), amphotericin B (AmB) and retinoic acid (RA), were used as matrix molecules in a matrix-assisted laser desorption/ionization time of flight mass spectrometry (MALDI-TOF MS) investigation. The drug molecules were analyzed in terms of their efficiency to act as matrix for different homopolymers and the block copolymer poly(ethylene glycol)-*block*-poly(ε-caprolactone) (PEG-*b*-PCL). The block copolymer was further utilized to prepare micellar solutions and to encapsulate the drug molecules previously investigated as matrix. The different micellar solutions were studied in terms of the detectability of the drug as well as the block copolymer to enable an imaging approach for the visualization of the micellar drug delivery system and the drug in *in vitro* and *in vivo* applications.

Keywords. Matrix-assisted laser desorption/ionization, matrix, drug, drug delivery system, mass spectrometry.

1. Introduction

The development of new drug molecules is a major task in pharmaceutical research as well as industry. The search for nature mimicking target structures has yielded many new chemical entities that are often proven to be active compounds.[1] A major issue results from the question of administration, as one third of all newly developed potential drug molecules are highly hydrophobic.[2] As these molecules cannot be dissolved in water or aqueous solutions that are tolerable for the human body, these molecules would be excluded from potential applications.[3]

Drug delivery systems (DDSs) have been developed to overcome this drawback.[4] These carrier systems can encapsulate hydrophobic drugs by forming hydrophobic cavities in hydrophilic environments with, *e.g.*, amphiphilic molecules. They can, furthermore, improve the pharmacokinetic

behavior of the drugs by increasing the apparent molar mass and prolonging, therewith, their circulation half life in blood. By this effect the targeting into, *e.g.*, cancer tissue is enhanced by utilizing the so-called enhanced permeability and retention (EPR) effect.[4–6] In particular, linear amphiphilic block copolymers gained significant attention to assemble into micelles and to solubilize therewith hydrophobic molecules far above their maximum solubility in water.[7,8] Although these carrier systems are characterized by a critical micelle concentration (cmc) meaning a limited stability at low concentrations, they gained broad attention due to the versatile possibilities for the synthesis of the block copolymers and the convenient formation of micellar structures.[9] As the stability of the micelle is highly dependent on the nature of the hydrophobic block and the ratio of the hydrophilic and hydrophobic segments, a sophisticated design of the block copolymer is necessary to obtain efficient micellar DDSs. Furthermore, the encapsulation efficiency of the micelles is influenced by the nature of the hydrophobic drug.[10–12]

The hydrophobic character of the drug molecules often arises from a π-system, either of aromatic or conjugated character. These π-systems result in a bathochromic shift of the absorption wavelength into the UV region or even to wavelengths of the visible part of the spectrum. A strong absorption of UV light is a basic prerequisite for the matrix in the matrix-assisted laser desorption/ionization (MALDI) process as well. This observation leads to the speculation that these systems might be excited by the UV laser and act as a potential matrix molecule in MALDI-time of flight (TOF) mass spectrometry (MS).

MALDI is an established method to volatilize substances to render them amenable for MS. The choice of matrix plays the central role in the success of a MALDI-TOF MS measurement.[13] Upon excitation by the laser beam, matrix molecules are transferred into the gas phase and co-desorb therewith analyte compounds, enabling their mass spectrometric analysis.[14]

It is generally known that the matrix has to meet several requirements determined by the role the matrix plays in the volatilization process. The matrix has to embed and separate the analytes by co-crystallization as well as absorb the energy from the laser pulse and the therewith connected ejection of matrix and analyte. For some analytes, it might play a role in the ionization process and, a sufficient vacuum stability and solubility within the solvent of the analyte is required. These materials are generally small, organic compounds that are readily absorbing light in the range of *e.g.* UV lasers.[13] But further structural requirements have not been established, and the choice of matrix is rather an empirical search than a rational choice. Nevertheless, efforts to rationalize this issue have been undertaken, *e.g.*, by Hoteling *et al*. comparing the retention times of polymers and matrices in high performance liquid chromatography (HPLC). The authors identified a good match between the retention times and the spectra quality, showing that similar polarity plays an important role to solubilize the polymers and to obtain good spectra qualities.[15] Similarly, Hanton and Owens established a matrix/polymer solubility scale, where the matrix can be chosen accordingly by comparing the polymers polarity.[16]

Assuming that a π-system is in principle sufficient to provide matrix qualities, several drug molecules might account as assistance in the MALDI process. This approach to use drug molecules as matrix could allow the detection of the drugs as well as the DDSs in *ex vivo* and *in vivo* applications. Moreover, MS imaging (MSI) would enable a spatially resolved detection of the amphiphilic block copolymers and the drug molecules on a cellular basis, as the spatial resolution of MALDI measurements could be

minimized to the diameter of the laser spot. Generally, MALDI MSI enables only a spatial resolution between 60 and 100 µm, depending on the matrix selection and its application on the tissue.[17] As this new approach already contains the matrix molecules as encapsulated drug, an additional application of a matrix is not required, permitting the MSI measurement with a spatial resolution predetermined by the laser diameter. This method has already been applied for the localization of secondary metabolites in plant tissue by means of matrix-free laser desorption/ionization (LDI) with a resolution down to 10 µm.[18]

Herein, we present the first application of the matrix-free LDI MS approach for the detection of copolymers as building blocks of micelles with the help of the encapsulated drug, which is acting as matrix. Five different drug molecules were chosen for a comparative study as matrix, namely madurahydroxylactone (MHL), tetrakis(4-hydroxyphenyl)-porphyrine (THP), chartreusin (Chart), amphotericin B (AmB) and retinoic acid (RA). MHL and Chart are natural products with antimicrobial, antimycobacterial and cytotoxic effects, respectively. MHL was also found to be useful in HIV therapy[19–21] and Chart was used as antitumor agent.[22,23] THP finds also its application in tumor therapy as a dye for photodynamic therapy.[24] AmB is an established standard drug for the treatment of fungal infections.[25-27] Finally, RA was also tested in cancer therapy for the treatment of acute promyelocytic leukemia.[28]

This choice of drugs includes RA as an already established matrix for MALDI measurements of polymers,[29–34] which was also used in LDI experiments,[35,36] and THP that was only once reported to be used as matrix.[37] The different molecules will be evaluated according to their ability to act as matrix for polymers in terms of the measurement range, the spectrum quality, laser threshold and their UV absorption behavior.

In a second step, the drug molecules will be encapsulated by an amphiphilic block copolymer and their inclusion efficiency, micelle formation, and micellar properties will be presented. A mass spectrometric analysis of the micellar solutions is performed subsequently to investigate whether the drug molecules also act under diluted conditions as matrix and assist to visualize the block copolymer.

2. Experimental Details

2.1. Materials

Tin(II) 2-ethylhexanoate (Aldrich), poly(methyl methacrylate) 2.5 kDa (PMMA, Polymer Standards Services GmbH, Mainz, Germany), poly(styrene) 2 kDa (PS, Polymer Standards Services GmbH, Mainz, Germany), and poly(ethylene glycol) methyl ether 2 kDa (PEG, Fluka) were used as received, if not otherwise stated. ε-Caprolactone (Aldrich) was dried for 2 d over CaH_2 before distillation and stored under argon. 2-Ethyl-2-oxazoline (Acros Organics) was distilled to dryness over barium oxide (BaO, Sigma Aldrich) and stored under argon. Methyl tosylate was distilled and subsequently stored under argon. Tetrahydrofuran (THF, Aldrich) and acetonitrile (99.8 %, Aldrich) were dried in a solvent purification system (Pure Solv EN, Innovative Technology) before use. *Trans*-2-[3-(4-*tert*-butylphenyl)-2-methyl-2- propenylidene] malononitrile (DCTB, Santa Cruz Biotechnology), retinoic acid (RA, Sigma), tetrakis(4-hydroxyphenyl)-porphyrine (THP, Aldrich), silver trifluoroacetate (AgTFA, Fluka) and sodium chloride (NaCl, 99.999%, Aldrich) were used as received. Madurahydroxylactone, chartreusin and amphotericin B were a generous gift of K. Martin of the Hans-Knöll-Institute (Jena, Germany).

2.2. Instrumentation

^{1}H nuclear magnetic resonance (NMR) spectra were recorded in $CDCl_3$ on a Bruker AC 300 MHz spectrometer at 298 K. Chemical shifts are given in parts per million (ppm, δ scale) relative to the residual signal of the deuterated solvent.

Size exclusion chromatography (SEC) was measured on a Shimadzu system equipped with a SCL-10A system controller, a LC-10AD pump, and a RID-10A refractive index detector using a solvent mixture containing chloroform, triethylamine, and isopropyl alcohol (94:4:2) at a flow rate of 1 mL min^{-1} on a PSS-SDV-linear M 5 μm column. The system was calibrated with PMMA (410 to 88,000 g mol^{-1}) and PEG (440 to 44,700 g mol^{-1}) standards.

MALDI-TOF spectra were recorded on an Ultraflex III TOF/TOF of Bruker Daltonics, Bremen, Germany equipped with a Nd:YAG laser. The instrument was calibrated prior to each measurement with an external PMMA standard from PSS Polymer Standards Services GmbH (Mainz, Germany). MS data were processed using PolyTools 1.0 (Bruker Daltonics) and Data Explorer 4.0 (Applied Biosystems).

Dynamic light scattering (DLS) measurements were performed on an ALV DLS/SLS equipment consisting of an ALV Laser CGS3 Goniometer with an ALV Avalanche correlator and a HeNe laser (λ = 632.8 nm) at 298 K. The aqueous polymer solutions as well as the THF solutions with concentrations of 1 mg mL^{-1} were filtered twice (GF 1 to 2 μm or PTFE 0.45 μm) and measured at an angle of 150 °. The hydrodynamic radius (R_h) was determined by the CONTIN algorithm. Angular dependent measurements were performed in the same manner in the range of 30 ° to 150 ° in 10 ° steps.

The ζ potential measurements were performed using a Zetasizer Nano ZS (Malvern instruments, Malvern, UK). The solutions were prepared with concentrations of 1 mg mL^{-1} polymer in deionized water and passed through 1-2 μm glass frit filters prior to measurement.

UV-Vis absorption measurements were performed on an Analytik Jena SPECORD 250 (Analytik Jena, Jena, Germany) at 298 K. Fluorescence emission as well as excitation spectroscopy has been measured on a Jasco FP-6500 spectrometer at 298 K. For the photometric absorbance measurement of the solid matrix, a TECAN Infinite M200 PRO plate reader (TECAN, Crailsheim, Germany) was used. Each well containing the sample was measured in 4 different spots each with 5 flashes per scan.

The AFM images have been recorded with a NanoScope IIIa Multimode instrument (Veeco) in semi-contact mode. MicroMasch NSC 35 cantilevers have been used for the investigations.

2.3. Experimental details

MALDI sample preparation. For the sample preparation, 1 μL of the polymer solution (10 mg mL^{-1}) in THF, 10 μL of the matrix solution (10 mg mL^{-1}) in THF, and 5 μL of NaCl or AgTFA in THF at a concentration of 100 mg mL^{-1} were mixed and the dried-droplet sample preparation method was applied. An array of three to fourteen spots was prepared for the fourteen different laser energies investigated. Automated MALDI measurements were carried out in triplicate and the obtained data are presented as the mean measured values with the confidence interval given in the SI.

Preparation of micelles. Of each matrix, a solution with 1.72 μmol mL^{-1} in acetone was prepared, except for AmB and Chart, which were dissolved in methanol. 1.5, 1, 0.5, 0.25 and 0.125 mL of MHL, THP and RA solutions were placed in separate vials, and the solvent was allowed to evaporate. For AmB and Chart, 1, 0.5, 0.25 and 0.125 mL were placed in the same manner into separate vials. Additionally, for each matrix 1 mL was placed into a vial and refilled after drying with 5 mL water as blank sample. To the other vials, 5 mL of water was added as well as 1 mL of a 5 mg mL^{-1} solution of

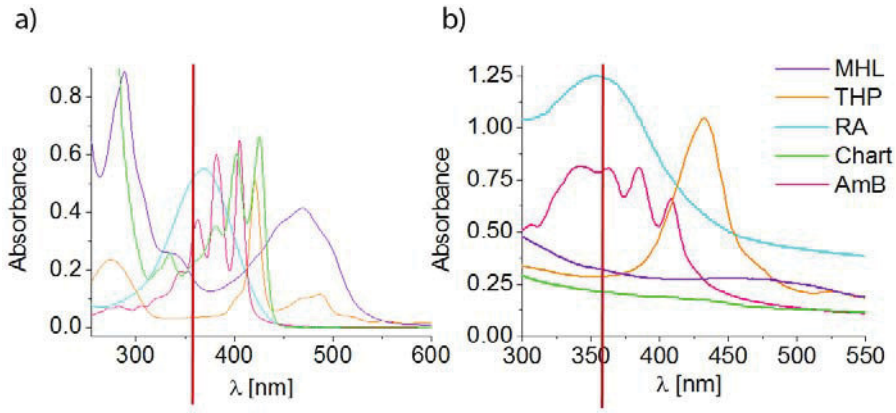

Figure 1: UV-Vis absorption data obtained for the five matrices (a) in chloroform, except AmB in methanol, and (b) in solid state. The red bar correlates to the wavelength of the Nd:YAG laser.

the PEG-*b*-PCL polymer in acetone (Synthesis of PEG-*b*-PCL described in the SI). The acetone was evaporated during two days and the water was subsequently refilled to 5 mL.

3. Results and discussion

UV investigations. When it comes to the question why a matrix delivers good results for a certain class of molecules, the literature is astonishing unknowing. This might be connected to the highly empirically developing history of the MALDI knowledge.[38] Systematical investigations are rare and were not able to identify the crucial parameters required to render a molecule a good or a bad matrix.[13,15,39,40] One of the basic prerequisites for the matrix is assumed to be a strong UV absorption to induce the desorption process.[14] Therefore, for the five chosen matrices the UV absorption was investigated (Figure 1). For the established matrix RA, an absorption maximum at the laser wavelength of 355 nm in solid state as well as in chloroform solution is detected. AmB and Chart show also good absorbance values at 355 nm in solution. However, THP has no absorption band in the emission region of the UV laser (Table 1).

Table 1. Characteristics of the drugs used as matrix.

Matrix/drug	Laser energy threshold [%][a]	Molar mass range of clusters[a]	ε_{max} (λ) [M^{-1} cm^{-1}][b]	ε_{355nm} [M^{-1} cm^{-1}][b]
MHL	33	0-1,000	5,745 (469 nm)[c]	2,657[c]
THP	23	0-1,400	17,546 (421 nm)[c]	1,057[c]
RA	13	0-700	44,785 (370 nm)[c]	40,886[c]
Chart	40	0-720	15,797 (425 nm)[c]	5,022[c]
AmB	40	0-475	39,113 (405 nm)[d]	14,701[d]

[a] Obtained by MALDI-TOF MS measurements. [b] Calculated from the slope of the absorptions at five different concentrations. [c] Measured in $CHCl_3$. [d] Measured in MeOH.

Evaluation of drugs as matrix. In a first MS approach, the selected drug molecules were submitted to LDI measurements to study their behavior under laser irradiation in positive mode as the majority of polymers is ionized and detected as cation. At the lowest laser energy required to obtain signals, the base peak was provided by the pseudo molecular ion for Chart, RA and THP, *i.e.* either a protonated

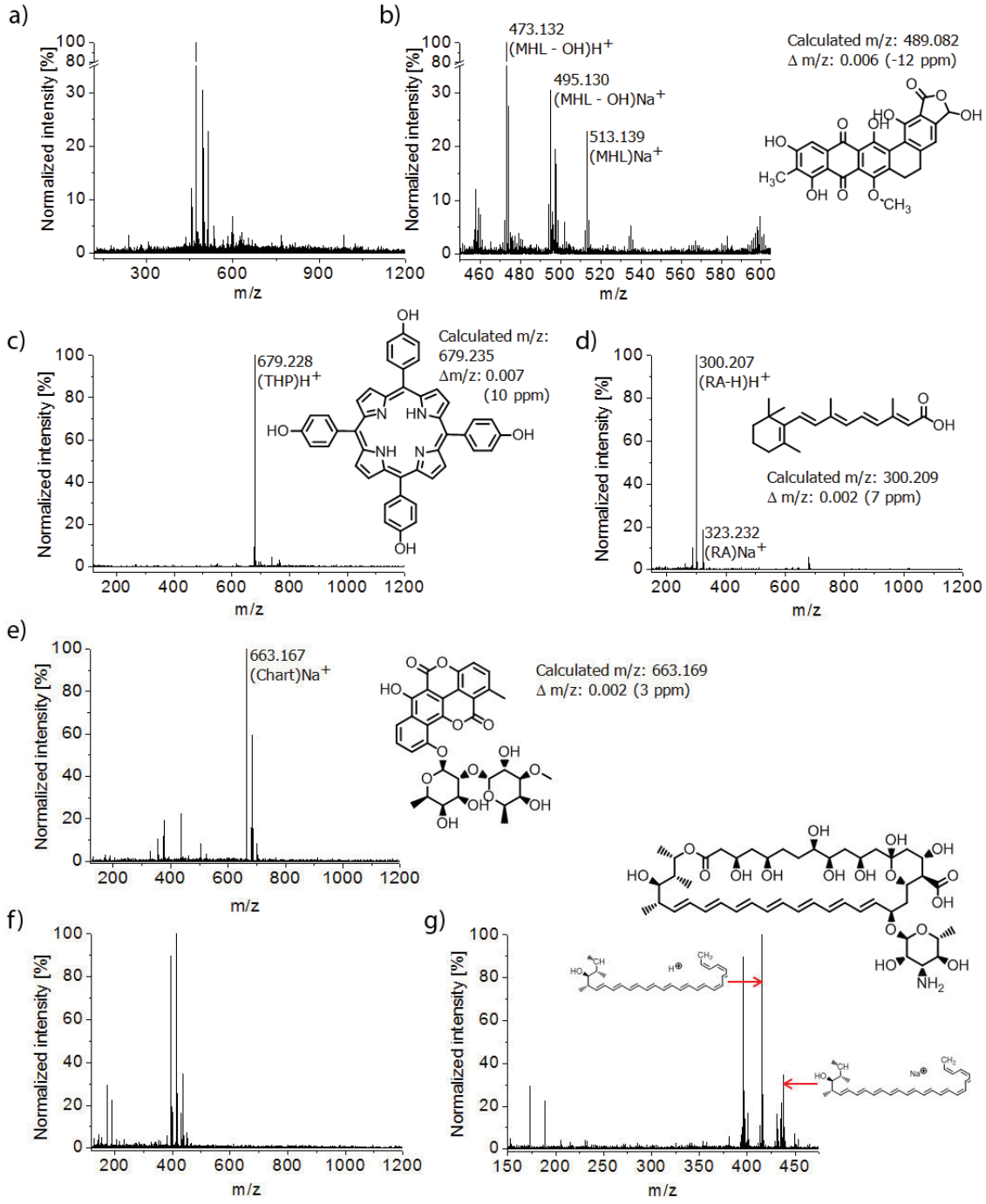

Figure 2: (a) Extended LDI spectrum of MHL. (b) Zoom into the LDI spectrum of MHL assigning the different fragments and ions. (c) LDI spectrum of THP with the assigned pseudo molecular ion peak. (d) LDI spectrum of RA with the two assigned pseudo molecular ion peaks. (e) LDI spectrum of Chart with the assigned pseudo molecular ion peak. (f) Extended LDI spectrum of AmB. (g) Zoom into the LDI spectrum of AmB with assigned fragment structures.

species (RA and THP) or a sodiated ion (Chart). Both AmB and MHL showed the formation of numerous, intensive fragments, whereas for AmB no molecular ion could be detected. Only few fragments could be assigned and were not in accordance with mechanisms observed earlier for persilylated AmB in electron impact (EI) MS.[41] THP and RA were the only molecules to show almost no fragment formation. This peculiarity might be attributed to the observation that for both matrices the lowest laser energies were required to obtain signals. In manual measurements (with the inevitable favoring of the sweet spots) laser energies above 13% and 23% for RA and THP, respectively, were used to obtain matrix signals (LDI spectra of all matrices are given in Figure 2). The MHL signals were visible above a laser energy of 33% and Chart signals as well as AmB fragment signals were observed above a laser energy of 40%. An additional explanation for the formation of fragments might be provided as for the latter molecules more labile structures are present in the molecules, such as the glycoside moiety of Chart or the polyol structure in AmB. These structural characteristics might act as predetermined breaking points resulting in the formation of more fragments during irradiation with the UV laser or later in the plume. Furthermore, it was observed that MHL and THP are only applicable above m/z 1,000 and m/z 1,400, respectively, as both drugs form clusters up to these molar masses (Table 1). The cluster formation is a serious limitation for the usage as matrix, as analyte ions are generally suppressed in this molar mass range by the formation of the aggregates. Therefore, both matrices should be preferably used above these molar mass thresholds.

From the LDI investigations it can be concluded that all drug molecules can be excited and transferred into the gas phase by the laser light, most probably due to their extended π-system. Only AmB showed a complete fragmentation behavior; the other molecules could be detected without the addition of a matrix by the assignment of their pseudo molecular ions. Subsequently, the ability to act as matrix was investigated for a choice of polymers, such as poly(ethylene glycol) (PEG) 2 kDa, poly(methyl methacrylate) (PMMA) 2.5 kDa, poly(styrene) (PS) 2 kDa, poly(2-ethyl-2-oxazoline) (PEtOx) 2 kDa and PEG 2 kDa-*block*-poly(*ε*-caprolactone) 0.9 kDa (PEG-*b*-PCL) (Scheme 1).

To balance the large variance of the results obtained in MALDI from one single measurement to the next, all measurements were performed by using the dried droplet preparation technique in triplicate on a separate spot. Four different spectra characteristics were evaluated in dependence of the investigated polymer, the matrix, and the laser energy (Figure 2). Firstly, the maximum peak of each obtained distribution was determined followed by its intensity, signal-to-noise (S/N) ratio, and resolution. The obtained information is given as diagrams in dependence on the laser energy. Figure 2 is represented in the SI once again with the confidence intervals for each value to obtain a notion of the deviation of the measurements (Figure S4). This graphical representation illustrates the difficulty that is faced in comparing different MALDI measurements to each other and should be kept in mind during the following discussion. However, for more clarity the confidence intervals are not shown in Figure 2.

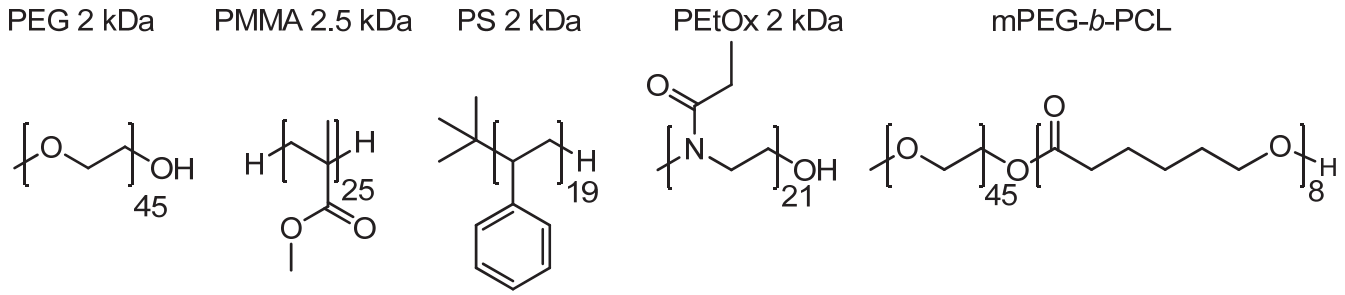

Scheme 1: Schematical representation of the polymer structures used for the matrix evaluation.

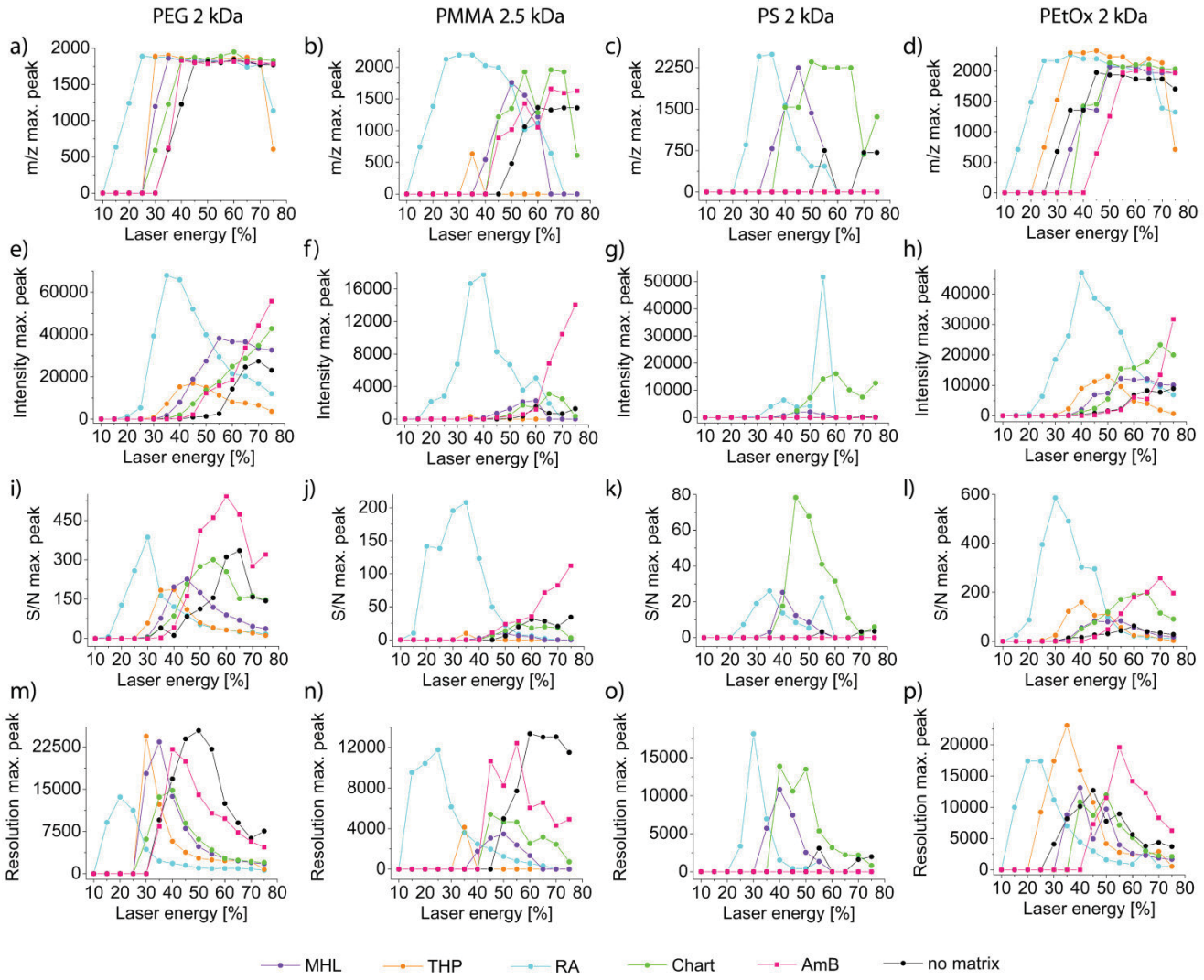

Figure 2: Evaluation of the characteristic parameters of the MALDI-TOF MS spectra on the basis of the maximum peak for PEG 2 kDa as a function of the laser energy against (a) the m/z value, (e) the intensity, (i) the S/N ratio, (m) the resolution; for PMMA 2.5 kDa as a function of the laser energy against (b) the m/z value, (f) the intensity, (j) the S/N ratio, (n) the resolution; for PS 2 kDa as a function of the laser energy against (c) the m/z value, (g) the intensity, (k) the S/N ratio, (o) the resolution; and for PEtOx 2 kDa as a function of the laser energy against (d) the m/z value, (h) the intensity, (l) the S/N ratio, (p) the resolution.

PEG. The maximum peak obtained for PEG with the different matrices shows rather the same m/z value around 1,900 Da, representing approximately the theoretical molar mass. Only the laser threshold for the different matrices varies showing for RA the smallest laser threshold of around 15%, followed by THP, MHL and Chart. AmB reveals only at a laser threshold of 35% a signal for PEG being therewith in the range of the measurement performed without matrix addition. After reaching the maximum value, the laser energy has almost no further influence on the maximum peak detected. Also Figure S4 shows that the confidence interval reaches rather high values for the increasing m/z value of the maximum peak, but remains very low in the constant area of the maximum peak m/z.

In contrast to the m/z value of the maximum peak, the intensity as well as the S/N ratio and the resolution show no plateau but a distinct maximum value indicating the optimum measurement conditions. For the intensity measured of the maximum peak, RA delivers the best values at the lowest

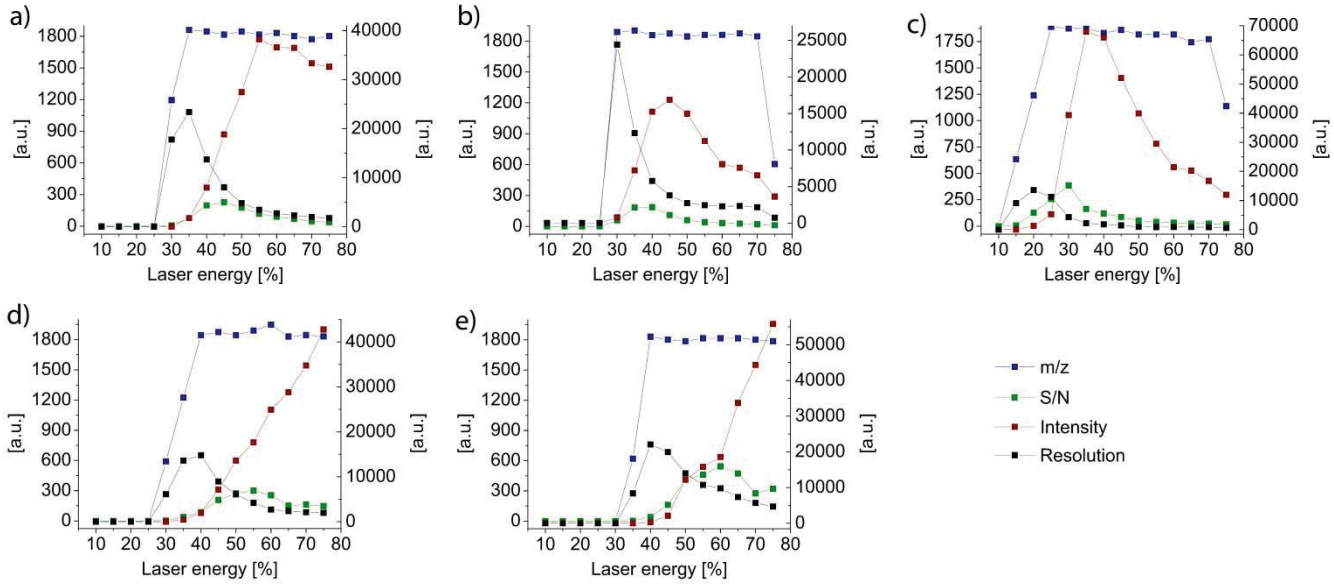

Figure 3: Evaluation of the characteristic parameters of the MALDI-TOF MS spectra on the basis of the maximum peak for PEG 2 kDa as a function of the laser energy for the different matrices: (a) MHL, (b) THP, (c) RA, (d) Chart and (e) AmB.

laser energies. According to empirical experiences, the laser energy required to obtain a distribution is not necessarily also showing the best intensity values, as the highest intensity is only reached at 35%. None of the other matrices is reaching the intensities obtained by RA. Although THP delivers a distribution at rather low laser energies it traverses the intensity maximum at relatively high laser energies, though still below those of MHL, Chart and AmB. The comparison of the S/N ratios shows surprisingly that AmB, which appears up to now ill qualified to act a matrix, results in higher S/N ratios than the RA, although high laser energies have to be applied to achieve this result. All matrices show a S/N maximum that is shifted to lower laser energies in comparison to the maximum peak intensity. The maximum value obtained for the resolution of the maximum peak is again shifted towards smaller laser energies approaching the laser energy values obtained within the comparison of the m/z value of the maximum peak.

The situation of divergent maxima for the different quality factors of the spectra is illustrated more clearly in Figure 3 for PEG and the five matrices. For each matrix the maxima obtained for the m/z value, the intensity, the S/N ratio and the resolution do not coincide. Therefore, the recommendation to measure at the lowest laser energy possible must not always deliver the best results for the measurement. The graphs rather suggest searching also at up to 20% higher laser energies for good measurement conditions in comparison to the laser threshold. Although these findings are not new for everybody working on the practical side of MALDI, they still confirm the accepted general knowledge that for each measurement the best conditions have to be found manually, and it is difficult to apply automated methods.

PMMA. Due to the fact that PEG can be rather easily measured other macromolecules like the hydrophobic PMMA were investigated. The curves obtained for PMMA clearly indicate that RA is the matrix of choice. The comparison of the maximum peak m/z, the intensity and the S/N ratio demonstrates the superiority of this matrix for PMMA in comparison to the other drug molecules. For each of the evaluation characteristics except the resolution with RA, the highest values are reached, for the intensity and the S/N ratio even far beyond the data observed for the other matrices. THP was shown

to be unsuitable for PMMA as only once a spectrum was obtained reflected in the outlier at 35% laser energy. Although for MHL and Chart m/z values for the maximum peak reach at least approximately the value obtained by RA, the intensity as well as the S/N ratio of the maximum peak are far below those obtained for RA. Surprisingly, AmB delivers relatively good values although at very high laser energies. It shows in all four compared characteristic values approaching those obtained for RA only at 20 to 40% higher laser energies.

PS. PS appears to be difficult to be transferred into the gas phase as for THP and AmB no signals at all could be detected. With RA, again best results are obtained regarding m/z value, intensity and resolution. But similar m/z values could be also obtained for MHL and Chart, although at higher laser energies, and Chart delivers very good S/N ratios in comparison to other matrices. As observed for PMMA, maximum values for each characteristic are observed revealing a narrow range of laser energies leading to good spectra qualities for the three matrices. Although Chart and MHL could deliver spectra in a reasonable quality, it was shown for PMMA and PS that RA is the best suited matrix for hydrophobic polymers.

PEtOx. For PEtOx, the m/z value obtained for the maximum peak does not traverse a maximum but stays rather on the same level once reached, as observed previously for PEG. Interestingly, PEtOx without matrix application can be distinguish very early at quite low laser energies before signals are obtained with MHL, Chart and AmB. However, by comparing the other characteristics the matrices show superior spectra quality in comparison to pure PEtOx apart from the resolution, where the values obtained for MHL and Chart are in the same range of the pure PEtOx. RA is shown to deliver the best results for intensity and S/N ratio of the maximum peak, and THP reveals the highest comparative resolution at laser energies of 35%.

As for PMMA and PS no spectra were obtained with THP as matrix, but for the hydrophilic polymers rather good spectra qualities were recorded, it can be concluded that this matrix is not suited for hydrophobic polymers. Furthermore, Chart and MHL deliver rather good results at relatively high laser energies, but constantly for all polymers. As expected RA is evaluated as best matrix for all polymers delivering not at all instances the best results but, on the whole, the most steady and robust spectra qualities. For the hydrophilic polymers it was observed that after reaching the maximum value the laser energy has almost no further influence on the maximum peak detected. This behavior was detected for PEG and to a smaller extent for PEtOx and seems to be typical for hydrophilic polymers.

Figure 2 and 3 raise the question whether AmB acts itself as matrix as the results obtained are very close to those measured without matrix. The impression gained by the individual evaluation of the spectra accounts for a slight matrix effect, although the absolute values obtained in comparison to the measurements without matrix do not show a clear distinction especially by considering the confidential intervals. For PS no matrix effect at all could be observed and for PEtOx even rather an ion suppressing effect. On the whole, a minor matrix role can be attributed to AmB by considering the intensity and S/N ratio values obtained for PEG as well as the data obtained for PMMA. In summary, RA as established matrix for MALDI delivered the best quality profile for all polymers. Nevertheless, volatilization enhancing effects have been detected for the four other drug molecules making them also suitable as matrix.

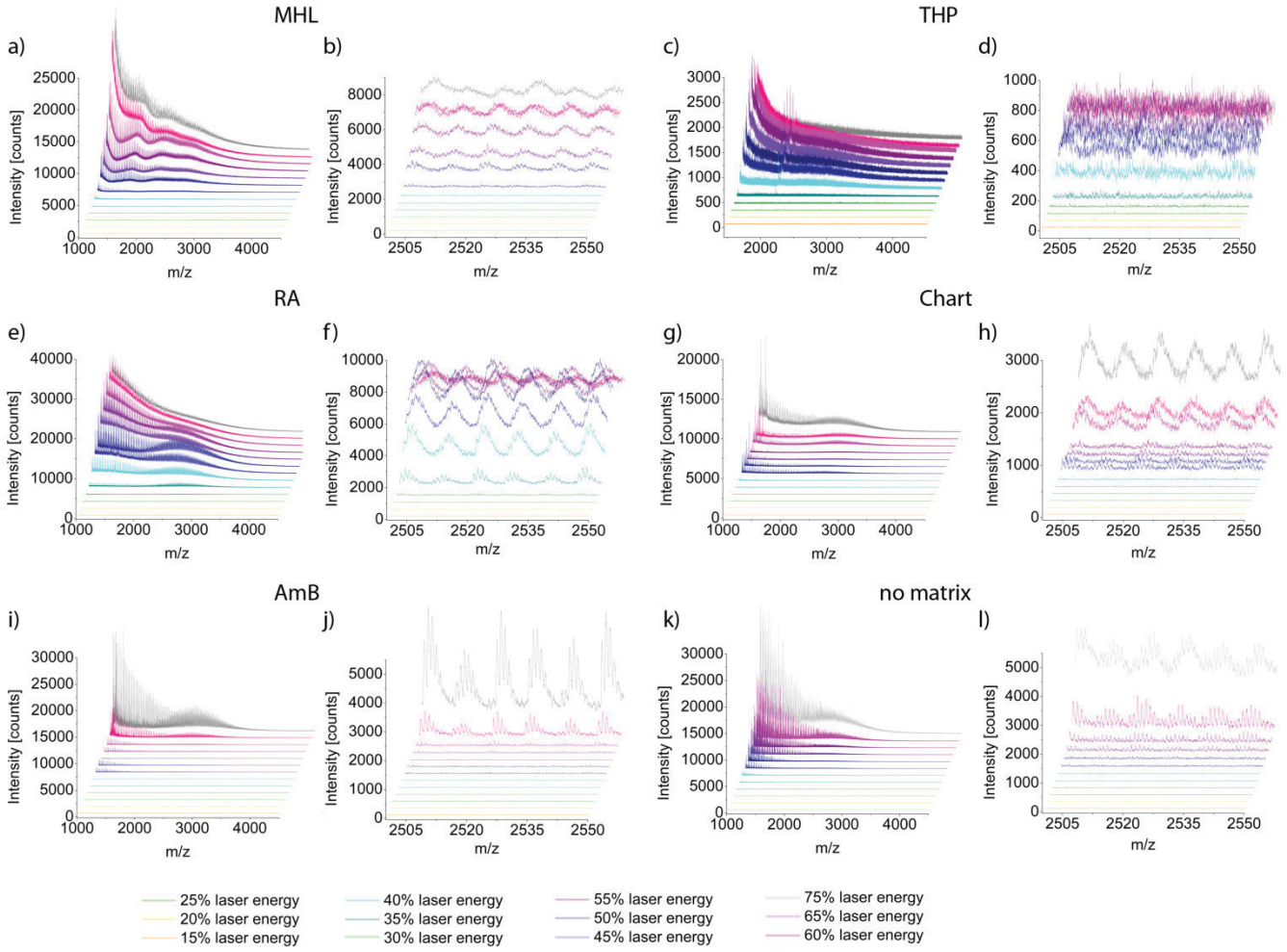

Figure 4: Comparison of the MALDI-TOF MS spectra of PEG-*b*-PCL with the different matrices at varying laser intensities. (a) Full spectrum and (b) zoom in with the MHL matrix. (c) Full spectrum and (d) zoom in with the THP matrix. (e) Full spectrum and (f) zoom in with the RA matrix. (g) Full spectrum and (h) zoom in with the Chart matrix. (i) Full spectrum and (j) zoom in with the AmB matrix. (k) Full spectrum and (l) zoom in without matrix application.

PEG-*b*-PCL. The spectra obtained for the block copolymer are not as easily evaluated as the spectra obtained for the homopolymers because the assignment of the peaks due to their multitude and overlapping character is not always performed properly by the applied software. Therefore, the spectra obtained for the five matrices and without matrix usage at different laser energies are plotted in Figure 4 to evaluate their potential as matrix for amphiphilic block copolymers. For THP, a broad baseline with a very high S/N ratio is detected at increasing laser energies, which might conceal the block copolymer as also an elevation in the baseline is observed. However, THP does not yield spectra with distinguishable peaks for PEG-*b*-PCL. Similarly, with MHL and Chart as matrices rather noisy, though distinguishable signals of the isotopic pattern of the block copolymer are obtained. However, whereas Chart shows in the full spectrum one hump in the region of the block copolymer with MHL, several distributions are observed leading to the assumption that it is decomposed during the measurement. By using AmB as matrix slightly better results could be obtained in comparison to the spectra obtained without matrix, as also observed in the investigations with the homopolymers. At 75% laser energy, a surprisingly well distinguishable distribution and isotopic pattern of the single peaks could be observed. But the very high laser fluences result also in a decomposition of the PEG-*b*-PCL. The RA delivers at quite low laser

energies (35%) separate isotopic pattern and only little fragmentation. But the window of the applicable laser energies is quite low as already at 40% laser energy considerable fragmentation of the block copolymer occurs, which is proven by the peaks appearing with increasing laser energy at the lower m/z side. Additionally, the resolution of the isotopic pattern is significantly decreasing.

Finally, RA and AmB seem to be the best suited matrices to measure PEG-*b*-PCL. However, by applying the other matrices a distribution is observable even though not with the same resolution of the isotopic pattern. In correlation to the UV spectroscopy, this result is in agreement with the hypothesis that an absorption at the laser wavelength leads to good matrix qualities, as RA was shown to result the best spectra for all polymer classes in comparison to the other matrices. Nevertheless, the remaining matrices do not confirm this assumption. AmB showing a rather high absorbance at 355 nm with a high molar absorptivity in solution and solid state provides only slightly better results than the measurement without matrix (Table 1). THP possesses the smallest molar absorptivity at 355 nm, and in the absorption spectra almost no signal can be traced at this wavelength, however, THP still shows for the hydrophilic polymers the second best results after RA. The same observation is valid for MHL and Chart; both are showing in the solid state UV-Vis spectroscopy almost no signal but a matrix property can be clearly attributed according to the results obtained for the polymers. These investigations reveal that the UV absorption cannot be a main prerequisite for the matrix. Moreover, different characteristics like the isolation of the analyte molecules in solid state or the disintegration process into the gas phase seem to play a more important role.[13,14]

All together, for all drugs a MALDI-enhancing property was asserted making them amenable as matrix. Although it was found that the strong UV absorption cannot be one of the basic prerequisites as not all matrices show an absorption at the wavelength of the laser, it can be regarded as indicator for a superior matrix.

Micelle preparation and drug inclusion. Although not all drugs show surpassing matrix properties they were all evaluated in terms of their suitability for inclusion into micelles of amphiphilic block copolymers formed by the amphiphilic block copolymer PEG-*b*-PCL.

To obtain information of the working range of the block copolymer, its critical micelle concentration (cmc) was determined by inclusion of pyrene and nile red. Both dyes indicate a cmc in the range of 0.1 mg mL^{-1}. This is a rather high value in comparison to other PEG-*b*-PCL systems, which can be attributed to the quite short hydrophobic block.[42,43] The block length of PCL was chosen to design a block copolymer that is still amenable to MALDI-TOF MS investigations, which is rendered more difficult with increasing overall molar mass and equalizing number of repeating units. The applicability of further PCL block lengths, to improve the micellar properties of PEG-*b*-PCL, might be subject of future studies.

All five matrices were used for encapsulation studies (Figure 6). The micelles were prepared with varying drug molecule to polymer molecule ratios and characterized subsequently in terms of their diameter, zeta potential and the inclusion of the drug by UV-Vis absorption measurements. For all matrices, except RA, an increase of the size with increasing dye molecule to polymer molecule ratio can be observed, probably attributed to an encapsulation of the drug. At the same time, an increase of the UV-Vis absorption should be observable as the matrix should then be more solubilized in water in comparison to pure water as solvent. This effect could not be observed for Chart and AmB, where the UV-Vis absorbance of the drug in water is in the range of the values obtained from the micellar solution. For both drug molecules this behavior is not unexpected, as both are rather hydrophilic

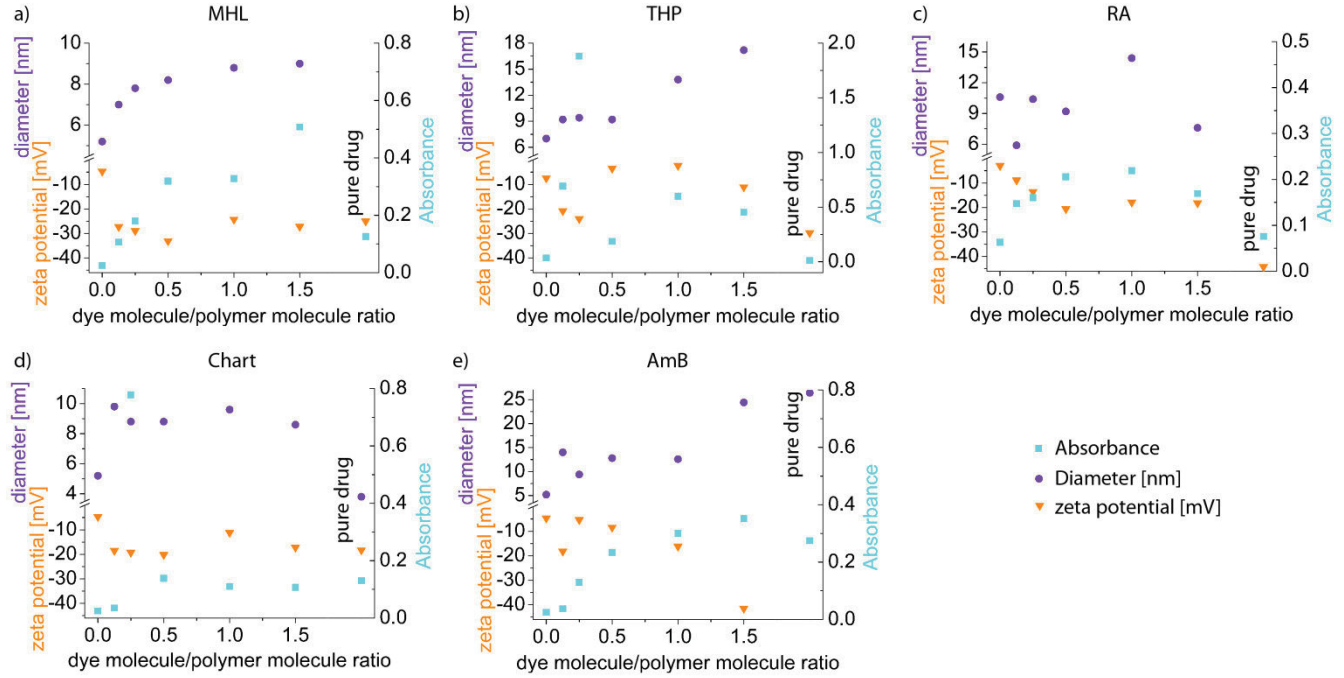

Figure 6: UV-Vis absorption data, diameter and zeta potentials of the micelles obtained by encapsulation of the five matrices: (a) MHL, (b) THP, (c) RA, (d) Chart and (e) AmB.

molecules that do not necessarily require a drug delivery system to be solubilized in water. For MHL, THP and RA, the UV-Vis data suggest an increased solubility of the matrix in water assisted by the block copolymer. For RA, no increase of the micelle size could be determined, but an optimum for the inclusion could be identified at the ratio of 0.5 dye molecules per polymer molecule showing the maximum UV absorbance. This is in accordance with the zeta potential, which is also not decreasing further by trespassing this ratio. For MHL, also a limit is reached at 0.5 dye molecules per polymer molecule, where neither the size increases considerably nor the zeta potential changes any longer. THP seems to reach this limit already at 0.25 THP molecules per polymer molecule, although the enhanced solubility provoked by the block copolymer is most obvious for this matrix.

In conclusion, Chart and AmB were excluded from further investigations, as no efficient encapsulation of the matrix was observed. From the remaining matrix molecules, the solution with the highest drug content was selected for further MALDI-TOF MS experiments. For this purpose, micellar solutions of RA and MHL with a ratio of 0.5 matrix molecules per polymer molecule as well as the THP solution containing 0.25 matrix molecules per polymer molecules were chosen. These solutions were submitted to an analysis whether such a small amount of matrix is sufficient to volatilize the polymer and render it therewith measurable by the MALDI process.

Evaluation of micellar solutions in (MA)LDI-MS. For the intended purpose of detection of both, drug and block copolymer, it is important to evaluate under which conditions the matrix or the DDS are visible in the mass spectrum. MALDI measurements of the chosen micellar solution showed that for RA and MHL the block copolymer was detectable. However, signals for the drug matrix could not be obtained disappearing most probably in the noise of the block copolymer fragments. Only for the micellar solution of THP, spectra of the drug as well as the block copolymer were obtained. In separate measurements below and above m/z 1000, THP and PEG-*b*-PCL, respectively, could be detected (Figure 7a).

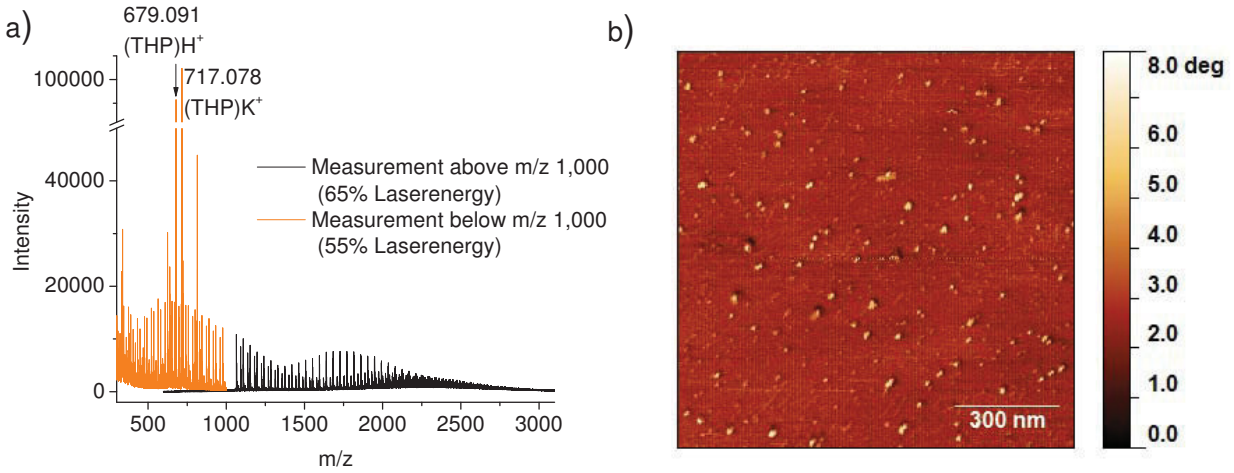

Figure 7: a) Detection of the THP matrix and the PEG-*b*-PCL block copolymer from the micellar solution. b) AFM phase image of the PEG-*b*-PCL block copolymer micellar solution containing THP.

However, for the intended purpose of imaging those structures, the dimensions of the obtained micelles are too small (Figure 7b). As the diameter of the laser is at least 10 µm, those single micelles would not be spatially resolved in the LDI-MSI approach. Therefore, future studies will focus on the preparation of larger micellar carrier systems or on nanoparticulate encapsulation systems to enable the detection by this laser focus size. An additional approach, separating the DDSs further, to detect per shot only on carrier will be followed by spin-coating or embedding techniques.

4. Conclusion

In this study we could show that drug molecules, bearing a π-system, can be used in the LDI as well as in the MALDI process. During the LDI process the drug is desorbed by the laser irradiation and for all drugs but the AmB the pseudo molecular ion could be detected. This investigation shows that the drug alone can be detected by LDI measurements. Within the MALDI approach the drugs were used as matrix for different homopolymers. Although the drugs Chart, MHL, THP and AmB did not reach the quality of the standard matrix RA, they showed surprisingly good results. In contrast, the assumption that a good UV absorbance represents a basic prerequisite for the application as matrix is not supported by this study. Although, for RA this supposition is true, for THP, showing a very minor absorbance at 355 nm but a superior matrix quality in comparison to the MHL, Chart and AmB drugs, it cannot be certified.

Micellar solutions of MHL, THP and RA encapsulated by PEG-*b*-PCL at the optimum inclusion capacities were selected for further MS investigations. However, only for the micellar solution of THP the drug as well as the block copolymer were detected in MALDI-TOF MS. Proving this system to be suitable for detection of a drug as well as its carrier. The imaging of these DDSs will be part of a future study as further optimization is required for the (MA)LDI-TOF MSI detection of this small entities.

Acknowledgment. Karin Martin is acknowledged for the generous gift of madurahydroxylactone, chartreusin and amphotericin B. A. Teichler and A. Urbanek are acknowledged for the kind help with the ink-jet equipment and for MALDI measurements, respectively. We thank Dr. S. Schubert for correction of the manuscript.

Supporting Information. Synthesis and Characterization of PEtOx and PEG-*b*-PCL.

References

[1] D. J. Newman, G. M. Cragg. Natural products as sources of new drugs over the 30 years from 1981 to 2010. *J. Nat. Prod.* **2012**, *75*, 311.

[2] C. A. Lipinski. Drug-like properties and the causes of poor solubility and poor permeability. *J. Pharmacol. Toxicol.* **2000**, *44*, 235–249.

[3] T. M. Allen, P. R. Cullis. Drug delivery systems: Entering the Mainstream. *Science* **2004**, *303*, 1818–1822.

[4] R. Duncan. The dawning era of polymer therapeutics. *Nat. Rev. Drug Discov.* **2003**, *2*, 347–360.

[5] K. Knop, R. Hoogenboom, D. Fischer, U. S. Schubert. Poly(ethylene glycol) in drug delivery: Pros and cons as well as potential alternatives. *Angew. Chem. Int. Ed.* **2010**, *49*, 6288–6308.

[6] H. Maeda, J. Wu, T. Sawa, Y. Matsumura, K. Hori. Tumor vascular permeability and the EPR effect in macromolecular therapeutics: A review. *J. Control. Release* **2000**, *65*, 271–284.

[7] S. Kim, Y. Shi, J. Y. Kim, K. Park, J.-X. Cheng. Overcoming the barriers in micellar drug delivery: Loading efficiency, in vivo stability, and micelle-cell interaction. *Expert Opin. Drug Deliv.* **2010**, *7*, 49–62.

[8] M. L. Adams, A. Lavasanifar, G. S. Kwon. Amphiphilic block copolymers for drug delivery. *J. Pharm. Sci.* **2003**, *92*, 1343–1355.

[9] J. F. Gohy. Block copolymers II. *Adv. Polym. Sci.* **2005**, *190*, 65–136.

[10] G. S. Kwon, K. Kataoka. Block copolymer micelles as long-circulating drug vehicles. *Adv. Drug Delivery Rev.* **1995**, *16*, 295–309.

[11] K. Letchford, H. Burt. A review of the formation and classification of amphiphilic block copolymer nanoparticulate structures: Micelles, nanospheres, nanocapsules and polymersomes. *Eur. J. Pharm. Biopharm.* **2007**, *65*, 259–269.

[12] J. Liu, Y. Xiao, C. Allen. Polymer-drug compatibility: A guide to the development of delivery systems for the anticancer agent, ellipticine. *J. Pharm. Sci.* **2004**, *93*, 132–143.

[13] S. M. A. B. Batoy, E. Akhmetova, S. Miladinovic, J. Smeal, C. L. Wilkins. Developments in MALDI mass spectrometry: The quest for the perfect matrix. *Appl. Spectrosc. Rev.* **2008**, *43*, 485–550.

[14] K. Dreisewerd. The desorption process in MALDI. *Chem. Rev.* **2003**, *103*, 395–426.

[15] A. J. Hoteling, W. J. Erb, R. J. Tyson, K. G. Owens. Exploring the importance of the relative solubility of matrix and analyte in MALDI sample preparation using HPLC. *Anal. Chem.* **2004**, *76*, 5157–5164.

[16] S. D. Hanton, K. G. Owens. Using MESIMS to analyze polymer MALDI matrix solubility. *J. Am. Soc. Mass Spectrom.* **2005**, *16*, 1172–1180.

[17] T. Greer, R. Sturm, L. Li. Mass spectrometry imaging for drugs and metabolites. *J. Proteomics* **2011**, *74*, 2617–2631.

[18] D. Hölscher, R. Shroff, K. Knop, M. Gottschaldt, A. Crecelius, B. Schneider, D. G. Heckel, U. S. Schubert, A. Svatos. Matrix-free UV-laser desorption/ionization (LDI) mass spectrometric imaging at the single-cell level: Distribution of secondary metabolites of Arabidopsis thaliana and Hypericum species. *Plant J.* **2009**, *60*, 907–918.

[19] C. Marchand, J. A. Beutler, A. Wamiru, S. Budihas, U. Möllmann, L. Heinisch, J. W. Mellors, S. F. Le Grice, Y. Pommier. Madurahydroxylactone derivatives as dual inhibitors of human immunodeficiency virus type 1 integrase and RNase H. *Antimicrob. Agents Chemother.* **2008**, *52*, 361–364.

[20] M. Badar, K. Hemmen, M. Nimtz, M. Stieve, M. Stiesch, T. Lenarz, H. Hauser, U. Möllmann, S. Vogt, M. Schnabelrauch, P. P. Mueller. Evaluation of madurahydroxylactone as a slow release antibacterial implant coating. *Open Biomed Eng J.* **2010**, *4*, 263–270.

[21] P. Jütten, W. Schumann, A. Härtl, L. Heinisch, U. Gräfe, W. Werner, H. Ulbricht. A novel type of nonsteroidal estrone sulfatase inhibitors. *Bioorg. Med. Chem. Lett.* **2002**, *12*, 1339–1342.

[22] B. E. Leach, K. M. Calhoun, L. E. Johnson, C. M. Teeters, W. G. Jackson. Chartreusin, a new antibiotic produced by streptomyces chartreusis, a new species. *J. Am. Chem. Soc.* **1953**, *75*, 4011–4012.

[23] Z. Xu, K. Jakobi, K. Welzel, C. Hertweck. Biosynthesis of the antitumor agent chartreusin involves the oxidative rearrangement of an anthracyclic polyketide. *Chem. Biol.* **2005**, *12*, 579–588.

[24] W. An, Y. Jiao, C. Dong, C. Yang, Y. Inoue, S. Shuang. Spectroscopic and molecular modeling of the binding of meso-tetrakis(4-hydroxyphenyl)porphyrin to human serum albumin. *Dyes Pigments* **2009**, *81*, 1–9.

[25] R. B. Greenwald, Y. H. Choe, J. McGuire, C. D. Conover. Effective drug delivery by PEGylated drug conjugates. *Adv. Drug Delivery Rev.* **2003**, *55*, 217–250.

[26] W. Wu, S. Wieckowski, G. Pastorin, M. Benincasa, C. Klumpp, J.-P. Briand, R. Gennaro, M. Prato, A. Bianco. Targeted delivery of amphotericin B to cells by using functionalized carbon nanotubes. *Angew. Chem. Int. Ed.* **2005**, *44*, 6358–6362.

[27] P. Legrand, M. Chéron, L. Leroy, J. Bolard. Release of amphotericin B from delivery systems and its action against fungal and mammalian cells. *J. Drug Target.* **1997**, *4*, 311–319.

[28] H. Meng-er, Y. Yu-chen, C. Shu-rong, C. Jin-ren, L. Jia-Xiang, Z. Lin, G. Long-jun, W. Zhen-yi. Use of all-trans retinoic acid in the treatment of acute promyelocytic leukemia. *Blood* **1988**, *72*, 567–572.

[29] S. J. Wetzel, C. M. Guttman, J. E. Girard. The influence of matrix and laser energy on the molecular mass distribution of synthetic polymers obtained by MALDI-TOF-MS. *Int. J. Mass Spectrom.* **2004**, *238*, 215–225.

[30] J. W. Leon, J. M. J. Frechet. Analysis of aromatic polyether dendrimers and dendrimer-linear block copolymers by matrix-assisted laser desorption ionization mass spectrometry. *Polym. Bull.* **1995**, *35*, 449–455.

[31] D. C. Schriemer, L. Li. Detection of high molecular weight narrow polydisperse polymers up to 1.5 million daltons by MALDI mass spectrometry. *Anal. Chem.* **1996**, *68*, 2721–2725.

[32] D. C. Schriemer, L. Li. Mass discrimination in the analysis of polydisperse polymers by MALDI time-of-flight mass spectrometry. 1. Sample preparation and desorption/ionization issues. *Anal. Chem.* **1997**, *69*, 4169–4175.

[33] L. Przybilla, J. Brand, K. Yoshimura, H. Rader, K. Muellen. MALDI-TOF mass spectrometry of insoluble giant polycyclic aromatic hydrocarbons by a new method of sample preparation. *Anal. Chem.* **2000**, *72*, 4591–4597.

[34] M. W. F. Nielen. MALDI time-of-flight mass spectrometry of synthetic polymers. *Mass Spectrom. Rev.* **1999**, *18*, 309–344.

[35] L. Cohen, A. Gusev. Small molecule analysis by MALDI mass spectrometry. *Anal. Bioanal. Chem.* **2002**, *373*, 571–586.

[36] T. Wingerath, D. Kirsch, B. Spengler, W. Stahl. Analysis of cyclic and acyclic analogs of retinol, retinoic acid, and retinal by laser desorption ionization-, matrix-assisted laser desorption ionization-mass spectrometry, and UV/Vis spectroscopy. *Anal. Biochem.* **1999**, *272*, 232–242.

[37] Y. C. Ling, L. Lin, Y. T. Chen. Quantitative analysis of antibiotics by matrix-assisted laser desorption/ionization time-of-flight mass spectrometry. *Rapid Commun. Mass Spectrom.* **1998**, *12*, 317–327.

[38] R. Knochenmuss. Ion formation mechanisms in UV-MALDI. *Analyst* **2006**, *131*, 966–986.

[39] B. J. Bauer, C. M. Guttman, D. Liu, W. R. Blair. Tri-α-naphthylbenzene as a crystalline or glassy matrix for matrix-assisted laser desorption/ionization: A model system for the study of effects of dispersion of polymer samples at a molecular level. *Rapid Commun. Mass Spectrom.* **2002**, *16*, 1192–1198.

[40] H. Ehring, M. Karas, F. Hillenkamp. Role of photoionization and photochemistry in ionization processes of organic molecules and relevance for matrix-assisted laser desorption ionization mass spectrometry. *Org. Mass Spectrom.* **1992**, *27*, 472–480.

[41] K. D. Haegele, D. M. Desiderio. The structural elucidation of polyene macrolide antibiotics by mass spectrometry. Nystatin, amphotericin B and pimaricin. *Biomed. Mass Spectrom.* **1974**, *1*, 20–28.

[42] K. Letchford, J. Zastre, R. Liggins, H. Burt. Synthesis and micellar characterization of short block length methoxy poly(ethylene glycol)-*block*-poly(caprolactone) diblock copolymers. *Colloids Surf., B* **2004**, *35*, 81–91.

[43] Y.-I. Jeong, M.-K. Kang, H.-S. Sun, S.-S. Kang, H.-W. Kim, K.-S. Moon, K.-J. Lee, S.-H. Kim, S. Jung. All-trans-retinoic acid release from core-shell type nanoparticles of poly(ε-caprolactone)/poly(ethylene glycol) diblock copolymer. *Int. J. Pharm.* **2004**, *273*, 95–107.

Supporting information

Drugs as matrix to detect their own drug delivery system of mPEG-*b*-PCL block copolymers in MALDI-TOF MS

*Katrin Knop,[1,2] Steffi Stumpf,[1,2] and Ulrich S. Schubert[1,2]**

[1] Laboratory of Organic and Macromolecular Chemistry (IOMC), Friedrich-Schiller-University Jena, Humboldtstrasse 10, 07743 Germany

[2] Jena Center for Soft Matter (JCSM), Friedrich-Schiller-University Jena, Philosophenweg 8, 07743 Germany

[*]Author for correspondence: Prof. Dr. U. S. Schubert. Telephone: +49(0) 3641 948200, Fax: +49(0) 3641 948202, E-mail: ulrich.schubert@uni-jena.de, Internet: www.schubert-group.com

Synthesis of Poly(ethylene glycol)-*block*-poly(*ε*-caprolactone) (mPEG-*b*-PCL). The synthesis of poly(ethylene glycol)-*block*-poly(*ε*-caprolactone) represents a standard procedure,[1–4] which was carried out according to the following protocol. Briefly, 5 g (2.5 mmol) poly(ethylene glycol) 2 kDa was coevaporated with toluene prior to use. 2.11 mL (2.28 g, 20 mmol) ε-caprolactone and 40 µL (51 mg, 0.12 mmol) of tin-(II) ethylhexanoate, set to 1/20 of the initiating hydroxy groups, were added under inert conditions. The reaction mixture was submitted to three freeze-pump-thaw cycles and, subsequently, stirred overnight at 80 °C. The resulting highly viscous block copolymer was dissolved in dichloromethane, precipitated into cold diethyl ether and dried *in vacuo*.

^{1}H NMR (300 MHz, $CDCl_3$): δ 4.20 (2H, t, PEG-CH_2-O-CO), 4.03 (15H, m, PCL-CH_2-O), 3.61 (176H, m, CH_2-OH, O-CH_2-CH_2-O), 3.35 (4H, m, PEG-O-CH_3 + carbon satellite), 2.28 (20H, m, CO-CH_2), 1.62 (34H, m, COCH_2-CH_2-CH_2CH_2CH_2O + COCH_2CH_2CH_2-CH_2-CH_2O), 1.36 (17H, m, COCH_2CH_2-CH_2-CH_2CH_2O).

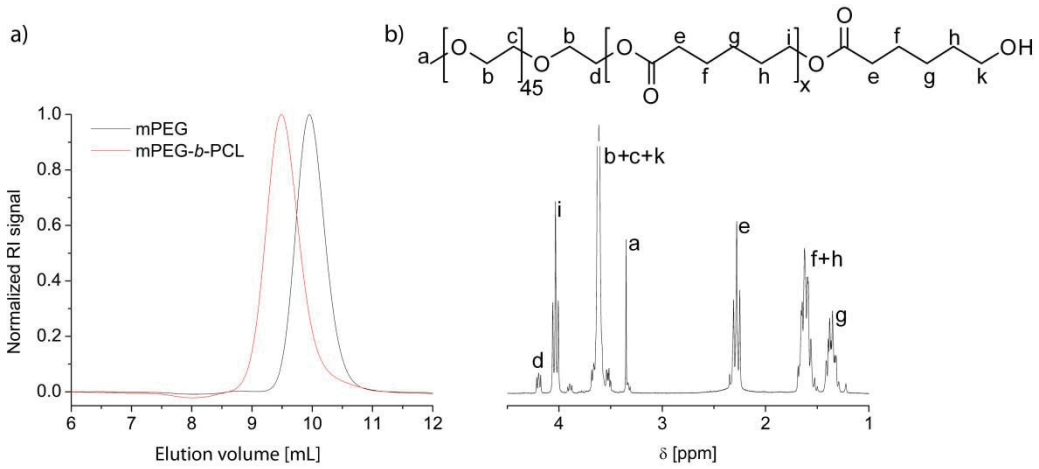

Figure S1: (a) SEC traces of the mPEG and mPEG-*b*-PCL copolymers. (b) ^{1}H-NMR spectrum of the mPEG-*b*-PCL copolymer in $CDCl_3$.

Table S1. Overview of analytical data obtained for the mPEG-*b*-PCL copolymer.

Polymer	DP PCL[a]	M_n [g mol^{-1}][a] ^{1}H NMR	M_n [g mol^{-1}][b] SEC	PDI	M_n [g mol^{-1}][c] MALDI	PDI
mPEG-*b*-PCL	8	2,900	1,700	1.08	2,600	1.04

[a]Calculated from ^{1}H NMR. [b] Obtained from SEC ($CHCl_3$:*i*-PrOH:TEA) using PEG calibration. [c] Obtained by MALDI-TOF MS.

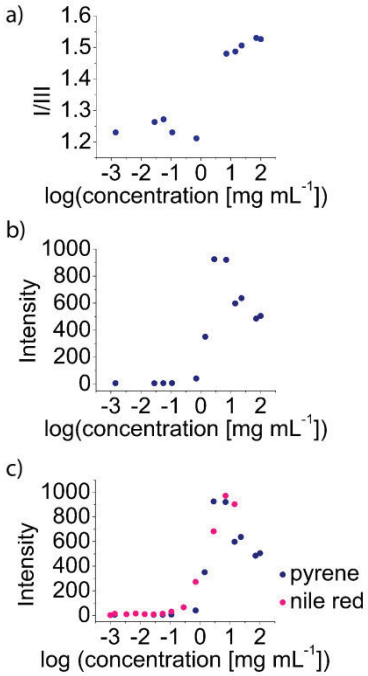

Figure S2: Determination of the critical micelle concentration for mPEG-*b*-PCL by means of (a) the ratio of band I to band III of the fluorescence emission of pyrene, (b) the fluorescence intensity of the pyrene fluorescence emission and (c) the intensity of the fluorescence emission of nile red.

Determination of the cmc with pyrene. 1 mL of the polymer in acetone solution was dropped into 5 mL water under stirring to obtain the final concentrations between 1.0×10^{-3} mg mL^{-1} and 100 mg mL^{-1}. 10 µL of a 0.254 mg mL^{-1} concentrated pyrene in acetone solution was added leading to a final pyrene concentration in water of 2.5×10^{-6} M. The acetone was evaporated for 2 days, the solutions were refilled with water to 5 mL and the vials were closed to equilibrate for further 2 weeks. The emission spectra were recorded between 350 nm and 500 nm with λ_{exc} = 335 nm. Excitation spectra were recorded from 300 nm to 380 nm. The emission wavelength was set to 390 nm.

Determination of the cmc with nile red. The aqueous polymer solutions were prepared in an analogue way as described for the cmc determination with pyrene. To each sample, 10 µL of nile red in acetone (0.4 mg mL^{-1}) were added to result in a final nile red in water concentration of 2.5×10^{-6} M. The acetone was evaporated for 2 days and refilled to 5 mL and equilibrated for 2 weeks. The emission spectra were recorded between 525 nm and 750 nm with λ_{exc} = 520 nm.

The cmc was determined from the plotting to be 0.1 mg mL^{-1}.

Synthesis of poly(2-ethyl-2-oxazoline) 2 kDa ($PEtOx_{20}$). The $PEtOx_{20}$ was synthesized according to a reported procedure.[5,6] Briefly, the required amount of initiator (methyl tosylate, 37.3 mg, 0.2 mmol), monomer (2-ethyl-2-oxazoline, 0.397 g, 0.413 mL, 4 mmol) and solvent (acetonitrile, 0.59 mL) were transferred under argon into a flame-dried microwave vial. The reaction mixtures were heated under microwave conditions to 140 °C for 190 s. The end capping was performed by adding 1 mL of concentrated sodium carbonate solution by syringe to the microwave vials and stirring at room temperature overnight. The reaction solution was diluted with dichloromethane, washed with aqueous sodium hydrogen carbonate solution and brine, dried with sodium sulfate, filtered and dried under vacuum. The repeating units were calculated by comparison of the signals at 6.06 ppm and 3.45 ppm.

^{1}H NMR (300 MHz, $CDCl_3$): δ 3.43 (85H, m, N-CH_2-CH_2), 3.00 (3H, m, N-CH_3), 2.32 (44H, m, CO-CH_2-CH_3), 1.09 (68H, m, CO-CH_2-CH_3).

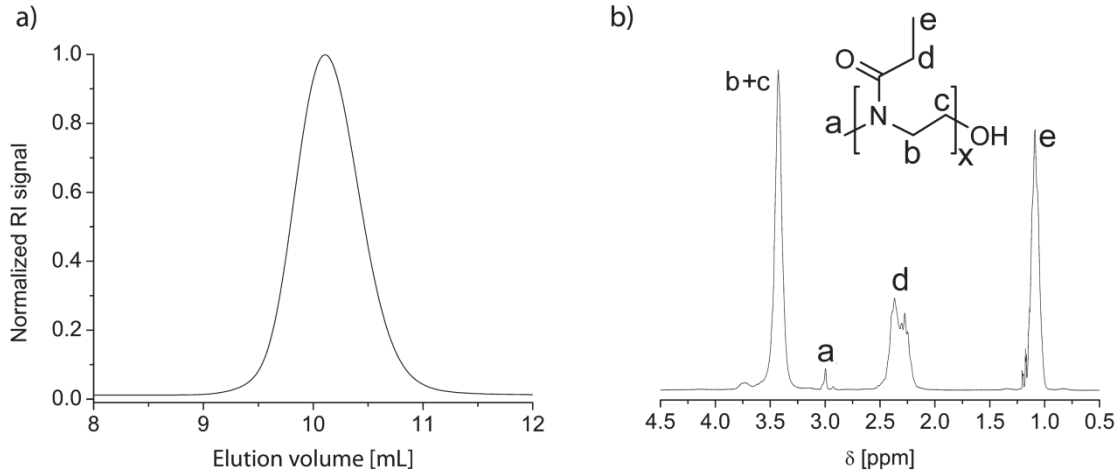

Figure S3: (a) SEC traces of the $PEtOx_{20}$ polymer. (b) ^{1}H-NMR spectrum of the $PEtOx_{20}$ polymer in $CDCl_3$.

Table S2. Overview of analytical data obtained for the PEtOx polymer.

Polymer	DP PEtOx[a]	M_n [g mol^{-1}][a] ^{1}H NMR	M_n [g mol^{-1}][b] SEC	PDI	M_n [g mol^{-1}][c] MALDI	PDI
$PEtOx_{20}$	21	2,100	2,000	1.14	2,200	1.04

[a]Calculated from ^{1}H NMR. [b] Obtained from SEC ($CHCl_3$:*i*-PrOH:TEA) using PMMA calibration. [c] Obtained by MALDI-TOF MS.

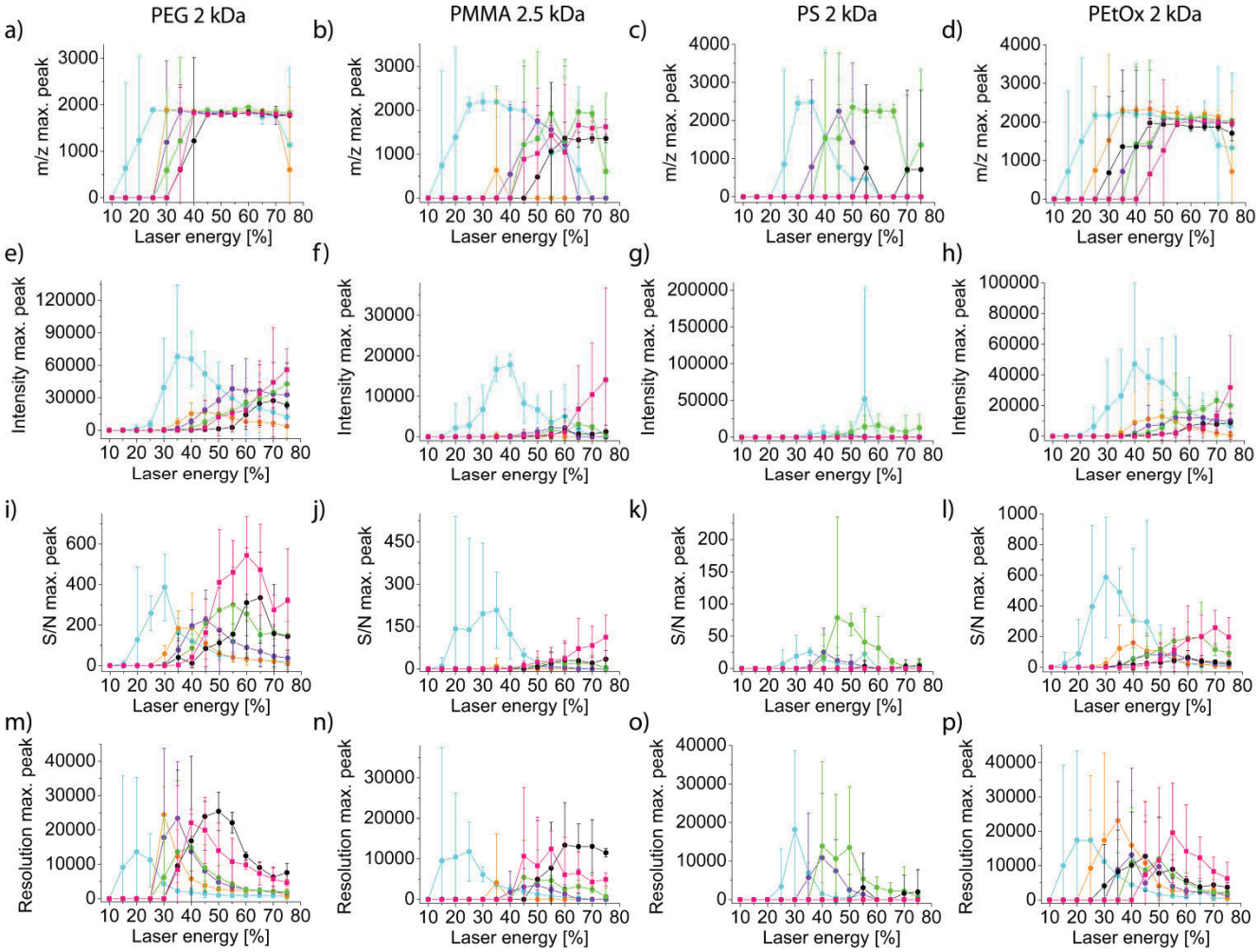

Figure S4: Evaluation of the characteristic parameters of the MALDI-TOF MS spectra shown with error bars on the basis of the maximum peak for mPEG 2 kDa as a function of the laser energy against (a) the m/z value, (e) the intensity, (i) the S/N ratio, (m) the resolution. Evaluation of the characteristic parameters of the MALDI-TOF MS spectra on the basis of the maximum peak for PMMA 2.5 kDa as a function of the laser energy against (b) the m/z value, (f) the intensity, (j) the S/N ratio, (n) the resolution. Evaluation of the characteristic parameters of the MALDI-TOF MS spectra on the basis of the maximum peak for PS 2 kDa as a function of the laser energy against (c) the m/z value, (g) the intensity, (k) the S/N ratio, (o) the resolution. Evaluation of the characteristic parameters of the MALDI-TOF MS spectra on the basis of the maximum peak for PEtOx 2 kDa as a function of the laser energy against (d) the m/z value, (h) the intensity, (l) the S/N ratio, (p) the resolution.

REFERENCES

[1] L. Luo, J. Tam, D. Maysinger, A. Eisenberg. Cellular internalization of poly(ethylene oxide)-*b*-poly(ε-caprolactone) diblock copolymer micelles. *Bioconjugate Chem.* **2002**, *13*, 1259–1265.

[2] C. Lu, S. Guo, L. I. Liu, Y. Zhang, Z. Li, J. Gu. Aggregation behavior of mPEG-PCL diblock copolymers in aqueous solutions and morphologies of the aggregates. *J. Polym. Sci., Part B: Polym. Phys.* **2006**, *44*, 3406–3417.

[3] K. Letchford, J. Zastre, R. Liggins, H. Burt. Synthesis and micellar characterization of short block length methoxy poly(ethylene glycol)-*block*-poly(caprolactone) diblock copolymers. *Colloids Surf. B* **2004**, *35*, 81–91.

[4] Y.-I. Jeong, M.-K. Kang, H.-S. Sun, S.-S. Kang, H.-W. Kim, K.-S. Moon, K.-J. Lee, S.-H. Kim, S. Jung. All-trans-retinoic acid release from core-shell type nanoparticles of poly(ε-caprolactone)/poly(ethylene glycol) diblock copolymer. *Int. J. Pharm.* **2004**, *273*, 95–107.

[5] C. Weber, C. R. Becer, A. Baumgaertel, R. Hoogenboom, U. S. Schubert. Preparation of methacrylate end-functionalized poly(2-ethyl-2-oxazoline) macromonomers. *Des. Monomers Polym.* **2009**, *12*, 149–165.

[6] F. Wiesbrock, R. Hoogenboom, M. A. M. Leenen, M. A. R. Meier, U. S. Schubert. Investigation of the living cationic ring-opening polymerization of 2-methyl-, 2-ethyl-, 2-nonyl-, and 2-phenyl-2-oxazoline in a single-mode microwave reactor. *Macromolecules* **2005**, *38*, 5025–5034.

Publication P10:

Matrix-free UV-laser desorption/ionization (LDI) mass spectrometric imaging at the single-cell level: distribution of secondary metabolites of *Arabidopsis thaliana* and *Hypericum* species

---

D. Hölscher, R. Shroff, K. Knop, M. Gottschaldt, A. C. Crecelius, B. Schneider, D. Heckel, U. S. Schubert, A. Svatoš

Plant J. **2009**, *60*, 907–918.

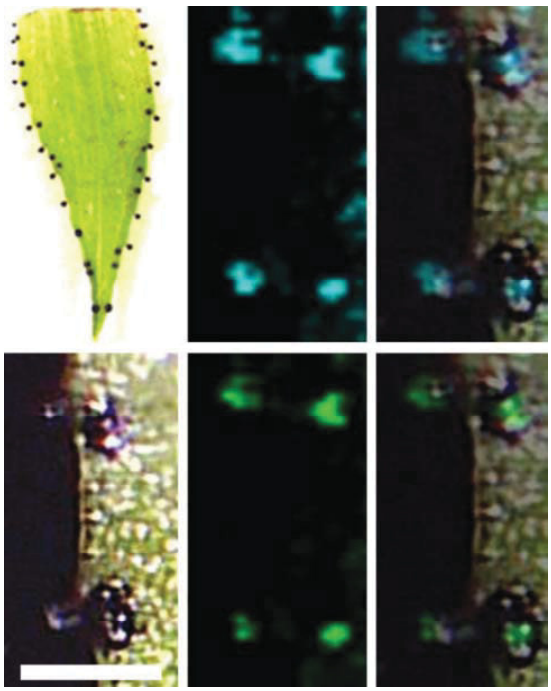

the plant journal

SEB SOCIETY FOR EXPERIMENTAL BIOLOGY

The Plant Journal (2009) **60**, 907–918 doi: 10.1111/j.1365-313X.2009.04012.x

TECHNICAL ADVANCE

Matrix-free UV-laser desorption/ionization (LDI) mass spectrometric imaging at the single-cell level: distribution of secondary metabolites of *Arabidopsis thaliana* and *Hypericum* species

Dirk Hölscher[1,*], Rohit Shroff[1], Katrin Knop[2], Michael Gottschaldt[2,3], Anna Crecelius[2,3], Bernd Schneider[1], David G. Heckel[1], Ulrich S. Schubert[2,3,4] and Aleš Svatoš[1,*]

[1]*Department of Entomology, Mass Spectrometry Research Group, and Biosynthesis/NMR Research Group, Max Planck Institute for Chemical Ecology, Hans-Knöll-Strasse 8, 07745 Jena, Germany,*

[2]*Laboratory of Organic and Macromolecular Chemistry, Friedrich-Schiller University of Jena, Humboldtstrasse 10, 07743 Jena, Germany,*

[3]*Dutch Polymer Institute (DPI), John F. Kennedylaan 2, 5612 AB Eindhoven, The Netherlands, and*

[4]*Laboratory of Macromolecular Chemistry and Nanoscience, Eindhoven University of Technology, Den Dolech 2, 5600 MB Eindhoven, The Netherlands*

Received 8 May 2009; revised 8 August 2009; accepted 24 August 2009; published online 27 October 2009.
[*]For correspondence (fax +49 3641 571701; e-mail svatos@ice.mpg.de or hoelscher@ice.mpg.de).

SUMMARY

The present paper describes matrix-free laser desorption/ionisation mass spectrometric imaging (LDI-MSI) of highly localized UV-absorbing secondary metabolites in plant tissues at single-cell resolution. The scope and limitations of the method are discussed with regard to plants of the genus *Hypericum*. Naphthodianthrones such as hypericin and pseudohypericin are traceable in dark glands on *Hypericum* leaves, placenta, stamens and styli; biflavonoids are also traceable in the pollen of this important phytomedical plant. The highest spatial resolution achieved, 10 μm, was much higher than that achieved by commonly used matrix-assisted laser desorption/ionization (MALDI) imaging protocols. The data from imaging experiments were supported by independent LDI-TOF/MS analysis of cryo-sectioned, laser-microdissected and freshly cut plant material. The results confirmed the suitability of combining laser microdissection (LMD) and LDI-TOF/MS or LDI-MSI to analyse localized plant secondary metabolites. Furthermore, *Arabidopsis thaliana* was analysed to demonstrate the feasibility of LDI-MSI for other commonly occurring compounds such as flavonoids. The organ-specific distribution of kaempferol, quercetin and isorhamnetin, and their glycosides, was imaged at the cellular level.

Keywords: ***Hypericum perforatum, Hypericum reflexum,*** **LDI mass spectrometric imaging, laser microdissection, naphthodianthrones, flavonoids.**

INTRODUCTION

Recently, a variety of technologies have been successfully used to obtain data from individual plant cells (Lange, 2005). Both laser microdissection (LMD) (Emmert-Buck *et al.*, 1996; Hölscher and Schneider, 2007; Li *et al.*, 2007a) and cell sap sampling using microcapillaries (Brandt *et al.*, 2002) have been reported to improve access to the contents of individual cells; these reports were based on analyses using both post-genomic bioanalytical technologies and spectroscopic methods (Lange, 2005). Techniques such as LMD allow researchers to avoid the averaging effects that occur when heterogeneous tissues, which represent the most abundant cell types, are pooled; however, as amplification methods such as commonly used for DNA and RNA are not available, highly sensitive detection methods are required for metabolites. Methods based on mass spectrometry offer the required high sensitivity and specificity (Sumner *et al.*, 2003).

MS-dependent imaging techniques have been developed in the past to study the localization on a small scale of compounds from complex biological systems. Recently, a method for MS imaging has been developed that offers information about the distribution of proteins, peptides or metabolites with 100–300 μm spatial resolution (Caprioli *et al.*, 1997; Cooks *et al.*, 2006; Li *et al.*, 2008; Seeley and Caprioli, 2008). Furthermore, when atmospheric pressure infrared matrix-assisted laser desorption/ionization mass spectrometry was used to study plant metabolites in the white lily (*Lilium candidum* L.) and other plants, over 50 small metabolites were discovered; these were involved in flavonoid biosynthesis and had a spatial resolution of 180–640 μm (Li *et al.*, 2008). MALDI imaging involves use of a conventional MALDI source to desorb ions of interest from the sample covered by a sprayed (Rubakhin *et al.*, 2005) or spotted matrix (Aerni *et al.*, 2006). MALDI imaging has been used to study the distribution of a wide variety of metabolites, including drugs, peptides and proteins, in animal tissues (Reyzer and Caprioli, 2007; Goodwin *et al.*, 2008), and herbicides (Mullen *et al.*, 2005), peptides (Kondo *et al.*, 2006) and sugars (Burrell *et al.*, 2007; Li *et al.*, 2007a,b) in plants. Recently, ion intensity maps were constructed from MALDI-TOF mass spectra to measure the spatial distribution of some secondary plant metabolites. The matrix 9-aminoacridine was evenly applied to the leaves of *Arabidopsis thaliana* (Col-0) in order to detect glucosinolates (Shroff *et al.*, 2008). However, applying MALDI matrices to the tissues complicates tissue preparation for imaging and can disturb the native distribution of the studied metabolites (Shroff *et al.*, 2008). Low-molecular-weight metabolites have been profiled and localized using colloidal graphite-assisted LDI (GALDI) MS in *A. thaliana* (Cha *et al.*, 2008). Profiles and spatially resolved images of phospholipids, cerebrosides, oligosaccharides, flavonoids and other secondary metabolites were obtained in negative and positive ion MS modes. Certain mass imaging methods, such as laser-assisted electrospray ionization (LAESI) (Vertes *et al.*, 2008), can reduce sample handling prior to analysis. However, the infrared laser currently used does not provide cell-like resolution for the obtained MS images.

The main secondary plant products of members of the genus *Hypericum* of the Hypericaceae plant family (Mabberley, 2008) are flavonoids (e.g. quercetin, hyperoside, rutin, quercitrin, isoquercitrin), xanthones (e.g. 1,3,6,7,-tetrahydroxyxanthone), prenylated phloroglucinols such as hyperforin and adhyperforin, biflavonoids [I3,II8-biapigenin and I3′,II8-biapigenin (amentoflavone)] and naphthodianthrones (Brockmann *et al.*, 1942; Wolfender *et al.*, 2003; Charchogylan *et al.*, 2007; Smelcerovic *et al.*, 2008) (Figure 1 and Table 1). Multi-cellular, globular or tunnel-shaped aggregates such as secretory canals, and dark and translucent glands have been reported to contain the secondary metabolites (Ciccarelli *et al.*, 2001; Robson, 2003). Dark and pale glands often occur in the stem, leaf, sepal, petal or anthers. In *Hypericum*, the stamens possess a connective terminating in a dark gland (Figure 2). The gynoecium of *H. perforatum* has three styles and contains relatively small red stigmata (Figure 2). There is a large variation in the glandularity of sepals in *Hypericum*, and some species (such

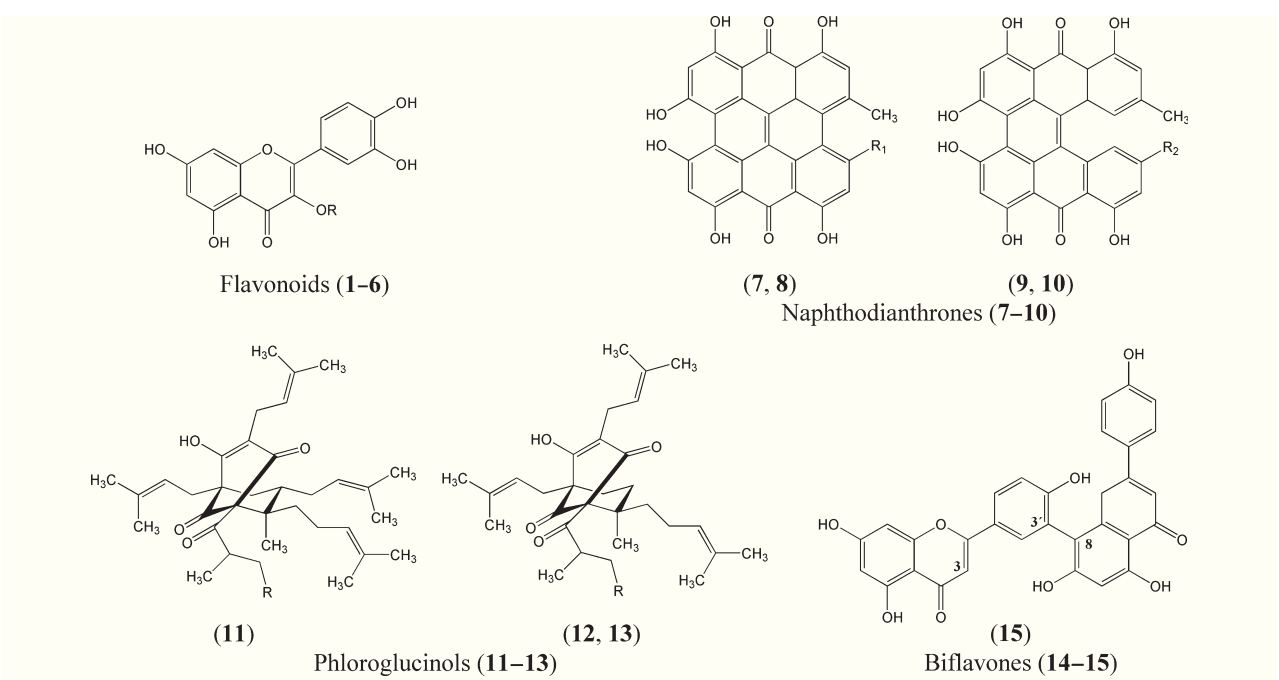

Figure 1. Chemical structures for the major secondary metabolites of *H. perforatum.*

Table 1 Names, deprotonated ion mass and UV adsorption wavelengths of the *Hypericum* sp. natural constituents (see Figure 1 for structural formula) (Jürgenliemk, 2001)

Number	Name	$[M-H]^-$ (*m/z*)	UV_{max} (nm)
(1)	Quercetin	301.03	256.8, 372.9
(2)	Quercitrin (R: 3-*O*-α-L-rhamnopyranosyl)	447.09	256.8, 349.3
(3)	Isoquercitrin (R: 3-*O*-β-D-glucopyranosyl)	463.08	256.8, 352.9
(4)	Hyperoside (R: 3-*O*-β-D-galactopyranosyl)	463.08	256.8, 352.9
(5)	Miquelianin (R: 3-*O*-α-D-glucuronopyranosyl)	477.07	256.8, 352.9
(6)	Rutin (R: 3-*O*-β-D-rutinosyl)	609.14	256.8, 352.9
(7)	Hypericin (R: $-CH_3$)	503.07	278.1, 317.2, 452.3, 539.5, 579.7
(8)	Pseudohypericin (R: $-CH_2OH$)	519.07	281.6, 324.3, 455.9, 539.5, 579.7
(9)	Protohypericin (R: $-CH_3$)	505.09	–
(10)	Protopseudohypericin (R: $-CH_2OH$)	521.08	–
(11)	Hyperforin (R: -H)	535.37	271.0
(12)	Adhyperfirin (R: $-CH_3$)	481.33	–
(13)	Hyperfirin (R: -H)	467.31	–
(14)	Biapigenin (I3,II8-biapigenin)	537.08	267.4, 331.4
(15)	Amentoflavone (I3′,II8-biapigenin)	537.08	–

as *H. reflexum*) have stalked glands (Robson, 2003). These glandular trichomes are often close neighbours of dark glands, which are located near the margins of the sepals (Esau, 1965; Piovan *et al.*, 2004). The short distance (<50 μm) between these glands makes the use of (MA)LDI techniques to acquire information from each dark gland extremely challenging.

Controlled clinical trials have shown the therapeutic efficacy of preparations from aerial parts of this medicinal plant for treating mild to moderate depression (Kaul, 2000; Butterweck, 2003; Gädcke, 2003; Müller, 2003). Hyperforin, in particular, a major acylphloroglucinol in *Hypericum perforatum* L. (Erdelmeier, 1998), exhibits intriguing pharmacological properties (Müller, 2003; Beerhues, 2006).

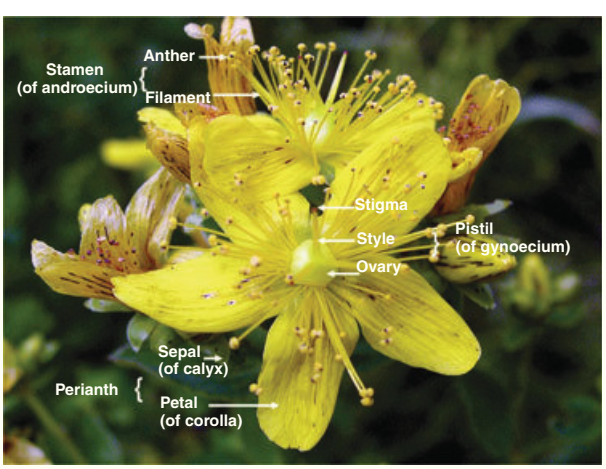

Figure 2. Photograph of a flower of *H. perforatum*, reproduced with permission from S. Imhof (University of Marburg, Germany).
The bisexual flower of *H. perforatum* shows a large number of stamens, collectively called the androecium, and three pistils, collectively called the gynoecium. The pistil comprises three styles with red stigmas. The ovary is the part of the pistil containing the ovules; these are connected to the placenta tissue by a stalk called the funicle (funiculus) (Figure 6a). The perianth of *H. perforatum* consists of two discrete whorls: the outer green photosynthetic calyx comprising leaf-like sepals, and the yellow corolla comprising individual petals.

Numerous studies have been published describing the various approaches to analysing the constituents of *H. perforatum*, commonly known as St John's wort. One of the best-selling herbal medicinal plants worldwide, this species is planted in several hundred hectares in Europe (Gaudin *et al.*, 2003). HPLC and RPLC separations have been performed to identify and quantify active compounds in extracts of St John's wort (Li and Fitzloff, 2001; Seger *et al.*, 2004; Pages *et al.*, 2006). Other publications reported analysis of the major secondary metabolites of *H. perforatum* based on measurements using LC/MS^2 (Brolis *et al.*, 1998; Ganzera *et al.*, 2002) and LC/NMR/MS (Hansen *et al.*, 1999). Previously, Tatsis *et al.* (2007) combined liquid chromatography/diode array detector/solid phase extraction/NMR spectroscopy and liquid chromatography/ultraviolet/tandem MS spectrometry. Generally speaking, modern techniques for identifying compounds are combined with a classical approach, namely extracting whole plant material such as leaves or flowers using organic solvents.

The model plant *A. thaliana* was chosen to investigate the tissue-specific accumulation of flavonoids in its flowers, sepals, petals and leaves, and thus to demonstrate the broader applicability of the matrix-free LDI-MSI method. Recently, flavonoids and cuticular waxes have been profiled and imaged from various plant surfaces, and cross-sections of *A. thaliana* were successfully probed by colloidal graphite-assisted LDI (GALDI) MS imaging (Cha *et al.*, 2008). The size and fragility of *A. thaliana* presented challenges when using the GALDI-MSI method to analyse the metabolome.

The present paper reports on the use of matrix-free laser desorption/ionization mass spectrometric imaging

(LDI-MSI) to study highly localized UV-absorbing secondary metabolites in plant tissues. The applicability of the method is demonstrated on the phytochemical contents of members of the plant genera Arabidopsis and *Hypericum*, and verified by mass spectrometry of the areas isolated using LMD in *Hypericum*.

RESULTS

Laser desorption/ionization time of flight (LDI-TOF) detection of *Hypericum* sp. and *A. thaliana* secondary metabolites

To prepare samples from various tissues of *Hypericum* sp. for LDI-TOF/MS analysis, two approaches were used: cell sap sampling using microcapillaries and LMD. The thickness of the plant cell walls and the fragility of the specially prepared fused silica capillaries (Figure 3c) (Kelly *et al.*, 2006; Sproß, 2007) made it difficult to obtain sufficient amounts of the dark glands.

Dark glands from petals (Figure 3b) and dark and translucent glands from leaves (Figure 3a,d) were successfully separated by LMD. As a control, green parenchyma tissue from the leaves of *H. perforatum* (Figure 3a) was collected and extracted using methanol. Aliquots (1 μl) of the individual sample solutions were dried on the stainless steel plate typically used in MALDI instruments. Because phenolic structures deprotonate easily, the MALDI analysis was carried out in negative ion mode using 9-aminacridine as the matrix. Moreover, these analytes did not require a chemical matrix for ionization, probably due to their strong UV absorption. They ionized very well under UV irradiation with a conventional nitrogen laser (λ = 337 nm) fitted to the MALDI instrument. A comparison of the MALDI (matrix 9-aminoacridine; Shroff *et al.*, 2007) and LDI spectra of hypericin and pseudohypericin showed no difference in sensitivity. Moreover, the LDI spectra were free of matrix peaks. Both MALDI and LDI methods showed comparable limit of detection for authentic compounds (5 pg).

We compared our data with the results of several phytochemical investigations of *Hypericum* secondary metabolites (Brockmann *et al.*, 1942; Wolfender *et al.*, 2003; Charchogylan *et al.*, 2007; Tatsis *et al.*, 2007; Smelcerovic *et al.*, 2008). In the dark glands of the petals of *H. perforatum*, we detected the naphthodianthrones hypericin (**7**) (*m/z* 503.07, $[M\text{-}H]^-$) and pseudohypericin (**8**) (*m/z* 519.07, $[M\text{-}H]^-$) and the flavonoids quercetin (**1**) (*m/z* 301.03, $[M\text{-}H]^-$), quercitrin (**2**) (*m/z* 447.07, $[M\text{-}H]^-$) and rutin (**6**) (*m/z* 609.14, $[M\text{-}H]^-$), as well as isoquercitrin (**3**) (*m/z* 463.08, $[M\text{-}H]^-$) and/or hyperoside (**4**) (*m/z* 463.08, $[M\text{-}H]^-$) (indistinguishable by our methods) (Figure 4a) (Tatsis *et al.*, 2007). Compared to the dark glands of the petals, the black nodules of the leaves show two additional compounds: protohypericin (**9**) (*m/z* 505.09, $[M\text{-}H]^-$) and protopseudophypericin (**10**) (*m/z* 521.08, $[M\text{-}H]^-$) (Figure 4b). The LDI-TOF/MS analysis of the translucent glands of the leaves showed signals for three phloroglucinols: hypeforin (**11**) (*m/z* 535.17, $[M\text{-}H]^-$), adhyperfirin (**12**) (*m/z* 481.33, $[M\text{-}H]^-$) and hyperfirin (**13**) (*m/z* 467.31, $[M\text{-}H]^-$) (Figure 4c) (Tatsis *et al.*, 2007). The LMD-prepared dark glandular cells of the connective tissue between the theca of the stamens (Figure 2) showed a signal profile comprising hypericin (**7**) (*m/z* 503.07, $[M\text{-}H]^-$), pseudohypericin (**8**) (*m/z* 519.07, $[M\text{-}H]^-$), protohypericin (**9**) (*m/z* 505.09, $[M\text{-}H]^-$) and protopseudophypericin (**10**), (*m/z* 521.08, $[M\text{-}H]^-$) and the flavonoid quercetin (**1**) (*m/z* 301.03, $[M\text{-}H]^-$). Furthermore, the most intense signal of this spectrum was produced by the biflavonoid biapigenin (**14**) (*m/z*

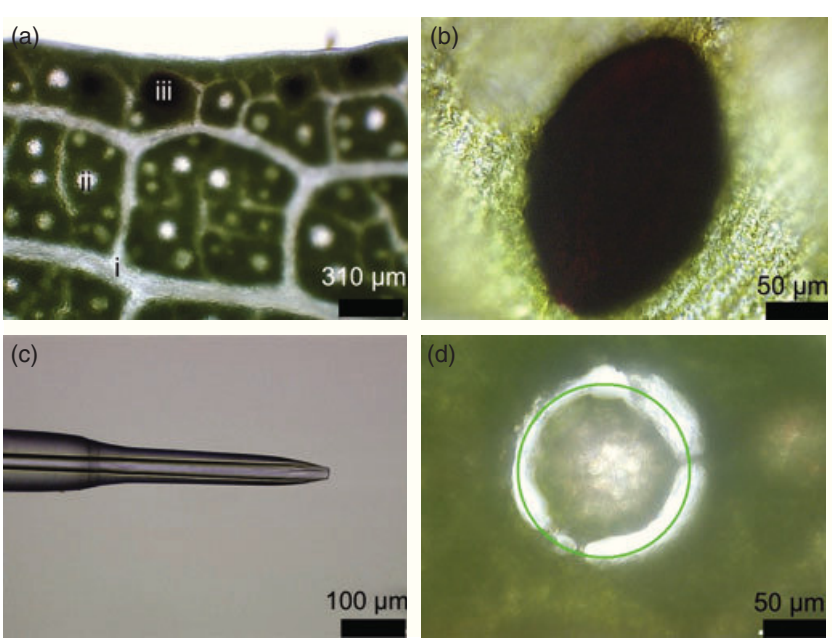

Figure 3. Localization of dark and translucent glands in various tissues of *H. perforatum*.
(a) Part of a green leaf of *H. perforatum* showing translucent leaf venation, and translucent and dark glands.
(b) Dark gland of a petal of *H. perforatum*.
(c) Fused silica capillary
(d) Laser-microdissected dark glands of a leaf of *H. perforatum*.

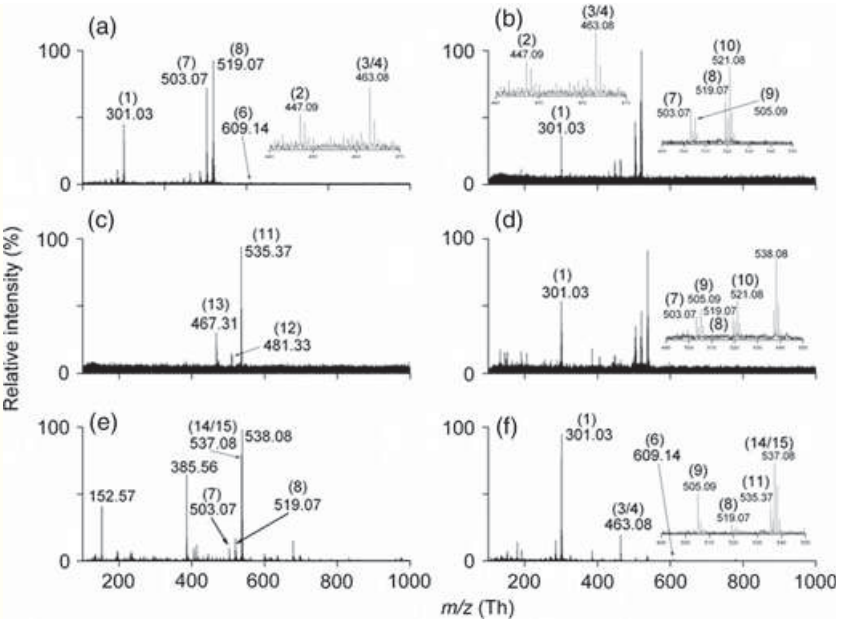

Figure 4. Representative LDI mass spectra of various parts of *H. perforatum*.
(a) Laser-microdissected dark glands from a leaf; (b) dark glands from a petal; (c) translucent glands from a leaf; (d) dark connective theca stamens; (e) pollen stamens; (f) red papillae styli.

537.08, [M-H]$^-$) (Figure 4d). In previous reports, only traces of isobaric amentoflavones were found in *H. perforatum* (Repčák and Martonfi, 1997; Nebelmeir, 2006). The prepared pollen showed the biapigenin signal almost exclusively (**14**) (*m/z* 537.08, [M-H]$^-$), and only traces of the naphthodianthrones hypericin (**7**) (*m/z* 503.07, [M-H]$^-$), pseudohypericin (**8**) (*m/z* 519.07, [M-H]$^-$), protohypericin (**9**) (*m/z* 505.09, [M-H]$^-$) and protopseudohypericin (**10**) (*m/z* 521.08, [M-H]$^-$) (Figure 4e). The spectra of the lighter red papillae of the styli showed signals for hypericin (**7**) (*m/z* 503.07, [M-H]$^-$), pseudohypericin (**8**) (*m/z* 519.07, [M-H]$^-$), protohypericin (**9**) (*m/z* 505.09, [M-H]$^-$), protopseudophypericin (**10**) (*m/z* 521.08, [M-H]$^-$), the flavonoids quercetin (**1**) (*m/z* 301.03, [M-H]$^-$), isoquercitrin (**3**) (*m/z* 463.08, [M-H]$^-$) and/or hyperoside (**4**) (*m/z* 463.08, [M-H]$^-$), and the phloroglucinol hyperforin (**11**) (*m/z* 535.37, [M-H]$^-$). Once again, the strongest signal was produced by the biflavonoid biapigenin (**14**) (*m/z* 537.08, [M-H]$^-$) (Figure 4f). Investigation of the non-secretory parenchyma tissue showed only traces of the flavonoids quercetin (**1**) (*m/z* 301.03, [M-H]$^-$) and rutin (**6**) (*m/z* 609.14, [M-H]$^-$) and the phloroglucinol hyperforin (**11**) (*m/z* 535.37, [M-H]$^-$).

Thus, use of LMD and MALDI- or LDI-MS has proven to be a powerful combination for obtaining information about the phytochemical profile of specialized plant areas. The ability to ionize the investigated hypericins without the use of matrix during the LDI process simplifies sample preparation and enables direct profiling of secondary plant metabolites by MSI.

Direct profiling/imaging of flavonoids, biflavonoids and hypericins by LDI-MSI

The commonly used MS imaging technique, which involves application of a matrix, has certain disadvantages. If the tissue is wetted when the matrix is applied, significant analyte de-localization may occur, leading to artefacts. Additionally, the size of matrix crystals formed after multiple spraying is highly variable and sometimes larger than the required spatial resolution. Hence, the best solution is to analyse the tissue without any chemical treatment in order to observe the native distribution of compounds. However, this is generally not feasible, as most analytes do not strongly absorb UV light and require a matrix to be desorbed. However, the efficient UV absorption of hypericins suggested that the LDI process could be used for imaging these compounds in *H. perforatum* tissues without the need for a matrix.

Preliminary experiments were performed using a MALDI micro instrument (Shroff *et al.*, 2008); however, the laser beam (approximately 50 μm) could not be focused to allow spatial information to be differentiated on a fine scale. Higher resolution could be achieved using the Ultraflex III®, in which the laser can be focused on spots of <10 μm. We were able to resolve the localized distribution of hypericin and pseudohypericin in both secretory cavities, separated from each other by the peduncle of the glandular trichomes (Figure 5), in *H. reflexum* leaves. Additionally, LDI-MSI made it possible to detect hypericin, pseudohypericin, quercetin and rutin in the small red appendices of the placenta; supposedly from one cell, these appendices are easily prepared from cryo-sectioned flower material (Figure 6). Difficulties in performing LDI-MSI experiments with the three-dimensional bulky stamens and styli were overcome by LMD. The filament was removed and samples suitable for measurement were obtained (Figure 7a,b). LDI-MSI allowed hypericin (*m/z* 503.07, [M-H]$^-$) (Figure 7c,e) and pseudohypericin (*m/z* 519.07, [M-H]$^-$) (Figure 7d,f) to be

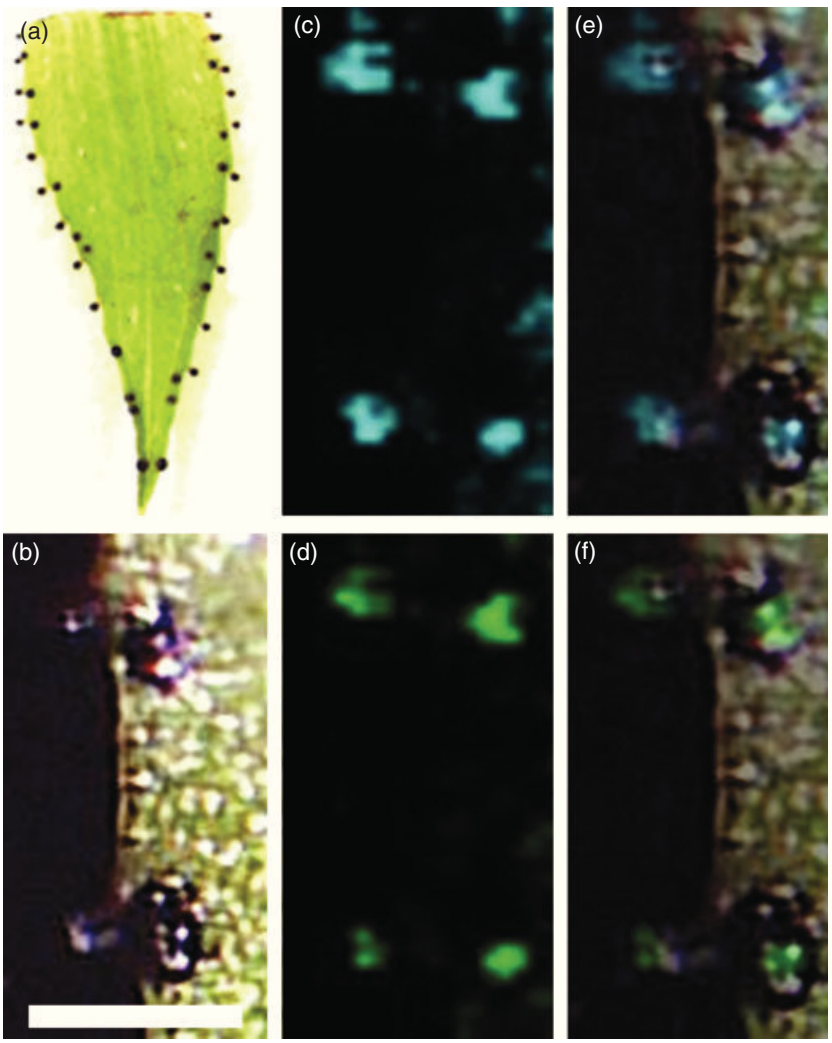

Figure 5. Detection of hypericins in the glandular trichomes of *H. reflexum*.
(a) Detail of *H. reflexum* leaf; (b) cut-out of measured region; glandular trichomes and secretory cavities are distinguishable; (c, d) molecular images of (b) for *m/z* 503 (blue) and *m/z* 519 (green); (e, f) overlays of optical image (b) and molecular images for *m/z* 503 (blue) and *m/z* 519 (green), respectively. Scale bar = 200 μm.

detected in the dark connective theca stamens. Signals for hypericins and biflavonoids were detectable on the stigma as a result of the presence of pollen grains on the papillae (image not shown, and Figure 8a). Signals typical for the biflavonoids biapigenin (*m/z* 537.08, $[M\text{-}H]^-$) and amentoflavone (*m/z* 537.08, $[M\text{-}H]^-$) were found in the pollen (Figure 8b). A laser intensity of 283 μJ mm^{-2} was sufficient for efficient desorption/ionization of the analytes. Images constructed for the whole leaf were composed of approximately 9000 pixels, and the images constructed for smaller structures such as the stamens, styli and pollen were all more than 1000 pixels. Although a spatial resolution of 10 μm was required to differentiate highly localized regions, the high frequency (200 Hz) of the Nd:YAG laser made it possible for the measurements to be performed in a reasonable time span.

The ease with which biflavonoids could be analysed using LDI inspired us to study whether other phenolic compounds could be desorbed from plant material. GALDI imaging has shown the distribution of three flavonoids (kaempferol, quercetin and isorhamnetin) and their glycosides at low spatial resolution in sepals and petals from *A. thaliana* (Cha *et al.*, 2008). Mounting detached *A. thaliana* Col-0 petals on conductive tape (Figure 9a,f) and LDI-MSI imaging using the Ultraflex III® at 10 μm resolution within the scanning range *m/z* 100–800 we were able to obtain highly resolved ion images with cell-like structures (Figure 9). Very strong signals for many putative flavonoids and corresponding glycosides were visible, with particular patterns for individual ions. Using CID spectra (TOF/TOF) and published data (Cha *et al.*, 2008), we were able to identify individual ions. The upper two-thirds of most petal surfaces contain kaempferol (*m/z* 285.02, Figure 9b) and kaempferol-rhamnoside (*m/z* 431.04, Figure 9d). Upon closer inspection, petal veins show very low concentrations of these compounds. An identical distribution was observed for highly glycosylated kaempferols (data not shown), e.g. *m/z* 577 (kaempferol-dirhamno-

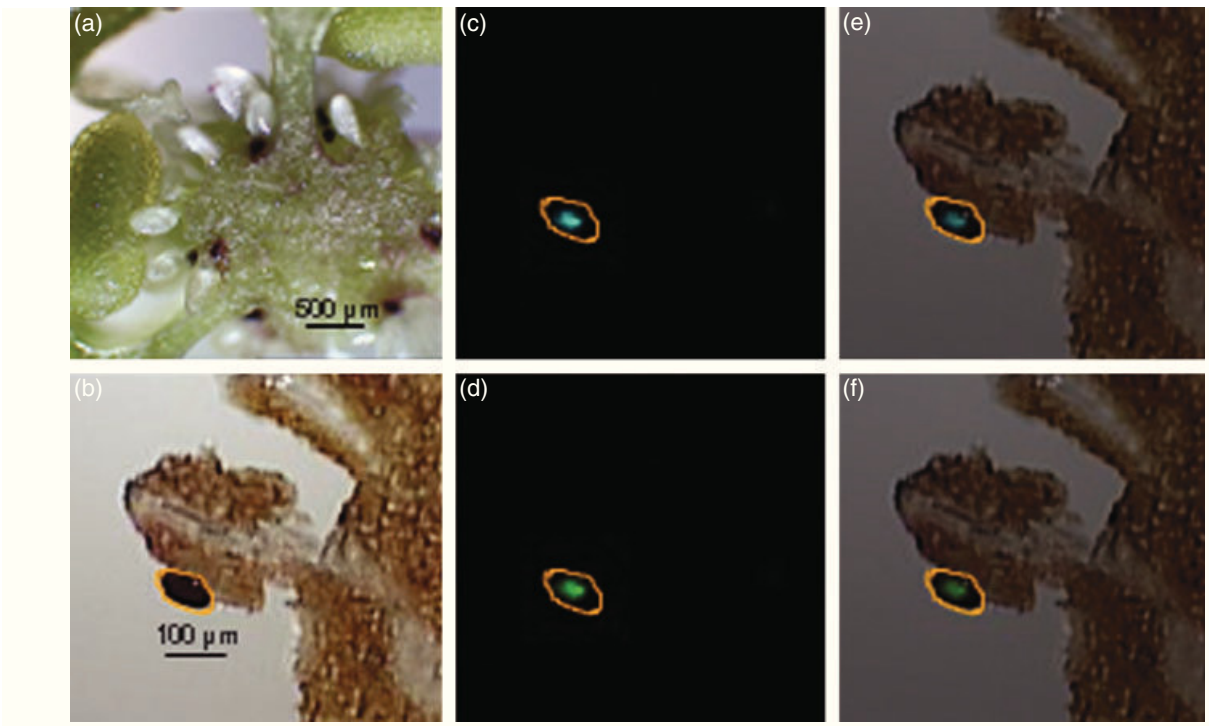

Figure 6. LDI-MSI detection of hypericins in appendices of the placenta of *H. perforatum*.
(a) Cryosection of the ovary of *H. perforatum* showing the placenta (ovary wall), the funiculi and ovules; (b) optical image of the measured region of placenta – the area circled in orange shows expected localization of secondary metabolites; (c, d) molecular images of (b) for *m/z* 503 (blue) and *m/z* 519 (green), respectively; (e, f) overlays of optical image (b) and molecular images for *m/z* 503 (blue) and *m/z* 519 (green), respectively.

side), *m/z* 593 (kaempferol-rhamnoside-glucoside) and *m/z* 739 (kaempferol-dirhamnoside-glucoside).

Quercetin and isorhamnetin (*m/z* 301, Figure 9c and *m/z* 315, Figure 9e, respectively) are co-localized in the lower third of the petal, and corresponding glycosylated forms showed an identical pattern, e.g. *m/z* 447 (quercetin-rhamnoside), *m/z* 461 (isorhamnetin-rhamnoside) and *m/z* 609 (quercetin-rhamnoside-glucoside). In contrast to the kaempferol family, quercetin and isorhamnetin were detected in petal veins. If the images from both distribution patterns are superimposed, all compounds are seen to be co-localized in the lower petal mid-vein, suggesting that they share a common means of transport. In sepals, kaempferol/quercetin and isorhamnetin show a somewhat less distinct distribution than in petals (Figure 9f–j). Kaempferol (Figure 9g) and its rhamnoside (Figure 9i) are more abundant in the internal parts of the plant, whereas quercetin (Figure 9h) and isorhamnetin (Figure 9j) occupy the whole leaf surface.

DISCUSSION

The detection of variations in the molecular content of cell populations requires analytical methods based on single cells to avoid the pooling of data that occurs when constituents are averaged over multiple cells. Therefore, we used various strategies to acquire information about the distribution of secondary natural products in cryo-sectioned, laser-microdissected or freshly cut plant samples of *Hypericum* sp. The results show the suitability of combining LMD and LDI-TOF/MS and LDI-MSI to analyse the localization of secondary metabolites of *H. perforatum*. This approach should minimize the negative effects caused by application of a matrix. No additional chemical interactions, no additional data-distorting diffusion processes, and no additional changes of the matrix-treated surface of the sample are expected.

The phytochemical constituents of members of the genus *Hypericum*, and especially *H. perforatum*, have been described frequently, allowing us to compare our molecular data for the secondary metabolites with published data. Recent publications that provide an overview of the phytochemical profiles of various parts of leaves and flowers of *H. perforatum* include those by Berghöfer and Hölzl (1989), Nebelmeir (2006) and Tatsis *et al.* (2007). Our methods permitted identification of most compounds described in these reports, but could not distinguish the biflavonoids biapigenin and amentoflavone from the flavonoids hyperoside and isoquercitrin, which would have required the use of LC-MS equipment.

Naphthodianthrones were detectable in the dark glands of leaves and petals and in certain parts of the connective tissue of the theca of the stamens. With the higher resolution afforded by use of the Ultraflex III® apparatus, we were able

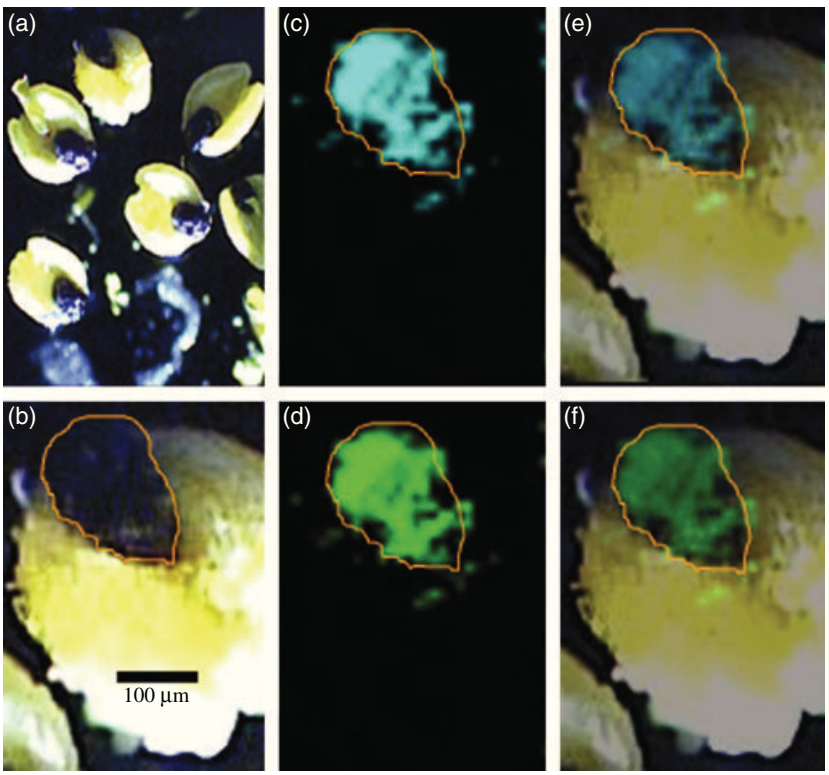

Figure 7. Visualization of hypericins in the stamen connective.
(a) Image of stamens of *H. perforatum* with a dark red region of the connective tissue between the thecae; (b) optical image of measured stamens of *H. perforatum* – the area circled in orange shows expected localization of secondary metabolites; (c, d) molecular images of (b) for *m/z* 503 (blue) and *m/z* 519 (green); (e, f) overlays of optical image (b) and molecular images for *m/z* 503 (blue) and *m/z* 519 (green), respectively.

to analyse the contents of closely adjacent anatomical structures on *H. reflexum* leaves that were separated from each other by only 50 μm; our analysis revealed highly localized hypericins in the glandular trichomes and dark glands of *H. reflexum*, and avoided the time-consuming steps required to mechanically isolate glandular trichomes and determine their natural products (Piovan *et al.*, 2004). Furthermore, the LDI-MSI results can be easily re-checked by LMD and LDI-TOF/MS or LC/MS/MS analysis.

The spatial resolution of the phytochemical profile of neighbouring secretory cavities of *Hypericum* was excellent, enabling us to investigate even smaller areas such as the small appendices of the placenta – to do this requires collection of data on a scale <10 μm. Proof of the presence of naphthodianthrones and flavonoids in the small appendices of the placenta was provided using the Smartbeam® optics of the Ultraflex III® equipment, which are able to acquire data from localized secondary metabolites.

Recently, hyperforin was detected in disc-shaped leaf material containing translucent glands of *H. perforatum* that was manually isolated using modified syringes (Soelberg *et al.*, 2007). Our approach, namely combining LMD with LDI-TOF/MS and LDI-MSI imaging, allowed phloroglucinols to be detected in individual translucent glands, and confirmed that hyperfirin and adhyperfirin accumulate in these secretory cavities (Soelberg *et al.*, 2007; Tatsis *et al.*, 2007). Surprisingly, adhyperfirin was not detected in our samples. This variability of the phytochemical profile could be due to different environmental factors (Nebelmeir, 2006). LMD was also used to prepare the papillae-containing styli of the stigma. In addition to hypericins, MS signals typical for the biflavonoids biapi-

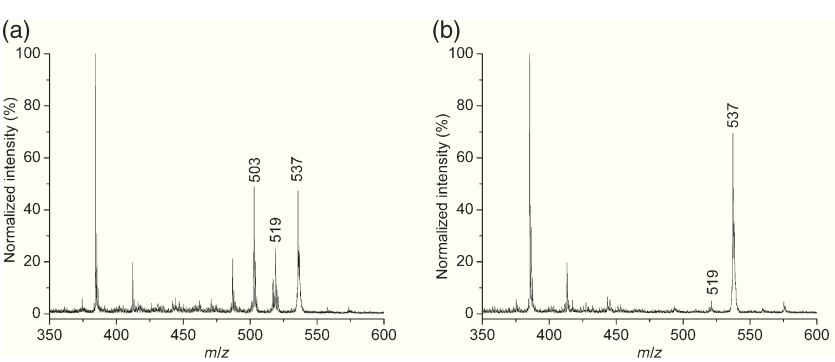

Figure 8. LDI-MS/TOF spectra of styli and pollen.
(a) A representative spectrum of styli of *H. perforatum* containing both hypericins and the signal for the biflavonoids biapigenin and amentoflavone, whose presence is due to pollen.
(b) No hypericins were detected in representative spectra of pollen.

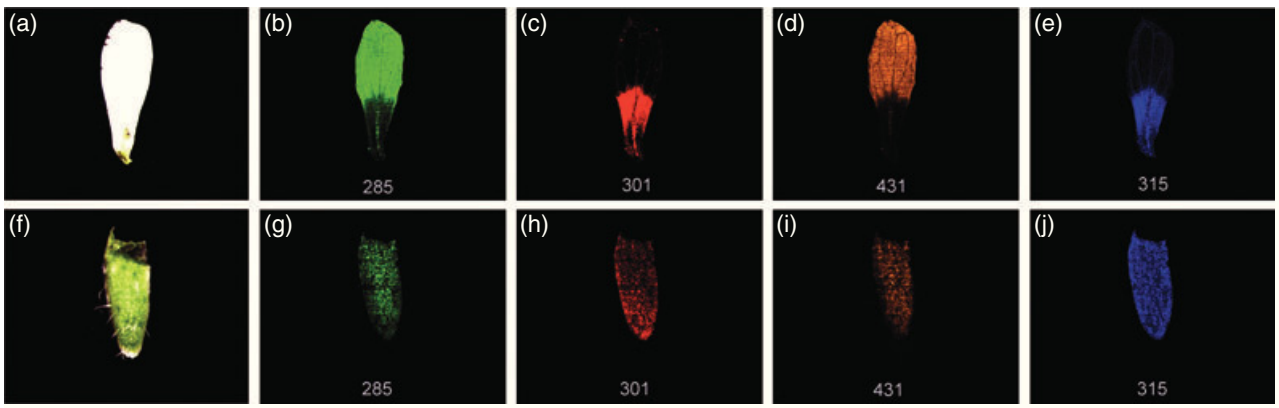

Figure 9. Distinct distribution of flavonoids in *A. thaliana* petals and sepals.
(a) Optical image of an *A. thaliana* Col-0 flower petal; negative ion mode LDI-MSI images constructed for the distribution of (b) the *m/z* 285 ion corresponding to kaempferol; (c) the *m/z* 301 ion corresponding to quercetin; (d) the *m/z* 431 ion corresponding to kaempferol rhamnoside; (e) the *m/z* 315 ion corresponding to isorhamnetin.
(f) Optical image of an *A. thaliana* Col-0 flower sepal; (g, h, i and j) correspond to the same ion images as described for (b–e), respectively.

genin and amentoflavone were detected. Both compounds are thought to be localized in the stamens (Repčák and Martonfi, 1997; Nebelmeir, 2006), and, in comparison to biapigenin, only traces of amentoflavone are verifiable. Evidence of biflavonoids in the papillae comes from the presence of pollen on the styli. The compounds were detected and separated using LC-MS techniques on extracts of LMD samples. The presence of flavonoids appears to be connected with hypericin-containing secretory structures. Only traces of quercetin and rutin were detectable in non-secretory parenchyma cells from *H. perforatum*.

The well-known UV demarcations of the flower of *H. perforatum* result from two categories of pigments, flavonoids and de-aromatized isoprenylated phloroglucinols (Gronquist *et al.*, 2001). Our investigation did not reveal any de-aromatized isoprenylated phloroglucinols. Future investigations will focus on the presence of secondary metabolites during the anatomical development of plant parts such as the leaves, stamens or placenta of *Hypericum* sp. The ability to analyse cell-specific metabolite patterns makes it possible to study the location of the biosynthesis of secondary metabolites and putative translocations. Furthermore, LDI-MSI will allow us to investigate the influence of genetic and environmental factors on the accumulation of secondary metabolites of *Hypericum* sp. and other plants without using a matrix.

Natural populations and breeding lines of *H. perforatum* possess a variety of bioactive constituents. LDI-MSI can be used on this important phytomedical plant to address harvest quality, the drying process, and storage of the plant material. Further experimental developments should enable us to analyse active compounds in species at various vegetative stages and in specific parts of the plant. Such analysis will help to define the optimal harvest time for obtaining high-quality raw material.

Anthracnose disease of *H. perforatum* caused by *Colletotrichum gloeosporioides* Penz. leads to the development of symptoms such as the reddish colour of infected plants (Gaudin *et al.*, 2003). LDI-MSI will be useful for studying the role of secondary plant metabolites such as phytoalexins, whose concentration increases after pathogen attack; it is an elegant tool for investigating the uptake, metabolism and distribution of polycyclic aromatic plant metabolites in host–pathogen interactions.

Using LDI-MSI on *A. thaliana* Col-0 petals and sepals provided clear MS images (Figure 9) at cellular resolution (approximately 10 μm), and indicates the broad scope of the method. The previously determined distribution of flavonoids reported by Cha *et al.* (2008) was re-examined. We found that all the compounds are co-localized in the main basal petal vein, and only glycosides of the quercetin and isorhamnetin type occur in small veins. The mechanistic cause of this pattern cannot be determined from the current dataset, but the transport from other plant parts is likely. A possible function of the observed distribution could be that the localization of highly UV-absorbing pigments (the quercetin and isorhamnetin series) in the petal base directs pollinators to the nectar source. A related UV-absorbing guide mark has been isolated from the petal base of the related species *Brassica rapa*, and identified as isorhamnetin-3,7-*O*-di-β-D-glucopyranoside (Sasaki and Takahashi, 2002).

In principle, any UV-absorbing compound could be imaged on the scale of individual cells as performed here. All compounds with condensed aromatic rings, such as flavonoids, flavanes, anthocyanins or similar plant pigments, or indolic alkaloids and related structures, are targets for future application of the LDI-MSI method illustrated here. It is encouraging that plants can be imaged without

cryo-sectioning, and that organs/glands in the body of the plant tissues are suitable for MSI. The UV laser is able to penetrate a few micrometres into the sample, enough to desorb and ionize the compounds of interest. This method could also be applied to samples of animal or microbial origin.

EXPERIMENTAL PROCEDURES

Plant material

Plants of *H. perforatum* L. were obtained from Agrarprodukte Ludwigshof eG and Martin Bauer GmbH Co. KG (http://www.martin-bauer.de). They were grown outside close to the greenhouse of the Max Planck Institute for Chemical Ecology. Plants of *H. reflexum* L. were obtained from the Botanical Garden of Martin Luther University (Halle-Wittenberg, Germany). These plants were grown in either sand or soil (Klasmann Erden (http://www.klasmann.deilmann.de) clay and sand in the ratio 1:2) under greenhouse conditions (day 20–22°C, night 18–20°C; 30–55% relative humidity; the natural photoperiod was supplemented by 8 h of light from a Philips Sun-T Agro 400 W sodium light, http://www.philips.com).

A. thaliana plants of Columbia accession (Col-0) were grown in a soil:vermiculite mixture (3:1) in a controlled environment chamber at 21°C, 55% relative humidity, 100 μmol m^{-2} sec^{-1} photosynthetically active radiation from a mixture of Fluora and Cool White lamps (Osram, http://www.osram.de), and a diurnal cycle of 10 h light/14 h dark.

Laser microdissection of secretory cavities

Using to the procedure described by Hölscher and Schneider (2007), leaves, sepals and petals of *H. perforatum* or *H. reflexum* were fixed between a thin glass slide (0.6 mm thickness, Menzel Gläser, http://www.menzel.de) and a specially manufactured metal frame. The dissection of the secretory cavities was made possible by use of a nitrogen solid-state diode laser of a Leica LMD6000 system (http://www.leica-microsystems.com/) with short pulse duration (355 nm). The microdissected secretory cavities were collected in the lid of an Eppendorf tube by the Leica LMD6000 system. The microtube was briefly centrifuged (1000 ***g***, 25°C, 1 min) to settle the contents. Methanol was added and the mixture was sonicated for 1 min, and then transferred to a MALDI plate for (MA)LDI-TOF/MS investigation.

Sap sampling using microcapillaries

Fused silica capillaries were used as microcapillaries. Their etching using hydrofluoric acid was performed as described previously (Kelly *et al.*, 2006; Sproß, 2007). The micro-injection apparatus consists of a stereo microscope (Zeiss Stemi SV11, http://www.zeiss.com/) with a magnification range of 6 × to 60 ×. The microcapillaries were connected with a micromanipulator and a home-made air-pulse controller system manufactured by the Max Planck Institute for Chemical Ecology workshop according to the plans described by Handler (2000). Injection of the microcapillaries and ejection of the contents of the specialized cells of *Hypericum* sp. were performed in the open air.

Mass spectrometry

A MALDI micro MX mass spectrometer (Waters, http://www.waters.com) fitted with a nitrogen laser (337 nm, 4 nsec laser pulse duration, 10 Hz and 154 μJ per pulse) was used in reflectron mode and negative polarity for data acquisition using MassLynx version 4.0 software. The chemical identity of the compounds observed was confirmed by comparing MS/MS spectra of standard compounds and the masses obtained using an LTQ ion trap instrument (Thermo Fisher, http://www.thermo.com) with an atmospheric pressure MALDI source equipped with a solid-state Nd:YAG UV laser (MassTech, http://www.apmaldi.com) and running Target 6 (MassTech) and Excalibur version 2.0 (Thermo Fisher) software for data acquisition.

Fixation of plant material for Ultraflex III

Sepal and petal (*A. thaliana*), laser-microdissected stigma, untreated leaves, theca and pollen (leaves from *H. reflexum*, others from *H. perforatum*) were manually separated from the rest of the stamens using micro chisels (Eppendorf, http://www.eppendorf.com) and fixed on carbon conductive adhesive tape (Plano, http://www.plano-em.de), which was in turn fixed on an ITO slide (Bruker Daltonic, http://www.bdal.com). The cryo-sectioned placenta slices (thickness 60 μm) were directly transferred to an indium-tin-oxide (ITO) glass slide. A Staedtler triplus gel-liner (silver, 0.4 mm; Staedtler-Mars, Nürnberg, Germany, http://www.staedler.com) was used to place marks close to the samples to define their position. The granular particles of this gel-roller marker were useful to alleviate the laser positioning during LDI-MSI. Stereomicroscopic images were developed using Image J software (National Institutes of Health, http://rsb.info.nih.gov/ij/).

Imaging on the Ultraflex III® mass spectrometer

An Ultraflex III® mass spectrometer (Bruker Daltonics) was used for the analysis. The instrument was equipped with a Nd:YAG laser. All spectra were measured in negative reflectron mode. To measure the pixels of ca 10 × 10 μm, the minimum laser focus setting (corresponding to a diameter of about 10 μm laser, under-usage of oversampling) was used. For each raster point, a spectrum was accumulated with 40 laser shots and fixed laser intensity. For image reconstruction, FlexImaging version 2.0 software (Bruker Daltonics) was used. For LDI-MSI of the placenta, 4633 raster positions were measured; 4125 positions for the stamens and 1107 positions for the styli and pollen. All signals within a mass range of m/z 300–600 were recorded. Leaf imaging was performed at 9262 raster positions within a mass range of m/z 300–700. Forty laser shots per pixel were collected from each position, and then the software calculated the average mass spectrum.

ACKNOWLEDGEMENTS

We wish to thank Tamara Krügel and the greenhouse team at the Max Planck Institute (Jena, Germany), for raising the *Hypericum* and Arabidopsis plants. We thank Eva Bremer and Sabine Stahl for providing *H. reflexum* (Botanical Garden, University Halle-Wittenberg, Halle, Germany), and Louise Hauke (Agrarprodukte Ludwigshof eG, Ranis-Ludwigshof, Germany) and Hans-Jürgen Hannig (Martin Bauer GmbH & Co. KG, Vestenbergsgreuth, Germany) for providing *H. perforatum*. We are also grateful to Regina Schenk (Humboldt University of Berlin, Germany), Ute Gärber (Julius Kühn-Institut, Bundesforschungsanstalt für Kulturpflanzen, Kleinmachnow, Germany), Wolf-Dieter Blüthner (N.L. Chrestensen GmbH, Erfurt, Germany), Heike Heklau (Botanical Garden University Halle-Wittenberg, Halle, Germany), Hermann Manitz (Herbarium Haussknecht, Jena, Germany) and Johannes Sebastian Nebelmeir (Technical University München-Weihenstephan, Germany) for helpful discussions. We thank Dr Wilmar Schwabe GmbH & Co. KG (Karlsruhe, Germany) for the generous gift of reference compounds, Finzelberg GmbH & Co KG (Andernach, Germany) for larger

amounts of herba hyperici perforati (minimum 0.1% dianthrone), Roland Kilper (aura optik GmbH, Jena, Germany) for help in establishing the sampling of cell contents using microcapillaries, Jens Sproß for introduction to the preparation of fused silica microcapillaries, and Stephan Imhof (Fachbereich Biologie, University of Marburg, Germany) for permission to use a photograph of a flower of *H. perforatum*. We also thank Sören-Oliver Deininger (Bruker Daltonics) for technical support and discussion. The authors gratefully acknowledge Emily Wheeler for editing help and Daniel Veit for constructing special slides for LMD and construction of the air-pulse controller system.

REFERENCES

Aerni, H.R., Cornett, D.S. and Caprioli, R.M. (2006) Automated acoustic matrix deposition for MALDI sample preparation. *Anal. Chem.* **78**, 827–834.

Albert, A. and Ritchie, B. (1942) 9-Aminoacridine. *Org. Synth.* **22**, 5–8.

Beerhues, L. (2006) Hyperforin. *Phytochemistry*, **67**, 2201–2207.

Berghöfer, R. and Hölzl, J. (1989) Isolation of I3,II8-biapigenin (amentoflavone) from *Hypericum perforatum*. *Planta Med.* **55**, 91.

Brandt, S., Kloska, S., Altmann, T. and Kehr, J. (2002) Using array hybridization to monitor gene expression at the single cell level. *J. Exp. Bot.* **53**, 2315–2323.

Brockmann, H., Pohl, F., Maier, K. and Haschad, M.N. (1942) Über das Hypericin, den photodynamischen Farbstoff des Johanniskrautes (*Hypericum perforatum*). *Justus Liebigs Ann. Chem.* **553**, 1–53.

Brolis, M., Gabetta, B., Fuzatti, N., Pace, R., Panzeri, F. and Peterlongo, F. (1998) Identification by high-performance liquid chromatography–diode array detection–mass spectrometry and quantification by high-performance liquid chromatography–UV absorbance detection of active constituents of *Hypericum perforatum*. *J. Chromatogr. A*, **825**, 9–16.

Burrell, M.M., Earnshaw, C.J. and Clench, M.R. (2007) Imaging matrix assisted laser desorption ionization mass spectrometry: a technique to map plant metabolites within tissues at high spatial resolution. *J. Exp. Bot.* **58**, 757–763.

Butterweck, V. (2003) Mechanism of action of St John's wort in depression – what is known? *CNS Drugs*, **17**, 539–562.

Caprioli, R.M., Farmer, T.B. and Gille, J. (1997) Molecular imaging of biological samples: localization of peptides and proteins using MALDI-TOF MS. *Anal. Chem.* **23**, 4751–4760.

Cha, S., Zhang, H., Ilarslan, H.I., Wurtele, E.S., Brachova, L., Nikolau, B.J. and Yeung, E.S. (2008) Direct profiling and imaging of plant metabolites in intact tissues by using colloidal graphite-assisted laser desorption ionization mass spectrometry. *Plant J.* **55**, 348–360.

Charchogylan, A., Abrahamyan, A., Fujii, I., Boubakir, Z., Gulder, T.A.M., Kutchan, T.M., Vardapetyan, H., Bringmann, G., Ebizuka, Y. and Beerhues, L. (2007) Differential accumulation of hyperforin and secohyperforin in *Hypericum perforatum* tissue cultures. *Phytochemistry*, **68**, 2670–2677.

Ciccarelli, D., Andreucci, A.C. and Pagni, A.M. (2001) Translucent glands and secretory canals in *Hypericum perforatum* L. (Hypericaceae): morphological, anatomical and histochemical studies during the course of ontogenesis. *Ann. Bot.* **88**, 637–644.

Cooks, R.G., Ouyang, Z., Takats, Z. and Wiseman, J.M. (2006) Ambient mass spectrometry. *Science*, **311**, 1566–1570.

Emmert-Buck, M.R., Bonner, R.F., Smith, P.D., Chuaqui, R.F., Zhuang, Z., Goldstein, S.R., Weiss, R.A. and Lotta, L.A. (1996) Laser capture microdissection. *Science*, **274**, 998–1001.

Erdelmeier, C.A.J. (1998) Hyperforin, possibly the major non-nitrogenous secondary metabolite of *Hypericum perforatum* L. *Pharmacopsychiatry*, **31**, 2–6.

Esau, K. (1965) *Plant Anatomy*. New York: Wiley, pp. 308–311.

Gädcke, F. (2003) Beispiel: Johanniskraut Herstell- und Qualitätsaspekte pflanzlicher Extrakte. *Pharm. Unserer Zeit*, **32**, 192–201.

Ganzera, M., Zhao, J. and Khan, I.A. (2002) *Hypericum perforatum* – chemical profiling and quantitative results of St. John's wort products by an improved high-performance liquid chromatography. *J. Pharm. Sci.* **91**, 623–630.

Gaudin, M., Simonnet, X. and Debrunner, N. (2003) *Colletotrichum gloeosporioides* as the cause of St John's wort (*Hypericum perforatum*) dieback in Switzerland and breeding for a tolerant variety. In *Hypericum: The Genus Hypericum* (Ernst, E., ed). London: Taylor & Francis, pp. 23–42.

Goodwin, R.J.A., Pennington, S.R. and Pitt, A.R. (2008) Protein and peptides in pictures: imaging with MALDI mass spectrometry. *Proteomics*, **8**, 3785–3800.

Gronquist, M., Bezzerides, A., Attygalle, A., Meinwald, J., Eisner, M. and Eisner, T. (2001) Attractive and defensive functions of the ultraviolet pigments of a flower (*Hypericum calycinum*). *Proc. Natl Acad. Sci. USA*, **98**, 13745–13750.

Handler, A.M. (2000) An introduction to the history and methodology of insect gene transfer. In *Insect Transgenesis* (Handler, A.M. and James, A.A., eds). Boca Raton, FL: CRC Press, pp. 14–16.

Hansen, S.H., Jensen, A.G., Cornett, C., Bjørnsdottir, I., Taylor, S., Wright, B. and Wilson, I.D. (1999) High-performance liquid chromatography on-line coupled to high-field NMR and mass spectrometry for structure elucidation of constituents of *Hypericum perforatum* L. *Anal. Chem.* **71**, 5235–5241.

Hölscher, D. and Schneider, B. (2007) Laser microdissection and cryogenic nuclear magnetic resonance spectroscopy: an alliance for cell type-specific metabolite profiling. *Planta*, **225**, 763–770.

Jürgenliemk, G. (2001) *Phenolische Inhaltsstoffe aus dem Kraut von Hypericum perforatum L. – analytische, biopharmazeutische und pharmakologische Aspekte*. PhD Thesis, University of Münster, pp. 69 and 77.

Kaul, R. (2000) In *Johanniskraut: Botanik, Inhaltsstoffe, Qualitätskontrolle, Pharmakologie, Toxikologie und Klinik*. Kapitel 7, Stuttgart, Germany: Wissenschaftliche Verlagsgesellschaft, pp. 136–171.

Kelly, R.T., Page, J.S., Luo, Q., Moore, R.J., Orton, D.J., Tang, K. and Smith, R.D. (2006) Chemically etched open tubular and monolithic emitters for nanoelectrospray ionization mass spectrometry. *Anal. Chem.* **78**, 7796–7801.

Kondo, T., Sawa, S., Kinoshita, A., Mizuno, S., Kakimoto, T., Fukuda, H. and Sakagami, Y. (2006) A plant peptide encoded by *CLV3* identified by *in situ* MALDI-TOF MS analysis. *Science*, **313**, 845–848.

Lange, B.M. (2005) Single-cell genomics. *Curr. Opin. Plant Biol.* **8**, 236–241.

Li, W.K. and Fitzloff, J.F. (2001) High performance liquid chromatographic analysis of St. John's wort with photodiode array detection. *J. Chromatogr. B*, **765**, 99–105.

Li, S.H., Schneider, B. and Gershenzon, J. (2007a) Microchemical analysis of laser-microdissected stone cells of Norway spruce by cryogenic nuclear magnetic resonance spectroscopy. *Planta*, **225**, 771–779.

Li, Y., Shresta, B. and Vertes, A. (2007b) Atmospheric pressure molecular imaging by infrared MALDI mass spectrometry. *Anal. Chem.* **79**, 523–532.

Li, Y., Shresta, B. and Vertes, A. (2008) Atmospheric pressure infrared MALDI imaging mass spectrometry for plant metabolomics. *Anal. Chem.* **80**, 407–420.

Mabberley, D.J. (2008) *Mabberley's Plant-Book: A Portable Dictionary of Plants, Their Classification and Uses*. Cambridge: Cambridge University Press.

Mullen, A.K., Clench, M.R., Crosland, S. and Sharples, K.R. (2005) Determination of agrochemical compounds in soya plants by imaging matrix-assisted laser desorption/ionisation mass spectrometry. *Rapid Commun. Mass Spectrom.* **19**, 2507–2516.

Müller, W.E. (2003) Current St. John's wort research from mode of action to clinical efficacy. *Pharmacol. Res.* **47**, 101–109.

Nebelmeir, J.S. (2006) *Züchtung von Johanniskraut (Hypericum perforatum L.): Entwicklung agronomischer und pharmakologischer Selektionskriterien*. PhD Thesis, Technical University of Munich, pp. 121–131, 141–144, 151–164.

Pages, G., Mazarin, M., Sergent, M., Phan-Tan-Luu, R. and Delaurent, C. (2006) Optimization of the assay of naphthodianthrones in dry St John's wort extract by reversed-phase liquid chromatography. *Anal. Bioanal. Chem.* **385**, 716–723.

Piovan, A., Filippini, R., Caniato, R., Borsarini, A., Maleci, L.B. and Cappelletti, E.M. (2004) Detection of hypericins in the 'red glands' of *Hypericum elodes* by ESI-MS/MS. *Phytochemistry*, **65**, 411–414.

Repčák, M. and Martonfi, P. (1997) The localization of secondary substances in *Hypericum perforatum* flowers. *Biologia*, **52**, 91–94.

Reyzer, M.L. and Caprioli, R.M. (2007) MALDI-MS-based imaging of small molecules and proteins in tissues. *Curr. Opin. Chem. Biol.* **11**, 29–35.

Robson, N.K.B. (2003) *Hypericum* botany. In *Hypericum: The Genus Hypericum* (Ernst, E., ed). London: Taylor & Francis, pp. 1–22.

Rubakhin, S.S., Jurchen, J.C., Monroe, E.B. and Sweedler, J.V. (2005) Imaging mass spectrometry: fundamentals and applications to drug discovery. *Drug Discov. Today*, **10**, 823–837.

Sasaki, K. and Takahashi, T. (2002) A flavonoid from *Brassica rapa* flower as the UV-absorbing nectar guide. *Phytochemistry*, **61**, 339–343.

Seeley, E.H. and Caprioli, R.M. (2008) Molecular imaging of proteins in tissues by mass spectrometry. *Proc. Natl Acad. Sci. USA*, **105**, 18126–18131.

Seger, C., Römpp, H., Sturm, S., Haslinger, E., Schmidt, P.C. and Hadacek, F. (2004) Characterization of supercritical fluid extracts of St. John's wort (Hypericum perforatum L.) by HPCL-MS and GC-MS. *Eur. J. Pharm. Sci.* **21**, 453–463.

Shroff, R., Muck, A. and Svatoš, A. (2007) Analysis of low molecular weight acids by negative mode matrix-assisted laser desorption/ionization time-of-flight mass spectrometry. *Rapid Commun. Mass Spectrom.* **21**, 3295–3300.

Shroff, R., Vergara, F., Muck, A., Svatoš, A. and Gershenzon, J. (2008) Non-uniform distribution of glucosinolates in *Arabidopsis thaliana* leaves has important consequences for plant defense. *Proc. Natl Acad. Sci. USA*, **105**, 6196–6201.

Smelcerovic, A., Zuehlke, S., Spiteller, M., Raabe, N. and Özen, T. (2008) Phenolic constituents of 17 *Hypericum* species from Turkey. *Biochem. Syst. Ecol.* **36**, 316–319.

Soelberg, J., Jørgensen, L.B. and Jäger, A.K. (2007) Hyperforin accumulates in the translucent glands of *Hypericum perforatum*. *Ann. Bot.* **99**, 1097–1100.

Sproß, J. (2007) *Monolithic columns for nanoLC-ESI-MS analysis of proteins and peptides*. Diploma Thesis, Friedrich-Schiller-University of Jena, pp. 25–30.

Sumner, L.W., Mendes, P. and Dixon, R.A. (2003) Plant metabolomics: large-scale phytochemistry in the functional genomics era. *Phytochemistry*, **62**, 817–836.

Tatsis, E.C., Boeren, S., Exarchou, V., Troganis, A.N., Vervoort, J. and Gerothanassis, I.P. (2007) Identification of the major constituents of *Hypericum perforatum* by LC/SPE/NMR and/or LC/MS. *Phytochemistry*, **68**, 383–393.

Vertes, A., Nemes, P., Shrestha, B., Barton, A.A., Chen, Z.Y. and Li, Y. (2008) Molecular imaging by MID-IR laser ablation mass spectrometry. *Appl. Phys. A Mat. Sci. Process*, **93**, 885–891.

Wolfender, J.-L., Verotta, L., Belvisi, L., Fuzzati, N. and Hostettmann, K. (2003) Structural investigations of isomeric oxidised forms of hyperforin by HPLC-NMR and HPLC-MS. *Phytochem. Anal.* **14**, 290–297.

Publication P11:

4-Deoxyaurone based UV nectar guide formation in *Bidens ferulifolia* (Jacq.) DC.

S. Miosic, K. Knop, D. Hölscher, J. Greiner, C. Gosch, J. Thill, M. Kai, B. Shreshta, B. Schneider, A. C. Crecelius, U. S. Schubert, S. Svatoš, K. Stich, H. Halbwirth

J. Exp. Botany **2012**, submitted.

4-Deoxyaurone based UV nectar guide formation in Bidens ferulifolia (Jacq.) DC.

Silvija Miosic[1], Katrin Knop[2], Dirk Hoelscher[3], Jürgen Greiner[1], Christian Gosch[1], Jana Thill[1], Marco Kai[3], Binita Kumari Shrestha[1], Bernd Schneider[3], Anna C. Crecelius[2], Ulrich S. Schubert[2], Aleš Svatoš[3], Karl Stich[1] and Heidi Halbwirth[1]*

[1]Institut für Verfahrenstechnik, Umwelttechnik und Technische Biowissenschaften, Technische Universität Wien, Getreidemarkt 9/1665, 1060 Wien, Austria

[2]Institut für Organische Chemie und Makromolekulare Chemie (IOMC, Lehrstuhl II/Schubert), Jena Centre for Soft Matter, Friedrich-Schiller Universität of Jena, Humboldtstrasse 10, 07743 Jena, Germany

[3]Max-Planck-Institut für chemische Ökologie, Hans-Knöll-Str. 8, 07745 Jena, Germany

*Corresponding author: Phone: +43-1-58801-166559, Fax: +43-1-58801-17399, hhalb@mail.zserv.tuwien.ac.at

Running title: 4-Deoxyaurone formation in *Bidens ferulifolia*

Key words: *Bidens ferulifolia,* pollinator attraction, floral pattern, yellow flower colour, anthochlor pigments (aurones and chalcones), aurone synthase, chalcone 3-hydroxylase

Valid email addresses of authors: silvija_miosic@yahoo.de, k.knop@uni-jena.de, hoelscher@ice.mpg.de, j.greiner@fastbone.com, christian.gosch@tuwien.ac.at, jthill@mail.zserv.tuwien.ac.at, mkai@ice.mpg.de, binita.shrestha88@yahoo.com, schneider@ice.mpg.de, anna.crecelius@uni-jena.de, Ulrich.Schubert@uni-jena.de, svatos@ice.mpg.de, kstich@mail.zserv.tuwien.ac.at,

Date of submission: April 13, 2012

Number of figures: 7 (2, 4, 5: in colour)

Number of tables: 1

Number of supplementary figures: 1

Number of supplementary tables: 2

Total word count: (6612 words).

Summary (250 words)

The formation of 4-deoxyaurones, which serve as UV nectar guides in *Bidens ferulifolia* (Jacq.) DC., was studied by combination of UV photography, mass spectrometry, and biochemical assays. The yellow flowering ornamental plant accumulates deoxy-type anthochlor pigments (6'-deoxychalcones and the corresponding 4-deoxyaurones) in the basal part of the flower surface whilst the apex contains only yellow carotenoids. For UV sensitive pollinating insects, this appears as a bicoloured floral pattern, the so-called bull's eye, which can be visualized *in situ* by specific ammonia staining of the anthochlor pigments. The petal back side, in contrast, shows a faintly UV absorbing centre and UV absorbing rays along the otherwise UV reflecting petal apex. Matrix-free UV laser desorption/ionisation mass spectrometric imaging (LDI-MSI) indicated the presence of 9 anthochlors in the UV absorbing areas. The prevalent pigments were derivatives of okanin and maritimetin. Enzyme preparations from flowers, leaves, stems and roots of *B. ferulifolia* and from plants, which do not accumulate aurones e.g. *Arabidopsis thaliana,* were able to convert chalcones to aurones. Thus, aurone formation could be catalyzed by a widespread enzyme and seems to depend mainly on a specific biochemical background, which favours the formation of aurones at the expense of flavonoids. In contrast to 4-hydroxyaurone formation, hydroxylation and oxidative cyclization to the 4-deoxyaurones does not occur in one single step but is catalyzed by two separate enzymes, chalcone 3-hydroxylase and aurone synthase. Aurone formation shows an optimum at pH 7.5 or above, which is another striking contrast to 4-hydroxyaurone formation in *Antirrhinum majus* L.

Abbreviations: ANS: anthocyanidin synthase, AUS: aurone synthase, CH3H: chalcone 3-hydroxylase, CHAPS: 3-[(3-cholamidopropyl)dimethylammonio]-1-propanesulfonate, CHI: chalcone isomerase, CHR: chalcone reductase, CHS: chalcone synthase, DOPA: 3,4-dihydroxyphenylalanine, DFR: dihydroflavonol 4-reductase, FHT: flavanone 3-hydroxylase, F3'H: flavonoid 3'-hydroxylase, FNSII: flavone synthase II, FW: fresh weight; HPLC: high-performance liquid chromatography, LC-MS: liquid chromatography-mass spectrometry, LDI-MSI: matrix-free UV-laser desorption/ionisation mass spectrometric imaging, PPO: polyphenol oxidase, UV: ultraviolet

Introduction

Flower colour is a result of the evolutionary development from undirected pollination by wind to directed pollination by a specific vector (Briscoe and Chittka 2001; Chittka *et al.* 1994; Harborne 1993; Menzel and Shmida 1993). Yellow coloration appeared as an adaptation to the colour sense of insects as the prevalent pollinators in temperate zones (Harborne 1993). Many Asteraceae species accumulate two types of yellow pigments, carotenoids and anthochlors. In *Bidens* sp., the carotenoids are uniformly distributed across the petal whereas the anthochlors are concentrated at the petal base (Harborne and Smith 1978; Scogin and Zakar 1976). Such patterns are know as nectar guides (synonym: honey guides, pollen guides) (McCrea and Levy 1983). For humans, the flowers are monochromatically yellow; however for UV sensitive insects the flowers appear bicoloured because of the different UV absorbance of carotenoids and anthochlors (Briscoe and Chittka 2001; Daumer 1958). *Bidens ferulifolia* is an interesting model plant for studying both nectar guide formation and anthochlor biosynthesis, which is not completely understood so far (Davies *et al.* 2006).

Although the occurrence of anthochlors (chalcones and aurones) is not restricted to flower tissues they are mostly noticed as the yellow flower pigments in Asteraceae species, snapdragon (*Antirrhinum majus* L.) and carnations (*Dianthus caryophyllus* L.) (Davies *et al.* 1997; Harborne 1967). Anthochlors are frequently ranked among flavonoids, but their structure cannot be derived from the flavonoid skeleton (Figure 1). Hydroxy-types and deoxy-types are distinguished, depending on whether or not the position 6' of chalcones and the corresponding position 4 of aurones carry a hydroxyl group. In Asteraceae, anthochlor pigments of the deoxy-type are typically found with the exception of *Helichrysum bracteatum* which accumulates the hydroxy-type pigments as *Antirrhinum majus* (Harborne 1967). Whereas 6'-hydroxychalcones rapidly isomerise - either chemically or enzymatically - to the corresponding flavanone, the 6'-deoxychalcones are chemically stable and are not converted by common chalcone isomerases (CHI). Anthochlors are easily detected by a specific colour switch from yellow to orange when exposed to ammonia or the alkaline vapour of a cigarette (Harborne 1967). This is due to the pH dependent transition of the undissociated phenol groups to phenolates. Consequently, the absorbance spectrum of the

pigments shows a bathochromatic shift of approx. 100 nm from the violet to the blue range of the spectrum (Supplementary Figure1). This results in a corresponding shift of the reflected wavelengths, which is perceived as colour switch by the human eye.

In contrast to the well-studied flavonoid pathway, the knowledge on the formation of anthochlors and particularly of aurones is still limited. The formation of aurones competes with flavonoid formation for chalcones as the immediate biochemical precursors. During the past decade, aurone formation in plants was exclusively studied in *A. majus*, (Nakayama *et al.* 2001; Nakayama *et al.* 2000; Ono *et al.* 2006a; Ono *et al.* 2006b; Sato *et al.* 2001). In addition it was shown that fungal catechol oxidases can also catalyze aurone formation (Nakayama *et al.,* 2000; Sanchez-Gonzalez and Rosazza 2006). Aureusidine synthase from *A. majus*, a soluble, bifunctional polyphenol oxidase (PPO) homologue (monooxygenase and dioxygenase activity) catalyzes the hydroxylation and oxidative cyclization of chalcones to aurones. In the suggested reaction mechanism (Nakayama 2002), the monoxygenase activity is particularly crucial to explain the occurring 3,4- and 3,4,5-hydroxylation pattern of the aurones present in *A. majus*. In addition, it is essential for the conversion of the monohydroxylated naringenin chalcone, because oxidative cyclization occurs only in the presence of hydroxyl groups in *ortho*-position. Aureusidine synthase accepted also 6'-deoxychalcones although they are not native substrates in *A. majus*. Thus, it was assumed that formation of 4-deoxyaurones in Asteraceae species follows a similar mechanism (Nakayama 2002); however, this was not tested so far in a 4-deoxyaurone producing plant.

Using a combined approach of mass spectrometry, biochemical assays, and UV photography, we investigated for the first time the formation of 4-deoxyaurones in *Bidens ferulifolia* (Jacq.) DC. We show that the hydroxylation step of the B-ring requires the presence of an additional hydroxylating enzyme. In addition, we demonstrate for the first time that the ability of aurone formation is frequently present in plants and not necessarily correlated to aurone accumulation, thereby contributing a novel perspective to the knowledge of aurone biosynthesis in general.

Results (1381 words)

Anthochlors and flavonoids in Bidens ferulifolia *petals*

The presence of anthochlor pigments and flavonoids in the *Bidens* petals was analysed by a combined approach of matrix-free UV laser desorption/ionisation mass spectrometric imaging (LDI-MSI), LC-MS and HPLC with emphasis on identifying the chalcone and aurone core structures. LDI-MSI demonstrated the presence of 9 mass peaks corresponding to 6 core structures of anthochlor pigments or flavonoids and the corresponding monoglucosides, respectively (Figure 2). A mass peak related to isoliquiritigenin 4'-*O*-β-D-glucoside (*m/z* 417) was not detected. Mass peaks *m/z* 269, 271, 285, 287, 431, 433, 447 and 449 were not clearly related to a specific compound because the presence of several mass isomers could be expected (Figure 3). The compounds were further identified by LC-MS measurement of exact mass and retention time in comparison to commercially available reference compounds (Figure 3). The native methanolic extracts contained anthochlors as aglycones and glycosides. The latter were not identified further because the glucosylation pattern of the pigments is not decisive for the nectar guide formation. The presence of those glycosides, which were not available as commercial references, was investigated after enzymatic hydrolysis and the glucose position was tentatively allocated according to the literature (Halbwirth *et al.* 1997; Harborne 1967). Thus, the LDI-MSI mass peaks could be allocated to specific compounds as follows: *m/z* 269 (sulfuretin), *m/z* 271 (butein), *m/z* 285 (maritimetin/luteolin), *m/z* 287 (okanin), *m/z* 431 (sulfuretin 6-*O*-β-D-glucoside), *m/z* 433 (butein 4'-*O*-β-D-glucoside), *m/z* 447 (maretimein/luteolin 7-*O*-β-D-glucoside) and *m/z* 449 (marein). The presence of 3',4',5',6-tetrahydroxyaurone and robtein and their glycosides could be excluded (Figure 3). The abundance of the main pigments was estimated by HPLC. After enzymatic hydrolysis of methanolic extracts, okanin (2.6 mg ± 0.5/10 g FW) followed by maritimetin (1.3 mg ± 0.7/10 g FW) and butein (0.4 mg ± 0.3/10 g FW) were the prevalent anthochlor pigments. High amounts of the flavone luteolin (1.4 mg ± 0.4/10 g FW) were also present.

Nectar guides

UV photography of *B. feruliulifolia* showed the presence of the typical bulls-eye, which is composed of a UV absorbing petal base and a UV reflecting apex (Figure 4 a). The back side, in contrast,

showed a different pattern with a faintly UV absorbing centre and UV absorbing rays along the otherwise UV reflecting petal apex (Figures 4 e). Staining with ammonia led to a colour switch of the petal base in the same areas (Figure 4 b, c, f, g), indicating that the UV nectar guides are based on the local accumulation of anthochlor pigments as described earlier (Scogin and Zakar 1976). Particularly the veins were intensively stained along the whole petal (Figure 4 d, g, h). The anthochlors are present in the epidermal layer of both sides of the petal base (Figure 4 i, j), whereas in the cross sections of the apex only the veins at the back side were stained (Figure 4 g, k, l). Petals from all developmental stages showed the typical colour switch after ammonia staining. However, petals of closed buds were two times folded and only the back side was visible at the early stages of flower anthesis. In contrast to *Bidens* sp*., Coreopsis grandiflora* Hogg ex Sweet and *Cosmos sulphureus* Cav showed a complete colour switch demonstrating the uniform distribution of anthochlor pigments in their petals (Figure 4 m-p).

In the LDI-MS image, all 9 mass peaks showed a similar distribution along the petal and were exclusively present at the base but not in the apex of the petals front side (Figure 2). LDI-MSI was also possible when the petals were stained with ammonia, however, this negatively affected leaf quality, with the exception of imaging of the veins. It appears that the ammonia might soften the relatively stiff structure of the veins thereby facilitating the extraction of the analytes. All mass peaks were found on both petal sides with the exception of the mass peaks *m/z* 433 and *m/z* 431, which were present only on the front side.

4-Deoxyaurone formation in B. ferulifolia

Incubation of butein with enzyme preparations from *B. ferulifolia* petals led to the formation of one product which was identified as sulfuretin by comparison with the authentic reference compound (Figure 6 a). No formation of robtein or 5'-hydroxysulfuretin could be observed under standard conditions. Apart from butein, the enzyme accepted the 6'-deoxychalcones okanin and robtein as substrates and converted them into the corresponding aurones maritimetin and 5'-hydroxysulfuretin. Butein 4'-*O*-glucoside was converted into sulfuretin 6-*O*-glucoside accordingly. Hydroxylating activity in addition to the ring closure could be observed in none of the assays. When marein was offered as a substrate, the formation of okanin and the corresponding aurone

maritimetin could be detected. No product formation could be observed when isoliquiritigenin or naringenin chalcone were offered, neither under standard conditions nor in the presence of 3-[(3-cholamidopropyl)dimethyl-ammonio]-1-propanesulfonate (CHAPS) and/or hydrogen peroxide (H_2O_2). Eriodictyol chalcone was also converted to aureusidine and bracteatin but was an unsuitable substrate for enzyme characterisation due to chemical instability in both acidic and alkaline environment.

Formation of aurones was cataylzed by enzyme preparations from flower tissues, leaves, stems and roots (Supplementary Table 1). Flower tissues included petals from disc florets and 3 developmental stages of ray florets and sepals. Highest activities were observed in roots followed by open flowers; lowest activities were found in leaves. The presence of ascorbate strongly influenced the AUS activity. When no ascorbate was present in the buffer during the enzyme preparation, neither the substrate nor the product could be detected in the assay. The presence of ascorbate concentrations up to 0.02 µM during enzyme preparation did not affect product formation. At higher concentrations, the AUS activity decreased steadily. Aurone formation showed a high dependence on substrate concentration. Thus, highest activities were observed in the presence of a substrate concentration as low as 0.5 mM and decreased steadily with increasing concentrations. However, product formation could be also observed in the presence of 30 mM.

Using butein as a substrate, the reaction showed highest activities at pH 7.5. At lower pH values, the activity decreased rapidly, at higher pH values slowly. At pH 5.5, 25 % of the activity compared to the pH optimum was observed (Table 1). pH Optima for okanin, robtein and butein 4'*O*-glucoside were slightly higher (Table 1). Eriodictyol chalcone was converted at acidic and alkaline conditions. Quantification, however, was not possible because of substrate instability. The reaction was characterized in more detail using [^{14}C]butein as substrate. Highest reaction rates were observed at 25 °C. At 60 °C, reaction rates still reached 21 % of the values measured at 25 °C; at temperatures higher than 60 °C no AUS activity could be observed. In the presence of heat inactivated preparations, no product formation was observed at any pH or temperature tested. The reaction was linear with time up to 15 min and with protein concentrations up to 3 µg.

Flavonoid metabolism in Bidens *petals*

Enzyme preparations from petals of *B. ferulifolia* were analysed for the presence of enzymes activities of the pathways leading to anthochlors and flavonoids. The activities of chalcone synthase/CHI, flavanone 3-hydroxylase, flavone synthase II, AUS, flavonoid 3'-hydroxylase, and CH3H could be detected in the petals (Supplementary Table 2). Dihydroflavonol 4-reductase (DFR) activity was not found. A type II CHI activity, which catalyzes the isomerisation of 6'-deoxychalcones to the corresponding 5-deoxyflavanones (Shimada *et al.* 2003) was not detected either. The presence of a chalcone reductase (synonyms: polyketide reductase, chalcone ketide reductase) (Welle and Grisebach 1988) activity (CHR) could not be demonstrated. All enzymes detected showed higher activities in the petal base compared to the apex but were clearly present in both parts.

4-Deoxyaurone formation with enzyme preparations from further plants

Enzyme preparations from further plants which do not naturally accumulate anthochlor pigments, were also able to catalyze the conversion of 6'-hydroxychalcones and 6'-deoxychalcones to the corresponding aurones (Figure 6). This included a number of other ornamental plants from the Asteraceae family e.g. *Tagetes erecta* and *R. hirta*, but also members of other plant families e.g. *A. majus*, *Petunia hybrida*, *D. caryophyllus* and *A. thaliana* (Figure 6). In *A. majus,* AUS activity was present in enzyme preparations from petals and leaves (Figure 6 c, d). *B. ferulifolia* and *A. majus* showed a striking difference in the acceptance of isoliquiritigenin as a substrate (Figure 6 i, j). Enzyme preparations from *A. majus* catalyzed the formation of butein and sulfuretin from isoliquiritigenin. Addition of H_2O_2 or CHAPS was not required. The presence of KCN strongly decreased the formation of butein and sulfuretin whereas the cytochrome P450 specific inhibitors ketoconazol and ancymidol did not. *B. ferulifolia,* in contrast, converted isoliquiritigenin only in the presence of NADPH to butein.

Discussion (1366 words)

The ornamental plant *B. ferulifolia* is an easily accessible model for studying UV nectar guides because a rapid visualization by ammonia staining instead of UV photography, which needs specialized equipment, is possible. In addition, *B. ferulifolia* offers the possibility to study for the

first time the biosynthesis of aurones in plants, which accumulate the deoxy type anthochlors as flower pigments. Studies on the deoxy type pathway have the advantage that the chemically stable 6'-deoxychalcones are the native substrates for aurone formation and no competition for common precursors for flavanone formation by CHI occurs. *B. ferulifolia* was preferred over other Asteraceae species as model plant because the irregular distribution in the petals and the striking presence particularly in veins offers interesting possibilities for future studies on the regulation and tissue or cell specific formation of anthochlors in the flowers.

4-Deoxyaurone formation

The presence of 9 compounds belonging to the class of anthochlor pigments was observed. Surprisingly 5 of them were aglycones although in the literature the corresponding glycosides are reported (Scogin and Zakar 1976). Whereas the presence of compounds based on isoliquiritigenin, butein, sulfuretin, okanin and maritimetin was expected for *Bidens* sp., the presence of anthochlor pigments carrying 3 hydroxyl groups in the B-ring was not reported and could not be demonstrated in our studies either. This allows important clues on the mechanism of 4-deoxyaurone formation, because it demonstrates that AUS does not introduce an additional hydroxyl group in the B-ring as part of the catalytic mechanism as is the case in 4-hydroxyaurone formation.

Formation of aurones has only been studied in the 4-hydroxyaurone accumulating *A. majus* so far and was shown to be catalyzed by the so-called 'aureusidine synthase' (Nakayama *et al.,* 2000). However, we favour the more general term 'aurone synthase' (AUS), because the enzyme catalyzes the formation of both aureusidine and bracteatin from eriodictyol chalcone and also accepts other chalcone substrates. This is also in better agreement with the physiological activity in Asteraceae where aureusidine formation is not native. In *B. ferulifolia*, AUS activity was present in different flower tissues including non-aurone accumulating sepals, but also in roots, stems and leaves. Furthermore, aurone formation could be demonstrated with enzyme preparations from a number of plants which do not naturally accumulate aurones including *A. thaliana*. Thus, the presence of AUS activity is not specifically correlated with aurone occurrence. One possible explanation is that aurone formation is catalyzed by an unspecific enzyme e.g. a PPO because

AUS was classified as being a Cu^{2+} containing PPO homologue. This is supported by the fact that the suggested reaction mechanism is actually based on an enzymatic *o*-quinone formation, which is a classical PPO reaction, followed by a non-enzymatic cyclization step (Strack and Schliemann 2001). The argument against is that the purified aureusidine synthase specifically acted on chalcones whereas DOPA, which is one of the most common substrates for PPOs, was not accepted (Nakayama *et al.,* 2000).

The observed ability of aurone formation in non-aurone accumulating plants and tissues is obviously not of physiological relevance and could be also due to the presence of PPOs, particularly from chloroplasts in the leaves. On the other hand, enzyme preparations from *B. ferulifolia* petals, in which aurone formation is of physiological relevance, did not show a specifically higher or different AUS activity than the other tissues and the observed substrate acceptance and product formation was in accordance with the anthochlors identified in the petals. Davies *et al.* (2006) showed that AUS expression in different *A. majus* lines did not correlate with aurone formation and suggested the presence of a multigene family.

An explanation for the absence of aurones in most plants despite the common presence of a PPO type AUS activity is that aurone formation can occur only in a special biochemical background. The formation of 4-deoxyaurones requires a 6'-deoxychalcone precursor, which is provided by a rare CHR (synonyms: polyketide reductase, chalcone ketide reductase) found only in few plants so far (Bomati *et al.* 2005; Welle and Grisebach 1988). The immediate biochemical precursors of 4-hydroxyaurones, in contrast, are commonly formed in ornamental species (Forkmann and Heller 1999). However, they need to be present in vacuoles where aurone formation is suggested to take place (Ono *et al.,* 2006b). This occurs only in mutants lacking the activities of CHI and of at least one further enzyme in the flavonoid pathway (Forkmann and Dangelmayr 1980). Thus, in the competition between flavanone and aurone formation velocity of the involved enzymes and further unknown factors must be decisive. AUS based biotechnological approaches to introduce yellow flower were not really convincing so far (Bradley *et al.* 2000; Ono *et al.,* 2006a). It appears that a careful selection of the parental line is essential.

Our studies have identified several crucial differences between the aurone formation in *A. majus* and *B. ferulifolia.* Most important is the lack of the monooxygenase activity during the reaction regardless which 6'-deoxychalcone substrate was used. Thus, butein was converted to sulfuretin only, and isoliquiritigenin was not accepted as substrate. This is supported by the fact that the presence of robtein and tetrahydroxychalcone in *Bidens* sp. has never been reported in literature and could also not be demonstrated in our investigations. Thus, the presence of two vicinal hydroxy groups in the chalcone precursor is indispensable, which must be introduced by a separate enzyme. Recently, chalcone 3-hydroxylase (CH3H) activity was described for the first time in *Cosmos sulphureus* (Schlangen *et al.* 2010) and was also demonstrated in our enzyme preparations from *B. ferulifolia* petals (Supplementary Table 2). This is in clear contrast to 4-hydroxyaurone formation where hydroxylation and cyclization can be catalyzed in one single step (Sato *et al.,* 2001). This is also supported by the fact that butein formation from isoliquiritigenin by enzyme preparations from *A. majus* decreased in the presence of the PPO inhibitor KCN whereas cytochrome P450 specific inhibitors had no influence.

A second important difference was the dependence of the reaction on pH. Highest activities were observed at alkaline conditions. Even though the observed optima for all substrates except butein were above physiological relevance, the activity was still high at pH 7.0, but low in the range of pH 5.0-6.5, where AUS shows it's pH maximum (Sato *et al.,* 2001). From the observed pH optima it is more likely that 4-deoxyaurone formation takes place in the cytosol and not in the vacuoles as shown for 4-hydroxyaurone formation in *A. majus* (Ono *et al.,* 2006b).

Nectar guides

Nectar guides are the most subtle visual signals of flowers aiming at 'brand recognition' and persistent attraction of individual pollinators to ensure directed and specific pollination of a plant species (Leonard and Papaj 2011). They are caused by the irregular spatial distribution of compounds with divergent light absorbance behaviour at the petal's front side. Depending on the absorbance spectrum of the pigments and the visual sense of the target pollinator such floral

322 patterns can be invisible to the human's eye and are typically visualized by UV photography
323 (McCrea and Levy 1983). Although the occurrence of UV nectar guides was largely investigated
324 (Clark 1979; Guldberg and Atsatt 1975; Harborne and Smith 1978; Rieseberg and Schilling 1985),
325 in-depth studies on the chemical base are so far limited to the flavonol-based UV nectar guides in
326 *R. hirta* (Schlangen *et al.* 2009; Thompson 1972) where it was shown that the spatial distribution of
327 specific flavonols rather than a +/- system of flavonols in general is creating the pattern. In
328 *B. ferulifolia*, however, nectar guides are based on other pigments and ammonia staining clearly
329 demonstrated the presence of a +/- system of anthochlor pigments on the petal front side. On the
330 back side, in contrast, anthochlor pigments are found at both the base and apex, but are restricted
331 to the veins in the apex. The typical bulls-eye pattern of the front side is established already in the
332 earliest developmental stages but remains hidden to pollinators until the buds are open and the
333 petals unfolded. Recently, LDI-MSI proved to be highly suitable for the localization of secondary
334 metabolites in plant tissues even at single-cell resolution (Hölscher *et al.* 2009). Our work
335 demonstrates the suitability of this technique for the non-destructive investigation of (UV) colour
336 patterns in plants providing information of the chemical composition and the local distribution
337 simultaneously.
338
339 *B. ferulifolia* flowers are yellow due to the absence of anthocyanins as a result of lacking DFR
340 activity. The enzyme activities required for the nectar guide formation could be detected in the base
341 and apex of the petals. Because anthochlor pigments are also present in the apex veins on the
342 back side this was not surprising. However, it remains a puzzle in which way the nectar guides are
343 formed. This requires a tight cell specific regulation, resulting in anthochlor pigment formation in
344 the epidermis at the front and back side of the petal base whereas in the apex the pathway is
345 exclusively activated in the veins. For anthocyanin formation in *A. majus*, it was recently shown
346 that epidermal specific venation is defined by overlapping expression domains of two coregulators
347 of the pathway (Shang *et al.* 2010).

348 **Conclusions**

349 Our knowledge on aurone biosynthesis is still limited in many aspects including the question how

tissue and cell specific formation is regulated. Our studies have shown that the presence of aurone synthase activity is more common than originally assumed. This strongly indicates that the decisive evolutionary step for *aurone* accumulation rather concerned the provision of suitable chalcone precursors than the actual ring closure step. The establishment of the 4-deoxyaurone pathway (Figure 7) is the first crucial step for future studies on aurone formation at the molecular level. Our studies have demonstrated the advantages of the 4-deoxyaurone system, particularly with respect to the chemical stability of the 6'-deoxychalcone substrates and the absence of immediate competition of CHI and AUS for the same precursors which allows directly studying aurone formation with enzyme preparations from different plant tissues. Thus, *Asteraceae* species could be an excellent model system to investigate various aspects of aurone formation including regulatory issues.

EXPERIMENTAL PROCEDURES (1004 WORDS)

Plant material

The investigations were carried out on *Bidens ferulifolia* L. flowers purchased as potted plants (Bellaflora, Vienna, Austria, www.bellaflora.at) and cultivated in the experimental field of TU Wien in Vienna in summers 2008-2011. Three developmental flower stages were collected: buds (folded petals, 5 mm length), opening flowers (unfolding petals, 9 mm length) and open flowers (unfolded petals, 12 mm length). Petals of *Rudbeckia hirta* L. cv. Indian Summer, *Tagetes erecta* L. cv. Antigua F_1 gelb and *Antirrhinum majus* L. cv. Sonnett F_1 gelb, *Petunia hybrida* cv. White Corso (all grown from seeds of Austrosaat, Vienna, Austria, www.austrosaat.at) were also collected from the experimental field, yellow and white carnations were purchased as cut flowers from a local flower shop. Seeds of *Arabidopsis thaliana* Col-0 were obtained from the European Arabidopsis Stock Centre NASC and cultivated at standard conditions.

UV photography

For UV photography, flowers or petals were radiated with a Camag Reprostar II at 366 nm (Camag, Muttenz, Switzerland). Pictures were taken with a Nikon D100 digital camera and a UV Nikkor lens (f=105 mm, 1:4.5, Nikon, Vienna, Austria, http://www.nikon.at) together with the UV

pass filter B+W 58 403 (Schneider, Bad Kreuznach, Germany, http://www.schneiderkreuznach.com) and are shown as monochromes.

Microsocopy

Petals were treated as described (Braune *et al.* 1967). The tissue was infiltrated with a series of glycerol-water dilutions (v/v 1:10, 1:5, 1:1) for one hour each. After the infiltration process, cross-sections were sliced manually from the petals still embedded in the glycerol-water 1:1. The slices were transferred to a microscope slide and were embedded either in water (native) or in a solution of 2 M ammonia in (1:1) glycerol-water. The preparations were examined under a Carl Zeiss Axio Scope A1 microscope (Zeiss, Vienna, Austria, http://www.zeiss.at) and pictures were taken using a Canon G10 (Canon, Vienna Austria, http://www.canon.at) connected to the microscope *via* a conversion Canon lens adapter LA-DC58K (Zeiss No. 426126).

Chemicals

[^{14}C]Isoliquiritigenin and [^{14}C]butein were synthesised as described (Halbwirth *et al.* 2006) from 4-hydroxy[ring-U-^{14}C]benzaldehyde (33.1 MBq/mg) (Amersham International, UK, http://www.gelifesciences.com). Isoliquiritigenin, butein, sulfuretin, luteolin, marein, maritimein, luteolin 7-*O*-glucoside and eriodictyol chalcone were purchased from Extrasynthesis (Genay, France, http://www.extrasynthese.com), robtein from TransMIT-MPC (Giessen, Germany, http://www.plantmetachem.com). Okanin and maritimetin were obtained by enzymatic hydrolysis from marein and maritimein, respectively. Briefly, 20 µg of the glycoside dissolved in 20 µL ethanol were incubated for 30 min at 30 °C with 10 µg naringinase (Sigma-Aldrich, Vienna, Austria, http://www.sigmaaldrich.com) in 80 µL 0.1 M McIlvaine buffer pH 5.5.

LC-MS analysis

The LC-MS analysis was performed using the Ultimate 3000 series RSLC (Dionex, Sunnyvale, CA, USA, http://www.dionex.com) system and the Orbitrap XL mass spectrometer (Thermo Fisher Scientific, Bremen, Germany, http://www.thermo.com) equipped with an ESI source. HPLC was accomplished using the Acclaim C18 Column (150 x 2.1 mm, 2.2 µm; Dionex) at a constant flow rate of 300 µL/min using a binary solvent system: solvent A contains water with 0.1 % formic acid (Roth, Karlsruhe, Germany, http://www.carl-roth.de) and solvent B contains acetonitrile

406 (hypergrade for LC MS, Merck KGaA, Darmstadt, Germany, http://www.merckchemicals.com) with
407 0.1% formic acid. Ten µL were injected into the HPLC gradient system started with 0.5% B and
408 linearly increased to 10 % B in 10 min and to 80 % in 14 min and was then held for 5 min, before
409 being brought back to the initial conditions and held for 6 min for re-equilibration of the column for
410 the next injection. Capillary voltage was set to 35 V and transfer capillary temperature to 275 °C.
411 Measurements were performed in negative mode using the Orbitrap analyzer. Full scan mass
412 spectra (x to y) were generated using 30,000 resolving power and processed and visualized using
413 Xcaliber xx software.

414 **Imaging on the Ultraflex III® mass spectrometer**

415 A carbon conductive adhesive tape (Plano, Wetzlar, Germany, http://www.plano-em.de) was fixed
416 on an Indium Tin Oxide slide (Bruker Daltonics, Bremen, Germany, http://www.bdal.com) to fix the
417 petals on the slide. The rims of the leave were used for the laser positioning during LDI-MSI. An
418 Ultraflex III® mass spectrometer (Bruker Daltonics) equipped with a Nd:YAG laser was used for the
419 analysis. All spectra were measured in negative reflectron mode. A raster of 75 x 75 µm and the
420 large laser focus settings with constant laser intensity and a shot rate of 50 Hz were used. For LDI-
421 MSI of the front side, 9494 raster positions were measured; and 19085 positions for the back side
422 were recorded within a mass range of *m/z* 100–1100. For each raster point, a spectrum was
423 accumulated with 230 laser shots for the front side; and 100 laser shots for the back side;
424 respectively. For image reconstruction, FlexImaging version software version 2.0 (Bruker
425 Daltonics) was used.

426 **HPLC**

427 HPLC analysis was performed on a Perkin Elmer Series 200 system (Perkin Elmer, Vienna,
428 Austria, http://www.perkinelmer.de) equipped with a photodiode array detector coupled with a
429 500TR Flow Scintillation Analyzer for the detection of radiolabeled substances according to
430 Chandra *et al.* (2001) for assays with okanin and marein as substrates and according to Vande
431 Casteele *et al.* (1982) for all other compounds.

432 **Enzyme preparation**

433 0.5 g plant material, 0.25 g polyclar AT (Serva, Mannheim, Germany, http:www.serva.de) and

434 0.25 g quartz sand (VWR Vienna, Austria, https://at.vwr.com) were homogenized with 3 mL buffer
435 in a mortar. The homogenate was centrifuged for 10 min at 10,000 x g and 4 °C. To remove low
436 molecular compounds, crude enzyme preparations were passed through a gel chromatography
437 column (Sephadex G25, GE Healthcare, Freiburg, Germany, http://www.gelifesciences.com).
438 Extraction buffers generally contained 0.4 % (v/v) sodium ascorbate (Sigma). For AUS assays,
439 enzyme preparations were liberated from ascorbate during the gel extraction step. Protein content
440 was determined by a modified Lowry procedure (Sandermann and Strominger 1972) using
441 crystalline bovine serum albumine as a standard.

442 **Enzyme assays**

443 Assays for CHS/CHI, CH3H, DFR, FHT, FNS II and F3'H were performed as described earlier
444 (Halbwirth *et al.* 2008; Schlangen *et al.,* 2010).

445 **Enzyme characterization**

446 All data represents an average of at least three independent experiments. Determination of the pH
447 optimum was carried out as described for the standard aurone synthase assay, but using 0.2 M
448 McIlvaine buffers with pH values between 4.5 and 9.0.

449 **Standard assay for aurone synthase**

450 The reaction mixture in a final volume of 100 µL contained: 1 nmol [^{14}C]butein (150 Bq) or 10 nmol
451 unlabelled anthochlor, 3 µg enzyme preparation, 90 µL 0.1 M K_2HPO_4/KH_2PO_4 buffer pH 7.5. The
452 reaction was started by the addition of the enzyme preparation and the assay was incubated for 15
453 min at 30 °C. The reaction was stopped by addition of 10 µL glacial acetic acid and 70 µL methanol
454 (both VWR). After centrifugation for 10 min at 22,000 x g 100 µL of the reaction mixture were
455 subjected to HPLC analysis.

ACKNOWLEDGEMENTS

These investigations were supported by grants from the Austrian Science Fund (FWF): [Projects V18-B03 and P24331-B16]. J. Thill acknowledges her Marie Curie scholarship from EU (MRTN_CT-2006-035805). H. Halbwirth and J. Greiner would like to thank Dr. Sylvia Plaschil (JKI Quedlinburg, Germany) for the introduction into microscopic techniques. U. S. Schubert thanks the Dutch Polymer Institute (DPI, technology area HTE) for financial support. This work was performed in the frame of Cost Action FA1006.

SUPPLEMENTAL INFORMATION

Additional information may be found in the online version of this article:

Supplementary Figure 1: Absorbance spectra of the chalcone butein and the aurone sulfuretin in acidic and alkaline environment.

Supplementary Table 1: AUS activity in different tissues of *B. ferulifolia*

Supplementary Table 2: Flavonoid and 4-deoxyaurone biosynthesis in the base and apex of the petals of buds and flowers

References

Bomati, E.K., Austin, M.B., Bowman, M.E., Dixon, R.A. and Noel, J.P. (2005) Structural elucidation of chalcone reductase and implications for deoxychalcone biosynthesis. *Journal of Biological Chemistry*, **280**, 30496-30503.

Bradley, J., Winefield, C., Schwinn, K., Martin, C., Bloor, S., Davies, K. and Spiller, G. (2000) Genetic engineering for yellow flower colours, pp. 39-44.

Braune, W., Leman, A. and Taubert, H. (1967) Pflanzenanatomisches Praktikum. Jena: Fischer VEV, pp. 23-39.

Briscoe, A.D. and Chittka, L. (2001) The evolution of color vision in insects. *Annual Review of Entomology*, **46**, 471-510.

Chandra, A., Rana, J. and Li, Y. (2001) Separation, identification, quantification, and method validation of anthocyanins in botanical supplement raw materials by HPLC and HPLC-MS. *Journal of agricultural and food chemistry*, **49**, 3515-3521.

Chittka, L., Shmida, A., Troje, N. and Menzel, R. (1994) Ultraviolet as a component of flower reflections, and the colour perception of Hymenoptera. *Vision Research*, **34**, 1489-1508.

Clark, C. (1979) Ultraviolet absorption by flowers of the Eschscholzioideae (Papaveraceae). *Madroño*, **26**, 22-25.

Daumer, K. (1958) Blumenfarben, wie sie die Bienen sehen. *Journal of Comparative Physiology A: Neuroethology, Sensory, Neural, and Behavioral Physiology*, **41**, 49-110.

Davies, K., Schwinn, K., Geneve, R., Preece, J. and Merkle, S. (1997) Flower colour. In *Biotechnology of ornamental plants.* (Geneve, R.L.P., J.E.Merkle, S.A. ed. Wallingford CAB INTERNATIONAL, pp. 259-294.

Davies, K.M., Marshall, G.B., Bradley, J.M., Schwinn, K.E., Bloor, S.J., Winefield, C.S. and Martin, C.R. (2006) Characterisation of aurone biosynthesis in *Antirrhinum majus*. *Physiologia Plantarum*, **128**, 593-603.

Forkmann, G. and Dangelmayr, B. (1980) Genetic control of chalcone isomerase activity in flowers of *Dianthus caryophyllus*. *Biochemical Genetics*, **18**, 519-527.

Forkmann, G. and Heller, W. (1999) Biosynthesis of flavonoids. In *Comprehensive Natural Products Chemistry* (D. Barton, K. Nakanishi, O. Meth-Cohn and Sankawa, U. eds): Elsevier Science, Amsterdam, pp. 713-748.

Guldberg, L.D. and Atsatt, P.R. (1975) Frequency of reflection and absorption of ultraviolet light in flowering plants. *American Midland Naturalist*, **93**, 35-43.

Halbwirth, H., Kahl, S., Jager, W., Reznicek, G., Forkmann, G. and Stich, K. (2006) Synthesis of (14C)-labeled 5-deoxyflavonoids and their application in the study of dihydroflavonol/leucoanthocyanidin interconversion by dihydroflavonol 4-reductase. *Plant Science*, **170**, 587-595.

Halbwirth, H., Muster, G. and Stich, K. (2008) Unraveling the Biochemical Base of Dahlia Flower Coloration. *Nat. Prod. Comm*, **3**, 1259-1266.

Halbwirth, H., Wimmer, G., Wurst, F., Forkmann, G. and Stich, K. (1997) Enzymatic glucosylation of 4-deoxyaurones and 6′-deoxychalcones with enzyme extracts of *Coreopsis grandiflora*, Nutt. I. *Plant Science*, **122**, 125-131.

Harborne, J.B. (1967) *Comparative Biochemistry of Flavonoids* London: Academic Press.

Harborne, J.B. (1993) *Introduction to ecological biochemistry*: Academic Press.

Harborne, J.B. and Smith, D.M. (1978) Anthochlors and other flavonoids as honey guides in the Compositae. *Biochemical Systematics and Ecology*, **6**, 287-291.

Hölscher, D., Shroff, R., Knop, K., Gottschaldt, M., Crecelius, A., Schneider, B., Heckel, D.G., Schubert, U.S. and Svatoš, A. (2009) Matrix free UV laser desorption/ionization (LDI) mass spectrometric imaging at the single cell level: distribution of secondary metabolites of *Arabidopsis thaliana* and *Hypericum* species. *The Plant Journal*, **60**, 907-918.

Leonard, A.S. and Papaj, D.R. (2011) 'X'marks the spot: The possible benefits of nectar guides to bees and plants. *Functional Ecology*, **25**, 1293–1301.

McCrea, K.D. and Levy, M. (1983) Photographic visualization of floral colors as perceived by honeybee pollinators. *American Journal of Botany*, 369-375.

Menzel, R. and Shmida, A. (1993) The ecology of flower colours and the natural colour vision of insect pollinators: the Israeli flora as a study case. *Biological Reviews*, **68**, 81-120.

Nakayama, T. (2002) Enzymology of aurone biosynthesis. *Journal of Bioscience and Bioengineering*, **94**, 487-491.

Nakayama, T., Sato, M., Fukui, Y., Yonekura-Sakakibara, K., Hayashi, H., Tanaka, Y., Kusumi, T. and Nishino, T. (2001) Specificity analysis and mechanism of aurone synthesis catalyzed by aureusidin synthase, a polyphenol oxidase homolog responsible for flower coloration. *FEBS letters*, **499**, 107-111.

Nakayama, T., Yonekura Sakakibara, K., Sato, T., Kikuchi, S., Fukui, Y., Fukuchi-Mizutani, M., Ueda, T., Nakao, M., Tanaka, Y. and Kusumi, T. (2000) Aureusidin synthase: a polyphenol oxidase homolog responsible for flower coloration. *Science*, **290**, 1163.

Ono, E., Fukuchi-Mizutani, M., Nakamura, N., Fukui, Y., Yonekura-Sakakibara, K., Yamaguchi, M., Nakayama, T., Tanaka, T., Kusumi, T. and Tanaka, Y. (2006a) Yellow flowers generated by expression of the aurone biosynthetic pathway. *Proceedings of the National Academy of Sciences*, **103**, 11075-11080.

Ono, E., Hatayama, M., Isono, Y., Sato, T., Watanabe, R., Yonekura Sakakibara, K., Fukuchi Mizutani, M., Tanaka, Y., Kusumi, T. and Nishino, T. (2006b) Localization of a flavonoid biosynthetic polyphenol oxidase in vacuoles. *The Plant Journal*, **45**, 133-143.

Rieseberg, L.H. and Schilling, E.E. (1985) Floral flavonoids and ultraviolet patterns in Viguiera (Compositae). *American Journal of Botany*, **72**, 999-1004.

Sanchez-Gonzalez, M. and Rosazza, J.P.N. (2006) Biocatalytic synthesis of butein and sulfuretin by *Aspergillus alliaceus*. *Journal of agricultural and food chemistry*, **54**, 4646-4650.

Sandermann, H. and Strominger, J.L. (1972) Purification and properties of C55-isoprenoid alcohol phosphokinase from *Staphylococcus aureus*. *Journal of Biological Chemistry*, **247**, 5123-5131.

Sato, T., Nakayama, T., Kikuchi, S., Fukui, Y., Yonekura-Sakakibara, K., Ueda, T., Nishino, T., Tanaka, Y. and Kusumi, T. (2001) Enzymatic formation of aurones in the extracts of yellow snapdragon flowers. *Plant Science*, **160**, 229-236.

Schlangen, K., Miosic, S., Castro, A., Freudmann, K., Luczkiewicz, M., Vitzthum, F., Schwab, W., Gamsjäger, S., Musso, M. and Halbwirth, H. (2009) Formation of UV-honey guides in *Rudbeckia hirta*. *Phytochemistry*, **70**, 889-898.

Schlangen, K., Miosic, S., Thill, J. and Halbwirth, H. (2010) Cloning, functional expression, and characterization of a chalcone 3-hydroxylase from *Cosmos sulphureus*. *Journal of Experimental Botany*, **61**, 3451-3459.

Scogin, R. and Zakar, K. (1976) Anthochlor pigments and floral UV patterns in the genus Bidens. *Biochemical Systematics and Ecology*, **4**, 165-167.

Shang, Y., Venail, J., Mackay, S., Bailey, P.C., Schwinn, K.E., Jameson, P.E., Martin, C.R. and Davies, K.M. (2010) The molecular basis for venation patterning of pigmentation and its effect on pollinator attraction in flowers of *Antirrhinum*. *New Phytologist*.

Shimada, N., Aoki, T., Sato, S., Nakamura, Y., Tabata, S. and Ayabe, S. (2003) A cluster of genes encodes the two types of chalcone isomerase involved in the biosynthesis of general flavonoids and legume-specific 5-deoxy (iso) flavonoids in *Lotus japonicus*. *Plant Physiology*, **131**, 941-951.

Strack, D. and Schliemann, W. (2001) Bifunctional polyphenol oxidases: Novel functions in plant pigment biosynthesis. *Angewandte Chemie International Edition*, **40**, 3791-3794.

Thompson, W.R., Meinwald, J., Aneshansley, D., Eisner, T. (1972) Flavonols: responsible for ultraviolet absorption in nectar guide of flower. *Science*, **177**, 528-530.

Vande Casteele, K., Geiger, H. and Van Sumere, C.F. (1982) Separation of flavonoids by reversed-phase high-performance liquid chromatography. *Journal of Chromatography A*, **240**, 81-94.

Welle, R. and Grisebach, H. (1988) Isolation of a novel NADPH-dependent reductase which coacts with chalcone synthase in the biosynthesis of 6'-deoxychalcone. *FEBS Letters*, **236**, 221-225.

Table 1: Dependence of the 4-deoxyaurone formation on pH. Relative activities were calculated in comparison to the activity at the optimal pH which was defined as being 100%. Substrate preference cannot be concluded from comparison of the activities.

Substrate	**pH optimum**	**activity at optimal pH (mol/s.g)**	**relative activity at pH 7.0 [%]**	**relative activity at pH 5.5 [%]**
butein	7.5	0.4 ± 0.1	97	25
okanin	8.5	2.4 ± 0.2	18	11
robtein	8.5	0.5 ± 0.05	18	9
butein 4-*O*-glucoside	8.25	0.01± 0.005	42	14

Figure legends

Figure 1: The basic chalcone-, aurone- and flavonoid structure. Please note the divergent ring numbering.

Figure 2: LDI-MS of a *Bidens ferulifolia* petal. a: a representative spectrum of the petal base containing nine *m/z* signals of anthochlors. b: no anthochlors were detected in representative spectra of the petal apex. For the allocation of *m/z* signals to compounds refer to Figure 3.

Figure 3: Anthochlors and flavonoids present or absent in *Bidens ferulifolia* petals

Figure 4: UV nectar guides. *Bidens ferulifolia* flower UV photography of front (a) and back (e) side, daylight photographies (b, f) and after (c, g) ammonia staining. Cross sections of *Bidens ferulifolia* petals base native (i) and stained (j) and petal apex native (k) and stained (l). Epi-illumination mode microscopic view of stained epidermis of petal front side base (d) and apex (h). *Coreopsis grandiflora* flower before (m) and after (n) ammonia staining. *Cosmos sulphureus* flower before (o) and after (p) ammonia staining.

Figure 5: Spatial distribution of okanin (*m/z* 287) along a *Bidens* petal fixed by adhesive tape on a Indium Tin Oxide glass slide, first row: front side, second row: back side; from left to right: daylight photos, UV photos, negative ion mode LDI-MSI images (green area indicates the presence of the target compound), negative ion mode LDI-MSI images overlapping the daylight photos. All mass peaks related to anthochlor pigments showed a similar distribution.

Figure 6: HPLC chromatograms from incubation of enzyme preparations from *B. ferulifolia* petals (a) and leaves (b), *Antirrhinum majus* petals (c) and leaves (d), *Arabidopsis thaliana* col-0 plants (e), *Tagetes erecta* petals (f), *Dianthus caryophyllus* petals (g), and *Petunia hybrida* petals (h) with butein and of enzyme preparations from *B. ferulifolia* petals (l) and *Antirrhinum majus* petals (j) with isoliquiritigenin.

Figure 7: Overview on flavonoid and anthochlor formation from *p*-coumaroyl-CoA. abbrev.: ANS:

anthocyanidin synthase, AUS: aurone synthase, CH3H: chalcone 3-hydroxylase, CHI: chalcone isomerase, CHR: Chalcone reductase, CHS: chalcone synthase, DFR: dihydroflavonol 4-reductase, FHT: flavanone 3-hydroxylase, F3'H: flavonoid 3'-hydroxylase, FNSII: flavone synthase II

Figure 1: The basic chalcone-, aurone- and flavonoid structure. Please note the divergent ring numbering.

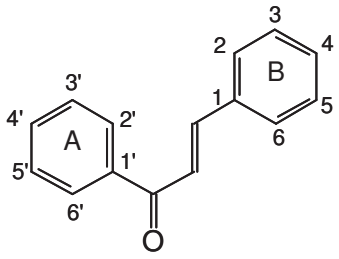

Chalcone

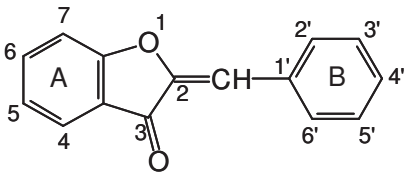

Aurone

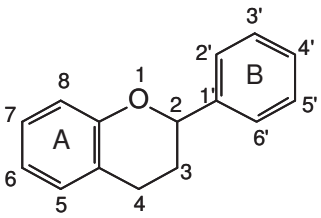

Flavan

Figure 2: LDI-MS image of a *Bidens ferulifolia* petal. above: no anthochlors were detected in representative spectra of the petal apex. below: a representative spectrum of the petal base containing nine *m/z* signals of anthochlors. For the allocation of *m/z* signals to compounds refer to Figure 3.

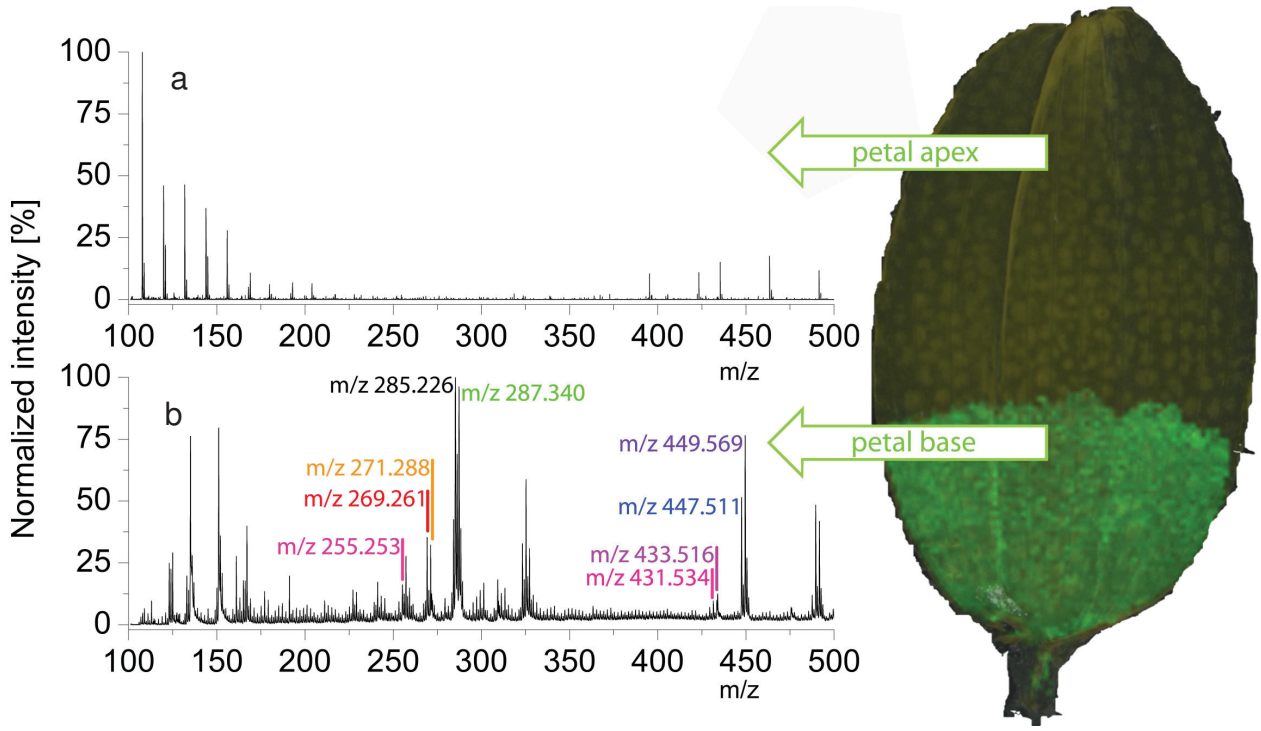

Figure 3: Anthochlor pigments and flavonoids in *Bidens ferulifolia* petals

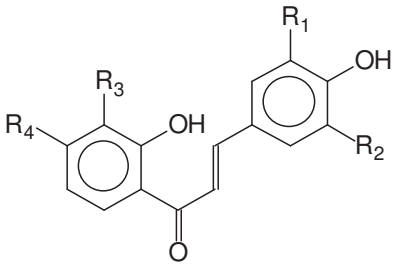

Chalcone (A)

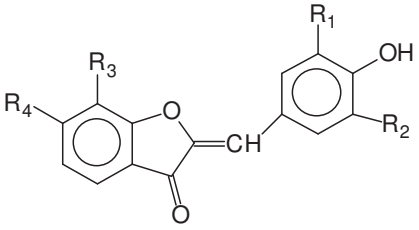

Aurone (B)

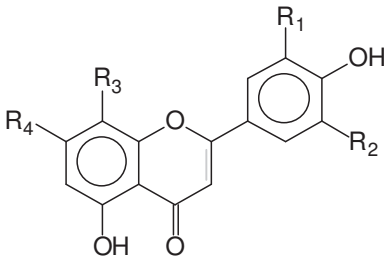

Flavanone (C)/Flavone (D)

Compounds present in B. ferulifolia petals	**Type**	**R_1**	**R_2**	**R_3**	**R_4**	**FW (g/mol)**	**$[M-H]^-$: m/z**	**R_t**	**detected by**
Isoliquiritigenin $C_{15}H_{12}O_4$	A	H	H	H	OH	256.25	255.07[1]	13.66	LDI-MSI
Sulfuretin $C_{15}H_{10}O_5$	B	OH	H	H	OH	270.24	269.05[1]	12.60	LC-MS
Butein $C_{15}H_{12}O_5$	A	H	OH	H	OH	272.25	271.06[1]	13.13	LC-MS
Maritimetin $C_{15}H_{10}O_6$	B	OH	H	OH	OH	286.24	285.04[1]	12.14	LC-MS
Luteolin $C_{15}H_{10}O_6$	D	OH	H	H	OH	286.24	285.07[1]	12.81	LC-MS
Okanin $C_{15}H_{12}O_6$	A	OH	H	OH	OH	288.24	287.06[1]	12.41	LC-MS
Sulfuretin 6-*O*-β-D-glucoside $C_{21}H_{20}O_{11}$	B	OH	H	H	OGlu	432.38	431		LDI-MSI
Butein 4'-*O*-β-D-glucoside $C_{21}H_{22}O_{10}$	A	OH	H	H	OGlu	434.39	433		LDI-MSI
Maritimetin 6-*O*-β-D-glucoside (Maritimein) $C_{21}H_{20}O_{11}$	B	OH	H	OH	OGlu	448.38	447.09	11.53	LC-MS
Luteolin 7-*O*-β-D-glucoside $C_{21}H_{20}O_{11}$	D	OH	H	H	OGlu	448.39	447		LDI-MSI
Okanin 4'- *O*-β-D-glucoside (Marein) $C_{21}H_{22}O_{11}$	A	OH	H	OH	OGlu	450.39	449.11[1]	12.14	LC-MS
Mass isomers not present[2]									
Apigenin $C_{15}H_{10}O_5$	D	H	H	H	OH	270.24	269.05[1]	13.26	
Naringenin $C_{15}H_{12}O_5$	C	H	H	H	OH	272.25	271.06[1]	13.30	
3',4',5',6-Tetrahydroxyaurone $C_{15}H_{10}O_6$	B	OH	OGlu	H	OH	286.24	285.07[1]	12.07	
Robtein $C_{15}H_{12}O_6$	A	OH	OH	H	OH	288.25	287.06[1]	12.56	
Eriodictyol $C_{15}H_{12}O_6$	C	OH	H	H	OH	288.25	287.06[1]	12.82	
Isoliquiritigenin 4'-*O*-β-D-glucoside $C_{21}H_{22}O_9$	A	H	H	H	OGlu	418.39			
Apigenin 7- *O*-β-D-glucoside $C_{21}H_{20}O_{10}$	D	H	H	H	OGlu	432.39	431		
Naringenin 7-*O*-β-D-glucoside $C_{21}H_{22}O_{10}$	C	H	H	H	OGlu	434.39	433		
3',4',5',6-Trihydroxyaurone 6- *O*-β-D-glucoside $C_{21}H_{20}O_{11}$	B	OH	OGlu	H	OH	448.38	447		
Robtein 4'-*O*-β-D-glucoside $C_{21}H_{22}O_{11}$	A	OH	OH	OH	OGlu	450.39	449		
Eriodictyol 7-*O*-β-D-glucoside $C_{21}H_{22}O_{11}$	C	OH	H	H	OGlu	450.39	449		

[1]exact mass obtained by LC-MS, [2] presence excluded by LC-MS

Figure 4: UV nectar guides. *Bidens ferulifolia* flower UV photography of front (a) and back (e) side, daylight photographies (b, f) and after (c, g) ammonia staining. Cross sections of *Bidens ferulifolia* petals base native (i) and stained (j) and petal apex native (k) and stained (l). Epi-illumination mode microscopic view of stained epidermis of petal front side base (d) and apex (h). *Coreopsis grandiflora* flower before (m) and after (n) ammonia staining. *Cosmos sulphureus* flower before (o) and after (p) ammonia staining.

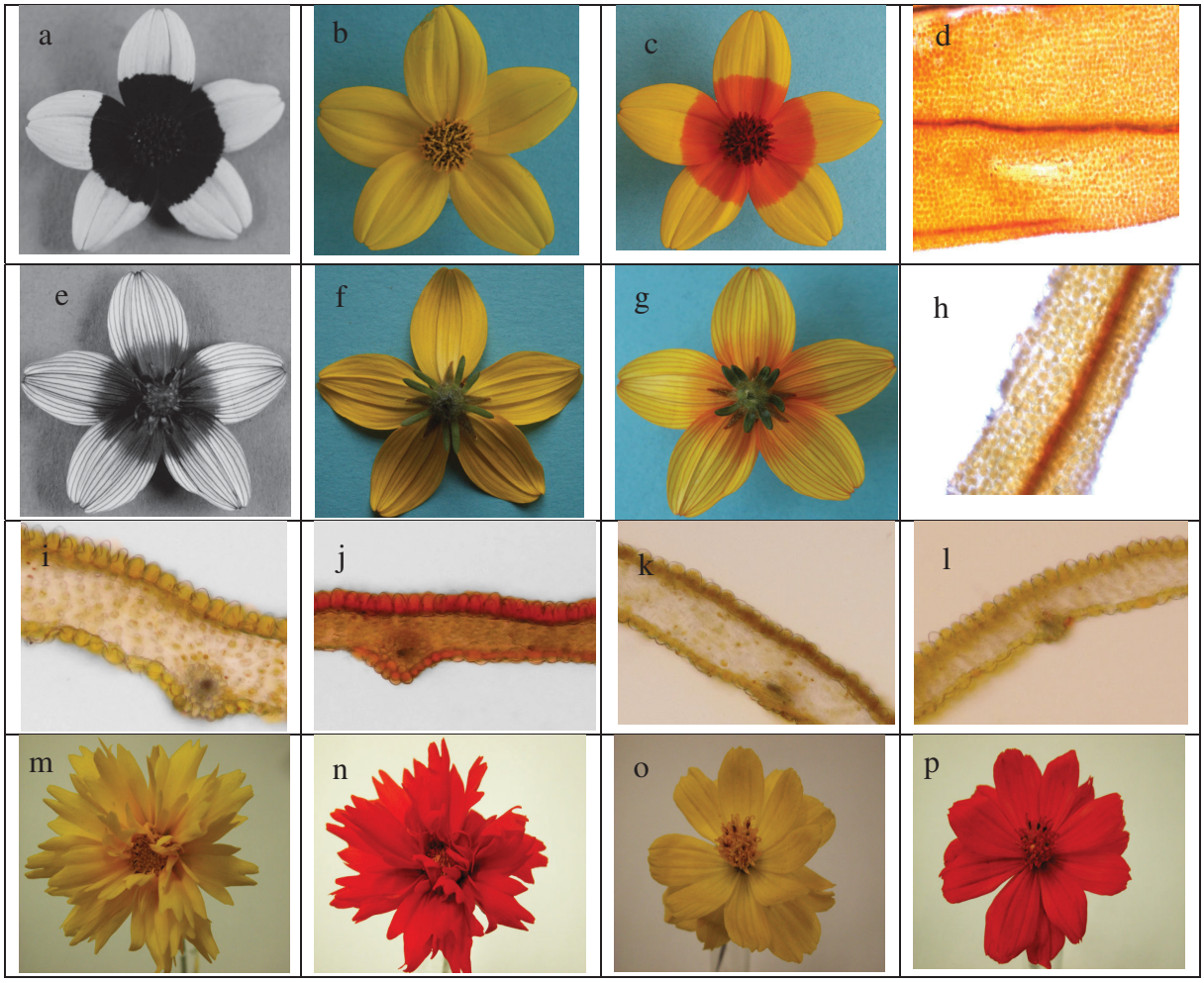

Figure 5: Spatial distribution of okanin (*m/z* 287) along a *Bidens* petal fixed by adhesive tape on a Indium Tin Oxide glass slide, first row: front side, second row: back side; from left to right: daylight photos, UV photos, negative ion mode LDI-MSI images (green area indicates the presence of the target compound), negative ion mode LDI-MSI images overlapping the daylight photos. All mass peaks related to anthochlors showed a similar distribution.

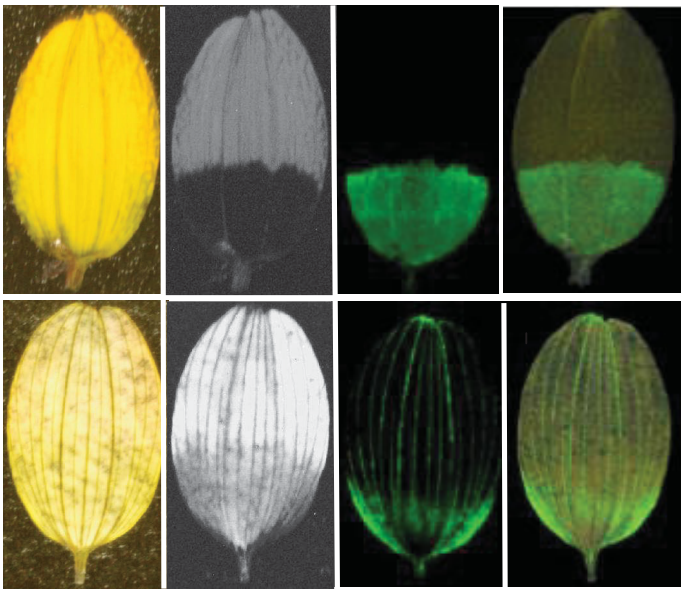

Figure 6: HPLC chromatograms from incubation of enzyme preparations from *B. ferulifolia* petals (a) and leaves (b), *Antirrhinum majus* petals (c) and leaves (d), *Arabidopsis thaliana* col-0 plants (e), *Tagetes erecta* petals (f), *Dianthus caryophyllus* petals (g), and *Petunia hybrida* petals (h) with butein and of enzyme preparations from *B. ferulifolia* petals (i) and *Antirrhinum majus* petals (j) with isoliquiritigenin.

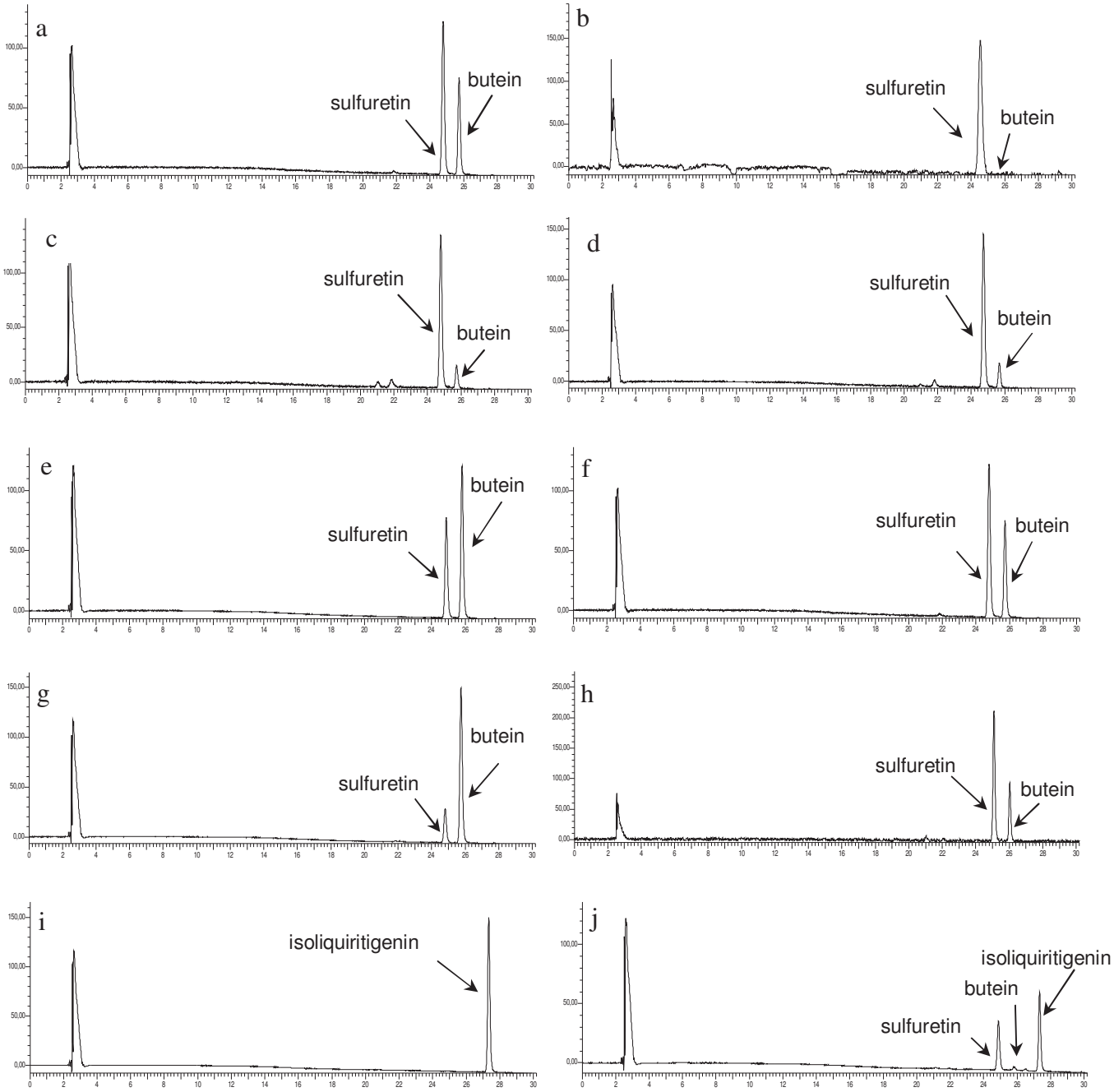

Figure 7: Overview on flavonoid and aurone formation from *p*-coumaroyl-CoA. abbrev.: ANS: anthocyanidin synthase, AUS: aurone synthase, CH3H: chalcone 3-hydroxylase, CHI: chalcone isomerase, CHR: Chalcone reductase, CHS: chalcone synthase, DFR: dihydroflavonol 4-reductase, FHT: flavanone 3-hydroxylase, F3'H: flavonoid 3'-hydroxylase, FNSII: flavone synthase II

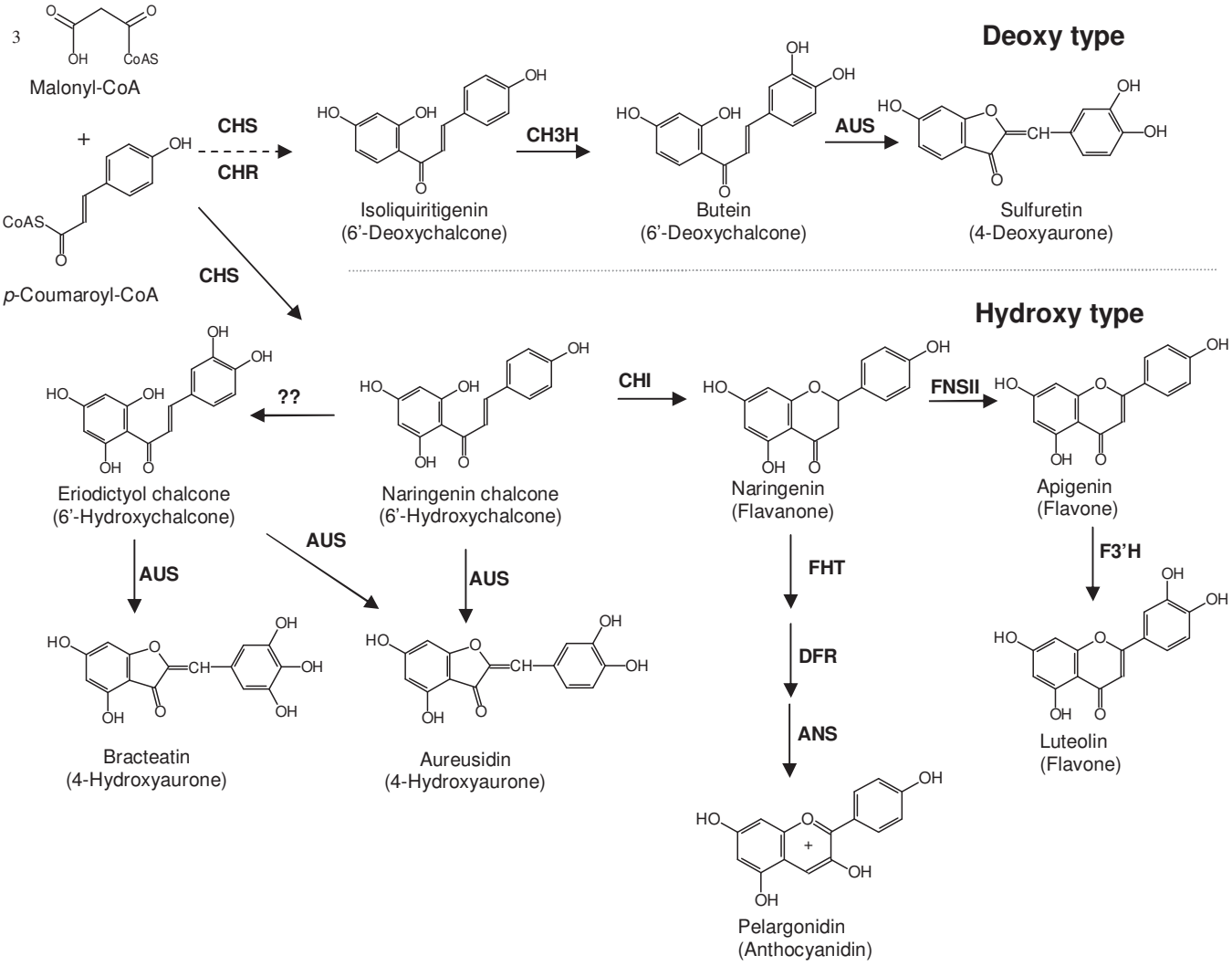

Publication P12:

Spatially-resolved qualitative and quantitative analysis of *Gossypium hirsutum* L. leaf pigments at single cell level

---

D. Hölscher, K. Knop, M. Kai, R. Maddula, C. Ritter, A. C. Crecelius, D. Heckel, B. Schneider, U. S. Schubert, T. Alexandrov, B. Zimmermann, A. Svatoš

Plant J. **2012**, submitted.

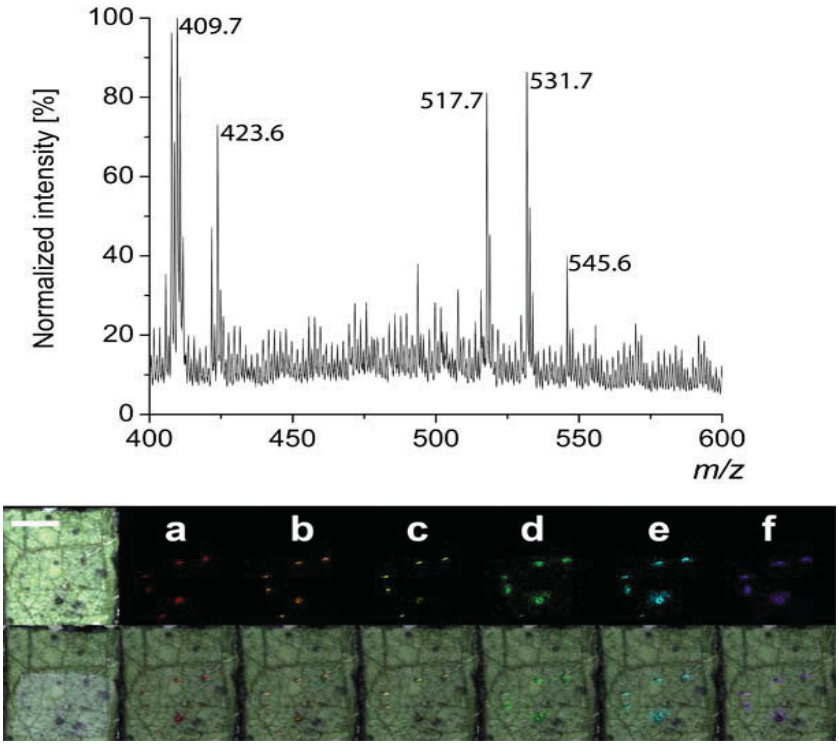

Spatially-resolved qualitative and quantitative analysis of *Gossypium hirsutum* L. leaf pigments at single cell level.

D. Hölscher,[1] K. Knop,[2,3] M. Kai,[1] R. Maddula,[1] C. Ritter,[1] A. C. Crecelius,[2,3] D. Heckel,[1] B. Schneider,[1] U. S. Schubert,[2,3] T. Alexandrov,[4] B. Zimmermann,[5] A. Svatoš[1]

[1] Department of Entomology, Mass Spectrometry Research Group, and Biosynthesis/NMR Research Group, Max Planck Institute for Chemical Ecology, Hans-Knöll-Str. 8, 07745 Jena, Germany

[2] Laboratory of Organic and Macromolecular Chemistry (IOMC), Jena Center for Soft Matter (JSCM), Friedrich-Schiller University of Jena, Humboldtstrasse 10, 07743 Jena, Germany

[3] Dutch Polymer Institute (DPI), John F. Kennedylaan 2, 5612 AB Eindhoven, The Netherlands

[4] Center for Industrial Mathematics (ZeTeM), University of Bremen, 28359 Bremen, Germany

[5] Institute of Nutrition and Food Sciences, University of Bonn,
Endenicher Allee 11-13, 53115 Bonn, Germany
Institut Prof. Dr. Kurz GmbH, Eupener Str. 161, 50933 Köln, Germany

Email: hoelscher@ice.mpg.de , svatos@ice.mpg.de

ABSTRACT

Matrix-free UV-laser desorption/ionization (LDI-MSI) mass spectrometric imaging of pigment glands of *Gossypium hirsutum* L. and its improved evaluation by exploiting spatial segmentation methods using edge-preserving image denoising and clustering are reported as efficient tools for the localized qualification of prominent secondary metabolites gossypol, methoxygossypol, 6,6'-dimethoxygossypol hemigossypolone, heliocide H-type and B-type isomers. All detected compounds are co-localized in cotton pigment glands. Their chemical identity was confirmed using TOF-TOF fragmentation data and by comparing to authentic standards. Theirs concentrations outside the glandular cells were negligible (less than 1%). The quantification of these naturally occurring compounds was performed by the combination of laser microdissection-based (LMD) isolation of pigment glands from young leaves of *G. hirsutum* with ultra performance liquid chromatography (UPLC-MS) methods. Amounts of cotton pigments were sufficient to determine cell-to-cell variance (e.g. hemigossypolone 67±13 and gossypol 46.5±7.8 ng/cell) corresponding to 980 nM / 340 nM concentration. Furthermore a determination of the gossypol enantiomer ratio of laser-microdissected (LMD) pigment glands is accomplished by a combination of high performance liquid chromatography mass spectrometry (HPLC-MS) and capillary electrophoresis (CE).

Keywords: *Gossypium hirsutum* L., LDI mass spectrometric imaging, laser microdissection, UPLC/MS, HPLC/MS, capillary electrophoresis, edge-preserving image denoising and clustering, segmentation map, gossypol, hemigossypolone, heliocides H_1, H_2, H_3, H_4 and B_1,

Abbreviation

LDI-MSI	matrix-free UV-laser desorption/ionization mass spectrometric imaging
PG	pigment gland
BF	bright field microscopy
LMD	laser microdissection
MS	mass spectrometry
UPLC	ultra performance liquid chromatography
HPLC	high performance liquid chromatography
CE	capillary electrophoresis

INTRODUCTION

Microscopy and different staining/labelling techniques offer an observation of biological materials or tissue samples lacking molecular specificity. Recently developed methods especially advances in mass spectrometric imaging MSI technology created a broad array of molecular imaging tools allowing a direct visualization of metabolites within the plant organism (Svatoš, 2010; Heinemann and Zenobi, 2011; Kaspar *et al.*, 2011; Thunig *et al.*, 2011, Svatoš A. 2011).

The development of matrix-free UV-laser desorption/ionization mass spectrometric imaging (LDI-MSI) at the single-cell level has proven the successful identification of secondary metabolites of *A. thaliana* and *Hypericum* species (Hölscher *et al.*, 2009). Furthermore, an exceeding analysis of the LDI imaging data could be supported by the usage of new computational methods originally created for matrix-assisted laser/desorption ionization mass spectrometric imaging (MALDI-MSI) data. A recently published approach to reduce the important issue of pixel-to-pixel variability in MALDI-MSI takes not only the similarity of mass spectra alone into account, it is improving the multivariate analysis of MALDI-MSI data sets by considering spatial relations of mass spectra for the first time (Alexandrov *et al.*, 2010). The procedure of edge-preserving image denoising allowed the compression of the full MALDI-MSI data set into one image. These segmentation maps revealed a superior quality in terms of smoothness, lack of noise, level of detail, and correlation with morphological structures of the sample (Alexandrov *et al.*, 2010).

Although offering almost exclusively qualitative information, the LDI-MSI method can be considered as a starting position for subsequent quantitative analysis by employing extraction procedures followed by liquid chromatography mass spectrometry (LC-MS) methods. Laser microdissection (LMD) has been proven to be a successful technique for isolating secretory cavities from leaves of of *Dilatris pillansii* (Haemodoraceae) (Hölscher

and Schneider, 2007) and stone cells of Norwegian spruce (Li *et al.*, 2007) for metabolic profiling studies.

To determine the localization and the concentration of plant secondary metabolites we addressed the challenging problems of spatial characterization and quantitative determination of secondary compounds of *Gossypium hirsutum* L. cotton by performing a LMD-based isolation of pigment glands from leaves of cotton. The Guatemalan native species *G. hirsutum* is the most widely cultivated (90%) industrial cotton among all *Gossypium* species. Its importance stimulated early investigations of its principal, intensely yellow colored pigment gossypol, an axial chiral, complex tautomerism exhibiting, dimeric sesquiterpene isolated from a large number of members of the Malvaceae family (Marchlewski, 1899; Boatner and Hall, 1946; Adams *et al.*, 1960; Bell and Stipanovic, 1986; Fryxell, 1992; Jaroszewski *et al.*, 1992; Sunilkumar *et al.*, 2006). Gossypol and related compounds like hemigossypolone and the heliocides H and B (Stipanovic *et al.*, 1977; Bell *et al.*, 1978) accumulate in subepidermal pigment glands found in all green tissues and in root epidermis of healthy, unstressed plants (Stanford and Viehoever, 1918; Boatner *et al.*, 1947). The phytochemical profile of the pigment glands varies considerably depending on the species, the environment, and specific varieties (Schwartze and Alzberg, 1923; Stansbury *et al.*, 1954; Bell *et al.*, 1986; Essenberg *et al.*, 1990).

Restricted rotation around the 2,2´-carbon-internaphthyl bond is resulting in atropisomerism of the gossypol molecule. The atropisomers are referred to as (+)-(*S*)-gossypol (P-form) and the in most commercial *G. hirsutum* cottonseed less abundant (-)-(*R*)-gossypol (M-form) which are separable from each other by chromatographic means (Freedman *et al.*, 2003; Kenar, 2006; Stipanovic *et al.*, 2009) (Fig.1). Serious side effects of the (*R*)-atropisomer of gossypol as male oral human contraceptive assisted the development of modified gossypol derivatives with new medical applications (Qian and Wang, 1984; Waites *et al.*, 1998). Possessing pharmacological activities especially pure (*R*)-gossypol is now used in phase II clinical trials of the pharmaceutical industry (Bauer *et al.*, 2005).

Protecting the plant from insect herbivores and pathogen attacks the effects of the gossypol atropisomers and other related terpenoid aldehydes like hemigossypolone and the heliocides are still under investigation (Bell, 1969; Elliger *et al.*, 1978; Stipanovic *et al.*, 2008). Since the times of establishing the basic procedure for the isolation of gossypol and related compounds from seed kernels in 1915 by Withers and Carruth some refinements in the method have been published (Withers and Carruth, 1915; Adams *et al.*, 1960; Cai *et al.*, 2004). A considerable variation in the atropisomer ratio of 671 different accessions of *Gossypium barbadense* L. was examined by preparing (*R*)-2-amino-1-propanol-derivatized, diastereoisomeric gossypol Schiff´s base sample mixtures for high performance liquid chromatography (HPLC) separation and quantification (Stipanovic *et al.*, 2009). Chiral HPLC was used recently for the first direct determination of the enantiomeric ratio of gossypol enantiomers in seeds, flowers, and roots in a number of cultivar samples of different *Gossypium* species (Cass *et al.*, 2004).

The increasing pharmacological importance of gossypol and the importance of the phytochemical composition of the PGs for pathogen protection of a plant whose products are most widely used as natural fiber cloth prompted us to combine an array of procedures and

methods to develop a fast approach for the detection and quantification of compounds in the PGs of *G. hirsutum*.

The first part of this work reports LDI-MSI of pigment glands of *G. hirsutum* and its improved evaluation by exploiting spatial segmentation methods based on using edge-preserving image denoising and clustering. The second part starts with a LMD-based isolation of PGs of *G. hirsutum* for a qualification of the terpenoid aldehydes detectable. Furthermore laser-microdissected PGs were used for the quantification of hemigossypolone and gossypol via ultra performance liquid chromatography mass spectrometry (UPLC-MS) combined with an investigation to check the minimum number of laser-microdissected PGs necessary for the determination of the phytochemical composition of PGs. A determination of the gossypol enantiomer ratio by a combination of high performance liquid chromatography mass spectrometry (HPLC-MS) and capillary electrophoresis (CE) (Ritter *et al.*, 2010).
The workflow of this study is presented in Figure 1/2.

RESULTS

Qualitative analysis of gossypol and related secondary plant metabolite compounds using LDI-MSI and edge-preserving image denoising

The ease with which flavonoids of *Arabidopsis thaliana* and especially biflavonoids of highly specialized plant tissue of *Hypericum perforatum* have been analysed using LDI-MSI (Hölscher *et al.*, 2009) encouraged us to study the phytochemical content of further plants possessing complex secretory structures. Using the state-of-the-art mass spectrometer Ultraflex III® achieving high lateral resolution of 20 µm, we were able to detect gossypol in the PGs of leaves of *Gossypium* plants. LDI-MSI allowed gossypol (*m/z* 517.7, $[M- H]^-$) to be detected in the crimson coloured PGs by superimposing the images of bright field microscopy (BF microscopy) and LDI-MSI as presented in Figure 3. The identity of gossypol was confirmed by obtaining CID mass spectra of the reference compound and the sample (Suppl. Fig. 1). Additionally there are more masses detectable in the gossypol region which can be aligned with phytochemical compounds isolated from *Gossypium* species before (Stipanovic *et al.*, 1977; Bell *et al.*, 1978; Stipanovic *et al.*, 2006). Signals showing a value of *m/z* 409 are attributable for the heliocide compounds of the H-type. Additionally signals for monomethylated heliocides (B-type) of *m/z* 423 are detectable. Hemigossypolone provides a value of *m/z* 273. The value of *m/z* 531.79 allowed methoxygossypol to be detected in the PGs. A signal typical for 6,6´-dimethoxygossypol was found in this region additionally. The images constructed for the measured part of the leaf were composed of approximately 10887 pixels. The spatial resolution of 20 µm and a frequency of 50 Hz of the Nd:YAG laser allowed measurement in a reasonable time span of 9 h. All the compounds were found to be localized in the pigment glands by performing spatial segmentation on the data sets and searching for *m/z* values with high signal intensities in these regions (Alexandrov *et al.*, 2010).
The processing of the *G. hirsutum* LDI-MSI dataset by spatial segmentation further reveals that the regions of the pigment glands, shown in Figure 4 as red coloured areas, are

surrounded by always an identical phytochemical content, highlighted in yellow. This very interesting information was only possible by the employed data processing steps.

Quantitative analysis of gossypol by LMD, UPLC-MS, HPLC-MS, and CE

Following the successful harvest of internal secretory cavities from leaves of *Dilatris pillansii* (Haemodoraceae) (Hölscher and Schneider, 2007) leaves of *G. hirsutum* provided a sufficient amount of laser-microdissected PGs (Stanford and Viehoever, 1918; Boatner *et al.*, 1946). No embedding material was required to dissect PGs of the plant material, which was simply fixed between a thin glass slide and a specially manufactured metal frame. The PGs were collected in a lid of a pcr cap using gravity. Repeated application of this technique on parts of fresh leaves of *G. hirsutum* provided sufficient material for the analysis of the phytochemical profile of PGs and for the determination of the concentration of gossypol. The easy UPLC-MS depending detection of hemigossypolone and its good solubility and stability in methanol allowed us to tackle the task of the determination of the minimum number of PGs necessary to achieve a reliable quantification of the phytochemical composition of the PGs. UPLC MS runs of the methanol-extracted samples of laser-microdissected PGs revealed signals for gossypol and its methylated derivatives methoxygossypol and 6,6'-dimethoxygossypol. Additionally the results were confirmed by using reference compounds of gossypol (Sigma-Aldrich), hemigossypolone, the heliocides H_1 to H_4 and heliocide B_1 (R.D. Stipanovic). The compounds were identified by their retention times and by UPLC-MS/MS measurements with the exception of heliocide B_1, which was not definitely assignable to the series of heliocide B-type candidates in the spectrum (Fig. 2). As two compounds were available at high purity (gossypol and hemigossypolone) we were able to quantify them even at single cell amounts (Table 1). A measurement series of 1, 3, 5, 7 and 10 laser-microdissected PGs with at least a triplicate for each laser-microdissected preparation were applied. A linear calibration grade of hemigossypolone with values of 0.1 µg/mL, 0.25 µg/mL, 0.5 µg/mL, 0.75 µg/mL, 1 µg/mL, 2.5 µg/mL, 5 µg/mL and 7.5 µg/mL was helpful to measure a mass of 67.0 ± 13.1 ng of this secondary metabolite for even one PG and 46.5 ± 7.8 ng for gossypol (Tab. 1) . The similar amounts were obtained from polled cells. From microscopy data the average diameter of the almost globular-shaped pigmented cells was determined (80 µm), which allows for molar concentration calculation. For individual cells the value was 920 nM and for pooled sampled was very similar (Table 1). A calculation of the number of pigmented cells of a young leaf revealed a total sum of approximately 2300 PGs per leaf with a density of almost 4 PGs / mm^2. The usage of the mass of the young leaf (68.345 mg) allows the determination of the percentage of mass of gossypol (0.16 %; 1.6 g/kg) and hemigossypolone (0.23 %; 2.3 g/kg) of the leaf material. The values show in the case of gossypol and hemigossypolone the similarity of the amount of these plant secondary metabolites with published results (Stipanovic *et al.*, 1988). Stipanovic et al. detected for the leaves of five different cotton varieties 0.08 – 0.5% for hemigossypolone and 0.04 – 0.1% for gossypol.

Finally the acidic extraction of the phytochemical content of PGs according to the official EU method of gossypol determination (European Commission, 1972) revealed in the case of gossypol only a yield of 18% and in the case of hemigossypolone a yield of 23% of the

amount of the secondary metabolites detectable with the UPLC MS data yields of the MeOH-based extraction method of laser-microdissected PGs.
Different approaches for the determination of the ratio of gossypol enantiomers and their differences in parts of cotton plants were published recently (Cass *et al.*, 2004; Stipanovic *et al.*, 2009). One of the prominent peaks in the HPLC chromatogram (data not shown) of the laser-microdissected PGs identified as gossypol, showing the characteristic masses (*m/z*) of 519 and 501 in positive mode, retention time (8.11 min) and UV spectrum were the same as of the reference compound. A chiral separation as for the reference compound was achieved in the fraction of the HPLC eluate (7.90-8.40 min) analyzed by CE (Fig. 5). The ratio of the two isomers in the laser-microdissected PGs samples of young leaves from *Gossypium. hirsutum* L. ”Deltapine cala 90” was 4.8:1.

DISCUSSION

First reasons for the isolation of pigment glands from economically valuable parts of cotton seed were due to public health issues. Health protection of humans and cattle demanded the removal of secondary metabolites like gossypol assumed to be toxic (Withers and Carruth, 1915; Boatner and Hall, 1946). A recently published *in situ* cell-by-cell imaging using laser ablation electrospray ionization (LAESI) MS excellently showed the metabolite concentration distributions of ablated oil glands from *Citrus aurantium* (Shresta *et al.*, 2011). Here the quantification of hemigossypolone and gossypol were used to show the possibility to determine the reproducible determination of the concentration of these secondary metabolites in even one PG. Furthermore the efficient UV absorption of an aromatic compound like gossypol and related compounds offer a direct imaging of the spatial distribution of these compounds in the highly specialized tissues. Needing no matrix minimizes sample preparation and is excluding all the disadvantages involved in the application of a matrix-demanding high lateral resolution measurement of MALDI MSI on plant material (Hölscher *et al.*, 2009) and is supporting the usefulness of advanced computational methods in analyzing large and complex MSI data sets by a procedure of edge-preserving image denoising and clustering (Alexandrov *et al.*, 2010). The high lateral resolution measurements of LDI MSI allow cellular features as small aromatic molecules to be observed. The achieved sensitivity is encouraging, individual PGs contain only ca 900 nM of gossypolone and ca 1 ng/laser spot was sufficient to obtain a strong signal in MSI-MS experiment, comparable or better to other methods for single cell analysis (Svatos, 2011). PGs and their direct surrounding are places of high concentration of gossypol and related compounds. These compounds in other regions are not detectable. By this procedure with its high sampling efficiency and spatial resolution important assumptions of the places of formation seem to be possible. No gossypol or related secondary metabolites were detected outside the region of the PGs using LC-MS analyses, which (especially their glandular epithelial cells) can be regarded as the centres of the biosynthesis of these secondary metabolites.
The qualification and the quantification of the ingredients of the phytochemical profile of PGs of cotton are not restricted to gossypol. Related compounds like the methylated gossypol derivatives should be treatable in the same way and differences of all possible ratios of the abovementioned applications should be quantifiable (McCormick, 1982; Opitz *et al.*, 2008).

Further research about gossypol and its related compounds resulted in a broad field of pharmacological applications stimulating intensified investigations. Especially the differences of biological activities of the gossypol enantiomers demanded the employment of sophisticated methods measuring its enantiomeric ratios. In all applications derivatizations to synthezise diastereoisomeric mixtures with separations on an achiral C18 column were necessary until a direct chiral HPLC method was established (Cass *et al.*, 2004). In all cases for the determination of gossypol enantiomer ratio in cotton plants intact parts of heterogeneous plant tissue were analyzed. The only to well known fact of the cell specific distribution of gossypol imbued us to use LMD as a fast tool to harvest PGs of cotton for the first time. A fast and gentle extraction of the secondary metabolites from the PGs was followed up by a purification of gossypol via UPLC-MS and the measurement of the enantiomeric ratio of this purified dimeric sesquiterpene using CE. Due to this powerful combination of tools for analyzing samples of a well-arranged, fortunately limited number of PGs a broad array of pigment glands either from different parts of the plant or from different cultivars or from plants raised under different nutritional value conditions or from pathogen-plant interactions can be performed.

The comparison of a hot extraction of terpenoid aldehydes used in the official EU method of gossypol determination with the cold organic solvent extraction of the plant secondary metabolites from laser-microdissected PGs showed the limited solvent power of the hot acidic extraction and an advantage of the cold methanolic extraction. The questionable specifity of the spectrophotometrical determination of gossypol as dianilino-gossypol (European Commission, 1972; Alexander *et al.*, 2008) in comparison with higher degrees of specificity offering HPLC methods and furthermore UPLC MS procedures is a point of recent discussions (Stipanovic *et al.*, 1988; Alexander *et al*., 2008).

Ongoing breeding programs yielding many varieties of cotton plants by selective breeding and hybridization of various species including wild cotton varieties can benefit from the proposed procedure of a specific analytical method of plant secondary metabolites to generate (transgenic) cotton cultivars, resistant to diseases and drought-tolerance.

MATERIALS and METHODS / EXPERIMENTAL PROCEDURES

Plant material

Plants *G. hirsutum* L. of a single variety, “Deltapine cala 90” (Delta and Pine Company – Hollandala, MS, USA) were grown in soil (Klasmann Erden clay substrate (Art. Nr. 4230, Klasmann-Deilmann GmbH, Geeste, Germany, http://www.klasmann-deilmann.com) and Lettischer Weisstorf / fibric peat (Letta Flor, Nordtorf Group, Aknistes, Latvia, http://www.nordtorf.eu) (1:1) and 1g/L Osmocote exact 16-11-11 (Scotts Germany GmbH, Nordhorn, Germany, http://www.scottsinternational.com). Plants were established in a growth chamber under high light intensity with high pressure sodium vapour lamps (Eye Sunlux Ace NH 360 FLX, Iwasaki Electric Co. Ltd., Tokyo, Japan, http://www.eye.co.jp) [749 μmol $(m^2)^{-1}$ s^{-1} of photosynthetically active radiation], 28°C/23°C (day/night), a 15-h light period, and 65% relative humidity.

Laser microdissection of pigment glands

Using the procedure described by Hölscher and Schneider (2007), leaves of *G. hirsutum* were cut in small pieces (length 1 cm) and fixed between a thin glass slide (0.6 mm thickness, Menzel Gläser, Braunschweig, Germany, http://www.menzel.de) and a specially manufactured metal frame. The nitrogen solid state diode laser of the Leica LMD6000 system (Leica Microsystems, Wetzlar, Germany, http://www.leicamicrosystems.com) with a short pulse duration (355 nm) enables the precise and fast cutting of the SC. Microdissection was performed at 10x (HC PL FLUOTAR 10x/0.30 Leica) and 20x (HCX PL FLUOTAR L20x/0.40 Leica) magnification. The laser-microdissected PGs were collected in the lid of a 0.5ml pcr-cup (Greiner Bio-One GmbH, Solingen-Wald, Germany, http://www.gbo.com) by the Leica LMD6000 system. The microtube was shortly centrifuged (1000 g, 25°C, 1 min) to settle the contents. 50 µl of methanol was added, the mixture was shaken for 30 minutes in a thermomixer at room temperature (Thermomixer comfort, Eppendorf AG, Hamburg, Germany, http://www.eppendorf.de) and the supernatant carefully transferred to a 0.1 ml micro inlet of a 1.5 ml short thread vial (Carl Roth GmbH + Co KG, Karlsruhe, Germany, http://www.carl-roth.de) for UPLC MS analysis as described below. In the case of the hot acidic extraction a mixture of 45 µl dimethylformamide (Sigma-Aldrich Chemie GmbH, Steinheim, Germany, http://www.sigmaaldrich.com) and 5 µl acetic acid (Carl Roth GmbH + Co KG, Karlsruhe, Germany) were added to the laser-microdissected PGs. The sample was shaken for 30 min at 99 °C in a thermomixer. After that the procedure followed the protocol described for the methanolic extraction of the PGs.

Fixation of plant material for Ultraflex III mass spectrometer

Small parts of leaves of *G. hirsutum* (0.5 x 0.5 cm) were fixed on carbon conductive adhesive tape (Plano, http://www.plano-em.de), which was in turn fixed on an ITO slide (Bruker Daltonic, http://www.bdal.de). The granular particles of the marks of a Staedtler triplus gel-liner (silver, 0.4 mm; Staedtler-Mars, Nürnberg, Germany, http://www.staedtler.com) were helpful to define the samples position and to alleviate the laser positioning during LDI-MSI.

LDI-MSI on the Ultraflex III® mass spectrometer

An Ultraflex III® mass spectrometer, equipped with a Nd:YAG laser, (Bruker Daltonics) was used for the analysis. All spectra were measured in negative reflectron mode. To measure the pixels of ca 20 x 20 µm, the minimum laser focus setting was used. For each raster point, a spectrum was accumulated with 300 laser shots and fixed laser intensity. For image reconstruction, FlexImaging version 2.0 software (Bruker Daltonics) was used. For LDI-MSI of the PGs, 10887 raster positions were measured. All signals with a mass range of *m/z* 100-300 were recorded. (300 laser shots per pixel were collected from each position, and then the software calculated the average mass spectrum.)

UPLC-MS

UPLC/ESI-MS was performed using the Ultimate 3000 series RSLC (Dionex, Sunnyvale, CA, USA) system and the Orbitrap XL mass spectrometer (Thermo Fisher Scientific, Bremen, Germany). UPLC was accomplished on an Acclaim C18 Column (150 × 2.1 mm, 2.2 µm; Dionex). A binary solvent system was used: solvent A consists of water with 0.1% formic acid and solvent B consists of acetonitrile with 0.1% formic acid. The flow rate was constantly kept at 300 µl min^{-1}. One µl were injected into the UPLC gradient system started with 5% B and linearly increased to 98% B in 28 min and was then held for 3 min, before being brought back to the initial conditions and held for 5 min for re-equilibration of the column for the next injection. ESI source were set to 275°C for capillary temperature and -35 V for capillary voltage. Full scan mass spectra were generated using 30,000 resolving power measured in negative mode using the Orbitrap analyzer. Identification was obtained by injection of the reference compounds gossypol (Sigma Aldrich), hemigossypolone, heliocide H_1, H_2, H_3 and H_4 (R.D. Stipanovic, Southern Plains Agricultural Research Center, College Stations, Texas) and comparisons of retention times of reference compounds with heliocides. Quantitative determination of hemigossypolone and gossypol was performed by generating a set of calibration solutions (0.1, 0.25, 0.5, 0.75, 1, 2.5, 5, 7.5 µg ml^{-1}). XCALIBUR (Thermo Fisher Scientific, Waltham, MA, USA) software was applied to analyze obtained data.

HPLC-MS and CE

An Acquity UPLC system by Waters (Waters Corporation, Milford, USA, http://www.waters.com) was used consisting of a binary pump (BSM), an autosampler (SM; injected volume: 2 µL for standards, 7.5 µL for samples), a column oven (CM) set at 40 °C, a diode array detector (PDA) scanning from 190 to 500 nm, and a triple quadrupole mass spectrometer (Acquity TQD) with electrospray interface operating in positive mode. Column: Acquity BEH Shield RP18, particle size 1.7 µm, internal diameter 2.1 mm, length 50 mm. Eluents: A: water (LC-MS-grade, Optigrade, LGC Standards, Wesel, Germany, http://www.lgcstandards.com) with 0.1% formic acid (LC-MS-grade, Fluka/Sigma Aldrich, Steinheim, Germany); B: acetonitrile (LC-MS-grade, Mallinckrodt Baker, Deventer, The Netherlands, http://www.mallbaker.com) with 0.1 % formic acid. Gradient: 0 min: 40% B; 10 min: 100% B, curve 8, i.e. a concave gradient; holding 100% B for 2 min; back to the initial 40% B within 0.5 min and re-equilibration with 40% B for 1.5 min. Flow: 0.6 mL/min. Detection wavelength: 254 nm.

The mass spectrometer was tuned using a solution of pure gossypol (Sigma Aldrich, Steinheim, Germany) dissolved in DMF. The resulting parameters were: capillary voltage 3.0 kV; cone voltage 52.0 V for m/z 501 and 21 V for m/z 519; extractor voltage 3.0 V; RF voltage 0.10 V; source temperature 150 °C; desolvation temperature 450 °C; cone gas (nitrogen) flow 50 L/h; desolvation gas (nitrogen) flow 900 L/h.

The mass traces of *m/z* 501.25, and 519.28 were recorded in single ion monitoring (SIM) mode. Peak identity was confirmed by comparison of retention time and UV spectra of pure gossypol.

All enantioselective separations were carried out on a Beckman P/ACE MDQ capillary electrophoretic system (Beckman Coulter Inc, Fullerton, CA, USA, http://www.beckmancoulter.com) equipped with a photo diode array detection system. The scan range was 190 to 600 nm. All electropherograms were recorded at 244 nm. Data was processed on an IBM personal computer with Beckman 32 Karat version 7.0. Uncoated fused-silica capillaries of 375 µm O.D. x 50 µm I.D. were obtained from Beckman and cut to 70.2 cm (effective length 60.0 cm). The capillary was first washed by 20 p.s.i. pressure with 0.25 mol/L NaOH for 15 min and finally with purified water for 10 min. For the running buffer boric acid (Merck, Darmstadt, Germany) and anhydrous sodium tetraborate ($Na_2B_4O_7$) (KMF (KMF Laborchemie Handels GmbH, Lohmar, Germany, http://www.kmf1.de) of c = 200 mM and (2-hydroxypropyl)-γ-cylodextrin (Fluka/Sigma Aldrich, Steinheim, Germany) of c = 2 mM was used. Between each run with 0.25 mol/L NaOH for 3 min and equilibrated with the running buffer for 5 min. The capillary temperature was set to 20 °C and the applied voltage was 20 kV. Samples were injected hydrodynamically (0.4 p.s.i.) for 4 s.
Peak identity was confirmed by comparison of retention time and UV spectra of pure gossypol.
Pure gossypol was dissolved in DMF (c = 1.2 mg/L) and diluted with DMF to a concentration of 0.051 mg/L. The laser dissected material was suspended in 100 µL DMF and sonicated for 10 min and centrifuged. The supernatant was injected into the HPLC system. For the CE analysis, the eluted solvent of the HPLC was collected from 7.9 to 8.2 min. The solvent was reduced to about 20 µL at 40 °C under a gentle nitrogen flow. This solution was injected into the CE system.

Spatial segmentation with edge-preserving image denoising

The recently published pipeline was exploited for the spatial segmentation of MALDI-imaging data (Alexandrov *et al.*, 2010) which is developed taking into account the important issue of pixel-to-pixel variability. The pipeline consists of three steps.
Peak picking**:** Given a pre-processed LDI-MSI data set (after spectra normalization, baseline correction, and binning), first of all the data set is reduced by performing peak picking on the full data set. Ten peaks with Orthogonal Matching Pursuit algorithm searching for peaks of the Gaussian shape were selected for each 10^{th} spectrum (Denis *et al.*, 2009). The Gaussian width was automatically estimated by a simple algorithm considering several large peaks. This spectrum-wise peak picking assigns to each *m/z*-value a number of spectra in which this *m/z*-value was selected as a peak. Then, 100 the most frequent peaks were taken. Often several *m/z*-values close to the center peak *m/z*-value are selected, because the Gaussian shape is just an approximation of a real peak shape and probably because of small mass shifts (the mass recalibration for each spectrum usually is not used in MSI). In order to prevent this redundant selection of several masses per peak, the peak picking was improved by aligning the selected *m/z*-values "moving them" uphill the data set mean spectrum so that they get in the local maxima of the mean spectrum.
Edge-preserving denoising: As discussed in Alexandrov *et al.*, 2010, MALDI-imaging data sets suffer from the strong pixel-to-pixel variability leading to noise in *m/z*-images and in the segmentation map as well. The same is true for an LDI-MSI data set. In order to reduce this

variability, image denoising was applied to each of the *m/z*-images selected after the peak picking. Spatially-adaptive edge-preserving denoising was exploited in order not to smooth out small spatial details. The number of clusters (colors) was selected manually as the most representative after considering maps with 2-10 clusters.
Clustering: After all selected *m/z*-images are processed with image denoising, the resulted spectra were clustered, i.e. group into several groups by their similarity, so that the spectra with similar peaks are put in one group. Finally, the pixels corresponding to spectra of one group are colored with the same color that results in a segmentation map.

Search for masses and their visualization

In this study, segmentation maps were used to get an overview of the data set, and, mainly, to find masses corresponding to regions of interest, that was done as follows. After examining the segmentation map, one color was selected manually. The regions corresponding to this color are taken as spatial mask. Then, the correlation of its *m/z*-image with the mask was calculated for each *m/z*-value (from the original data set, before peak picking). High correlation points out those pixels of the image inside the regions of interest have high intensity and other pixels have low intensity. The *m/z*-image were considered for those the correlation was significant (p-value is less than 0.05) and the correlation coefficient was larger than 0.2. The resulted *m/z*-images have been processed with edge-preserving denoising (the same used in the segmentation) to remove the noise and make their structure more visible.

ACKNOWLEDGEMENTS

We are grateful to Robert D. Stipanovic, USDA-ARS, Southern Plains Agricultural Research Center (College Stations, Texas) for the generous gift of authentic samples of hemigossypolone, heliocide H_1, H_2, H_3, H_4 and B_1. We wish to thank Tamara Krügel and the greenhouse team at the Max Planck Institute (Jena, Germany) for raising the *Gossypium* plants. The authors gratefully acknowledged Emily Wheeler for editing help and Daniel Veit for constructing special slides for LMD.

Tables and figures captions

Table 1. Determination of the amount of hemigossypolone and gossypol detectable in a measurement series of 1, 3, 5, 7, and 10 pigment glands of cotton leaves.

number of PGs	hemigossypolone (ng) total ± SDEV	hemigossypolone (ng) per PG ± SDEV and molar concentration per pigment gland (nM)[y]		gossypol (ng) total ± SDEV and	gossypol (ng) per PG ± SDEV molar concentration per pigment gland (nM)[y]	
1	67 ± 13.1	67 ± 13.1	912 ± 178	46.5 ± 7.8	46.5 ± 7.8	334 ± 56
3	176.5 ± 38.1	58.8 ± 12.7	800 ± 173	122.4 ± 20.7	40.8 ± 6.9	293 ± 50
5	378.5 ± 7.9	75.7 ± 2.6	1030 ± 35	262.6 ± 44.3	52.5 ± 8.9	378 ± 64
7	478.5 ± 6.3	68.4 ± 2.1	931 ± 29	332.0 ± 56.0	47.4 ± 8.0	341 ± 58
10	692.0 ± 11.0	69.2 ± 3.7	942 ± 50	480.1 ± 81.0	48.0 ± 8.1	345 ± 58

y) based on average PG diameter 80 μm

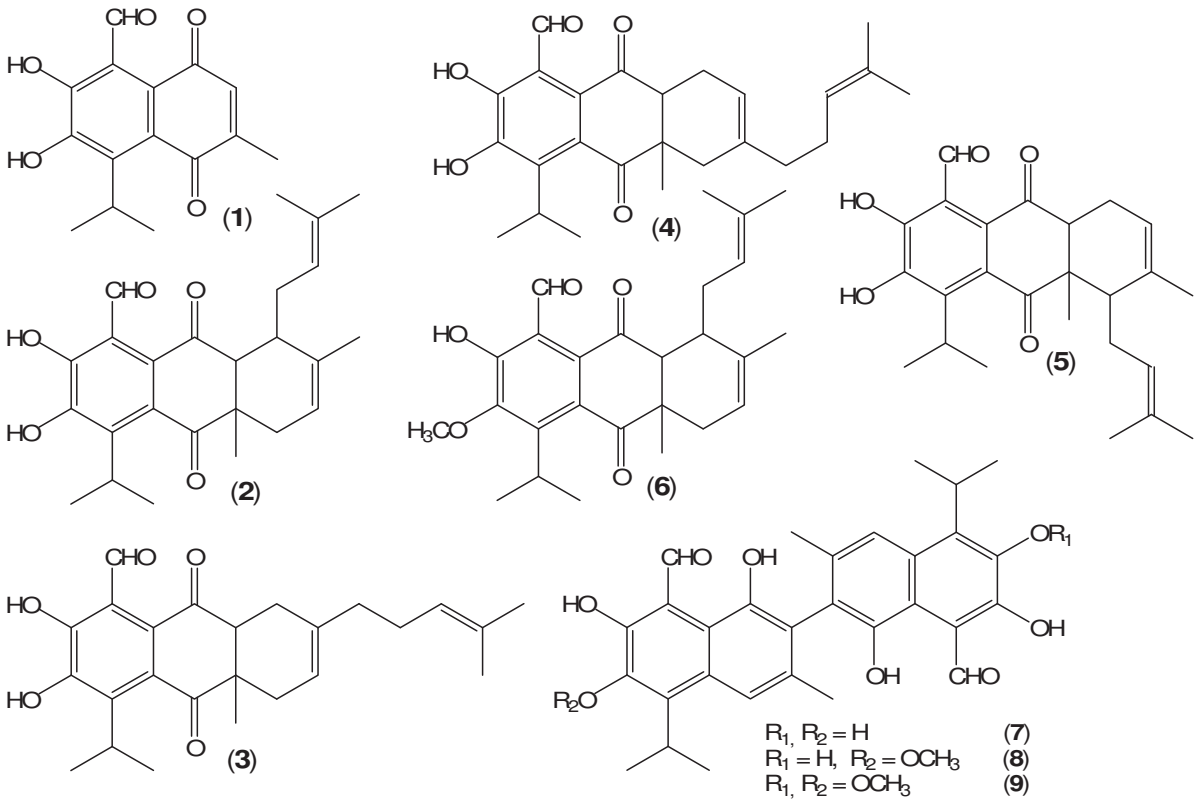

Figure 1. Chemical structures of identified compounds.

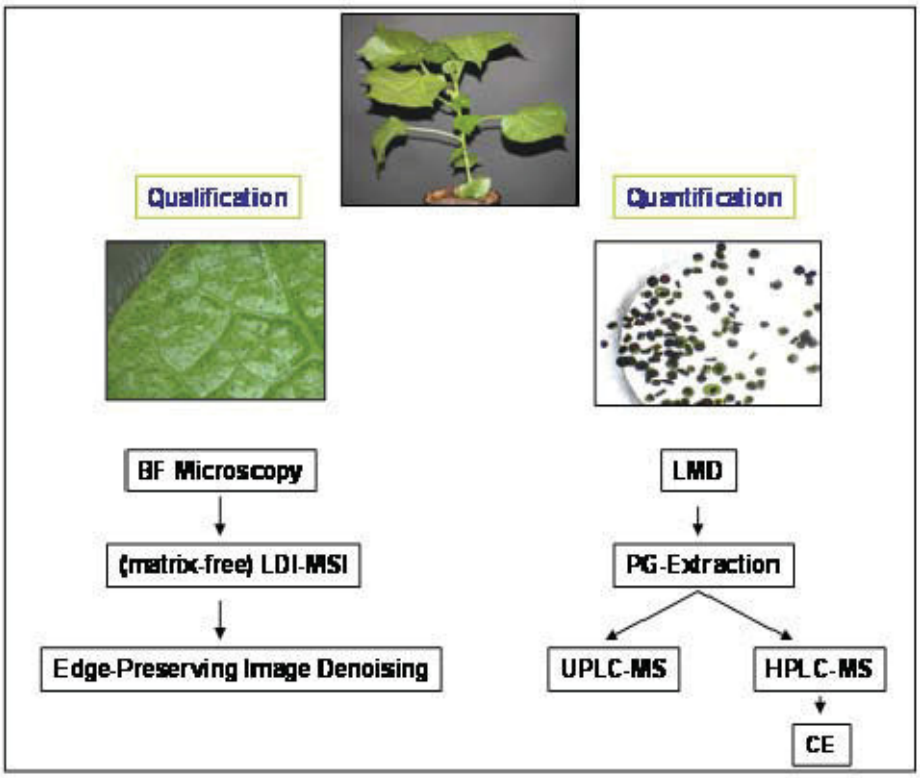

Figure 2. Workflow of the qualitative and quantitative analysis of secondary metabolites from leaves of *G. hirsutum*.

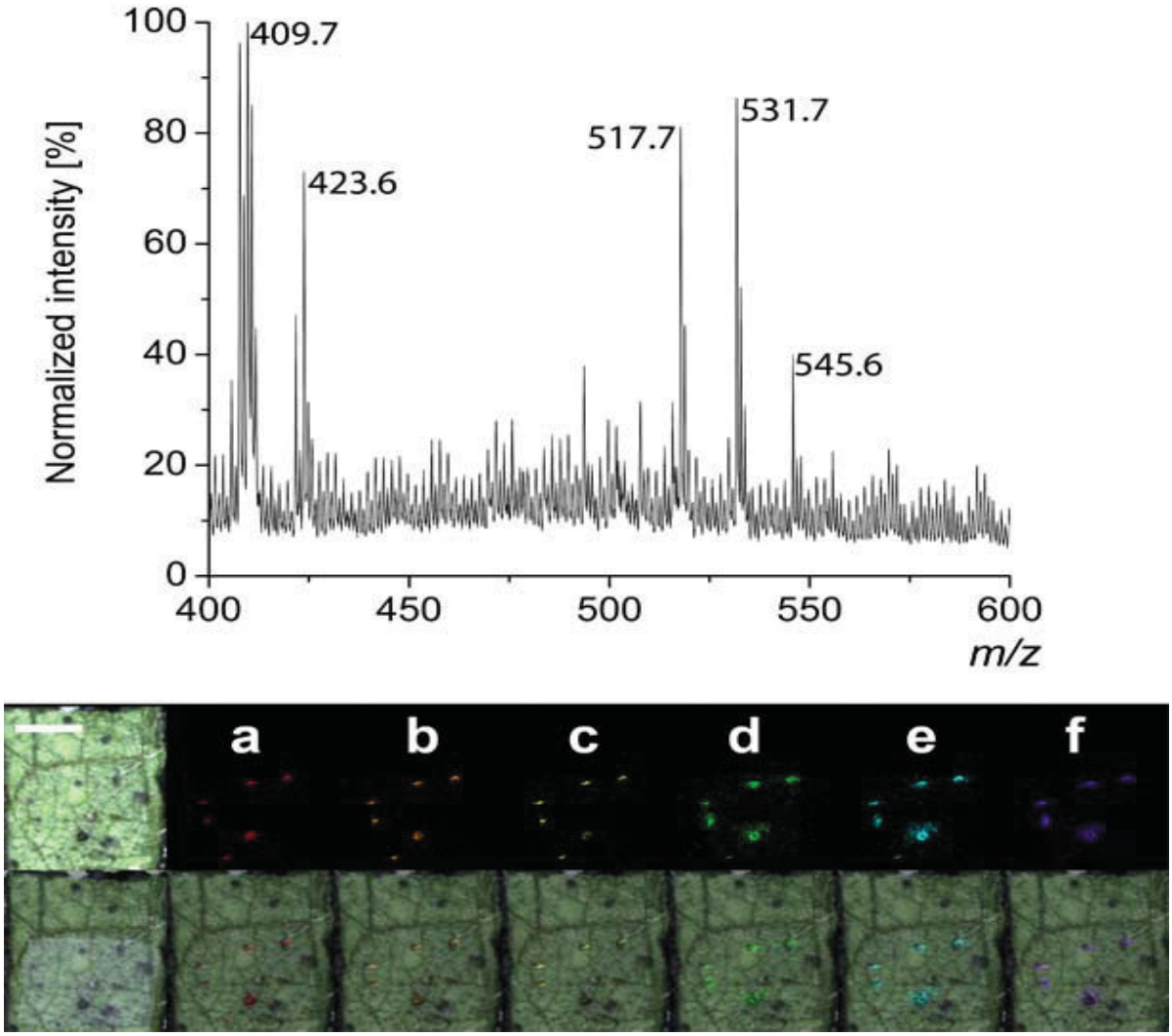

Figure 3. A section of average MALDI-TOF/MS spectra obtained from pigment glands occurring on young *G. hirsutum* leaves (upper panel). Microphotography of the cotton leaf imagined with a scale bar and MSI images platted at *m/z* of individual metabolites: gossypol (**a**, *m/z* 517, minimum intensity 15 %), methoxygossypol (**b**, *m/z* 531, 15 %), 6,6'-dimethoxygossypol (**c**, *m/z* 545, 15 %), hemigossypolone (**d**, *m/z* 273, 55 %), heliocide H-type compounds (e, *m/z* 409, 30 %), heliocide B-type compound (**f**, *m/z* 423, 30 %) are shown in middle panel. The overlays of the leaf micrograph and individual MSI images are shown in the low panel. Scale bar = 500 μm.

Figure 4. Segmentation map with two clusters. One cluster (red) corresponds to the pigment glands, the other one (yellow) is covering the proximate surrounding area of the pigment glands.

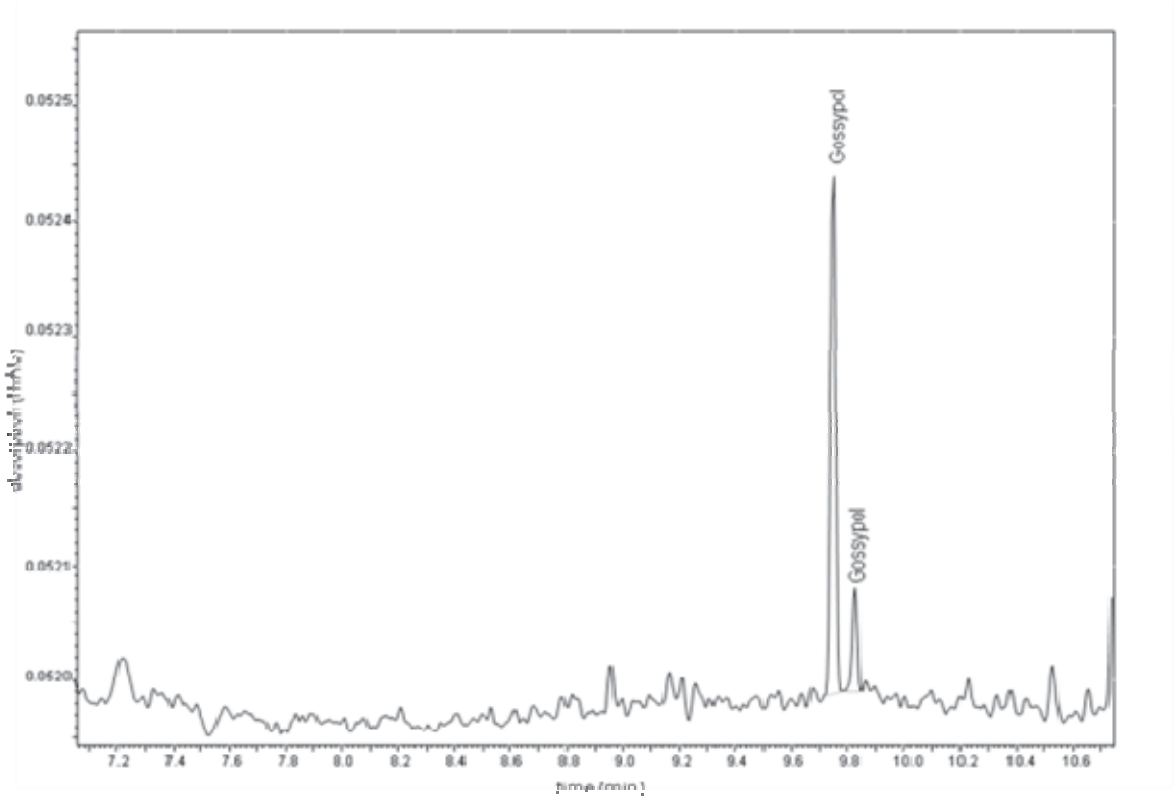

Figure 5. Enantioresolution of gossypol atropisomers on a Beckman P/ACE MDQ capillary electrophoretic system with detection at 244 nm. Laser-microdissected sample from pigment glands of *G. hirsutum*.

REFERENCES

Alexander, J., Benford, D., Cockburn, A., Cravedi, J.-P., Dogliotti, E., Di Domenico, A., Férnandez-Cruz, M.L., Fürst, P., Fink-Gremmels, J., Galli, C.L., Grandjean, P., Gzyl, J., Heinemeyer, G., Johansson, N., Mutti, A., Schlatter, J., van Leeuwen, R., Van Peteghem, C. and Verger, P. (2008) Scientific Opionion - Gossypol as undesirable substance in animal feed – Scientific Opinion of the Panel on Cotaminants in the Food Chain. *The EFSA Journal* **908**, 1-55.

Adams, R., Geissman, T.A. and Edwards, J.D. (1960) Gossypol, a pigment of cottonseed. *Chem. Rev.* **60**, 555-574.

Alexandrov, T., Becker, M., Deininger, S.O., Ernst, G., Wehder, L., Grasmair, M., von Eggeling, F., Thiele, H. and Maass, P. (2010) Spatial segmentation of imaging mass spectrometry data with edge-preserving image denoising and clustering. *J. Proteome Res.* **9**, 6535-6546.

Bauer, J.A., Trask, D.K. and Kumar, B. (2005) Reversal of cisplatin resistance with a BH3 mimetic, (-)-gossypol, in head and neck cancer cells: role of wild-type p53 and Bcl-x_L. *Mol. Cancer Ther.* **4**, 1096-1104.

Bell, A.A. (1969) Phytoalexin production and Verticillium wilt resistance in cotton. *Phytopathology* **59**, 1119-1127.

Bell, A.A., Stipanovic, R.D., O'Brien, D.H. and Fryxell P.A. (1978) Sesquiterpenoid aldehyde quinones and derivatives in pigment glands of Gossypium. *Phytochemistry* **17**, 1297-1305.

Bell, A.A. and Stipanovic, R.D. (1986) Biochemistry of disease and pest resistance in cotton. *Mycopathologia* **65**, 91-106.

Boatner, C.H. and Hall, C.M. (1946) Selective hydrogenation in the preparation of purified oleic acid from animal fats. Elimination of extremely low crystallization temperatures. *J Am Oil Chem Soc* **23**, 128-133.

Boatner, C.H., Hall, C.M., O´Connor, R.T. and Castillon, L.E. (1947) Pigment glands of cottonseed. III. Distribution and some properties of cottonseed pigments. *Bot Gaz* **109**, 108-120.

Cai, Y., Zhang, H., Zeng, Y., Mo, J., Bao, J., Miao, C., Bai, J., Yan, F. and Chen, F. (2004) An optimized gossypol high-performance liquid chromatography assay and its application in evaluation of different gland genotypes of cotton. *J. Biosci.* **29**, 67-71.

Cass, Q.B., Oliveira, R.V. and de Pietro, A.C. (2004) Determination of gossypol enantiomer ratio in cotton plants by chiral higher-performance liquid chromatography. *J. Agric. Food Chem.* **52**, 5822-5827.

Denis, L., Lorenz, D.A. and Trede, D. (2009) Greedy solution of ill-posed problems: error bounds an exact inversion. *Inverse Probl* **25**, 115017 (24pp) ***[artnum 115017].***

Elliger, C.A., Chan, B.G. and Waiss, A.C. (1978) Relative toxicity of minor cotton terpenoids compared to gossypol. *J. Econ. Entomol.* **71**, 161-164.

Essenberg, M., Grover, P.B. and Cover, E.C. (1990) Accumulation of antibacterial sesquiterpenoids in bacterially inoculated *Gossypium* leaves and cotyledons. *Phytochemistry* **29**, 3107-3113.

European Commission (1972). Third Commission Directive 72/199/EEC of 27 April 1972 establishing Community Methods of Analysis for the official Control of Feedingstuffs (OJ L123, 29.5.1972, p.6).

Freedman, T.B., Cao, X., Oliveira, R.V., Cass, Q.B. and Nafie, L.A. (2003) Determination of the absolute configuration and solution confirmation of gossypol by vibrational circular dichroism. *Chirality* **15**, 196-200.

Fryxell, P.A. (1992) A revised taxonomic interpretation of *Gossypium* L. (Malvaceae). *Rheedea* **2**, 108-165.

Heinemann, M. and Zenobi, R. (2011) Single cell metabolomics. *Curr. Opin. Biotechnol.* **22**, 26-31.

Hölscher, D. and Schneider, B. (2007) Laser microdissection and cryogenic nuclear magnetic resonance spectroscopy: an alliance for cell type-specific metabolite profiling. *Planta* **225**, 763-770.

Hölscher, D., Shroff, R., Knop, K., Gottschaldt, M., Crecelius, A., Schneider, B., Heckel, D.G., Schubert, U.S. and Svatoš, A. (2009) Matrix-free UV-laser desorption/ionization (LDI) mass spectrometric imaging at the single-cell level: distribution of secondary metabolites of *Arabidopsis thaliana* and *Hypericum* species. *Plant J.* **60**, 907-918.

Jaroszewski, J.W., Strøm-Hansen, T., Hansen, L.L. (1992) Optical stability of gossypol. *Chirality* **4**, 216-221.

Kaspar, S., Peukert, M., Svatoš, A., Matros, A. and Mock, H.-P. (2011) MALDI-imaging mass spectrometry – an emerging technique in plant biology. *Proteomics* **11**, 1840-1850.

Kenar, J.A. (2006) Reaction chemistry of gossypol and its derivatives. *J Am Oil Chem Soc* **83**, 269-302.

Li, S.H., Schneider, B. and Gershenzon, J. (2007) Microchemical analysis of laser-microdissected stone cells of Norway spruce by cryogenic nuclear magnetic resonance spectroscopy. *Planta* **225**, 771-779.

Marchlewski, L. (1899) Gossypol, ein Bestandtheil der Baumwollsamen. *Adv. Synth. Catal.* **60**, 84-90.

McCormick, J.P. (1982) Secondary metabolites of gossypium – a biogenetic analysis. **ACS Symposium Series 189**, 275-300.

Opitz. S., Kunert, G. and Gershenzon, J. (2008) Increased terpenoid accumulation in cotton (*Gossypium hirsutum*) foliage is a general wound response. *J. Chem. Ecol.* **34**, 508-522.

Qian, S.Z. and Wang, Z.G. (1984) Gossypol: A potential antifertility agent for males. *Annu. Rev. Pharmacol. Toxicol.* **24**, 329-360.

Ritter, C., Zimmermann, B.F. and Galensa R. (2010) Chiral separation of (+)/(-)-catechin from sulfated and glucorinated metabolites in human plasma after cocoa consumption. *Anal Bioanal Chem* **397**, 723-730.

Schwartze, E.M. and Alsberg, C.L. (1923) Quantitative variation of gossypol and its relation to the oil content of cottonseed. *J Agric Res* **25**, 285-295.

Shresta, B., Patt, J.M. and Vertes, A. (2011) In situ cell-by-cell imaging and analysis of small cell populations by mass spectrometry. *Anal. Chem.* **83**, 2947-2955.

Stanford, E.E. and Viehoever, A. (1918) Chemistry and histology of the glands of the cotton plant, with notes on the occurrence of similar glands in related plants. *J Agric Res* **13**, 419-435.

Stansbury, M.F., Cucullu, A.F. and den Hartog, G.T. (1954) Cottonseed contents variation. Influence of variety and environment on oil content of cottonseed kernels. *J. Agric. Food Chem*. **2**, 692-696.

Stipanovic, R.D. Bell, A.A. and Lukefahr, M.J. (1977) 14 Natural insecticides from cotton (*Gossypium*), Hedin PA (Ed.), Host plant resistance. *American Chemical Society*, 197-214.

Stipanovic, R.D., Altman, D.W., Begin, D.L., Greenblatt, G.A., Benedict, J.H. (1988) Terpenoid aldehydes in upland cottons: analysis by aniline and HPLC methods. *J. Agric. Food Chem.* **36**, 509-515.

Stipanovic, R.D., Puckhaber, L.S., Reibenspies, J.H. and Williams, H.J. (2006) The absolute configuration of (-)-3-hydroxy-a-calacorene. *Phytochemistry* **67**, 1304-1308.

Stipanovic, R.D., López, J.D., Dowd, M.K., Puckhaber, L.S. and Duke, S.E. (2008) Effect of racemic, (+) and (-)- gossypol on survival and development of *Heliothis virescens* larvae. *Environmental. Entomol.* **37**, 1081-1085.

Stipanovic, R.D., Puckhaber, L.S., Liu, J. and Bell, A.A. (2009) Total and percent atropisomers of gossypol and gossypol-6-methl ether in seeds from pima cottons and accessions of *Gossypium barbadense* L. *J. Agric. Food Chem.* **57**, 566-571.

Sunilkumar, G., Campbell, L.M., Puckhaber, L., Stipanovic, R.D. and Rathore, K.S. (2006) Engineering cottonseed for use in human nutrition by tissue-specific reduction of toxic gossypol. *Proc. Natl. Acad. Sci. U.S.A.* **103**, 18054-18059.

Svatoš, A. (2010) Mass spectrometric imaging of small molecules. *Trends Biotechnol.* **28**, 425-434.

Svatoš, A. (2011) Single-cell metabolomics comes of age: new developments in mass spectrometry profiling and imaging. *Anal. Chem.* **83**, 5037-5044.

Thunig, J., Hansen, S.H. and Janfelt, C. (2011) Analysis of secondary plant metabolites by indirect desorption electrospray ionization imaging mass spectrometry. *Anal. Chem.* **83**, 3256-3259.

Waites, G.M.H., Wang, C. and Griffin, P.D. (1998) Gossypol: reasons for its failure to be accepted as a safe, reversible male antifertiliy drug. *Int. J. Androl.* **21**, 8-12.

Withers, W.A. and Carruth, F.E. (1915) Gossypol, the toxic substance in cottonseed meal. *J Agric Res* **5**, 261-288.

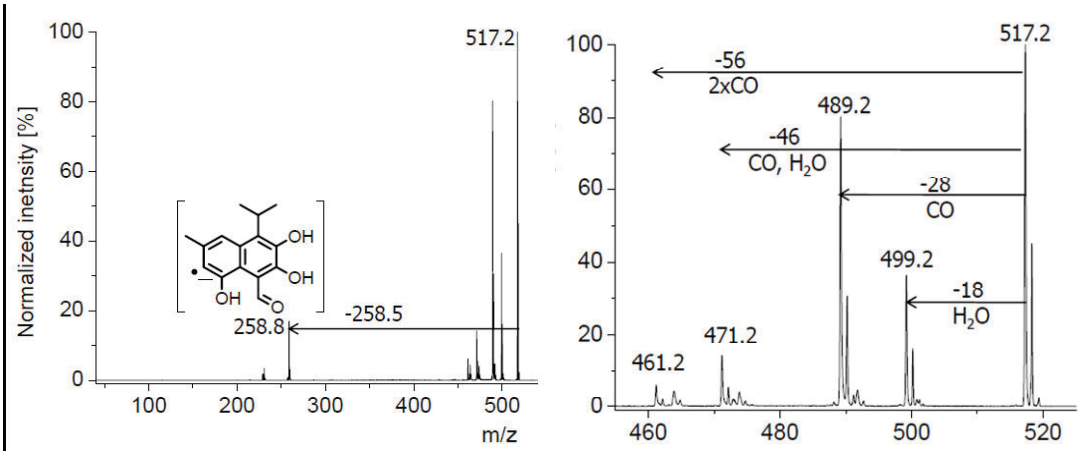

Suppl. Figure 1. TOF/TOF mass spectra of *m/z* 517 corresponding to gossypol. Characteristic fragments and losses are highlighted.

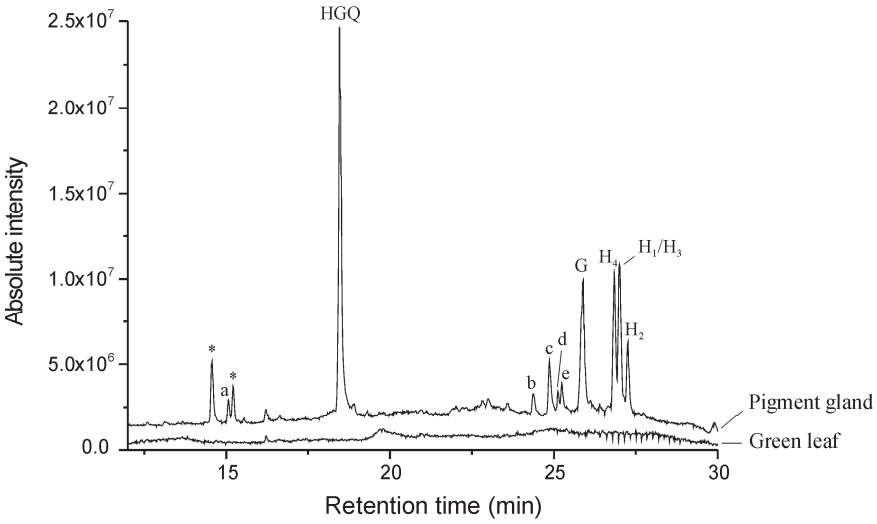

Suppl. Figure 2. UPLC/MS chromatogram of pigment glands and green leaf extracts of *G. hirsutum*. Peaks labelled with an asterisk were also detected in HGQ reference compound. Compounds represent further peaks have a m/z of (a) 271.0606, (b) 531.1649, (c) 423.2164, (d) 423.1809, (e) 423.2170. Compounds represent peaks c, d and e are heliocide B candidates. The mass deviation is – 0.47 ppm resp. 0.97 ppm.

Publication P13:

Phenalenone-type phytoalexins mediate resistance of banana plants (Musa spp.) to the burrowing nematode *Radopholus similis*

D. Hölscher, S. Dhakshinamoorthy, T. Alexandrov, M. Becker, T. Bretschneider, A. Bürkert, A. C. Crecelius, D. De Waele, D. G. Heckel, H. Heklau, C. Hertweck, M. Kai, K. Knop, C. Krafft, R. K. Madulla, C. Matthäus, J. Popp, B. Schneider, U. S. Schubert, R. Sikora, A. Svatoš, R. Swennen

Nature Chem. Biol. **2013**, in preparation.

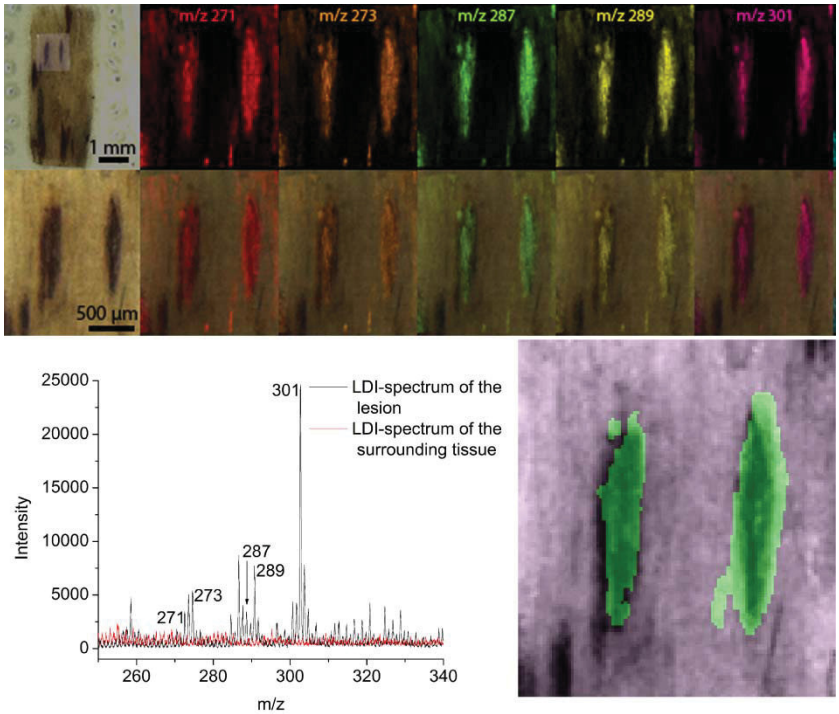

Journal:
Nature Chemical Biology

Phenalenone-type phytoalexins mediate resistance of banana plants (*Musa* spp.) to the burrowing nematode *Radopholus similis*

Dirk Hölscher[1,2,18*], Suganthagunthalam Dhakshinamoorthy[3,18], Theodore Alexandrov[4,5], Michael Becker[6], Tom Bretschneider[7], Andreas Buerkert[2], Anna C. Crecelius[8], Dirk De Waele[3], Annemie Elsen[9], David G. Heckel[10], Heike Heklau[11], Christian Hertweck[6], Marco Kai[12], Katrin Knop[8], Christoph Krafft[13], Ravi Kumar Maddula[12], Christian Matthäus[13], Jürgen Popp[13,14], Bernd Schneider[1], Ulrich S. Schubert[8,15], Richard A. Sikora[16], Aleš Svatoš[12] & Rony Swennen[3,17]

[1]NMR Research Group, Max Planck Institute for Chemical Ecology, Jena, Germany. [2] Organic Plant Production and Agroecosystems Research in the Tropics and Subtropics, University of Kassel, Witzenhausen, Germany. [3]Laboratory of Tropical Crop Improvement, Division of Crop Biotechnics, Department of Biosystems, Faculty of Bioscience Engineering, University of Leuven (KU Leuven), Leuven, Belgium. [4]Center for Industrial Mathematics, University of Bremen, Bremen, Germany. [5]Steinbeis Innovation Center for Scientific Computing in Life Sciences, Bremen, Germany. [6]Bruker Daltonik GmbH, Bremen, Germany. [7]Department of Biomolecular Chemistry, Leibniz Institute for Natural Product Research and Infection Biology (HKI), Jena, Germany. [8]Laboratory of Organic and Macromolecular Chemistry (IOMC), Jena Center for Soft Matter (JSCM), Friedrich Schiller University of Jena, Jena, Germany. [9]Bodemkundige Dienst van België, Leuven, Belgium. [10]Department of Entomology, Max Planck Institute for Chemical Ecology, Jena, Germany. [11] Martin Luther University of Halle-Wittenberg, Institute of Biology / Geobotany and Botanical Garden, Halle (Saale), Germany. [12]Mass Spectrometry Research Group, Max Planck Institute for Chemical Ecology, Beutenberg Campus, Jena, Germany. [13]Institute of Photonic Technology (IPHT), Jena, Germany. [14]Institute for Physical Chemistry and Abbe School of Photonics, Friedrich Schiller University of Jena, Jena, Germany. [15]Dutch Polymer Institute (DPI), Eindhoven, The Netherlands. [16]Institute of Crop Science and Resource Conservation (INRES) - Phytomedicine, Rheinische Friedrich-Wilhelms-Universität Bonn, Bonn, Germany. [17] Bioversity International, Leuven,

Belgium. [18]These authors contributed equally to this work. *email: hoelscher@ice.mpg.de

ABSTRACT

The global yield of bananas, one of the most important food crops, is severely hampered by parasites such as nematodes which cause yield losses up to 75%.

Plant-nematode interactions of two banana cultivars differing in susceptibility to *Radopholus similis* were investigated by a novel strategy combining the conventional and spatially-resolved analytical techniques ^{1}H NMR spectroscopy, matrix-free UV-laser desorption/ionization mass spectrometric imaging (LDI-MSI) and Raman microspectroscopy. This innovative combination of analytical techniques was applied to isolate, identify and locate the banana specific type of phytoalexins – phenylphenalenones – in the distinct lesions *R. similis* causes in the studied *Musa* cultivars. The striking anti-nematode activity of the phenylphenalenone anigorufone, its ingestion by the nematode and its subsequent localization in lipid droplets within the nematode is reported. The importance of varying local concentrations of these specialized metabolites in infected plant tissues, their involvement in the plant's defense system and derived strategies for improving banana resistance are given.

INTRODUCTION

Bananas and plantains (*Musa* spp.) are among the world's most important food and cash crops with a global production of about 138 million tonnes in 2010. They are part of a well-balanced human diet and are a major food staple for more than 400 million people in the tropics[1].

About 82% of the world's banana production is consumed locally, particularly in India, China and many African countries[1]. Export bananas represent an important source of employment and income in many countries, especially in the export leaders Costa Rica, Ecuador, Colombia and the Philippines, who ship the majority of their production to the northern hemisphere. Banana yields are severely hampered by fungi, insects and plant-parasitic nematodes. Of the approximately 150 different nematode species associated with *Musa*, the burrowing nematode, *Radopholus*

similis (Cobb, 1893) Thorne, 1949, is the key pathogen causing yield losses up to 75%[2-4].

R. similis is found in all major banana producing regions of the world. Its best-known hosts are bananas, black pepper (*Piper nigrum* L.), *Citrus* spp.[5,6] and more recently coffee (*Coffea* spp.)[7]. It causes extensive root lesions that can lead to toppling of banana plants[8]. A complete eradication of this most damaging nematode from infested banana plantations would require a five-year plant-free fallow as the nematode can survive on weed hosts[9,10]. Therefore, a variety of less time-consuming practices such as physical, chemical, cultural and biological control measures are typically applied to control this parasite[11].

Plant-parasitic nematodes have been effectively managed through the use of nematicides. However, their high toxicity has adverse effects on humans and their toxic residues are known to accumulate through non-target organisms in the food chain[12]. After the withdrawal of many effective nematicides such as methyl bromide from the market[13], organophosphate and carbamate nematicides are still intensively applied to banana and therefore continue to threaten the health of agricultural workers[14] and the environment.

The in-depth investigation of the plant-nematode interactions on the cellular and molecular level could lead to the development of more rational and efficient control strategies[15]. The production of toxic, herbivore-deterrent and/or repellent secondary metabolites which is typical for many plant defense systems is particularly interesting in this context[16]. *Musa* cultivars resistant to *R. similis* have been identified[17]. Especially the cultivar Yangambi km5 is often used as a reference resistant cultivar[18]. Histochemical and ultrastructural investigations of lesions caused by *R. similis* in Yangambi km5 revealed the accumulation of phenolic compounds in response to infection[19]. Unfortunately, many of these studies were based solely on histochemical staining methods and did not identify the chemical structures of nematicidal secondary metabolites[12,20,21]. Initial phytochemical analyzes of *R. similis*-infected roots of the *Musa* cultivar Pisang sipulu identified the phenylphenalenone anigorufone (**1**) as a phytoalexin produced in response to nematode damage and confirmed earlier suggestions of the significant role of phytoalexins in the plant defense system[22,23,24]. Phenylphenalenones are a group of special phenylpropanoid-derived natural products[25], which are known as Musaceae phytoalexins[22]. The activity of phenylalanine ammonia lyase (PAL, EC 4.3.15), the entry-point enzyme of

the phenylpropanoid pathway, is correlated to the biosynthesis of specific phenylpropanoids involved in defense and was substantially induced in nematode infected roots of Yangambi km5[26]. Phenylphenalenone-related compounds show biological activity against bacteria, fungi, algae and diatoms[22,27-34]. Their formation has been elicited in banana leaves by *Mycosphaerella fijiensis* (Black Sigatoka leaf streak disease), in the peel of the fruits by *Colletotrichum musae* (anthracnose disease)[22,28,34,35] and in roots and rhizomes by *Fusarium oxysporum* f. sp. *cubense* (Panama disease) and *R. similis*[23,34,36].

In the present study, we report on the results of an innovative combination of analytical techniques that we applied to isolate and identify phenylphenalenones and their tissue-specific localization in *R. similis* lesions in the *R. similis* susceptible and resistant *Musa* AAA cultivars, Grande Naine (GN) and Yangambi km5 (Ykm5). The anti-nematode activity of selected phenylphenalenones is demonstrated. Ingestion of phenylphenalenones by the nematode and its localization within lipid droplets within the nematode body is also reported. The importance of the local concentration of specialized metabolites in plant defense systems and strategies for improving banana resistance are discussed.

RESULTS

Root damage and root lesions

In the greenhouse, potted Grande Naine (GN) and Yangambi km5 (Ykm5) plants, were inoculated with the burrowing nematode *Radopholus similis*. Roots of 20-week-old plants were monitored for nematode damage 12 weeks after infection. Damage was more severe in roots of GN than in those of Ykm5. Visual observation of infected GN roots revealed large, continuous and tunnel-like lesions (**Fig. 1a, 1b**). Moreover, root damage extended to the root bases near the GN corms (**Fig. 1c**). Newly formed root lesions were identified by means of their light red color. Older lesions were dark red-brownish. In Ykm5, no corm infection was observed and both newly formed and older root lesions were small, discontinuous, dark red-brown in color and non-expanding (**Fig. 1d, 1e**). Uninfected roots of Ykm5 and GN, used as controls, showed no lesions and appeared healthy upon visual inspection.

Isolation and identification of metabolites

R. similis lesions from GN and Ykm5 roots were mechanistically dissected from healthy material and extracted with ethanol. Equal amounts of root tissue from uninfected healthy roots were used as control samples. Liquid-liquid separation resulted in $CHCl_3$, ethyl acetate, *n*-butanol and aqueous subfractions. Preliminary ^1H NMR analysis of subfractions of the *R. similis*-infected GN and Ykm5 root material revealed signals in the aromatic range of the spectrum of the $CHCl_3$ extract, while the other subfractions did not show aromatic signals of notable intensity. The $CHCl_3$ subfractions were further analysed for the occurrence of phenylphenalenones. In a first step, the $CHCl_3$ subfractions of *R. similis*-infected and uninfected root extracts of GN and Ykm5 were purified by semi-preparative HPLC. The individually collected fractions were subjected to ^1H NMR spectroscopy for identification and the structures of all compounds were identified as typical metabolites and major phytoalexins of *Musa* species (**Fig. 2**)[22,32,37]. The phytochemical profiles and the number of secondary metabolites in GN and Ykm5 (**Fig. 2**) are slightly different. Anigorufone (**1**)[38], hydroxyanigorufone (**2**)[38], irenolone (**5**)[22], 4-phenyl-*1H,3H*-benzo[*de*]isochromene-1,3-dione (**7**)[38] and 4-(4-hydroxyphenyl)-*1H,3H*-benzo[*de*]isochromene-1,3-dione (**8**)[37] were detectable in the extracts of lesions from both cultivars. (2*S*,3*R*)-2,3-Dihydro-2,3-dihydroxy-9-phenylphenalen-1-one (**3**)[36], isoanigorufone (**4**)[39] and anigorootin (**9**)[40] were exclusively found in Ykm5 and methylirenolone (**6**)[34] only in GN. Twice as much anigorufone (**1**), the major specialized metabolite of lesions in both cultivars was found in Ykm5 compared to GN. Additionally, all minor compounds were present in smaller amounts- per- kg-root- material in GN compared to Ykm5. The amounts of the isolated compounds are recorded in **Table 1**.

Analysis and interpretation of LDI-MSI data

The suitability of matrix-free UV-laser desorption/ionization mass spectrometric imaging (LDI-MSI) to identify secondary metabolites of *Arabidopsis thaliana* and *Hypericum* species[41] encouraged us to use this spatially-resolved bioanalytical technique to study the presence of phenylphenalenones in the lesions of GN and Ykm5. The Ultraflex III®- and the ultrafleXtreme® mass spectrometers allowed the application of a high lateral resolution of 10 µm, enabling the localization of phenylphenalenones in the area of lesions (100 to 200 µm).

The accumulation of secondary metabolites in the lesions was detected by LDI-MSI. The LDI-MSI data obtained from the lesion and the surrounding tissues (**Fig. 3**) show mass signals of phenylphenalenones precisely at the site of nematode infection. The LDI-MSI images were plotted in SCiLS Lab software (SCiLS, Bremen, Germany) after spectra baseline correction, hotspot removal (by suppressing 1% of most intense pixels) and edge-preserving image denoising to reduce the pixel-to-pixel variation[42]. Within the lesions *m/z* values of the discovered secondary metabolites (**1**-**9**) were detected, which are consistent with compounds resulting from the phytochemical investigations of the dissected lesions. The *m/z* value of 271 detected within the lesions was assigned to $[M-H]^+$ of the compounds anigurofone (**1)**, **4** or both (**Fig. 3c**). A signal for compound **7** (*m/z* 273) was found in this area (**Fig. 3d**) as well as signals of **2** and its 4-phenyl analog **5** (*m/z* 287) (**Fig. 3e**). The signal *m/z* 289 is attributable to the secondary metabolites **3**, **8** or both (**Fig. 3f)**. A signal for the *O*-methyl phenylphenalenone (**6**) of *m/z* 301 is also detectable (**Fig. 3g**). Furthermore, using the ultrafleXtreme®, we were able to detect a signal for the dimer **9** at *m/z* 573.
The areas of the lesions were strikingly different from the healthy, uninfected surrounding regions with regard to the presence of secondary metabolites, both in the isolation experiments and in the LDI-MSI investigations. Nevertheless, an elevated background in single LDI measurements caused by high laser intensities was observed within the uninfected regions of the tissue. As the color mapping indicates only the signal intensity at specific raster points and not the occurrence of a certain compound, color signals appear where only background is detected (**Fig. 4**).

Effect of phenylphenalenones in *R. similis* motility bioassay

To test for anti-nematode properties of the phenylphenalenone-type phytoalexins an *in vitro* bioassay on the motility (capability of movement) of *R. similis* was performed with 13 selected phenylphenalenones and related compounds (**Table 2** and **Fig. 2**). The percentage of inhibition of nematode motility (nematostatic effect) was monitored after 24, 48 and 72 h of exposure to the compounds.
At both tested concentrations (50 and 100 ppm) **1**, **2** and monohydroxyanigorootin (**13**) showed a nematostatic effect as of 24 h of incubation. This effect was either constant (**13**) or increased over time up to 72 h (**1** and **2**). Anigorufone (**1)** showed the strongest activity with 89% of the nematodes becoming immotile after 72 h of incubation. Similar nematostatic effects were observed for **2**, **4**, **8** and 4-hydroxy-2-

methoxy-9-phenylphenalenone (**11**) at a concentration of 100 ppm. Exposure to 50 ppm resulted in higher percentages of immotile nematodes of 48 h of exposure in comparison to the 1% ethanol control. The compounds **5**, **9**, methoxyanigorufone (**10**), musanolone C (**12**) and perinaphthenone (**15**) revealed inconsistent nematostatic effects. Methylirenolone (**6)** and dihydroxyanigorootin (**14**) did not show any significant inhibition of nematode motility (not included in **Table 2**). The solvent (1% ethanol) exhibited a negligible effect on nematode motility comparable to sterile distilled water.

Dosage effect of anigorufone (1) on *R. similis* motility bioassay

Among the phenalenones tested in the *R. similis* motility bioassay, **1** was the most active compound at a concentration of 100 ppm (**Table 2**). Therefore **1** was selected for a more detailed investigation of its nematostatic potential. The data obtained at 10, 20, 40, 50 and 100 ppm clearly showed a concentration-dependent effect of **1** on nematode motility (**Fig. 5**). At an incubation time of 24 h, the percentage of immotile *versus* the total number of nematodes increased from non-significant 26% at a concentration of 10 ppm to significant 50.2% at 40 ppm and 74.3% at 100 ppm. Hence, significantly ($P < 0.05$) higher levels of nematostatic effects were observed from 40 ppm upwards compared to the control (1% ethanol). Increasing the concentration to 150 ppm resulted in partial precipitation of **1** and non-reproducible results (data not shown). As compared to the values obtained after 24 h, the motility of nematodes further decreased at incubation times of 48 h and 72 h (**Fig. 5**). The concentration of **1** which inhibited the motility of 50% of the nematodes (IC_{50}) in the bioassay was 59 µg/mL for an incubation time of 24 h. For an exposure time of 48 h, IC_{50} was 38 µg/mL and only 23 µg/mL for 72 h of exposure.

Nematode ingestion of anigorufone (1) and its detection by LDI-MSI

A surprising observation was made during the evaluation of the *R. similis* motility bioassay with **1**. Under bright field microscopy (BF), yellow droplets were seen in parts of the bodies of nematodes exposed to high concentrations of **1** (**Fig. 6**). These were readily visible due to the natural transparency of the nematode cuticle. Nematodes containing such yellow droplets were subjected to LDI-MSI in order to identify the yellow pigment. The drying of the nematodes on the indium tin oxide (ITO) coated conductive glass slides and the high field vacuum conditions of the LDI-

MSI process preserved the position of the nematodes on the slides and allowed pointing the laser precisely at the target region. This was important since the shape of the yellow droplets changed during the drying on the glass slides and during the LDI-MSI measuring process because the droplets converged. LDI-MSI spectra recorded from yellow regions of *R. similis* nematodes showed an ion peak of *m/z* 273 $[M+H]^+$, corresponding to the molecular mass of **1** (**Fig. 7**). LDI-MSI spectra of control nematodes, not exposed to **1**, did not show such a signal. Ingestions of large enough amounts of **1** to be visible by BF always led to nematode mortality. Thus it has become obvious that **1** is not only a nematostatic but also a nematocidal compound.

Raman microspectroscopy

Studies were conducted to analyze the chemical composition of the yellow droplets appearing in the bodies of *R. similis* after ingestion of **1**. Recent developments in combining Raman spectroscopy with optical microscopy provided a new non-invasive technique to assess and image biological samples and processes. The technique has recently been successfully applied to identify and visualize lipid droplets in nematodes[43]. **Fig. 8a** shows a bright field image of part of a *R. similis* nematode using a 60x / NA=1 water immersion objective. The Raman image reconstructed from the integrated areas of the scattering intensities originating from C-H stretching vibrations of organic molecules of part of the image in **Fig. 8a** is shown in **Fig. 8b**. **Fig. 8c** was generated from **Fig. 8b** using a spectral decomposition algorithm that searches for the greatest spectral contrast within a given dataset. Subsequently the abundances of the spectral information were plotted. The distribution of lipids is shown in red in **Fig. 8c**, the protein distribution in light blue. Apparently, the lipids are arranged in rather large fat droplets, whereas the abundance of the proteins reveals the internal organisation of the organism. **Fig. 8d** shows the associated spectral information. The spectrum shown in light blue exhibits all characteristic features associated with proteins. For example, the scattering intensities between 2800 and 3100 cm^{-1} originate from C-H stretching vibrations of the protein residues, the band centered around 1650 cm^{-1} is due to stretching motions of the C=O bonds of the peptide backbones and CH_2 scissoring motions can be observed at 1450 cm^{-1}. The red spectrum resembles a typical spectrum of lipids. The intensities of C-H stretching bands between 2800 and 3100 cm^{-1} and C-H deformation bands between 1300 and 1440 cm^{-1} are more intense than in proteins. Further bands are assigned to C=O

bonds of ester groups at 1740 cm^{-1}, C=C groups of unsaturated fatty acid chains at 1260 and 1660 cm^{-1} and C-C groups near 1060 cm^{-1}.

DISCUSSION

Banana cultivars show different grades of susceptibility to the burrowing nematode *R. similis*. The cultivar Grande Naine (GN), which is extensively cultivated for banana fruit production, is susceptible to *R. similis* and, in contrast, the cultivar Yangambi km5 (Ykm5) is largely resistant. The objective of this study was to investigate if secondary metabolites of the *Musa* plant could be the reason for these differences in plant-nematode interaction.

This study provides evidence for the local induction of phenylphenalenone-type secondary metabolites in response to *R. similis* infection in *Musa* spp. Nine phenylphenalenone-type compounds were detected in nematode-induced lesions using LDI-MSI, elucidated by NMR analyses and identified as typical metabolites and major phytoalexins of *Musa* species[22,32,37]. Anigorufone (**1**) was the most abundant phenylphenalenone-type secondary metabolite present in the nematode-induced lesions of the resistant cultivar Ykm5 as well as in the susceptible cultivar GN. As recently reported for secondary metabolites of *Arabidopsis thaliana* and *Hypericum* species, LDI-MSI is an effective technique of localizing secondary metabolites in plant tissues[41]. Here this technique revealed that the location of phenylphenalenones in *Musa* roots is restricted to the lesions created by *R. similis*.

A significant difference between the two *Musa* cultivars was observed when the mass fraction of the compounds in the lesions was determined. A greater concentration of **1** and other anti-nematode phenylphenalenones was discovered in the small lesions in Ykm5 roots than in the large lesions in GN roots. *In vitro* bioassays revealed the IC_{50} concentrations of **1** and other active phenylphenalenones necessary to immobilize and kill *R. similis*. These critical concentrations of active phenylphenalenones are not reached in the lesions of GN roots. In this sensitive GN cultivars, nematodes are neither immobilized nor killed, and continue feeding and invading more tissue, creating larger lesions. By contrast, these critical concentrations are reached in Ykm5 roots and lead to the immobilization and eventual death of *R. similis in situ*. Hence, it appears that the systemic production of high concentrations of phenylphenalenones in the nematode-infected tissues in the

roots of Ykm5 is the key mechanism responsible for Ykm5's resistance to *R. similis*. Phenylphenalenones do not create a nematode-toxic environment when they are present in roots at low concentrations. The local increase in concentration of these specialized metabolites upon nematode attack in resistant Ykm5 roots causes reduced motility and mortality preventing nematodes from migrating to neighboring regions outside the initial infection zone.

To the best of our knowledge, the present bioassay-based study provides the first evidence of anti-nematode properties of phenylphenalenones and related compounds. Compound **1** is the most abundant phenylphenalenone in root lesions of Ykm5 and GN and also proved to be the most active anti-nematode compound in the *in vitro* bioassays with *R. similis*. Of the compounds tested **1** caused the greatest nematostatic and nematocidal effects. Immotility data (**Table 2**) revealed different grades of activity of individual compounds. In addition to anigorufone (**1**), the compounds **2**, **4**, **8**, **11**, and **13** also had substantial nematostatic and –cidal effects on *R. similis*, while others had less (**5**, **9**, **10**, **12**, **15**) or no effect at all (**6**, **14**). Whether or not the composition of the phytoalexin mixture present in lesions also contributes to the resistance seen in Ykm5 remains to be investigated. Testing selected combinations of different phenylphenalenones and whole extracts could reveal synergistic or antagonistic effects of individual phenylphenalenones[12]. Furthermore, the cellular concentration of anigorufone (**1**) and other nematocidial phenylphenalenones in lesions in the roots of other *R. similis*-resistant *Musa* cultivars is the subject of ongoing investigations.

For the first time, the uptake of a plant secondary metabolite, namely anigorufone (**1**)**,** into the body of individual *R. similis* nematodes was detected by LDI-MSI. No extraction of nematodes was necessary to analyse the ingested metabolites. Whether phenylphenalenones were incorporated into the nematode with the diet, via the skin or via both routes was not addressed in this study. However, once taken up, non-glucosidic phenylphenalenones such as anigorufone (**1**), which are poorly soluble in water may converge with lipids. In this context, it was a remarkable finding that Raman microspectroscopy confirmed lipids as the major contents of droplets in *R. similis*, which were exposed to anigorufone (**1**). The readily visible yellow color and LDI-MSI confirmed the accumulation of anigorufone (**1**) in the lipid droplets present in the bodies of *R. similis* exposed to anigorufone (**1**). In *Caenorhabditis elegans*, intestinal oil droplets - storage components for lipophilic compounds - are

involved in minimizing the toxicity of polychlorinated biphenyl[44]. A similar process may be indicated in *R. similis* by the observed formation of bulky oil droplets containing anigorufone (**1**). However, the oil droplets in *R. similis* become very large and this process is not accompanied by an expansion of the body. The droplets ultimately take-up the space available to the nematode's internal organs, thereby hampering essential life processes. As opposed to the observed retention of lipids and the formation of bulky droplets in *R. similis*, a variety of stressors increased the excretion and stopped the pharyngeal pumping as a response in *C. elegans*. In this organism, a complex system of regulatory mechanisms can minimize the toxic effects of alcohol or heavy metals, at least for a limited time[45]. Exposure of *C. elegans* to quercetin and caffeic acid resulted in an altered lipid metabolism. The determination of the fat status of these nematodes revealed a significant reduction in the fluorescence intensity of Nile Red, indicating reduced intestinal fat deposition. In contrast to the toxic effect of phenylphenalenones on *R. similis*, the tested compounds quercetin and caffeic acid caused an effect which is linked to longevity in *C. elegans*[46]. Genes involved in regulation of lipid storage and mobilization, e.g. enlarged fat droplets in *C. elegans*, have been reported[47]. Thus the formation of large lipid droplets in *R. similis* upon exposure to phenylphenalenones may be an effect of these plant metabolites on the lipid regulatory system. The development of such bulky lipid droplets as part of the *Musa*-*R. similis*-interaction may be comparable to the role of lipids in the aging of *C. elegans*[48].

Extrapolating data from laboratory bioassays to the field situation should be done with caution[49]. Nevertheless, phenylphenalenones, both natural phytoalexins and synthetics, are potential pest control agents. However, regardless of their origin from plants or from chemical synthesis, phenylphenalenones as polycyclic aromatic compounds hold potential risks for farmers, consumers, non-target organisms and the environment. Adverse effects such as phototoxicity of phenylphenalenone-producing plants and pure phenylphenalenones have been reported[50-52]. Hence, further investigations and risk assessments are necessary before phenylphenalenones should be considered as model compounds for the development of nematocides[12].

Metabolic engineering[53] to enhance the cellular concentration of inducible phenylphenalenones (phytoalexins) could be an appealing way to develop commercially important banana cultivars which are as resistant to *R. similis* as Ykm5

and as productive as GN is. Engineering of specialized metabolite pathways for enhancing the disease resistance represents a feasible strategy[54,55], but requires the genes and enzymes of the pathway and its regulation to be fully known. So far this is not the case for phenylphenalenone biosynthesis and, as a consequence such studies are a necessary prerequisite. Moreover, the identification of the genes involved in local response to nematode attack and local induction of phenylphenalenone biosynthesis, as seen in Ykm5 and resulting in concentrations sufficient to control nematodes (or other pests), is challenging. The recent description of the draft sequence of the 523-megabase genome of a *Musa acuminata* doubled-haploid genotype represents a major advance to elucidate the complex biochemical processes of banana-pathogen interactions[56].

METHODS

Plant material

Plant material, the *R. similis*-resistant *Musa* cultivar Yangambi km5 (*Musa acuminata* AAA, Ibota subgroup, ITC 1123) and the *R. similis*-susceptible *Musa* cultivar Grande Naine (*Musa acuminata* AAA, Cavendish subgroup, ITC 1256) were originally provided by the International Transit Centre (ITC), Bioversity International, KU Leuven, Belgium. The planting material was further multiplied and cultured individually according to standard procedures[57]. Eight-week-old tissue culture plants with roots were transplanted to pots with 8 L of a sterile quartz-peat mixture (2:1). At weekly intervals, each plant received a dose of commercial liquid fertilizer mixture for leafy plants (Aveve Group, Leuven, Belgium, http://www.aveve.be). The plants were maintained under greenhouse conditions at an ambient temperature of 27/20 °C (day/night), 80% relative humidity, 12 h photoperiod and irrigated as needed.

Nematodes

A population of *Radopholus similis* (*Radopholus similis* (Cobb, 1893) Thorne, 1949) originally isolated from banana roots in Uganda was used in the experiments. The nematode population was maintained as monoxenic culture on sterile carrot disks and on sterile alfalfa callus tissues at 25±1 °C in the dark[2,58]. A mixture of adult and juvenile nematodes extracted from six to eight-week-old carrot disk cultures was

collected in distilled water; a concentration of 500 active nematodes was adjusted in 1 mL of water and used to inoculate the banana plants.

Six-week-old alfalfa callus tissue-based nematode cultures were used in *in vitro* bioassays to test anti-nematode properties of the phenylphenalenones.

Nematode inoculation

Eight weeks after being transplanted and placed in the greenhouse, six plants of each cultivar were inoculated with 8000 nematodes. Six uninfected control plants were maintained per cultivar (total of 12 plants per cultivar).

Twelve weeks after inoculation with *R. similis*, the banana plants were uprooted. The extent of root necrosis was estimated using the root necrosis index according to the established protocol[59]. Roots were cleaned, snap-frozen in liquid nitrogen and stored at -80 °C prior to the phytochemical analysis. A portion of young roots with newly developing lesions was preserved separately for localization of secondary compounds using LDI-MSI.

Isolation and structure elucidation of phenylphenalenones

Root tissues with lesions were manually micro-dissected using a scalpel, frozen with liquid nitrogen, ground, and exhaustively extracted with ethanol at room temperature. The crude extract was evaporated (<40 °C) and partitioned between $CHCl_3$-H_2O and ethyl acetate-H_2O, followed by *n*-butanol-H_2O. Purifications were achieved by means of semi-preparative reversed-phase HPLC on a Nucleosil 100 RP-18 column (10 µm, 250×10 mm, UV 284 nm) using a gradient MeCN-H_2O (0.1% TFA) from 15 to 95% MeCN in 120 min at a flow rate of 3.5 mL/min (Merck Hitachi LiChrograph L-6200A gradient pump, Merck KGaA, Darmstadt, Germany, http://www.merckgroup.com).

^{1}H NMR spectroscopy

^{1}H NMR spectra were measured on an AV 500 NMR spectrometer (Bruker, Rheinstetten, Germany, http://www.bruker.com) at 500.13 MHz. The spectrometer was equipped with a 5 mm Bruker TCI Cryoprobe™. Standard Bruker pulse sequences were used to record spectra in acetone-d_6 at 300 K. Spectra were referenced to tetramethylsilane, which was used as an internal standard.

LDI-MSI on the Ultraflex III® and ultrafleXtreme® mass spectrometers

Thin, small longitudinal sections of the *Musa* root epidermis, rich in lesions, were cryosectioned and fixed on a carbon conductive adhesive tape (Plano, Wetzlar, Germany, http://www.plano-em.de), which was in turn fixed on an ITO slide (Bruker Daltonics, Bremen, Germany, http://www.bdal.com)[60]. A gel-liner (Staedtler triplus gel-liner, silver, 0.4 mm; Staedtler-Mars, Nürnberg, Germany, http://www.staedtler.com) was used to place marks surrounding the sections to define their position. The gel-silver points served as reference points when overlaying the optical image with the LDI-MSI data.

An Ultraflex III® mass spectrometer (Bruker Daltonics), equipped with a Nd:YAG laser was used for the analysis of plant material. All spectra were measured in the negative reflector mode. To measure the pixels of ca. 10 × 10 µm, the minimum laser focus setting (corresponding to a diameter of about 10 µm laser, under usage of oversampling) was used. For each raster point, a spectrum was accumulated with 100 laser shots in the range of *m/z* 100 to 1000 Da and fixed laser intensity. For data acquisition, the FlexImaging version 2.0 software (Bruker Daltonics)® was used. For advanced image visualization (**Fig. 3**), SCiLS Lab software was used. Each image corresponding to a *m/z* value was visualized by overlaying the image with the optical image of the lesion. Each signal intensity in the *m/z* image is represented by a specific color corresponding to the mass of the metabolites hereby visualized.

An ultrafleXtreme® mass spectrometer was used for the detection of **1** in the *R. similis* bioassay. Nematodes were pipetted directly onto conductive coated ITO glass slides (Bruker Daltonics) and residual water was evaporated.

Subsequently, the ITO glass slide was clamped into a MTP slide adapter II and inserted into an ultrafleXtreme® mass spectrometer operating with flexControl 3.0 (Bruker Daltonics). The data were collected in the range of *m/z* 0 to 440 Da in the positive reflector mode with a raster width of 10 µm in XY at 90% laser power with 1000 Hz laser frequency. One thousand spectra at each raster spot were recorded with a sample rate of 4.00 GS/s. After data acquisition from flexImaging 2.0®, the resultant sum spectra was filtered manually. Masses were picked with a mass range of 0.5 Da and visualized by overlaying with the optical image.

Anti-nematode properties of phenylphenalenones in a *R. similis* motility bioassay

Two series of *in vitro* bioassay experiments were carried out. In the first series, the effect of 13 phenylphenalenone-type compounds on the motility of *R. similis* was assayed **(Fig. 2, Table 2)**. Two concentrations (50 and 100 ppm) were tested. Each treatment was replicated three times and for each compound, the assay was repeated at least twice.

In the second experiment, the dosage effect of **1** on the motility of *R. similis* was tested using a gradient of six concentrations (10, 20, 40, 50, 100, 150 ppm). Each treatment was replicated six times and the bioassay was repeated twice to confirm the results. Dose-dependent effects allowed the calculation of IC_{50} values, defined as the concentration of a compound required to cause 50% of nematodes to become immotile, at 24, 48 and 72 h of incubation. Compound **1** was considered toxic when at least 10% more nematodes become immotile in a treatment than in the solvent control. Nematicidal effects were checked by transferring the nematodes to sterile distilled water after 72 h in contact with **1**. The number of live and dead nematodes was counted under a fluorescence microscope (Leica Dialux 20, Leica Microsystems, Wetzlar, Germany, http://www.leica-microsystems.com) at 96 h[61]. To be sure nematodes were dead and not just immotile they were poked with a needle.

Experimental procedure used in both bioassay series: with the exception of **15** (Sigma Aldrich, Deisenhofen, Germany, http://www.sigmaaldrich.com) all phenylphenalenones were extracted from *Musa* spp. and *Anigozanthos* spp. and purified using semi-preparative HPLC. The compounds were dissolved in aqueous ethanol (1%). Stock solutions (200 µg/mL) were prepared aseptically and stored as aliquots at -20 °C.

All the experiments were performed in 24-well-plates under aseptic conditions. The control consisted of 1% ethanol in an aqueous solution. A sterile distilled water control was also included to test the solvent effects on motility. An aliquot of 100 µL sterile nematode suspension containing 80 to 100 adult and juvenile *R. similis* was added to each well and the exact number of motile and immotile nematodes in each well was counted prior to the addition of the compounds. Nematodes were counted using an inverted compound microscope (Nikon TMS-F, 40×, Nikon Belux, Brussels, Belgium, http://www.nikon.be). A total volume of 400 µL, composed of different volumes of compound stock solution (200 ppm) and of sterile distilled water were

added to each well to obtain the desired concentrations. Plates were incubated in the dark at 25±1 °C. The number of immotile nematodes was counted after 24, 48 and 72 h of incubation.

The percentages of immotile nematodes were calculated relative to the number of actively moving and immotile nematodes at the onset of the experiment. Compounds were considered motility inhibitive (nematostatic) when significantly ($P \leq 0.05$) more nematodes became immotile than in the solvent control at any assayed concentration.

Statistical data analysis: Statistical data analysis was performed using STATISTICA version 9 (StatSoft, Tulsa, OK, USA, http://www.statsoft.com). Data on motility assay were analyzed using the Kruskal-Wallis analysis of variance by ranks. When the Kruskal-Wallis analysis of variance ranks was significant, each group mean was compared with the control by multiple comparisons of mean ranks.

Data on dosage effect of **1** on *R. similis* motility were analyzed by analysis of variance (ANOVA) provided the conditions of ANOVA (normal distribution and homogeneity of variance) were met. The percentage motile nematodes were arcsin (x/100) transformed prior to the analysis. When significant differences ($P \leq 0.05$) were observed, Tukey's HSD test was applied for multiple comparisons of group means. The IC_{50} values were obtained by interpolating the corresponding percentage of immotile nematodes *vs*. **1** concentration in scatter plots.

Raman data acquisition and data analysis

Raman spectra were acquired using a WITec Model CRM 300 Confocal Raman Microscope (WITec GmbH, Ulm, Germany, http://www.witec.de). Excitation at 785 nm (ca. 10 mW per sample) was achieved by a single mode diode laser. The exciting laser radiation was coupled into a microscope through a wavelength-specific single mode optical fiber. The incident laser beam was collimated *via* an achromatic lens and passed a holographic band pass filter, before it was focused onto the sample through the microscope objective. A Nikon Fluor (60x/1.00 NA, WD = 2.0 mm) water immersion objective was used in the studies reported here (Nikon GmbH, Düsseldorf, Germany, http://www.nikon.de). The sample was scanned through the laser focus in a raster pattern at a constant stage speed of fractions of a micrometer per second. The continuous motion prevents sample degradation in the focal point of the laser beam. Spectra were collected at a 0.5 µm grid, with a dwell time of 0.25 s. The

spectral resolution was about 6 cm^{-1} and the spectral window ranged from 300 to 3200 cm^{-1} [62].

References

1. FAOSTAT. *Food and Agriculture Organization of United Nations.* (Crops-Faostat, 23rd Feb 2012, faostat.fao.org/site/567/default.aspx.).
2. Speijer, P.R. & De Waele, D. *Screening of* Musa *germplasm for resistance and tolerance to nematodes* (INIBAP Technical Guidelines 1. Montpellier, France, 1997, http://www.bioversityinternational.org/publications/search.html.).
3. Sarah, J.L. in *Diseases of* Banana*,* Abacá *and* Ensete (ed. Jones, D.R.) 295-303 (CABI Publishing, Wallingford, UK, 1999).
4. Gowen, S.R., Quénéhervé, P. & Fogain, R. *Plant Parasitic Nematodes in Subtropical and Tropical Agriculture* 2nd edn. (eds. Luc, M., Sikora, R.A. & Bridge, J.) 611-644 (CABI Publishing, Wallingford, UK, 2005).
5. Holdeman, Q.L. The burrowing nematode *Radopholus similis sensu lato*. (Nematology Publication, California Department of Food and Agriculture, Division of Plant Industry, Sacramento, CA, USA, 1986).
6. Moens, M. & Perry, R.N. Migratory plant endoparasitic nematodes: a group rich in contrasts and divergence. *Annu. Rev. Phytopathol.* **47**, 313-332 (2009).
7. Campos, V.P. & Villain, L. in *Plant Parasitic Nematodes in Subtropical and Tropical Agriculture* 2nd edn. (eds. Luc, M., Sikora, R.A. & Bridge, J.) 529-579 (CABI Publishing, Wallingford, UK, 2005).
8. Leach, R. Blackhead toppling disease of bananas. *Nature* **181**, 204-205 (1958).
9. Sarah, J.L., Pinochet, J. & Stanton, J. *The burrowing nematode of bananas,* Radopholus similis *Cobb.* (INIBAP, Musa Pest Fact Sheet No.1, Montpellier, France, 1996).
10. Bulletin OEPP/EPPO Bulletin. European and Mediterranean Plant Protection Organization (EPPO) Diagnostics Report. *Radopholus similis*. *Eppo Bulletin* **38**, 374-378 (2008).
11. Chabrier, C., Tixier, P., Duyck, P.F., Carles, C. & Quénéhervé, P. Factors influencing the survivorship of the burrowing nematode, *Radopholus similis* (Cobb.) Thorne in two types of soil from banana plantations in Martinique. *Agric., Ecosyst. Environ., Appl. Soil Ecol.* **44**, 116-123 (2010).

12. Chitwood, D.J. Phytochemical based strategies for nematode control. *Annu. Rev. Phytopathol.* **40**, 221-249 (2002).
13. Quénéhervé, P., Valette, C., Topart, P., Tezenas du Montcel, H. & Salmon, F. Nematode resistance in bananas: screening results on some wild and cultivated accessions of *Musa* spp. *Euphytica* **165**, 123-126 (2009).
14. Wesseling, C. *et al*. Symptoms of psychological distress and suicidal ideation among banana workers with a history of poisoning by organophosphates or *N*-methyl carbamate pesticides. *Occup. Environ. Med.* **67**, 778-784 (2010).
15. Grunewald, W., Cannoot, B., Friml, J. & Gheysen, G. Parasitic nematodes modulate PIN-mediated auxin transport to facilitate infection. *PloS Pathog.* **5**, e1000266 (2009).
16. Hopkins, R.J., van Dam, N.M. & van Loon, J.J.A. Role of glucosinolates in insect-plant relationships and multitrophic interactions. *Annu. Rev. Entomol.* **54**, 57-83 (2009).
17. Dochez, C., Whyte, M., Tenkouano, A., Ortiz, R. & De Waele, D. Response of east African highland bananas and hybrids to *Radopholus similis*. *Nematology* **7**, 655-666 (2005).
18. Price, N.S. Field trial evaluation of nematode susceptibility within *Musa*. *Fundam. Appl. Nematol.* **17**, 391-396 (1994).
19. Valette, C., Andary, C., Geiger, J.P., Sarah, J.L. & Nicole, M. Histochemical and cytochemical investigations of phenols in roots of banana infected by the burrowing nematode *Radopholus similis*. *Phytopathology* **88**, 1141-1148 (1998).
20. Beckman, C.H. Phenolic-storing cells: keys to programmed cell death and periderm formation in wilt disease resistance and in general defence responses in plants? *Physiol. Mol. Plant Pathol.* **57**, 101-110 (2000).
21. Wuyts, N. *et al*. Potential physical and chemical barriers to infection by the burrowing nematode *Radopholus similis* in roots of susceptible and resistant banana (*Musa* spp.). *Plant Pathol.* **56**, 878-890 (2007).
22. Luis, J.G. *et al*. Irenolone and emenolone: two new types of phytoalexin from *Musa paradisiaca*. *J. Org. Chem.* **58**, 4306-4308 (1993).
23. Binks, R.H., Greenham, J.R., Luis, J.G. & Gowen, S.R. A phytoalexin from roots of *Musa acuminata* var. Pisang Sipulu. *Phytochemistry* **45**, 47-49 (1997).

24. Collingborn, F.M.B., Gowen, S.R. & Mueller-Harvey, I. Investigations into the biochemical basis for nematode resistance in roots of three *Musa* cultivars in response to *Radopholus similis* infection. *J. Agric. Food Chem.* **48**, 5297-5301 (2000).
25. Cooke, R.G. & Edwards, J.M. Naturally occurring phenalenones and related compounds. *Prog. Chem. Org. Nat. Prod.* **40**, 153-190 (1981).
26. Wuyts, N., de Waele, D. & Swennen, R. Activity of phenylalanine ammonia-lyase, peroxidase and polyphenol oxidase in roots of banana (*Musa acuminata* AAA, cvs Grande naine and Yangambi km5) before and after infection with *Radopholus similis*. *Nematology* **8**, 201-209 (2006).
27. Winters, K., Batterton, J.C. & Van Baalen, C. Phenalen-1-one: Occurrence in a fuel oil and toxicology to microalgae. *Environ. Sci. Technol.* **11**, 270-272 (1977).
28. Kamo, T. *et al*. Phenylphenalenone-type phytoalexins from unripe Bungulan banana fruit. *Biosci. Biotechnol. Biochem.* **62**, 95-101 (1998).
29. Quiñones, W. *et al*. Synthesis and antifungal activity of *Musa* phytoalexins and structural analogs. *Molecules* **5**, 974-980 (2000).
30. Lazzaro, A. *et al*. Light and singlet oxygen-mediated antifungal activity of phenylphenalenone phytoalexins. *Photochem. Photobiol. Sci.* **3**, 706-710 (2004).
31. Qin, B., Shao, Z.Y., Zeng, W., Wang, H.Q. & Zhu, D.Y. Musellactone, a new lactone from *Musella lasiocarpa*. *J. Chin. Chem. Soc.* **53**, 475-478 (2006).
32. Otálvaro, F. *et al*. Phenalenone-type compounds from *Musa acuminata* var. “Yangambi km 5” (AAA) and their activity against *Mycosphaerella fijiensis*. *J. Nat. Prod.* **70**, 887-890 (2007).
33. Jitsaeng, K. & Schneider, B. Metabolic profiling of *Musa acuminata* with *Sporobolomyces salmonicolor*. *Phytochem. Lett*. **3**, 84-87 (2010).
34. Luis, J.G., Fletcher, W.Q., Echeverri, F. & Grillo T.A. Phenalenone-type phytoalexins from *Musa acuminata* - synthesis of 4-phenyl-phenalenones. *Tetrahedron* **50**, 10963-10970 (1994).
35. Kamo, T., Hirai, N., Tsuda, M., Fujioka, D. & Ohigashi, H. Changes in the content and biosynthesis of phytoalexins in banana fruit. *Biosci. Biotechnol. Biochem.* **64**, 2089-2098 (2000).

36. Luis, J.G *et al*. Musanolones: four 9-phenylphenalenones from rhizomes of *Musa acuminata*. *Phytochemistry* **41**, 753-757 (1996).
37. Hirai, N., Ishida, H. & Koshimizu, K. A phenalenone-type phytoalexin from *Musa acuminata*. *Phytochemistry* **37**, 383-385 (1994).
38. Cooke, R.G. & Thomas, R.L. Colouring matters of Australian plants XVIII. Constituents of *Anigozanthos rufus*. *Aust. J. Chem.* **28**, 1053-1057 (1975).
39. Luis, J.G., Lahlou, E.H. & Andrés, L.A. 4'-dehydroxy-irenolone, a new phytoanticipin from the resistant *Musa* selected hybrid SH-3481. *Nat. Prod. Lett.* **13**, 299-304 (1999).
40. Hölscher, D. & Schneider, B. HPLC-NMR analysis of phenylphenalenones and a stilbene from *Anigozanthos flavidus*. *Phytochemistry* **50**, 155-161 (1999).
41. Hölscher, D. *et al*. Matrix-free UV-laser desorption/ionization (LDI) mass spectrometric imaging at the single-cell level: distribution of secondary metabolites of *Arabidopsis thaliana* and *Hypericum* species. *Plant J.* **60**, 907-918 (2009).
42. Alexandrov, T. *et al*. Spatial segmentation of imaging mass spectrometry data with edge-preserving image denoising and clustering. *J. Proteome Res.* **9**, 6535-6546 (2010).
43. Klapper, M. *et al*. Fluorescence-based fixative and vital staining of lipid droplets in *Caenorhabditis elegans* reveal fat stores using microscopy and flow cytometry approaches. *J. Lipid Res.* **52**, 1281-1292 (2011).
44. Menzel, R. *et al*. Cytochrome P450s and short-chain dehydrogenases mediate the toxicogenomic response of PCB52 in the nematode *Caenorhabditis elegans*. *J. Mol. Biol.* **370**, 1-13 (2007).
45. Jones, D. & Candido, E.P.M. Feeding is inhibited by sublethal concentrations of toxicants and by heat stress in the nematode *Caenorhabditis elegans*: relationship to the cellular stress resonance. *J. Exp. Zool. Part A Comp. Exp. Biol.* **284**, 147-157 (1999).
46. Pietsch, K., *et al*. Hormetins, antioxidants and prooxidants: defining quercetin-, caffeic acid- and rosmarinic acid-mediated life extension in *C. elegans*. *Biogerontology* **12**, 329-347 (2011).
47. Ashrafi, K. *et al*. Genome-wide RNAi analysis of *Caenorhabditis elegans* fat regulatory genes. *Nature* **421**, 268-272 (2003).

48. Hou, N.S., & Taubert, S. Functions and regulation of lipid biology in *Caenorhabditis* aging. *Front. Physiol.* **3**, 143 (2012).
49. Spence, K.O., Lewis, E.E. & Perry, R.N. Host-finding and invasion by entomopathogenic and plant-parasitic nematodes: evaluating the ability of laboratory bioassays to predict field results. *J. Nematol.* **40**, 93-98 (2008).
50. Darwin, C. *On the Origin of Species by Means of Natural Selection* 4th British edn. 12 (John Murray, London, UK, 1866) (darwin-online.org.uk/Variorum/1866/1866-12-dns.html).
51. Webb, L.J. *Guide to the medicinal and poisonous plants of Queensland* 65 (Council for Scientific and Industrial Research, Bulletin No. 232, Melbourne, Australia, 1948).
52. Flors, C., *et al*. Phototoxic phytoalexins. Processes that compete with the photosensitized production of singlet oxygen by 9-phenylphenalenones. *Photochem. Photobiol.* **82**, 95-103 (2006).
53. Misawa, N. Pathway engineering for functional isoprenoids. *Curr. Opin. Biotechnol*. **22**, 727-633 (2011).
54. Dixon, R.A. Natural products and plant disease resistance. *Nature* **411**, 843-847 (2001).
55. Collinge, D.B., Jørgensen, H.J.L., Lund, O.S. & Lyngkjær, M.F. Engineering pathogen resistance in crop plants: current trends and future prospects. *Annu. Rev. Phytopathol*. **48**, 269-291 (2010).
56. D'Hont, A. *et al*. The banana (*Musa acuminata*) genome and the evolution of monocotyledonous plants. *Nature* **488**, 213-217 (2012).
57. Banerjee, N. & De Langhe, E. A tissue culture technique for rapid clonal propagation and storage under minimal growth conditions of *Musa* (banana & plantain). *Plant Cell Rep.* **4**, 351-354 (1985).
58. Elsen, A. *et al*. Aseptic culture systems of *Radopholus similis* for *in vitro* assays on *Musa* spp. and *Arabidopsis thaliana*. *J. Nematol.* **33**, 147-151 (2001).
59. Carlier, J., De Waele, D. & Escalant, J.-V. *Global evaluation of Musa germplasm for resistance to Fusarium wilt, Mycosphaerella leaf spot diseases and nematodes* (eds. Vézina, A. & Picq, C.) 56-57 (INIBAP Technical Guidelines 6. The International Network for the Improvement of Banana and Plantain, Montpellier, France, 2002).

60. Hölscher, D. & Schneider, B. Laser microdissection and cryogenic nuclear magnetic resonance spectroscopy: an alliance for cell type-specific metabolite profiling. *Planta* **225**, 763-770 (2007).
61. Forge, T.A. & MacGuidwin, A.E. Nematode autofluorescence and its use as an indicator of variability. *J. Nematol.* **21**, 399-403 (1989).
62. Hedegaard, M. *et al*. Spectral unmixing and clustering algorithms for assessment of single cells by Raman microscopic imaging. *Theor. Chem. Acc.* **130**, 1249-1260 (2011).

Acknowledgments

The authors thank Lut Ooms and the greenhouse team at the University of Leuven (Division of Crop Biotechnics, Department of Biosystems), and Tamara Krügel and the greenhouse team at the Max Planck Institute for Chemical Ecology (Jena, Germany) for the help in raising *Musa* plants. D.H and B.S. wish to thank the German Research Council for financial support (Grant No. HO 4380/1 and SCHN 450/10). S.D. acknowledges the Interfaculty Council for Development Co-operation, University of Leuven (KU Leuven) for a PhD scholarship and a grant by COST action 872 for a short-term scientific mission to the MPI for Chemical Ecology. U.S. Schubert thanks the Dutch Polymer Institute (DPI, technology area HTE), Thüringer Ministerium für Bildung, Wissenschaft und Kultur (Grant No. B515-07008) and the Deutsche Forschungsgemeinschaft for financial support. The authors gratefully acknowledge Alexandra zum Felde for editorial help in the preparation of the manuscript.

Author Contributions

D.H., S.D., B.S., A.B., D.G.H., R.A.S. and R.S. developed the concept. S.D. inoculated nematodes and carried out the nematode bioassay. D.H., S.D., M.K. and R.M.K. isolated and identified the metabolites. D.H. and H.H. made the microscopic pre-examinations. K.K., S.D., D.H., H.H., A.C.C., U.S.S. performed the ultraflex®-examination of nematode lesions in roots. T.B., D.H., M.B., S.D. and C.H. examined and evaluated nematodes from the bioassay using the ultraflextreme®. T.A. statistically analysed the LDI MSI data. A.E., D.D.W. and R.S. all supervised S.D. Both C.K. and J.P supervised C.M., while both A.C.C. and U.S.S supervised K.K. A.S. supervised both M.K. and R.K.M., and C.H. supervised T.B. C.M. and D.H.

performed the Raman microspectroscopy, C.M., C.K. and J.P. carried out its data analysis.

All authors discussed the results and commented on the manuscript.

Competing financial interests

The authors declare no competing financial interests.

Additional information

Supplementary information is available online at http://www.nature.com/naturechemicalbiology/. Reprints and permissions information is available online at http://www.nature.com/reprints/index.html. Correspondence and requests for materials should be addressed to D.H.

TABLE AND FIGURE CAPTIONS

Table 1 | Masses of phenylphenalenones extracted from *Radopholus similis* induced legions on *Musa* spp. cv. Yangambi km5 (Ykm5) and Grande Naine (GN) roots and the calculation of their mass fractions using the necrosis factor. (**a**) Results for Ykm5 (270 g root material, necrosis factor: 20%) and (**b**) results for GN (253 g root material; necrosis factor: 80%).

Table 1 | (a) Results for Ykm5 (270 g root material, necrosis factor: 20%)

Compound (No.)	**Yield (mg)**	**Amount per kg root material**	**Amount per kg lesion material**
Anigorufone (**1**)	2.106	7.8	39.0
Hydroxyanigorufone (**2**)	0.486	1.8	9.0
(*2S,3R*)-2,3-Dihydro-2,3-dihydroxy-9-phenyl-phenalenone (**3**)	0.405	1.5	7.5
Isoanigorufone (**4**)	1.134	4.2	21.0
Irenolone (**5**)	0.729	2.7	13.5
4-Phenyl-1*H*,3*H*-benzo[*de*]isochromene-1,3-dione (**7**)	0.810	3.0	15.0
4-(4-Hydroxyphenyl-1*H*,3*H*-benzo[*de*]isochromene-1,3-dione (**8**)	0.270	1.0	5.0
Anigorootin (**9**)	0.135	0.5	2.5

Table 1 | (b) Results for GN (253 g root material, necrosis factor 80%)

Compound (No.)	**Yield (mg)**	**Amount per kg root material**	**Amount per kg lesion material**
Anigorufone (**1**)	0.987	3.9	4.9
Hydroxyanigorufone (**2**)	0.304	1.2	1.5
Irenolone (**5)**	0.127	0.5	0.6
Methylirenolone (**6**)	0.105	0.4	0.5
4-Phenyl-1*H*,3*H*-benzo[*de*]isochromene-1,3-dione (**7**)	0.100	0.4	0.5
4-(4-Hydroxyphenyl-1*H*,3*H*-benzo[*de*]isochromene-1,3-dione (**8**)	0.076	0.3	0.4

Table 2 | Percentage of immotile *Radopholus similis* in solutions of 11 selected phenylphenalenones at two concentrations (conc.) over three days (n = 3). All the presented means are significantly from the percentage immotile nematodes present in the control solution according to Kruskal-Wallis analysis. No significant difference was observed.

Compound (No.)	Concentration (ppm)	Immotile nematodes (%)		
		24 h	48 h	72 h
Anigorufone (**1**)	100 50	70.0 51.4	86.1 70.7	89.1 67.9
4-Hydroxy-2-methoxy-9-phenylphenalenone (**11**)	100 50	38.1 -	76.7 74.9	75.9 72.2
Isoanigorufone (**4**)	100 50	25.5 -	74.4 71.9	72.8 68.8
Hydroxyanigorufone (**2**)	100 50	47.7 22.3	67.6 55.4	68.7 69.3
4-(4-Hydroxyphenyl)-1*H*,3*H*-benzo[*de*]isochromene-1,3-dione (**8**)	100 50	26.6 -	66.1 54.7	66.3 65.2
Monohydroxyanigorootin (**13**)	100 50	35.9 23.7	59.4 57.8	51.2 54.3
Irenolone (**5**)	100 50	- -	55.4 -	- -
Anigorootin (**9**)	100 50	- -	- 51.3	- -
Methoxyanigorufone (**10**)	100 50	41.5 -	- -	- -
Perinaphthenone (**15**)	100 50	33.4 -	- -	- -
Musanolone C (**12**)	100 50	- -	31.9 -	26.1 -

-: No significant inhibitory effect was observed.

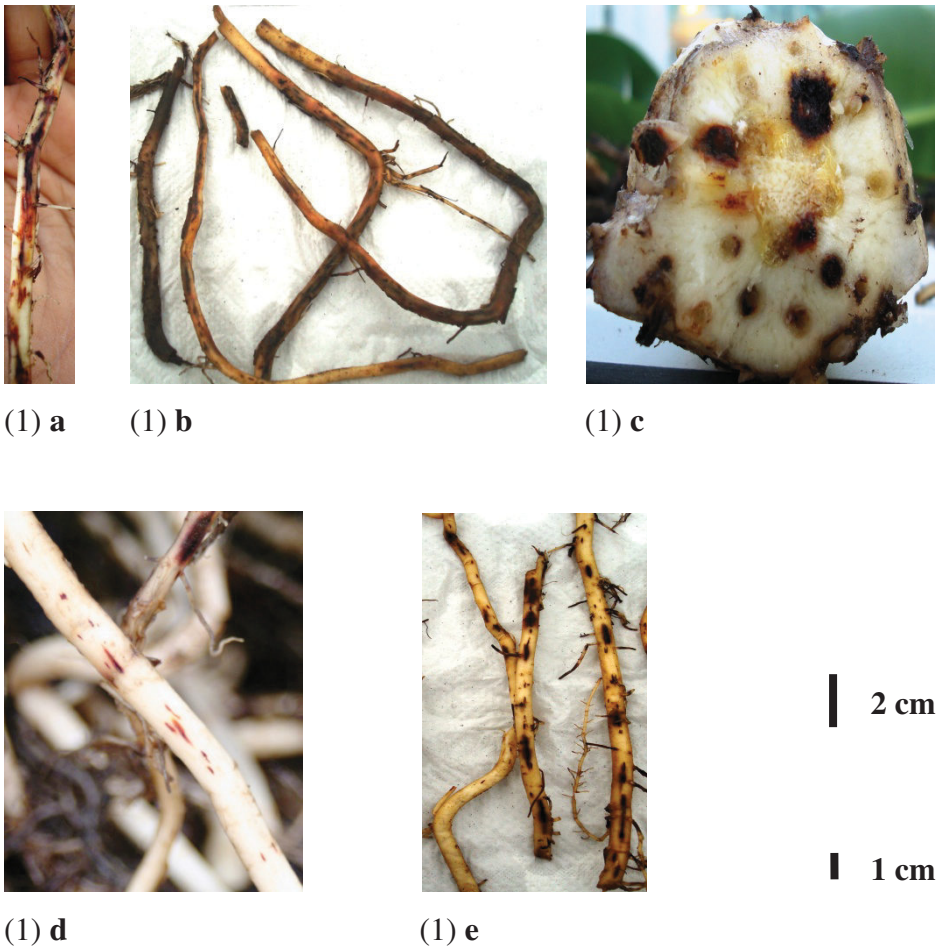

Figure 1 | Photographs of the root system of *Musa* spp. cv. Grande Naine (GN) and cv. Yangambi km5 (Ykm5) infected with *Radopholus similis*. **(a)** Young, developing, reddish brown lesions on GN roots. **(b)** Well developed, tunnel-like, dark brown, older lesions on GN roots. **(c)** Lesions on the root bases of the GN corm. **(d)** Young, developing, reddish brown lesions on Ykm5 roots. **(e)** Older, small, discontinuous, dark brown lesions on Ykm5 roots. [1 cm – 1a, 1b, 1c, 1e, 2 cm – 1d]

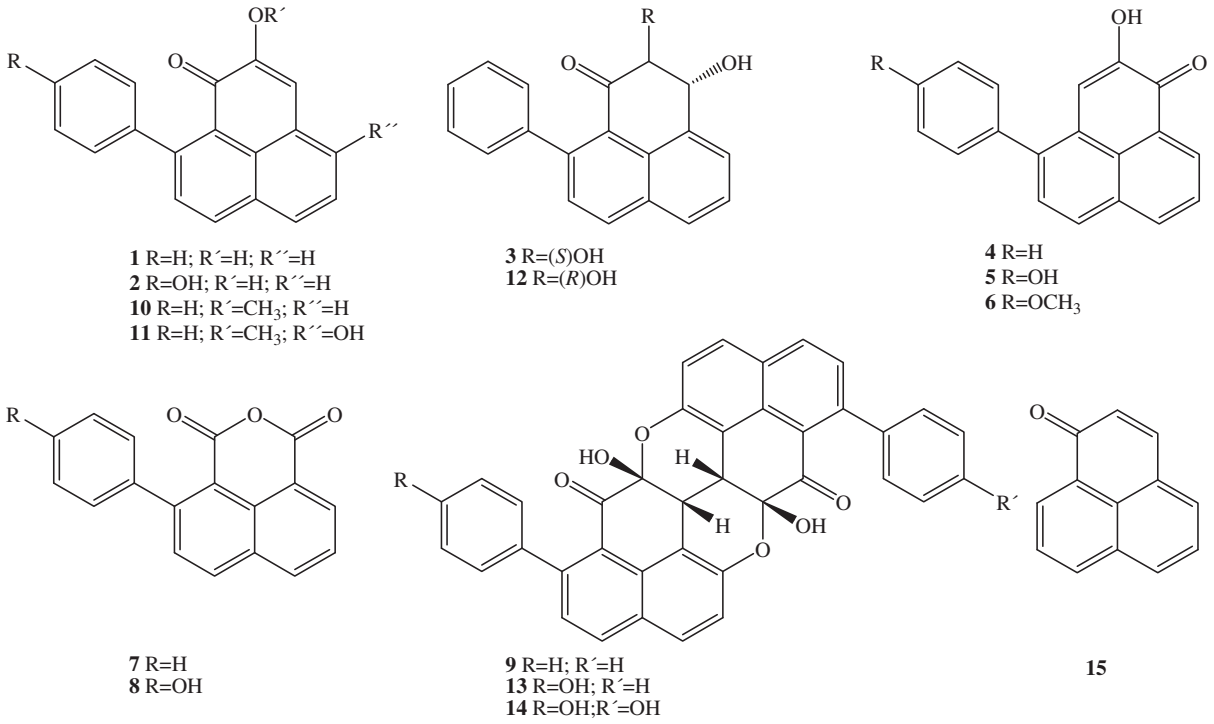

Figure 2 | Structures of all isolated phenylphenalenone type phytoalexins (1-9) and additional compounds tested in the *R. similis* motility bioassay (10-15). (**1**) anigorufone; (**2**) hydroxyanigorufone; (**3**) (2*S*,3*R*)-2,3-dihydro-2,3-dihydroxy-9-phenylphenalen-1-one; (**4**) isoanigorufone; (**5**) irenolone; (**6**) methylirenolone; (**7**) 4-phenyl-1*H*,3*H*-benzo[*de*]isochromene-1,3-dione; (**8**) 4-(4-hydroxyphenyl)-1*H*,3*H*-benzo[*de*]isochromene-1,3-dione; (**9**) anigorootin; (**10**) methoxyanigorufone; (**11**) 4-hydroxy-2-methoxy-9-phenalen-1-one; (**12**) musanolone C; (**13**) monohydroxyanigorootin; (**14**) dihydroxyanigorootin; (**15**) perinaphthenone.

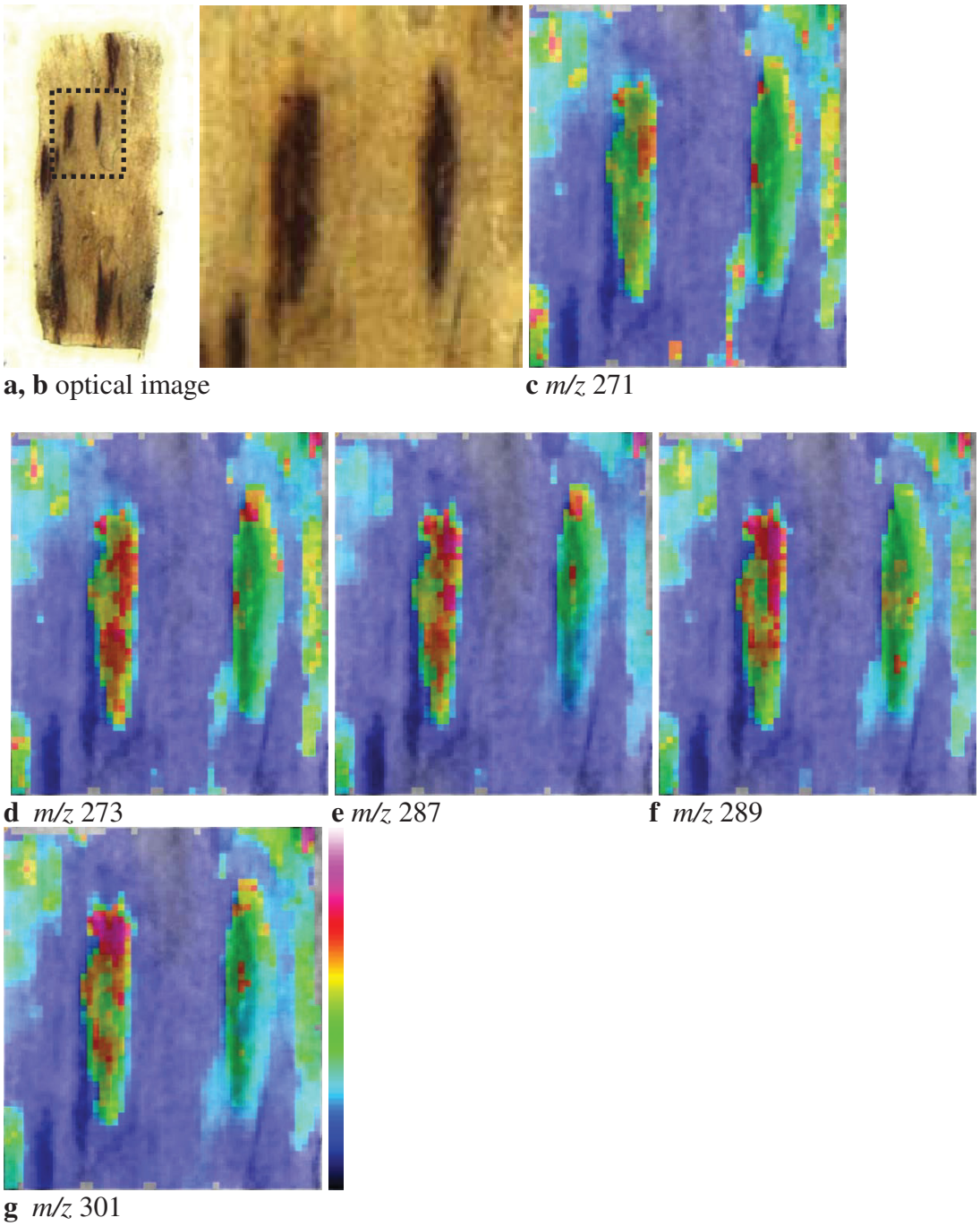

Figure 3 | Negative ion mode LDI-MSI of the lesions of Ykm5. (**a**) Optical image of the lesions on Ykm5 roots. (**b**) The region of the lesions subjected to LDI-MSI. The molecular image of section (**b**) for the *m/z* (**c**) 271 (**d**) 273 (**e**) 287 (**f**) 289 and (**g**) 301.

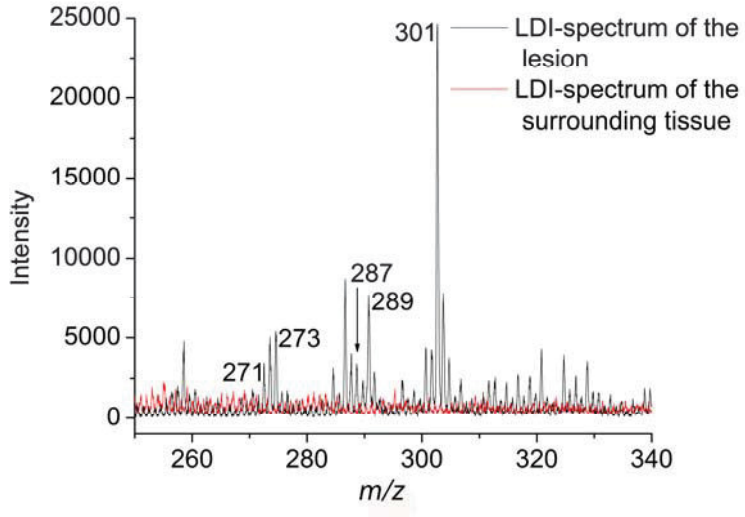

Figure 4 | A section of a LDI-TOF/MS negative ion mode spectrum (*m/z* 250-340) obtained from lesions of Ykm5.

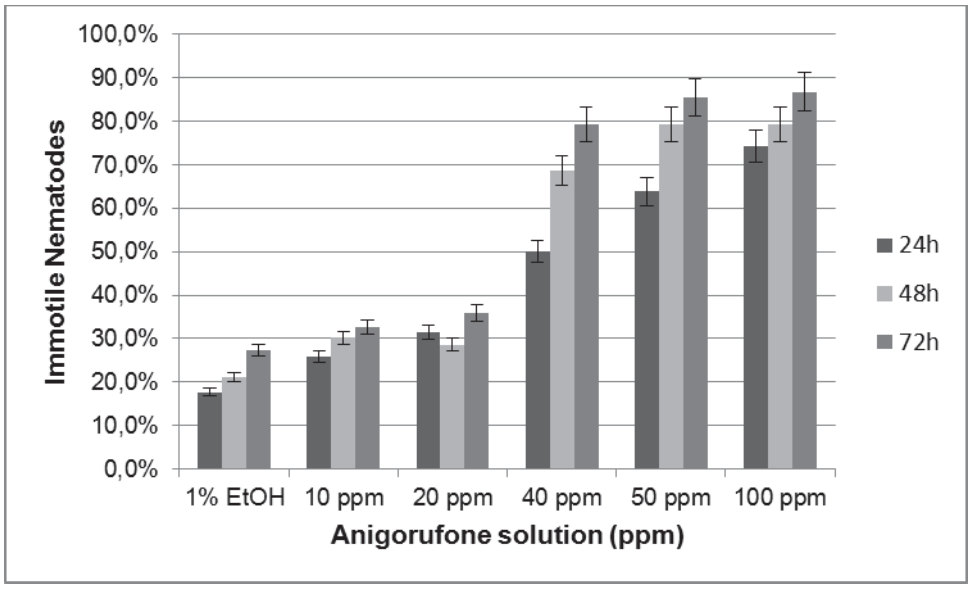

Figure 5 | *R. similis* nematode motility bioassay. Percentage of immotile nematodes *versus* the total number of nematodes exposed to anigorufone (**1**) solutions of different concentrations.

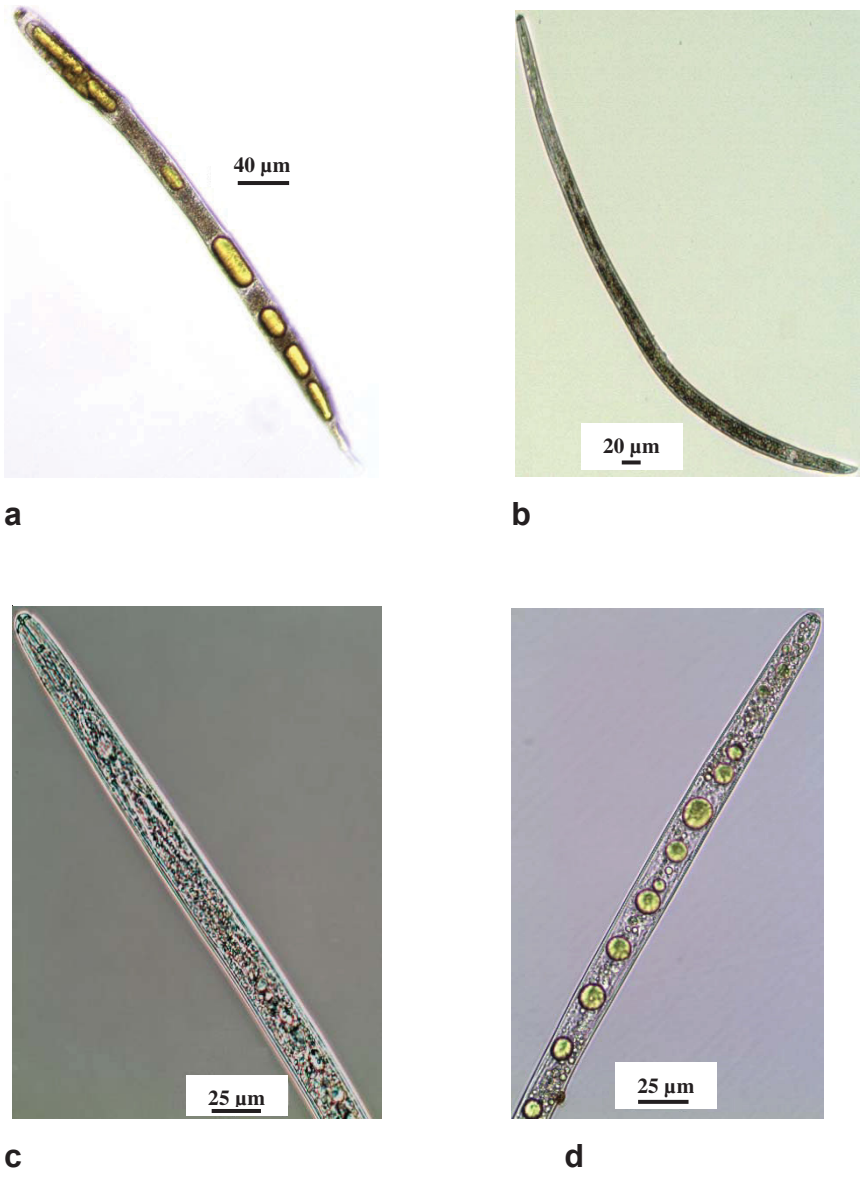

Figure 6 | Bright field microscopic images of *R. similis* from bioassay with anigorufone (1) (a and c) and from negative control, 1% ethanol (b and d). Nematodes were temporarily fixed for imaging purpose. (a) Dead *R. similis* from bioassay with anigorufone (**1**) – note yellow droplets in body. **(b)** Adult female *R. similis* after 72 h incubation in control. **(c)** Accumulation of anigorufone (**1**) in small oil droplets throughout the body of a juvenile *R. similis* nematode. **(d)** Anterior body of a *R. similis* showing normal digestive tract.

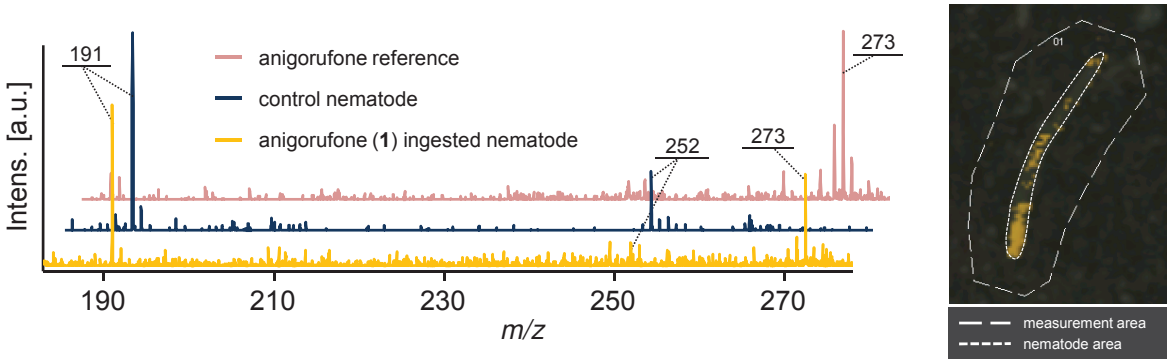

Figure 7 | Positive ion mode LDI-MSI of *R. similis* after motility bioassay with anigorufone (1). (**a**) Mass spectra in the range of *m/z* 185-285 from an imaging run of a nematode that had ingested anigorufone (**1**) and a control nematode in comparison to a mass spectrum of the anigorufone reference compound (**1**). (**b**) Image of a dried *R. similis* nematode before LDI-MSI overlaid with the image for the signal of *m/z* 273 $[M+H]^+$, representing anigorufone (**1**).

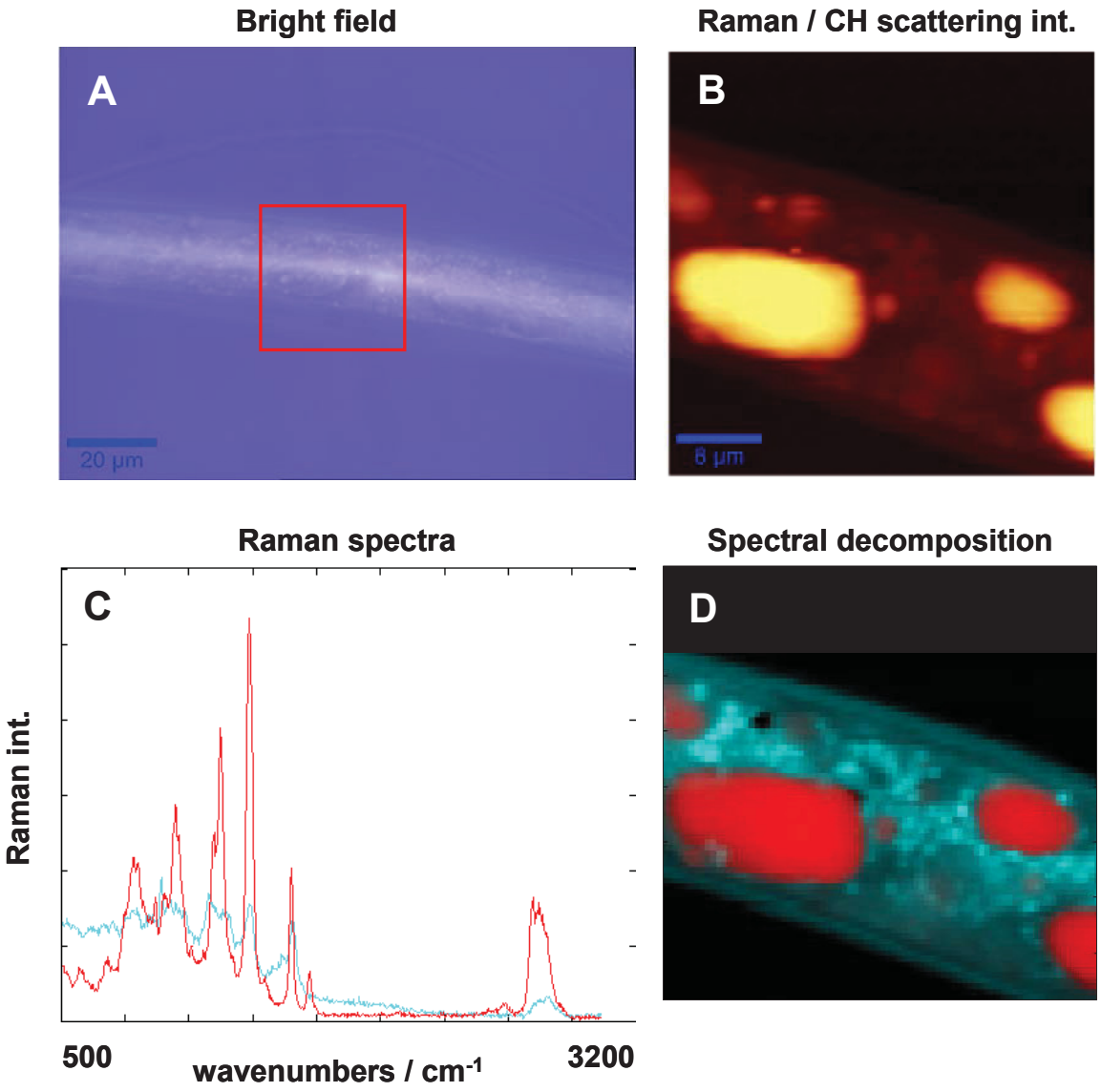

Figure 8 | Bright field picture of a nematode: (a) in comparison with a Raman image generated from the integrated Raman scattering intensities of C-H stretching vibrations **(b)**. The plotted associated spectral information **(c)** and an image **(d)** was generated by plotting the abundances of the spectra associated with lipids (red) *vs.* proteins (light blue).